Materials Horizons: From Nature to Nanomaterials

Kaviyarasu Kasinathan
Mohamed S. Elshikh
Dunia Abdul-Aziz Al Farraj *Editors*

# Nanomaterials for Energy Conversion, Biomedical and Environmental Applications

Springer

# Materials Horizons: From Nature to Nanomaterials

**Series Editor**

Vijay Kumar Thakur, School of Aerospace, Transport and Manufacturing, Cranfield University, Cranfield, UK

Materials are an indispensable part of human civilization since the inception of life on earth. With the passage of time, innumerable new materials have been explored as well as developed and the search for new innovative materials continues briskly. Keeping in mind the immense perspectives of various classes of materials, this series aims at providing a comprehensive collection of works across the breadth of materials research at cutting-edge interface of materials science with physics, chemistry, biology and engineering.

This series covers a galaxy of materials ranging from natural materials to nanomaterials. Some of the topics include but not limited to: biological materials, biomimetic materials, ceramics, composites, coatings, functional materials, glasses, inorganic materials, inorganic-organic hybrids, metals, membranes, magnetic materials, manufacturing of materials, nanomaterials, organic materials and pigments to name a few. The series provides most timely and comprehensive information on advanced synthesis, processing, characterization, manufacturing and applications in a broad range of interdisciplinary fields in science, engineering and technology.

This series accepts both authored and edited works, including textbooks, monographs, reference works, and professional books. The books in this series will provide a deep insight into the state-of-art of Materials Horizons and serve students, academic, government and industrial scientists involved in all aspects of materials research.

**Review Process**

The proposal for each volume is reviewed by the following:

1. Responsible (in-house) editor
2. One external subject expert
3. One of the editorial board members.

The chapters in each volume are individually reviewed single blind by expert reviewers and the volume editor.

Kaviyarasu Kasinathan · Mohamed S. Elshikh ·
Dunia Abdul-Aziz Al Farraj
Editors

# Nanomaterials for Energy Conversion, Biomedical and Environmental Applications

Springer

*Editors*
Kaviyarasu Kasinathan
Materials Research Group
iThemba LABS-National Research Foundation
Faure, Cape Town, South Africa

Mohamed S. Elshikh
Department of Botany and Microbiology, College of Sciences
King Saud University
Riyadh, Saudi Arabia

Dunia Abdul-Aziz Al Farraj
Department of Botany and Microbiology, College of Sciences
King Saud University
Riyadh, Saudi Arabia

ISSN 2524-5384 ISSN 2524-5392 (electronic)
Materials Horizons: From Nature to Nanomaterials
ISBN 978-981-19-2638-9 ISBN 978-981-19-2639-6 (eBook)
https://doi.org/10.1007/978-981-19-2639-6



This Springer imprint is published by the registered company Springer Nature Singapore Pte Ltd.
The registered company address is: 152 Beach Road, #21-01/04 Gateway East, Singapore 189721, Singapore

# Preface

At present, most people get exposed to information about health care sector, climate change and environmental management only through stories publicized in the media. One of the clean energy sources with zero carbon emissions is hydrogen. It is expected that soon hydrogen will take one of the main places among energy sources. In some instances, responses demonstrated a lack of knowledge about basic materials science that may have significant implications for public education measures in materials design, cost-benefit likely processing, and analysis in industrial manufacturing.

In this book, entitled *Nanomaterials for Energy Conversion, Biomedical and Environmental Applications*, there are eighteen chapters. We have finalized the following chapters: I mean ordering the chapters. We have two subsections (Part I) Nanomaterials for Energy Conversion & (Part II) is Biomedical and Environmental Applications. The first part includes eight chapters discussing photoelectrochemical water splitting to produce fuel, storage, and conversion of energy using sunlight. Insight, we discussed about optical transport, nanocomposites, phosphate glass bioactive, perovskite nanomaterials, MgSn alloys and metal additive manufacturing via post-processing heat treatments too. Applied biomedicine and environmental science is the focus of the second part. Nine chapters have been indexed in this section that were found relevant to biomedical applications such as tissue engineering, drug delivery, nanodiagnostics, polymeric chain mechanisms of chitosan and cellulose as well as metal oxide nanoparticles for antimicrobial applications. We make ensure this book *Nanomaterials for Energy Conversion, Biomedical and Environmental Applications* is succinctly formulated, captures the focus, contains moral ambiguities, and grabs the reader's interest. We believe in this book reaching large research and development audience in the frame of energy storage revisited for new methods. To increase readers, identifying all appropriate topics within this series is important.

In this book *Nanomaterials for Energy Conversion, Biomedical and Environmental Applications*, Undoubtedly, the main objective of the proposed book has addressed several issues, and in the future, this book will become a good platform for understanding the future developments in metal oxide nanostructures for energy conversion, biomedical and environmental management. A bioinspired material for environmental applications may support or act as a carrier for antibacterial behavior,

pathogenic infections, and antimicrobial behavior. Appropriately, *Nanomaterials for Energy Conversion, Biomedical and Environmental Applications*, we recommend the book to undergraduates, postgraduates, and doctoral students those who are working in material science and researchers across the world working in interdisciplinary research. Thus, major concerns have been raised about materials synthesis and energy harvesting following the efficient and selective mechanisms of biology.

Cape Town, South Africa — Kaviyarasu Kasinathan
Riyadh, Saudi Arabia — Mohamed S. Elshikh
Riyadh, Saudi Arabia — Dunia Abdul-Aziz Al Farraj

# Contents

# Contributors

**Ali Amjad** Department of Physics, University of Okara, Okara, Pakistan

**Alikhanov N. M. R.** Dagestan State University, Makhachkala, Russia;
Amirkhanov Institute of Physics of Dagestan Federal Research Center, Russian Academy of Sciences, Makhachkala, Russia

**Aravindan S.** PG and Research Department of Physics, Government Arts College (Autonomous), Salem, Tamil Nadu, India

**Asim Jamil** University of Okara, Okara, Pakistan;
Faculty of Computer Science and Information Technology, Universiti Malaysia Sarawak, Kota Samarahan, Malaysia

**Ayeshamariam A.** Department of Physics, Khadir Mohideen College (Affiliated to Bharathidasan University, Thiruchirappalli), Adirampattinam, Tamil Nadu, India

**Babujanarthanam Ranganathan** Nano and Energy Bioscience Laboratory, Department of Biotechnology, Thiruvalluvar University, Vellore, Tamil Nadu, India

**Balaji P.** PG and Research Centre in Biotechnology, MGR College, Hosur, Tamil Nadu, India

**Basha S. Khaleel** Department of Chemistry, C. Abdul Hakeem College, Melvisharam, Tamil Nadu, India

**Bavani Thirungnanam** Solar Energy Lab, Department of Chemistry, Thiruvalluvar University, Vellore, Tamil Nadu, India

**Beer Mohamed S.** Department of Material Science, Central University of Tamil Nadu, Thiruvarur, Tamil Nadu, India

**Dallaev R. S.** Department of Physics, Faculty of Electrical Engineering and Communication, Brno University of Technology, Brno, Czech Republic

**Danielwillson A.** Department of Materials Science, Central University of Tamil Nadu, Tamil Nadu, Thiruvarur, India

**Eyini M.** PG and Centre for Research in Botany, Thiagarajar College, Madurai, Tamil Nadu, India

**Fathima Mubashira G. T.** Department of Physics, Sacred Heart College (Autonomous), Tirupattur, Tamil Nadu, India

**Girisan Elliangal Kunhappa** Department of Computer Applications, Sree Narayana Guru College, Coimbatore, Tamil Nadu, India

**Gopalakrishnan Velliyur Kanniappan** School of Medicine, Bule Hora University Institute of Health, Bule Hora University, Bule Hora, Ethiopia

**Guru Kumar Dugganaboyana** Division of Biochemistry, School of Life Sciences, JSS Academy of Higher Education and Research, Mysuru, Karnataka, India

**Honey Shehla** Department of Physics, University of Okara, Okara, Pakistan;
Centre for Nanosciences, University of Okara, Okara, Pakistan;
NPU-NCP Joint International Research Center on Advanced Nanomaterials and Defects Engineering, Northwestern Polytechnical University, Xi'an, China;
College of Graduate Studies, UNESCO-UNISA Africa Chair in Nanosciences/Nanotechnology, University of South Africa, Pretoria, South Africa;
Nanosciences African Network (NANOAFNET), iThemba LABS, National Research Foundation, Somerset West, South Africa

**Isaev A. B.** Department of Inorganic Chemistry and Chemical Ecology, Dagestan State University, Makhachkala, Dagestan Republic, Russia

**Ismail Fathima M.** Department of Physics, Mangayarkarasi College of Arts and Science College for Women, Madurai, Tamil Nadu, India

**Ismailov A. M.** Department of Inorganic Chemistry and Chemical Ecology, Dagestan State University, Makhachkala, Dagestan Republic, Russia

**Jayachandran M.** Department of Physics, Sethu Institute of Technology, Pulloor, Kariyapatti, Tamil Nadu, India

**Jayaganthan R.** Department of Engineering Design, Indian Institute of Technology Madras, Tamil Nadu, Chennai, India

**Kamran Muhammad Arshad** Department of Physics, University of Okara, Okara, Pakistan

**Kanimozhi K.** Department of Chemistry, Global Institute of Engineering and Technology, Melvisharam, Tamil Nadu, India;
PG Research & Department of Chemistry, Auxilium College (Autonomous), Vellore, Tamil Nadu, India

**Kannan Karthikeyan** Gujarat Institute of Desert Ecology, Gujarat, Bhuj, India

**Kasinathan Kaviyarasu** College of Graduate Studies, UNESCO-UNISA Africa Chair in Nanosciences/Nanotechnology, University of South Africa, Pretoria, South Africa;

Nanosciences African Network (NANOAFNET), iThemba LABS, National Research Foundation, Somerset West, South Africa

**Kaviarasu C.** Department of Mechanical Engineering, Arasu Engineering College, Tamil Nadu, Kumbakonam, India

**Kaviyarasu K.** UNESCO-UNISA Africa Chair in Nanosciences/Nanotechnology Laboratories, College of Graduate Studies, University of South Africa (UNISA), Pretoria, South Africa;
Nanosciences African Network (NANOAFNET), Materials Research Group (MRG), iThemba LABS-National Research Foundation (NRF), Somerset West, Western Cape Province, South Africa

**Kumar M.** Department of Plant Biology and Plant Biotechnology, Madras Christian College (Autonomous), Tambaram, Tamil Nadu, India

**Kumari V. Sugantha** PG Research & Department of Chemistry, Auxilium College (Autonomous), Vellore, Tamil Nadu, India

**Kuppanan Nanthakumar** The Energy and Resources Institute (TERI), New Delhi, India

**Maaza M.** College of Graduate Studies, UNESCO-UNISA Africa Chair in Nanosciences/Nanotechnology, University of South Africa, Pretoria, South Africa;
Nanosciences African Network (NANOAFNET), iThemba LABS, National Research Foundation, Somerset West, South Africa

**Madhavan Jagannathan** Solar Energy Lab, Department of Chemistry, Thiruvalluvar University, Vellore, Tamil Nadu, India

**Mazhar Muhammad Ehsan** Department of Physics, Bahuaddin Zakariya University, Multan, Pakistan

**Meenakshi Periasamy** Department of Biochemistry, Tamil Nadu Agricultural University, Coimbatore, Tamil Nadu, India

**Munusamy Ayyasamy Pudukkadu** Department of Microbiology, Periyar University, Salem, India

**Muthukumaran Azhaguchamy** Department of Biotechnology, Kalasalingam Academy of Research and Education, Krishnankoil, Tamilnadu, India

**Naveenkumar Suresh** Department of Biotechnology, Kalasalingam Academy of Research and Education, Krishnankoil, Tamilnadu, India

**Nishara Begum A.** PG and Research Department of Physics, Chikkaiah Naicker College, Erode, Tamil Nadu, India

**Omarov G. M.** Department of Inorganic Chemistry and Chemical Ecology, Dagestan State University, Makhachkala, Dagestan Republic, Russia

**Orudzhev F. F.** Dagestan State University, Makhachkala, Russia;
Amirkhanov Institute of Physics of Dagestan Federal Research Center, Russian Academy of Sciences, Makhachkala, Russia

**Parasaran M.** Department of Physics, Sacred Heart College (Autonomous), Tirupattur, Tamil Nadu, India

**Pothiraj C.** Department of Botany, Government Arts College, Melur, Tamil Nadu, India

**Ramazanov Sh. M.** Amirkhanov Institute of Physics of Dagestan Federal Research Center, Russian Academy of Sciences, Makhachkala, Russia

**Ramesh R.** Department of Physics, Sacred Heart College (Autonomous), Tirupattur, Tamil Nadu, India;
Department of Physics, Islamiah College (Autonomous), Vaniyambadi, Tamil Nadu, India

**Rasool Atif** Department of Physics, University of Okara, Okara, Pakistan

**Rathi Muthaiyan Ahalliya** Department of Biochemistry, FASCM and Karpagam Cancer Research Center, Karpagam Academy of Higher Education, Coimbatore, Tamil Nadu, India

**Sackey J.** Nanosciences African Network (NANOAFNET), iThemba LABS-National Research Foundation, Somerset West, South Africa;
UNESCO-UNISA Africa Chair in Nanosciences/Nanotechnology, College of Graduate Studies, University of South Africa (UNISA), Pretoria, South Africa

**Sathiyaraj Sivaji** Nano and Energy Bioscience Laboratory, Department of Biotechnology, Thiruvalluvar University, Vellore, Tamil Nadu, India

**Selvaraj Selvajeyanthi** Department of Microbiology, Shri Nehru Maha Vidyalaya College of Arts and Science, Coimbatore, India

**Shabanov N. S.** Department of Inorganic Chemistry and Chemical Ecology, Dagestan State University, Makhachkala, Dagestan Republic, Russia;
Dagestan Federal Research Centre of the Russian Academy of Sciences, Analytical Center for Collective Use, Makhachkala, Russia

**Sivabharathy M.** Department of Physics, Sethu Institute of Technology, Pulloor, Kariyapatti, Tamil Nadu, India

**Sivaranajani S.** Department of Physics, St. Antony's College of Arts and Sciences for Women, Dindigul, Tamil Nadu, India

**Sobola D.** Dagestan State University, Makhachkala, Russia;
Department of Physics, Faculty of Electrical Engineering and Communication, Brno University of Technology, Brno, Czech Republic;
Department of Inorganic Chemistry and Chemical Ecology, Dagestan State University, Makhachkala, Dagestan Republic, Russia;

Department of Physics, Faculty of Electrical Engineering and Communication, Laboratory of Environmental Science and Technology, Brno University of Technology, Brno, Czech Republic;
Central European Institute of Technology BUT, Brno, Czech Republic

**Suriyakala Gunasekaran** Nano and Energy Bioscience Laboratory, Department of Biotechnology, Thiruvalluvar University, Vellore, Tamil Nadu, India

**Uthrakumar R.** PG and Research Department of Physics, Government Arts College (Autonomous), Salem, Tamil Nadu, India

**Valan Arasu Mariadhas** Department of Botany and Microbiology, College of Science, King Saud University, Riyadh, Saudi Arabia

**Velmurugan C.** Department of Mechanical Engineering, Indian Institute of Information Technology, Tamil Nadu, Tiruchirappalli, India

**Venkateshan Narayanan** Department of Pharmaceutical Chemistry, Arulmigu Kalasalingam College of Pharmacy, Krishnankoil, Tamil Nadu, India

**Vijaya Chitra Arumugam** Department of Microbiology, Sri Ramakrishna College of Arts and Science for Women, Coimbatore, India

# Abbreviations

| | |
|---|---|
| ACM | Alcoholic cardiomyopathy |
| AFM | Atomic force microscopy |
| AgNPs | Silver nanoparticles |
| AIDS | Acquired immunodeficiency syndrome |
| ALD | Atomic layer deposition |
| AOP | Advanced Oxidation Process |
| APP | Amyloid precursor protein |
| ATR-FTIR | Attenuated total reflection-Fourier transform infrared spectroscopy |
| BET | Brunauer–Emmett–Teller |
| BiOX | Bismuth oxyhalides |
| CB | Conduction band |
| CMC | Ceramic Matrix Composite |
| CNTs | Carbon Nanotubes |
| Cu NWs | Copper nanowires |
| D/F P | Dew/Frost Point |
| DC | Direct current |
| DMEM | Dulbecco's modified Eagle medium |
| DMRP | Diagnostic magnetic resonance platform |
| DNA | Deoxyribonucleic acid |
| DRS | Diffuse reflectance spectroscopy |
| DTA | Differential Thermal Analysis |
| E.Coli | Escherichia Coli |
| EDS | Energy dispersive spectrometry |
| EDX | Energy dispersive X-ray spectroscopy |
| ELISA | Enzyme-linked immunosorbent assay |
| ESCA | Electron spectroscopy for chemical analysis |
| FESEM | Field emission scanning electron microscopy |
| FTIR | Fourier transform infrared spectroscopy |
| FWHM | Full width half maximum |
| G-Negative | Gram negative bacteria |
| G-Positive | Gram positive bacteria |

| | |
|---|---|
| $H_M$ | Microhardness |
| ITO's | Indium tin oxides |
| JCPDS | Joint committee for powder diffraction studies |
| LEDs | Light emitting diodes |
| MAC | Mycobacterium avium complex |
| MBAS | Magnetic barcode assay system |
| MFM | Magnetic force microscopy |
| MG | Malachite green |
| M-H | Magnetic hysteresis loops |
| MMC | Metal Matrix Composite |
| MNWs | Metallic nanowires |
| MO | Methyl orange |
| MRI | Magnetic resonance imaging |
| m-RNA | Messenger ribonucleic acid |
| NEMO | Nano-based capsule-endoscopy with molecular imaging and optical biopsy |
| NPs | Nanoparticles |
| NSI | Natural sunlight irradiation |
| OFNASET | Oral Fluid NanoSensor Test |
| $P_2O_5$ | Phosphorous pentoxide |
| PBS | Phosphate Buffer Saline |
| PCR | Polymerase Chain Reaction |
| PFM | Piezoelectric response |
| PG | Panchagavya |
| PLD | Pulse laser deposition |
| PMC | Polymer Matrix Composite |
| PPM | Parts Per Million |
| PPMv | Parts Per Million by Volume fraction |
| PPMw | Parts Per Million by Molecular weight |
| PVP | Poly(vinyl alcohol) |
| RH | Relative Humidity |
| RhB | Rhodamine B |
| RIA | Radioimmunoassay |
| ROS | Reactive oxygen species |
| S.aureus | Staphylococcus aureus |
| SAED | Selected area electron diffraction |
| SAp | Sodium alginate polymers |
| SBF | Stimulated body fluid |
| SEM | Scanning electron microscopy |
| SIMS | Secondary-ion mass spectrometry |
| SPM | Scanning probe microscopy |
| TCEs | Transparent Conducting Electrodes |
| TE | Tissue engineering |
| TEM | Transmission electron microscopy |
| TPP | Thiamine pyrophosphate |

| | |
|---|---|
| t-RNA | Transfer ribonucleic acid |
| UV-vis | Ultraviolet-visible |
| VB | Valence band |
| VLA | Visible light active |
| VLI | Visible light irradiation |
| XPS | X-ray photoelectron spectroscopy |
| XRD | X-ray diffraction |
| ZnSe | Zinc selenide |

# Symbols and Explanations

| | |
|---|---|
| % | percentage |
| ($^{\bullet}OH$) | hydroxyl |
| ($O_2^{\bullet-}$) | superoxide radicals |
| μm | micrometer |
| $E_g$ | bandgap energy |
| Hc | Coercivity |
| hν | light quantum |
| mg | milligram |
| mL | milliliter |
| mM | milli Molar |
| Mr | retentivity |
| Ms | saturation magnetization |
| nm | nanometer |
| λ | wavelength of light |

# Part I
# Nanomaterials for Energy Conversion

# Chapter 1
# ZnO/Chalcogenides Semiconductor Heterostructures for Photoelectrochemical Water Splitting


**A. B. Isaev, N. S. Shabanov, D. Sobola, K. Kaviyarasu, A. M. Ismailov, and G. M. Omarov**

## 1 Introduction

With the depletion of hydrocarbon energy sources, the production of environmentally friendly and renewable fuels is becoming more and more important. One of the clean energy sources with zero carbon emissions is hydrogen. It is expected that soon hydrogen will take one of the main places among energy sources. The way to obtain hydrogen is through the water splitting. Various methods are currently used for water splitting. Among them, one can single out the electrochemical water splitting [1–3], photocatalytic [4–8], and photoelectrochemical water splitting [9–11] using

A. B. Isaev (✉) · N. S. Shabanov · D. Sobola · A. M. Ismailov · G. M. Omarov
Department of Inorganic Chemistry and Chemical Ecology, Dagestan State University, St. M. Gadjieva 43-a, Makhachkala, Dagestan Republic 367000, Russia
e-mail: abdul-77@yandex.ru

N. S. Shabanov
Dagestan Federal Research Centre of the Russian Academy of Sciences, Analytical Center for Collective Use, Gadzhiyev str. 45, 367000 Makhachkala, Russia

D. Sobola
Department of Physics, Faculty of Electrical Engineering and Communication, Laboratory of Environmental Science and Technology, Brno University of Technology, Technická 2848/8, Brno 61600, Czech Republic

Central European Institute of Technology BUT, Purkyňova 123, Brno 61200, Czech Republic

K. Kaviyarasu
College of Graduate Studies, UNESCO-UNISA Africa Chair in Nanoscience's/Nanotechnology Laboratories, University of South Africa (UNISA), Muckleneuk Ridge, P.O. Box 392, Pretoria, South Africa

Nanosciences African Network (NANOAFNET), Materials Research Group (MRG), iThemba LABS-National Research Foundation (NRF), 1 Old Faure RoadWestern Cape Province, P.O. Box 722, Somerset West 7129, South Africa



K. Kasinathan et al. (eds.), *Nanomaterials for Energy Conversion, Biomedical and Environmental Applications*, Materials Horizons: From Nature to Nanomaterials,
https://doi.org/10.1007/978-981-19-2639-6_1

light energy. For hydrogen production, considerable attention was drawn to the water splitting by solar energy and semiconductors [12–16]. Photoelectrochemical splitting of water is one of the most suitable methods to converting sunlight into hydrogen because of its practicality and efficiency. The photoelectrochemical splitting of water and the production of hydrogen in large volumes require cheap, efficient, and stable semiconductor photoelectrodes in a photoelectrochemical cell. The materials used in a device for photoelectrochemical production of hydrogen must be cheap, photoactive, provide chemical and stability, and have a sufficient efficiency of converting solar energy into photoelectrochemical hydrogen. Until now, a lot of types of semiconductor materials have been investigated, including composites and nanostructures [17, 18]. But unfortunately, these materials do not have the necessary efficiency of energy conversion. High-energy conversion efficiency is typical for materials operating in the ultraviolet region of the spectrum. However, there is not enough ultraviolet in the solar spectrum for water splitting in industrial scale [19]. Among the most studied materials about photoelectrochemical splitting of water, zinc oxide got an important place [20–28]. Zinc oxide (ZnO) belongs to an n-type semiconductor material with anisotropic crystal structure. It has low cost, wide distribution in the earth, non-toxicity, ease synthesis, high thermal stability, wide bandgap, etc. [21]. The development of semiconductor materials with a small bandgap, high photoelectrochemical activity, and stability based on ZnO are of particular interest for creating a competitive technology for photoelectrochemical water splitting [26, 27, 29, 30].

This review is mainly devoted to efficient photocatalysts based on ZnO and chalcogenides for photoelectrochemical water splitting. Because of its properties of increasing the efficiency of photoelectrochemical water splitting under sunlight irradiation, sensitization of ZnO by chalcogenides has attracted wide research interest [22]. In this review, we mainly focus on strategies of synthesis and control of properties (morphology, bandgap structure), photocatalytic and photoelectrochemical water splitting using ZnO/chalcogenide heterostructures. The combination of ZnO materials with chalcogenides to obtain heterostructures is a promising approach for obtaining a highly efficient composite photocatalyst, since chalcogenides are materials that have a bandgap greater than 1.23 V (the water splitting potential) [20].

## 2 The General Principles of Photoelectrochemical Water Splitting

The photoelectrochemical splitting of water using $TiO_2$ as a photocatalyst was earlier noted by Fujishima and Honda [31]. A minimum bandgap of 1.23 eV is required for the photocatalytic water splitting. This value corresponds with the redox potentials of the $H^+/H_2$ and $O_2/H_2O$ pairs [32]. To ensure the electron transfer process and the subsequent stages of hydrogen evolution, a large bandgap (>2.0 eV) is often required. Simultaneously, the photocatalyst must have a sufficiently small bandgap (e.g., <3.0 eV) for efficient use of solar spectrum [33]. Compared to the photocatalytic

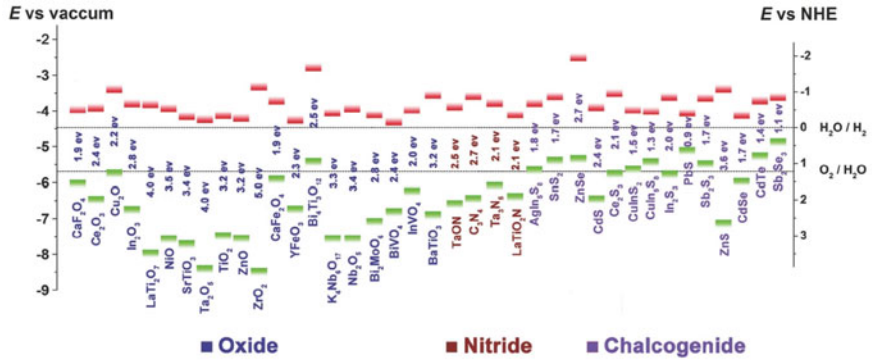


**Fig. 1** Bandgaps and bandedge values with respect to the vacuum level and normal hydrogen electrode [32]

water splitting by powder photocatalyst, photoelectrochemical splitting promotes the separation of electrons and holes [34]. There are few semiconductor materials that meet these criteria. The authors of [32] classified semiconductor materials according to their bandgaps, which can be used in water splitting reactions to hydrogen production as photocatalysts or cocatalysts, including chalcogenides, oxides, and nitrides (Fig. 1). The oxygen is released when *n*-type material is used as a photoanode, and electron vacancies are generated on it during irradiation by sunlight (Eq. 1). The generated electrons then move to the photocathode where the reaction of hydrogen evolution occurs (Eq. 2).

$$2H_2O + 4h^+ \rightarrow O_2 + 4H^+, \quad E^0_{(O_2/H_2O)} = 1.23\,\text{V vs. RHE} \tag{1}$$

$$2H^+ + 2e^- H_2, \quad E^0_{(H^+/H_2)} = 0\,\text{V vs. RHE} \tag{2}$$

The oxygen evolution reaction has thermodynamic limitations, the minimum of the conduction band for the semiconductor is supposed to have more negative in comparison to the energy level $H^+/H_2$, while the maximum of the valence band should have more positive value than the energy level $O_2/H_2O$ [33]. ZnO is an *n*-type wide bandgap semiconductor (≈3.3 eV) at room temperature. It is of great interest for photoelectrochemical hydrogen production [34]. But the large bandgap and fast recombination of photogenerated carriers are the reason of low light absorption and decrease of photocatalytic quantum yield, prevent using ZnO as a photocatalyst [35–38]. The preparation of ZnO nanostructures can reduce the diffusion path of charge carriers with increasing of the reaction surface area [39–41]. However, this is insufficient to enhance the photocatalytic activity of wide bandgap ZnO in visible light. For this, numerous approaches were used, such as regulation of the parameters of surface morphology and using graphene derivatives as acceptors [42–44] doping of various metals into the crystal lattice structure [45, 46] and obtaining heterostructures [47–49]. The construction of a ZnO heterojunction with narrow bandgap semiconductors

is a favorable method to increase absorption of light and boost light utilization [50]. Basically, ZnO-based heterostructures contain type II electron hole transition forms (Fig. 2a), p–n junction (Fig. 2b), Z-based systems (Fig. 2c), and hot-electron injection (Fig. 2d).

A lot of efforts have been devoted to research on the optical properties, and the morphology of heterostructures based on ZnO and chalcogenides for their use in various photoconverters [52]. Metal chalcogenides materials have a narrower bandgap in comparison with ZnO. Therefore, transferring photogenerated electrons from the conduction band of chalcogenides to the ZnO conduction band is possible (Table 1). This leads to a more efficient separation of photogenerated charge carriers. Currently, the main task for photoelectrochemical splitting of water is the preparation of photoanodes, that have high charge transfer and light-collecting efficiency. In this regard, much attention is paid to the preparation of ZnO in the form of various nanostructures. Primarily, special attention is given to the preparation of ZnO in the nanorods form. ZnO nanorods obtained by the hydrothermal method can be utilized as photoanodes in photoelectrochemical water splitting. These highly ordered ZnO nanorod arrays exhibit increased light-harvesting efficiency originated from light scattering [63].

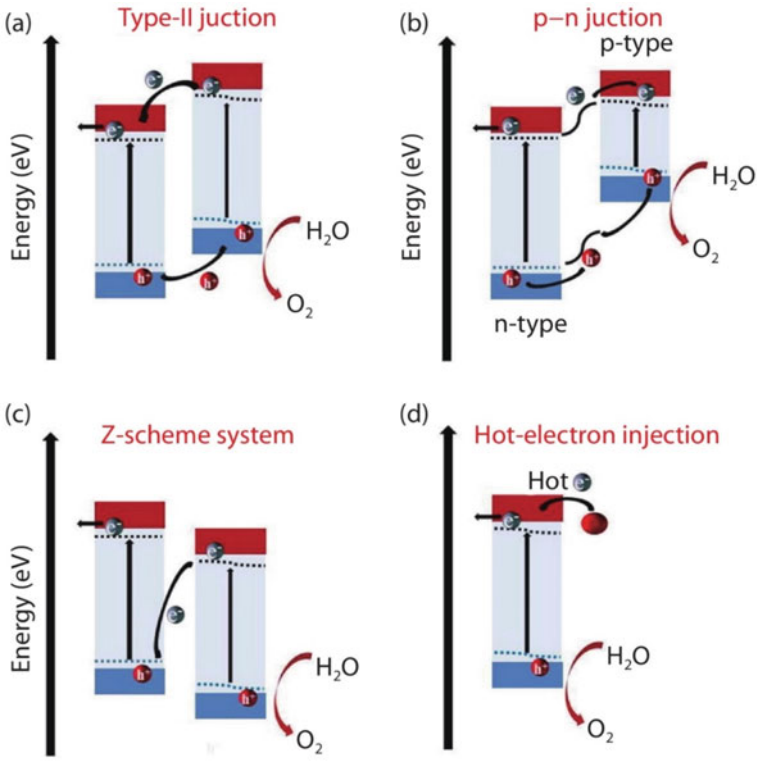


**Fig. 2** Design scheme of **a** type-II junction, **b** p–n junction, **c** Z-scheme system, and **d** hot-electron injection [34, 51]

**Table 1** The bandgap of chalcogenides and zinc oxide relative to hydrogen reference electrode

| Materials | Bandgap, eV | References |
|---|---|---|
| ZnO | 3.2 | Ma et al. [34] |
| ZnS | 3.6–3.7 | Kurnia and Hart [53], D'Amico [54], Schrier et al. [55], Jiang et al. [56] |
| ZnSe | 2.84 | Ye et al. [57] |
| ZnTe | 2.1 | Zaari et al. [58] |
| CdS | 2.5 | Wei et al. [59] |
| CdSe | 1.76 | Wei et al. [59] |
| CdTe | 1.61 | Wei et al. [59] |
| PbS | 1.31 | Yeon et al. [60] |
| $MoS_2$ | 1.48 | Miller et al. [61] |
| CuS | 3.10–3.94 | Dolui et al. [62] |

## 3 ZnO/ZnS Heterostructures

ZnS is a semiconductor material with a bandgap of 3.7 eV and a conduction band of 1.04 eV [56, 64]. This value is more negative than the reduction potential of $H^+$ to $H_2$. Studies of ZnS as a photocatalyst for water splitting have shown its certain activity. In this case, it is proposed to increase the activity of ZnS with the use of additives of noble metals Pt and Au [65, 66]. The use of a ZnS heterostructure with ZnO accelerates the photogenerated $e^-/h^+$ separation. ZnO has a more positive position in the conduction band (–0.31 eV) and the valence band (2.89 eV) in comparison with ZnS. It provides a better separation of charge carriers [66]. ZnO and ZnS heterostructures show a high efficiency of hydrogen evolution during water splitting [67, 68]. It is assumed that the ZnO/ZnS heterostructure may be more promising for the photoelectrochemical production of hydrogen due to the ease of formation of a heterojunction during direct ion exchange or thermal diffusion [69], as well as easy charge transfer inside the electrodes of the heterostructure [70].

In this case, the bands are aligned, which causes improved separation of electrons and holes and the generation of a higher photocurrent and greater oxidative capacity in relation to water splitting (Fig. 3). Under the action of irradiation, the shift of the band promotes an enhancement in charge separation, which leads to an increased photocurrent of the electrode of the ZnO/ZnS heterostructure. On the other hand, preparation of heterostructure is favorable to improve the transfer of charge between ZnS and ZnO, even in the dark, resulting in a higher dark current. The direction of the dark current and photocurrent is the same. Additionally, the migrated charges of the ZnS shells can be supplemented by ion diffusion from the electrolyte [70]. The chemical transformation of ZnO to zinc sulfide is used to obtain a ZnS shell over the ZnO single crystal nanowire. A decrease in visible light transmission (by about 15%) is found in ZnO–ZnS core–shell nanowires, which provides larger light

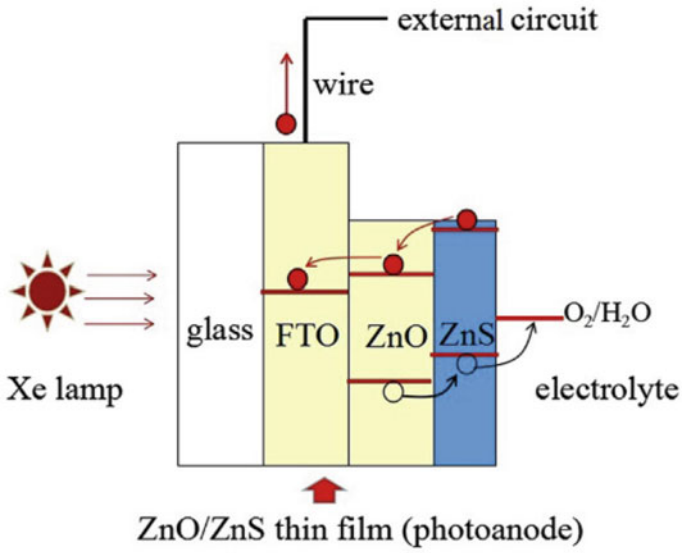


**Fig. 3** The scheme and diagram of energy bands of type-II-staggered ZnO/ZnS heterostructure [70]

absorption. Compared to the initial ZnO, the photocurrent for the ZnO–ZnS core–shell stays unchanged with no significant fluctuations for several hours. It means that the functionalization of ZnS provides stability to the unstable photoanode from ZnO. The higher position of the ZnS conduction band increases the photovoltage in the open circuit and decreases the rate of photocarrier recombination. This fact leads to a lifetime increase in photocarriers [71]. Modifications of ZnO nanosheets with ZnS layer show a decreased bandgap (2.72 eV) and, nevertheless, a small increased minimum of the conduction band, which significantly expands the wavelength range for light absorption [72].

Numerous studies have been carried out to obtain heterostructures with different morphologies to enhance the transfer of electrons over the interface when using photocatalysis or photoelectrocatalysis to decompose water [73–75]. In [76], ZnO/ZnS heterostructures were obtained by electrochemical deposition of an array of ZnO nanorods, followed by their sulfonation in a hydrothermal process with the preparation of a core–shell heterojunction structure. It is assumed that the combination of two different dissolution–crystallization and substitution reactions is responsible for the growth of well-aligned arrays of ZnO/ZnS heterostructures [77]. The heterostructures of ZnO/ZnS nanowire arrays were synthesized using ammonium persulfate as an oxidizing agent for direct oxidation of zinc foil and then by a sulfidization process to replace oxygen with sulfur in an alkaline solution (Fig. 4). The photocatalytic activity was noticeably enhanced at mentioned heterostructures because of electron transfer between ZnS and ZnO in comparison with pure ZnO nanofibers. The bandgap of a sulfur-doped ZnO film obtained with the use of pulsed

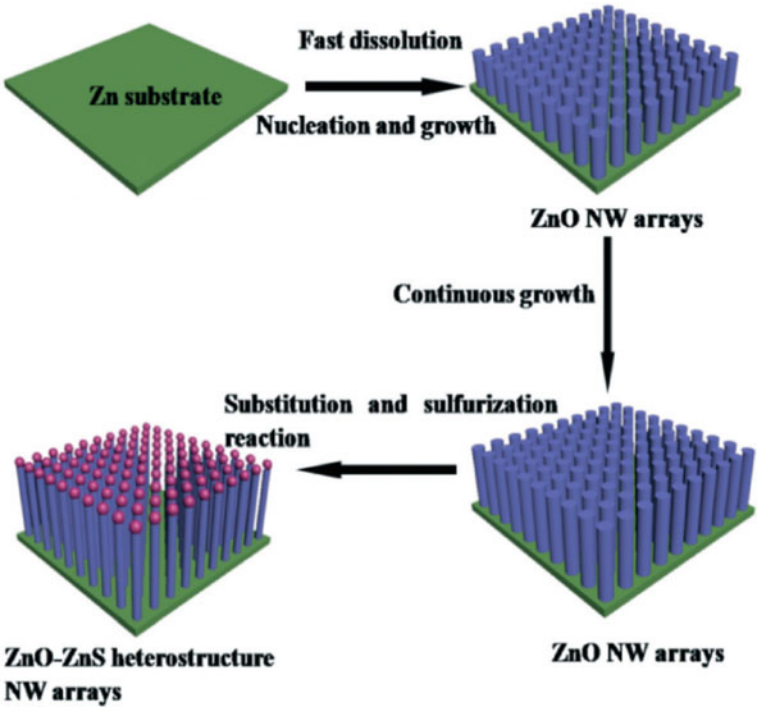


**Fig. 4** Schematic representation of the fabrication of ZnO/ZnS heterostructure [77]

laser deposition shifts to a lower level as sulfur is included [69], which leads to better absorption of visible spectra of sunlight. A new approach to the production of ZnO–ZnS on an array of ZnO nanowires for the generation of hydrogen with a significantly increased photocurrent was demonstrated [78].

ZnS–ZnO composite heterostructures were also prepared at low temperatures by the solvothermal method by partial sulfidation of ZnO with the use of thiourea. The obtained materials demonstrated functionality in the production of hydrogen. In this case, the addition of methanol caused an increase in the amount of $H_2$ formed up to five times as correlated with the most effective photocatalyst with no methanol addition [79]. Electrochemical methods are one of the most promising approaches for obtaining ZnO/ZnS heterostructures. The results of a study on the preparation of the obtained ZnO/ZnS heterostructures by anodizing zinc in water and glycerol/water/$NH_4F$ electrolytes with various additions of $Na_2S$ are presented [80]. The results obtained prove that the hydrodynamic conditions favor the ordered nanotube morphology. This makes the separation of electrons and holes easier. This, in turn, increases the photoelectrochemical activity in the splitting of water. Another approach of the electrochemical method was demonstrated in [81], which consisted of electrodeposition of ZnO nanorods on an ITO substrate and sulfidation of the surface by ion exchange in an aqueous solution of $Na_2S$. The ultrasonic method provides

a number of advances as a rapid, easy, and large-scale synthesis ZnO/ZnS core–shell nanorods [82]. The nanorods were obtained by successive reactions, including the ZnO nanorods synthesis and transformation of their surface into the ZnS on a fluorine-doped tin oxide (FTO) substrate by sonochemical methods. ZnO/ZnS nanorods demonstrated higher photocurrents in contrast to ZnO nanorods for the reaction of water splitting. The ZnS passivates the defects at ZnO surface when the water splitting reaction occurs. It causes enlarged charge separation in ZnO nanorods. Heterostructures core–shell ZnO/ZnS core–shell used as a photoanode in the photoelectrochemical production of hydrogen and obtained by chemical vapor deposition on Si (100) substrates also show high efficiency [83]. Freshly prepared ZnO/ZnS heterostructures had a photocurrent density of 1.21 mA/cm$^2$, this value is 8.5 times larger than that of pure ZnO nanocrystals.

To increase the separation efficiency, the ZnO/ZnS heterostructure is proposed to be modified using various materials. In [84], photoelectrodes coated with polyaniline ZnS film/ZnO nanorods for splitting water were evaluated for their photocorrosion properties. Modification of ZnO/ZnS heterostructures with metals, as well as alloys with metals, leads to an increase in the efficiency of photoelectrochemical water splitting. Au nanoparticles were deposited on the ZnO/ZnS heterostructure for more efficient water splitting [85]. The optimal heterostructure decorated with Au demonstrates a high rate of hydrogen formation [86]. Doping with cerium also leads to an increase in the hydrogen yield, as reported in [87]. The attachment of other inorganic compounds to the surface of ZnO/ZnS heterostructures leads to a reduction in the charge migration distance, supplying an immense number of active centers and increasing the absorption of visible light. Deposition of $Cu(OH)_2$ clusters on the surface of ZnO/ZnS nanorods helps to increase the charge transfer and consequently the production of hydrogen by photocatalysis. The uncoated ZnO and ZnS catalysts exhibit a low $H_2$ formation rate due to their wide bandgaps under visible light conditions. As seen in Fig. 8a, the loading of $Cu(OH)_2$ has a significant impact on the activity of the ZnO/ZnS heterostructure [88].

Nowadays, triple heterostructures consisting of three semiconductors attract considerable interest due to the efficient separation and transfer of photogenerated charge carriers in these materials. The addition of other chalcogenides to the ZnO/ZnS heterostructures helps to increase the efficiency of absorption and conversion of solar energy into hydrogen. Sulfides of metals CdS [89–93], $Ag_2S$ [94–97], $Cu_2S$ [94, 98], CuS [94], CoS [99], and sulfides of bimetals [92]. Ternary CdS/ZnS/ZnO heterostructures were accurately prepared in form of one-dimensional (1D) nanofibers by the combination of various processes as electrospinning of ZnO, then in situ sulfurization of ZnO with the formation of ZnS/ZnO heterostructures, and in situ deposition of CdS quantum dots on the ZnS/Zn heterostructure. The optimized CdS/ZnS/ZnO heterostructure showed an $H_2$ evolution rate of 51.45 mmol$\cdot$ h$^{-1}\cdot$g$^{-1}$ with quantum efficiency of 26.88% at 420 nm at no cocatalyst used. It is 93,54 and 2.28 times more than for the initial ZnO and ZnS/ZnO, respectively, at similar process parameters [89]. The ZnO/ZnS/CdS heterostructures as nanorods were obtained by the ion-exchange method for the photoelectrochemical production of hydrogen [90]. The ZnO nanorods arrays can be used as sources for the synthesis of homogeneous

ZnS layers and their further transformation into CdS. The CdS content in films can be easily modified by the variation in process temperature. Photoelectrodes with an array of ZnO/CdS/ZnS and ZnO/ZnS/CdS nanorods were designed and CdS and ZnS layers were prepared by alternative chemical deposition in a bath on the surfaces of ZnO nanorods. The photoelectrochemical characteristics of photoelectrodes with a composite structure and the concept of action of ZnS buffer layers were studied. Outcomes of the research confirm that the photoelectrode with an array of ZnO/ZnS/CdS nanorods has an increased hydrogen yield. This boost can be assigned to ZnS buffer layers. As was mentioned above, these layers are useful for separating and transporting photogenerated charge carriers in photoelectrodes with nanorod array of ZnO/ZnS/CdS [100].

An easier way to obtain ZnO/ZnS/$M_xS$ (metal sulfide) core/shell/shell nanorod heterostructures, ZnO/ZnS/CuS, ZnO/ZnS/$Ag_2S$, ZnO/ZnS/CdS, ZnO/ZnS/$Cu_2S$, and ZnO/ZnS/$Bi_2S_3$ was demonstrated in [94]. The ion–ion growth mechanism is an intermediate path to the transformation of ZnO nanorods into ZnO/ZnS and ZnO/ZnS/$M_xS$ nanostructures. This transformation is possible due to significant differences between the constants of the solubility of ZnO, ZnS, and $M_xS$ products. The photocurrent density and hydrogen generation efficiency in the ZnO/ZnS/$Ag_2S$ nanostructure were obtained up to 15.28 mA/cm$^2$ and 15.92%, respectively [94]. Another approach to the preparation of ternary heterostructures for the water splitting upon irradiation with sunlight was demonstrated using the example of ZnO–ZnS–$Cu_2S$ [98]. The production of a heterostructure is a three-stage process, including the growth of an array of ZnO nanorods in solution, followed by the deposition of $Cu_2O$ followed by its sulfonation. The addition of an intermediate ZnS layer to the ZnO–$Cu_2S$ core–shell arrays additionally expands the absorption range of visible spectrum and supports the efficient separation of charge carriers (Fig. 5). In this case, the transformation of $Cu_2O$ into $Cu_2S$ provides efficient contact of the core–shell heterostructure with the surface of ZnS. It is a reason for forming a configuration of energy levels and, therefore, the spectral bands which make possible proper separation of photogenerated electrons and holes. The release of $H_2$ upon irradiation with visible light was 436 $\mu mol \cdot h^{-1} \cdot g^{-1}$ for arrays of ZnO–ZnS–Cu2S (8 h) nanorods, which is 2.55 and 1.61 times larger in comparison to ZnO–$Cu_2O$ and ZnO–$Cu_2S$.

The process of sulfonation of ZnO nanostructures with the subsequent production of ZnO/ZnS/$M_xS$ heterostructures can be represented in the form of a diagram as presented in Fig. 6. The hydrolysis of thiourea and the formation of gaseous $H_2S$ happen when a substrate from a conductive glass is coated by ZnO nanorods and submerged in a solution containing sulfur, where the ZnO sulfonation reaction occurs. This is the effect of significant variation between values of ZnO and ZnS solubility constants. The interaction of ZnO with $H_2S$ on the NR surface leads to the appearance of NR ZnO/ZnS core/shell (stage 1) [94].

ZnO/ZnS/CdS/$CuInS_2$ core–shell nanowires arrays with increased photoelectrochemical performance in visible spectrum have been effectively obtained using ion-exchange and hydrothermal synthesis, the preparation of which is shown in Fig. 7. The photoanode p–n junction heterostructure ZnO/ZnS/CdS/$CuInS_2$ exhibits an improved photoelectrocatalytic activity during water splitting in comparison

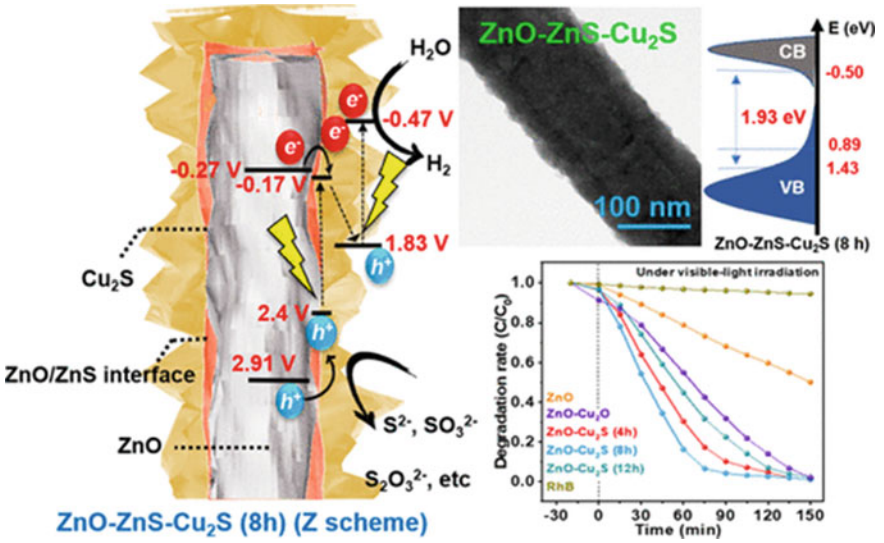


**Fig. 5** Charge transfer scheme and performance of the process of solar energy conversion for the ZnO/ZnS/$Cu_2S$ heterostructure [98]

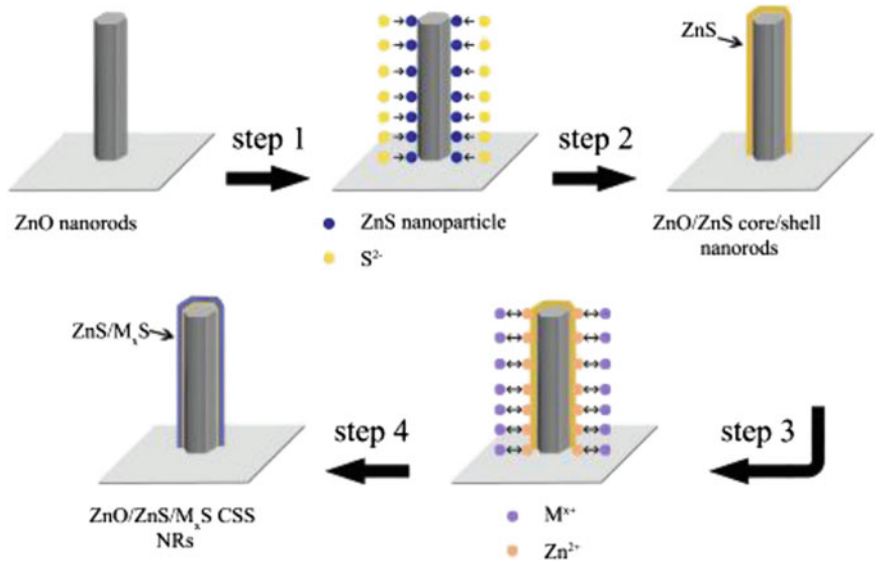


**Fig. 6** Stepwise scheme of ZnO/ZnS/$M_xS$ NRs preparation [94]

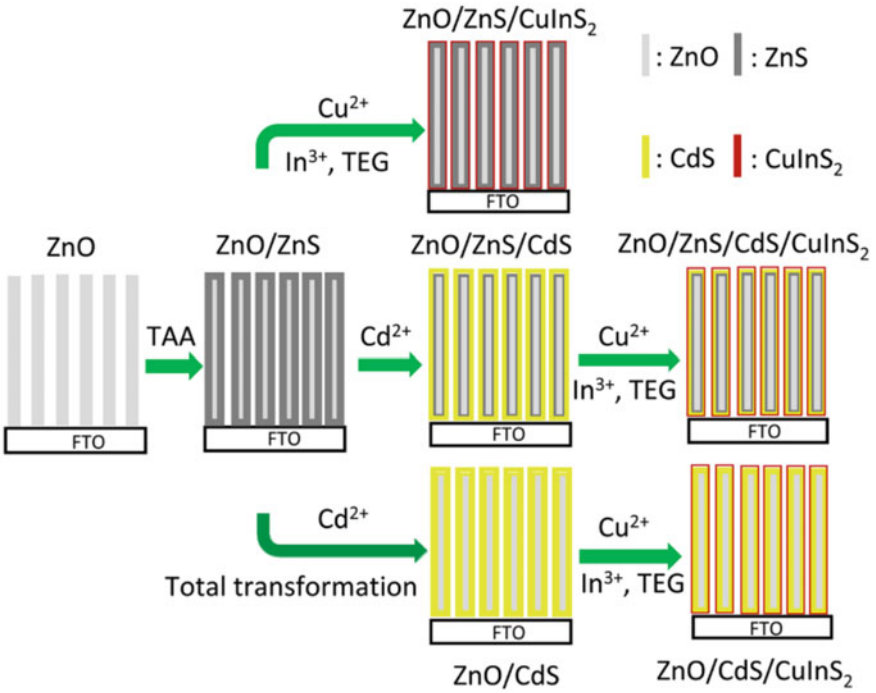


**Fig. 7** Scheme of Core−Shell structures formation [92]

with thin films from ZnO/ZnS/CdS and ZnO/ZnS. The optimized structure of ZnO/ZnS/CdS/$CuInS_2$ film exhibits values of photocurrent equal to 10.5 mA/$cm^2$ and high incident photon-to-current conversion efficiency (IPCE) of 57.7% for 480 nm at bias potential of 0 V compared to Ag/AgCl. CdS and ZnS have an important role in the ZnO/ZnS/CdS/$CuInS_2$ structure. Particularly, ZnS, as a passivating layer, reduces the recombination of charge carriers at the oxide/$CuInS_2$ interface. The CdS and $CuInS_2$ create a p–n junction and the absorption in visible spectrum grows. In its turn, it facilitates the charge transport and slows down the carrier's recombination in $CuInS_2$ which leads to the enhancement of characteristics of the heterostructure ZnO/ZnS/CdS/$CuInS_2$ [92].

The ternary heterostructures based on $Ag_2S$ obtained by ion exchange on a $SnO_2$ surface doped with fluorine also showed high efficiency in the photoelectrochemical water splitting [95]. Heterostructures of ZnO/ZnS nanorods bound to $Ag_2S$ were prepared at substrates of wire mesh from stainless steel. The preparation was carried out along the axis by sulfonating arrays of ZnO nanorods as immobilized hierarchical photocatalysts ($Ag_2S$-bound ZnO/ZnS/metal wire mesh) to obtain $H_2$. The yield of $H_2$ for photocatalysts ZnO@ZnS/metal wire mesh bound with $Ag_2S$ values of 5870 and 168 $\mu mol \cdot g^{-1} \cdot h^{-1}$ at visible and ultraviolet radiation [97]. Another way to prepare the ternary heterostructures on the Sonova of ZnO and metal chalcogenides is the use of organometallic compounds as precursors [99]. Sulfurization of organometallic

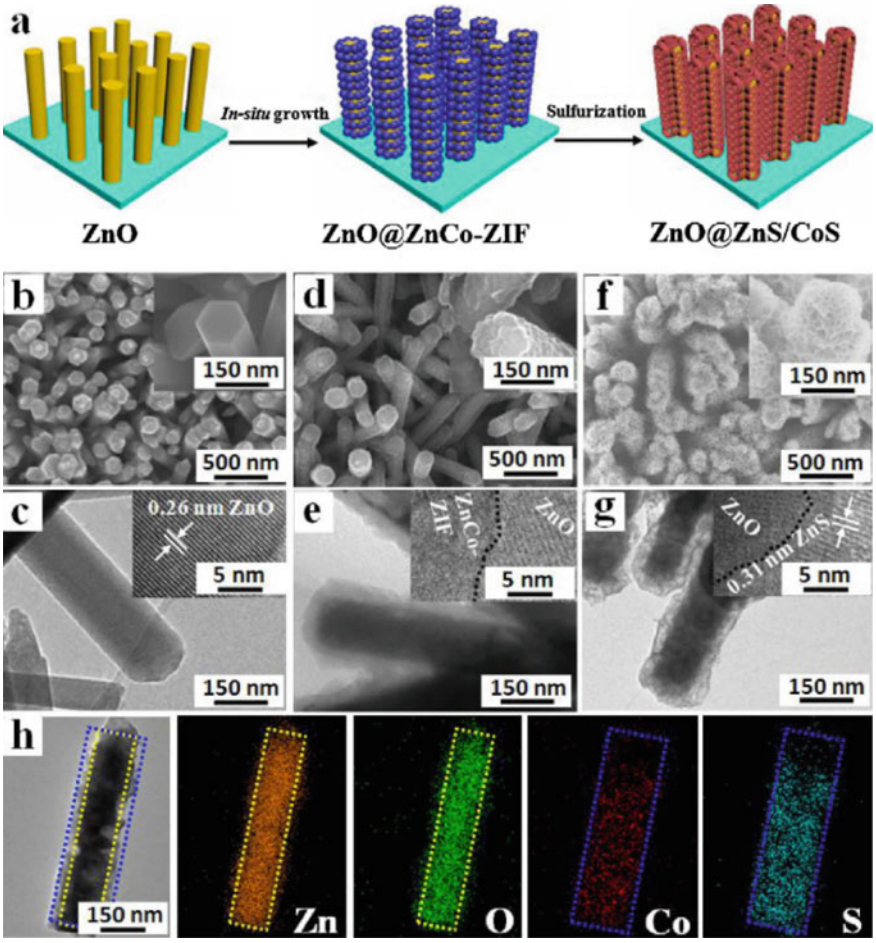


**Fig. 8** **a** Scheme of cellular ZnO/ZnS/CoS preparation, **b** SEM image of ZnO, **c** TEM image of ZnO, **d** SEM image of ZnO@ZnCo-ZIF, **e** TEM image of ZnO@ZnCo-ZIF, **f** SEM image of ZnO@ZnS/CoS, **g** TEM image of ZnO@ZnS/CoS [99]

scaffolds on semiconductor ZnO leads to the formation of cellular heterostructured catalysts ZnO/ZnS/CoS for water splitting (Fig. 8). The obtained structures show a high photoconversion efficiency (0.65% at 0.14 V) and a photocurrent density (2.46 mA/cm$^2$ at 0.6 V) at all ranges of irradiation, surpassing the performance of the described above catalysts on the basion of ZnO into unbiased environment. CoS, acting as a cocatalyst, can accelerate the transfer of holes and concurrently take part in the oxidation of surface water. It decreases the oxygen evolution barrier at heterostructures ZnO/CoS and ZnO/ZnS/CoS [99].

There are also studies on the techniques of hydrogen production by the splitting of water irradiated with sunlight using ZnO–ZnS/graphene heterostructures [101]. The

inclusion of graphene can improve photogenerated charge separation across ZnO–ZnS/graphene contact area and increase the rate of hydrogen production by photocatalysts. The use of composite materials for photocatalysts has shown enhanced performance due to more intensive charge separation and increased absorption of radiation. The addition of glycerine and other organic compounds increases the efficiency of hydrogen production. The addition of organic compounds leads to the elimination of the charge recombination. Due to the reaction with photogenerated holes, the photocatalytic activity in the production of $H_2$ increases [50, 102]. The rates of hydrogen formation are 193.3, 269.9, and 587.6 $\text{lmol}\cdot\text{h}^{-1}\cdot\text{g}^{-1}$ at a glycerol concentration of 10, 20, and 30 vol%, respectively [101].

## 4 ZnO/ZnSe Heterostructures

The use of narrow-gap semiconductors such as zinc selenide (ZnSe) in combination with one-dimensional metal oxide semiconductors (for example, ZnO) to encourage the absorption efficiency in visible spectrum has been extensively studied. Metal selenides are generally characterized by a narrow bandgap, decreased internal resistance, high usage of sunlight, and excellent photoelectrochemical performance. The bandgap of ZnSe is 2.56 eV and an exciton binding energy is 21 meV at room temperature [103, 104]. Selenium doping of ZnO leads to an increase in light absorption when compared to undoped ZnO nanocrystals. The density of photocurrent for Se-doped ZnO nanoplates reaches ~0.2 $\text{mA/cm}^2$. This value is larger than for undoped ZnO nanocrystals (~0.015 $\text{mA/cm}^2$ [105]; therefore, the use of zinc selenide as a material to increase the conversion efficiency of sunlight is justified [106, 107]. Pure ZnSe in the form of nanorods has also been used to production of hydrogen using splitting of water upon sunlight irradiation, with a quantum yield of $50 \pm 4\%$ ($\lambda = 400$ nm) [108]. Studies have shown that ZnSe is a potential photocatalyst for the reduction of water to $H_2$ The use of ZnSe as a cocatalyst in the preparation of heterostructures allows to considerably improve the photocatalytic activity to produce $H_2$ [109]. In recent years, the ZnSe-based heterostructures studies have begun [110–112] for use in sunlight conversion [113]. Thus, the $FeSe_2$/ZnSe heterostructure obtained by depositing ZnSe nanoparticles on $FeSe_2$ nanorods was used as an electrode in photoelectrochemical splitting of water [114]. The photoelectrochemical activity, as well as the rate of $H_2$ formation, were three times higher than that of ZnSe in terms of photoelectrochemical activity, it was also 2.3 times higher in the rate of $H_2$ production. Most ZnSe-based heterostructures are staggered core–shell heterostructures such as (ZnSe/CdS)/CdS [115], ZnSe/CdS/ZnSe [116] and ZnSe/CdS(or CdS/ZnSe) [117]. ZnO/ZnSe heterostructures were investigated for photoelectrochemical water splitting and hydrogen production. Yong Zhang et al. [118] noted that conversion of sunlight using a heterostructure based on arrays of ZnO/ZnSe core–shell nanorods. Heterostructures based on ZnO and ZnSe show the high efficiency of absorption of sunlight in a wide spectral range. For some heterostructures, the absorbed energy extends to the near-infrared range [119].

Heterostructures based on ZnO and zinc selenide are also actively studied for photoelectrochemical water splitting. Nanocrystalline FTO/ZnO/ZnSe heterostructures were obtained from ZnO films obtained by electrodeposition. Afterward, it transformed into FTO/ZnO/CuSe heterostructures by completely replacing zinc (II) in composition of zinc selenide with copper (II). The heterostructures such as FTO/ZnO/ZnSe proved to be efficient photoanodes in absorbing sunlight [120]. Heterostructures of ZnO nanofibers/ZnSe nanoparticles (ZS1) were also formed by the dissolution–recrystallization method [121]. With a longer time and higher concentrations of solution during the reaction, the arrays of nanostructures were changed to arrays of ZnO nanowire/ZnSe nanospheres (ZS2) heterostructures. Photoanodes with an array of ZnO/ZnSe heterostructures exhibit absorption at the visible part of spectrum (wavelength <550 nm) with IPCE up to 47% (ZS1) or 57% (ZS2) at zero potential relative to Ag/AgCl (Fig. 9) [122]. The insertion of ZnSe can significantly increase the absorption edge of visible spectrum. In addition, the formation of the ZnO/ZnSe heterostructure makes it possible to efficiently transfer photoexcited

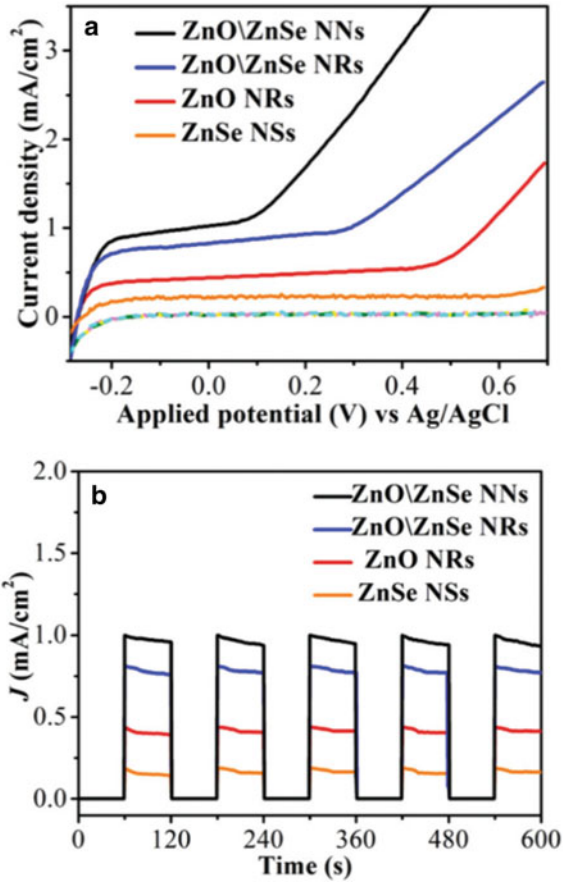


**Fig. 9** **a** Curves of photocurrent density/potential (I–V) and **b** Curves of photocurrent density/time for photoelectrochemical water oxidation (The material of electros and voltages are shown in graphs) [123]

carriers of charge, which are expected to significantly modify the characteristics of the photoelectrochemical water oxidation [123].

An easy way for fabrication of ZnO heterostructure arrays of ZnSe nanonails on substrates of FTO glass using a simple two-step hydrothermal synthesis was proposed in [123]. As shown in Fig. 10, ZnO nanorods arrays are obtained for the first time on the FTO surface by a hydrothermal process. ZnSe nanoparticles on a ZnO nanorod were obtained by in situ ion exchange. Likewise, ZnSe nanoribbons are also formed in situ and coat the surface of ZnO nanorods. The photocurrent density in such heterostructures of the ZnO/ZnSe nanorod array reaches 1.01 mA/cm$^2$ at an applied potential of 0.1 V (relative to Ag/AgCl). This is an enormously large value

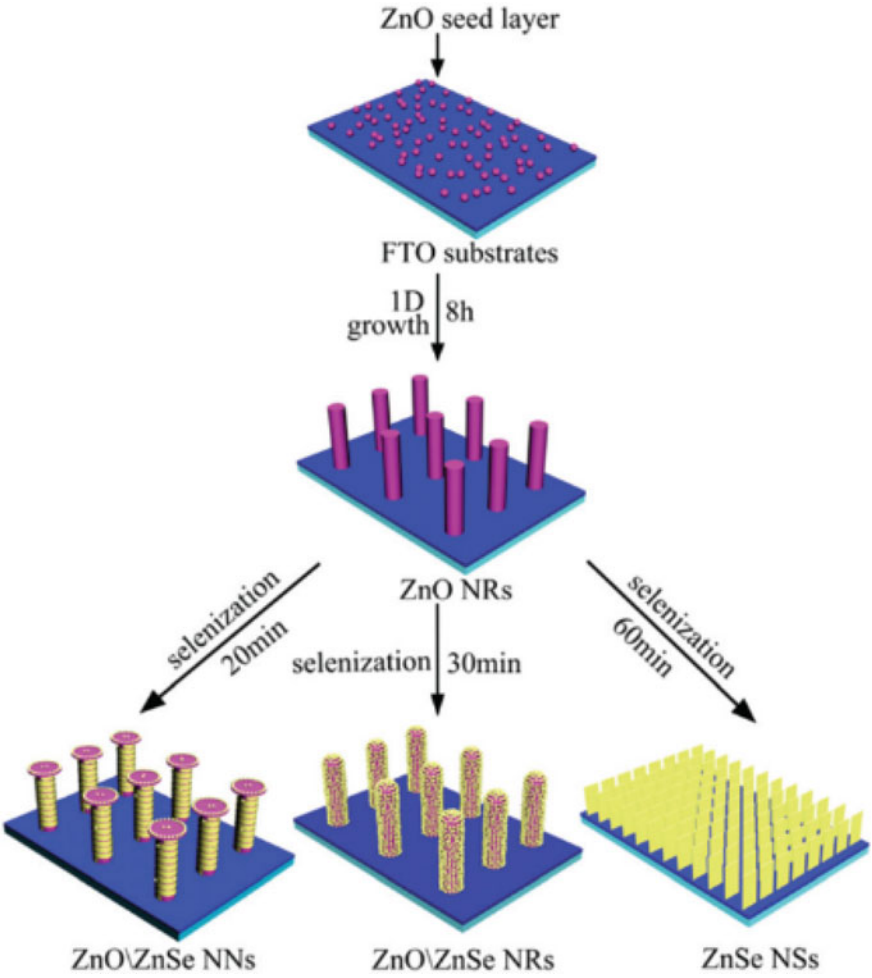


**Fig. 10** Scheme of preparation process of the ZnO/ZnSe heterostructure arrays on substrates of FTO glass [123]

in comparison with the ZnO/ZnSe nanorod array (0.71 mA/cm$^2$), an array of ZnO nanorods (0.39 mA/cm$^2$), and a ZnSe electrode (0.21 mA/cm$^2$), which indicates its significant activity under visible light irradiation for the photoelectrochemical oxidation of water.

The formation of ZnO/ZnSe/CuSe heterostructures using the ion-exchange method was studied in [124]. This heterostructure provides enhancement of photocatalytic activity, and at the same time the photocurrent density is up to 5.70 mA/cm$^2$. According to the authors, the use of a double shell based on the composite structure of ZnO can make this material inspirational for design of techniques for the water splitting [124]. Ternary heterostructures using ZnO/ZnSe and other chalcogenides are mainly obtained by the ion-exchange method [125, 126]. Nanofiber arrays from ZnO/ZnSe/CdSe/$Cu_xS$ core–shell heterostructures achieve a sunlight conversion efficiency of 89.5% at 500 nm (at 0.2 V) relative to Ag/AgCl. In this case, CdSe acts as an immensely efficient absorber of visible light. It creates heterojunctions with surrounding components to increase the separation and transport of photoinduced carriers. $Cu_xS$ is supposed to be used as a passivating layer and an very active p-type mediator, so the goal is passivation of defects and various states of semiconductors surface and formation of p–n junctions with CdSe, facilitating the transport of holes at the interface of semiconductor and electrolyte. The surface of ZnO/ZnSe/CdSe/$Cu_xS$ core–shell nanowire arrays with nanoporous morphology, concurrently with the tunneling transport of charge carriers in ZnSe and CdSe thin films, promotes the kinetics of reactions under irradiation and increase absorption of light [125, 126].

Clearly, defined porous heteronanostructures with a broad interval of light absorption and efficient charge transfer are main problems in the development of efficient photoanodes for the photoelectrochemical water splitting. Paper [127] reports on the formation of a ZnO/$Zn_xCd_{1-x}Se$ heterostructure on an FTO surface. The heteroepitaxy of shell layers from the $Zn_xCd_{1-x}Se$ on the surface of ZnO allows to achieve a photoconversion efficiency of 10.64%. However, the problem of erosion of a film of arrays of ZnO nanorods is the main obstacle to the sensitization of its surface. Coating the ZnO surface with zinc selenide and cadmium selenide show the high stability of such heterostructures [128]. A typical synthesis of a ZnO/CdS/CdSe ternary heterostructure on FTO is presented in Fig. 11. After growing the ZnO nanorods in various ways, a ZnO/ZnSe structure is obtained on the substrate surface due to the transformation of the ZnO surface to ZnSe through the reaction of an anion exchange (stage 2). To conclude, ZnSe/CdS/CdSe photoelectrodes with triple sensitization were prepared by sequential CdS and then CdSe deposition on preliminarily fabricated ZnO/ZnSe nanorods (stages 3 and 4), respectively [129]. Increased interface areas and interface uniformity can enhance the efficiency of photoelectrochemical water oxidation. Moreover, for heterostructures based on ZnO and ZnSe, no noticeable weakening of the photocurrent density is observed after long operating cycles, which perfectly demonstrates their high stability [123].

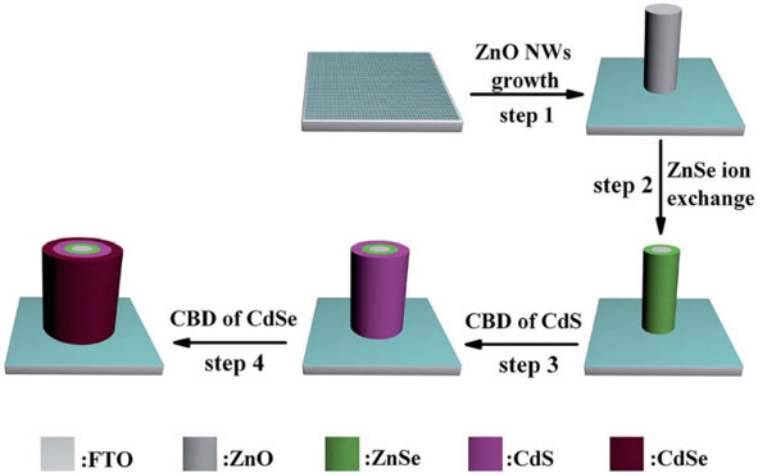


**Fig. 11** Sketch of preparation procedure of photoelectrodes from ZnSe/CdS/CdSe [129]

## 5 ZnO/ZnTe Heterostructures

Zinc telluride (ZnTe) is appeared to be a desirable material for the role of a photocathode in water splitting by photocatalysis. ZnTe has a demanded bandgap value (2.26 eV) for efficient light absorption. The most negative position of the conduction band edge (which is −1.63 V RHE) in comparison with other semiconductors of p-type, provides a huge stimulation of electron transfer at the interface from the semiconductor towards acceptors in electrolyte [130, 131]. A pure ZnTe photocathode exhibits moderate activity, high overvoltage, and low stability. The combined modification of a ZnTe-based photocathode using carbon and MoS2 improves its photoelectrochemical characteristics with a decrease in overvoltage, increased photoactivity, and improved stability [132]. A wide range of irradiation absorption and a high efficiency of photogenerated charges separation are expected from high-performance photoelectrodes. Ternary heterostructures based on ZnO and tellurides in the form of an array of core/shell ZnO/ZnxCd$_{1-x}$Te nanowires, characterized by a wide edge of absorption from UV (380 nm) to near IR (855 nm) were obtained by chemical vapor deposition [133]. The ZnO/Zn$_x$Cd$_{1-x}$Te core/shell nanowire array was a monocrystalline triple shell, which significantly increases the efficiency of charge separation, extends the lifetime of charge carriers, and promotes growth of photocatalytic and photoelectrocatalytic performance under light irradiation. Additionally, the ZnO/Zn$_x$Cd$_{1-x}$Te heterostructure showed high photocatalytic activity of $H_2$ production due to the synergistic absorption of light by the Zn$_x$Cd$_{1-x}$Te triple shell and the making of a heterostructure between the boundaries of ZnO core and the Zn$_x$Cd$_{1-x}$Te shell [133].

## 6 ZnO/Cadmium Chalcogenides Heterostructures

Among the chalcogenides for the preparation of heterostructures based on ZnO, CdS is of the greatest interest to researchers due to the similarities of crystal lattice structures of CdS and ZnO. Additionally, the ZnO/CdS heterojunction can form a type II structure of energy bands. ZnO conduction band is situated between the valence and the conduction bands of CdS. This fact can prevent the recombination of photogenerated charge carriers. The photocatalytic activity of pure ZnO is lower than of ZnO/CdS heterostructures when sunlight is irradiated [134–136]. Various methods were used to synthesize ZnO/CdS heterostructures for the photoelectrochemical water splitting. In particular, the hydrothermal method [137, 138], the electrochemical deposition method [136], the ion-exchange method [139], the photodeposition method [140], etc. were used. The use of the hydrothermal method makes obtaining heterostructures of ZnO/CdS with uniform deposition of CdS on the ZnO nanorods surface. The ZnO/CdS heterostructure film with a three-dimensional structure shows a significant increase in light absorption and photoelectrochemical characteristics [137]. Figure 12 shows a linear sweep of the I–V curve with intermittent illumination of ZnO/CdS samples. The samples exhibit an excellent performance when the light is turned on and off. During illumination, the density of photocurrent of the samples constantly grows with increasing the applied voltage [137].

A modified process of sequential adsorption and reaction of the ionic layer was applied for the deposition of bound quantum dots of CdS and CdSe on the surface of

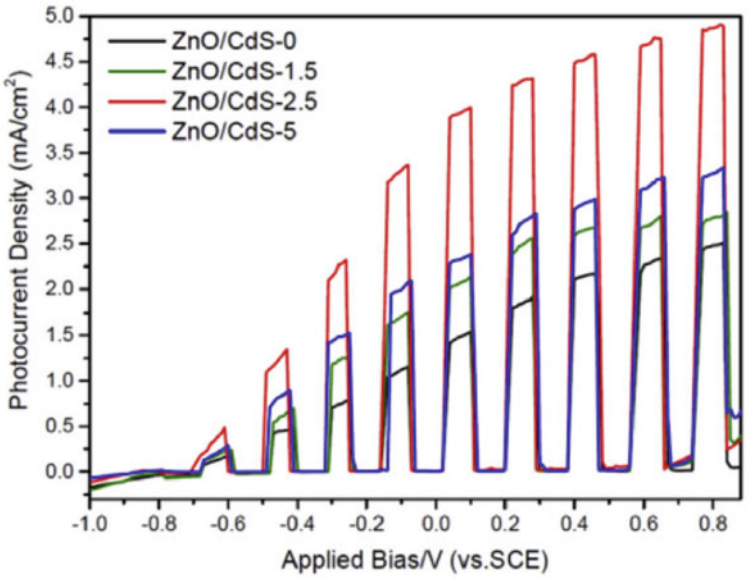


**Fig. 12** The I–V curve of ZnO/CdS samples under illumination by 100 mW/cm$^2$ [137]

highly oriented ZnO nanorods [139]. The approach ensures conformal and uniform deposition of quantum dots subsequently with ZnO nanorods arrays. Photoanodes with CdSe/CdS/ZnO nanorods are highly sensitive to visible spectrum and demonstrate intensified ion diffusion and effective suppression of recombination of charge pairs. ZnO/CdS heterostructures show the good photocatalytic activity of $H_2$ evolution in aqueous solutions, which is confirmed by the data presented in [140]. An increase in the CdS content in the ZnO/CdS heterostructure to 22.91% leads to a higher rate of hydrogen production ($1725 \cdot \mu mol \cdot g^{-1} \cdot h^{-1}$), which is approximately 9.2 and 34.5 times higher than for ZnO and CdS separately. The formation of a photocatalytic system according to the Z-scheme significantly contributes to the separation and migration of photogenerated carriers. To achieve efficient charge separation in ZnO/CdS heterostructures, it is proposed to obtain pseudomicrospherical ZnO/CdS core–shell structures. Homogeneous ZnO pseudomicrospheres with a diameter of about 2 μm were obtained, which were subsequently used as core materials for a CdS shell coated with different amounts of nanoparticles [138]. ZnO microspheres show a relatively low rate of hydrogen evolution (0.16 mmol $g^{-1}$ $h^{-1}$), CdS nanoparticles showed a little bit higher hydrogen evolution rate ($1.69 \ \mu mol \cdot g^{-1} \cdot h^{-1}$) due to the narrow bandgap. The sample of ZnO + CdS was obtained by mechanical stirring and showed a decreased hydrogen evolution rate (about $0.76 \ \mu mol \cdot g^{-1} \cdot h^{-1}$). This value can be attributed to the worst contact between CdS and ZnO. The heterostructures of CdS/ZnO have a high hydrogen evolution rate ($22.12 \ mmol \cdot g^{-1} \cdot h^{-1}$) (Fig. 13) [138]. The increased photocatalytic activity of CdS/ZnO heterostructures is associated with

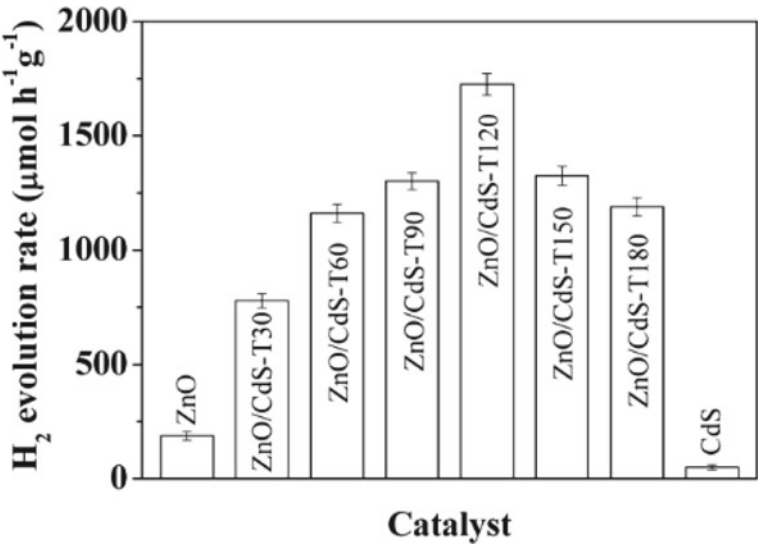


**Fig. 13** Dependence of hydrogen evolution rate for ZnO, CdS, and ZnO/CdS samples with various amounts of CdS [140]

a decrease in the recombination of charge carriers, which are originated from electron transfer from CdS to ZnO. Additionally, the hydrogen yield in the CdS/ZnO heterostructures increases with the growth of the CdS/ZnO mass ratio from 0.01 to 0.10. It decreases with a further increase in the amount of CdS, despite the light absorption range of the CdS/ZnO samples [141].

The heat treatment of the heterostructure causes an increase in the rate of hydrogen evolution during the water splitting. This is due to an increase in the crystallinity of the heterostructure and a more efficient separation of the charge generated by irradiation with sunlight. $CdCl_2$ treatment of the ZnO/CdS heterostructure promotes recrystallization, as well as densification of the CdS shell layer. It makes possible the formation of an intermediate $Zn_xCd_{1-x}S$ layer at the interface of ZnO and CdS, which facilitates the separation and transport of photogenerated carriers and broaden the range of light absorption [142]. The presence of CdO in the heterostructure also leads to an increase in the rate of hydrogen release in comparison with the use of ZnO/CdS [143]. There is also information that an increase in the efficiency of photoelectrochemical water splitting in heterostructures based on ZnO is associated with the formation of CdSSe by the core–shell type. The data are presented on the synthesis with a 10–50 nm shell thickness by chemical vapor deposition of CdSSe on previously grown arrays of ZnO nanowires [144]. In another work [145], heterostructures based on sulfides of two metals (ZnCdS) and ZnO were studied. In this case, ZnS and ZnO were prepared on one procedure at the sulfonation stage. In this case, ZnS acts as a barrier to the localization of ZnO particles and it feels the free areas inside the ZnS layers. The obtained multilayer ZnCdS/ZnO/ZnCdS heterostructures show the $H_2$ formation rate of 28.6 $mmol \cdot g^{-1} \cdot h^{-1}$. A photoanode consisting of open top arrays of ZnO/CdS/PbS nanotubes and several heterojunctions, synthesized with successive use of hydrothermal treatment, adsorption reaction, and chemical deposition showed a high photoelectrochemical action in the hydrogen evolution [146]. Improved photoelectrochemical activity could be associated with the morphology of the heterostructure; open-top nanotubes significantly increase the surface area, which contributes to efficient light absorption and rapid mass transfer. Arrays of ZnO/CdS/$CuSbS_2$ nanofibers core–shell as a photoanode for hydrogen evolution were obtained by electrodeposition from non-aqueous electrolytes and exchange of cation. The ZnO/CdS/$CuSbS_2$ photoanode obtained under optimal conditions provides a photocurrent of 6.48 $mA/cm^2$ at 0 V compared to Ag/AgCl and a solar light conversion efficiency of about 52% at 480 nm. In this research, the electrolyte solution contained 0.35 M of $Na_2SO_3$ and 0.25 M of $Na_2S$ [147].

Another approach to increasing the efficiency of hydrogen production using CdS/ZnO heterostructures is to modify them with metals and obtain an M/CdS/ZnO heterostructure by metal photodeposition. The Pt/CdS/ZnO and Pd/CdS/ZnO heterostructures showed the same hydrogen yields. The values were larger than for Ni/CdS ZnO yields. The hydrogen yield for Pt (0.5%)/CdS/ZnO was increased in comparison with Pt (0.1%)/CdS/ZnO. It is noteworthy that the yield of hydrogen from CdS/Pt/ZnO was less than from Pt/CdS/ZnO [141].

Photoanodes based on ZnO/CdS heterostructures have excellent photoelectrochemical characteristics for the water splitting with the purpose of hydrogen formation. Unfortunately, its practical application is strongly hampered by photocorrosion caused by generated holes on the CdS surface. To increase the resistance to photocorrosion, it is proposed to cover the ZnO/CdS heterostructure with other compounds. In [148], the ZnO/CdS/BiOI heterostructure in the form of nanorods was obtained using the solvothermal method. At illumination by visible light ($\lambda > 420$ nm), the ZnO/CdS/BiOI photoanode demonstrates high activity in the photoelectrochemical process and produces a photocurrent density of 9.12 mA/cm$^2$ at 1.1 V compared to RHE. This value is 1.8 times higher than the photoanode. photoanode ZnO/CdS in alkaline electrolyte and, in this case, the stability of the photoanode made more than 6000 s. The use of heterostructures based on ZnO, cadmium telluride, and cadmium selenide for the photoelectrochemical water splitting was demonstrated in [149, 150]. Arrays of ZnO/CdTe heterostructure nanotubes of the core–shell type were synthesized using two-stage electrochemical deposition [149]. It was found that freshly prepared ZnO/CdTe nanotube arrays demonstrate significantly increased density of photocurrent at water decomposition in comparison with ZnO nanorod arrays (Fig. 14). The reason is a smaller bandgap or a reduced density of defect states such as oxygen vacancies, etc.

The ZnO/selenide heterostructure in combination with high values of electron mobility in ZnO and a large range of optical absorption of selenide also makes it possible to achieve high efficiency of photoelectrochemical conversion of sunlight [151]. The dense shell of CdTe and the interface of ZnO/CdTe provide rapid transfer

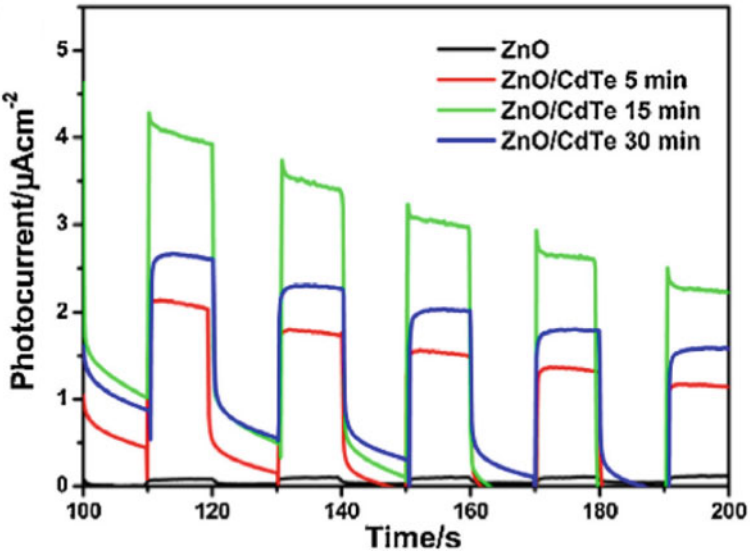


**Fig. 14** Values of photocurrent at light on–off for photoanodes based on ZnO and ZnO/CdTe core–shell nanostructures (illumination $\lambda \geq 420$ nm) [149]

of photogenerated electrons with high efficiency from the shell of CdTe to the nanorods of ZnO. It provides a significant drop in anodic decomposition/corrosion and a significant improvement in the stability of photodevices. Second, the CdTe cladding improves absorption in the visible range of light and promotes charge separation [149, 152, 153]. The presence of a CdSe layer on the ZnO surface also promotes more efficient charge separation [153]. Cadmium selenide was mainly deposited using ion-exchange technology [150]. In situ preparation of a CdSe layer on the surface of nanorods from ZnO optimizes contact at the interface of the CdSe and ZnO, which lowers the barrier to electron transfer.

## 7 ZnO/Molybdenum, Lead, Copper, and Silver Chalcogenides Heterostructures

To obtain ZnO-based semiconductors, heterostructures with a narrow bandgap are used in some semiconductors, which shows high photoactivity and good separation of photogenerated charge carriers [154]. Chalcogenides of various metals such as PbS, $Ag_2S$, CuS, and $MoS_2$ were used as materials that have a narrow bandgap. Despite the enhanced efficiency of using chalcogenides in the photoelectrochemical conversion of sunlight into gaseous hydrogen, the number of published works on ZnO/molybdenum, lead, copper, and silver chalcogenides heterostructures is still limited. Nowadays, the published studies are related to the use of heterostructures ZnO/chalcogenides of molybdenum, lead, copper, and silver for the photoelectrochemical production of hydrogen, as well as heterostructures ZnS/CuS [155] and ZnS/$Ag_2S$ [156] using ZnO as source material with following sulfonation and reaction of ion exchange. At the same time, the problem is to manage both the electrical and chemical energy efficiency of composites and materials while maintaining their photocorrosion resistance. For this purpose, molybdenum disulfide $MoS_2$ is one of the promising candidates for binding to ZnO due to its narrow bandgap (1.7 eV), photocorrosion resistance inside the electrochemical cells, and its advanced characteristics for the reaction of hydrogen evolution [157]. Firstly, the study of Paquin et al. [158] mentioned the synthesis of hybrid ZnO photocatalysts coated with layered $MoS_2$ nanosheets using the hydrothermal method for the photocatalytic production of $H_2$. The efficiency of the ZnO/$MoS_2$ heterostructure modified with gold nanoparticles to produce $H_2$ was also investigated [159]. Despite these studies, $MoS_2$/ZnO heterostructures remain relatively poorly understood for the photoelectrochemical water splitting compared to other types of heterostructures based on ZnO and metal chalcogenides.

The $MoS_2$/ZnO heterostructure prepared by electrodeposition on a mesh substrate from stainless steel for the photoelectrochemical production of hydrogen have investigated [160]. $MoS_2$ can have a function of a cocatalyst to restrain electron–hole pair recombination, providing prevention of ZnO photocorrosion. The 1D–2D heterostructures based on nitrogen-doped ZnO nanorods covered by defective nanosheets of $MoS_2$ with many edge sulfur atoms were synthesized according to

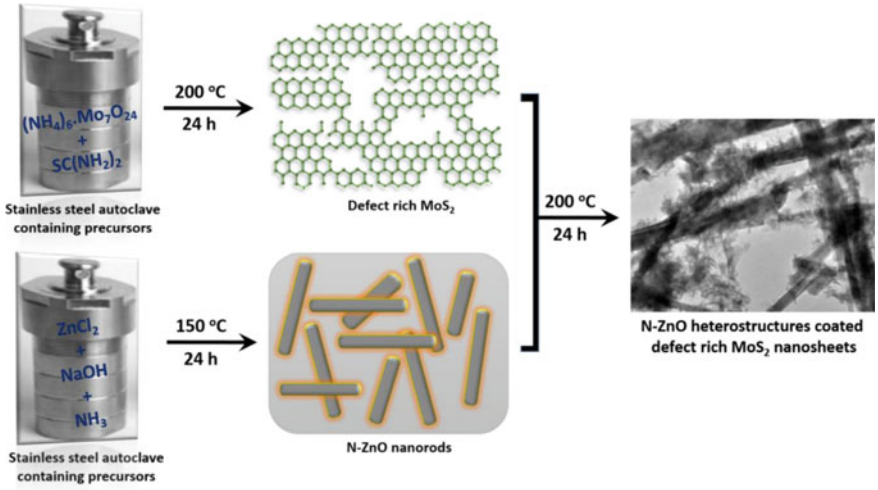


**Fig. 15** Illustration of the Procedure for the Fabrication of N-ZnO Nanorods Coated with Defect-Rich $MoS_2$ Nanosheets [161]

the scheme shown in Fig. 15 and were used to obtain hydrogen by irradiation with sunlight in [161]. The most optimal heterostructure consisting of 15 wt% $MoS_2$ nanosheets coated with N-ZnO demonstrates a hydrogen evolution rate of about 17.3 mmol/h when exposed to sunlight.

The enhanced rate of hydrogen evolution on $MoS_2$/ZnO heterostructures can be associated with a growth in the density of charge carriers. Therefore, it was noted that the ZnO/$MoS_x$ heterostructure shows an almost 7.4 times higher charge carrier density in contrast to pure ZnO [162]. The addition of reduced graphene oxide to the ZnO/$MoS_2$ heterostructure leads to an even greater increase in the efficiency of the hydrogen evolution process. A ternary heterostructure which contains nanoparticles of ZnO fixed on $MoS_2$-reduced graphene oxide (RGO) nanosheets shows a hydrogen evolution rate of 28.616 $mmol \cdot h^{-1} \cdot g_{cat}^{-1}$ under solar illumination, which is 56 times higher than the value of pure ZnO [163]. In this case, graphene provides a two-dimensional platform, which ensures the formation of $MoS_2$ heterojunctions and allows to receive and transfer photogenerated electrons to the reaction sites from the semiconductors at the course of photoelectrochemical hydrogen evolution, which increases the activity of the ZnO/$MoS_2$ heterostructure.

PbS is another narrow bandgap candidate for the production of a ZnO-based heterostructure with subsequent use for the photoelectrochemical method of water splitting. The addition of PbS results in improved absorption of the visible part of light spectrum. It is an essential way to optimize the photoelectrochemical functioning of ZnO. The ZnO/PbS photoanode demonstrates a significant increase in the photocurrent density, which is approximately ten times greater than that of pure ZnO nanocrystals [164]. The same high efficiency in the photoelectrochemical splitting of water is demonstrated by the ZnO/PbS heterostructure obtained by sequential

**Table 2** Activity values for ZnO-based heterostructures during the evolution of hydrogen

| No. | Heterostructure | Light source | $H_2$ evolved | References |
|---|---|---|---|---|
| 1 | ZnO/$MoS_2$ | Sunlight | 17,363 μmol $h^{-1}$ $g^{-1}{}_{cat}$ | Kumar et al. [161] |
| 2 | ZnO/$MoS_2$/RGO | Sunlight | 28,616 μmol $h^{-1}$ $g^{-1}{}_{cat}$ | Kumar et al. [163] |
| 3 | ZnO/PbS | UV light irradiation (254 nm) | 7.38 μmol $cm^{-2}$ $h^{-1}$ | Carrasco-Jaim et al. [169] |
| 4 | ZnO/CuS | Solar irradiation | 10,113.59 μmol·$g^{-1}$ $h^{-1}$ | Yendrapati et al. [170] |
| 5 | Ag2S/ZnO@ZnS | Visible light | 5870 μmol·$g^{-1}$ $h^{-1}$ | Hsu et al. [97] |

two-stage deposition of semiconductors [165]. The highest photocurrent density obtained at this electrode was ~13.6 mA/$cm^2$ (+1.0 V) compared to Ag/AgCl at sunlight illumination. A photoelectrode consisting of ZnO nanorods and being the core for a heterostructure with a shell of $Cu_2S$ nanoparticles sequentially located on the surface shows an increase in the absorption of sunlight [166]. The $Ag_2S$-based heterostructure has a narrow bandgap, e.g., ~0.9–1.05 eV. It showed high efficiency of sunlight conversion, it is supposed to be associated with the ability of $Ag_2S$ to facilitate the generation and injection of electrons and holes at the heterojunction boundary [167]. The attachment of nanosized particles to the ZnO surface leads to a boost in photoactivity, facilitating the transfer of charge carriers and suppressing the recombination process [168]. Table 2 shows the comparative characteristics of hydrogen evolution on various ZnO/metal chalcogenides heterostructures.

A comparison of the efficiency of hydrogen evolution during water decomposition using ZnO-based heterostructures and chalcogenides shows that hydrogen is evolved at a relatively high rate. The high activity of such heterostructures can be associated with the coating of ZnO in the form of various nanostructures with chalcogenides, which have a smaller bandgap and contribute to charge transfer and a lowering of recombination. Additionally, the activity is associated with the presence of active catalytic sites with many open unsaturated atoms of S at the edges and high affinity for $H^+$ ions. In turn, these ions are reduced by photogenerated electrons with the release of $H_2$ on the catalyst surface [161].

## 8 Conclusions and Future Perspectives

Metal oxides are often used for the photoelectrochemical water splitting when exposed to sunlight. However, their large bandgap, absorption of irradiation in a narrow spectral range, and fast rate of recombination of charge carriers significantly limit their use in the photoelectrochemical production of hydrogen. For this purpose, hybrid heterostructures based on ZnO and metal chalcogenides (sulfides, selenides,

and tellurides) have been studied for their use as effective materials for the photoelectrochemical water splitting upon irradiation with sunlight. To increase the efficiency of converting sunlight into photoelectrochemical hydrogen obtained by irradiation with sunlight and visible light, heterostructures are synthesized by combining materials to increase the active area and increase photocatalytic activity. Often, studies of semiconductor heterostructures based on ZnO and chalcogenides are aimed at reducing the bandgap and expanding the range of absorbed wavelengths towards near-infrared light. For this, various approaches are used, doping, or adding particles of metals, non-metals, and various semiconductors, which have low values of the bandgap. The mentioned processes allow to enhance the sensitivity and effectivity of photocatalysts to visible light. Over the past few years, a lot of research work was done to obtain heterostructures with different morphologies using various technologies to increase the efficiency of photoelectrochemical water splitting.

There are still problems associated with resistance to photocorrosion, long-term stability in hydrogen production, increased rate of charge transfers across the interface of heterostructures, and broadening of the absorption spectrum of daylight. Therefore, obtaining heterostructures with many active centers using various combined methods is a promising task. In addition, attention should be paid to the creation of ternary heterostructures in combination with new materials to avoid the recombination processes of charge carriers. To date, the question of the interfacial interaction between ZnO-based heterostructures and metal chalcogenides remains practically unexplored. Understanding the processes of interfacial interaction will allow the development of heterostructures with better photoelectrochemical characteristics. Another important task is to increase the efficiency of conversion of sunlight to photoelectrochemical hydrogen (more than 15–20%), which would retain their efficiency over a long period of operation. In this aspect, ternary heterostructures using nanostructured carbon-based materials can play a main role.

## References

1. Xu Y, Zhang B (2019) Recent advances in electrochemical hydrogen production from water assisted by alternative oxidation reactions. ChemElectroChem 6:3214–3226
2. Wang M, Chen L, Sun L (2012) Recent progress in electrochemical hydrogen production with earth-abundant metal complexes as catalysts. Energy Environ Sci 5:6763–6778
3. Chen Z, Wei W, Ni BJ (2021) Cost-effective catalysts for renewable hydrogen production via electrochemical water splitting: recent advances. Curr Opin Green Sustain Chem 27:100398
4. Mohd Shah NRA et al (2021) Current progress on 3D graphene-based photocatalysts: from synthesis to photocatalytic hydrogen production. Int J Hydrogen Energy 46:9324–9340
5. Yang Y et al (2021) Recent advances in application of transition metal phosphides for photocatalytic hydrogen production. Chem Eng J 405:126547
6. Kumaravel V, Mathew S, Bartlett J, Pillai SC (2019) Photocatalytic hydrogen production using metal doped TiO2: a review of recent advances. Appl Catal B Environ 244:1021–1064
7. Corredor J, Rivero MJ, Rangel CM, Gloaguen F, Ortiz I (2019) Comprehensive review and future perspectives on the photocatalytic hydrogen production. J Chem Technol Biotechnol 94:3049–3063

8. Sarkar J, Bhattacharyya S (2012) Application of graphene and graphene-based materials in clean energy-related devices Minghui. Arch Thermodyn 33:23–40
9. Ahmed M, Dincer I (2019) A review on photoelectrochemical hydrogen production systems: challenges and future directions. Int J Hydrogen Energy 44:2474–2507
10. Aydin MI, Karaca AE, Qureshy AMMI, Dincer I (2021) A comparative review on clean hydrogen production from wastewaters. J Environ Manage 279:111793
11. Siavash Moakhar R et al (2021) Photoelectrochemical water-splitting using CuO-based electrodes for hydrogen production: a review. Adv Mater 33
12. Tournet J, Lee Y, Karuturi SK, Tan HH, Jagadish C (2020) III–V Semiconductor materials for solar hydrogen production: status and prospects. ACS Energy Lett 5:611–622
13. Hisatomi T, Domen K (2019) Reaction systems for solar hydrogen production via water splitting with particulate semiconductor photocatalysts. Nat Catal 2:387–399
14. Alexander BD, Kulesza PJ, Rutkowska I, Solarska R, Augustynski J (2008) Metal oxide photoanodes for solar hydrogen production. J Mater Chem 18:2298–2303
15. Liao CH, Huang CW, Wu JCS (2012) Hydrogen production from semiconductor-based photocatalysis via water splitting. Catalysts 2:490–516
16. Zhang K, Guo L (2013) Metal sulphide semiconductors for photocatalytic hydrogen production. Catal Sci Technol 3:1672–1690
17. Tahir MB et al (2020) Recent advances on photocatalytic nanomaterials for hydrogen energy evolution in sustainable environment. Int J Environ Analyt Chem 101:2016–2034.https://doi.org/10.1080/03067319.2019.1691188
18. El Nazer HA, Mohamed YMA (2021) Chalcogenide-based nanomaterials as photocatalysts for water splitting and hydrogen production. Chalcogenide-Based Nanomater Photocatal 173–183 https://doi.org/10.1016/B978-0-12-820498-6.00007-X
19. Saraswat SK, Rodene DD, Gupta RB (2018) Recent advancements in semiconductor materials for photoelectrochemical water splitting for hydrogen production using visible light. Renew Sustain Energy Rev 89:228–248
20. Reddy CV et al (2020) Hetero-nanostructured metal oxide-based hybrid photocatalysts for enhanced photoelectrochemical water splitting—a review. Int J Hydrogen Energy 45:18331–18347
21. Desai MA, Vyas AN, Saratale GD, Sartale SD (2019) Zinc oxide superstructures: recent synthesis approaches and application for hydrogen production via photoelectrochemical water splitting. Int J Hydrogen Energy 44:2091–2127
22. Altaf CT et al (2020) Highly efficient 3D-ZnO nanosheet photoelectrodes for solar-driven water splitting: chalcogenide nanoparticle sensitization and mathematical modeling. J Alloys Compd 828:154472
23. Ong CB, Ng LY, Mohammad AW (2018) A review of ZnO nanoparticles as solar photocatalysts: synthesis, mechanisms and applications. Renew Sustain Energy Rev 81:536–551
24. Zhang X et al (2019) Fabrication of 3-D ZnO/CN nanorods for photo-/electrocatalytic water splitting: an efficient morphology for charge carriers transportation. Int J Hydrogen Energy 44:21821–21836
25. Sreedhar A, Neelakanta Reddy I, Ta QTH, Namgung G, Noh JS (2019) Plasmonic Ag nanowires sensitized ZnO flake-like structures as a potential photoanode material for enhanced visible light water splitting activity. J Electroanal Chem 832:426–435
26. Abdullayeva N et al (2019) Investigation of strain effects on photoelectrochemical performance of flexible ZnO electrodes. Sci Rep 9:1–14
27. Barreca D et al (2017) Vapor phase fabrication of nanoheterostructures based on ZnO for photoelectrochemical water splitting. Adv Mater Interfaces 4:1–9
28. Desai MA, Vyas AN, Saratale GD, Sartale SD (2019) Zinc oxide superstructures: recent synthesis approaches and application for hydrogen production via photoelectrochemical water splitting. Int J Hydrogen Energy 2091–2127. https://doi.org/10.1016/j.ijhydene.2018.08.042
29. Lu X, Liu Z (2017) Efficient all p-type heterojunction photocathodes for photoelectrochemical water splitting. Dalt Trans 46:7351–7360

30. Eftekhari A, Babu VJ, Ramakrishna S (2017) Photoelectrode nanomaterials for photoelectrochemical water splitting. Int J Hydrogen Energy 42:11078–11109
31. Fujishima A, Honda K (1972) Electrochemical photolysis of water at a semiconductor electrode. Nature 238(5358):37–38
32. Lu Q, Yu Y, Ma Q, Chen B, Zhang H (2016) 2D transition-metal-dichalcogenide-nanosheet-based composites for photocatalytic and electrocatalytic hydrogen evolution reactions. Adv Mater 28:1917–1933
33. Qu Y, Duan X (2013) Progress, challenge and perspective of heterogeneous photocatalysts. Chem Soc Rev 42:2568–2580
34. Ma M et al (2020) Engineering the photoelectrochemical behaviors of ZnO for efficient solar water splitting. J Semicond 41:091702. https://doi.org/10.1088/1674-4926/41/9/091702
35. Ma S, Xue J, Zhou Y, Zhang Z (2014) Photochemical synthesis of ZnO/Ag2O heterostructures with enhanced ultraviolet and visible photocatalytic activity. J Mater Chem A 2:7272–7280
36. Rai SC et al (2015) Piezo-phototronic effect enhanced UV/visible photodetector based on fully wide band gap type-II ZnO/ZnS core/shell nanowire array. ACS Nano 9:6419–6427
37. Chen YC et al (2015) ZnO-graphene composites as practical photocatalysts for gaseous acetaldehyde degradation and electrolytic water oxidation. Appl Catal A Gen 490:1–9
38. Wang T, Lv R, Zhang P, Li C, Gong J (2015) Au nanoparticle sensitized ZnO nanopencil arrays for photoelectrochemical water splitting. Nanoscale 7:77–81
39. Shao M, Ning F, Wei M, Evans DG, Duan X (2014) Hierarchical nanowire arrays based on ZnO core-layered double hydroxide shell for largely enhanced photoelectrochemical water splitting. Adv Funct Mater 24:580–586
40. Patel PP et al (2015) Nitrogen and cobalt co-doped zinc oxide nanowires—viable photoanodes for hydrogen generation via photoelectrochemical water splitting. J Power Sources 299:11–24
41. Kargar A et al (2013) ZnO/CuO heterojunction branched nanowires for photoelectrochemical hydrogen generation. ACS Nano 7:11112–11120
42. Kim JK et al (2015) Nano carbon conformal coating strategy for enhanced photoelectrochemical responses and long-term stability of ZnO quantum dots. Nano Energy 13:258–266
43. Chandrasekaran S, Chung JS, Kim EJ, Hur SH (2016) Exploring complex structural evolution of graphene oxide/ZnO triangles and its impact on photoelectrochemical water splitting. Chem Eng J 290:465–476
44. Guo CX, Dong Y, Yang HB, Li CM (2013) Graphene quantum dots as a green sensitizer to functionalize ZnO nanowire arrays on F-doped SnO2 glass for enhanced photoelectrochemical water splitting. Adv Energy Mater 3:997–1003
45. Zong X et al (2013) Activation of photocatalytic water oxidation on N-doped ZnO bundle-like nanoparticles under visible light. J Phys Chem C 117:4937–4942
46. Barreca D et al (2017) Vapor phase fabrication of nanoheterostructures based on ZnO for photoelectrochemical water splitting. Adv Mater Interfaces 4:1700161
47. Liu C et al (2017) Electrodeposition of ZnO nanoflake-based photoanode sensitized by carbon quantum dots for photoelectrochemical water oxidation. Ceram Int 43:5329–5333
48. Li C et al (2015) 3D ZnO/Au/CdS sandwich structured inverse opal as photoelectrochemical anode with improved performance. Adv Mater Interfaces 2. https://doi.org/10.1002/admi.201500428
49. Li Y et al (2012) ZnO/CuInS2 core/shell heterojunction nanoarray for photoelectrochemical water splitting. Int J Hydrogen Energy 37:15029–15037
50. Wang M et al (2015) Construction of FeS2-sensitized ZnO@ZnS nanorod arrays with enhanced optical and photoresponse performances. Adv Mater Interfaces 2:1500163
51. Qiu Y et al (2019) Current progress in developing metal oxide nanoarrays-based photoanodes for photoelectrochemical water splitting. Sci Bull 64:1348–1380
52. Tian W et al (2013) Low-cost fully transparent ultraviolet photodetectors based on electrospun ZnO-SnO2 heterojunction nanofibers. Adv Mater 25:4625–4630
53. Kurnia F, Hart JN (2015) Band-gap control of zinc sulfide: towards an efficient visible-light-sensitive photocatalyst. ChemPhysChem 16:2397–2402

54. D'Amico P, Calzolari A, Ruini A, Catellani A (2017) New energy with ZnS: novel applications for a standard transparent compound. Sci Rep 7:1–9
55. Schrier J, Demchenko DO, Wang LW, Alivisatos AP (2007) Optical properties of ZnO/ZnS and ZnO/ZnTe heterostructures for photovoltaic applications. Nano Lett 7:2377–2382
56. Jiang J, Wang M, Ma L, Chen Q, Guo L (2013) Synthesis of uniform ZnO/ZnS/CdS nanorod films with ion-exchange approach and photoelectrochemical performances. Int J Hydrogen Energy 38:13077–13083
57. Ye HY et al (2018) Germanene on single-layer ZnSe substrate: Novel electronic and optical properties. Phys Chem Chem Phys 20:16067–16076
58. Zaari H, Boujnah M, El Hachimi A, Benyoussef A, El Kenz A (2014) Optical properties of ZnTe doped with transition metals (Ti, Cr and Mn). Opt Quantum Electron 46:75–86
59. Wei SH, Zhang SB, Zunger A (2000) First-principles calculation of band offsets, optical bowings, and defects in CdS, CdSe, CdTe, and their alloys. J Appl Phys 87:1304–1311
60. Yeon DH, Lee SM, Jo YH, Moon J, Cho YS (2014) Origin of the enhanced photovoltaic characteristics of PbS thin film solar cells processed at near room temperature. J Mater Chem A 2:20112–20117
61. Miller EM et al (2016) Revisiting the valence and conduction band size dependence of PbS quantum dot thin films. ACS Nano 10:3302–3311
62. Dolui K, Rungger I, Sanvito S (2013) Origin of the n-type and p-type conductivity of MoS2 monolayers on a SiO2 substrate. Phys Rev B—Condens Matter Mater Phys 87:1–7
63. Hu Y et al (2015) Large-scale patterned ZnO nanorod arrays for efficient photoelectrochemical water splitting. Appl Surf Sci 339:122–127
64. Hernández-Gordillo A, Tzompantzi F, Gómez R (2012) An efficient ZnS-UV photocatalysts generated in situ from ZnS(en) 0.5 hybrid during the H 2 production in methanol-water solution. Int J Hydrogen Energy 37:17002–17008
65. Zhang J et al (2013) Enhanced photocatalytic hydrogen production activities of Au-loaded ZnS flowers. ACS Appl Mater Interfaces 5:1031–1037
66. Wu A et al (2015) ZnO-dotted porous ZnS cluster microspheres for high efficient, Pt-free photocatalytic hydrogen evolution. Sci Rep 5:1–9
67. Sang HX, Wang XT, Fan CC, Wang F (2012) Enhanced photocatalytic H2 production from glycerol solution over ZnO/ZnS core/shell nanorods prepared by a low temperature route. Int J Hydrogen Energy 37:1348–1355
68. Wang Z, Cao SW, Loo SCJ, Xue C (2013) Nanoparticle heterojunctions in ZnS-ZnO hybrid nanowires for visible-light-driven photocatalytic hydrogen generation. CrystEngComm 15:5688–5693
69. Gu X, Zhang S, Zhao Y, Qiang Y (2015) Band alignment of ZnO/ZnS heterojunction prepared through magnetron sputtering and measured by X-ray photoelectron spectroscopy. Vacuum 122:6–11
70. Wang L et al (2018) Preparation of ZnO/ZnS thin films for enhancing the photoelectrochemical performance of ZnO. Vacuum 148:201–205
71. Kushwaha A, Aslam M (2014) ZnS shielded ZnO nanowire photoanodes for efficient water splitting. Electrochim Acta 130:222–231
72. Zhang X et al (2018) ZnO nanosheets with atomically thin ZnS overlayers for photocatalytic water splitting. J Mater Chem A 6:9057–9063
73. Zhao H et al (2015) Facile preparation of a ZnS/ZnO nanocomposite for robust sunlight photocatalytic H2 evolution from water. RSC Adv 5:6494–6500
74. Wei C et al (2019) Enhanced photoelectrochemical activities of ZnO nanorod arrays after a modification of ZnS or ZnIn2S4. J Electron Mater 48:7345–7351
75. Hassan MA et al (2020) Single-step fabrication of 3D hierarchical ZnO/ZnS heterojunction branched nanowires by MOCVD for enhanced photoelectrochemical water splitting. J Mater Chem A 8:8300–8312
76. Liu C et al (2017) Design of core–shell-structured ZnO/ZnS hybridized with graphite-like C3N4 for highly efficient photoelectrochemical water splitting. Adv Mater Interfaces 4:1–11

77. Gao X, Wang J, Yu J, Xu H (2015) Novel ZnO-ZnS nanowire arrays with heterostructures and enhanced photocatalytic properties. CrystEngComm 17:6328–6337
78. Chen HM et al (2011) A new approach to solar hydrogen production: a ZnO-ZnS solid solution nanowire array photoanode. Adv Energy Mater 1:742–747
79. Piña-Pérez Y et al (2018) Novel ZnS-ZnO composite synthesized by the solvothermal method through the partial sulfidation of ZnO for H2 production without sacrificial agent. Appl Catal B Environ 230:125–134
80. Sánchez-Tovar R, Fernández-Domene RM, Montañés MT, Sanz-Marco A, Garcia-Antón J (2016) ZnO/ZnS heterostructures for hydrogen production by photoelectrochemical water splitting. RSC Adv 6:30425–30435
81. Brayek A et al (2018) The structural and the photoelectrochemical properties of ZnO-ZnS/ITO 1D hetero-junctions prepared by tandem electrodeposition and surface sulfidation: on the material processing limits. RSC Adv 8:11785–11798
82. Cheon SY et al (2017) Sonochemical synthesis of ZnO-ZnS core-shell nanorods for enhanced photoelectrochemical water oxidation. J Am Ceram Soc 100:3825–3834
83. Hassan MA, Johar MA, Waseem A, Bagal IV, Ha JS, Ryu SW (2019) Type-II ZnO/ZnS core-shell nanowires: earth-abundant photoanode for solar-driven photoelectrochemical water splitting. Optics Express 27:184–196
84. Kim H, Oh MH, Yang BL (2020) Photocorrosion of polyaniline-ZnS–ZnO photoelectrode for water splitting. Thin Solid Films 693:137678
85. Liu Y et al (2015) Design of sandwich-structured ZnO/ZnS/Au photoanode for enhanced efficiency of photoelectrochemical water splitting. Nano Res 8:2891–2900
86. Ma D et al (2019) Au decorated hollow ZnO@ZnS heterostructure for enhanced photocatalytic hydrogen evolution: the insight into the roles of hollow channel and Au nanoparticles. Appl Catal B Environ 244:748–757
87. Chang CJ, Huang KL, Chen JK, Chu KW, Hsu MH (2015) Improved photocatalytic hydrogen production of ZnO/ZnS based photocatalysts by Ce doping. J Taiwan Inst Chem Eng 55:82–89
88. Madhusudan P et al (2019) Nature inspired ZnO/ZnS nanobranch-like composites, decorated with Cu(OH)2 clusters for enhanced visible-light photocatalytic hydrogen evolution. Appl Catal B Environ 253:379–390
89. Sun D et al (2020) CdS/ZnS/ZnO ternary heterostructure nanofibers fabricated by electrospinning for excellent photocatalytic hydrogen evolution without co-catalyst. Chin J Catal 41:1421–1429
90. Li C, Chen S, Wang Y, Hou Z (2019) ZnO/ZnS heterostructures grown on Zn foil substrate by hydrothermal method for photoelectrochemical water splitting. Int J Hydrogen Energy 44:25416–25427
91. Zhang R et al (2017) Macroporous ZnO/ZnS/CdS composite spheres as efficient and stable photocatalysts for solar-driven hydrogen generation. J Mater Sci 52:11124–11134
92. Yu YX, Ouyang WX, Liao ZT, Du BB, Zhang WD (2014) Construction of ZnO/ZnS/CdS/CuInS2 core-shell nanowire arrays via ion exchange: P-n junction photoanode with enhanced photoelectrochemical activity under visible light. ACS Appl Mater Interfaces 6:8467–8474
93. Liu Z et al (2014) Preparation of cauliflower-like CdS/ZnS/ZnO nanostructure and its photoelectric properties. J Nanoparticle Res 16
94. Han J et al (2014) Synthesis of metal sulfide sensitized zinc oxide-based core/shell/shell nanorods and their photoelectrochemical properties. J Power Sources 268:388–396
95. Zhang Y et al (2016) Facile preparation of one dimension ZnO/chalcogenide semiconductor heterostructure for efficient photoelectrochemical water splitting. J Alloys Compd 685:581–586
96. Yadian B et al (2017) Metal-sulfide-decorated ZnO/Si nano-heterostructure arrays with enhanced photoelectrochemical performance. Mater Res Bull 96:503–508
97. Hsu MH, Chang CJ, Weng HT (2016) Efficient H2 production using Ag2S-coupled ZnO@ZnS core-shell nanorods decorated metal wire mesh as an immobilized hierarchical photocatalyst. ACS Sustain Chem Eng 4:1381–1391

98. Ranjith KS et al (2020) Promotional effect of Cu 2 S-ZnS nanograins as a shell layer on ZnO nanorod arrays for boosting visible light photocatalytic H 2 evolution. J Phys Chem C 124:3610–3620
99. Zhou J et al (2018) Cellular heterojunctions fabricated through the sulfurization of MOFs onto ZnO for high-efficient photoelectrochemical water oxidation. Appl Catal B Environ 226:421–428
100. Wu LP, Zhang YL, Long LZ, Cen CP, Li XJ (2014) Effect of ZnS buffer layers in ZnO/ZnS/CdS nanorod array photoelectrode on the photoelectrochemical performance. RSC Adv 4:20716–20721
101. Chang CJ, Lin YG, Weng HT, Wei YH (2018) Photocatalytic hydrogen production from glycerol solution at room temperature by ZnO-ZnS/graphene photocatalysts. Appl Surf Sci 451:198–206
102. Castañeda C, Tzompantzi F, Rodríguez-Rodríguez A, Sánchez-Dominguez M, Gómez R (2018) Improved photocatalytic hydrogen production from methanol/water solution using CuO supported on fluorinated TiO2. J Chem Technol Biotechnol 93:1113–1120
103. Zhang Q, Li H, Ma Y, Zhai T (2016) ZnSe nanostructures: synthesis, properties and applications. Prog Mater Sci 83:472–535
104. Thirumavalavan S, Mani K, Sagadevan S (2016) A study of structural, morphological, optical and electrical properties of Zinc Selenide (ZnSe) thin film. Mater Today Proc 3:2305–2314
105. Chen Y, Wang L, Wang W, Cao M (2017) Synthesis of Se-doped ZnO nanoplates with enhanced photoelectrochemical and photocatalytic properties. Mater Chem Phys 199:416–423
106. Huang HC, Yang CL, Wang MS, Ma XG (2018) Optical absorption enhancement of Hg-doped ZnX (X= S, Se) for hydrogen production from water splitting driven by solar energy. Vacuum 157:36–44
107. Gu Y et al (2019) Inverted ZnSe/CdSe core-shell nanobelts with type-I behavior: preparation, photoelectrochemical and photocatalytic performances. CrystEngComm 21:5482–5491
108. Kuehnel MF et al (2019) ZnSe nanorods as visible-light absorbers for photocatalytic and photoelectrochemical H 2 evolution in water. Angew Chemie 131:5113–5117
109. Ren C et al (2020) ZnSe nanoparticles with bulk WC as cocatalyst: a novel and noble-metal-free heterojunction photocatalyst for enhancing photocatalytic hydrogen evolution under visible light irradiation. Appl Mater Today 20:100731
110. Tian P et al (2020) High photocatalytic and photoelectrochemical performance of a novel 0D/2D heterojunction photocatalyst constructed by ZnSe nanoparticles and MoSe2 nanoflowers. Ceram Int 46:13651–13659
111. Liu S et al (2016) ZnSe sensitized and Co-Pi catalyzed TiO 2 nanowire array photoanode for solar-driven water splitting. J Electrochem Soc 163:H744–H749
112. Sun C, Gu Y, Wen W, Zhao L (2018) ZnSe based semiconductor core-shell structures: from preparation to application. Opt Mater (Amst) 81:12–22
113. Wang W et al (2015) Ultrawide photoresponse in ZnO/ZnSe coaxial nanowires with a threshold of 0.8 eV. Int J Hydrogen Energy 40:10788–10794
114. Zhang J et al (2020) Excellent photoelectrochemical hydrogen evolution performance of FeSe2 nanorod/ZnSe 0D/1D heterostructure as efficiency carriers migrate channel. Int J Hydrogen Energy 45:8526–8539
115. Hewa-Kasakarage NN et al (2009) Radiative recombination of spatially extended excitons in (ZnSe/CdS)/CdS heterostructured nanorods. J Am Chem Soc 131:1328–1334
116. Hewa-Kasakarage NN et al (2010) Ultrafast carrier dynamics in type II ZnSe/CdS/ZnSe nanobarbells. ACS Nano 4:1837–1844
117. Verma S, Kaniyankandy S, Ghosh HN (2013) Charge separation by indirect bandgap transitions in CdS/ZnSe type-II core/shell quantum dots. J Phys Chem C 117:10901–10908
118. Zhang Y et al (2012) ZnO/ZnSe type II core-shell nanowire array solar cell. Sol Energy Mater Sol Cells 102:15–18
119. Ghoul M et al (2015) Synthesis of core/shell ZnO/ZnSe nanowires using novel low cost two-steps electrochemical deposition technique. J Alloys Compd 647:660–664

120. Kozytskiy AV, Stroyuk OL, Kuchmiy SY (2014) Inorganic photoelectrochemical solar cells based on nanocrystalline ZnO/ZnSe and ZnO/CuSe heterostructures. Catal Today 230:227–233
121. Cho S et al (2011) Three-dimensional type II ZnO/ZnSe heterostructures and their visible light photocatalytic activities. Langmuir 27:10243–10250
122. Cho S et al (2011) Solution-based fabrication of ZnO/ZnSe heterostructure nanowire arrays for solar energy conversion. J Mater Chem 21:17816–17822
123. Wang L, Tian G, Chen Y, Xiao Y, Fu H (2016) In situ formation of a ZnO/ZnSe nanonail array as a photoelectrode for enhanced photoelectrochemical water oxidation performance. Nanoscale 8:9366–9375
124. Hong T et al (2015) Preparation and enhanced photoelectrochemical performance of selenite-sensitized zinc oxide core/shell composite structure. J Mater Chem A 3:4239–4247
125. Ouyang WX, Yu YX, Zhang WD (2015) High and stable photoelectrochemical activity of ZnO/ZnSe/CdSe/CuxS core-shell nanowire arrays: nanoporous surface with CuxS as a hole mediator. Phys Chem Chem Phys **17**:14827–14835
126. Chen Y, Wang L, Wang W, Cao M (2017) Enhanced photoelectrochemical properties of ZnO/ZnSe/CdSe/Cu2-xSe core–shell nanowire arrays fabricated by ion-replacement method. Appl Catal B Environ 209:110–117
127. Zeng Y et al (2019) ZnxCd1-xSe nanoparticles decorated ordered mesoporous ZnO inverse opal with binder-free heterojunction interfaces for highly efficient photoelectrochemical water splitting. Appl Catal B Environ 245:469–476
128. Li C et al (2020) Enhanced photoelectrochemical performance based on conformal and uniform ZnO/ZnSe/CdSe heterostructures on Zn foil substrate. Int J Hydrogen Energy 45:8257–8272
129. Xu H et al (2014) ZnSe/CdS/CdSe triple-sensitized ZnO nanowire arrays for multi-bandgap photoelectrochemical hydrogen generation. RSC Adv 4:47429–47435
130. Zhang L et al (2017) Scalable low-band-gap Sb2Se3 thin-film photocathodes for efficient visible-near-infrared solar hydrogen evolution. ACS Nano 11:12753–12763
131. Xiong X, Forster M, Major JD, Xu Y, Cowan AJ (2017) Time-resolved spectroscopy of ZnTe photocathodes for solar fuel production. J Phys Chem C 121:22073–22080
132. Jang YJ, Lee J, Lee J, Lee JS (2016) Solar hydrogen production from zinc telluride photocathode modified with carbon and molybdenum sulfide. ACS Appl Mater Interfaces 8:7748–7755
133. Zhan X et al (2014) Composition-tuned ZnO/ZnxCd1-xTe core/shell nanowires array with broad spectral absorption from UV to NIR for hydrogen generation. ACS Appl Mater Interfaces 6:2878–2883
134. Xu F et al (2012) Synthesis of ZnO/CdS hierarchical heterostructure with enhanced photocatalytic efficiency under nature sunlight. CrystEngComm 14:3615–3622
135. Kundu P, Deshpande PA, Madras G, Ravishankar N (2011) Nanoscale ZnO/CdS heterostructures with engineered interfaces for high photocatalytic activity under solar radiation. J Mater Chem 21:4209–4216
136. Ding M et al (2016) ZnO@CdS core-shell heterostructures: fabrication, enhanced photocatalytic, and photoelectrochemical performance. Nanoscale Res Lett 11:205
137. Xu S et al (2020) Construction of ZnO/CdS three-dimensional hierarchical photoelectrode for improved photoelectrochemical performance. Renew Energy 153:241–248
138. Ma D et al (2017) Highly efficient photocatalyst based on a CdS quantum dots/ZnO nanosheets 0D/2D heterojunction for hydrogen evolution from water splitting. ACS Appl Mater Interfaces 9:25377–25386
139. Lin CJ, Kao LC, Huang Y, Bañares MA, Liou SYH (2015) Uniform deposition of coupled CdS and CdSe quantum dots on ZnO nanorod arrays as electrodes for photoelectrochemical solar water splitting. Int J Hydrogen Energy 40:1388–1393
140. Zhao H et al (2015) Light-assisted preparation of a ZnO/CdS nanocomposite for enhanced photocatalytic H2 evolution: an insight into importance of in situ generated ZnS. ACS Sustain Chem Eng 3:969–977

141. Kim YG, Jo WK (2017) Photodeposited-metal/CdS/ZnO heterostructures for solar photocatalytic hydrogen production under different conditions. Int J Hydrogen Energy 42:11356–11363
142. Chen W et al (2018) CdCl2-assisting heat-treatment: enhanced photoelectrocatalytic hydrogen generation and stability of CdS/ZnO nanoheterojunction arrays. Int J Hydrogen Energy 43:9969–9977
143. Bak D, Kim JH (2017) Facile fabrication of pseudo-microspherical ZnO/CdS core-shell photocatalysts for solar hydrogen production by water splitting. Ceram Int 43:13493–13499
144. Myung Y et al (2010) Composition-tuned ZnO-CdSSe core-shell nanowire arrays. ACS Nano 4:3789–3800
145. Chen J et al (2018) Fabricating sandwich-shelled ZnCdS/ZnO/ZnCdS dodecahedral cages with "one stone" as Z-scheme photocatalysts for highly efficient hydrogen production. J. Mater. Chem. A 6:19631–19642
146. Wang R et al (2019) ZnO/CdS/PbS nanotube arrays with multi-heterojunctions for efficient visible-light-driven photoelectrochemical hydrogen evolution. Chem Eng J 362:658–666
147. Su RR, Yu YX, Xiao YH, Yang XF, Zhang WD (2018) Earth abundant ZnO/CdS/CuSbS2 core-shell nanowire arrays as highly efficient photoanode for hydrogen evolution. Int J Hydrogen Energy 43:6040–6048
148. Ye YQ et al (2019) 3D cross-linked BiOI decorated ZnO/CdS nanorod arrays: a cost-effective hydrogen evolution photoanode with high photoelectrocatalytic activity. Int J Hydrogen Energy 44:21865–21872
149. Liu ZQ et al (2013) Electrochemical synthesis of ZnO/CdTe core-shell nanotube arrays for enhanced photoelectrochemical properties. Electrochim Acta 98:268–273
150. Wang L et al (2019) Conductive polymer nanolayer modified one-dimensional ZnO/CdSe photoanode with enhanced photoelectrochemical properties by in-situ ions exchange method. Chem Eng J 368:710–718
151. Hou J et al (2016) High performance of Mn-doped CdSe quantum dot sensitized solar cells based on the vertical ZnO nanorod arrays. J Power Sources 325:438–445
152. Chen HM et al (2010) Quantum dot monolayer sensitized ZnO nanowire-array photoelectrodes: true efficiency for water splitting. Angew Chemie 122:6102–6105
153. Wang X et al (2010) Aligned ZnO/CdTe core−shell nanocable arrays on indium tin oxide: synthesis and photoelectrochemical properties. ACS nano 4:3302–3308
154. Holi AM et al (2018) Effect of heat treatment on photoelectrochemical performance of hydrothermally synthesised Ag2S/ZnO nanorods arrays. Chem Phys Lett 710:100–107
155. Shao YB, Wang LH, Huang JH (2016) ZnS/CuS nanotubes for visible light-driven photocatalytic hydrogen generation. RSC Adv 6:84493–84499
156. Yang X et al (2014) Synthesis of porous ZnS:Ag2S nanosheets by ion exchange for photocatalytic H2 generation. ACS Appl Mater Interfaces 6:9078–9084
157. Li Y et al (2011) MoS2 nanoparticles grown on graphene: an advanced catalyst for the hydrogen evolution reaction. J Am Chem Soc 133:7296–7299
158. Paquin F, Rivnay J, Salleo A, Stingelin N, Silva C (2015) Significant enhancement in photocatalytic hydrogen evolution from water by MoS2 nanosheet-coated ZnO heterostructure photocatalyst. Dalt Trans 44:10715–10722
159. Guo S, Li X, Zhu J, Tong T, Wei B (2016) Au NPs@MoS2 sub-micrometer sphere-ZnO nanorod hybrid structures for efficient photocatalytic hydrogen evolution with excellent stability. Small 12:5692–5701
160. Lamouchi A, Assaker IB, Chtourou R (2019) Enhanced photoelectrochemical activity of MoS 2 -decorated ZnO nanowires electrodeposited onto stainless steel mesh for hydrogen production. Appl Surf Sci 478:937–945
161. Kumar S et al (2019) Defect-rich MoS2 ultrathin nanosheets-coated nitrogen-doped ZnO nanorod heterostructures: an insight into in-situ-generated ZnS for enhanced photocatalytic hydrogen evolution. ACS Appl Energy Mater 2:5622–5634
162. Sharma MD, Mahala C, Basu M (2020) Sensitization of vertically grown ZnO 2D thin sheets by MoSx for efficient charge separation process towards photoelectrochemical water splitting reaction. Int J Hydrogen Energy 45:12272–12282

163. Kumar S et al (2017) Efficient electron transfer across a ZnO–MoS2–reduced graphene oxide heterojunction for enhanced sunlight-driven photocatalytic hydrogen evolution. Chemsuschem 10:3588–3603
164. Li X, Li J, Cui C, Liu Z, Niu Y (2016) PbS nanoparticle sensitized ZnO nanowire arrays to enhance photocurrent for water splitting. J Phys Chem C 120:4183–4188
165. Kumar D, Bai R, Chaudhary S, Pandya DK (2017) Enhanced photoelectrochemical response for hydrogen generation in self-assembled aligned ZnO/PbS core/shell nanorod arrays grown by chemical bath deposition. Mater Today Energy 6:105–114
166. Guo K, Chen X, Han J, Liu Z (2014) Synthesis of ZnO/Cu2S core/shell nanorods and their enhanced photoelectric performance. J Sol-Gel Sci Technol 72:92–99
167. Kumar S et al (2016) Fabrication of TiO2/CdS/Ag2S Nano-heterostructured photoanode for enhancing photoelectrochemical and photocatalytic activity under visible light. ChemistrySelect 1:4891–4900
168. Chen C et al (2016) Enhanced visible light photocatalytic performance of ZnO nanowires integrated with CdS and Ag2S. Dalt. Trans. 45:3750–3758
169. Carrasco-Jaim OA, Ceballos-Sanchez O, Torres-Martínez LM, Moctezuma E, Gómez-Solís C (2017) Synthesis and characterization of PbS/ZnO thin film for photocatalytic hydrogen production. J Photochem Photobiol A Chem 347:98–104
170. Yendrapati TP, Gautam A, Bojja S, Pal U (2020) Formation of ZnO@CuS nanorods for efficient photocatalytic hydrogen generation. Sol Energy 196:540–548

# Chapter 2
# Argon Ions Beam Irradiation of Copper Nanowires for Transparent Electrodes


**Shehla Honey, Kaviyarasu Kasinathan, Muhammad Ehsan Mazhar, Atif Rasool, Muhammad Arshad Kamran, Amjad Ali, Jamil Asim, and M. Maaza**

## 1 Introduction

Transparent Conducting Electrodes (TCEs) are major parts of optoelectronic devices such as solar cells and light emitting diodes (LEDs). TEs should be highly transparent and conductive to integrate in optoelectronic devices [1]. Until now, the most excellent TEs are indium tin oxides (ITO's), but major reasons for their demise are brittleness of ITO, high production costs and shortage of indium. Besides, it is difficult to keep safe the underneath substrates made up of organic material during depositing

S. Honey (✉) · A. Rasool · M. A. Kamran · A. Ali
Department of Physics, University of Okara, Okara, Pakistan
e-mail: shehlahoney@yahoo.com

S. Honey
Centre for Nanosciences, University of Okara, Okara, Pakistan

J. Asim
University of Okara, Okara, Pakistan

Faculty of Computer Science and Information Technology, Universiti Malaysia Sarawak, Kota Samarahan, Malaysia

S. Honey
NPU-NCP Joint International Research Center on Advanced Nanomaterials and Defects Engineering, Northwestern Polytechnical University, Xi'an 710072, China

M. E. Mazhar
Department of Physics, Bahuaddin Zakariya University, Multan, Pakistan

S. Honey · K. Kasinathan · M. Maaza
College of Graduate Studies, UNESCO-UNISA Africa Chair in Nanosciences/Nanotechnology, University of South Africa, Muckleneuk ridge, Pretoria, South Africa

Nanosciences African Network (NANOAFNET), iThemba LABS, National Research Foundation, Old Faure Road, Somerset West 7129, South Africa



K. Kasinathan et al. (eds.), *Nanomaterials for Energy Conversion, Biomedical and Environmental Applications*, Materials Horizons: From Nature to Nanomaterials,
https://doi.org/10.1007/978-981-19-2639-6_2

by sputtering [1–4]. The above-mentioned challenges of ITO's urge the scientific community to search for alternative materials which can replace ITOs from market. To replace ITO, many nanomaterials come on front line such as graphene, metallic nano-grids, metallic nanowires (MNWs) meshes and carbon nanotubes (CNTs) [5–7]. However, MNWs mesh-based TEs are mechanically flexible, having high aspect ratio and good physical properties which make them capable to replace ITO. Moreover, methods for deposition of MNWs meshes are trouble-free [8]. MNWs meshes can be deposited in the form of thin films using simple techniques, for example, rod coating [9–12], drop casting [13], spin coating and spray coating [14–17]. The most convenient and inexpensive method from all the deposition techniques is drop casting. Colloidal solutions can also be handled easily in depositing thin films of MNWs meshes by drop casting technique [18, 19]. To integrate MNWs meshes as TEs in optoelectronic devices, the major challenges are enhancement in optical transparency and electrical conductivity of the mesh. Recently, Argon ions beam irradiation technique were used in order to alter the properties of NTs/NWs [20]. In a previous report, properties of Ni NWs mesh have been altered using Argon ions beam irradiation technique [21]. Moreover, Ahmad et al. utilized beam of Argon ions to alter the properties of carbon nanotubes (CNT's) [22]. In the present work, copper nanowire (Cu NWs) meshes are coated on glass substrates in the form of thin film by an inexpensive drop casting method. Afterward, meshes of Cu NWs are irradiated by MeV $Ar^+$ ions beam for the first time to the best of our knowledge. The changes in optical and electrical properties are required for optoelectronic applications of Cu NWs meshes as TEs.

## *1.1 Ion Beam Irradiation on Materials*

The idea of ion beam irradiation is to collect beams of ions from a source and accelerate them at a specified voltage, which is usually between 50 and 250 keV, with a desired energy of up to 10 meV, before transferring and encroaching on the target or surface. The ions contact with the specimen surface because of the impingement, and some get lodged in the specimen while others scatter. Ion beam irradiation is a clever way to modify the surface of materials while keeping their bulk characteristics. Toughness, fatigue, wear, hardness, friction, dielectric, magnetic, electronic, resistive and superconducting characteristics may all be improved or degraded by ion beam irradiation process. These impacts are influenced by how the produced materials are used. Ceramics, insulators, semiconductors, metals, alloys and polymers are all good candidates for ion beam irradiation. The mass of the incoming ion to the specimen, the accelerating voltage utilized for the beam, the thermal characteristics of the point defects limiting the cascade area and the crystalline structure of the sample all have a role in the extent of the defect created in the materials. The creation of disordered lattice, which may be increased by low dose energy of heavy ions, is the most distinguishing property of ion beam irradiation of materials. Ion beam irradiations are frequently used in optical materials to generate luminescence to assess the purity and

point flaws in the material. In some crystal materials, the ion beam irradiation effect causes light. The brightness seen during ion beam placement in substances provides information on dynamic defect states due to transitory characteristics caused by the movement of difficult-to-excite ions. The flaws seen can subsequently be detected using ion beam-induced fluorescence, sharing information on the sample's intrinsic defect state's decay, impurities and progression [23].

## 2 Argon Ions Beam Irradiation of Copper Nanowires

To see the influence of $Ar^+$ ions on the properties of Cu NWs, experimental steps were performed and discussed in Sect. 2.1.

### *2.1 Experimental Procedure*

Cu NWs were supplied from Plasma Chem (Germany). The diameters of pristine Cu NWs were in the range 100–300 nm and lengths were 100–200 μm approximately. At first, the Cu NWs were received in the form of powder. The aqueous dispersion of Cu NWs in isopropanol solution was prepared from the powder form. 5 mg of Cu NWs powder was dissolved in one millilitre of isopropanol solution. Later, Cu NWs solution was deposited on glass substrates and copper grids using a drop casting method. These samples were irradiated with a 4 meV $Ar^+$ ions beam of different fluencies $1 \times 10^{14}$ ions/cm$^2$, $1 \times 10^{15}$ ions/cm$^2$, $1 \times 10^{16}$ ions/cm$^2$ and $1 \times 10^{17}$ ions/cm$^2$ in 5-UDH Pelletron Accelerator at room temperature. The ion implantation within lattices of Cu NWs during ion beam irradiation was examined through a SRIM computer simulation program [24]. Before and after irradiation, structure of Cu NWs was characterized through x-ray diffraction (XRD) and morphological analysis was done through transmission electron microscopy (TEM) techniques.

## 3 Results and Discussion

### *3.1 TEM Analysis of Argon Ions Irradiated Copper Nanowires*

Before and after irradiation by Argon ions, The Cu NWs were characterized through transmission electron microscopy (TEM) technique. The pristine Cu NWs are having diameters in the range of approximately 100–300 nm as can be observed in Fig. 1a representing the TEM image. Moreover, it is observed in HRTEM image of Fig. 1b that nature of Cu NWs is polycrystalline and poly crystallinity of materials is also

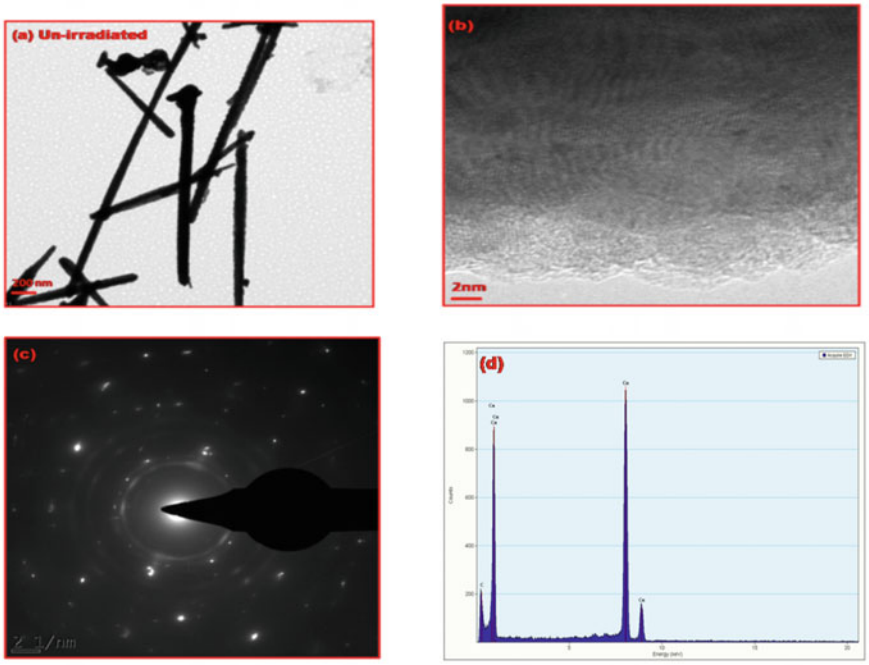


**Fig. 1** **a** TEM image of pristine Cu NWs mesh **b** HRTEM **c** SAED **d** EDX spectrum

verified through selected area electron diffraction (SAED) image and is shown in Fig. 1c. EDX spectrum of pristine Cu NWs network is shown in Fig. 1d, which shows the presence of trace elements Cu and C. Main trace element is Cu, whereas C might have appeared due to carbon coating during TEM analysis.

However, when Cu NWs are irradiated at a dose $1 \times 10^{14}$ ions/cm$^2$ of $Ar^+$ ions, the diameters of Cu NWs are reduced slightly, which can be seen in Fig. 2. Some nanowires relate to each other as appeared in Fig. 2. When the dose is further increased upto $1 \times 10^{15}$ ions/cm$^2$, diameters are not decreased significantly, but interconnections are improved as shown in TEM image of Fig. 3. Same findings have been observed in the case of high irradiation dose at $1 \times 10^{16}$ ions/cm$^2$ (see in Fig. 4). It is observed from TEM results that nanowires are not damaged or lose their shapes under irradiation in the range of doses $1 \times 10^{14}$ ions/cm$^2$ to $1 \times 10^{16}$ ions/cm$^2$. NWs were destroyed and lose their shapes when irradiated by high dose of Argon ions at $1 \times 10^{17}$ ions/cm$^2$ as shown in the TEM image of Fig. 5 where thinning and melting of NWs have been found.

The diameters of Cu NWs are reduced slightly after irradiation by Argon ions, which is due to the ejection of atoms from the surfaces of Cu NWs. Continuous hitting of Argon ions on surfaces of Cu NWs produces collision cascade effect in NWs and atoms will be ejected from surface of Cu NWs. There are two types of interactions between energetic ions and Cu NWs: elastic and inelastic collision. A

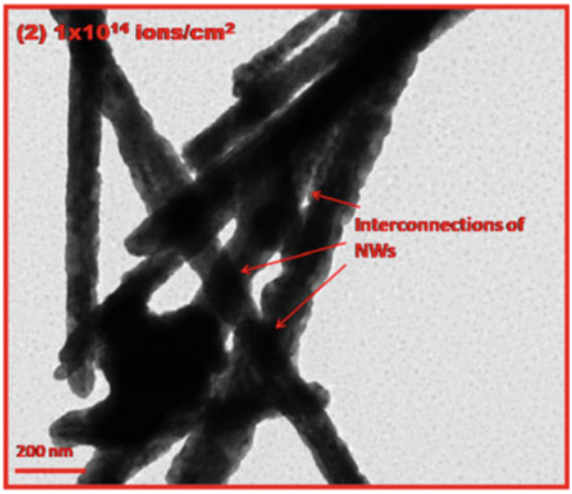


**Fig. 2** Cu NWs network irradiated at a dose of ~1 × $10^{14}$ ions/$cm^2$

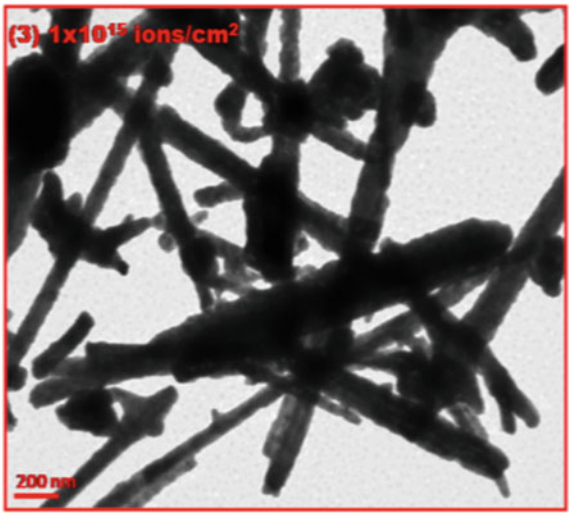


**Fig. 3** Cu NWs network irradiated at a dose of 1 × $10^{15}$ ions/$cm^2$

series of collisions will be produced after elastic collision between an energetic ion and Cu NWs, and the energetic ion lastly releases its kinetic energy. Consequently, series of collisions will generate a large string of recoiling atoms in Cu NWs and this process will carry on and is called collision cascade effect. During this process, some atoms will gain enough amount of energy that is sufficient to remove the atom from lattice; atoms finally gain this energy and ejected from lattice of NWs [25, 26]. If atoms removed from the surfaces are in huge amount, then diameters of Cu NWs will be lessened. If energetic ions of energies in keV range are interacting with NWs, then nuclear collision will occur dominantly and atoms will be removed due

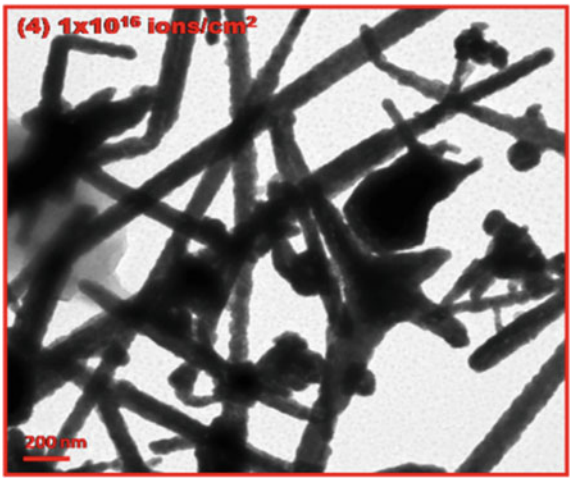


**Fig. 4** Cu NWs network irradiated at a dose of 1 × $10^{16}$ ions/cm$^2$

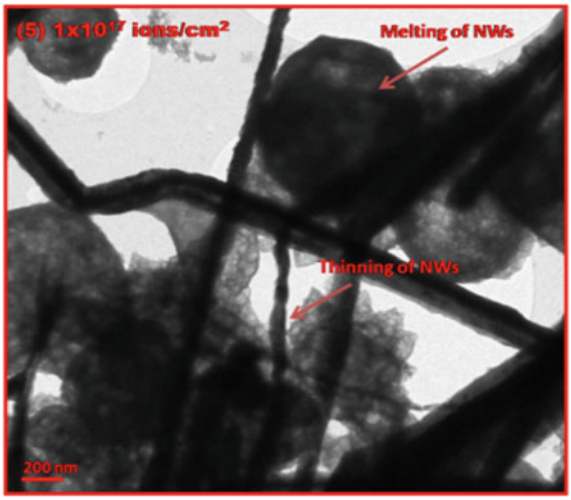


**Fig. 5** Cu NWs network irradiated at a dose of 1 × $10^{17}$ ions/cm$^2$

to collision cascade [27, 28]. This removal of atoms from surfaces of Cu NWs is verified because diameters of Cu NWs were decreased after irradiation. The kinetic energy will be transferred to electrons (electronic energy loss, *Se*) if energetic argon ions are fast moving ($\geq$ 0.11 meV) and due to which *Se* is playing an important role in transporting the atoms at joints between individual Cu NWs [28, 29]. A small fraction of kinetic energy of energetic ion will be lost due to columbic interaction with atomic electrons in case of inelastic collision between an energetic ions and atoms [30]. As per thermal spike model, the excited electrons remain in a thermodynamic equilibrium for the time interval $10^{-15}$ s and finally release their energy into the lattice for the time interval $10^{-13}$–$10^{-10}$ s. This energy will be deposited to Cu lattice

along ions track and produce localized heat spikes. Due to heat spikes, temperature along the path of ions and melting point of material may be increased significantly due to which a liquid melted zone of material is formed of small depth (few nm) at crossing regions between Cu NWs [29]. However, these heated zones of materials are momentary and soon ions track turns to cold resulting in accumulation of atoms at crossing positions. So, heat spikes are localized and increases with an increase in incident flux of ions causing Cu NWs to weld with each other [31]. Damage due to surplus ions beam irradiation can be avoided by selecting middle-range ion energies and fluencies in the medium range and temperature as room temperature. If beam fluence of ions is less, then less heat or defects will be produced during irradiation. Restructured surface atoms, vacancies or heat produced was insufficient to connect or making bond between nanowires. In case of high beam fluence, excessive power will destroy interface regions or internal structure of Cu NWs [28]. It is seen from the results that the above phenomenon are taking place at the same time within Cu NWs after ions beam irradiation. We will perform SRIM simulation to obtain verification of the heat production due to ionization and removal of surface atoms due to collision cascade effect.

## 3.2 *SRIM Analysis of Agron Ions Irradiated Copper Nanowires*

SRIM calculation was performed by selecting incident ions = 2500 and energy of Argon ions = 4 meV at incident angle 0°. Figure 6 shows the graphs of path of ions and collision events. SRIM results are shown in Table 1. Parameters for ions represent the loss of energy occurred due to ions in Cu, whereas parameters for recoils show energy losses that occurred because of recoiling of Cu atoms. Results in Table 1 show the contact of MeV Argon ions with Cu NWs producing both phenomena such as production of lattice defects and generation of heat.

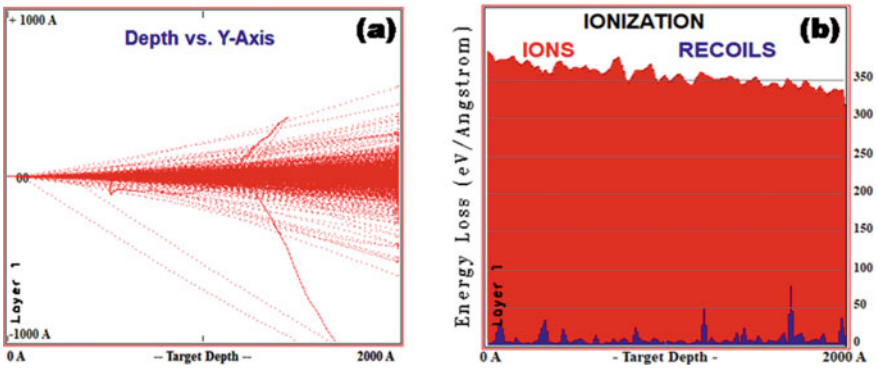


**Fig. 6** Graphs of SRIM simulation for the contact of MeV Argon ions with Cu material **a** depth versus Y-Axis (ions track) **b** events of collision

**Table 1** SRIM results of 4 meV Argon ions in Cu

| Ion | Total vacancies produced/ion | % Loss of energy due to ion | | % Loss of energy due to recoil atom | |
|---|---|---|---|---|---|
| | | Ionization | Phonons | Ionization | Phonons |
| Argon | 399.4 | 94.54 | 0.06 | 2.05 | 3.20 |

## *3.3 Structural Analysis of Argon Ions Irradiated Copper Nanowires*

After irradiating Cu NWs by different fluencies of Argon ions, structural alterations are analyzed by x-ray diffraction (XRD). XRD was performed to observe structural stability of Cu NWs during and after ions beam irradiation. XRD results of Fig. 7 demonstrates that the un-irradiated Cu NWs show 2θ peaks corresponding to planes (111) and (200) of cubic structure. After irradiation by fluencies of Argon ions $1 \times 10^{14}$, $1 \times 10^{15}$ and $1 \times 10^{16}$ ions/cm$^2$, crystalline structure of NWs is remained unaffected. However, after irradiation by the first two beam fluencies, intensities of XRD peaks are observed to be increased which shows the improvement in crystallinity of material. Thereafter, the intensity of XRD peaks was decreased after irradiating by beam fluence $1 \times 10^{17}$ ions/cm$^2$ which indicates the destruction of the structure of NWs at this dose and can be seen in the spectra shown in Fig. 7. Later the intensities decreased after irradiating by beam fluence $1 \times 10^{17}$ ions/cm$^2$ which indicates the destruction of the structure of NWs at this dose. XRD peaks intensities are decreased after irradiation at beam fluence $1 \times 10^{17}$ ions/cm$^2$ which is possibly due to vacancies and defects generated by Argon ions. These defects reduced the crystallinity of Cu

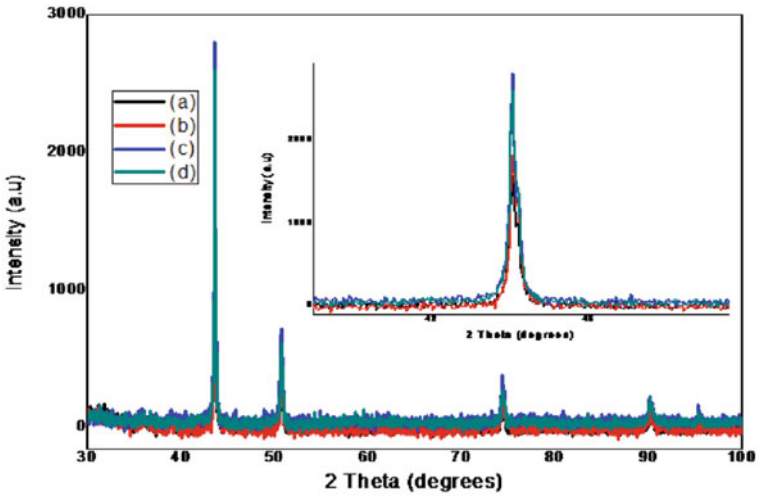


**Fig. 7** **a–d** XRD spectra of Cu NWs before and after irradiating at different doses of Argon ions

NWs that might have arised due to collision cascade and get accumulated in the form of amorphous clusters in the material. TEM image (see in Fig. 5) of relevant irradiated Cu NWs mesh shows that Cu NWs are melted and lost their shapes as compared to un-irradiated Cu NWs. Destruction of structures of Cu NWs is confirmed by the melting of Cu NWs. Therefore, TEM and XRD results are in agreement.

Grain size (i.e. crystallite size) of Cu NWs was evaluated by using X-ray diffraction data and presented in Fig. 8. Grain size "D" was calculated by Scherer's equation [32] $D = K\lambda/\beta\text{Cos}\theta$; Where "β" shows the broadening of diffraction line, which is measured at half of the maximum intensity (FWHM) of diffraction line, λ (=1.5418 Å) is the wavelength of X-rays, K is the shape factor and its value is 0.9 for polycrystalline films, angle of diffraction is θ [33]. Scherrer's equation relies on the fact that large size grains produce sharp XRD peaks. The changes in average grain sizes versus beam fluencies of Argon ions are shown in Fig. 8. After and before irradiation, average grain sizes of Cu NWs are found to be 50 nm, 71 nm, 71 nm and 57 nm, respectively. Figure 7 (curve (a)) shows sharp diffraction peaks indicating large sizes of crystallites. After irradiating Cu NWs with $Ar^+$ ions, the values of crystallite sizes were increased from 50 to 71 nm which does not change at $1 \times 10^{16}$ ions/cm$^2$ (see Fig. 8). At $1 \times 10^{17}$ ions/cm$^2$, the grain size was decreased to 57 nm showing a reduction in crystallinity of Cu NWs. Reduction in crystallinity is found in Cu NWs after irradiation with high fluencies of Argon ions, whereas Cu NWs are found to be crystalline after irradiation with low beam fluencies. The Lorentz polarization factor (LPF) was also calculated by XRD data. The formula for LPF is given below. Lorentz polarization factor $= 1 + \cos^2 2\theta / \sin^2\theta$; The major role of the Lorentz polarization (LP) factor is to manage X-ray intensity with respect to the diffraction angle. At low

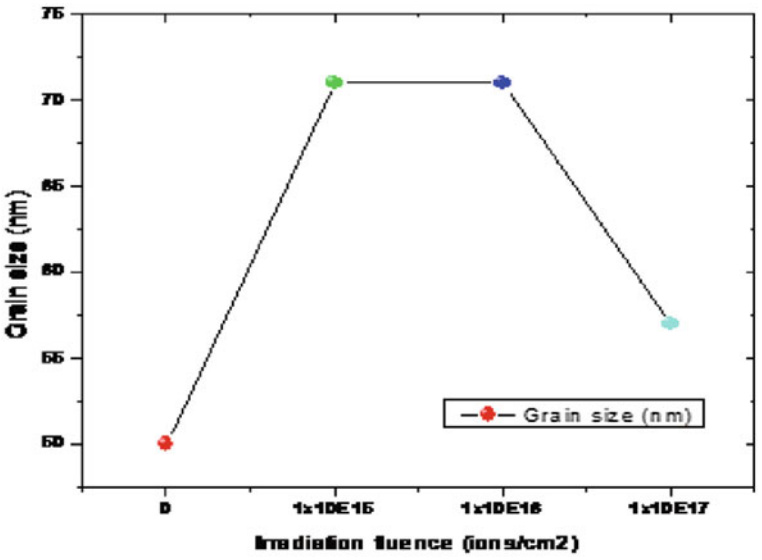


**Fig. 8** Average grain sizes versus various beam fluencies of Argon ions

angles, values of LPF are found to be very large which reached a minimum value of around 43.53° as shown in Fig. 10. For each reflection, LPF is inversely proportional to the velocity of reflection and directly proportional to the time taken. The values of LPF are decreasing with an increase in angles because of the reasons that low-angle peaks are of greater intensity in X-ray diffraction pattern as compared to high angle peaks [34]. So, the intensity profile in the X-ray diffraction pattern of Cu NWs is as per Lorentz polarization factor.

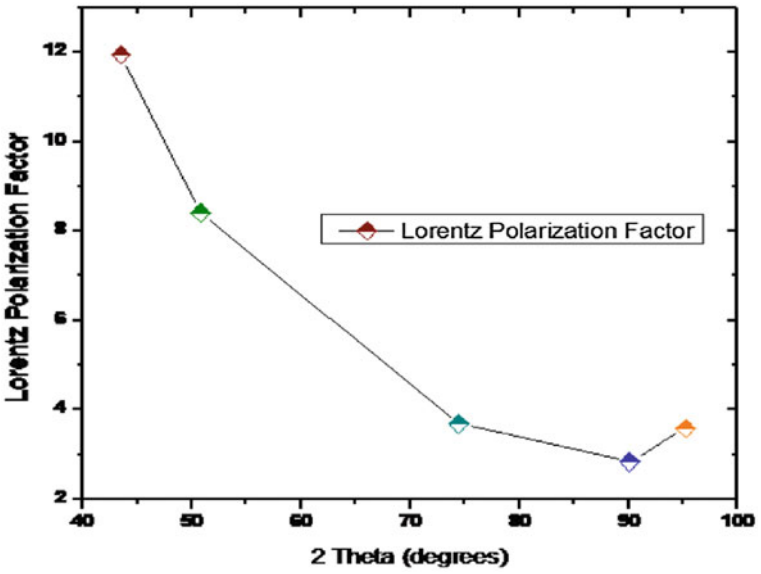


**Fig. 9** The lorentz polarization factor of Cu NWs

**Fig. 10** **a–d** Plots of transmittance versus wavelength for Cu NWs meshes

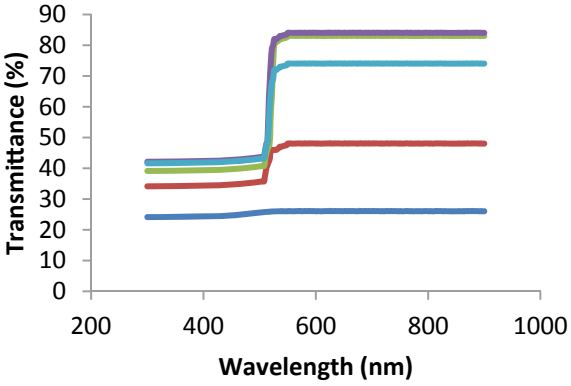

### *3.4 Optical Analysis of Argon Ions Irradiated Copper Nanowires*

The optical properties of bulk and nano-scaled materials are different and originated from surface plasmonic resonance. In fact, an electromagnetic field will contact conduction electrons of Cu NWs and produce an oscillating electric field. Excitations in the electrons of conduction band at surfaces of Cu NWs will be produced due to the oscillating electric field and displace them with respect to nuclei as a cloud of electrons. The coulombic attraction force will be raised between nuclei and electron cloud which will cause the electronic cloud to oscillate with respect to nuclei. The collective effect of oscillations of electron cloud on surfaces of NWs is called surface plasmonic resonance [18, 35]. Before and after exposing Cu NWs meshes to Argon ions, optical transmittance spectra are shown in Fig. 10a–d. It is observed from the spectra that optical transmittance is less in the visible (Vis) region of the ultraviolet–visible (UV–vis) spectrum at 500 nm and the strong absorption of light in this region is due to surface plasmonic resonance. In case of NWs of copper material, an absorbance band usually appears in the visible zone on UV–visible spectra and this band appears because of the contact of an electromagnetic field with conduction electron which might have arised due to surface plasmonic resonance [33, 36]. In this band, the amount of transmitted light is reduced, whereas absorbed and scattered light will be increased. A major advantage of a surface plasmonic band of MNWs is exploiting this band in controllable and tunable optoelectronic properties. In the above results, the optical transmittance of Cu NWs meshes has been increased with the first three beam fluencies of Argon ions and then decreased at a higher dose, as seen in Fig. 10. This increase in transmittance might be related to an increase in spaces between Cu NWs. The spaces produced or increased in Cu NWs are due to the removal of atoms from the surfaces of NWs after irradiation, which is confirmed through TEM results of Fig. 1a–d where the diameters of Cu NWs are slightly decreasing.

## 4 Conclusions

Optical properties can successfully be changed by irradiating Cu NWs with Argon ions. Atomic removals occurred from surfaces of Cu NWs after irradiation which resulted in the reduction of thicknesses of Cu NWs. Spaces in individual Cu NWs are increased because of the reduction in thicknesses of Cu NWs. Argon ions beam irradiation is found to be a valuable technique to alter the optical properties of NWs which happens due to a reduction in the diameters of Cu NWs. The reduction of diameters is occurring might possibly be due to ejection of atoms from Cu NWs surfaces. Tuning the optical properties of Cu NWs can be advantageous in opto-electronic applications. XRD analysis revealed no destruction and perseverance of crystalline structure of Cu NWs after ion beam irradiation. TEM analysis shows

slight reduction in diameters of Cu NWs with increase of beam fluencies of Argon ions.

**Conflict of Interest** The authors hereby declare that they have no conflict of interest.

## References


1. Groep JV, Spinelli P, Polman A (2012) Nano Lett 3:138
2. Catrysse PB, Fan S (2010) Nano Lett 10:2944
3. Kuang P, Park JM, Leung W, Mahadevapuram RC, Nalwa KS, Kim TG, Chaudhary S, Ho KM, Constant K (2011) Adv Mater 23:2469
4. Hecht DS, Hu L, Irvin G (2011) Adv Mater 23:1482
5. Kumar A, Zhou C (2010) ACS Nano 4:11
6. Hu L, Wu H, Cui Y (2011) MRS Bull 36:760
7. Ellmer K (2012) Nat Photon 6:809
8. Jeongmo K, Wilson JS, Rashid MY, Jin J (2016) Sci Rep 6:19813
9. Chung CH, Song TB, Bob B, Zhu R, Yang Y (2012) Nano Res 5:805
10. Leem DS, Edwards A, Faist M, Nelson J, Bradley DDC, deMello JC (2011) Adv Mater 23:4371
11. Lee JY, Connor ST, Cui Y, Peumans P (2010) Nano Lett 10:1276
12. Hardin BE, Gaynor W, Ding IK, Rim SB, Peumans P, McGehee MD (2011) Org Electron 12:875
13. Liu CH, Yu X (2011) Nanoscale Res Lett 6:75
14. Tenent RC, Barnes TM, Bergeson JD, Ferguson AJ, To B, Gedvilas LM, Heben MJ, Blackburn JL (2009) Adv Mater 21:3210
15. Lu YC, Chou KS (2010) Nanotechnology 21:21570
16. Scardaci V, Coull R, Lyons PE, Rickard D, Coleman JN (2011) Small 7:2621
17. Kim T, Canlier A, Kim GH, Choi J, Han SM (2013) ACS Appl Mater Interfaces 5:788
18. Honey S, Naseem S, Ishaq A, Maaza M, Bhatti MT, Wan D (2016) Chin Phys B 25:046105
19. Leem DS, Edwards A, Faist M, Bradley DDC, deMello JC (2011) Adv Mater 23:4371
20. Ishaq A, Zhichun N, Long Y, Jinlong G, Dezhang Z (2010) Rad Phys Chem 79:687
21. Honey S, Asim J, Ahmad I, Zhao TK, Maaza M, Naseem S (2020) Modification in optical properties of Ni-NWs networks by $Ar^{+}$ ion beam irradiation for TCEs. Mater Res Express 7:065008
22. Ishaq A, Waheed A, Husnain G, Long Y, Xingtai Z (2011) Curr Nanosci 7:790
23. Honey S et al (2020) Ion implantation in metal nanowires. In: Ion beam techniques and applications. IntechOpen
24. Ziegler JF, Biersack JP Littmark U (1985) Perganom Press, New York
25. Honey S, Naseem S, Ishaq A, Maaza M, Bhatti MT, Wan D (2016) J Nanomater Mol Nanotechnol 6
26. Honey S, Ishaq A, Madhuku M, Naseem S, Maaza M, Kennedy JV (2017) Mater Res Exp 4:075042
27. Asha A, Ajit K, Shammi V, Sunil O, Kandasami A, Lekha N (2013) Nanoscale Res Lett 8:433
28. Dee CF, Ahmad I, Long Y, Xingtai Z, Salleh MM, Majlis BY (2011) Phys E 43:1857
29. Wang ZG, Dufour C, Euphrasie S, Toulemonde M (2003) Nucl Instrum Methods Phys Res B 209:194
30. Li X, Gao F, Gu Z (2011) Open Surf Sci J 3:91
31. Asha A, Ajit K, Shammi V, Sunil O, Kandasami A, Lekha N (2013) Nanoscale Res Lett 8(433):31
32. Cullity BD (1978) Addison Wesley, New York 324

33. Kumar N, Kumar R, Kumar S, Chakarvarti SK (2014) Curr Appl Phys 14:046105
34. Sarkar S, Das R (2018) Indian J Pure Appl Phys 56:765–772
35. Honey S, Asim J, Ahmad I, Zhao TK, Maaza M, Naseem S (2020) Mater Res Express 7:065008
36. Pallavi R, Chauhan RP (2014) Phys B 45:26

# Chapter 3
# The Recent Developments on Bismuth Oxyhalides (BiOX; X = Cl, Br, and I) Based Nanocomposite Materials for Environmental Remediation


**Thirungnanam Bavani and Jagannathan Madhavan**

## 1 Introduction

Environmental contamination is a serious concern owing to the inappropriate discharge of organic/inorganic contaminants into freshwater bodies. Generally, water scarcity is caused by water contamination, which raises harmful health issues to terrestrial lives [1–3]. Mainly the developments in living standards generate the demand for the regular utilization of clothes, cosmetics, products of leathers, etc. Therefore, the industries are increasing the amount of utilization of synthetic dyes to enhance the quality of the product that becomes a menace to the ecological environment [3–5]. Still, the industries continue to dispose of the wastes in the freshwater bodies every day. Hence, it is vital to eliminate those organic pollutants from the water bodies. For this, different chemical, physical, and biological methods are operated to detoxify contaminated water [6]. However, some processes such as ozonation, electro-oxidation, reverse osmosis, adsorption, ion exchange, and membrane filtration are time-consuming, high cost, and generate additional pollutants. The advanced oxidation process with the semiconductor photocatalyst is operated as an environmentally friendly and economical method to degrade the contaminants without causing secondary pollutants [7–9]. The photocatalyst and the source of light are vital in the photocatalytic removal of contaminants. Here, the structure of the photocatalyst favors the light absorption in the visible region. As well, $TiO_2$ is a conventional photocatalyst owing to its inexpensive and non-toxic nature. On the contrary, its wide bandgap energy (~3.2 eV) limits its large-scale applications [10]. Therefore, various semiconductor photocatalysts such as $Bi_2WO_6$ [11], $WO_3$ [12], ZnO [13], $BiFeO_3$ [14], CuS [15], g-$C_3N_4$ [16], AgI [17], $V_2O_5$ [18], etc.

T. Bavani · J. Madhavan (✉)
Solar Energy Lab, Department of Chemistry, Thiruvalluvar University, Vellore, Tamil Nadu 632115, India
e-mail: jagan.madhavan@tvu.edu.in



K. Kasinathan et al. (eds.), *Nanomaterials for Energy Conversion, Biomedical and Environmental Applications*, Materials Horizons: From Nature to Nanomaterials,
https://doi.org/10.1007/978-981-19-2639-6_3

are prepared to replace the $TiO_2$. Among them, the bismuth-based photocatalysts include $Bi_2MoO_6$, $Bi_2O_3$, $BiVO_4$, and BiOX (X = Cl, I, Br) [19–21], etc. gained greater attention.

Moreover, the bismuth-based metal–oxide photocatalysts have greater visible light absorption and have lower bandgap energy, leading to an excellent photocatalytic performance against various pollutants. In that, BiOX shows some unique layered structures with a tetragonal phase. Here, four halogen and oxygen atoms are encircled on the central bismuth atom of the BiOX and make a unique layered structure [X-Bi-O-Bi-X] as shown in Fig. 1. These layers are bonded with the halides by van der Walls interaction, the internal electrical field generated by this interaction is perpendicular to each layer, resulting in the formation of appropriate band structures of the semiconductor that are favorable for greater visible light absorption. The BiOCl has a broader bandgap energy (~3.0–3.2 eV) and it exhibits greater photocatalytic performances in the presence of ultraviolet (UV) light [22]. The BiOI has a remarkable photocatalytic ability due to its lower band structure (~1.6–1.9 eV), leading to more excellent visible light absorption [23]. Also, BiOBr exhibits good photocatalytic activity in the visible region (~2.6–2.8 eV) [24]. The BiOX photocatalysts are

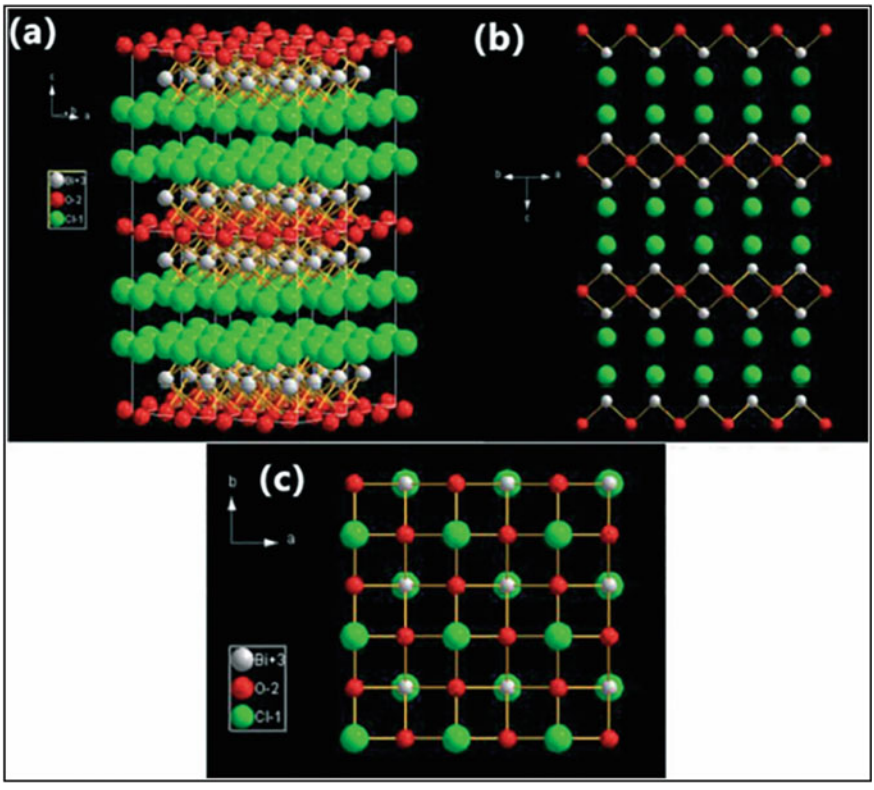


**Fig. 1** Lattice structure of BiOCl **a** 3D structure, **b** crystal facets {110}, **c** crystal facets {001} [25]

p-type semiconductors, and are extensively used in the degradation of contaminants from wastewater. This book chapter presents the recent developments of BiOX-based nanocomposite photocatalysts for environmental remediation. Greater significance has been concentrated to increase the photocatalytic performance toward the elimination of organic/inorganic contaminants. The degradation pathway and mechanism behind the removal of wastewater contaminants are discussed in detail.

## 2 General Photocatalytic Degradation Mechanism

Generally, photocatalysis is an operative, persistent, and ecofriendly technique for removing highly toxic contaminants in the presence of light [26]. Figure 2 presents the schematic representation of the general mechanism for the decomposition of pollutants under visible light irradiation (VLI). Under illumination, the photocatalytic reaction is stimulated once the photoelectrons on the completely occupied valence band (VB) get excited, leaving a hole ($h^+$) present in the VB and electron ($e^-$) present in the conduction band (CB). After, $e^-$ on the surface of CB reduces the oxygen, and the $h^+$ on the surface of the VB oxidizes the pollutant to create hydroxyl ($^{\bullet}OH$) and superoxide ($O_2^{\bullet -}$) radicals. These radicals react with contaminants, as presented in Eqs. (2–4).

$$\text{Photocatalyst} + h\nu \rightarrow e^-(\text{CB}) + h^+(\text{VB}) \tag{1}$$

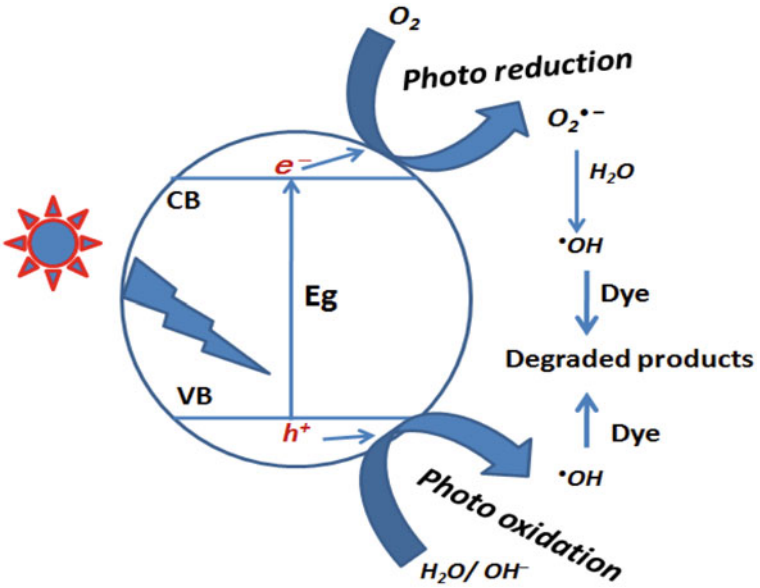


**Fig. 2** Photocatalytic mechanism of BiOCl-based nanocomposite [26]

$$e^{-}_{CB} + O_2 \rightarrow O_2^{\bullet -} \quad (2)$$

$$h^{+}_{VB} + H_2O \rightarrow {}^{\bullet}OH + H^{+} \quad (3)$$

$$O_2^{\bullet -} + {}^{\bullet}OH + \text{pollutant} \rightarrow \text{Degradation products} \quad (4)$$

## 3 BiOCl-Based Nanocomposite for the Degradation of Pollutants

Kong et al. inspected the photocatalytic ability of β-$Bi_2O_3$/BiOCl composite for the tetracycline (TC) degradation with a 300 W Xe lamp under VLI [27]. The hollow flower-like β-$Bi_2O_3$/BiOCl composites were prepared by an impregnation process. The β-$Bi_2O_3$/BiOCl composite showed an excellent photocatalytic degradation efficiency than bare β-$Bi_2O_3$ and BiOCl, this is due to the specific surface area (SSA) of the β-$Bi_2O_3$/BiOCl composite with 0.5 mol/L of HCl is (27.711 $m^2$/g) comparatively higher than the β-$Bi_2O_3$ is (17.06 $m^2$/g), owing to the surface of pure β-$Bi_2O_3$ covered by BiOCl nanosheets on the surface. This increase might be owing to the creation of β-$Bi_2O_3$/BiOCl heterojunction, it greatly improves the separation of $e^-$–$h^+$ pairs. Tahmasebi et al. designed the $Bi_2WO_6$/BiOCl composite through a facile one-step hydrothermal process [28]. Further, $Bi_2WO_6$/BiOCl composites were employed to evaluate the photocatalytic degradation efficiency by the removal of methyl orange (MO), malachite green (MG), and rhodamine B (RhB) under the condition of natural sunlight irradiation (NSI) or LED light. In this study, RhB dye showed complete (~100%) degradation within 80 min under NSI, whereas the irradiation of LED light toward the elimination of RhB exhibits ~ 91% after 100 min. The photocatalytic ability of the $Bi_2WO_6$/BiOCl composite is significantly affected by the presence of tungsten ions, the BET surface area of the $Bi_2WO_6$/BiOCl composites with different amounts of HCl are 0.5, 1.3, and 2.2 mL are 37.50, 24.50, 19.95, and 1.14 $m^2g^{-1}$ correspondingly, and these are mesoporous materials which show type-4 adsorption isotherm (H3- hysteresis loop) and the sample without tungsten ion displays type-3 adsorption isotherm, which matches with the microporous and non-porous materials containing smaller 1.14 $m^2g^{-1}$ specific BET surface area. This remarkable improvement of photocatalytic efficiency is due to the generation of heterojunction as given in Fig. 3, making close interfacial contact between BiOCl and $Bi_2WO_6$, it suppresses the rejoining of $e^-$–$h^+$ pairs on the semiconductor surface.

Bao et al. fabricated the BiOCl/$TiO_2$ composite by the combination of electrospinning and solvothermal methods [29]. The photocatalytic ability of BiOCl/$TiO_2$ composite was assessed for the removal of different antibiotic contaminants like TC, demeclocycline, chlortetracycline, oxytetracycline, and doxycycline in the presence of VLI. Then, after 120 min of illumination, the BiOCl/$TiO_2$ composite degraded

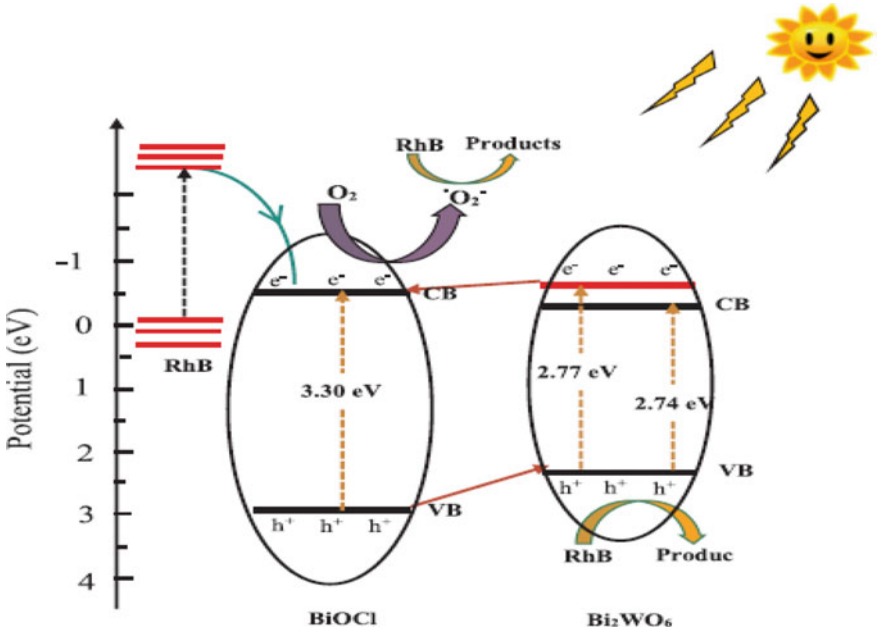


**Fig. 3** A schematic sketch of the band diagram and photocatalytic mechanism of $Bi_2WO_6$/BiOCl [28]

84.04% of TC (0.0137 $min^{-1}$) than pure BiOCl and $TiO_2$. The separation of $e^-$–$h^+$ pairs and effective adsorption greatly induces the photocatalytic ability. Yosefi et al. prepared $Mn_3O_4$/BiOCl nanocomposite via a simple precipitation process and used it for the removal of acid orange-7 (AO7) in VLI [30]. The $Mn_3O_4$/BiOCl nanocomposite presented greater photocatalytic performance than the bare materials. They reported that after four cycles of run, the $Mn_3O_4$/BiOCl composite showed higher reusability, which makes it a reliable material for the photocatalytic process. Further, the improved photocatalytic ability was credited to the development of $Mn_3O_4$/BiOCl heterojunction, and the huge SSA of the nanocomposites that offered a much greater number of active sites for the degradation, which increases the charge separation and migration efficiency. Zhao et al. constructed a Z-scheme between phosphotungstic acid (HPW) and BiOCl by a one-step hydrothermal route, and the sequence of BiOCl-HPW composites was prepared by varying the amount of HPW (0.02, 0.03, and 0.04 g) [31]. The TC is taken to estimate the photocatalytic ability of BiOCl/HPW composite in the presence of a 300 W Xe lamp under VLI. As expected, 0.03 g of HPW on the BiOCl-HPW composite exhibited superior photocatalytic activity of 92.2% and a rate constant ($k_{app}$) of 0.0195 $min^{-1}$ within 120 min due to the heterojunction that controlled the separation of photoproduced $e^-$–$h^+$ pairs. Xiao et al. constructed a Z-scheme $CdIn_2S_4$/BiOCl heterostructure via the hydrothermal method and the photocatalytic ability was assessed toward the decomposition of MO, TC, and RhB in solar light [32]. Among the prepared samples, the 6.0 wt.% of $CdIn_2S_4$-BiOCl

composite possesses a higher photocatalytic activity, it is 3.6- and 2.59-fold greater than bare $CdIn_2S_4$ and BiOCl. The observed degradation is credited to its higher SSA (50.96 $m^2/g$) of the $CdIn_2S_4$–BiOCl composite, a key factor for photocatalytic degradation. The exclusive Z-scheme face-to-face heterostructure with close interface contact affords more charge separation and reduces the charge transfer distance of the photoinduced $e^-$–$h^+$ pairs, thereby increasing the photocatalytic performance of the $CdIn_2S_4$–BiOCl composite.

Zhao et al. designed a visible light active (VLA) 3D hierarchical BiOBr/BiOCl microspheres and the effect of synthesis time with a different molar ratio of Br:Cl studied through a one-pot solvothermal process to evaluate the photocatalytic ability toward the removal of RhB [33]. Besides, the PL intensity of the sample decreases with the synthesis time and the samples with a shorter duration of the synthesis are red-shifted than the sample with a longer time of the synthesis. From the results, the BiOBr/BiOCl composite displays an improved photocatalytic ability with the $k_{app}$ value of the BiOBr/BiOCl composite (0.0290 $min^{-1}$), which is 4.5- and 8.8-fold greater than BiOCl and BiOBr individually. The enhancement in the photocatalytic performance is owing to the generation of BiOBr/BiOCl heterojunction, which efficiently improves the migration and separation of photoproduced $e^-/h^+$ pairs.

## 4 BiOBr-Based Nanocomposites for Pollutant Degradation

Hu et al. applied a solvothermal method to synthesize $Bi_2MoO_6$/BiOBr composite photocatalyst, and their photocatalytic ability was estimated toward the removal of MB under VLI (50 W LED lamp) [34]. The $Bi_2MoO_6$/BiOBr composite showed a higher surface area which improved photocatalytic performance toward the removal of MB under VLI. This enhancement is also credited to the effective VLA and construction of Z-scheme $Bi_2MoO_6$/BiOBr heterojunction, which effectively separates the charge carriers during the photo-degradation process. Ye et al. constructed the BiOBr/g-$C_3N_4$ composite through a facile one-step chemical bath technique and examined their photocatalytic performance toward the RhB degradation in VLI, and the BiOBr/g–$C_3N_4$ composite shows excellent photocatalytic degradation efficiency than pristine BiOBr and g-$C_3N_4$ photocatalysts [35]. The structural and morphological results reveal the construction of facet coupling between BiOBr (001) and g-$C_3N_4$ (002). In BiOBr/g–$C_3N_4$ composite, the charge carrier transfer efficiency is mainly influenced by the facet coupling during the photocatalytic process (Fig. 4). Cao et al. invented a VLA$CdWO_4$/BiOBr composite photocatalyst by hydrothermal process [36]. Furthermore, the $CdWO_4$/BiOBr composite is subjected to analyze the photocatalytic ability toward the decomposition of RhB in the presence of a 300 W Xe lamp. In the series of composites, the 15%-$CdWO_4$/BiOBr composite photocatalyst displays a superior photocatalytic efficiency toward RhB within 8 min. The BET surface area results of bare BiOBr, $CdWO_4$, and 15%-$CdWO_4$/BiOBr are 24.2, 27.6, and 21.7 $m^2/g$, separately. The formation of $CdWO_4$/BiOBr p-n heterojunction induces the creation of more photoexcited $e^-$–$h^+$ pairs on their interfaces.

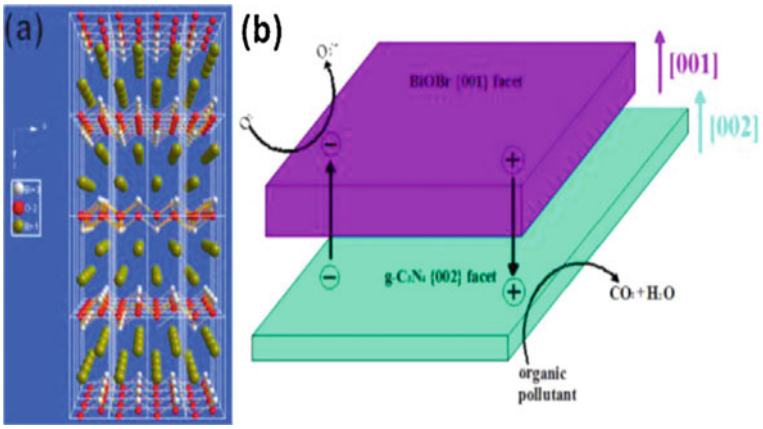


**Fig. 4** **a** Crystal structure of BiOBr; and **b** coupling model of BiOBr-g-$C_3N_4$ [35]

Lu et al. employed the facile hydrothermal method to synthesize BiOBr/$BiFeWO_6$ composites by adding different amounts of (20, 40, and 60 mg) $BiFeWO_6$ [37]. The RhB was taken to assess the photocatalytic efficiency under VLI (300 W Xe lamp). The BiOBr/$BiFeWO_6$ composite has higher degradation activity, due to the increasing amount of the $BiFeWO_6$ will increases the surface area of the BiOBr/$BiFeWO_6$ composite increases the number of active sites for the removal of RhB. Tang et al. prepared a sequence of the VLA β-$Bi_2O_3$/BiOBr heterojunction via the precipitation method [38]. The β-$Bi_2O_3$/BiOBr heterojunction showed an enhanced photodegradation ability around ~ 99.6% toward RhB under 300 W Xe-arc lamp within 35 min. From Fig. 5, β-$Bi_2O_3$/BiOBr heterojunction facilitates the

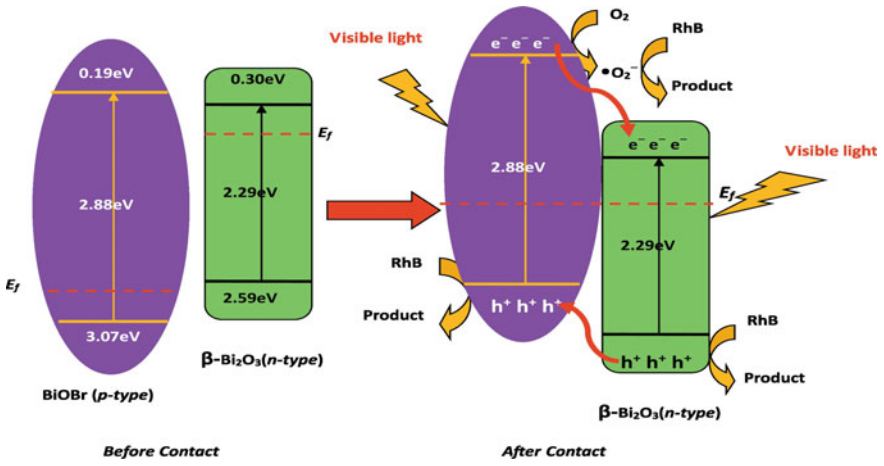


**Fig. 5** Schematic diagram of the possible visible light photodegradation mechanism [38]

flow of $e^-$ on the surface of BiOBr to β-$Bi_2O_3$, and at the same time, the flow of $h^+$ on the surface of β-$Bi_2O_3$ to BiOBr generates an internal electric field between the interfaces of β-$Bi_2O_3$ and BiOBr, which greatly separates the $e^-$–$h^+$ pairs across the interface. From the above results, the β-$Bi_2O_3$/BiOBr photocatalyst is a potential material for the remediation of wastewater treatment.

Chai et al. constructed the type-II heterojunction between $Bi_2SiO_5$/BiOBr via an in situ ion-exchange approach [39]. The as-prepared $Bi_2SiO_5$/BiOBr photocatalyst displayed a superior photocatalytic activity of RhB degradation under VLI. The higher degradation of $Bi_2SiO_5$/BiOBr heterojunction significantly rises the absorption of visible light, suitable band structure, and strong interfacial contact. Long et al. synthesized BiOBr–$Bi_2S_3$ heterojunction by ion-exchange process, further it operated toward the Cr(VI) reduction under VLI [40]. Within 12 min of illumination, a complete Cr(VI) reduction is observed in BiOBr with 2 mmol of $Na_2S_2O_3{\cdot}5H_2O$ at pH 6.0, and it is 28.9- and 184.6-fold greater than that of bare $Bi_2S_3$ and BiOBr. The optical and electrochemical studies present the development of BiOBr–$Bi_2S_3$ heterojunction, which effectively enhancing the separation of the $e^-$–$h^+$ pairs. Yan et al. designed visible light driven ZnS/BiOBr nanocomposite for the decomposition of TC and it possesses 82% of degradation after 25 min of illumination [41]. Also, even it maintained 70% in 25 min of irradiation after five consecutive cycles, which indicates the excellent reusability property of ZnS/BiOBr photocatalyst. Here, the improved photocatalytic degradation efficiency is owing to the suppression of rapid reconnection of charge carriers.

## 5 BiOI Based Nanocomposites for Pollutant Degradation

He et al. fabricated BiOI/g-$C_3N_4$ composite using in situ transformation process at room temperature [42]. Subsequently, the photocatalytic degradation ability of BiOI/g–$C_3N_4$ composite was assessed through the removal of phenol pollutant under LED light illumination ($\lambda > 400$ nm). Further, BiOI/g–$C_3N_4$ composite presents greater photocatalytic ability than bare BiOI and g-$C_3N_4$. Here, the Brunauer, Emmett, and Teller (BET) SSA for g-$C_3N_4$, BiOI, and BiOI/g- g-$C_3N_4$ was measured to be 80, 6, and 78 $m^2$/g, individually, and the greater surface area of g-$C_3N_4$ and BiOI/g-$C_3N_4$ is due to the volume of micropores. The density functional theory (DFT) computation results reveal the improved photocatalytic efficiency, which is mainly credited to the generation of the internal electric field between the g-$C_3N_4$ and BiOI (Fig. 6). Jiang et al. constructed BiOI/g–$C_3N_4$ heterojunction [43]. The BiOI/g-$C_3N_4$ samples were further used for the Cr(VI) reduction under VLI. The 20% mechanical mixture of BiOI/g-$C_3N_4$ has noticeably reduced the Cr(VI) after 15 min illumination. The obtained photocatalytic reduction is owing to the development of a nonradiative recombination center that promotes the $e^-$–$h^+$ pairs migration and separation on the interface of BiOI/g-$C_3N_4$ Z-scheme heterojunction. Song et al. fabricated three-dimensional (3D) nanoplate-built $CdWO_4$/BiOI using low-temperature chemical bath process by adding different ratios of $CdWO_4$ [44]. The morphology of

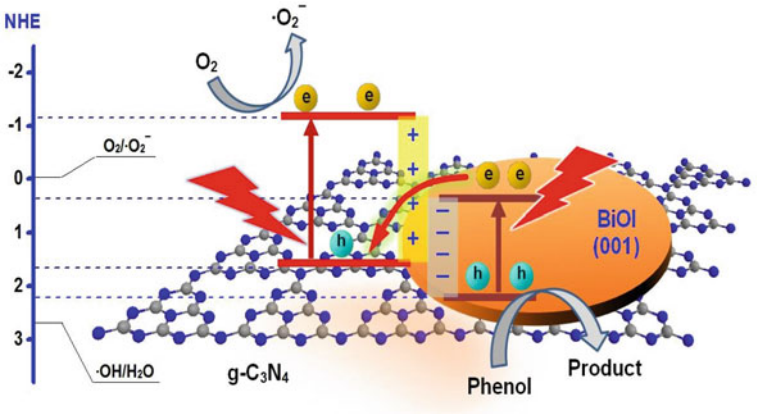


**Fig. 6** Schematic diagram of the direct Z-scheme charge migration of the BiOI/g-$C_3N_4$ composite [42]

$CdWO_4$ exhibits nanorods structure and the morphology of $CdWO_4$/BiOI composite exhibits 3D flower-like morphology with a 9.1 $m^2$/g surface area. The photocatalytic degradation performance of the $CdWO_4$/BiOI composite was assessed toward the removal of RhB under VLI. The $CdWO_4$/BiOI composite with the addition of a 0.07 molar ratio of $CdWO_4$ showed a greater photocatalytic degradation efficiency (95.1%) toward the removal of RhB. The creation of the $CdWO_4$/BiOI *p–n* junction greatly increases the separation and reduces the reconnection of photoexcited $e^-/h^+$ pairs thus favoring the photodegradation efficiency.

Chen et al. prepared the AgI/BiOI photocatalyst via a simple in situ ion exchange route presented in Fig. 7 [45]. By altering the ratio of bismuth precursor, a sequence of AgI/BiOI composites was prepared. The scanning electron microscope (SEM) results show the formation of flower-like AgI/BiOI hierarchical microspheres with a size of 2–5 μm. The photocatalytic efficiency of AgI/BiOI nanocomposite was evaluated through the decomposition of RhB and phenol in VLI. The AgI/BiOI composite

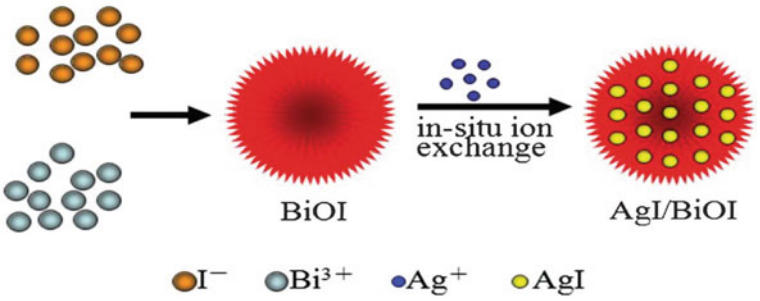


**Fig. 7** Schematic illustration of the proposed formation mechanism of the hierarchical AgI/BiOI microspheres [45]

presents improved photocatalytic ability in visible light, owing to the greater $e^-$–$h^+$ pairs separation between BiOI and AgI.

Lv et al. designed AgI/BiOI composite by ion-exchange method, and the composites were prepared by adding different amounts (10, 40, 60%) of AgI into the BiOI sample [46]. Further, the as-synthesized AgI/BiOI composites were employed for the removal of MO, RhB, and MB in the presence of VLI using a 300 W Xe arc lamp. The 40% AgI/BiOI composites showed a higher degradation performance, and this enhancement is credited to the migration and separation of photogenerated $e^-/h^+$ pairs. Liu et al. designed $BiPO_4$/BiOI composite using an anion-exchange process [47]. The $BiPO_4$/BiOI composite was further operated for the degradation of phenol under VLI. From the structural morphology results, the BiOI exhibited a nanosheet-like structure, after the anion exchange with $PO_4^{3-}$ from $BiPO_4$ the BiOI nanosheets are topped with the $BiPO_4$ nanorods. The photocatalytic decomposition results displayed that the $BiPO_4$/BiOI composite shows improved degradation ability than BiOI. This improvement in the photocatalytic ability is mainly credited to the transfer of photogenerated $e^-$–$h^+$ pairs between the interface of $BiPO_4$ donor and BiOI acceptor. Liu et al. constructed the ZnO–BiOI heterostructure to study the photocatalytic ability toward the removal of RhB in the presence of VLI (350 W xenon lamp) [48]. This ZnO–BiOI heterostructure model displays the catalytic effect on the interface of the heterostructure. Comprehensively, this is the study of different structural properties for the ZnO–BiOI heterostructures. There is an effective contact between $Bi^{3+}$ and ZnO that confirms the growth and nucleation on the ZnO surface to form ZnO–BiOI nanorod heterostructure. Conversely, the nucleation and the growth of the BiOI followed by the reaction with the ZnO nanorods present the heterostructure constituted by decorating the ZnO nanorod surface by BiOI nanoflowers (Fig. 8). Comparably, the ZnO–BiOI nanorod heterostructure showed 12-fold greater photocatalytic performance than the ZnO–BiOI nanoflower heterostructure, due to the greater interface in the ZnO–BiOI nanorod heterostructure that facilitated the formation and the separation of photoproduced $e^-$–$h^+$ pairs under VLI. Malefane et al.

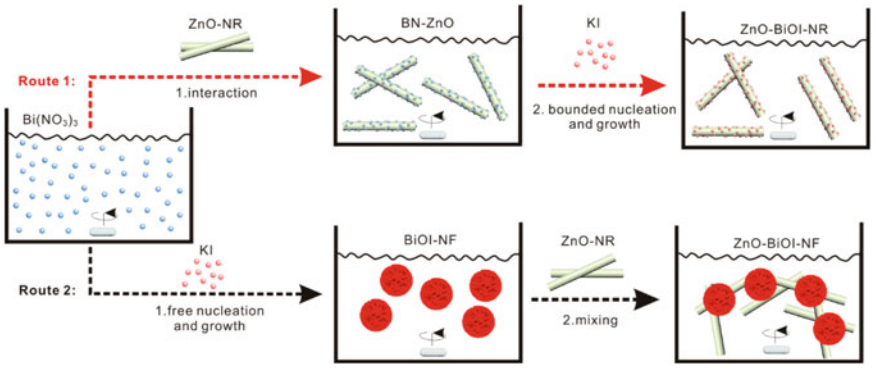


**Fig. 8** Schematic Illustration of the synthesis procedures for ZnO/BiOI heterostructures [48]

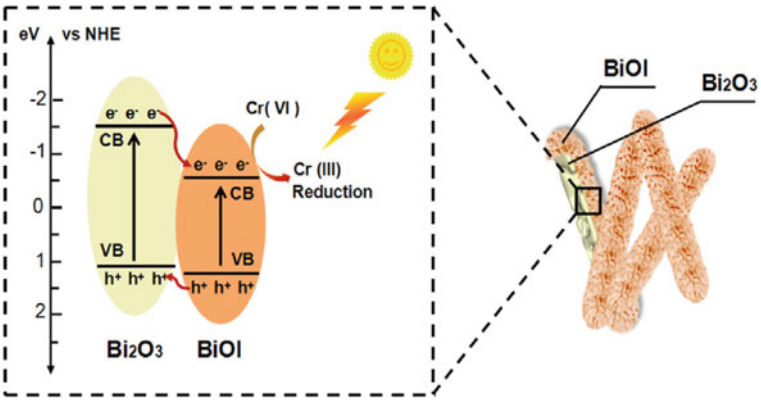


**Fig. 9** The photocatalytic reduction mechanism of Cr(VI) by $Bi_2O_3$/BiOI under visible-light irradiation [50]

designed a $Co_3O_4$/BiOI composite by facile self-assembly method for the degradation of ibuprofen using a 60 W LED lamp [49]. The construction of Z-scheme heterojunction creates the electric field between the $Co_3O_4$ worm-like spheroids and BiOI sphere-like flower structure, which leads to showing excellent degradation ability.

Wei et al. prepared a one-dimensional $Bi_2O_3$/BiOI composite by a simple *one-pot* precipitation method by adding different amounts of 30, 50, and 70% of $Bi_2O_3$, and the synthesized samples were treated for the Cr(VI) reduction under VLI [50]. The structural analysis displays the formation of a 3D flower-like BiOI microsphere containing several nanosheets with 10–15 nm thickness. The $Bi_2O_3$ exhibits a porous nanorod structure with a 300–350 nm diameter. From BET measurement, the SSA of the 50%–$Bi_2O_3$/BiOI, bare BiOI, and $Bi_2O_3$ are 135.9, 118.9, and 83.4 $m^2$/g, separately. The optimized 50%–$Bi_2O_3$/BiOI showed a superior photoreduction ability (94.5%), which is significantly greater than its individual BiOI and $Bi_2O_3$ materials, and it is mainly attributed to its higher surface area. Figure 9 represents the mechanism for the photoreduction of Cr(VI) by $Bi_2O_3$/BiOI under VLI.

## 6 Conclusions and Future Directions

In summary, this book chapter overviews the recent developments of BiOX-based nanocomposites for the degradation of organic/inorganic contaminants in the wastewater. Based on the above discussions, the BiOX-based heterostructures are having unique structures and showed enhanced photocatalytic activity than conventional photocatalysts. Several articles reveal that the photocatalytic ability of BiOX greatly increases through the addition of another semiconductor. The surface tailored

morphology and the development of heterojunction significantly improve the migration and separation of the photoexcited $e^-$–$h^+$ pairs, thereby reducing their recombination. The future consideration of pollutant degradation by BiOX photocatalyst desires a simple synthesis of scalable, reliable, and long-term BiOX composite photocatalysts for wastewater remediation treatment. Moreover, improved, cost-effective, and facile preparation methods are interpreted with enhanced photocatalytic activity. In contrast, laboratory research of the BiOX photocatalyst further improves commercial environmental wastewater remediation applications using a visible light source.

## References


1. Ge J, Zhang Y, Heo YJ, Park SJ (2019) Advanced design and synthesis of composite photocatalysts for the remediation of wastewater: a review. Catalyst 9:122. https://doi.org/10.3390/catal9020122
2. Koutavarapu R, Tamtam MR, Lee SG, Rao MC, Lee DY, Shim J (2021) Synthesis of 2D $NiFe_2O_4$ nanoplates/2D $Bi_2WO_6$ nanoflakes heterostructure: an enhanced Z-scheme charge transfer and separation for visible-light-driven photocatalytic degradation of toxic pollutants. J Environ Chem Eng 105893
3. Leena VB, Rajubhai KM (2017) Visible/solar light active photocatalysts for organic effluent treatment: fundamentals, mechanisms and parametric review. Renew Sust Energ Rev 76:1393–1421. https://doi.org/10.1016/j.rser.2017.01.130
4. Malathi A, Arunachalam P, Madhavan J, Al-Mayouf AM, Ghanem MA (2018) Rod-on-flake α-FeOOH/BiOI nanocomposite: facile synthesis, characterization and enhanced photocatalytic performance. Colloids Surf A Physicochem Eng Asp 537:435–445
5. Malathi A, Yiseul Y, Hyeon JJ, Sanghun Y, Hyeyeon L, Theerthagiri J, Lee SJ, Choi MY (2021) Solvent-mediated synthesis of BiOI with a tunable surface structure for effective VLAphotocatalytic removal of Cr(VI) from wastewater. Env Res 197:111080
6. Priya A, Arunachalam P, Selvi A, Madhavan J, Al-Mayouf AM (2018) Synthesis of $BiFeWO_6/WO_3$ nanocomposite and its enhanced photocatalytic activity towards degradation of dye under irradiation of light. Colloids Surf A Phys Eng Asp 559:83–91
7. Theerthagiri J, Murthy AP, Elakkiya V, Chandrasekaran S, Nithyadharseni P, Khan Z, Senthil RA, Shanker R, Raghavender M, Kuppusami P, Madhavan J, Ashokkumar M (2018) Recent development on carbon based heterostructures for their applications in energy and environment: a review. J Ind Eng Chem 64:16–59
8. Malathi A, Arunachalam P, Grace AN, Madhavan J, Al-Mayouf AM (2017) A robust visible-light driven $BiFeWO_6$/BiOI nanohybrid with efficient photocatalytic and photoelectrochemical performance. Appl Surf Sci 412:85–95. https://doi.org/10.1016/j.apsusc.2017.03.199
9. Sandeep K, Sharma S, Swati S, Ahmad U, Kansal SK (2016) Bismuth sulfide ($Bi_2S_3$) nanotubes decorated $TiO_2$ nanoparticles heterojunction assembly for enhanced solar light driven photocatalytic activity. Ceram Int 42(15):17551–17557
10. Priya A, Arunachalam P, Selvi A, Madhavan J, Al-Mayouf AM, Ghanem MA (2018) A low-cost VLABiFe$WO_6$/$TiO_2$nanocompositewith an efficient photocatalytic and photoelectrochemical performance. Opt Mater 81:84–92
11. Gui MS, Zhang WD, Su QX, Chen CH (2011) Preparation and visible light photocatalytic activity of $Bi_2O_3/Bi_2WO_6$ heterojunction photocatalysts. J Solid State Chem 184:1977–1982
12. Chena X, Lia Y, Lis L (2020) Facet-engineered surface and interface design of $WO_3/Bi_2WO_6$ photocatalyst with direct Z-scheme heterojunction for efficient salicylic acid removal. Appl Surf Sci 508:144796

13. Theerthagiri J, Salla S, Senthil RA, Nithyadharseni P, Madankumar A, Arunachalam P, Maiyalagan T, Kim HS (2019) A review on ZnO nanostructured materials: energy, environmental and biological applications. Nanotechnol 30:392001. https://doi.org/10.1088/1361-6528/ab268a
14. Bavani T, Madhavan J, Prasad S, AlSalhi MS, ALJaffreh M (2021) A straightforward synthesis of visible light driven $BiFeO_3/AgVO_3$ nanocomposites with improved photocatalytic activity. Env Poll 269:116067
15. Theerthagiri J, Senthil RA, Malathi A, Selvi A, Madhavan J, Ashokkumar M (2015) Synthesis and characterization of a CuS–$WO_3$ composite photocatalyst for enhanced visible light photocatalytic activity. RSC Adv 5:52718–52725
16. Theerthagiri J, Senthil RA, Priya A, Madhavan J, Michael RJV, Ashokkumar M (2014) Photocatalytic and photoelectrochemical studies of visible-light active α-$Fe_2O_3$–g-$C_3N_4$ nanocomposites. RSC Adv 4:38222–38229
17. Wang X, Yang J, Ma S, Zhao D, Dai J, Zhang D (2016) In situ fabrication of AgI/$AgVO_3$ nanoribbon composites with enhanced visible photocatalytic activity for redox reactions. Catal Sci Technol 6:243–253
18. Theerthagiri J, Senthil RA, Priya A, Madhavan J, Michael RJV, Ashokkumar M (2015) Synthesis of a visible-light active $V_2O_5$–g-$C_3N_4$ heterojunction as an efficient photocatalytic and photoelectrochemical material. New J Chem 39:1367–1374
19. Li WT, Zheng YF, Yin HY, Song XC (2015) Heterojunction BiOI/$Bi_2MoO_6$ nanocomposite with much enhanced photocatalytic activity. J Nanoparticle Res 17:271
20. Malathi A, Arunachalam P, Kirankumar VS, Madhavan J, Al-Mayouf AM (2018) An efficient visible light driven bismuth ferrite incorporated bismuth oxyiodide ($BiFeO_3$/BiOI) nanocomposite photocatalytic material for degradation of pollutants. Opt Mater 84:227–235
21. Wu X, Ng YH, Wang L, Du Y, Dou SX, Amal R, Scott J (2017) Improving the photo-oxidative capability of BiOBr via crystal facet engineering. J Mater Chem A 5:8117. https://doi.org/10.1039/C6TA10964K
22. Changa JQ, Zhonga Y, Hua CH, Luo JL, Wang PG (2018) Synthesis and significantly enhanced visible light photocatalytic activity of BiOCl/AgBr heterostructured composites. Inorg Chem Commun 96:145–152
23. Bavani T, Madhavan J, Prasad S, AlSalhi MS, ALJaffreh M, Vijayanand S (2021) Fabrication of novel $AgVO_3$/BiOI nanocomposite photocatalyst with photoelectrochemical activity towards the degradation of Rhodamine B under visible light irradiation. Environ Res 200:111365. https://doi.org/10.1016/j.envres.2021.111365
24. Li J, Zhou Q, Yang F, Wu L, Li W, Ren R, lv Y (2019) Uniform flower-like BiOBr/BiOI prepared by a new method: visible-light photocatalytic degradation, influencing factors and degradation mechanism. New J Chem 43:14829-14840
25. Sharma K, Dutta V, Sharma S, Raizada P, Hosseini-Bandegharaei A, Thakur P, Singh P (2019) Recent advances in enhanced photocatalytic activity of bismuth oxyhalides for efficient photocatalysis of organic pollutants in water: a review. J Ind Eng Chem 78:1–20
26. Kumar AA, Rajini A, Venkatathri N (2017) Synthesis and characterization of magnetically separable porous titanium silicate nanocomposite catalyst for environmental applications. Mater Today Proc 4(1):19–24
27. Kong S, An Z, Zhang W, An Z, Yuan M, Chen D (2020) Preparation of hollow flower-like microspherical β-$Bi_2O_3$/BiOCl heterojunction and high photocatalytic property for tetracycline hydrochloride degradation. Nanomaterials 10:57. https://doi.org/10.3390/nano10010057
28. Tahmasebi N, Maleki Z, Farahnak P (2019) Enhanced photocatalytic activities of Bi2WO6/BiOCl composite synthesized by one-step hydrothermal method with the assistance of HCl. Mater Sci Semicond Process 89:32–40
29. Bao S, Liang H, Li C, Bai J (2020) A heterostructure BiOCl nanosheets/$TiO_2$ hollow-tubes composite for visible light-driven efficient photodegradation antibiotic. J Photochem Photobiol A Chem 397:112590

30. Yosefi L, Haghighi M (2019) Sequential precipitation design of p-BiOCl-p-$Mn_3O_4$ binary semiconductor nanoheterojunction with enhanced photoactivity for acid orange 7 removal from water. Ceram Int 45(7):8248–8257
31. Zhao H, Liu X, Dong Y, Xia Y, Wang H (2019) A special synthesis of BiOCl photocatalyst for efficient pollutants removal: new insight into the band structure regulation and molecular oxygen activation. Appl Catal B Environ 256:117872
32. Chen Y, Hu Q, Yu M, Gong X, Li S, Wang S, Li Z (2021) In situ construction direct Z-scheme $CdIn_2S_4/TiO_2$ heterojunction for improving the photocatalytic properties. Cryst Eng Comm 23(29):5070–5077
33. Zhao C, Liang Y, Li W, Chen X, Tian Y, Yin D, Zhang Q (2020) 3D BiOBr/BiOCl heterostructure microspheres with enhanced photocatalytic activity. J Mater Sci Mater El 31(3):1868–1878
34. Hu T, Yang Y, Dai K, Zhang J, Liang C (2018) A novel Z-scheme $Bi_2MoO_6$/BiOBr photocatalyst for enhanced photocatalytic activity under visible light irradiation. Appl Surf Sci 456:473–481
35. Ye L, Liu J, Jiang Z, Peng T, Zan L (2013) Facets coupling of BiOBr-g-$C_3N_4$ composite photocatalyst for enhanced visible-light-driven photocatalytic activity. Appl Catal B Environ 142:1–7
36. Cao QW, Cui X, Zheng YF, Song XC (2016) A novel $CdWO_4$/BiOBr p–n heterojunction as visible light photocatalyst. J Alloys Compd 670:12–17
37. Lu C, Wu W, Zhou H (2021) In situ fabrication of BiOBr/$BiFeWO_6$ heterojunction with excellent photodegradation activity under visible light. J Solid State Chem 303:122465
38. Tang X, Wang Z, Wu N, Liu S, Liu N (2019) A novel visible-light-active β-$Bi_2O_3$/BiOBr heterojunction photocatalyst with remarkably enhanced photocatalytic activity. Catal Commun 119:119–123
39. Chai B, Yan J, Fan G, Song G, Wang C (2019) In-situ construction of $Bi_2SiO_5$/BiOBr heterojunction with significantly improved photocatalytic activity under visible light. J Alloys Compd 802:301–309
40. Long Z, Zhang G, Du H, Zhu J, Li J (2021) Preparation and application of BiOBr-$Bi_2S_3$ heterojunctions for efficient photocatalytic removal of Cr (VI). J Hazard Mater 407:124394
41. Yan S, Yang J, Li Y, Jia X, Song H (2020) One-step synthesis of ZnS/BiOBr photocatalyst to enhance photodegradation of tetracycline under full spectral irradiation. Mater Lett 276:128232
42. He R, Cheng K, Wei Z, Zhang S, Xu D (2019) Room-temperature in situ fabrication and enhanced photocatalytic activity of direct Z-scheme BiOI/g-$C_3N_4$ photocatalyst. Appl Surf Sci 465:964–972
43. Jiang J, Mu Z, Zhao P, Wang H, Lin Y (2020) Photogenerated charge behavior of BiOI/g-$C_3N_4$ photocatalyst in photoreduction of Cr (VI): A novel understanding for high-performance. Mater Chem Phys 252:123194
44. Song H, Wu R, Liang Y, Xiong H, Ji G (2017) Facile synthesis of 3D nanoplate-built $CdWO_4$/BiOI heterostructures with highly enhanced photocatalytic performance under visible-light irradiation. Colloids Surf A Physicochem Eng Asp 522:346–354
45. Chen L, Jiang D, He T, Wu Z, Chen M (2013) In-situ ion exchange synthesis of hierarchical AgI/BiOI microsphere photocatalyst with enhanced photocatalytic properties. Cryst Eng Commun 15(37):7556–7563
46. Lv Y, Liu H, Zhang W, Ran S, Chi F, Yang B, Xia A (2013) Room-temperature synthesis and high visible-light-induced photocatalytic activity of AgI/BiOI composites. J Environ Chem Eng 1(3):526–533
47. Liu Y, Yao W, Liu D, Zong R, Zhang M, Ma X, Zhu Y (2015) Enhancement of visible light mineralization ability and photocatalytic activity of $BiPO_4$/BiOI. Appl Catal B Environ 163:547–553
48. Liu J, Zou S, Lou B, Chen C, Xiao L, Fan J (2019) Interfacial electronic interaction induced engineering of ZnO-BiOI heterostructures for efficient visible-light photocatalysis. Inorg Chem 58(13):8525–8532

49. Malefane ME, Feleni U, Mafa PJ, Kuvarega AT (2020) Fabrication of direct Z-scheme $Co_3O_4$/BiOI for ibuprofen and trimethoprim degradation under visible light irradiation. Appl Surf Sci 514:145940
50. Wei Z, Zheng N, Dong X, Zhang X, Ma H, Zhang X, Xue M (2020) Green and controllable synthesis of one-dimensional $Bi_2O_3$/BiOI heterojunction for highly efficient visible-light-driven photocatalytic reduction of Cr (VI). Chemosphere 257:127210

# Chapter 4
# Additive-Based Structure and Bioactivity Modifications of Phosphate Glasses


**S. Aravindan, A. Nishara Begum, and R. Uthrakumar**

## 1 Introduction

Phosphate glass is one of the curious glassy structures that reveals the scope of utilization in diverse fields of application. Its characteristics have been studied extensively but still more to be explored in many areas including one in the field of biomaterials. In the earlier observations, the phosphate glasses prepared employing melt quench technique were found to be more corrosive in refractory utilities and it has been found as a major limitation for their usage. To enhance the utility aspects of the phosphate-based glasses, variety of methods have been attempted including the incorporation of various foreign elements within the phosphate glass network. It is important to note that the incorporation of other elements including metal oxides the characteristic behaviour of the phosphate glasses is found to be entirely altered and rendered a novel characteristic that could never be expected from the phosphate glass systems. The characteristics, which include the mechanical, elastic, bioactive, etc., are the few that have shown the variations to a greater extent by virtue of the inclusion of external elements with the phosphate glassy network. The application potential of phosphate glasses is substantial in the field of biomaterials as bioactive glasses. In the broad realm of materials science, biomaterials are one of the significant twigs that facilitate the development of substantial components that help for extending healthy human life. As stated earlier by Williams [1], biomaterial is a nonviable clinical material developed intentionally to interact with a living organism.

S. Aravindan (✉) · R. Uthrakumar
PG and Research Department of Physics, Government Arts College (Autonomous), Salem, Tamil Nadu 636007, India
e-mail: aravindan.sp@gmail.com

A. Nishara Begum
PG and Research Department of Physics, Chikkaiah Naicker College, Erode, Tamil Nadu 638004, India



K. Kasinathan et al. (eds.), *Nanomaterials for Energy Conversion, Biomedical and Environmental Applications*, Materials Horizons: From Nature to Nanomaterials,
https://doi.org/10.1007/978-981-19-2639-6_4

**Table 1** Biomaterials and their mode of working nature [2]

| Utility of biomaterial | Variety of biomaterial |
|---|---|
| Replacement of diseased/damaged parts | Prosthetic implants (soft or hard tissue), cardiac valves, renal dialysis machines, tissue scaffolds, etc |
| Healing assist | Sutures, bone plates, adhesives, sealants, screws, nails, etc |
| Functioning enhancement | Cardiac pacemakers, intraocular lenses, etc |
| Functional abnormality corrections | Cardiac defibrillators, cardiac pacemakers, etc |
| Cosmetic problem corrections | Tissue implants (breast, chin, etc.) |
| Disease diagnosing tool | Biosensors, probes, etc |
| Disease treatment kid | Implantable pumps, catheters, drains, drug delivery systems, etc |

It is an element made either by natural or synthesis and that enables interaction with living elements of a biological system to replace or augment any tissue or organ to retain or extend the healthy function of the body. In clinical activity, biomaterial is used for both therapeutic and diagnostic purposes as well. As of the present status, numerous varieties of biomaterials are in clinical practice with a specific target of application. Biomaterials are classified majorly into seven basic categories based on metal, polymers, ceramics, inorganic glass, regenerative and hybrid combinations, etc. All these branches are gaining substantial attention and developed mainly based on their clinical demands. Each element of biomaterials has a unique design and functionality based on the end-user need. The uses of biomaterials in the general perspective are given in Table 1. It reveals the clinical issues in various medical areas and the respective biomaterials may be used in specific forms and structures.

In the human body, the skeletal system is a prominent physical entity that decides the structure. It includes bones, joints, tendons, ligaments, and muscles, and the branch of medicine dealing with its care is orthopedics. Bone is a unique substance connecting the matrices of calcified elements with organic components. Bone tissue organization is a unique and complex one, which may either be in dense or spongy frames having pores ranging from 1 to 100 $\mu$m [3]. Although the structural and dimensional aspects of bone differs from part to part, its chemical composition is found to be similar all over. Bone mineral is an evident natural hybrid composite accommodating organic and inorganic phases inseparably. Bone is a multicomponent solid structure composed of the phases of bioorganic and inorganic phases of minerals [4] as given in Table 2. In both organic and inorganic phases of minerals, many trace elements could be identified. In the organic phase, numerous non-collagenous proteins such as osteonectin, osteocalcin, osteopontin, morphogenetic protein, thrombospondin, serum protein, sialoprotein, etc. exist in various percentages depending on the nature of bone. Among the trace elements exist in the inorganic composition, ionic elements of chlorine ($Cl^-$), fluorine (F), potassium ($K^+$), strontium ($Sr^{2+}$), lead ($Pb^{2+}$), zinc ($Zn^{2+}$), copper ($Cu^{2+}$), ferrous ($Fe^{2+}$), etc. are the few prominent species that exist in the fractional count.

**Table 2** Bone mineral composition [4]

| S. No. | Organic phase | Weight percentage (wt.%) |
|---|---|---|
| 1 | Collagen | 20 |
| 2 | Water | 9 |
| 3 | Non-collagenous protein | 3 |
| 4 | Other traces | – |
| | *Inorganic phase* | |
| 5 | Biological apatite (CaP) | 60 |
| 6 | Carbonates | 4 |
| 7 | Citrates | 0.9 |
| 8 | Sodium | 0.7 |
| 9 | Magnesium | 0.5 |
| 10 | Other traces | – |

Recent reports of materials science acknowledge the development of promising elements, particularly, as biomaterials to meet the clinical requirements for orthopedic surgical treatments. These biomaterials, based on the tissue interaction with them, can be classified majorly into four categories such as i) nearly inert, porous, bioactive, and resorbable as given in Table 3. It is essential that any bioactive material to be implanted in a living skeletal system should have mere similarities in chemical compositions and the characteristic of the living bone as well.

As described in Table 3, the third category of bioactive substance is gaining significance as a second generation of biomaterials [6]. The generation of biomaterials deviated from the first generation more than four decades ago. While describing the term biofunctionality, any external substance implanted within the living system could be expected to exhibit reactive responses either in favor or in an adverse way. If the implanted material could exhibit a favorable effect while interacting with the host system and it could continue as an active element in responses with surrounding tissues, it can be termed as a bioactive element. In general, the bioactive element is intended to exhibit appropriate and controlled interactions with the surrounding tissues. The general characteristics of second-generation biomaterials are given in Table 4.

**Table 3** Types of biomaterial categories with tissue interactions [5]

| Biomaterial type | Interaction with tissue | Element details |
|---|---|---|
| Nearly inert | Mechanical fixation | Metal, ceramic, polymer |
| Porous | Biological fixation | Calcium-rich phosphate (HAp), porous material with HAp coating |
| Bioactive | Bioactive fixation | Bioactive glasses and glass ceramics, HAp |
| Bioresorbable | Tissue replacement | Tricalcium phosphate, polylactic acid |

**Table 4** Second-generation biomaterial—characteristics [6]

| Element | Activity |
|---|---|
| Bioactive | Provokes interaction in a controlled way between the implant and surrounding tissues |
| Biodegradable | Elicits controlled chemical interaction and thereby breakdown and adsorption |
| Bioresorbable | Provokes functional tissue to grow within the network structure of implant material |

## *1.1 Bioactive Glass*

Bioactive material is the one that elicits specific biological reactions at the interface between the implant material and the host living system enabling it to extend the linkages with living tissues without any adverse effect [7]. In solid structure especially materials like glasses, glass ceramics and ceramics elicit a favorable response within the living body by extending tissue connectivity and thereby developing mechanically stable bonding to the bone. These bioactive substances are like to have better time-dependent and surface modification ability after implantation with the living body [8]. In the field of orthopedics, a biocompatible element that supports the cell attachment by enhancing the bone matrix generation and formation is found to be the bioactive glass. These glasses are mainly helpful to replace and regenerate the hard tissues of the bone matrix. In the past few decades, various bioactive materials have been developed and proven their bone-bonding ability. Bioglass®, A/W glass ceramics, Ceravital®, dense calcium phosphate, etc. are the few to be noted as worthy. All these materials are different in their chemical composition, their functionality, etc. Among the material listed above, Bioglass® is the foremost element that demonstrated its bone-bonding ability with the living bone by L.L. Hench [9]. It is termed as "45S5 Bioglass®" and its chemical composition is 45% of silica, 24.5% of $Na_2O$, 24.5% of CaO, and 6% of $P_2O_5$. The bone-bonding mechanism of all these materials are different and their time-dependent functionality for bone bonding is unique. In addition, the strength and thickness of bone-bonding are also dissimilar as reported elsewhere [5]. As an index of bioactivity of the respective system, the rate at which the implant material could possibly develop its interfacial bond with the living system shows its bioactivity. In the mechanism of bioactivity of a material, development of adherent interface between the implant material and host is essential, since it can resist the influence of any mechanical forces.

With the success of bioactive materials based on their exclusive bone-bonding ability, many trials have been attempted across the globe to derive novel materials with improved bioactive ability. The derived glasses are different in their route of synthesis, elements of compositions, and quantity. It has been observed that altering the chemical composition of glass material could possibly develop new varieties of glasses with tailor-made properties. Mainly, the bioactivity of glass systems is determined by their reactions with body fluid (or) stimulated body fluid (SBF) in the stipulated period and to form the hydroxycarbonate apatite layer [9]. In the bioactivity

mechanism, when the glass of specific composition is insert into the body fluid, it will immediately leach the sodium ions by dissolving the calcium and phosphate ionic components. By virtue of surface reactive responses in the glass structure due to the body fluid elements, a calcium-rich phosphate apatite has been formed. Any changes in the elemental composition and their content could lead to exhibiting different behaviors not only in bioactive response rather in its mechanical, solubility, elastic constants, etc. It attracts the research community to develop a variety of bioactive glasses with newer combinations with a variety of inorganic elements inclusions to obtain a newer combination of materials with unique properties. This could possibly be used to identify newer glasses having control and altered resorption rates in vivo. In continuation of developments, the phosphate-based bioglass has been established as an alternative element to silica-based bioglass.

## *1.2 Phosphate-Based Glass*

Phosphorous pentoxide ($P_2O_5$) is the one among the four glass-forming oxides including $SiO_2$, $GeO_2$, and $B_2O_3$ to be able to form phosphate-based glass with different characteristics from the other three glasses with limitations due to hygroscopic nature. A deeper understanding of the phosphate-based glassy structure and its network forming ability will help one to explore more possible ways to derive the glasses with tailor-made properties. Phosphate-based glasses have limitation because of their meager mechanical strength and are hence not suitable for load-bearing application. For the past few decades, researchers have attempted many trials to enhance its superior quality at par with other superior high-mechanical strength elements to enhance its application potential in various fields including biomaterials. The ternary and quaternary phosphate-based glass systems with $P_2O_5$, CaO, $Na_2O$, and other metal oxides have the potential to render phosphate-based glasses with unique and enhanced characteristic features. To develop phosphate-based glasses with superior characteristics, a deeper understanding of its structural components is essential. Basically, phosphate glass structure consisting of $PO_4$ tetrahedral unit of oxygens with weak van der Waals attraction is represented with $Q^n$, where n denotes the number of bridging oxygen, as shown in Fig. 1.

A phosphate ($P_2O_5$) glass system consists of a 3D network of elements branching with $Q^3$ units with three bridging oxygens and the remaining one is double-bonded

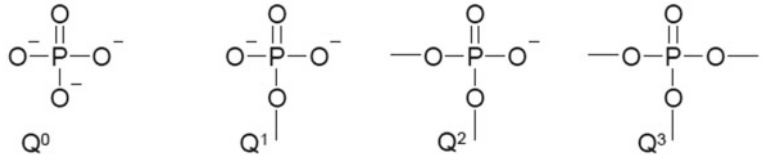


**Fig. 1** Phosphate glasses of four different $Q^n$ species

oxygen per basic tetrahedral structure. In case of incorporation of any network modifier element such as alkaline earth or alkali cation influenced to modify the $Q^3$ units to $Q^2$ with increasing ionic cross-link formations between phosphate units. The phosphate glass network consists only of $Q^2$ branches of linear phosphate units with the concentration of $P_2O_5$ with less than or equal to 50 mol%, wherein the $Q^3$ units are disappeared. Increasing the concentration of network modifier content above 50 mol% within the phosphate glass network leads to altering the $Q^2$ structure to $Q^1$ and then $Q^0$. It shows that polymerization of phosphate glass network is feasible only with low or zero content of network modifying metal cations, increasing modifier content leads to inhibiting the polymerizing ability of the $P_2O_5$ glass network. This is by virtue of a decrease in the availability of bridging oxygen per phosphate anion. Figure 2 reveals the formation of network elements in phosphate glasses with network former, modifier, bridging, and non-bridging oxygen. Phosphate-based glass system is a familiar one to accommodate foreign elements of different categories. Any elements, more specifically inorganic metal oxides, can get feasible accommodation within the phosphate glass network and shows entirely altered properties. Although a wide range of inorganic metal oxides is readily available to incorporate within the phosphate-based glass network, few metal oxides such as $Na_2O$, $Ag_2O$, and ZnO show their feasibility to enhance the bioactive behavior of the phosphate glass structure.

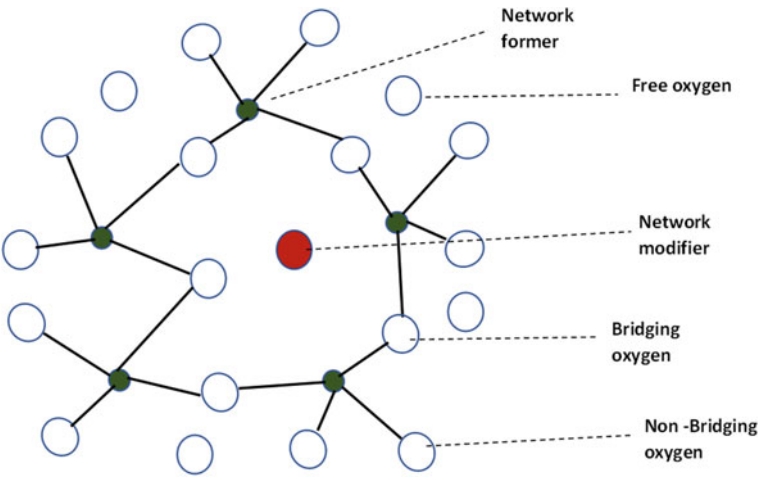


**Fig. 2** Glass network elements coordination

## *1.3 Glass Structural Examination*

Among the variety of experimental methods to evaluate the structural features of the glasses/solid materials, the ultrasonic nondestructive evaluation method is one of the promising techniques that can be used to explore the glass structure. It is known well that glass is one of the amorphous network structures that doesn't have definite crystalline order of atomic arrangements. Hence, the ultrasonic nondestructive evaluation method is an appropriate one for evaluating the glass structure features. In this method, by observing the time duration taken by the ultrasonic RF signals of a specific frequency to transmit within the upper and lower wall of a glass medium, one can estimate the elastic constants with the predefined equations as described elsewhere [10] and by knowing the density (ρ) of the glass by employing Archimedes' principle. By exploring the values of elastic constants such as longitudinal modulus (L), shear modulus (G), bulk modulus (K), Young's modulus (Y), and Poisson's ratio, their variations against the compositional changes could possibly be used to reveal the changes in the structural features of the glass medium. The following equations give the relation between the elastic constants:

$$\text{Longitudinal modulus } L = U_L^2 \rho. \tag{1}$$

$$\text{Shear modulus } G = U_S^2 \rho \tag{2}$$

$$\text{Bulk modulus } K = L - \left(\frac{3}{4}\right)\text{G} \tag{3}$$

$$\text{Youngs modulus } Y = (1 + \sigma)2\text{G} \tag{4}$$

$$\text{Poisson ratio } \nu \frac{L - 2G}{2(L - G)} \tag{5}$$

where $U_L$ and $U_S$, respectively, represent the ultrasonic longitudinal and shear velocity in the glass medium.

### 1.3.1 Density and Molar Volume of Phosphate Glass with Additives

#### (a) Increase of $Na^+$ against $Ca^{2+}$ in $P_2O_5$ network

As an attempt of observation to explore the changes in density value of the phosphate glass observed by Archimedes' principle against the compositional changes reveal the structural deformation of phosphate-based glass network by virtue of increasing $Na_2O$ content at the cost of CaO element with fixed $P_2O_5$. Density is an effective

tool that can explore the structural changes in the glass network as a result of compositional changes. These changes in composition by increasing network modifier ($Na_2O$) leads to altering the polymerization of phosphate glass network and thereby increasing the nonbridging oxygen by altering P–O–P bonding. While increasing the $Na_2O$ content with the fixed $P_2O_5$ glass network against CaO content, every $Na^+$ cation was found to interact with the P–O–P bonding structure of the glass and resulted in depolymerization. The increasing nonbridging oxygen elements results of $Na^+$ interactions lead to accommodating more content of alkali cations in the network structure. As discussed in the phosphate glass structure, during the increase of network modifier, the ultra-phosphate ($Q^3$) to metaphosphate ($Q^2$) and followed by pyrophosphate ($Q^3$). This structural deformation alters the density values to a greater extent in decreasing trend. In this structure, the increasing $Na_2O$ is made by decreasing the CaO content. Calcium ion ($Ca^{2+}$) is well known as an effective element in increasing the cross-link density of the glass structure by connecting two or more nonbridging oxygen linkages. The decrease of CaO content is also one of the reasons for decreasing the network connectivity between the constituent elements and thereby decreasing density values. Molar volume is also one of the structural parameters that can exhibit the changes in the glass structure against compositional changes. It is by trend against the density values of the glass system as increasing against the decreasing of density. The replacement of $Ca^{2+}$ by $Na^+$ is known well that the replacement of high field strength cation by the low field strength cation. The field strength of $Ca^{2+}$ is $0.33 \times 10^{20}$ $m^{-2}$ while the $Na^+$ value is $0.19 \times 10^{20}$ $m^{-2}$. The reductions in the density of high field strength ionic elements with an increase of low field strength cation lead to enhancing the molar volume of the glassy structure and thereby creating more terminal tangling oxygens at corners. Increasing nonbridging oxygen, on the other hand, enhances the volume space in the glassy network.

(b) **Increase of $Ag^{2+}$ against $Ca^{2+}$ in $P_2O_5$ glass network**

In phosphate-based glasses of the quaternary system, in addition to the components $P_2O_5$, CaO, $Na_2O$ an additive element $Ag_2O$ has been incorporated by replacing the CaO content with constant $P_2O_5$ and $Na_2O$. The structural modifications if any depends on the composition of the glass system and particularly, CaO and $Ag_2O$ are the key elements that hold the responsibility for changes. Density is the key physical parameter that can exhibit the structural compactness of the glass network. In this system, replacing calcium oxide with $Ag_2O$ helps to enhance the density of the glass sample considerably. The increase in density values is mainly because of the higher molecular weight of additive components $Ag_2O$ (231.7394 g $mol^{-1}$), which is significantly higher than CaO. Increasing density and decreasing molar volume are by the contraction in molecular volume space in the glass network. The atomic volume of Ag is very less comparatively than any other component in the quaternary glass system. The atomic volume of silver (Ag) is 10.3 $cm^3$ $mol^{-1}$. It causes the volume of the quaternary glass system to become compact with an increase of $Ag_2O$ content at the cost of CaO and hence increases its density.

(c) **Increase of ZnO against CaO in $P_2O_5$ glass system**

In this quaternary glass system, $P_2O_5$ and $Na_2O$ contents are considered to have fixed chemical compositions while the additive ZnO is incorporated to replace an equivalent definite amount of CaO. As stated elsewhere [11], the density of the glass system and its molar volume details can explore its structural features such as geometrical structure, elemental coordination, cross-link density, interstitial species dimension, etc. Although the additive component ZnO and replaced element CaO are both divalent cations, the structural deformation could possibly be observed by virtue of its compositional changes. The elemental parameters such as atomic mass, ionic density, etc. are quite different in these two elements. The atomic mass of replacing ZnO is higher as 81.389 g $mol^{-1}$ than that of CaO, i.e., 56.077 g $mol^{-1}$. Similarly, the ionic density of $Zn^{2+}$ is very larger at 7.14 g $cm^{-3}$ than $Ca^{2+}$ has 1.55 g $cm^{-3}$. These are the main cause of increase in the density value of this glass system increases with increasing ZnO content. As expected, the observed variations in the molar volume of this glass system exhibit a reverse trend to the density variations observed. The electrical field strength of progressively incorporated $Zn^{2+}$ element is much higher than the replacement $Ca^{2+}$, it enhances the attractive forces between the structural components and thereby reductions in interatomic spacing lead to lowering the molar volume space in the glass network. In addition, the elemental features such as atomic volume, ionic radius, etc. have significant differences in values of these two elements $Zn^{2+}$ and $Ca^{2+}$. The atomic volume of replaced $Ca^{2+}$ is much higher (29.9 $cm^3$ $mol^{-1}$) than the replacing $Zn^{2+}$, its value is 9.2 $cm^3$ $mol^{-1}$ and hence, this huge reduction in volume leads to a decrease in the space of molar volume in glass network structure. The ionic radius of $Zn^{2+}$ less value 0.88 Å than that of replaced $Ca^{2+}$, which has 1.14 Å, this reduction in ionic radius value also leads to a decrease in the volume space of the zinc oxide added phosphate glass network. The reduction of molar volume space and increase in density as a result of ZnO addition against CaO help the phosphate glass structure to attain a very compact and stable glass network.

### 1.3.2 Thermal Behaviour of $P_2O_5$ Glass Against Additives

(a) **Variations in thermal property of $P_2O_5$ network with increasing $Na^+$**

Thermal behavior of any glass structure can be observed by exploring the Differential Thermal Analysis (DTA). The phosphate glassy structure with increasing sodium oxide content and decreasing calcium oxide at the constant $P_2O_5$ network content. As observed in density variations the glass transition temperature value and crystallization temperature values are lowering result of increasing sodium oxide content. As discussed in the density variations, the phosphate glassy structure become less stable against the increase of $Na_2O$ and decreasing CaO although with constant $P_2O_5$. The ionic components exchanges, and their different field strengths are playing vital role in deciding the thermal behaviour. It reveals the increasing content of $Na_2O$ makes the phosphate glassy structure become thermally least stable. In addition, the content of $P_2O_5$, although it is constant, if it is lesser than 50 mol% then the

phosphate chain in the network will be shorter and hence, the glassy structure less viscous and more fluid. Phosphate glassy structure having least thermal stability may because of the lesser $P_2O_5$ in the over all composition than 50 mol%. The reductions in the bridging oxygen density in the glassy structure may lead to lowering the glass transition temperature and thereby increasing viscous nature of the glass structure. This will be resulted in decreasing the crystallisation temperature of the phosphate glass network by virtue of the reduction in CaO content by $Na_2O$.

(b) **Variations in thermal behavior of $P_2O_5$ glass with increasing $Ag_2O$**

Thermal behavior observations on the phosphate-based quaternary glass network reveal different trends of variation against the inclusion of $Ag_2O$ against CaO. Increasing the content of network modifier $Ag_2O$ leads to altering the structural features of the phosphate glass network to the greater extent. Thermal parameter, glass transition temperature ($T_g$) of this $Ag_2O$ included quaternary glass system are found to be decreasing linearly with increasing $Ag_2O$. Glass transition temperature ($T_g$) is one of the fundamental thermal properties of the glass system could exhibit the viscous nature of the glass system. The increasing network modifier content and thereby enhancing structural rearrangements will lead to altering the structural features of the glass and thereby increasing the viscous nature. On the other hand, the incorporated $Ag_2O$ leads to structural disruptions as a network modifier and shortens the phosphate chain lengths by converting the ultraphosphate ($Q^3$) groups into the chains of metaphosphate ($Q^2$) and pyrophosphate ($Q^1$). This, in turn, is reflected in the observed decreasing trend of $T_g$ values. The same trend of variation could be expected in crystallization temperature ($T_P$) data also, by exploring a similar trend of variation for $Ag_2O$ inclusions as for $T_g$ variations. It reveals that structural modifications enhance the rearrangements in glass networks under the influence of thermal energy. The increasing viscous nature of the glass network also leads to the occurrence of the crystallization of the glass structure at an earlier stage.

(c) **Variations in thermal property of $P_2O_5$ network with increasing ZnO**

The quaternary phosphate glass structure with increasing ZnO by replacing the CaO exhibits a unique thermal response in DTA analysis. Its thermal parameters such as glass transition temperature ($T_g$) and crystallization temperature ($T_P$) reveal variation against the compositional modification and exhibit unusual thermal behavior than any other phosphate-based glass. Glass transition temperature ($T_g$) is a parameter that could reflect the values with respect to the bonding strength between the constitutional elemental in the network. This glass system also reports reductions in $T_g$ values against the inclusion of ZnO. Before incorporating ZnO, the phosphate-based glass structure is dominant with the strong bonding of Ca–O–P bonding elements. While replacing $Ca^{2+}$ with $Zn^{2+}$ leads to altering the interstitial bonding structure by replacing stronger Ca–O–P with weaker Zn–OP [12]. Still, $Zn^{2+}$ has higher ionic field strength, its inclusion and thereby an increase in the structural network lead to enhancing the network connectivity of the species by increasing the cross-link density by interconnecting various disrupted network chains. This helps the structure become

thermally stable with increasing content of ZnO. This increasing thermal stability of phosphate-based ZnO-added glasses showed increasing crystallization ($T_P$) temperature value. When the glass structure becomes stable by its composition and thereby reducing its viscous nature and extending its crystallization temperature value.

### 1.3.3 Elastic Moduli of $P_2O_5$ Glass Network with Varying Additive Contents

(a) **Variations in elastic moduli of phosphate glass with increasing $Na^+$**

Through the observation of ultrasonic velocity during its transmission within the glassy medium, one could explore the glassy structural features to a greater extent. This is mainly because of the interaction of ultrasonic waves with the elements of the glassy network and their elemental bonding and thereby reduction in its speed due to the effective interactions. As the composed and dense network of glassy structures will absorb ultrasonic signals in a greater amount rather than the loosely packed network structure. In this way of observation, by estimating the velocity of ultrasonic signal through the phosphate glass medium, one can explore the changes that occurred in the network species as a result of composition changes. The increasing $Na^+$ density by decreasing $Ca^{2+}$ content has been explored as loosening the package structure of the glass network. By increasing the loose packaging structure, the transmission possibility of ultrasonic waves also finds difficulty and thereby lowering its speed with higher sodium content than the lower one. The structural depolymerization by the increasing content of network modifier content ($Na_2O$) leads to an increase in the population of nonbridging oxygen in the network content. This increasing nonbridging oxygen never hails the proper transmission of ultrasonic waves throughout the medium. It disrupts the signal transmission and hence a reduction in the ultrasonic signal velocity could be observed. Using the elastic moduli equations, the data of longitudinal modulus (L), shear modulus (G), bulk modulus (K) are representing a similar trend of structural fractions as observed in density against the increase of $Na_2O$. The increasing content of network modifier, nonbridging oxygen, molar volume, etc. leads to lowering the structural compactness and hence reductions in the elastic moduli values.

(b) **Variations in elastic moduli of phosphate glass with increasing $Ag_2O$**

While dealing with a quaternary phosphate glass system with stable $P_2O_5$ and $Na_2O$ content and by increasing $Ag_2O$ by replacing CaO, the elastic moduli observations are entirely in a new trend than observed in any other glass system. The observed ultrasonic velocity in the selected glassy medium is decreased considerably due to the compositional changes. The inclusion of $Ag_2O$ in the phosphate glass network influenced to alter its phosphate chain networks into various structures such as metaphosphate chains, pyrophosphate chains, etc. This leads the structure to get altered to a greater extent. This structural deformation makes the glass system become less connective and doesn't help the transmission of ultrasonic waves promptly. This

could reflect in the observation of elastic moduli such as Young's modulus (Y), shear modulus (G), and bulk modulus (K) to show decreasing trends in their values against the inclusion of $Ag_2O$ content. The reductions in the elastic moduli values are exploring the increasing nonbridging oxygen density in the glass network as a result of compositional modifications. This also exhibits the disruption of phosphate network chain connectivity and becomes shortened in length of the entire structure. As observed earlier [13], incorporation of monovalent cation ($Ag^+$) with phosphate network leads to disrupting the network structure and depolymerize it to get shorter phosphate chain lengths.

(c) **Variations in elastic moduli of phosphate glass with increasing ZnO**

Elastic property observations on ZnO-added quaternary phosphate glasses reveal increasing glass stability as with compositional changes. The observed ultrasonic velocity values while transmitting in the present glass system increases as increasing the ZnO content. ZnO is a network modifier content that disrupts the phosphate glass network connectivity, but the higher field strength of $Zn^{2+}$ enhances the interconnectivity between the disrupted chains of the phosphate-based glass structure. Zinc is an element that provides additional coordination sites to bond with nonbridging oxygen. It helps to increase the interconnectivity between the disrupted unlinked elements. The increase in glass network interconnectivity also enhances the cross-link density in the phosphate-based glass system. This helps the structure become dense with interconnecting bonds and thereby enhancing the speed of ultrasonic wave transmission. The estimation of elastic constants, Young's modulus (Y), longitudinal modulus (L), shear modulus (G), and bulk modulus (K) is exhibiting a similar trend of increasing values with increasing the ZnO content. The quaternary phosphate glass structure is becoming denser by the inclusion of ZnO at the cost of CaO.

### 1.3.4 Microhardness of $P_2O_5$ Network with Changing Additive Content

(a) **Variations in microhardness of $P_2O_5$ network with increasing $Na^+$**

Composition-dependent characteristic modifications on phosphate glasses reveal the role of constituent elements behind the changes. Microhardness is one of the key observations that could exhibit the physical strength and stability of the glass structure by revealing the internal structural aspects. Employed compositional changes with increasing alkali modifier content ($Na_2O$) with CaO leads to lowering its physical characteristics. Estimation of microhardness using the observed Young's modulus (Y) and Poisson's ratio ($\nu$) reveal the changes in the internal stability of glass structure against compositional modifications. The formula used to estimate the microhardness ($H_M$) is given as follows:

$$\text{Microhardness } (H_M) = (1 - 2\nu)\left[\frac{Y}{6(1+\nu)}\right]\text{Gpa} \tag{6}$$

As observed earlier, the structural deformations in the glass by virtue of alkali content increase also leading to lowering the microhardness of the sample. It is obvious that the alkali additions loosen the structural network of phosphate glass and thereby less compact. It has been observed with the experimental proof as increasing alkali ion content ($Na^+$) reduces the microhardness of the phosphate glass system. It reveals the structural deformation of phosphate glass with lower densification and higher interatomic spacing in the molecular arrangements of the glass system.

(b) **Variations in microhardness of $P_2O_5$ glass with increasing $Ag_2O$**

Microhardness ($H_M$) is one of the physical properties of the glass network which depends on the participant elements of chemical composition. Based on the compositional changes, the microhardness of the glass system either decrease or increase. The quaternary phosphate-based glass system with increasing incorporation of $Ag_2O$ by replacing CaO content reveals the decreasing trend of microhardness variations. As discussed earlier, the incorporation of monovalent cation ($Ag^+$) disrupts the phosphate glass network structure to great extent and thereby increasing the quantity of nonbridging oxygens at terminal ends. This leads to large structural deformation with every incorporation of $Ag_2O$ and thereby converting the basic polymeric chains structure of metaphosphate into pyro and orthophosphate units. These converting phosphate units have very short length in network connectivity with large number of discontinuities. The phosphate glass structure with this disrupted network connection could be explored by observing the microhardness estimation with the relation given in Eq. (6). As reported in elastic moduli observations for $Ag_2O$-included phosphate glass system, the microhardness values also confirm the structural deformation with a large number of nonbridging oxygen and disrupted a network of phosphate chains.

(c) **Variations in microhardness of $P_2O_5$ glass network with increasing ZnO**

Quaternary phosphate glass system with increasing content of ZnO by replacing alkaline earth metal oxide CaO exhibit different trends of microhardness results. Both these replaced and replacing elements are divalent cations with different functional parameters. It is expected that zinc oxide is a network modifier and its inclusion in the phosphate glass system leads to disruption the network connectivity. On contrary, the increasing addition of ZnO helps the phosphate glass system to get a more stable glass system with enhanced physical parameters. The main cause behind this observation is the higher field strength of $Zn^{2+}$. This high field strength cation overcomes the phosphate chain networks disruption by interconnecting different nonbridging oxygens of different network linkages. This interconnection is possibly enhancing the cross-link density between the structural network species and their linkages. It reflects in the microhardness observations. As observed in other elastic moduli investigations, this increasing network connectivity by the incorporated additive element ($Zn^{2+}$) helps the phosphate glass system to become more stable even at the decreasing content of CaO.

### 1.3.5 In vitro Behavior of $P_2O_5$ Glass Network Against Additive Content

In vitro characterization is an experimental method to explore the bioactive response of the glass in the aqueous solution, which has a similar ionic concentration as that of human blood plasma. The phosphate glasses with varying alkali and alkaline earth elements have been subjected to exploring their structural modification due to the compositional changes, revealing the influence of alkali content in altering the glass properties. Bioactive response (in vitro) reveals the bone-bonding ability of the glass composition in the living system. In vitro analysis is a testing method proposed to employ for a specified period of time, say 21 days by immersing the glass sample in a simulated body fluid (SBF), which has similar ionic concentrations as that of human blood plasma. After the targeted period, the sample has been examined to expose the formation of any calcium-rich apatite layer on its surface. By ensuring the elemental compositions of the apatite layer, the bioactive ability of the sample can be determined. During the in vitro analysis, the exchange of ionic components between the aqueous medium and immersed sample lead to dissolving the sample in the medium at a particular rate. In vitro behavior of the glass depends on various factors including the sample composition, its stability against the aqueous content, its ionic exchange proportions, etc. Based on the rate of dissolution of the glass sample in the immersed aqueous medium, the possibilities of ionic exchanges between the medium and glass can be determined. These ion-exchanging factors ensure the growth of calcium-rich apatite layer on the surface of the sample and thereby evident its bone-bonding ability. Although in vitro mechanism analyzes the ability of the sample to form calcium-rich apatite on its surface during the specified period of incubation time, based on the ratio of calcium to phosphate the apatite may be categorized with different names as listed in Table 5. Elemental composition of the apatite layer, particularly the calcium phosphate ratio is crucial in deciding its bone-bonding ability since the Ca/P ratio is not similar in all apatite layers which may be grown. The significance of the Ca, P ratio lies with the value of 1.67, hydroxyapatite ($Ca_{10}(PO_4)_6(OH)_2$) can bond with bone rather than any other calcium apatite mineral. Based on this observation, the

**Table 5** Various calcium phosphate with their respective Ca/P atomic ratios [14]

| Apatite mineral | Chemical formula | Ca/P ratio |
|---|---|---|
| Calcium dihydrogen phosphate | $Ca(H_2PO_4)2H_2O$ | 0.5 |
| Dicalcium phosphate dihydrate | $CaHPO_4.2H_2O$ | 1.0 |
| Dicalcium phosphate anhydrous | $CaHPO_4$ | 1.0 |
| Octacalcium phosphate | $Ca_8H_2(PO_4)_6.5H_2O$ | 1.33 |
| Tricalcium phosphate | $Ca_3(PO_4)_2$ | 1.5 |
| Hydroxyapatite | $Ca_{10}(PO_4)_6(OH)_2$ | 1.67 |
| Tetracalcium phosphate | $Ca_4O(PO_4)_2$ | 2 |

bioactive ability of the phosphate glass has been examined and its variation with respect to its modifier content is analyzed. Classification of apatite with the Ca, P ratio is given as follows.

After the incubation period in SBF medium (in vitro analysis), the sample has been examined to explore its bone-bonding ability. The characteristic studies such as X-ray diffraction (XRD) studies, Fourier transform infrared (FTIR) spectroscopy, scanning electron microscopy (SEM), energy dispersive X-ray analysis (EDAX), etc. are the key tools in disclosing the in vitro bioactivity of the glass sample. In X-ray studies, by ensuring the formation of a specific hydroxyapatite crystalline arrangement one can assure the emergence of calcium-rich apatite layer on the surface, since the glass doesn't have crystalline characteristics. FTIR can reveal the existence of molecular elements belonging to the hydroxyapatite combinations. Its functional vibrations could be explored using this spectroscopic analysis and ensured with the observation of specific absorption bands at specific wavenumbers. By comparing the scanning electron microscopic images before and after in vitro analysis, one can expose the surface modifications during the in vitro analysis. It helps to depict the growth of the apatite layer on the glass sample surface.

(a) **In vitro behavior of $P_2O_5$ glass network against the addition of $Na_2O$**

A series of phosphate glasses with increasing $Na_2O$ content by decreasing CaO gives different behavioral changes due to its structural modifications. Due to the structural modifications, its stability, elastic moduli, etc. its physical nature also change accordingly. During the in vitro analysis, the phosphate glass with increasing $Na_2O$ reveals different behaviors in ion-exchange properties and dissolution behavior. Increasing the $Na_2O$ content in the glass samples, increases the ability in apatite layer formation. Since it is a ternary-based glass with $P_2O_5$, $Na_2O$, and CaO, the possibility of calcium-rich apatite formation is prominent. After the in vitro analysis, XRD results of the ternary phosphate glasses exhibit their ability to develop a hydroxyapatite layer on its surface by exchanging the ionic elements with the surrounding immersion medium. The emergence of crystalline peaks and its data agreement with the standard JCPDS card including nos.74–0566, etc. This analysis also reveals the formation of polycrystalline nature of the surface by revealing the emergence of crystalline phases such as calcium metaphosphate, calcium metaphosphate hydroxide, calcium orthophosphate hydroxide, etc. Figure 3a, b, respectively, reveals the recorded SEM images of phosphate-based ternary glasses ($P_2O_5$–$Na_2O$–CaO) showing the formation of the apatite layer by comparing its surface before and after in vitro analysis.

In vitro response of any sample depends on the soluble nature of the immersed glass sample. Although the phosphate glasses with increasing $Na_2O$ are expected to have the ability for the kinetic growth of the CaP layer during in vitro analysis, their stability also plays a vital role. The dissolution rate of phosphate glass is its index of a physical stable structure. The dissolution behavior of the phosphate glass must be at a controlled rate. High-dissolution of phosphate ions are effective species in complex formations in the aqueous medium. The formation of such complexes in immersed medium suppress the functional group activity and thereby reduces the possibility of kinetic condensation for apatite layer growth [15]. Calcium-rich apatite

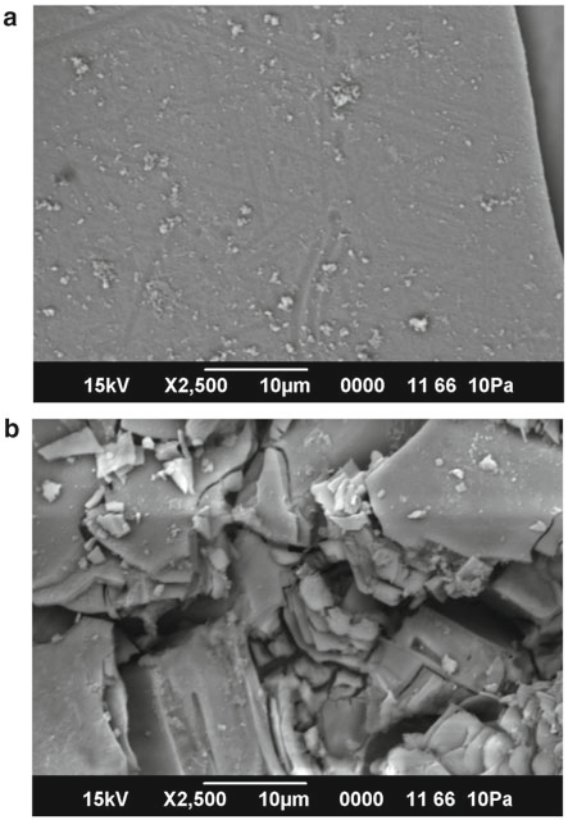


**Fig. 3** **a** Ternary phosphate glass surface before in vitro analysis. **b** Phosphate glass surface after in vitro analysis

formation is enhanced by the release of glass network species in more numbers due to the hydration effect. On contrary, exceeding the quantity of $PO_4^{3-}$ in the aqueous medium does not encourage the apatite formation on the glass surface rather it hinders the deposition of calcium-rich apatite layer. Hence, the releasing quantity of $PO_4^{3-}$ species in SBF medium is crucial and must be within a controlled rate. It should not exceed its alarming quantity before the formation of an apatite layer on its surface. As observed, the phosphate glasses are evident in the increasing ability of hydroxyapatite layer formation during in vitro analysis. By virtue of its $Na_2O$ content, its composition must be appropriate to exhibit controlled dissolution during the in vitro analysis in the aqueous medium. In a ternary phosphate glass system replacing $Na_2O$ components with CaO is always not helpful to show good bioactivity and it depends on the stable glass structure and controlled release of phosphorus ionic species during in vitro. The controlled release of ionic species including $PO_4^{3-}$ is essential in the ionic activity during bioactive mechanism and thereby forming calcium-rich apatite layer on the glass surface. Increasing of $PO_4^{3-}$ ionic species leads to an increase in the acidic nature in the aqueous medium wherein the incubation is occurring. The formation of

acidic nature does not encourage the apatite deposition and rather hinders the kinetic condensation.

(b) **In vitro behaviour of $P_2O_5$ glass network against addition of $Ag_2O$**

In vitro bioactivity of a phosphate-based glass system is tunable to different values based on the chemical species comprised in the glass structure. Quaternary phosphate-based glasses with stable $P_2O_5$ and $Na_2O$ and replaced CaO content with $Ag_2O$ reveal their chemical composition is dependent on in vitro bioactivity. Figure 4a shows the surface of low content (<5 mol%) silver oxide incorporated phosphate glass before in vitro analysis. In this glass system, the introduced $Ag^+$ monovalent ion disrupts the phosphate network chains and thereby leads to affecting the stability of the glass network. These phosphate glasses have shown poor bioactive behavior with increasing $Ag_2O$ content. During the *in vitro* analysis, the glass samples are set to incubate within the SBF solution for a stipulated period enabling to exchange the ionic components between the sample and immersed medium. The stability of glass sample is a key parameter, since the release of ionic species and its quantity depend on the glass dissolution rate. In the present $Ag_2O$ phosphate glass system, the glass

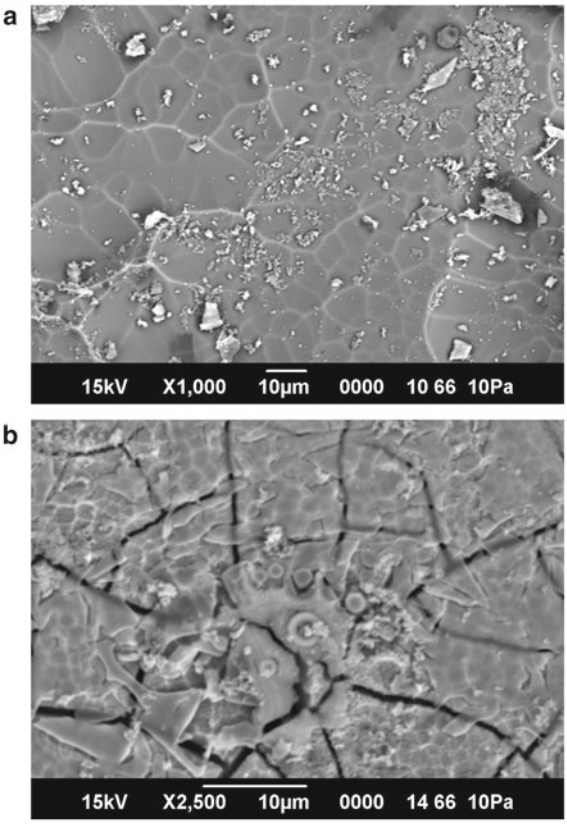


**Fig. 4** **a** Surface of $Ag_2O$-added quaternary phosphate glass before in vitro analysis. **b** Surface of $Ag_2O$-added quaternary phosphate glass after in vitro analysis

samples with lower $Ag_2O$ exhibit high stability and thereby low dissolution during in vitro analysis. Release of ionic species from this glass is in a controlled manner rather than other glasses with increased or higher $Ag_2O$ additions.

Due to the poor stability and thereby random release of ionic species could possibly lead to converting the aqueous medium to acidic in due course of the incubation period. This acidic nature will hinder the possibility calcium-rich apatite layer formations. The release of abundant ionic species in the earlier stage of in vitro (within a few days) analysis may lead to affecting the ionic activity mechanism drastically. In phosphate glasses with higher $Ag^+$, the dissolution rate of glass during in vitro is higher and thereby the possibility of higher $Ag^+$ ion release is high in the surrounding medium. It has been observed earlier that [16], the release of a high amount of $Ag^+$, on the other hand, impedes the possible growth of calcium-rich apatite layer on the glass surface. The ionic activity of $Ag^+$ disrupts the medium and thereby reduces the quantity of Ca, P ionic components necessary to form a calcium–phosphate layer. Released $Ag^+$ into the aqueous medium, in turn, lowers its pH value and becomes acidic, this doesn't encourage the activity of functional ionic products necessary for hydroxyapatite formations. Figure 4b shows the surface of the low-content silver oxide added phosphate-based glass network with the deposition of HAp layer. Thus, the phosphate glasses with lesser $Ag_2O$ content (<5 mol%) exhibited a controlled dissolution of glass samples in an aqueous medium and thereby releasing less amount of $Ag^+$ which could not be possible at the level to hinder the growth of calcium-rich apatite layer on the surface of the sample.

### (c) In vitro behavior of $P_2O_5$ glass network against the addition of ZnO

Observations on the in vitro bioactivity of ZnO-added quaternary phosphate-based glass system exhibit its non-productive nature with higher ZnO content. In this glass system, ZnO is an additive component progressively increased within the phosphate glass network by replacing an equivalent quantity of CaO. Figure 5a shows the surface of low content (<3 mol%) zinc oxide added phosphate-based glass system. As discussed above, the ZnO-added glass structure becomes more stable by enhancing the cross-link density by connecting various disrupted phosphate chains of shorter length. Although $Zn^{2+}$ is a network modifier, its high ionic field strength facilitates enhancing glass stability. In vitro bioactivity of the glass medium is depending on how the sample is managed within the physiological solution in a stipulated period to release and exchange its ionic components with the surrounding medium. Not lesser, the desired quantity of ionic products is essential to initiate the CaP layer during the in vitro analysis. In vitro analysis facilitates the two mediums such as the sample and surrounding medium to exchange ionic species to grow a crystalline layer on the surface. During the growth, the initial release of Ca and P made the physiological medium supersaturated, and the glass surface was used to absorb such calcium phosphate ionic components to form a gel-like amorphous calcium-rich layer on its surface. Nucleation sites for the calcium apatite layer can be formed only on this gel-like structure in due course of the incubation period. Due to the initiation of nucleation sites with the available product and thereby enhanced release of other

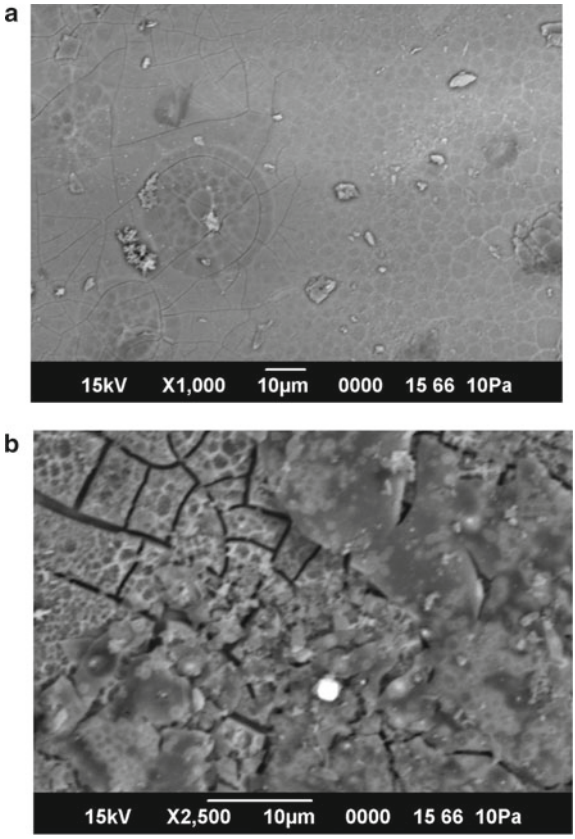


**Fig. 5** **a** Surface of ZnO-added quaternary phosphate glass before in vitro analysis. **b** Surface of ZnO-added quaternary phosphate glass after in vitro analysis

ionic products lead to the hydroxyapatite layer formation in the upcoming days. This is the mechanism of in vitro bioactivity phosphate-based glass system.

In zinc oxide incorporated phosphate-based glass system, the leaching of ionic products is not at the desired rate required for apatite layer formation. It has been evident that incorporation of $Zn^{2+}$ made the phosphate glass structure become more stable and hence, during the incubation period in physiological solution it affects the dissolution of glass and results in very slow degradability. This low dissolution, on the other hand, is not enough to promote the ionic activity necessary for hydroxyapatite formations. It is obvious that zinc is an amphoteric element possessing very low solubility by nature. Its lower dissolution doesn't favor the growth of the apatite layer in the sample surface within a stipulated time. Zinc oxide added phosphate-based glasses exhibit delayed apatite formation during in vitro analysis [17] mainly because of its low degradation profile.

## 2 Conclusion

Phosphate based glass is one of the prominent non-crystalline systems has unique structure readily available to alter its structural aspects under the influence of suitable foreign elements. Its property limitations are proven to be overcome by incorporating appropriate metal oxides of desired quantity. It has remarkable application potential mainly because of their flexible nature enable for structural modifications. Thermal, mechanical and dissolution ability of phosphate based glass network is quite alterable based on the incorporation of suitable amount of metal oxide component and hence, its bioactive nature also found to be tuneable. Inclusion of metal oxides such as $Ag_2O$ and ZnO into the phosphate glass network exhibit its different and quantity dependent bioactive responses.

## References

1. Williams DF (1987) Definitions in biomaterials. In: Proceedings of a consensus conference of the European society for biomaterials, vol. 4. Chester, England, March 3–5 1986, Elsevier, New York
2. Park JB (1995) Biomaterials. In: Bronzino JD (ed) The biomedical engineering handbook. CRC Press LLC, Boca Raton, FL
3. Lane JM, Tomin E, Bostrom MPG (1999) Biosynthetic bone grafting. Clin Orthop Relat Res 65:107–117
4. Murugan R, Ramakrishna S (2005) Development of nanocomposites for bone grafting. Compos Sci Technol 367:2385–2406
5. Cao W, Hench LL (1996) Bioactive materials. Ceram Int 22(6):493–507
6. Hench LL, Polak JM (2002) Third-generation biomedical materials. Science 295(5557):1014–1017
7. Hulbert SF, Hench LL, Forbers D, Bowman LS (1982) History of bioceramics. Ceram Int 8(4):131–140
8. Hench LL, Andersson O (1993) Chapter 3, Bioactive glasses, An introduction to Bioceramics, vol 1, 1st edn. World Scientific, Singapore, pp. 41–62
9. Hench LL, Splinter RJ, Allen WC, Greenlec TK (1971) Bonding mechanisms at the interface of ceramic prosthetic materials. J Biomed Mater Res 2(1):117–141
10. Rajendran V, Palanivelu N, El-Batal HA, Khalifa FA, Shafi NA (1999) Effect of $Al_2O_3$ addition on the acoustical properties of Lithium Borate glasses. Acoust Lett 23(6):113–121
11. Barbieri L, Corradi AB, Leonelli C, Siligardi C, Manfredini T, Pellacani GC (1997) Effect of $TiO_2$ addition on the properties of complex aluminosilicate glasses and glass-ceramics. Mater Res Bull 32(6):637–648
12. Neel EAA, O'Dell, LA, Smith ME, Knowles JC (2008) Processing, characterisation and biocompatibility of zinc modified metaphosphate based glasses for biomedical application. J Mater Sci Mater Med 19(4):1669–79
13. Brow RK, Kirkpatrick RJ, Turner GL (1990) The short-range structure of sodium phosphate glasses I. MAS NMR studies. J Non-Cryst Solids 116(1):39–45
14. Vallet-Regı M, lez-Calbet JMG (2004) Calcium phosphates as substitution of bonetissues. Prog Solid State Chem 32:1–31
15. Peltola T, Jokinen M, Rahiala H, Levänen E, Rosenholm JB, Kangasniemi I, Yli-Urpo A (1999) Calcium phosphate formation on porous sol-gel-derived $SiO_2$ and CaO-$P_2O_5$-$SiO_2$ substrates in vitro. J Biomed Mater Res 44(1):12–21

16. Shirkhanzadeh M, Azadegan M (1998) Formation of carbonate apatite on calcium phosphate coatings containing silver ions. J Mater Sci Mater Med 9(7):385–391
17. Haimi S, Gorianc G, Moims L, Lindroos B, Huhtala H, Raty S (2009) Characterisation of Zinc releasing three-dimensional bioactive glass scaffolds and their effect on human adipose stem cell proliferation and osteogenic differentiation. Acta Biomater 5(8):3122–3131

# Chapter 5
# Bio-synthesized and Photocatalytic Effectiveness of Date Pit Mediated Magnesium Oxides Nanoparticles


**J. Sackey and M. Maaza**

## 1 Introduction

The textile-manufacturing sector is reflected as one of the principal canals for water contamination worldwide. The industry faced problems with the treatment and disposal of effluent streams containing organic compounds. Water contamination of organic textile dyes makes up 80% of the waste from the sector. Textile dyes are organic compounds with an aromatic structure having the ability to impact colours on a given substrate. Organic textile dyes including acid orange 8, methylene blue, acid red 14 and methyl are highly toxic and non-degradable [1]. Due to hydrolysis, reactive dyes discharged into wastewater become non-reusable because they become non-reactive [2]. The organic compound become a major source of environmental contamination and cause a great hazard to human health due to their degradation inabilities. Sub-Saharan Africa is disadvantaged in catering to the water needs of its citizens, thus making children, women and elders victims of death as the result of drinking contaminated water. For instance, in Ghana, industry textile effluents and metal pollutants from illegal mining activities are the main drivers of fresh-water contamination. With a population of about 31 million, 5 million people rely on surface water for daily use leaving them exposed to water-related illnesses and diseases [3]. Cameroon faces a similar challenge with a high infant mortality rate owning to drinking contaminated water. The majority of the people do not have toilet facilities in Senegal. Therefore, exposure to faecal contamination occurs both inside and outside the household paving way for microbial contamination. Drinking

J. Sackey (✉) · M. Maaza
Nanosciences African Network (NANOAFNET), iThemba LABS-National Research Foundation, Old Faure Road, Somerset West 7129, South Africa
e-mail: sackey@tlabs.ac.za

UNESCO-UNISA Africa Chair in Nanosciences/Nanotechnology, College of Graduate Studies, University of South Africa (UNISA), Muckleneuk ridge, P.O. Box 392, Pretoria, South Africa



K. Kasinathan et al. (eds.), *Nanomaterials for Energy Conversion, Biomedical and Environmental Applications*, Materials Horizons: From Nature to Nanomaterials,
https://doi.org/10.1007/978-981-19-2639-6_5

such contaminated water leads to water-borne diseases like diarrhoea, dysentery and cholera causing a high infant mortality rate. The situation is even worse in developing countries in Africa like Malawi with limited access to clean water, sanitation and hygiene. With a population of 19 million, 4 million Malawians use infested river water for daily use exposing 78% of children under the age of 2 years to water-related illnesses that may lead to a great infant mortality rate. The WHO states that if the issue of water contamination is not addressed, the world population will live in water scarcity by 2025. Hence, it is imperative and important to design a more sustainable solution that will remove the organic compounds from the wastewater. This is because investing ineffective wastewater treatment and hygiene is an essential foundation for good health, saving millions of lives. Therefore, in response to addressing the existing problem and in compliance with the Sustainable Development Goal 6, several researchers have used different methods to remove organic compounds from wastewater. Amongst the many techniques such as electrochemical coagulation, reverse osmosis, nanofiltration used, adsorption is considered one of the best, simple, eco-friendly and cost-efficient methods of dye elimination in wastewater [4–9].

## *1.1 Aims and Objectives of the Chapter*

The chapter discusses the different water treatment techniques with an emphasis on the green nanochemistry approach. The objective is to describe via the green nanochemistry method the synthesis of MgO nanoparticles and their effectiveness in wastewater treatment. In this chapter, MgO nanoparticles will be synthesized via the green chemistry approach and characterized using scanning and transmission electron microscopy, energy-dispersive spectroscopy as well as X-ray diffraction spectroscopy. The optical properties of the MgO nanoparticles are also discussed. The discussion was further extended toward the MgO nanoparticle's ability to remediate industry textile organic dye. In this case, the photocatalysis technique is employed to investigate the degradation ability of the metal–oxide nanoparticles against acid orange 8 dye.

## *1.2 Wastewater Treatment by Coagulation*

Coagulation is a technique of treating wastewater by the addition of chemicals. The coagulant can either be aluminium or iron based. The coagulation process involves trivalent chemicals, whose positive charges neutralize the negative charges of the contaminants in the wastewater. Subsequently, the dirt particles bind to the chemicals to form floc, which is removed from the water via sedimentation. As a result, the clean water is passed through the filtration system which encompasses sand, gravel and charcoal. This is done to remove excess or additional dust particles. The coagulation

process is fast and efficient for the removal of insoluble contaminants. However, its capability to remove arsenic is very low. The technique also requires the use of non-reusable chemicals.

## *1.3 Wastewater Treatment by Chlorination*

Chlorination is a process of removing microbial, disease-causing pathogens and other microorganisms from contaminated water. The parameters such as water concentration, water pH, contact time and water temperature all are associated with chorine disinfection effectiveness. Normally, when chlorine is added to the water, it quickly reacts with the microorganism. Chlorination can be accomplished with either power chlorine (calcium hypochlorite) or liquid chlorine (sodium hypochlorite). Chlorination oxidized iron and manganese to be filtrated out and hydrogen sulphide to reduce the odour. Chorine disaffection is not efficient for large contaminants in water. It is also an expensive technique that requires monitoring and management.

## *1.4 Wastewater Treatment by Reversed Osmosis*

Reserved osmosis is the process of cleaning wastewater whereby a cell phone like a membrane is used to separate purified water from contaminated water. Reserve osmosis acts as an ultra-filter blocking large particles unable to pass through the membrane pores. A wide range of membranes such as thin-film composites, cellulose acetate, cellulose triacetate is rated based on their capability to reject contaminates from water. The process of reserved osmosis does not require chemicals and is efficient at the elimination of solids and also microorganism, yet its maintenance and operation cost is expensive. It also presents issues with the low flow rate as well as rapid membrane clogging. Some factors including pressure, temperature, membrane type and flow control affect the performance of the reserved osmosis system.

## *1.5 Wastewater Treatment by Advanced Oxidation*

Advanced oxidation process (AOP) is an in situ technique for the generation hydroxyl and sulphate radicals to degrade the organic pollutant in wastewater. The process involves mineralizing the pollutant to carbon dioxide and water. The reagent used is ozone and chlorine, which mostly leave behind carcinogenic by-products. There are several AOPs such as the use of microwave, plasma, electron beam and electrochemical treatment. The advantages of using the AOP are its effectiveness for recalcitrant and rapid degradation ability. However, it presents some technical constraints and low throughput. Further, this technique is not economical for small industries.

### *1.6 Wastewater Treatment by Nanofiltration Membrane*

Nanofiltration membrane technology is a non-destructive pressure-driven process of wastewater treatment. Some factors affecting pollutant separation via nanofiltration membrane are the particle size and charge effect [10]. Like reverse osmosis, this technology doesn't require chemicals and generates very small solid waste. It is also characterized by its fast reaction kinetics and rapid selectivity. Nonetheless, it requires high energy and is not economic for medium or small industries.

### *1.7 Water Treatment by Metal–Oxide Nanoparticles*

Recently researchers have confirmed metal–oxide nanoparticles effectiveness in the removal of organic compounds from effluents. Cleansing contaminated wastewater using nanoparticles are reliable and affordable and offers a better alternative Preparation and processing of metal–oxide nanoparticles including CuO, MgO, NiO and ZnO are on the increase. These nanoparticles have specific properties that make them attractive to be used in many applications including wastewater treatment. Manipulating the morphology and architecture of metal oxide, especially MgO nanoparticles provides ample scope for researchers to establish correlation with their properties.

## 2 Green Nanochemistry Method

Green nanochemistry synthesis of transition metal–oxide nanomaterial, which involves the use of various plant or agro-waste products as reducing agents, is preferred over the chemical and physical processes. The green bio-synthesis method requires the use of eco-friendly, non-toxic and easy synthesizing methods [11]. The use of plant extracts via the green chemistry approach to preparing metal–oxide nanoparticles has been widely reported. For example, Yulizar et al. [12] used Theobroma cacao seed bark extract to synthesize ZnO/CuO nanocomposites to decrease the high bandgap energy of ZnO. Similarly, Mohammadi-Aloucheh et al. [13] used Mentha longifolia leaf extract to synthesize ZnO/CuO nanocomposites and investigated their anti-bacterial activities. In the same manner, Ezhilarasi et al. [14] used Moringa Oleifera to synthesize NiO nanoparticles and tested them for cytotoxicity and antibacterial studies. Raja et al. [15] synthesized ZnO nanoparticles using extracts obtained from Tabernaemontana divaricate. Diallo [16] reported comprehensive studies on using natural extracts of Aspalathus linearis to synthesize different sizes of $SnO_2$ nanoparticles. The nanoparticles proved efficient against methylene blue, Congo red and Eosin Y. In addition to the plant extracts, researchers have used

the agro-waste products known to contain a high number of antioxidants and phytochemical constituents to synthesize a variety of metal oxides for different applications. For example, Fuku et al. [17] synthesize $Cu_2O$/CuO/ZnO nanocomposite using the peel extracts of Punica granatum to investigate their electrochemical properties. Mohammadi-Aloucheh et al. [18] prepared ZnO/CuO nanocomposites by using Vaccinium Arctostaphylos L. fruit extract and studied their antibacterial activities. Ibrahim [19] synthesized AgNPs from aqueous extracts of banana peels and investigated the antibacterial properties. Leong [20] used banana peels extracts to synthesize copper (II) oxide nanoparticles to investigate their photocatalytic activity. Similarly, Bankar et al. [21] used banana peel extracts to synthesize gold nanoparticles and studied their antimicrobial activity. Aminuzzaman et al. [22] reported on the green synthesis of CuO NPs from peels of banana extract and studied the photodegradation ability. The aqueous extracts from Zea mays were used to synthesize $Cu_2O$ nanoparticles and tested for photodegradation ability against organic dyes and textile wastes [23]. In the same manner, Sackey et al. [24] biosynthesized single-phase $Cr_2O_3$ with the extract obtained from peels of Ipomoea batatas L. A composite of $NiFe_2O_4$ was successfully synthesized via extracts from Persa Americano seeds, which showed excellent electrochemical properties [25].

## *2.1 MgO Nanoparticles Synthesis*

MgO is thermally and stoichiometrically stable with a very simple sodium–chloride structure and high corrosion-resistant behaviour [26]. Nanocrystalline MgO displays low heat capacity, chemical inertness and optical transparency [27]. In addition, MgO exhibits a high surface area and hence can be used as an excellent material to remediate various harmful chemicals [28–30]. Due to its wide bandgap, MgO has applications in antibacterial studies, sensors and in optical coating. Generally, MgO is not toxic and hence can be found in crucibles, refractory materials and coatings. Given its excellent abovementioned physiochemical attributes, MgO is classified as an eco-friendly and industrially essential material used as semi-conductor and absorbent for the organic and inorganic pollutants in wastewater. They also possess excellent antioxidant properties with application in wound healing, tissue regeneration and bioimaging [31, 32]. Parameters such as pH, annealing temperature, different synthesizing routes and ionic strength affect dimensions and morphology of the MgO nanoparticle formation. MgO enables the transfer of electrons and is hence used as a support for active species of catalyst [33]. For instance, Almerindo et al. [34] used MgO as a promoter in the transesterification reaction of oil for diesel production by means of short-chain alcohols. MgO is used as a heterogeneous catalyst to improve the synthesis method [35].

## 2.2 Physical and Chemical Synthesis of MgO Nanoparticles and Applications

MgO nanoparticles are synthesized via various physical and chemical routes. Each route produces a different morphology of MgO nanoparticles. For example, Qiu et al. employed the surfactant-mediated solution method to synthesize nanosized $Mg(OH)_2$ and obtained needle- or lamella-like $Mg(OH)_2$ nanoparticles [36]. Pei et al. [37] used a sol–gel technique with magnesium chloride as the precursor to synthesize fine magnesium oxide. They obtained single-phase MgO after thermal decomposition at 800 °C and nanoparticle dimension of 100 nm. Shimpi et al. [38] employed a double-step successive hydrothermal process at a low temperature of 155 °C to synthesize nanocomposite of MgO/ZnO. Stankic et al. [39] reported the synthesis of cubic-shaped MgO nanoparticles using the chemical vapour deposition (CVD) method together with successive thermal activation steps. Fang, Haihong, et al. synthesized MgO via the sol–gel auto-combustion method [40]. Niu et al. demonstrated the large-scale synthesis of bone-like MgO nanocrystals via a solvothermal process [41]. Many other synthesis routes including laser vaporization [42], wet chemical method [43], surfactant methods [44], combustion aerosol synthesis [45], chemical vapour deposition [46] provide nanoscale MgO. Purwajanti et al. obtained porous nano-MgO via the mesoporous carbon hard template method [47]. Sirota et al. [48] synthesized MgO nanopowder via thermal plasma in a thermal DC plasma touch. The high purity nanopowders recorded a particle size of 100–150 nm. In another paper, MgO nanoparticles were hydrothermally synthesized and used as adsorbents for the degradation of azo and anthraquinone dyes from an aqueous medium [49]. Yet the aforementioned technique presents numerous disadvantages. For example, the use of the thermal plasma technique requires high-frequency discharge, high AC or DC arcs and reactive submerge arc. Hydrothermal techniques equally require expensive raw materials and numerous processing steps. The CVD method involves high thermal activation and high vacuum conditions to obtain an almost perfect shape nanomaterial.

## 2.3 Green Nanochemistry Preparation of MgO NPs and Applications

Several researchers used an environmentally friendly and economic green chemistry process of synthesizing MgO for various applications [50–53]. The green method requires no sophisticated machinery or harmful chemicals yet the production of large-scale MgO nanoparticles is achievable. This methodology involved the use of plants, fungus, bacterial and algae, which have proven to be more convenient and preferred over the physical and chemical methods [54, 55]. Many have successfully synthesized via this approach crystalline MgO nanoparticles using any precursor of magnesium. Such precursors include chlorides, acetate, sulphate and nitrate [56, 57].

Generally, extracts obtained from plants, or templates from the biological species serve as stabilizing agents for the preparation of MgO nanomaterial [58, 59]. For example, Saied et al. [60] used Aspergillus terreus S1 to synthesize spherical well-dispersed MgO nanoparticles with an average particle size of 8–38 nm. The authors reported that the MgO nanoparticles showed high growth inhibition of gram-positive and gram-negative. Furthermore, they confirmed that the MgO nanoparticles exhibited a 97.5% ability to eliminate chromium ions from effluent. In another study by Hassan et al. [61], they reported successful biosynthesis of MgO nanoparticles using Rhizopus oryzae as a catalyst. The fungal-strain-assisted MgO nanoparticles with particle sizes ranging from 9 to 20 nm showed enhanced potential as a good antibacterial candidate against several pathogens such as Staphylococcus aureus, Bacillus subtilis as well as Escherichia coli and Candida albicans. Similarly, Ahmed et al. [62] synthesized MgO nanoparticles using Acinetobacter johnsonii $RTN_1$ and investigated its antibacterial activity against Acidovorax oryzae. Sushma et al. [63] also synthesized MgO nanoparticles using aqueous extracts of C. ternatea plant. They reported a 65% maximum inhibition activity, which was attributed to the antioxidant properties in the plant extracts.

The plant extract is also important in limiting agglomeration to produce well-crystalline nanoparticles. Plant extracts are reported to contain some active compounds, which act as free radicals and assist in neutralizing reactive oxygen species. The formation of MgO nanoparticles is examined as the chemical interaction between the precursor and the extract, which results in the reduction of the metal salt to its nano form. More precisely, the phytochemicals of the antioxidant obtained in the extract form a covalent bond between the precursor salt, which is broken down via thermal oxidation resulting in the MgO nanoparticles [64–66]. Das et al. [54] used Bauhinia purpurea leaf extracts to bio-synthesize MgO nanoflakes with a particle size of 11 nm. According to the authors, the extracts contain active compounds such as phenolic, flavonoids and antioxidants, which act as reducing agents for the synthesis of MgO nanoflakes. The Bauhinia purpurea leaf mediated MgO nanoflakes showed an excellent antibacterial study against S. aureus. Dobrucka [67] prepared MgO nanoparticles using A. abrotanum extracts and obtained high purity particles with a size of 10 nm. The author concluded that the MgO nanoparticles showed good antioxidant properties and excellent photodegradation of methyl orange. Moorthy et al. [51] used extracts from neem leaves to synthesize MgO nanoparticles. Vijayakumar et al. [68] studied extensively the antimicrobial properties of MgO nanoparticles synthesized by aqueous extracts of Capparis zeylanica L. leaf. The tetragonal MgO nanoparticle with a crystallite size of 32.6 nm was effective against several pathogens.

Similarly, Akshaykranth et al. [69] gave a comparative analysis of the effectiveness of an antibacterial activity against the strain of bacterial for MgO NPs. The MgO nanoparticle was prepared by extracts of Lawsonia inermis leaves and via the chemical method. As per their investigation, the green chemistry approach recorded a smaller particle size of 20 nm and better antibacterial studies and enhanced inhibition zoon at 80 μL concentration. In another report by Essien et al. [70] they synthesized MgO nanoparticles from Chromolaena odorata leaf extracts based on

the chemical reaction between the magnesium sulphate and extract phytochemicals. They obtained well-distributed nanoparticles with an average size of 12.3 nm. Using the same eco-friendly and simple green synthesizing approach, Ammulu et al. [66] reported the synthesis of MgO nanoparticles from heartwood extracts of Pterocarpus marsupium. The authors confirmed the presence of polyphenolic and flavonoids in the extracts, which assisted in the formation of polydispersed nanoparticles with particle sizes between 15 and 25 nm. The spherical shaped MgO nanoparticles showed great potent against gram-positive bacteria and gram-negative bacterial. In another investigation, the authors used strawberry leaf extract to bio-synthesize MgO nanoparticles [71]. Recently, MgO nanoparticles are also synthesized via extracts obtained from ago-waste products [72]. Fruits and vegetables as well as their by-products are reported to contain active phytochemical properties essential for MgO nanoparticle formation [73]. Nazeer et al. [74] reported that the phenolic groups in Coriandrum sativum and Moringa oleifera assisted in the reduction of the salts to the metallic oxide nanoparticle. They investigated the MgO nanoparticle's ability to treat chlorosis and confirmed its biocompatibility with the human embryonic kidney cell line. Li et al. [75] synthesized MgO hybrid carbonaceous composite via extracts obtained from sugarcane. The nanocomposite is used as a good material to eliminate organic contaminants in wastewater. Similarly, Qin et al. synthesized MgO-modified biochar from rice straw at a varying temperature [76]. Suresh et al. [77] reported that Nephelium lappaceum L. peel acted as natural ligation agents in the synthesis of MgO nanoparticles. Sugirtha et al. [78] used extracts of cauliflower and pomegranate peels to synthesize MgO nanoparticles, which showed good anti-cancer and photocatalytic activity. MgO nanoflakes of dimension 12 nm was synthesized from citrus lemon extracts at room temperature [79]. Vergheese and Vishal [80] reported on the green chemistry synthesis and characterization of MgO nanoparticles from Trigonella foenum-graecum aqueous extracts. The antibacterial properties of the MgO were investigated against gram-positive and gram-negative bacteria and it showed good results in both stains. Vijayakumar et al. [81] used citrus Aurantium peel extracts to prepare MgO nanoparticles and reported their antimicrobial activities. Furthermore, Essien et al. [82] identified the phytochemical in the leave extracts of Manihot esculenta to serve as reducing and capping agents in the synthesis of MgO NPs. They obtained hexagonal and less agglomerated microstructure with a practice size of 37.3 nm.

## *2.4 Green Synthesis of MgO Nanoparticle via Date Pit Extracts*

This contribution reports on the green nanochemistry synthesis of MgO nanoparticles using date pits extracts and its application toward photocatalytic degradation against acid orange 8. The fruits date scientifically known as Phoenix dactylifera is a rich source of fibres, protein and carbohydrates, which is cultivated mostly in the

Arab world [83]. Its by-products, which are the date pits are also known to contain minerals, lipids and protein. Phytochemical studies showed that the fruits and their waste products have some phenolic, carotenoids and flavonoid compounds useful for anti-mutagenic, anti-microbial, anti-cancer as well as antioxidant benefits [84]. In the study, the green nano-chemistry synthesis approach uses water as the universal solvent. The synthesis processes that will be discussed in detail involved the phyto-chemicals in the date pit will react chemically with the molten salts of the precursor reducing them to the nanoscale. The precursor, magnesium acetate was purchased from Sigma-Aldrich while the date was bought from Strand Cash & Carry in South Africa. The date fruits were eaten, and date pits were sent to the laboratory to be used in the preparation of the extracts. The preparation of the extracts was done following a cost-effective method described elsewhere [85]. Briefly, 30.0 g of the date pit was washed and placed in 200 ml distilled water. The content was brought to boil at a temperature of 80 °C for 2 h under constant magnetic stirring. The obtained yellowish extracts were filtrated twice under Whatman filter paper to remove any excess residue. The aqueous extracts, which recorded a pH of 6 were kept ready to be used for the synthesis of MgO nanoparticles. The synthesis routes for MgO nanoparticles are described as follows: 2.0 g of the precursor was dissolved in a 50 ml of the date pits extracts under constant magnetic stirring. The suspension was centrifuged and washed two times with distilled water. Subsequently, a laboratory oven dried up the precipitate to obtain a creamish powder. Afterwards, a laboratory furnace annealed the cream-ish powder at 500 °C for 2 h. A schematic diagram of the procedure is shown in Fig. 1. Later, the samples were characterized for structural, optical and morphological properties via the different characterization techniques. As a direct application, the MgO nanoparticles were tested against acid orange 8 dye degradation.

## 3 Application of MgO Nanoparticles in Wastewater Treatment

The use of bio-synthesized nanomaterial in environmental remediation such as wastewater treatment via photocatalysis process is pivotal. Bioassisted MgO NPs are promising materials for the elimination of organic dyes in an aqueous medium. Several morphologies including nanoflakes, a nanoplate, nanorods, nanowires and varying particle sizes of MgO nanomaterial are used as an adsorbent in the photocatalysis against pollutants in wastewater. Choudhury et al. [86] synthesized nanoflakes MgO using an aqueous extract from Madhuca longifolia flower. The authors tested the MgO nanoparticle calcined at 450 °C against the elimination of nigrosine dye via photocatalysis process using the Taguchi approach. They reported 86% dye removal ability by the MgO nanoparticles. Similarly, Khan et al. [87] used aqueous extracts from Dalbergia sissoo leaves to prepare MgO nanoparticles having varying bandgap energies. According to their analysis, MgO nanoparticles with a lower bandgap of

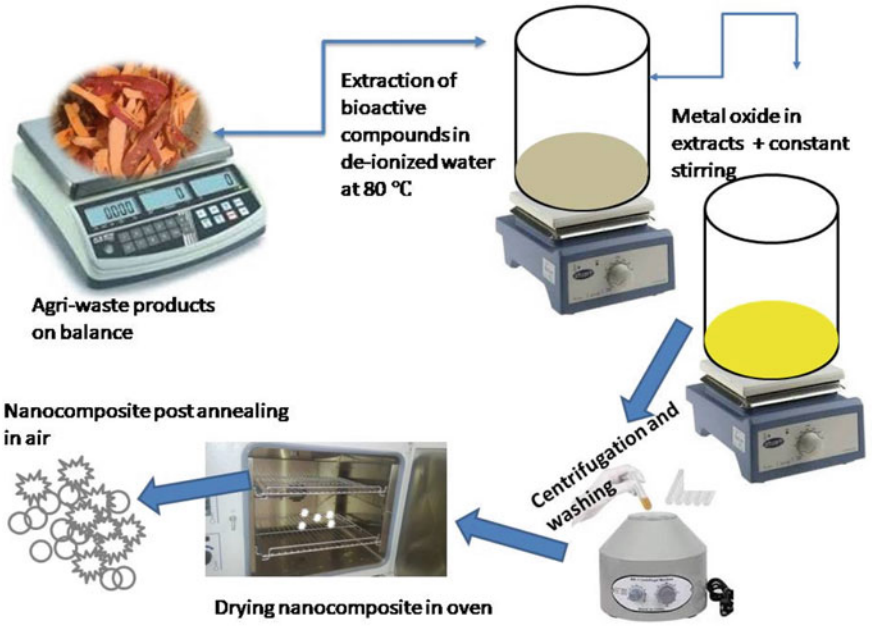


**Fig. 1** Pictorial illustration of the biosynthesis process of biogenic engineered MgO NPs

4.175 eV recorded the maximum degradation efficacy of 81% against methylene blue dye. In another study by Fouda et al. [88], they used metabolites secreted by Aspergillus niger strain F1 as a template to synthesize MgO nanoparticles. Their report shows that the photocatalysis efficacy of nanoparticles was investigated under visible light irradiation. They reported a high adsorption capacity of the MgO nanoparticles to remove heavy metals including lead, nickel and chromium present in tanning wastewater.

## *3.1 Photocatalysis of MgO Nanoparticles with Acid Orange 8(AO8)*

Photocatalysis is an alternative technology for the treatment of contaminated water. It is the phenomenon, where a substance changes the chemical reaction rate in the presence of light. The process involves the creation of electron–hole pair ($e^-/h^+$) when the semiconductor is exposed to light. Generally, photocatalysts are semiconductors. The electron–hole pair forms a hydroxyl radical that displays oxidation of the organic matter. Photocatalysis is a very simple yet efficient technique with the ability to eliminate organic compounds, and in addition leads to the production of energy. In this contribution, the photocatalytic activity of the date pit mediated

MgO nanoparticles was tested against an aqueous solution of acid orange 8 under a UV lamp (Mega-Ray 160 W/240 V MR160 SPL11/14). The methodology used is described as follows. A small amount of the MgO NPs was added to a volume of 25 ml aqueous solution of acid orange 8. The mix was allowed to sit without illumination under constant magnetic stirring for some time to acquire adsorption stability. Before being exposed to light irradiation, 4 ml of the samples are taken for UV-vis absorbance measurement. Subsequently, samples were taken every 5 min for 35 min.

### *3.2 Characterization of Date Pit Assisted MgO Nanoparticles Techniques*

The biosynthesized MgO nanoparticles were characterized for morphological, structural and optical properties instantly without any surface modification. The different characterization techniques used are described here. Tecnai 720 TEM and Zeiss Ultra plus 55 FE-SEM connected to Oxford instrument with an X-max solid state silicon drift detector were used to characterize the morphology and chemical analysis of the MgO nanoparticle. X-ray diffraction analysis of the MgO nanoparticles was performed using Bruker AXS D8 Advance. UV-vis absorbance measurement of the aqueous date pits extracts and the MgO nanoparticles were measured on Cary 5000 UV-vis NIR spectrophotometer within the wavelength of 200–500 nm. The diffuse reflectance measurement of the MgO nanoparticles was recorded using a Cary 5000 UV-vis NIR spectrophotometer equipped with an interpreting sphere.

## 4 Morphological and Chemical Element Analysis of MgO Nanoparticles

The morphology and the chemical elements with their respective weight and atomic percentages (see inset) of MgO nanoparticles are shown in Fig. 2a. The scanning electron microscopy (SEM) image shows spherical shaped and agglomerated MgO nanoparticles. The agglomeration is attributed to the photochemical reactions in the date pits extracts. The chemical elements obtained from the energy-dispersive spectroscopy (EDS) analysis displayed in the inset show that the nanoparticles are predominately rich in Mg followed by O. The presence of C originates from the carbon coating of the sample before SEM analysis while the other elements in very small quantities emanated from the date pits extracts. Therefore, from the EDS analysis, it can be confirmed that MgO nanoparticles have been successfully synthesized. The transmission electron microscopy (TEM) image and its corresponding selection electron area diffraction (SEAD) image is shown in Fig. 2b, c respectively. The

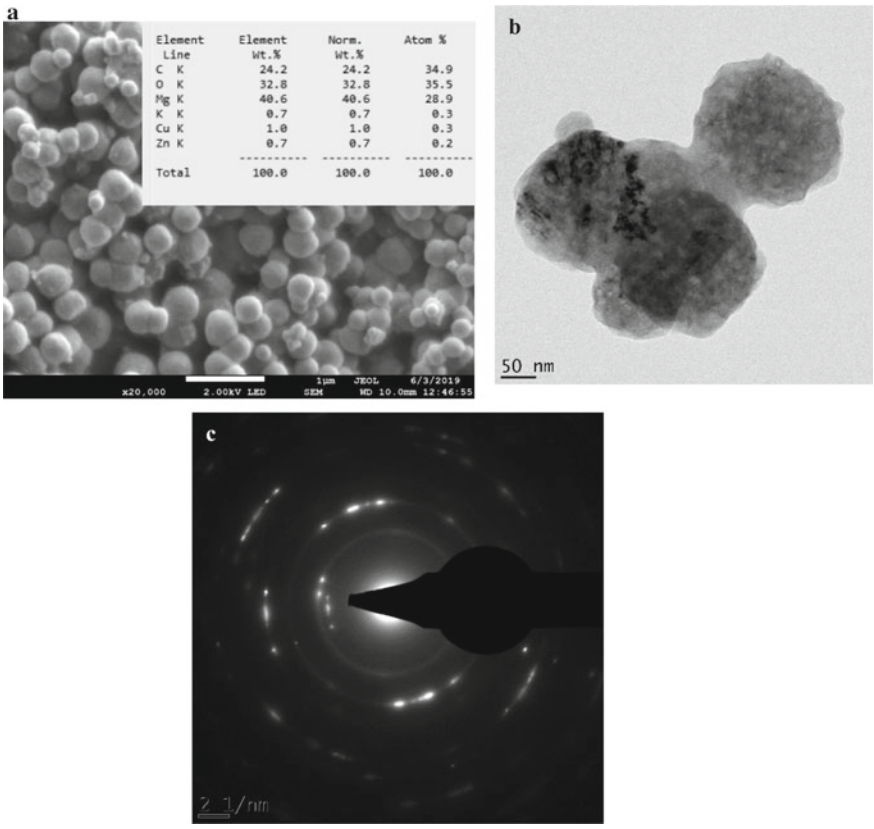


**Fig. 2** Morphological and chemical elements analysis of MgO nanoparticle displaying **a** SEM images, **b** TEM images and **c** SAED image. Inset is the EDS analysis

diffraction pattern is evident in both images. Specifically, the SAED image clearly shows the diffraction spot making up the rings, which confirms the crystallinity of the MgO nanoparticles.

## *4.1 Phase Identification Analysis*

To investigate the phase and crystallinity of the MgO nanoparticles, an X-ray diffraction analysis is performed. Figure 3 shows an experimental and calculated diffraction pattern for MgO nanoparticles. The XRD datasets of the MgO nanoparticles are analysed qualitatively using Materials Analysis Using Diffraction (MAUD) software. MAUD is a Rietveld technique for fitting X-ray diffraction datasets. According to Fig. 3, all reflections appearing at peak positions at $2\theta^\circ = 36.9^\circ$, $42.9^\circ$, $62.3^\circ$, $74.6^\circ$, $78.6^\circ$ correspond respectively to the crystal planes (111), (200), (220), (311),

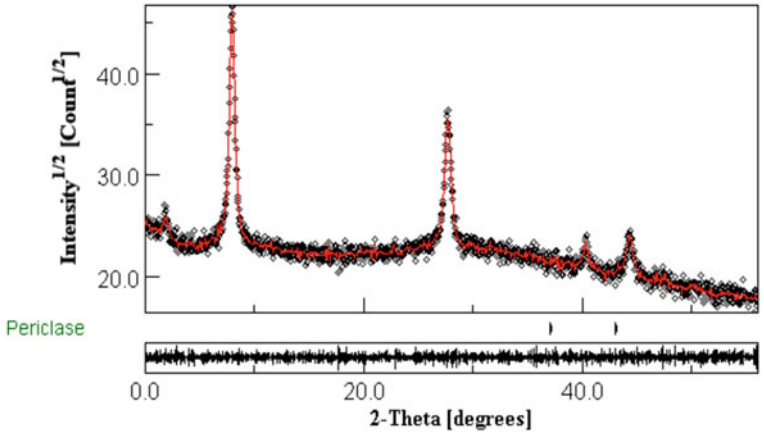


**Fig. 3** Datasets showing experimental (black diamond) and calculated (red lines) XRD pattern of MgO nanoparticles

**Table 1** Structural parameters extracted from MAUD analysis

| Atom | x | y | z | Biso |
|---|---|---|---|---|
| Mg | 0.5 | 0.5 | 0.5 | 0.3399 |
| O | 0 | 0 | 0 | 0.369 |

**Table 2** Refined structural parameters extracted from MAUD analysis

| Sample | Size (Å) | Strain ε(*1e$^{-4}$) | a (Å) |
|---|---|---|---|
| MgO | 999.98 | 5.99 | 4.211 |

(222). Retinal structural parameters such as atomic positions, size, strain and lattice parameters reported in Tables 1 and 2 are retrieved from the MAUD analysis. Face-centred cubic structure with a space group 'Fm3m' proposed by Hazen [89] fit well with the experimental X-ray dataset. This further confirms the synthesis of pure and well-crystalline MgO nanoparticles.

## *4.2 Optical Properties Analysis*

The optical properties of the MgO NPs are evaluated based on the UV–vis absorbance and the diffuse reflectance measurements. Figure 4a shows the absorbance spectra of both the date pit extract and the MgO nanoparticles measured within the wavelength range of 200–500 nm. The date pit extract presents two peaks at 280 and 330 nm, which are associated with the contained phytochemicals. The prominent peak is attributed to the B-ring cinnamoyl system and the latter at 330 nm to the A-ring

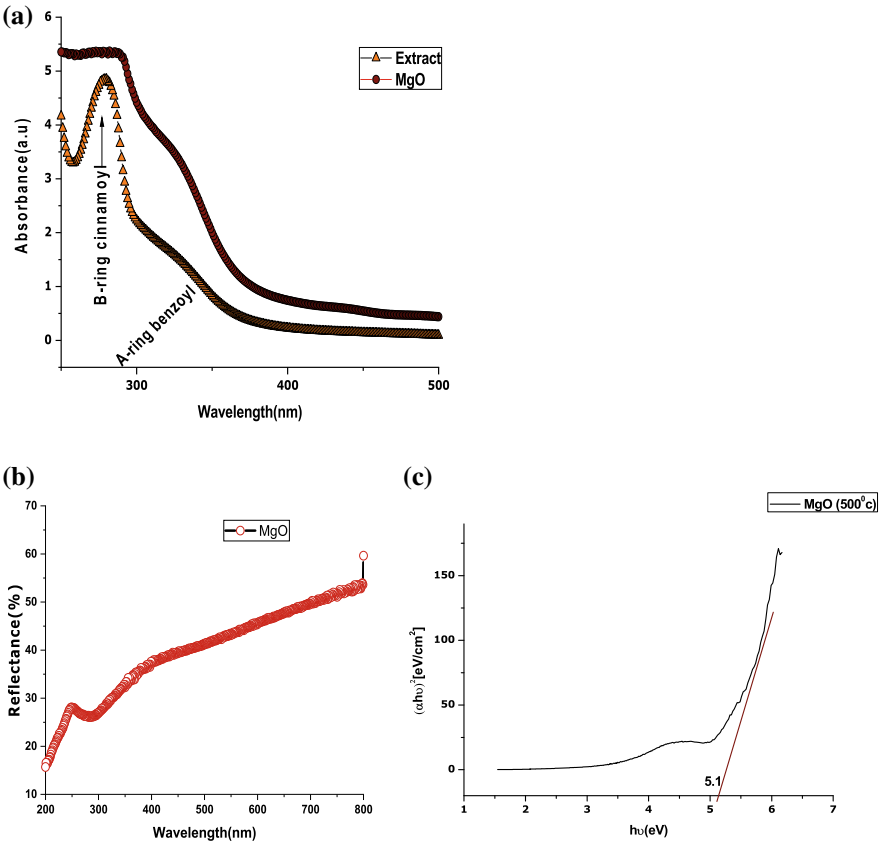


**Fig. 4** Optical properties showing **a** UV-vis absorbance spectra of peaks associated with the date pits extract and the MgO nanoparticles, **b** diffuse reflectance spectrum, **c** the bandgap energy

benzoyl system of flavonoid. These active compounds in the date pits extract act as reducing agents in the MgO nanoparticle synthesis. The peak appearing at 290 nm on the MgO is evidence of the formation of MgO nanoparticles established on the chemical collaboration between the flavonoids and the salt. The diffuse reflectance measurement of the sample is shown in Fig. 4b. By applying the Kubelka–Munk [85] equation written below, the optical energy bandgap is calculated as

$$F(R) = \alpha = (1 - R)^2/2R$$

where $R$ is the light that is reflected in percentage, $\alpha$ is the optical absorption coefficient. The bandgap (see Fig. 4c) is estimated at 5.1 eV, which is consistent with the value in the literature. The energy bandgap of the material plays a significant role in the photocatalysis process.

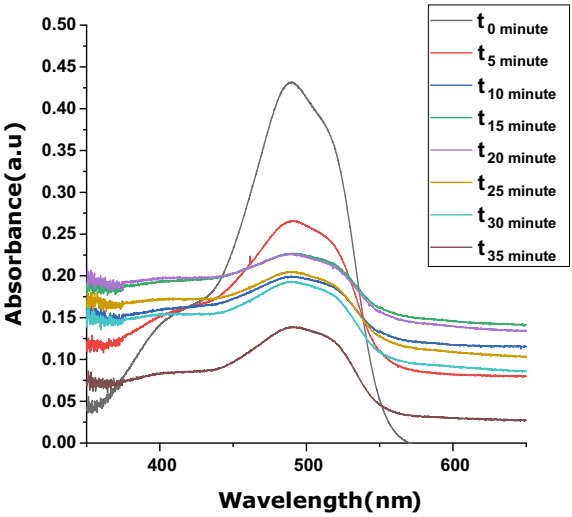


**Fig. 5** Photocatalysis activity of MgO nanoparticle against Acid orange 8 under UV lamp within 35 min

## 4.3 Photocatalysis Analysis

To test date pits assisted MgO nanoparticle ability to remove organic compounds in the aqueous medium, the photocatalysis analysis is conducted. Figure 5 shows the UV-vis absorbance spectra within the wavelength range of 350–700 nm. Specifically, $t = 0$ shows the absorbance peak of the MgO nanoparticle in acid orange 8 in the dark without light irradiation. Subsequently, absorbance peaks are recorded for the MgO nanoparticles in the acid orange under visible light illumination every 5 min. The dye degradation ability is monitored by the decrease in intensity of the peaks with respect to the time elapse. As seen at $t = 35$ min, the shape of the peak begins to broaden in comparison to at $t = 0$ min. This signifies the complete degradation ability of the acid's orange 8 dye.

## 4.4 Photodegradation Efficiency Analysis

The photodegradation efficiency can be calculated following the equation given below.

$$\delta(\%) = \frac{(A_0 - A_t)}{A_0} \times 100$$

where $A_{0\,\mathrm{is}}$ the absorbance of mixture at 0 min ($t = 0$, before illumination) and $A_t$ is the absorbance at sampling time. The photodegradation efficiency of the acid orange 8 dye is estimated at 68% as shown in Fig. 6. The high photodegradation

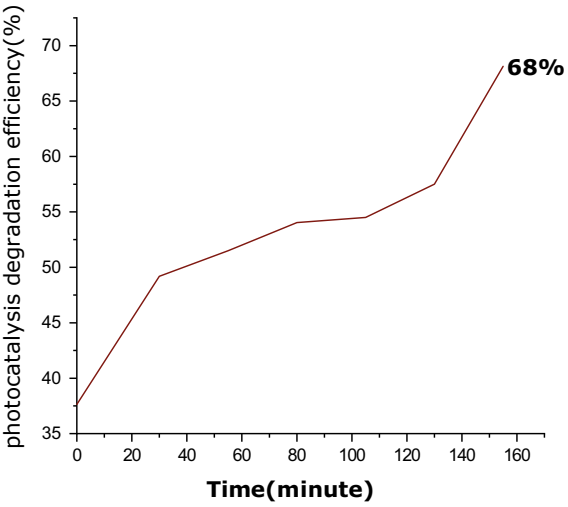


**Fig. 6** Photodegradation efficiency of MgO nanoparticles

efficiency could be attributed to the smaller bandgap of the MgO, which favours the movement of electrons from the valence to the conduction band.

### *4.5 Removal Kinetics Analysis*

The photocatalysis degradation obeys the first-order kinetics expressed as

$$\ln\left(\frac{A_t}{A_o}\right) = kt$$

where $k$ is the reaction rate constant and t is the irradiation time. The reaction rate constant was calculated from the slope of $\ln\left(\frac{A_t}{A_o}\right)$ versus the irradiation time t as $0.00341 \pm 6.03\ \text{min}^{-1}$ ($R^2 = 0.86505$). The reaction rate constant versus time as shown in Fig. 7 further confirms the efficient photodegradation ability of the MgO nanoparticles.

## 5 Conclusion

The current chapter highlighted different techniques with an emphasis on the green chemistry approach for wastewater remediation. In recent times, a more sustainable, cost-effective and environmentally friendly green chemistry methodology for synthesizing metal–oxide nanoparticles is being intensively researched. The metal

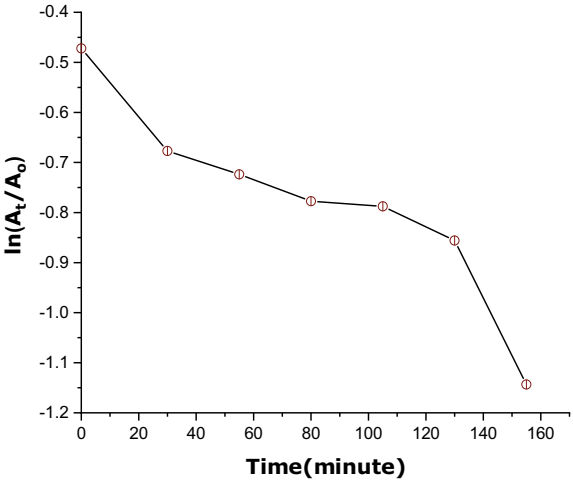


**Fig. 7** Removal kinetics showing reaction rate constant versus time

oxides including MgO nanoparticles are efficient in removing organic pollutants in wastewater. The chapter reported numerous plants, agro-wastes and fungi that have been investigated by many authors as biocatalysts for synthesizing MgO nanoparticles. The phytochemical in each material serves as reducing, capping and stabilizing agents during the synthesis process. MgO nanoparticles are synthesized following the green chemistry approach using date pit extracts. The purity and the crystallinity of the MgO nanoparticles are confirmed via the EDS and the XRD analysis. The spherical-shaped MgO nanoparticles demonstrate a smaller energy bandgap of 5.1 eV as evident from the UV–vis absorbance measurement. As a direct application, the MgO nanoparticles are tested against acid orange 8 under a UV lamp. The MgO nanoparticles showed an excellent photodegradation ability of 68%, which indicates that our material is a promising candidate for the removal of organic compounds in water effluent.

**Acknowledgements** The authors acknowledge UNESCO-UNISA Africa Chair in Nanosciences/Nanotechnology Laboratories, College of Graduate Studies, University of South Africa (UNISA) for funding the project. All research facilities are accessed at iThemba LABS National Research Foundation of South Africa.

## References

1. Hassan MM, Carr CM (2018) A critical review on recent advancements of the removal of reactive dyes from dyehouse effluent by ion-exchange adsorbents, vol 209
2. Aquino JM, Rocha-Filho RC, Ruotolo LA, Bocchi N, Biaggio SR (2014) Electrochemical degradation of a real textile wastewater using β-$PbO_2$ and DSA® anodes, vol 251
3. Gbedemah CM (1998) Potential for radiation processing as a technique for the conservation of the environment in Ghana, vol 1023

4. Sivamani S, Prakash C, Shoba U, Parvathi C (2019) Manihot esculenta peel powder: effective adsorbent for removal of various textile dyes from aqueous solutions. J Test Eval 46(6)
5. Mohan D, Sarswat A, Ok YPJ (2014) Organic and inorganic contaminants removal from water with biochar, a renewable, low cost and sustainable adsorbent–a critical review. Bioresour Technol 160:191–202
6. Verma A, Dash R, Bhunia P (2012) A review on chemical coagulation/flocculation technologies for removal of colour from textile wastewaters. J Environ Manag 93(1):154–168
7. Allegre C, Maisseu M, Charbit F, Moulin P (2004) Coagulation–flocculation–decantation of dye house effluents: concentrated effluents. J Hazard Mater 116(12):57–64
8. Nataraj S, Hosamani K, Aminabhavi T (2009) Nanofiltration and reverse osmosis thin film composite membrane module for the removal of dye and salts from the simulated mixtures. Desalination 249(1):12–17
9. Qiu M, He C (2019) Efficient removal of heavy metal ions by forward osmosis membrane with a polydopamine modified zeolitic imidazolate framework incorporated selective layer. J Hazard Mater 367:339–347
10. Mulyanti R, Susanto H (2018) Wastewater treatment by nanofiltration. In: IOP Conf. Ser.
11. Sackey J, Akbari M, Morad R, Bashir AKH, Ndiaye NM, Matinise N, Maaza M (2021) Molecular dynamics and bio-synthesis of phoenix dactylifera mediated $Mn_3O_4$ nanoparticles: electrochemical application. J Alloy Compd 854:156987
12. Yulizar Y, Bakri R, Apriandanu DOB, Hidayat T (2018) ZnO/CuO nanocomposite prepared in one-pot green synthesis using seed bark extract of Theobroma cacao. Nano-Struct Nano-Objects 16:300–305
13. Mohammadi-Aloucheh R, Habibi-Yangjeh A, Bayrami A, Latifi-Navid S, Asadi A (2018) Green synthesis of ZnO and ZnO/CuO nanocomposites in Mentha longifolia leaf extract: characterization and their application as anti-bacterial agents. J Mater Sci: Mater Electron 29(16):13596–13605
14. Ezhilarasi AA, Vijaya JJ, Kaviyarasu K, Maaza M, Ayeshamariam A, Kennedy LJ (2016) reen synthesis of NiO nanoparticles using Moringa oleifera extract and their biomedical applications: cytotoxicity effect of nanoparticles against HT-29 cancer cells. J Photochem Photobiol B 164:352–360
15. Raja A, Ashokkumar S, Marthandam RP, Jayachandiran J, Khatiwada CP, Kaviyarasu K, Swaminathan M (2018) Eco-friendly preparation of zinc oxide nanoparticles using Tabernaemontana divaricata and its photocatalytic and antimicrobial. J Photochem Photobiol B 181:53–58
16. Diallo A, Manikandan E, Rajendran V, Maaza M (2016) Physical & enhanced photocatalytic properties of green synthesized $SnO_2$ nanoparticles via Aspalathus linearis. J Alloy Compd 681:561–570
17. Fuku X, Kaviyarasu K, Matinise N, Maaza M (2016) Punicalagin green functionalized $Cu/Cu_2O$/ZnO/CuO nanocomposite for potential electrochemical transducer and catalyst. Nanoscale Res Lett 11(1):386
18. Mohammadi-Aloucheh R, Habibi-Yangjeh A, Bayrami A, Latifi-Navid S, Asadi A (2018) Enhanced anti-bacterial activities of ZnO nanoparticles and ZnO/CuO nanocomposites synthesized using Vaccinium arctostaphylos L. fruit extract. Artif Cells Nanomedicine Biotechnol 46:1200–1209
19. Ibrahim HM (2015) Green synthesis and characterization of silver nanoparticles using banana peel extract and their antimicrobial activity against representative microorganisms. J Radiat Res Appl Sci 8(3):265–275
20. Leong MK (2016) Green synthesis, characterization of copper (II) oxide nanoparticles and their photocatalytic activity. Universiti Tunku Abdul Rahman, UTAR
21. Bankar A, Joshi B, Kumar AR, Zinjarde S (2010) Banana peel extract mediated novel route for the synthesis of silver nanoparticles. Colloids Surf A: Physicochem Eng Asp 368(1–3):58–63
22. Aminuzzaman M, Kei LM, Liang WH (2017) Green synthesis of copper oxide (CuO) nanoparticles using banana peel extract and their photocatalytic activities. In: AIP Publishing

23. Nwanya AC, Razanamahandry LC, Bashir AKH, Ikpo CO, Nwanya SC, Botha S, Maaza M (2019) Industrial textile effluent treatment and antibacterial effectiveness of Zea mays L. dry husk mediated bio-synthesized copper oxide nanoparticles. J Hazard Mater 375:281–289
24. Sackey J, Morad R, Bashir A, Kotsedi L, Kaonga C, Maaza M (2021) Bio-synthesised black α-$Cr_2O_3$ nanoparticles; experimental analysis and density function theory calculations. J Alloys Compd 850
25. Bashir AKH, Matinise N, Sackey J, Kaviyarasu K, Kodseti MIGL, Maaza M (2020) Investigation of electrochemical performance, optical and magnetic properties of $NiFe_2O_4$ nanoparticles prepared by a green chemistry method. Phys E: Low-Dimens Syst Nanostructures 119:114002
26. Choudary B, Mulukutla R, Klabunde K (2003) Benzylation of aromatic compounds with different crystallites of MgO. J Am Chem Soc 125(8):2020–2021
27. Gao D, Watkins M, Shluger A (2012) Transient mobility mechanisms of deposited metal atoms on insulating surfaces: Pd on MgO (100). J Phys Chem C 116(27):14471–14479
28. Mahdavi S, Jalali M, Afkhami A (2013) Heavy metals removal from aqueous solutions using $TiO_2$, MgO, and $Al_2O_3$ nanoparticles. Chem Eng Commun 200(3):448–470
29. Salomao R, Milena L, Wakamatsu H, Pandolfelli V (2011) Hydrotalcite synthesis via co-precipitation reactions using MgO and $Al(OH)_3$ precursors. Ceram Int 37(8):3063–3070
30. Carnes C, Kapoor P, Klabunde K, Bonevich J (2002) Synthesis, characterization, and adsorption studies of nanocrystalline aluminum oxide and a bimetallic nanocrystalline aluminum oxide/magnesium oxide. Chem Mater 14:292
31. Azmi S, Nil B, Emek M, Nurcan T, Sabriye P (2014) Effect of magnesium borates on the fire-retarding properties of zinc borates. J Chem Neuroanat
32. Wahid F, Zhao XJ, Jia SR, Bai H, Zhong C (2020) Nanocomposite hydrogels as multifunctional systems for biomedical applications: current state and perspectives. Compos Part B: Eng 108208
33. Scarsella M, de Caprariis B, Damizia M, De Filippis P (2020) Heterogeneous catalysts for hydrothermal liquefaction of lignocellulosic biomass: a review. Biomass Bioenergy 140:105662
34. Almerindo GI, Probst LF, Campos CE, De Almeida RM, Meneghetti SM, Meneghetti MR, Clacens JM, Fajardo HV (2011) Magnesium oxide prepared via metal–chitosan complexation method: application as catalyst for transesterification of soybean oil and catalyst deactivation studies. J Power Sources 196(19):8057–8063
35. Liu X, Piao X, Wang Y, Zhu S (2008) Calcium ethoxide as a solid base catalyst for the transesterification of soybean oil to biodiesel. Energy Fuels 22(2):1313–1317
36. Qiu L, Xie R, Ding P, Qu B (2003) Preparation and characterization of Mg (OH) 2 nanoparticles and flame-retardant property of its nanocomposites with EVA. Compos Struct 62(3–4):391–395
37. Pei LZ, Yin WY, Wang JF, Chen J, Fan CG, Zhang QF (2010) Low temperature synthesis of magnesium oxide and spinel powders by a sol–gel process. Mater Res 13:339–343
38. Shimpi P, Gao PX, Goberman DG, Ding Y (2009) Low temperature synthesis and characterization of MgO/ZnO composite nanowire arrays. Nanotechnology 20(12):125608
39. Stankic S, Müller M, Diwald O, Sterrer M, Knözinger E, Bernardi J (2005) Size-dependent optical properties of MgO nanocubes. Angew Chem Int Ed 44(31):4917–4920
40. Fang H, Hu B, Wang L, Lu R, Yang C (2008) Preparation of nanometer MgO by sol–gel auto-combustion. Front Chem China 3(2):193–197
41. Niu H, Yang Q, Tang K, Xie Y (2006) Large-scale synthesis of single-crystalline MgO with bone-like nanostructures. J Nanopart Res 8(6):881–888
42. El-Shall M, Slack W, Vann W, Kane D, Hanley D (1994) Synthesis of nanoscale metal oxide particles using laser vaporization/condensation in a diffusion cloud chamber. J Phys Chem 98(12):3067–3070
43. Bhargava A, Alarco J, Mackinnon I, Page D, Ilyushechkin A (1998) Synthesis and characterisation of nanoscale magnesium oxide powders and their application in thick films of $Bi_2Sr_2CaCu_2O_8$. Mater Lett 34(3–6):133–142
44. Khairallah F, Glisenti A (2007) Synthesis, characterization and reactivity study of nanoscale magnesium oxide. J Mol Catal A: Chem 274(1–2):137–147

45. Helble J (1998) Combustion aerosol synthesis of nanoscale ceramic powders. J Aerosol Sci 29(5–6):721–736
46. Matthews J, Just O, Obi-Johnson B, Rees W Jr (2000) CVD of MgO from a Mg (β-ketoiminate) 2: preparation, characterization, and utilization of an intramolecularly stabilized, highly volatile, thermally robust precursor. Chem Vap Depos 6(3):129–132
47. Purwajanti S, Zhang H, Huang X, Song H, Yang Y, Zhang J, Yu C (2016) Mesoporous magnesium oxide hollow spheres as superior arsenite adsorbent: synthesis and adsorption behavior. ACS Appl Mater Interfaces 8(38):25306–25312
48. Sirota V, Selemenev V, Kovaleva M, Pavlenko I, Mamunin K, Dokalov V, Prozorova M (2016) Synthesis of magnesium oxide nanopowder by thermal plasma using magnesium nitrate hexahydrate. Phys Res Int
49. Moussavi G, Mahmoudi M (2009) Removal of azo and anthraquinone reactive dyes from industrial wastewaters using MgO nanoparticles. J Hazard Mater 168(2–3):806–812
50. Khan MI, Akhtar MN, Ashraf N, Najeeb J, Munir H, Awan TI, Kabli MR (2020) Green synthesis of magnesium oxide nanoparticles using Dalbergia sissoo extract for photocatalytic activity and antibacterial efficacy. Appl Nanosci 10(7):2351–2364
51. Moorthy SK, Ashok CH, Rao KV, Viswanathan C (2015) Synthesis and characterization of MgO nanoparticles by Neem leaves through green method. Mater Today: Proc 2(9):4360–4368
52. Abdallah Y, Ogunyemi SO, Abdelazez A, Zhang M, Hong X, Ibrahim E, Chen J (2019) The green synthesis of MgO nano-flowers using Rosmarinus officinalis L. (Rosemary) and the antibacterial activities against Xanthomonas oryzae pv. Oryzae. BioMed Res Int
53. Singh A, Joshi NC, Ramola M (2019) Magnesium oxide nanoparticles (MgONps): green synthesis, characterizations and antimicrobial activity. Res J Pharm Technol 12(10):4644–4646
54. Das B, Moumita S, Ghosh S, Khan MI, Indira D, Jayabalan R, Balasubramanian P (2018) Biosynthesis of magnesium oxide (MgO) nanoflakes by using leaf extract of Bauhinia purpurea and evaluation of its antibacterial property against Staphylococcus aureus. Mater Sci Eng C 91:436–444
55. Dobrucka R (2018) Synthesis of MgO nanoparticles using Artemisia abrotanum herba extract and their antioxidant and photocatalytic properties. Iran J Sci Technol Trans A Sci 42(2):547–555
56. Ali R, Shanan ZJ, Saleh GM, Abass Q (2020) Green synthesis and the study of some physical properties of MgO nanoparticles and their antibacterial activity. Iraqi J Sci 266–276
57. Jeevanandam J, San Chan Y, Danquah MK (2017) Biosynthesis and characterization of MgO nanoparticles from plant extracts via induced molecular nucleation. New J Chem 41(7):2800–2814
58. Ali MI, Sharma G, Kumar M, Jasuja ND (2015) Biological approach of magnesium oxide nanoparticles synthesize by Spirulina platensis. World J Pharm Res 4(7):1234–1241
59. Jhansi K, Jayarambabu N, Reddy KP, Reddy NM, Suvarna RP, Rao KV, Rajendar V (2017) Biosynthesis of MgO nanoparticles using mushroom extract: effect on peanut (Arachis hypogaea L.) seed germination. 3 Biotech 7(4):1–11
60. Saied E, Eid AM, Hassan SED, Salem SS, Radwan AA, Halawa M, Fouda A (2021) The catalytic activity of biosynthesized magnesium oxide nanoparticles (MgO-NPs) for inhibiting the growth of pathogenic microbes, tanning effluent treatment, and chromium ion removal. Catalysts 11(17):821
61. Hassan SED, Fouda A, Saied E, Farag M, Eid AM, Barghoth MG, Awad MF (2021) Rhizopus oryzae-mediated green synthesis of magnesium oxide nanoparticles (MgO-NPs): a promising tool for antimicrobial, mosquitocidal action, and tanning effluent treatment. J Fungi 7(5):372
62. Ahmed T, Noman M, Shahid M, Hahid MS, Li B (2021) Antibacterial potential of green magnesium oxide nanoparticles against rice pathogen Acidovorax oryzae. Mater Lett 282:128839
63. Sushma NJ, Prathyusha D, Swathi G, Madhavi T, Raju BDP, Mallikarjuna K, Kim HS (2016) Facile approach to synthesize magnesium oxide nanoparticles by using Clitoria ternatea—characterization and in vitro antioxidant studies. Appl Nanosci 6(3):437–444

64. Nijalingappa TB, Veeraiah MK, Basavaraj RB, Darshan GP, Sharma SC, Nagabhushana H (2019) Antimicrobial properties of green synthesis of MgO micro architectures via Limonia acidissima fruit extract. Biocatal Agric Biotechnol 18:100991
65. Ogunyemi SO, Zhang F, Abdallah Y, Zhang M, Wang Y, Sun G, Li B (2019) Biosynthesis and characterization of magnesium oxide and manganese dioxide nanoparticles using Matricaria chamomilla L. extract and its inhibitory effect on Acidovorax oryzae strain RS-2. Artif Cells Nanomed Biotechnol 47(1):2230–2239
66. Ammulu MA, Viswanath KV, Giduturi AK, Vemuri PK, Mangamuri U, Poda S (2021) Phytoassisted synthesis of magnesium oxide nanoparticles from Pterocarpus marsupium rox. b heartwood extract and its biomedical applications. J Genet Eng Biotechnol 19(1):1–18
67. Dobrucka R (2028) Synthesis of MgO nanoparticles using Artemisia abrotanum herba extract and their antioxidant and photocatalytic properties. Iran J Sci Technol Trans A Sci 42(2):547–555
68. Vijayakumar S, Nilavukkarasi M, Praseetha PK (2021) Synthesis of MgO nanoparticles through green method and evaluation of its antimicrobial activities. Vegetos 34(3):719–724
69. Akshaykranth A, Jayarambabu N, Tumu VR, Rajaboina RK (2021) Comparative study on antibacterial activity of MgO nanoparticles synthesized from Lawsonia inermis leaves extract and chemical methods. J Inorg Organomet Polym Mater 31(6):2393–2400
70. Essien ER, Atasie VN, Oyebanji TO, Nwude DO (2020) Biomimetic synthesis of magnesium oxide nanoparticles using Chromolaena odorata (L.) leaf extract. Chem Pap 1–9
71. Bayat M, Zargar M, Astarkhanova T, Pakina E, Ladan S, Lyashko M, Shkurkin SI (2021) Facile biogenic synthesis and characterization of seven metal-based nanoparticles conjugated with phytochemical bioactives using Fragaria ananassa leaf. Molecules 26(10):3025
72. Sackey J, Bashir AKH, Ameh AE, Nkosi M, Kaonga C, Maaza M (2020) Date pits extracts assisted synthesis of magnesium oxides nanoparticles and its application towards the photocatalytic degradation of methylene blue. J King Saud Univ-Sci 32(6):2767–2776
73. Oz AT, Kafkas E (2017) Superfood and functional food. In: Superfood and functional food. IntechOpen, London, pp 175–184
74. Nazeer AA, Udhayakumar S, Mani S, Dhanapal M, Vijaykumar SD (2018) Surface modification of $Fe_2O_3$ and MgO nanoparticles with agrowastes for the treatment of chlorosis in Glycine max. Nano Converg 5(1):1–8
75. Li R, Liang W, Wang JJ, Gaston LA, Huang D, Huang H, Zhang Z (2018) Facilitative capture of As (V), Pb (II) and methylene blue from aqueous solutions with MgO hybrid sponge-like carbonaceous composite derived from sugarcane leafy. J Environ Manag 212:77–87
76. Qin X, Luo J, Liu Z, Fu Y (2020) Preparation and characterization of MgO-modified rice straw biochars. Molecules 25(23):5730
77. Suresh J, Yuvakkumar R, Sundrarajan M, Hong SI (2014) Green synthesis of magnesium oxide nanoparticles. Adv Mater Res 952:141–144
78. Sugirtha P, Divya R, Yedhukrishnan R, Suganthi KS, Anusha N, Ponnusami V, Rajan KS (2015) Green synthesis of magnesium oxide nanoparticles using Brassica oleracea and Punica granatum peels and their anticancer and photocatalytic activity. Asian J Chem 27(7):2513
79. Awwad AM, Ahmad AL (2014) Biosynthesis, characterization, and optical properties of magnesium hydroxide and oxide nanoflakes using Citrus limon leaf extract. Arab J Phys Chem 12(1):66
80. Vergheese M, Vishal SK (2018) Green synthesis of magnesium oxide nanoparticles using Trigonella foenum-graecum leaf extract and its antibacterial activity. J Pharmacogn Phytochem 7(3):1193–1200
81. Vijayakumar S, Punitha VN, Parameswari N (2021) Phytonanosynthesis of MgO nanoparticles: green synthesis, characterization and antimicrobial evaluation. Arab J Sci Eng 1–6
82. Essien ER, Atasie VN, Okeafor AO, Nwude DO (2020) Biogenic synthesis of magnesium oxide nanoparticles using Manihot esculenta (Crantz) leaf extract. Int Nano Lett 10(1):43–48
83. Baliga MS, Baliga BRV, Kandathil SM, Bhat HP, Vayalil PK (2011) A review of the chemistry and pharmacology of the date fruits (Phoenix dactylifera L.). Food Res Int 44(7):1812–1822

84. Al-Farsi MA, Lee CY (2008) Nutritional and functional properties of dates: a review. Crit Rev Food Sci Nutr 48(10):877–887
85. Sackey J, Nwanya A, Bashir AKH, Matinise N, Ngilirabanga JB, Ameh AE, Maaza M (2020) Electrochemical properties of Euphorbia pulcherrima mediated copper oxide nanoparticles. Mater Chem Phys 244:122714
86. Choudhury R., Kodape SM, Bansod PG (2021) Removal of nigrosine by MgO nanoparticles, green synthesized using Madhuca longifolia flower extract. Environ Dev Sustain 1–22
87. Khan MI, Akhtar MN, Ashraf N, Najeeb J, Munir HATI, Kabli MR (2020) Green synthesis of magnesium oxide nanoparticles using Dalbergia sissoo extract for photocatalytic activity and antibacterial efficacy. Appl Nanosci 10(7):2351–2364
88. Fouda A, Hassan SED, Saied E, Hamza MF (2021) Photocatalytic degradation of real textile and tannery effluent using biosynthesized magnesium oxide nanoparticles (MgO-NPs), heavy metal adsorption, phytotoxicity, and antimicrobial activity. J Environ Chem Eng 9(4):105346
89. Hazen R (1976) Effects of temperature and pressure on the cell dimension and X-ray temperature. Am Mineral 61:266–271

# Chapter 6
# Property Management of $BiFeO_3$-Based Multifunctional Perovskite Nanomaterials: Nanoparticles, Ceramics, and Thin Films


**F. F. Orudzhev, Sh. M. Ramazanov, D. Sobola, N. M. R. Alikhanov, and R. S. Dallaev**

## 1 Introduction

Bismuth ferrite (Bi–Fe–O)-based compounds have a wide range of features that are of interest both for basic science and applied research. The Bi–Fe–O material, identical in chemical composition but different in structure, has a number of promising optical, magnetic, electrical, and mechanical properties. Practically significant is the ability to control and manage these properties through external influences. The problems of materials science, which can be found in pure phase preparation, make the progress of Bi–Fe–O adaptation slower for new-generation electronic devices such as spintronic, quantum optics, magneto-optics, etc. In the presence of a mixture of phases, each contributes to the magnetic properties. $Bi_2Fe_4O_9$ – antiferromagnet with Neel temperature of 264 K; $Bi_{25}FeO_{39}$– paramagnet (from 5 to 950 K) (from 5 to 950 K) [1], ferrimagnetic and paramagnetic regions of $Bi_3Fe_5O_{12}$ was found to be reported on yttrium iron garnet substrates [2]. Each phase individually has several features that expand the use of the Bi–Fe–O system in various fields of science and production. Thus, $Bi_2Fe_4O_9$ is promising for the manufacture of semiconductive chemical gas sensors and as a cheap replacement of catalysts in the oxidation of ammonia to NO in the industrial production of nitric acid. It has a photocatalytic activity for organic contaminants with absorption in the near-infrared region

F. F. Orudzhev (✉) · D. Sobola · N. M. R. Alikhanov
Dagestan State University, Dagestan Republic, Makhachkala 367000, Russia
e-mail: ff.orudzhev@dgu.ru

F. F. Orudzhev · Sh. M. Ramazanov · N. M. R. Alikhanov
Amirkhanov Institute of Physics of Dagestan Federal Research Center, Russian Academy of Sciences, Makhachkala 367003, Russia

D. Sobola · R. S. Dallaev
Department of Physics, Faculty of Electrical Engineering and Communication, Brno University of Technology, Brno 61600, Czech Republic



K. Kasinathan et al. (eds.), *Nanomaterials for Energy Conversion, Biomedical and Environmental Applications*, Materials Horizons: From Nature to Nanomaterials,
https://doi.org/10.1007/978-981-19-2639-6_6

[3]. $Bi_2Fe_4O_9$ electrode is reported to be a photoanode for solar water splitting [4]. $Bi_2Fe_4O_9$ has an orthorhombic structure of mullite, a space group Pbam with coexistence of [$FeO_6$] octahedra and [$FeO_4$] tetrahedra, and its band gap with reported to be 1.57–2.01 eV [5]. $Bi_{25}FeO_{39}$ in nano-dispersed state also exhibits photocatalytic properties in the visible range (during the decomposition of phenol and orange methylene), however, it is inferior to the properties of $BiFeO_3$ and $Bi_2Fe_4O_9$. Besides optical and piezo-response, its humidity sensing application was recently mentioned due to the effect of rendering charge carriers caused by water [6]. $Bi_{25}FeO_{39}$ has a cubic structure of selenite with space group I23 [7]. Electrical properties of this were reported as a mixed conductor of oxide ions and electronic holes [1]. Amorphous Bi–Fe–O nanoparticles were shown in recent works [8] to have photo-Fenton-like catalytic activity for typical organic contaminant RhB. Bandgap 2.2 $\sim$ 2.8 eV makes it useful for photocatalysts activated by visible light. The amorphous composition prepared with Zn inclusion indicates a speromagnet structure [9]. Such structures were recently reported for "ideal" high-entropy alloys [10].

The greatest interest of researchers is attracted to the $BiFeO_3$ phase due to the presence of the magnetoelectric effect at room temperature. Pseudo-cubic unit cells are interconnected along a diagonal line passing through their center. This arrangement forms a rhombohedral, $ABO_3$ distorted perovskite structure. An electric dipole moment is formed because of the displacement of bismuth atoms relative to the $FeO_6$ octahedron. For the presence of the piezoelectric effect, the paired bismuth electrons (6s2) respond. The partially filled 3d orbitals of ferric iron determine the presence of antiferromagnetism. In the R3c crystal structure, spontaneous polarization arises in the [111] direction of 6.1 $\mu C\ cm^2$, and in the direction [100] with a magnitude of 3.5 $\mu C\ cm^2$. The properties could be tuned by variation in morphology, thickness, microstructure, and crystallinity [11]. The presence of many methods for producing multiferroics, as well as the influence of various parameters on the resulting sample, makes the assessment of their properties a challenging task. Pulse laser deposition (PLD) and atomic-layer deposition (ALD) are effective methods for the low-temperature synthesis of thin bismuth ferrite films. The ability to vary temperature over a wide range is important in the production of functional structures of optical devices (optical sensors, solar cells, light-emitting diodes) and electronics (memory cells, magnetic field sensors, etc.) due to the possible reaction of other materials and components to the temperature.

## 2 Pulsed Laser Deposition Film of the Bi–Fe–O System

The method of pulsed laser spraying belongs to the group of methods of physical deposition from the gas phase. The process of laser ablation occurs when focusing high-power laser radiation on the surface of a solid target. The effect of the laser on the substance leads to the rapid absorption of radiation energy, heating, and explosive evaporation of the substance from the target surface. The process is accompanied

by the propagation of a shock wave in the environment. As a result of the interaction of radiation with the target material, the matter is removed from the target and ionized. The resulting hot plasma expands, during the expansion, the plasma experiences additional heating by laser radiation. Depending on the intensity of the laser radiation, the ablation products can be either atoms, ions, molecules of a substance, or formed clusters and nanoparticles emanating from a zone of exposure with high kinetic energy. Atoms ablated at a high temperature can interact with environmental molecules to form new compounds. Deposition can also be accompanied by partial mixing of the surface layer due to thermal motion and diffusion. An increase in the energy of the laser flow, accompanied by an increase in ionic collisions, can compensate for a decrease in the temperature of the substrate, which in turn will lead to an increase in the crystallization of the film. The required chemical composition of the film is achieved by varying the gas pressure, the temperature of the substrate during deposition, the modes of subsequent annealing, and the type of gas used during the process. The energy of the deposited material flow affects the adhesion coefficients and the formation of chemical bonds. This has a double effect: on the one hand, it can be effectively used to control the film growth mechanism, and on the other hand, it leads to modification of the surface of the sprayed target. As a result, the selected power of the deposition laser affects not only such parameters of the film as the crystal structure and orientation of the film, density, and content of defects, but also the composition of the film due to degradation of the initial material. The high energy of the erosive laser emitter particles allows the synthesis of films at low (down to room) substrate temperatures.

As for the distance from the target to the substrate, it is usually chosen empirically, considering the characteristic distance of the plasma. This is the distance over which the flow loses direction and disperses. There are several models describing optimal geometry: the model of a “strong shock wave”, “entrainment force”, etc. The electrical and optical parameters of samples obtained by pulsed laser deposition even at room temperature of the substrate are comparable with the parameters of films obtained by other methods at higher temperatures. However, despite the technological simplicity, physical phenomena such as self-atomization, the interaction of atoms with the surface, kinetic diffusion, island formation, and the shadow effect complicate the explanation of the film growth mechanism.

*Advantages of PLD:*

- Except for the cleaning, there is no need to activate the surface of the substrate;
- Simple and chemically pure synthesis of end products;
- A high degree of compliance of cationic stoichiometry of the formed films with the composition of the target material;
- The possibility of the formation of metastable phases;
- A high deposition rate of thin films;
- A direct relationship between the energy parameters of radiation and the kinetics of layer growth;
- Obtaining films with a high degree of crystallinity;

- Strict dosage of material supply, including multicomponent ones with high evaporation temperature.

*Disadvantages:*

- The possibility of contamination of the film by the products of the melt of the target material at high-laser powers;
- Small geometric sample size.

The data about the growth of bismuth ferrite of PLD is present in the literature. Mostly, it concerns such substrates as $SrTiO_3$ [12], $SrRuO_3$ [13], FTO glass [14], even specific like $Ca_{0.96}Ce_{0.04}MnO_3$, [15] etc. The structures proved to be prospective besides ferroelectricity and magnetic ordering, even demonstrated photovoltaic behavior. Nevertheless, several questions, such as the influence of oxygen vacancies or the type of electrode (or substrate) material are still open for discussion. The application of scanning probe microscopy (SPM) is essential for the description of surface properties. Among different techniques for surface imaging (optical methods, scanning electron microscopy, etc.) AFM proves to be the most reliable option when it comes to the 3D analysis of surface topography or surface modification with exact values of the Z-axis. The most widespread SPM type is atomic force microscopy (AFM). The basis of the AFM measurement process is the interaction between a probe and a sample surface. Aside from the topographical analysis with actual height values, AFM has several different modes which facilitate the study of the mechanical and electrical properties of materials. The use of scanning microscopy of the piezoelectric response (PFM) and magnetic force microscopy (MFM) was described in [16, 17]. In the study of magnetoelectric materials, AFM measurements using a conductive probe allow both local (units of nanometres) polarization of the sample and measurements of its characteristics on the microscale. The results allow evaluation of the domain structure, including the size and morphology of the domains. In addition to recording the displacement of the probe due to the presence of electric and magnetic domains, it is possible to carry out the polarization of surface areas and its subsequent registration. The use of external influences (temperature, magnetic field) and various configurations of the electrodes allow in situ determination of the physical characteristics of the samples (Fig. 1). The probe is in the form of an elastic cantilever with a sharp tip (10 nm) on its free end is used in this work for PFM and MFM. It allows tracing surface topography and its electrical properties with nanometer resolution.

The bending of the cantilever is often detected by a laser beam reflected from the probe to a detector. The location of the incident beam on the detector is then looped back to move the probe up or down to preserve constant force between the probe and the sample, thus forming a 3D image of the surface [18]. The scheme in Fig. 1 demands the use of the tips with conductive or magnetic properties. The application of additional contacts (Fig. 1b, c) to the sample has some advantages as the possibility to apply higher voltages (independent of microscope configuration) and differential geometry of contacts to measure PFM at different planes. In this case, there is no necessity to use the conductive probe for PFM and even subnanometer

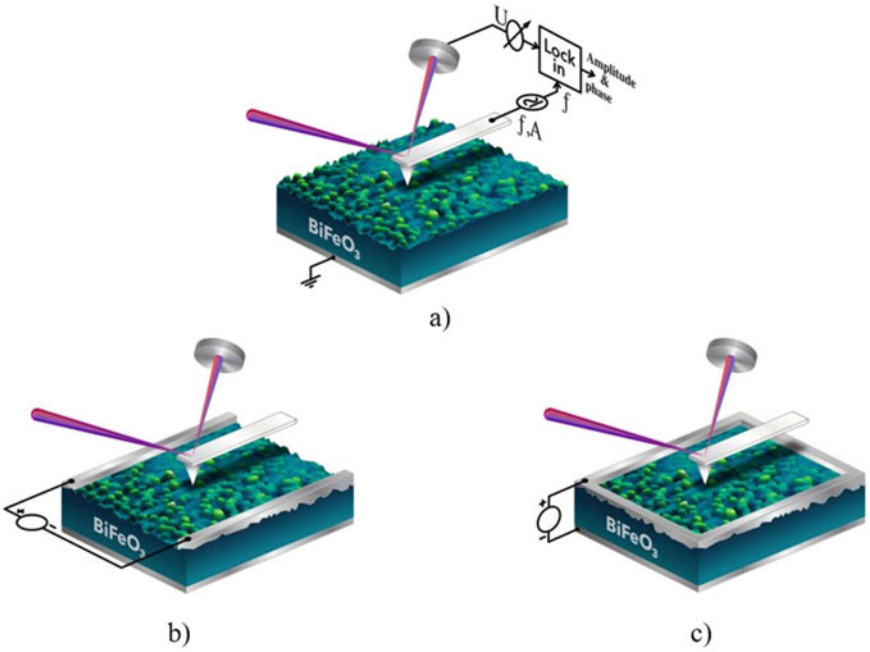


**Fig. 1** Measurement of electrical characteristics by AFM: **a** using metal conductive probe and **b**, **c** using external contacts

local bending of the sample will be detected. In this case, there is also a choice of scanning mode; both noncontact, tapping, and contacted modes could be used. The rest of the scanning parameters should be well-adjusted, for example, set-point and feedback loop parameters or scanning rate. The last was mentioned by Ch. C. Glover et al. [19]. Considering set-point and humidity conditions.

Silicon technology is one of the most developed in the field of obtaining structures for electronics. The market offers a wide selection of monocrystalline silicon of different sizes, structures, and doping levels. Silicon oxidation and surface oxide stability should be taken into consideration. Due to the oxygen-containing atmosphere, the silicon surface is oxidized, forming a layer of about 1 nm. This layer begins to form when preparing the silicon substrate to be inserted into the deposition unit. This complicates the preparation of bismuth ferrite directly on the silicon surface. The deposition on silicon substrates was carried out after the deposition of a metal layer, since silicon demonstrates chemical activity toward the growing perovskite structure and can be embedded in it, violating the structure, and forming a wide transition zone. The growth of bismuth ferrite on substrates of single-crystal silicon is carried out using buffer layers. This prevents the possibility of chemical interaction and diffusion of silicon with the growing layer. For deposition of the film by the PLD method, the metalized silicon substrates were used. The wafers were

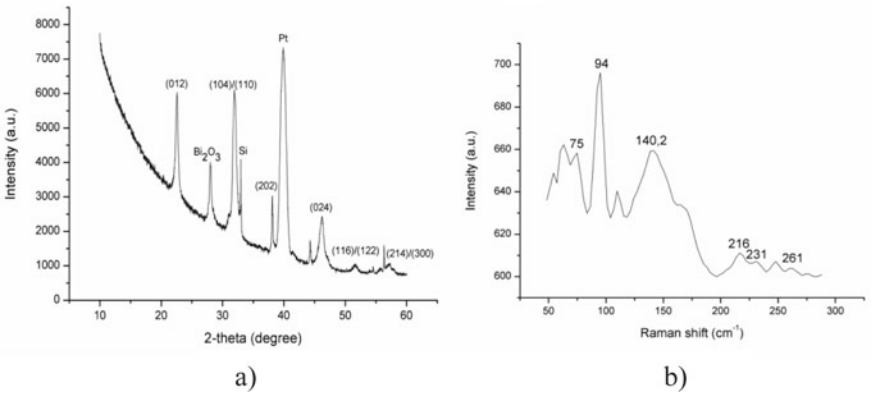


**Fig. 2** Structural study of BFO/Pt/$SiO_2$/Si **a** XRD spectra; **b** Raman spectra

purchased from Miro Chemicals GmbH, 4-inch, thickness 525 ± 25 μm, (100), 1-side polished, p-type (boron), $1^{-10}$ Ω cm. A platinum layer of 20 nm was deposited by magnetron sputtering on the substrates. PLD parameters: Spot size: 1.01 × 2.33 $mm^2$; Mask: 5.5 × 18 $mm^2$; Energy 22,7 mJ; Fluency: 1.08 J/$mm^2$; $O_2$ pressure: 0,1 mBar; Scanning diameter: 6,06 × 4,66 $mm^2$; Pulses: 50 000; Scan speed: 0,7 mm/s; Temperature control is essential to provide bonding of the film and substrate and control films stoichiometry. Following temperatures were chosen substrate temperature 250 °C, Ramp 25 °C /min; Annealing 500 °C for 5 min at $O_2$ 100 mBar.

X-ray diffraction analysis shows the polycrystalline phase of bismuth ferrite with a predominant structure of R3c (Fig. 2a). The peak at 28° shows the bismuth oxide phase in the structure, presumably which was formed due to the predominance of bismuth over iron in the phase.

Several Raman active modes in the shown spectral window are observed (Fig. 2b). The 140.2 $cm^{-1}$ and 216 $cm^{-1}$ are of A1 symmetry, and those at 75 $cm^{-1}$, 261 $cm^{-1}$ belong to E symmetry and confirmed the rhombohedral structure. 231 $cm^{-1}$ indicates a distorted rhombohedral-like (R-like) phase formed in the highly strained BFO thin film. According to the first principle calculation, Bi atoms' contributions lies in the low-frequency modes below 167 $cm^{-1}$, Fe atoms' contribution is mainly found in the modes between 152 and 262 $cm^{-1}$, whereas for higher frequency modes above 262 $cm^{-1}$, the prevalence of oxygen atoms can be observed. The Raman band located at 94 $cm^{-1}$ is assigned to lattice vibrations of β-$Bi_2O_3$ crystalline phase. Piezo response force microscopy and AC-magnetic force microscopy (Distance sample-probe for MFM 100 nm) were performed at room temperature (Figs. 3 and 4). MFM measurements with a voltage supply (+10 V, −10 V) of the obtained films give us information on the relationship between the electrical and magnetic subsystems in a bismuth ferrite film. As can be seen from the figures, when the polarity of the voltage changes, the magnetization of certain domains changes. Thus, the magnetic field can control the electrical properties of the resulting film.

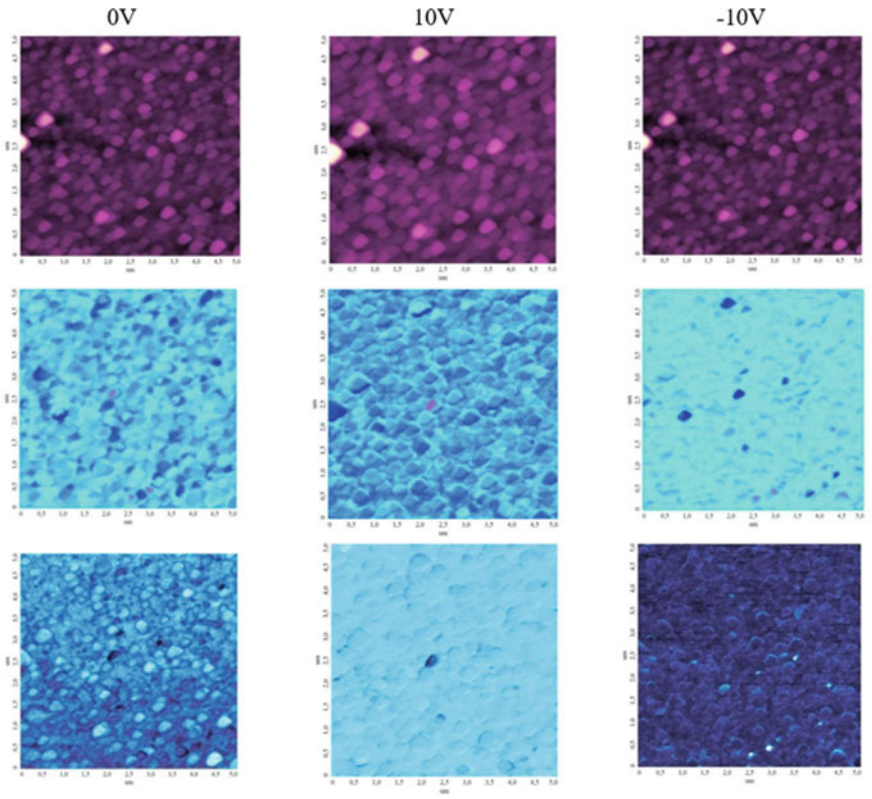


**Fig. 3** PFM of BFO/Pt/$SiO_2$/Si at 0, 10, and −10 V

PFM analysis of the obtained films gives information on the polarization of domains and their phase contrast depending on the voltage applied to the probe (0 V, +10 V, −10 V). As can be seen from the figures, the domains are about 300–500 nm in size. Depending on the direction of the applied voltage, the polarization and phase of some of the domain change. This will allow creating a structure with films of bismuth ferrite with controlled electric polarization. When a voltage polarity is applied, the structure undergoes some lattice distortions.

Ar ion etching was applied four times with the following parameters: 10 keV Ar1000 + , Raster size 3 × 3 mm, pre-etch and post-etch times 5 s. Cluster beam etching is less destructive and, according to the carbon level, only the surface layers were etched. Changes in the composition of iron and bismuth are associated with surface modification due to etching (Figs. 5 and 6).

Plasma modification of the surface makes it possible to create the desired properties in the surface region of the sample, as can be seen from the figures for changes in the $Fe^{3+}/Fe^{2+}$ ratio, it indicates the formation of oxygen vacancies, which allows changing of the electrical, magnetic, and optical properties of the obtained bismuth

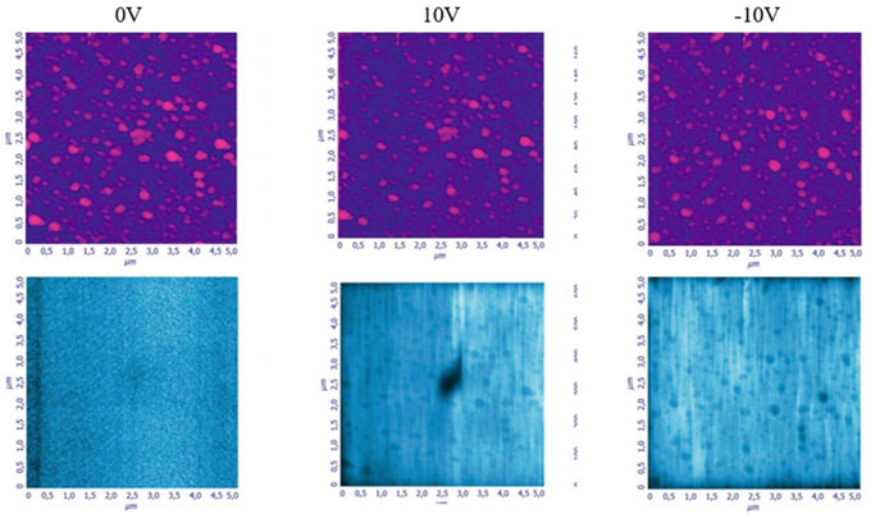


**Fig. 4** MFM of BFO/Pt/$SiO_2$/Si at 0, 10, and −10 V

ferrite films. The predominance or excess in the phase of metallic bismuth is associated with this same feature. The longer the surface is etched, the more metallic bismuth is in the phase. Thus, by controlling the composition of the resulting target, it is possible to control the properties of the resulting films.

Ceramic bismuth ferrite targets were prepared for (PLD) using the Spark Plasma Sintering (SPS) method based on synthesized powder. Analytically pure nitrates of iron $Fe(NO_3)_3 \cdot 9H_2O$ and bismuth $Bi(NO_3)_3 \cdot 5H_2O$ were used in stoichiometric proportions. Fossil fuel's role was played by glycine, which during combustion served as a platform for redox reaction between the reagents. Due to their natural hygroscopicity, metal nitrates mixed with glycine demonstrate the tendency toward the suspension mixture formation. Dehydration of the mixture was carried out by heating (up to 315 °C). Then, a hot stove was used to heat the dried mixture for the purpose of the combustion process initiation. Since the metals nitrates also serve as oxidizing agents, the process of combustion can proceed efficiently utilizing the oxygen that exists in the reagents themselves. Combustion process results in the formation of voluminous ash as well as a release of thick yellowish vapor. Afterward, the product is thoroughly grinded in a mortar and then subjected to temperature treatment for one hour at 600 °C. PLD is a process of rapid melting and evaporation of a target material because of exposure to high-energy laser radiation, followed by transfer of the sprayed material from the target to the substrate in vacuum and its deposition. The mechanism includes the ablation of the target material with laser irradiation, the development of a plasma torch containing high-energy ions and electrons, as well as the crystal growth of the coating itself on the substrate. The PLD process can be divided into four stages:

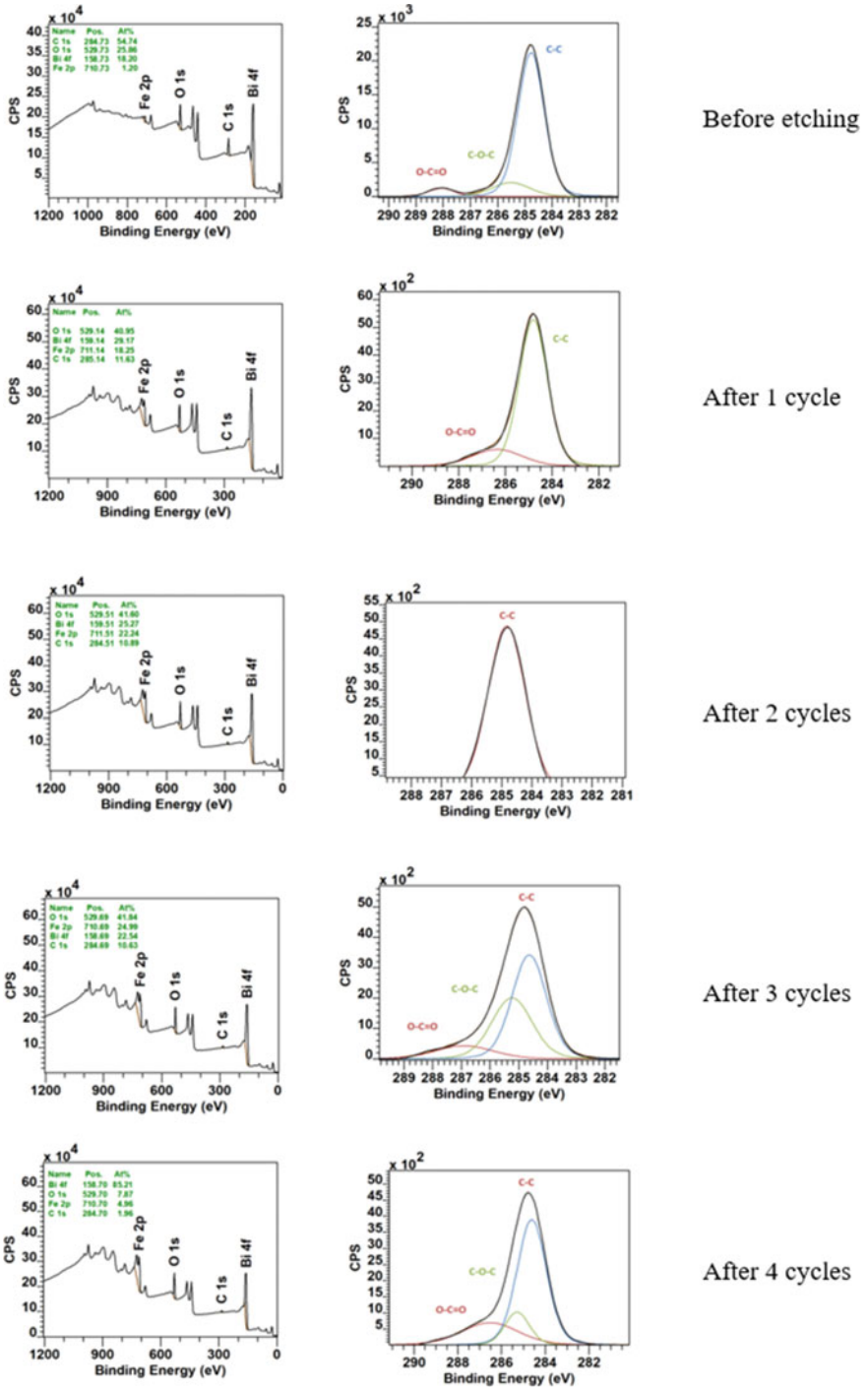


**Fig. 5** XPS wide and element (carbon) spectra of BFO/Pt/$SiO_2$/Si during depth profiling

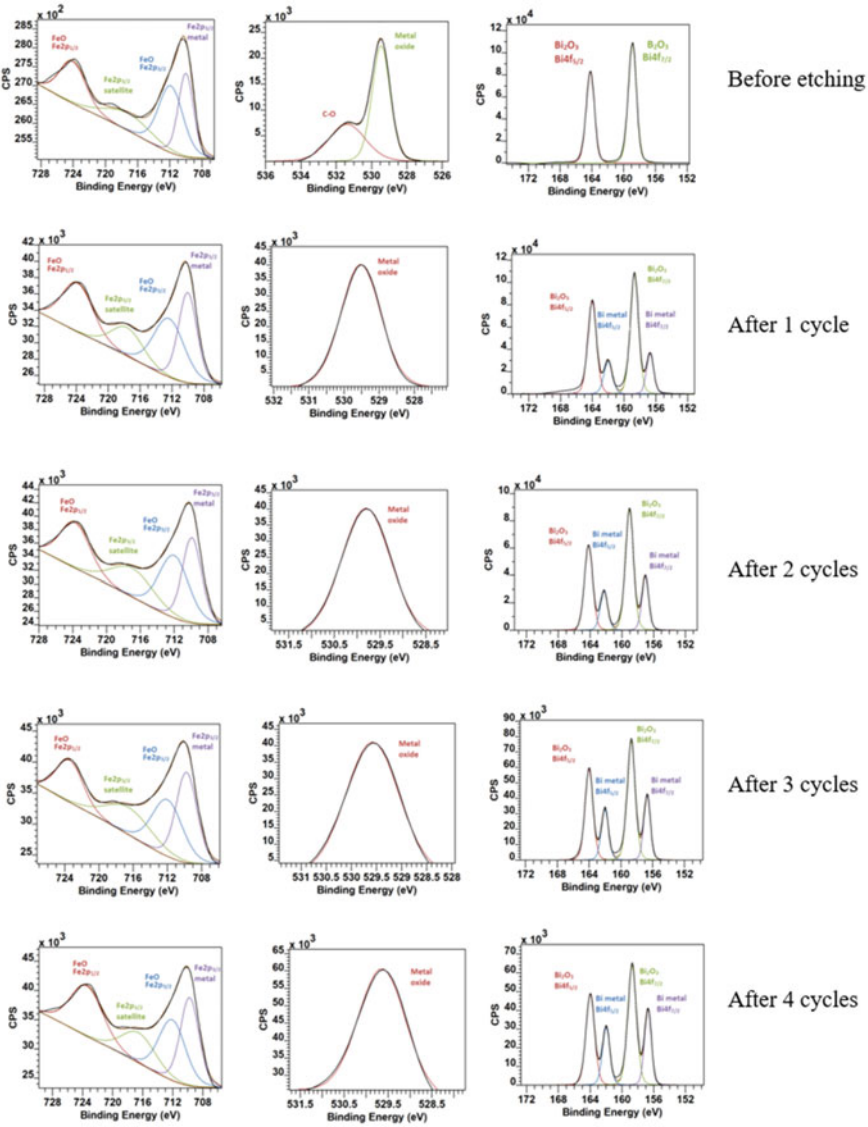


**Fig. 6** XPS element (iron, oxygen, and bismuth) spectra of BFO/Pt/$SiO_2$/Si during depth profiling

- Interaction of laser radiation with the target—ablation of the target material and the creation of plasma;
- Plasma dynamics—its expansion;
- Applying the material to the substrate;
- Film growth on the surface of the substrate.

Each of these steps is critical to the physicomechanical and chemical parameters of the coating. The removal of atoms from the bulk of the material is carried out by evaporation of the mass of the substance to the surface. The initial emission of electrons and coating ions occurs, the evaporation process by its nature is most often thermal. The depth of penetration of laser radiation at this moment depends on the wavelength of the laser radiation and the refractive index of the target material, as well as the porosity and morphology of the target. Due to the complex nature of such a process, it is impossible to calculate (simulate) it in advance. For example, during the evaporation process, the near-surface volume of the target undergoes significant modifications under certain conditions. And this affects the angular, mass, charge, and energy distribution of emitted particles, which, in turn, affects the mechanism and kinetics of the formation of condensate on the substrate. Therefore, studies aimed at establishing the relationship between the processes on the surface of the target and the growing film are relevant.

The stoichiometric composition, structure, and topography of the target used for PLD films of the $BiFeO_3$ multiferroic should be controlled before the deposition process. A change in the stoichiometric composition can affects the composition and structure of the resulting films. Given the fact that the PLD process uses an oxygen medium, the probability of the formation of additional oxygen bonds with the metals of iron and bismuth is highly probable. The target was pre-polished with diamond powder, ~0.25 μm in size. Further cleaning consisted of washing in an ultrasonic bath in $C_3H_8O$, then in ethanol and in demineralized water. The target was sputtered with a laser beam at the following parameters: Spot size: 2.85 × 0.82 $mm^2$, mask: 3 × 15 $mm^2$, energy 23.5 mJ, fluency: 1.093 J/$mm^2$, $O_2$ pressure: 0,1 mBar, scan speed: 0.7 mm/s, pre-ablation 10 Hz, and 1000 pulses for the first experiment and 100,000 for the second experiment. To understand the mechanisms of degradation of the target surface during the PLD process, the target was studied using SEM Tescan Lyra 3 with an EDX Oxfords Instruments X-Max 50 detector and determined the qualitative and quantitative characteristics of the sample. SEM and EDX data (Fig. 7) show the effect of laser annealing of the target surface at pulses: 10 000 to compare the target surface before the experiment. The appearing surface features at 100 000 were similar. It is seen from SEM–EDX that the surface topography changes significantly, and a quantitative change in the composition of the surface region of the target occurs. Depending on the number of laser pulses during the evaporation process, the amount of bismuth is mainly affected (see Table 1), which is relatively mobile in contrast to iron atoms (Table 1). Figure 8 shows how a laser beam acts on the surface of a ceramic target.

Thus, as can be seen from Fig. 8, with laser radiation from the target, the beam practically melts the evaporation region, and a liquid phase is created, which tends up the sides of the crater. The liquid phase creates elevations and forms a surface topography (Fig. 6). Since it is possible to control the amount of oxygen introduced into the chamber in the atmosphere of the evaporated substance, saturation, or excess of oxygen vacancies in the resulting $BiFeO_3$ film is possible (the dependence of the oxygen vacancies in the composition of the obtained film on the pressure of the oxygen introduced into the chamber will be studied in further work). A parallel

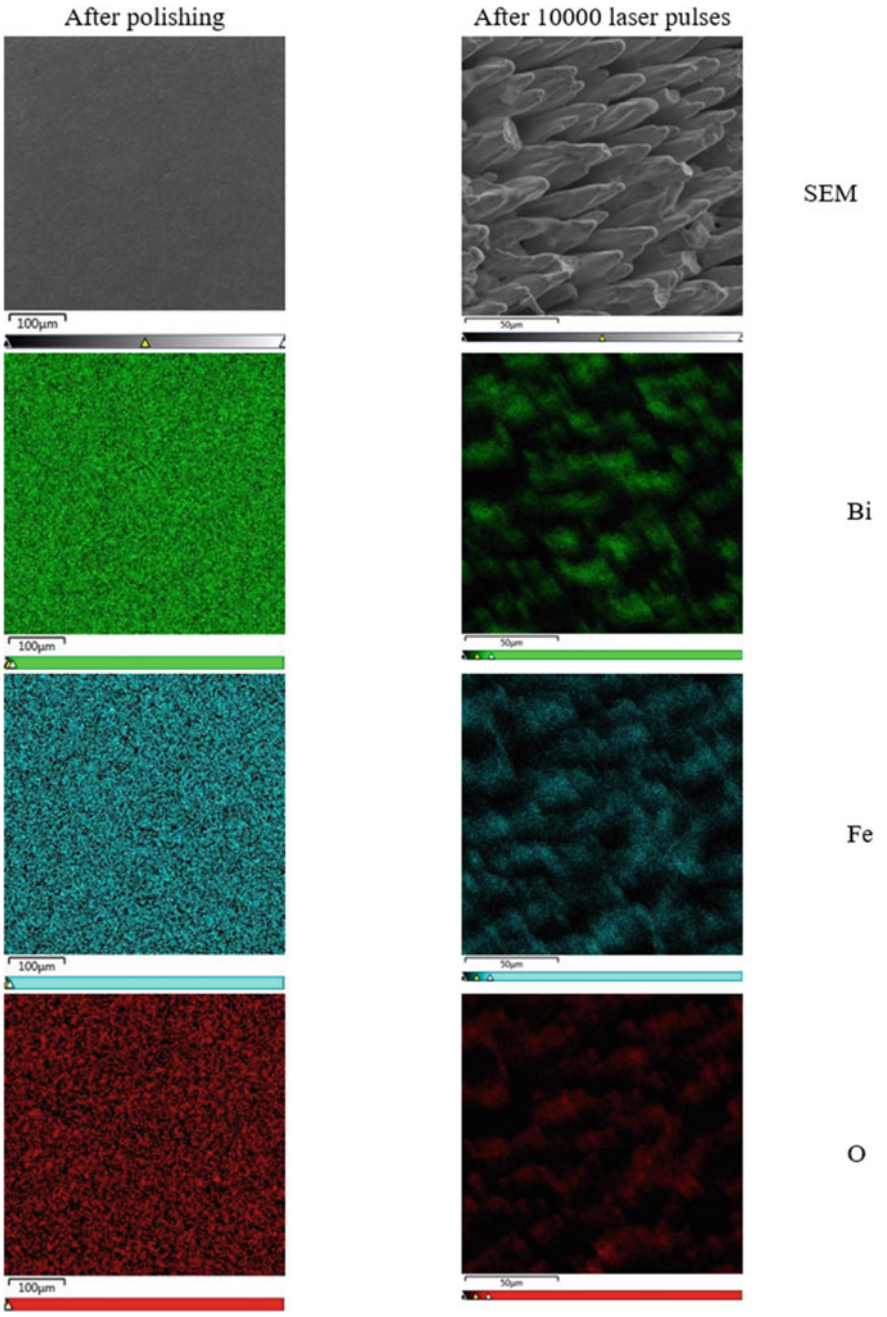


**Fig. 7** SEM–EDX analysis of the $BiFeO_3$ target before the process and after 10 000 laser pulses

**Table 1** EDX analysis of the $BiFeO_3$ target composition

| No ablation | Pulses: 10 000 | Pulses: 100 000 |
|---|---|---|
| Atomic % | Atomic % | Atomic % |
| O 41.45 | O 44.2 | O 47.0 |
| Fe 12.35 | Fe 23.9 | Fe 25.1 |
| Bi 12.30 | Bi 6.4 | Bi 6.0 |

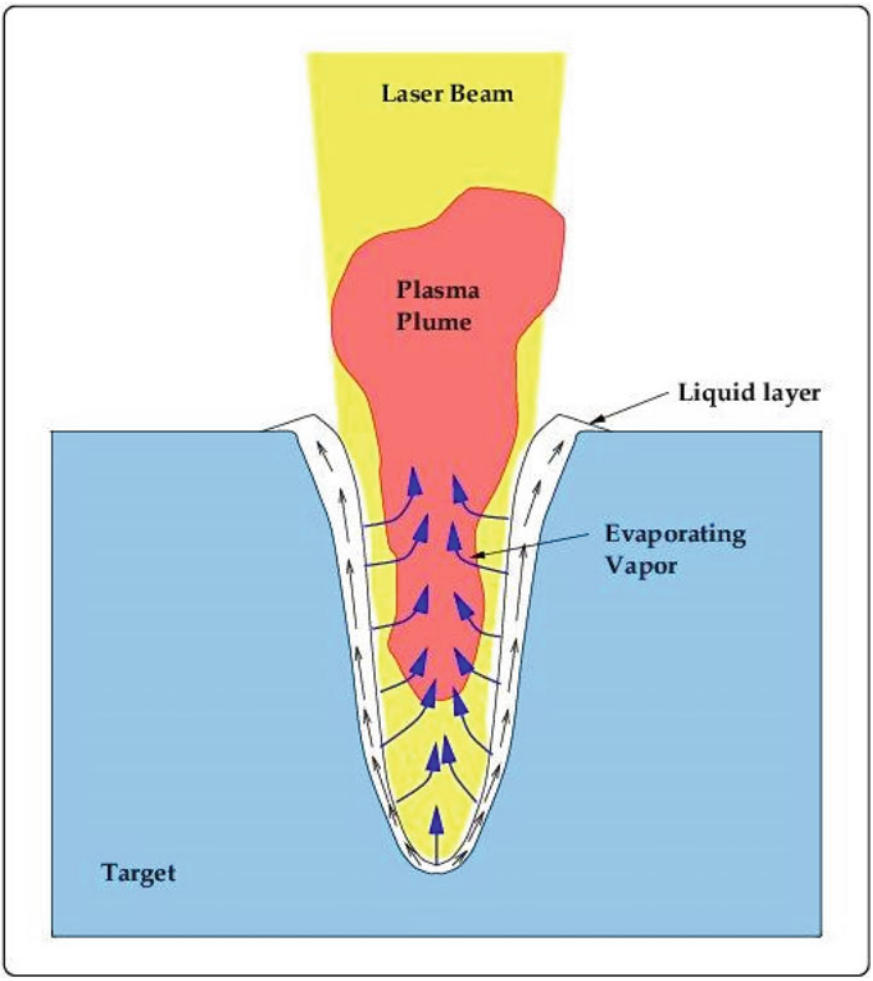


**Fig. 8** Schematic of laser–material interaction [20]

study of the target surface and the resulting film allows us to create the prerequisites for modeling the technological process for producing $BiFeO_3$ multiferroic films with desired properties. Changes in the phase and structural composition of the surface of the bismuth ferrite target were studied by XRD with brightness source Rigaku SmartLab 3 kW. Figure 9 shows the comparison of XRD spectra of the $BiFeO_3$ target after ablation, the data are systemized in Table 2.

From the XRD data, it follows that the ratio of the phase composition of the surface region of the target varies (see table). Due to changes in the morphology of the target surface in the PLD process, due to thermal processes, the number of non-$BiFeO_3$ phases increases several times. Obviously, this is due to the technological features of this process: oxygen atmosphere, thermal modification of the target surface, evaporation of elements or agglomerates from the target surface, quantitative ratios of elements in the laser-modified target surface, structural changes, etc. As the laser

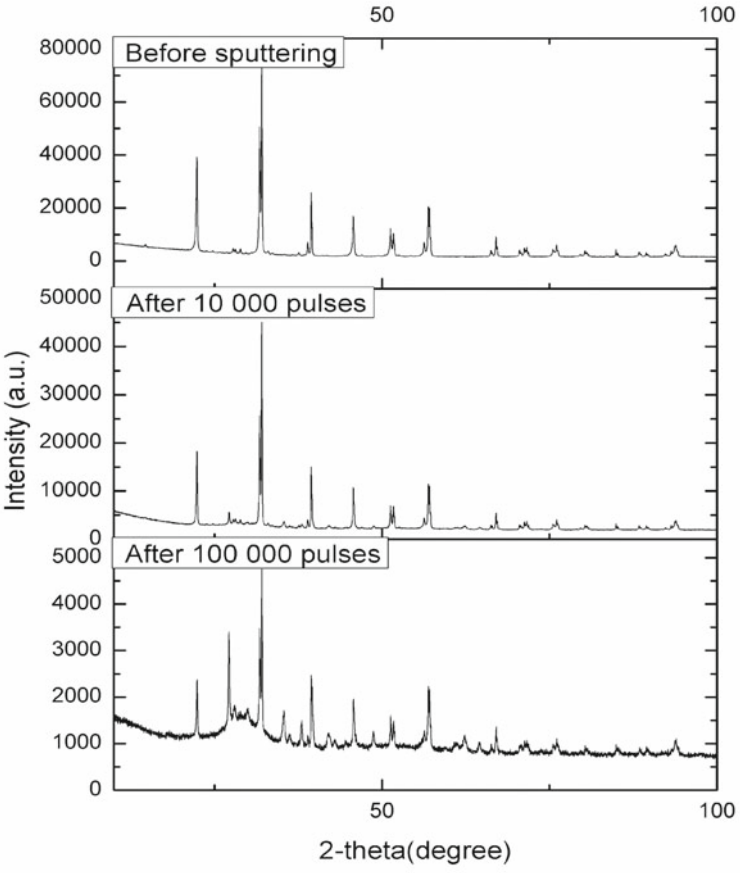


**Fig. 9** XRD of the $BiFeO_3$ target before and after ablation

**Table 2** Phase composition of the target before and after 100 000 pulses

| | Before sputtering | After 100 000 pulses |
|---|---|---|
| Target phase | Content (%) | Content (%) |
| $BiFeO_3$ | 89.9 | 34.1 |
| $Bi_2Fe_4O_9$ | 6.8 | 49.4 |
| $Bi_{25}FeO_{40}$ | 3.3 | 16.5 |

acts on the target, the crystal lattice structure of the near-surface region of the target changes; the selenite phase, $Bi_2Fe_4O_9$, grows to a greater extent (Fig. 10).

To study the structural properties of the target, Raman spectroscopy studies were additionally carried out. Raman spectra were excited by a solid-state laser ($\lambda$ = 532.0 nm), the diameter of the focused beam was 2 μm. Peaks positions (139 $cm^{-1}$, 172 $cm^{-1}$, 219 $cm^{-1}$, 264 $cm^{-1}$, 265 $cm^{-1}$, 364 $cm^{-1}$, 440 $cm^{-1}$, 480 $cm^{-1}$, 525 $cm^{-1}$, and 618 $cm^{-1}$) from the $BiFeO_3$ target coincides with literature data [21]. Being more sensitive to the surface, Raman spectra of sputtered targets demonstrate the presence of bismuth oxidation on the surface.

## 3 Atomic-Layer Deposition of Bi–Fe–O System

Atomic-layer deposition (ALD) belongs to a group of methods based on chemical processes. This technology is based on sequential chemical reactions between the gaseous precursor and the substrate material. When using multiple precursors to produce films of complex composition, the precursors are introduced alternately. As a result of repeated reactions of precursors with a surface, a thin film is deposited. The ALD process is a self-regulatory process. Since the reactions are self-limiting, the amount of deposited material in each reaction cycle is constant. Self-limitation of surface reactions makes it possible to control deposition at the atomic level. ALD supports the use of large geometric dimensions of samples with high uniformity. Substrates can be of various shapes and structures. It is also possible to obtain films of transparent conductive coatings with good optical and electrical characteristics at relatively low substrate temperatures. The advantage of ALD over other epitaxy methods (plasma-layer deposition, magnetron sputtering, and electron beam sputtering) is the possibility of more detailed control of growth. This avoids the violation of stoichiometry and structure of the films. ALD provides a choice of various precursors and options for the Bi–Fe–O composed films preparation. It creates opportunities for controlling stoichiometry and perfection of the films. At the same time, this complicates the task of evaluating the properties and parameters of the prepared structures before the processed will be completely tuned. By varying the concentration of precursors interacting with the surface layer of the substrate material, it is possible to self-organize nanoparticles of individual reaction components on the surface without additional thermal annealing. ALD is a surface-controlled process because of self-limiting reactions, where the process parameters, with exception of

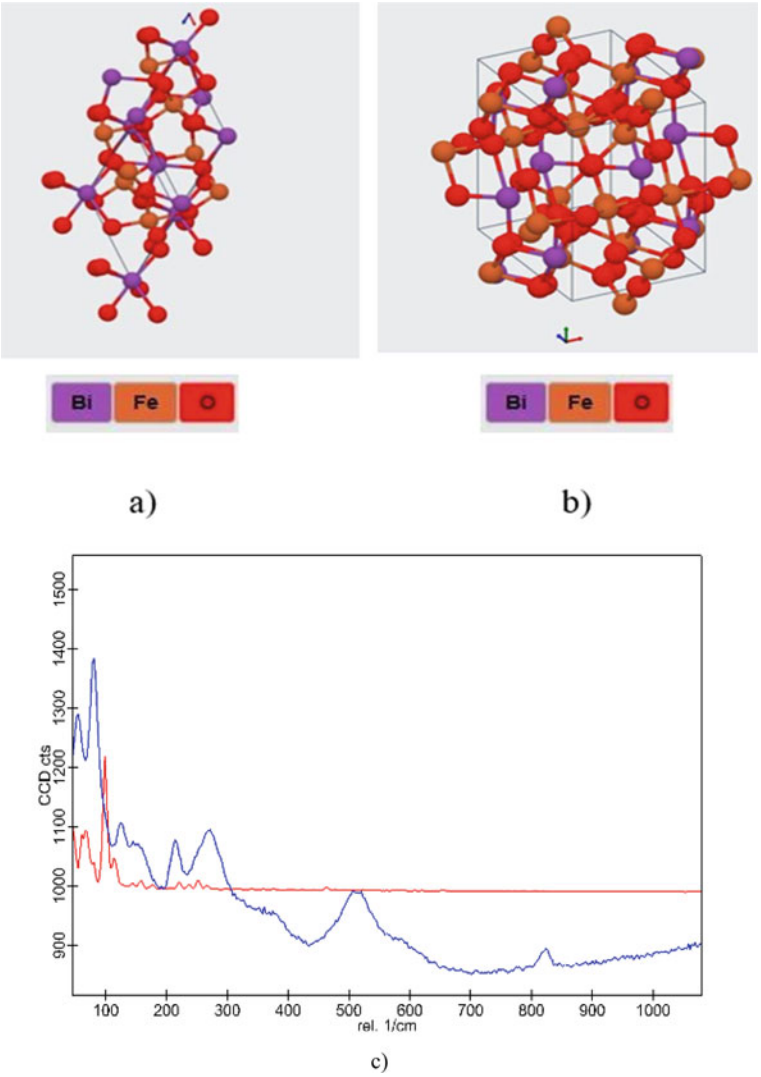


**Fig. 10** Structure of **a** $BiFeO_3$, **b** $Bi_2Fe_4O_9$, and **c** Raman spectra of the target before and after 100 000 ablation pulses

the composition of precursors, substrate, and temperature, have no significant effect. Due to this, the films grown by the ALD process have an exceptionally uniform composition and thickness. These thin films can be used in combination with films made by other common methods.

*Advantages of ALD:*

- Chemisorption of precursors with the surface provides excellent adhesion;

- Self-limiting surface reactions allow for automatic processing and eliminate the need for extra precise dosing;
- Surface reactions ensure the application of uniform protective coatings, regardless of the substrate material (dense, porous, tubular, powder, or other complex in shape);
- The combination of a protective coating with specific substrates creates completely new possibilities, for example, changing the diffusion properties of battery materials and much more;
- Allows deposition of layers less than one nanometer thick.

ALD supports the use of large geometric dimensions of samples with high uniformity. Substrates can be of various shapes and structures. It is also possible to obtain films of transparent conductive coatings with good optical and electrical characteristics at relatively low substrate temperatures. The advantage of ALD over other epitaxy methods (plasma-layer deposition, magnetron sputtering, electron beam sputtering) is the possibility of more detailed control of growth. This avoids the violation of stoichiometry and structure of the films. ALD provides a choice of various precursors and options for the Bi–Fe–O composed films preparation. It creates opportunities for controlling stoichiometry and perfection of the films. At the same time, this complicates the task of evaluating the properties and parameters of the prepared structures before the process will be completely tuned. By varying the concentration of precursors interacting with the surface layer of the substrate material, it is possible to self-organize nanoparticles of individual reaction components on the surface without additional thermal annealing. The main difference between ALD films and other chemical vapor deposition techniques is the completely heterogeneous nature of the reaction of two precursors (reagents), which leads to the growth of a film on a substrate. This is achieved by the cyclic feeding of the first and second precursors into the chamber, separated in time. In general, the required ALD phases include:

- Dosed injection of vapors of the first precursor into the reactor chamber;
- Purging and pumping out the chamber, after which strictly one monolayer of the precursor chemisorbed on the surface remains on the surface of the thermally stabilized substrate;
- Introduction of the second precursor and the occurrence of a heterogeneous reaction resulting in the formation of the film monolayer with a known composition;
- Pumping out gaseous reaction products.

Typically, the most important factor in the ALD process is the "ALD Window," where the growth per cycle (GPC) is nearly constant, allowing reliable and repeatable results to be obtained despite minor temperature changes. Figure 11 shows the possible growth behavior per cycle depending on the deposition temperature and the cause of the impairment of the ALD growth mechanism.

As region 1 (Fig. 11) demonstrates, GPC decreases with increasing deposition temperature due to the physical sorption of precursors. As a result, condensation of the precursors occurs. The adsorption can be separated into two general types

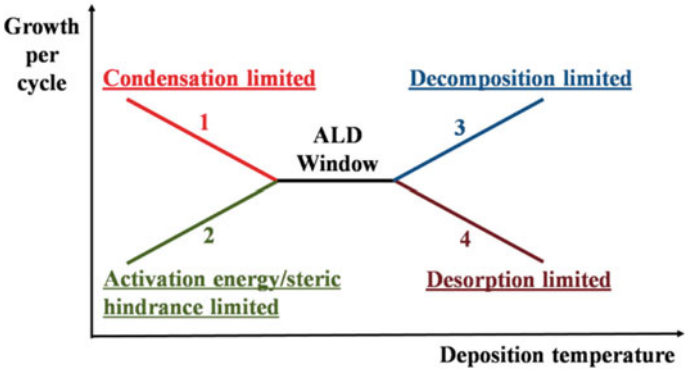


**Fig. 11** ALD window layout: possible growth behavior per cycle depending on the deposition temperature and the reasons for the disturbance of the ALD growth mechanism [22]

depending on the interaction strength between the solid surface and the adsorbing molecules: the first is physical adsorption (i.e., physical adsorption) and the second is chemisorption (i.e., chemical adsorption). Chemisorption also includes the breaking of chemical bonds between adsorbing molecules and a surface. Consequently, the surface accepts only one layer, while adsorption results in a monolayer formation of adsorbed molecules. However, physical adsorption occurs due to weak interactions (Van der Waals force), and minimal changes usually appear in the adsorbing molecule's structure. Interactions are not representative of the molecule/surface pair in physical sorption, so adsorption can form multilayer structures. Due to physical adsorption, ALD is sometimes not self-limiting (not forming a monolayer), but a multilayer "sandwich". In region 2 (Fig. 11), an increase in the temperature entails an increase in the GPC, which can be attributed to the decreasing steric hindrance effect of precursor ligands or to the reaction activation between the precursors and reagents. Ligands steric hindrance can result in a blockage of a part of the surface by ligands of adsorbed molecules (precursors) from access to another precursor molecule, thereby limiting the surface density of adsorbed precursors. This can limit the total amount of adsorbed precursors on the surface and the limitation of the film thickness in the ALD process. On the other hand, surface reactions between adsorbed precursors and reactants may not be activated at low deposition temperatures, which also limits GPC. In region 3, the GPC rises with the temperature, this is since the precursors decompose on their own during the ALD cycle. The surface particles' decomposition can take place even at the minimum possible temperature necessary for surface reactions, which renders the ALD process not self-limiting, and the process starts to resemble the chemical vapor deposition (CVD) mode. As shown in region 4, an increase in the temperature results in a decrease in GPS, this is explained by the precursors' desorption occurring on the surface. Thus, in accordance with the above effects, an ideal model for ALD (a self-limiting single monolayer growth mechanism) cannot always be attained in certain ALD processes.

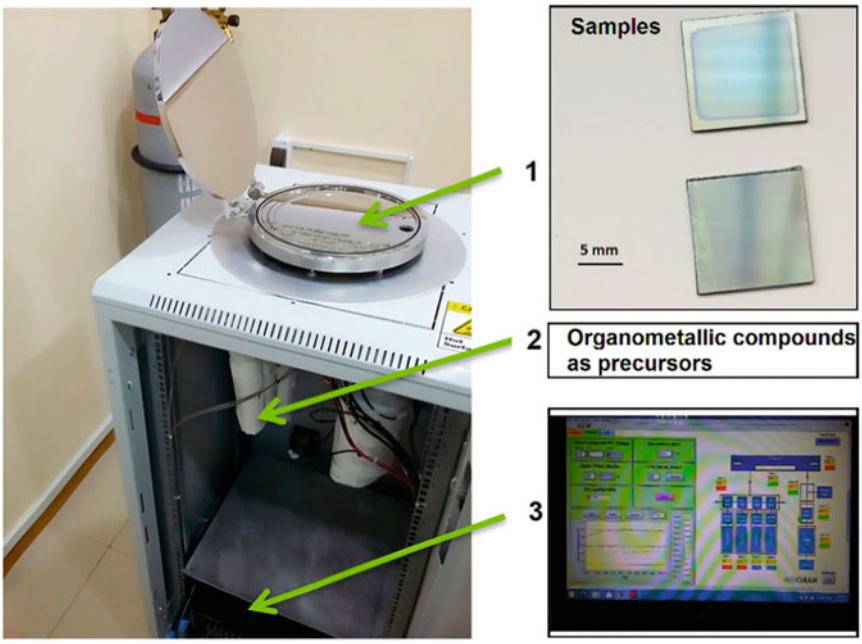


**Fig. 12** Atomic-layer deposition (ALD) instrument and its main parts: (1) vacuum chamber, (2) section for precursors containers, and (3) controller with custom-made software

In this review, we focus on ALD film growth in the Bi–Fe–O system. Thin BFO films were obtained on various substrates and heterostructures. The growth regime was practically the same, differing in the type of substrates, the number of cycles, and the substrate temperature. The film was deposited using ALDCERAM ML-200 (ALDCERAM, LLC, Boulder, CO, USA, located in the Engineering Center of the Dagestan State University, Makhachkala, Russia), shown in Fig. 12.

Bi-containing organometallic precursor with the formula tris(1-methoxy-2-methyl-2-propoxy) bismuth-$C_{15}H_{33}O_6Bi$ or $(Bi(mmp)_3)$ was used to deposit a thin film of amorphous bismuth ferrite on the substrate surface by ALD method. The precursor was purchased from Sigma-Aldrich, Schnelldorf, Germany. Evaporation occurred at 408–418 K temperature range. Ferrocene was used as the precursor for iron. The ferrocene formula is $Fe(C_5H_5)_2$ (also purchased from Sigma-Aldrich, Schnelldorf, Germany). For optimal evaporation of ferrocene, the temperature should be around 364 K. For oxidation purposes, an ozonizer was utilized which produced $O_3$ directly into the chamber. Oxidation with ozone using low temperatures is a simple method that was introduced by Iatsunskyi I et al. in their work [23]. Purging was carried out with the use of an $N_2$ gas carrier, the purity of which is up to 99.999%. The placement of the substrate was done in such a way that the distance between the inlet and the substrate was 4 cm. Then, the uniform heating of the chamber was initiated ($T = 523$ K). The initial value of the chamber pressure was $10^{-3}$ torr. The

constant temperature as the outlet for the purge gases was kept at 423 K. Since the ALD method has the capability of covering the surface with maximum conformity, $TiO_2$ nanotubes previously prepared on a titanium surface were used [24, 25, 26]. The ALD process diagram is shown in Fig. 13.

In the case of the $Bi_2O_3$–$TiO_2$ composition, Aurivillius phases compounds occur at n(Bi)/n(Ti) > 1. Lu et al. conducted a study on compounds' formation processes, which take place at the phase boundaries of $TiO_2$ and $Bi_2O_3$ within the $TiO_2$–$Bi_2O_3$–$TiO_2$ sandwich structure [26, 27]. The conclusion was that the titanium diffusion leads to the formation of a rather stable compound–$Bi_4Ti_3O_{12}$, within the $Bi_2O_3$ layer. Additionally, the γ-$Bi_2O_3$ melting point ($T_m \approx 550$–$630$ °C) is close to the annealing temperature (660 °C). This results in a considerable increase in the rate of mass transfer and chemical reaction initiation, which is considered an additional contribution to reaction 1.

As a result of this increased $Bi_2O_3$ mass transfer rate along the surface of a growing layer under annealing, a solid-phase reaction takes place in the near-surface region

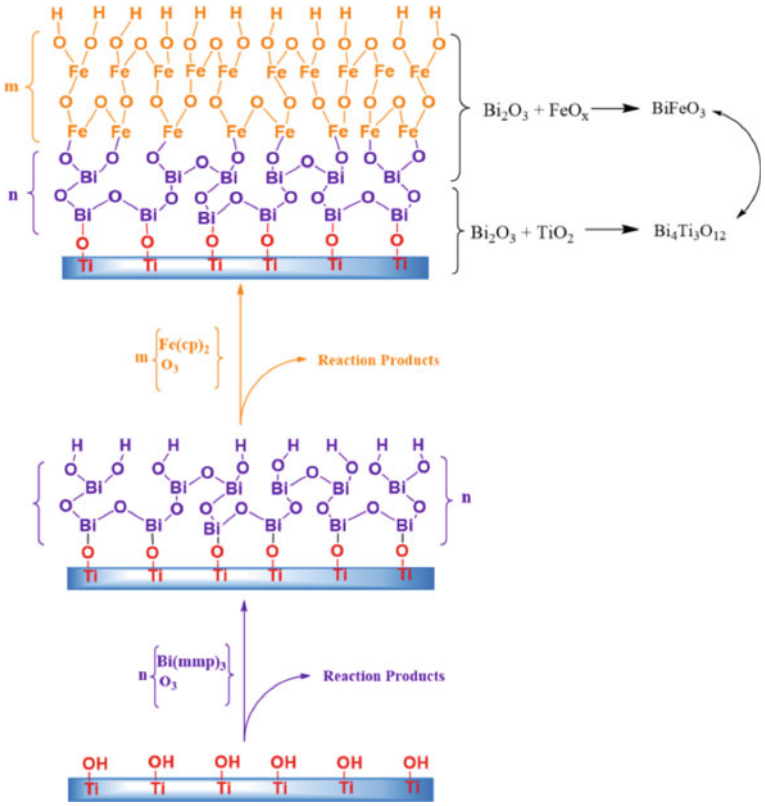


**Fig. 13** Schematic process of the ALD Aurivillius phase formation

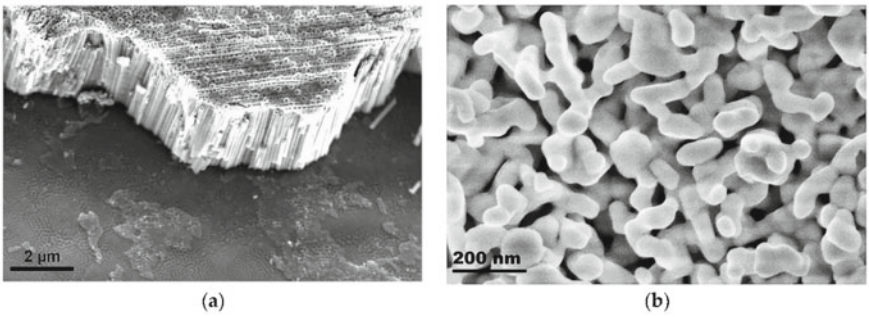


**Fig. 14** Scanning electron microscopy (SEM) images of **a** pure and **b** ALD-coated $TiO_2$ nanotubes (Nt) on Ti foil

$$3TiO_2 + 2Bi_2O_3 = Bi_4Ti_3O_{12} \quad (1)$$

Equation 2 describes the reaction that occurs in the $Bi_2O_3$-$FeO_x$ region due to the mass transfer:

$$2FeO_x + Bi_2O_3 = 2BiFeO_3 \quad (2)$$

The $BiFeO_3$–$Bi_4Ti_3O_{12}$ phases interact during the annealing process as demonstrated in Fig. 13, this interaction entails the formation of an Aurivillious phase layered structure [28]. The number of layers in that structure is explained by the fact the perovskite-like block contains $BiFeO_3$ [29]. SEM images of $TiO_2$ Nt surface before and after deposition are given in Fig. 14.

As Fig. 14a demonstrates, there is an array of $TiO_2$ Nt covering the substrate surface. These $TiO_2$ Nt are vertically oriented and have a length of approximately 2 μm and a diameter of 100 nm. Figure 14b shows the nanotubes' surface after the deposition of $Bi_2O_3$–$FeO_x$. It can be observed that there is an inhomogeneous layer of nanostructures (~100 nm in diameter) covering the nanotubes' surface. The nanotubes surfaced can be seen through the pores with a width of ~ 50 nm. To provide a more detailed characterization, TEM analysis has been performed on the coating (Fig. 15). Figure 15a contains a TEM image of a single $TiO_2$ Nt coated by ALD. There is a film with a thickness of ~ 20 nm covering a single nanotube in a uniform manner. Dark areas indicate nanocrystals grains with the size of 10–15 nm, which are in the film. Light areas represent the presence of an amorphous phase. According to the experimental data on the formation kinetics of layered perovskite-like compounds in BFTO systems, the formation of the Aurivillius phase occurs at 600 °C [30]. An enlarged area at the nanotube–film interface is given in Fig. 15b. It indicates that annealing at 660 °C leads to the formation of a complex layered structure in the nanotube–film interface, which is characteristic of Aurivillius phases. There are two types of layers that make up the crystal lattice of all Aurivillius phases. These are perovskite-like layers $(A_{n-1}B_nO_{3n+1})^{2-}$ and bismuth-oxygen layers $(Bi_2O_2)^{2+}$, which

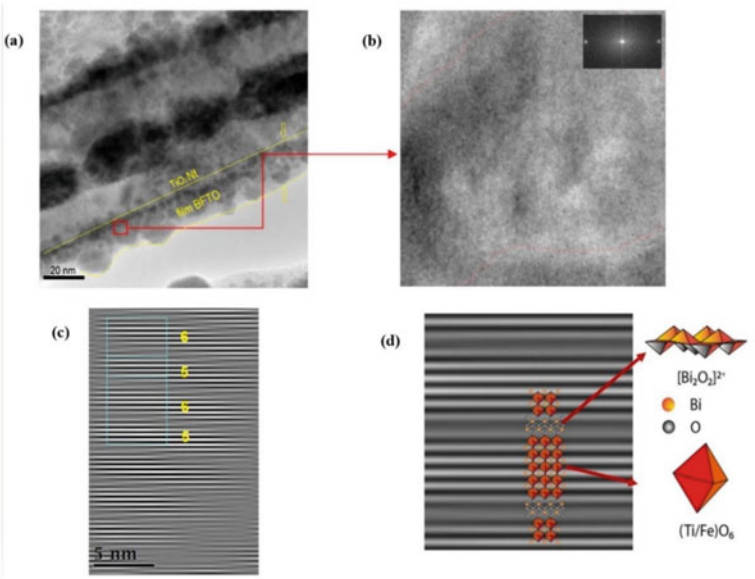


**Fig. 15** Transmission electron microscopy (TEM) analysis: **a** image of a single TiO2 Nt coated by ALD, **b** magnified area (7 × 7 nm2) at the nanotube–film interface where the layered structure is presented, and **c**, **d** Fourier masked micrographs of the region with a layered structure

alternate with each other as demonstrated in Fig. 15c. Fourier analysis of the high-resolution region (Fig. 15c, d) enabled visualization of phase-modulated structures, which are one-dimensional (1D) and consist of two different layered Aurivillius phases where arrays of five and six perovskite-like layers alternate with each other (Fig. 15c). There have been reports on the interface modulation in the periodically laid structures; however, it was commonly implemented through doping of the various structure positions with rare-earth metal or alkaline-earth ions. Stacking defects in the $(Bi_2O_2)^{2+}$ layer accompany the transition between layers with a different number of blocks. Complex deformations and distortions can take place in the interfaces comprised of 5- and 6-layer blocks. In this case, the perovskite structure remains, and regular lattice distortions occur in certain regions without any change in the general arrangement and formation of regions with morphotropic phase transitions. Probably, these regions are associated with the replacement of $Fe^{3+}$ ions by $Ti^{4+}$ ions in octahedral cells in a narrow range (0.58–0.65) [31]. Furthermore, Kikuchi suggests that the formation of these regions can be explained by the fact that ionic radii of titanium and iron have a 6% difference, which results in a displacement of these ions with respect to the $(Bi_2O_2)^{2+}$ layers.

Figure 16 contains characteristic XRD patterns of pure $TiO_2$ and $TiO_2$ deposited on Ti substrate by ALD. It is discovered that the phase of anatase (ICSD reference code: 98–015-4603) and Ti (ICSD reference code: 98-065-3275) are present in the pure $TiO_2$ Nt. The multitude of phases in the resulting structure explains the occurrence

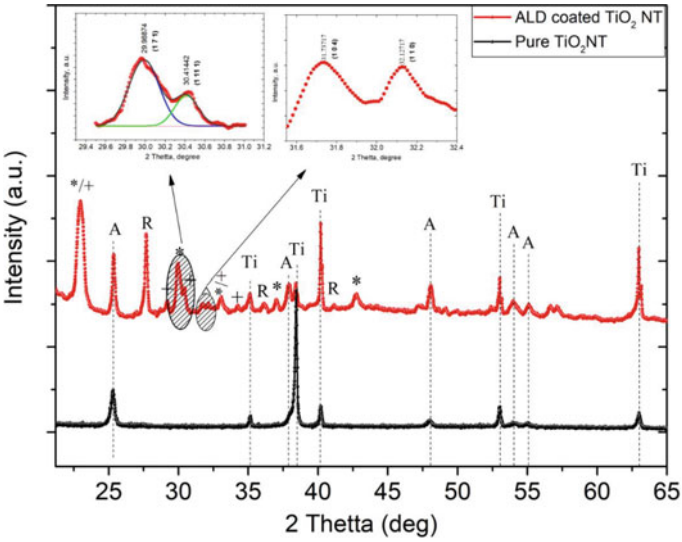


**Fig. 16** XRD patterns for $TiO_2$ (pure and coated by ALD). R-rutile; A-anatase; Ti-titanium; *-$Bi_4Ti_3O_{12}$; + -$Bi_6Fe_2Ti_3O_{18}$; ^-$BiFeO_3$. Left insert–deconvoluted $Bi_4Ti_3O_{12}$/$Bi_6Fe_2Ti_3O_{18}$ peaks, Right insert–$BiFeO_3$ peaks

of the XRD peaks overlap. The partial transformation of anatase phase into the rutile phase with the distinctive peak at $2\theta = 27.7°$ (110) is caused by annealing at 660 °C [32]. The diffraction peaks occurring at $2\theta = 30.1°$ (171), 33.1° (200), and 42.8° (113) are assigned to orthorhombic Bi4Ti3O12 with the Aba2 space group (ICSD reference code: 98–008-7809) [33]. The peaks that appear at around $2\theta = 31.7°$ (104) and 32.1° (110) (ICSD Reference code: 98–001-5299) [34] can be assigned to a pure $BiFeO_3$ hexagonal structure with an R3c space group. These peaks are presented in Fig. 16 (right insert). The other peaks are related to orthorhombic $Bi_6Fe_2Ti_3O_{18}$[18] with the Fmm2 space group. Figure 16 (left insert) contains deconvolution of the peaks, which indicates the $Bi_4Ti_3O_{12}$ phase at 29.9° (171) as well as of $Bi_6Fe_2Ti_3O_{18}$ phase at 30.4° (11 11). Thus, the proposed method of Aurivillius phase structure formation is confirmed by the presence of $Bi_4Ti_3O_{12}$ and $BiFeO_3$ phases.

1D phase phase-modulated; layered structures of Aurivillius phases with 5- and 6-layer perovskite-like blocks alternating with each other were deposited by ALD on $TiO_2$ Nt surface with the use of a two-layer $Bi_2O_3$–$FeO_x$ sandwich structure technique. It has been demonstrated that the self-organization under temperature treatment (660 °C) leads to the formation of the layered structure. The PL spectroscopy results show that due to the decrease in the charges radiative recombination, there is a high potential for application. Bandgap narrowing was demonstrated by diffuse reflection spectroscopy. This narrowing is explained by defective energy states affiliated with the crystal lattice disorder. $TiO_2$ Nt coated by ALD shows an increase in the Urbach energy with a magnitude of 4.2x. Such an increase indicates a disorder in the structure related to the bismuth and oxygen vacancies presence

as well as the simultaneous existence of 1D phase-modulated structures which are comprised of two different Aurivillius layered phases where the number of 5 or 6 alternating perovskite-like layers with varied Fe/Ti ratio in octahedrons. The performance of electrons photon excitation is improved by the incorporation of the ALD coating, which is evidenced by transient photocurrent responses under irradiation in the UV–vis range. It can be inferred based on MO photodegradation and the PEC experiments that the obtained structures display great potential as photocatalysts. BFO films can also be adapted to produce smooth surfaces used for optics. Thus, the surface morphology and structure of the BFO films obtained on the $Ta_2O_5$/Si surface can be changed [35]. Some of the largest consumers of energy resources are the centers designed for data storage and processing. The demand for energy will keep increasing due to the ever-growing industry of social networks, mobile applications, and cloud storage services. Thus, the implementation of novel electronic components is a key to further improvement of the capacity and functioning rates of these resources. The list of these components includes new kinds of logical elements, memristors, which serve as a basis for non-volatile memories with information storage of high density. In this regard, tantalum pentoxide ($Ta_2O_5$) attracts increasing attention from the scientific community nowadays due to its remarkable electrical and optical properties [36]. A large refractive index (RI) along with a high dielectric constant makes $Ta_2O_5$ a rather favorable option that can be considered in a variety of different applications. One such application, for example, involves the usage of $Ta_2O_5$ as an insulating material in various "sandwich" structures such as metal/insulator/metal (MIM) or metal/insulator/semiconductor (MIS) [37, 38]. $Ta_2O_5$/Si heterostructures were utilized as substrates in which $Ta_2O_5$ thickness was between 20 and 100 nm. After the film's deposition, the samples were subjected to annealing in vacuum under 600 °C for 1 h. Figure 17 contains AFM characterization of $Ta_2O_5$ films with different thickness values. The general trend here is that the average value of $Ta_2O_5$ surface roughness increases as the layer grows thicker. In order to achieve reliable results for the characterization of the 3D surface microtexture with high resolution, special attention must be paid to the correct choice of scanning parameters [39–42].

As Fig. 17 demonstrates, there is no significant variation in the surface topography with the increase in the thickness between 20 and 100 nm. Every 20 nm of thickness results in the heights difference of only about 0.1–0.2 nm. A feature that is characteristic of the heteroepitaxial growth is the pseudo-cubic structure formation in the deposited film, which is caused by the lattice mismatch between the film and the substrate. Crystallization of this type is common for ion-plasma methods, where the sprayed particles demonstrate additional kinetic energy. During the ALD process, a chemical reaction takes place on the surface, whereas for the formation of the crystallites on the surface a further heat treatment is necessary. It was reported the fractal mechanism is involved in the formation of $Ta_2O_5$ films. This study also investigated the dependency of 3D micromorphology and the thickness of the $Ta_2O_5$ films. Probably, this growth mechanism is repeated for thin films of BFO at smaller thicknesses (~50 nm). Figure 18 contains topography images of BFO thin films deposited on the surface of $Ta_2O_5$/Si with varied values of thickness.

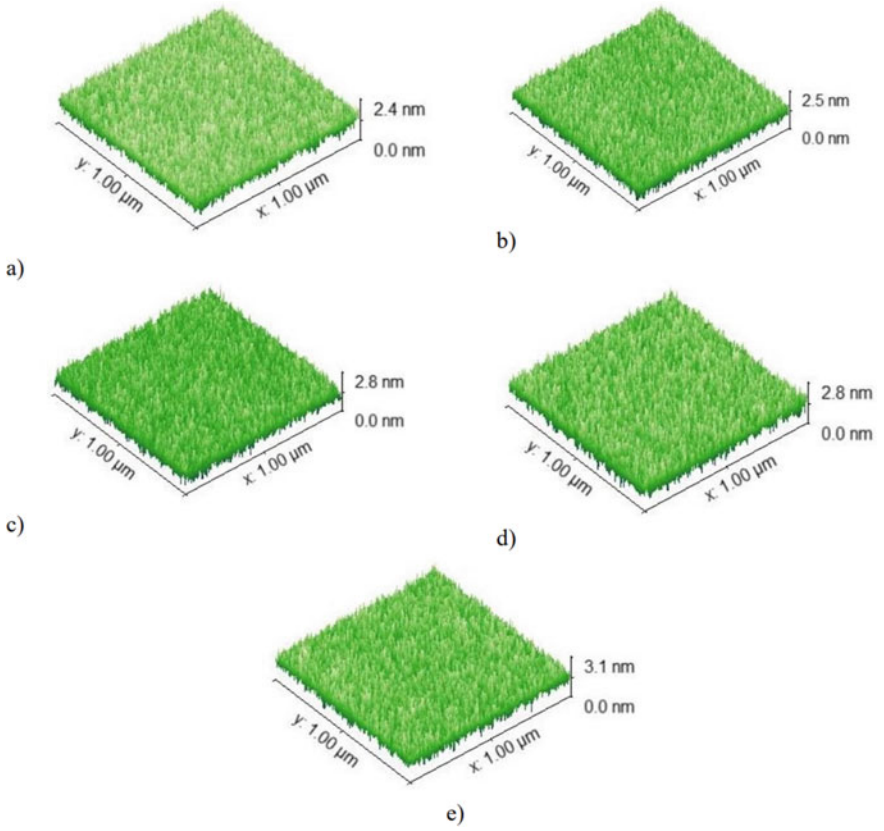


**Fig. 17** AFM topography images of $Ta_2O_5$ films with various thickness: **a** 20 nm; **b** 40 nm; **c** 60 nm; **d** 80 nm; **e** 100 nm

In this work, the surface of $Ta_2O_5$ was chosen for the deposition of the BFO thin films. Several depositions were performed to obtain BFO films with varied thickness. It can be noticed in the AFM images that the roughness of the deposited BFO films is in direct ratio with the initial values of $Ta_2O_5$ layer thickness. The acquired data indicate that there were several nm oxide layers present on the as-deposited film. The following annealing procedure led to the removal of this oxide layer to a large extent. The fields of nanotechnology and nanophysics require a carbon structure of a specific type and shape. This is why HOPG was chosen as a substrate for the deposition of smooth and stable films. The process for fabrication of this carbon type (HOPG) involves pyrolysis at a very high temperature (~2300 K) in carbon-containing steam followed by the second stage, which is annealing at ~3275 K [43]. The carbon material obtained by this method has a very strong bond in its hexagonal structure with $sp^2$ hybridization. The bonds between places on the other hand are relatively weak which greatly facilitates the separation. In this study, HOPG of ZYA quality and dimensions

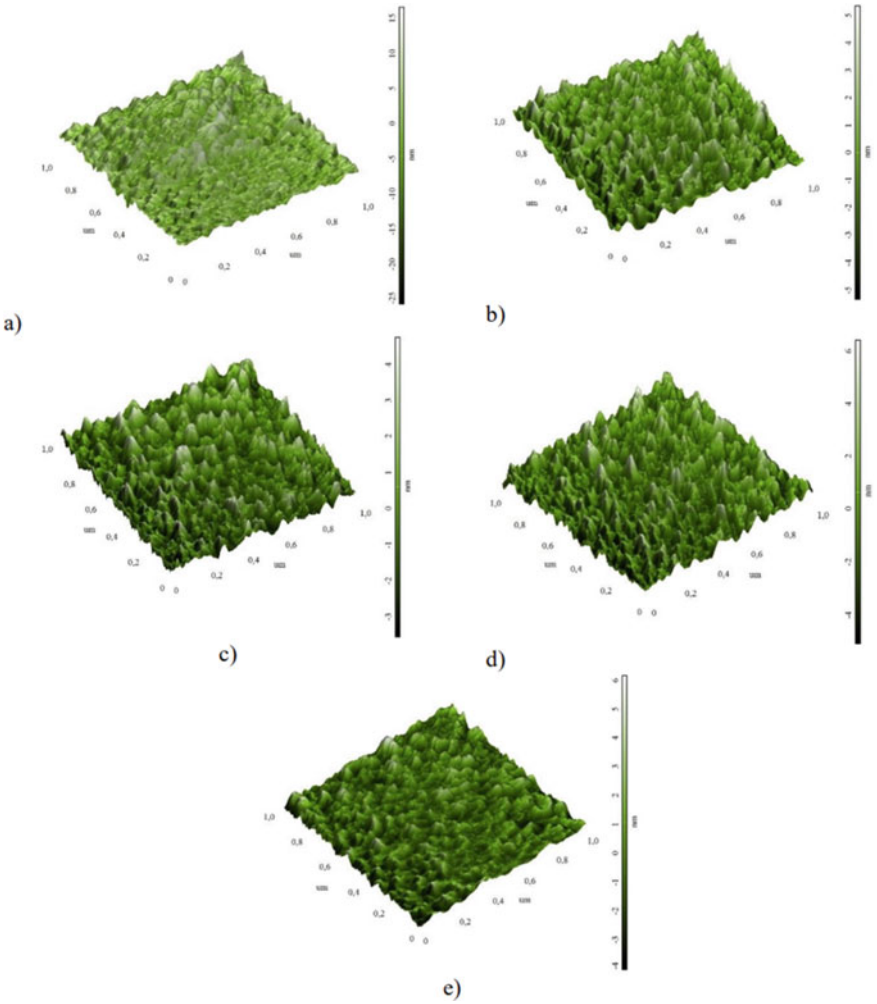


**Fig. 18** AFM topography images of the BFO film deposited on the surface of $Ta_2O_5$ layers with various thicknesses: **a** 20 nm; **b** 40 nm; **c** 60 nm; **d** 80 nm; **e** 100 nm

7 × 7 mm was procured from NT-MDT Spectrum Instruments in Moscow, Russia. The grain size of the ZYA type is up 10 μm and its mosaic distribution is 0.8° ± 0.2°. Then we adapted the same technological mode to obtain films on the highly oriented pyrolytic graphite (HOPG) surface [44, 45]. Preliminary studies on the processing and oxidation of the HOPG surface showed the formation of bubbles on its surface [46]. The total amount of sub-cycles within the process was 150 (for each precursor in a single technological mode). The sequence of the ALD process is presented in Fig. 19. The sub-cycles durations are 15.2 s and 16 s for $t_{Bi}$ and $t_{Fe,}$ respectively.

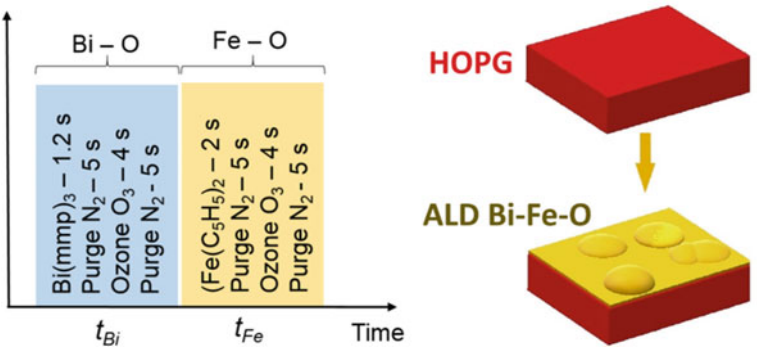


**Fig. 19** Sequence of ALD process including sub-cycles for Bi and Fe precursors

At first, the $BiO_x$ layer was obtained upon which the layer of $FeO_x$ was deposited later. The resulting thickness of the Bi–Fe–O layer was around 40 nm. As a result, the near-surface layer of graphite which contains graphene as well as low quantities of hydrogen and oxygen is modified. In our case, this mechanism manifests during the initial growth stage of the $BiO_x$ layer. The final structure of $BiO_x$–$FeO_x$ grown on HOPG as well as the operations sequence for the oxide's synthesis are given in Fig. 19. The ion beam method known as secondary-ion mass spectrometry (SIMS) was utilized to obtain the depth profile of the deposited layers. The following parameters were used: $Bi^+$ 30 kV primary ions for imaging mode, area of the beam is 200 $\mu m^2$; $O_2^+$ 500 V primary ions for sputtering mode. The analysis was implemented with the use of TOF-SIMS[5] equipment (IONTOF). Figure 20 contains the resulting relative concentrations of bismuth and iron. Bismuth ferrite, which is partially formed at 523 K, is represented by yellow parts in Fig. 20. Bismuth amount at the near-surface region is indicated by green sections. Figure 20 also demonstrates SIMS images of $Fe^+$, $Bi^+$, $C^+$ components as well as their composite RGB image of a sample not exposed to thermal treatment.

Detection of $Bi^+$ and $Fe^+$ ions allows us to see the etched area which is presented in Fig. 20a. The arrows indicate the spots where iron and bismuth were mixed prior to the BFO phase formation. It is worth noticing that this phase mostly occurs on the film's sections surface with more pronounced exfoliation, which is probably related to the oxidative reaction resulting in partial emissions of carbon oxides. $Bi_{1+x}FeO_3$ structure is formed in the near-surface region, where the amount of bismuth ions is prevailing (Fig. 20, green spots) [44]. Bismuth with its oxides creates several formal oxidation states, particularly $3^+$($Bi_2O_3$) and $5^+$ ($Bi_2O_5$) as well as some $3/5^+$ mixed-valence states ($Bi_2O_4$ and $Bi_4O_7$). Furthermore, the formation of substoichiometric phases, such as $Bi_2O_{2.75}$, $Bi_2O_{2.33}$, and BiO is also possible, however, mostly in a form of $Bi_2O_3$ impurity phases. Moreover, heat treatment or radiation exposure usually leads to the reduction of Bi to a metallic state [47]. Thereby, a reasonable approach is the formation of the $BiO_x$ initial layer by ALD for its further mixing with the $FeO_x$ phase in a homogenous manner. As Fig. 20b demonstrates, the near-surface region contains

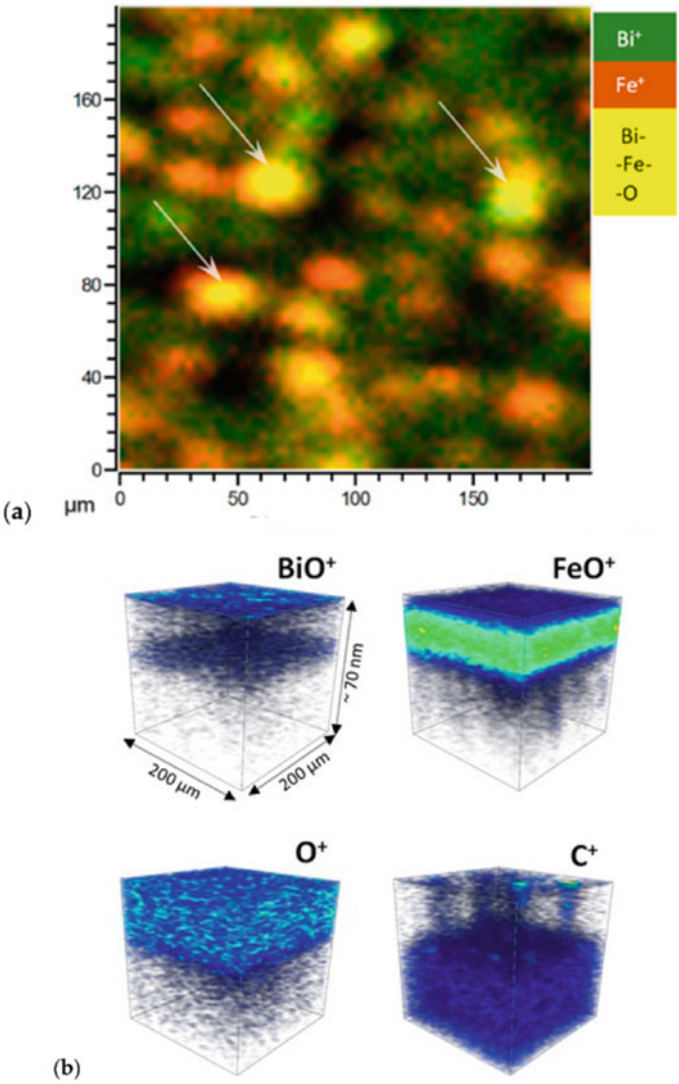


**Fig. 20** SIMS analysis of the sample surface: **a** the combined image of the Fe, Bi, C components and their composition; **b** depth profiles demonstrating the BFO phase which occurs during the film deposition process

some parts of $BiO_x$, which can be explained by the bismuth proclivity to diffuse towards the surface [48]. The delamination phenomenon is another evidence of the fact that the spherical elements observed in the surface morphology are hollow in nature and do not depict the difference in the compounds' composition. The only probable exception is the gas phase formation, which occurs due to adjacent compounds such as CO and $CO_2$. During the deposition process, the HOPG surface

is oxidized by ozone introduced into the chamber which leads to the formation of so-called nanobubbles. Additionally, Sobola et al. demonstrated in their work that the oxidation of HOPG surface with $HNO_3$ unambiguously results in the coverage of the entire surface with nanobubbles [46]. In this regard, it can be stated that the oxidation process results in the swelling of the surface. The oxygen distribution in the structure is not uniform and there are oxygen deficiency areas, which is demonstrated in Fig. 20b. The partial formation of $FeO^+$ at the stage of synthesis is also represented by Fig. 20b.

XPS analysis within situ heating capabilities was implemented to understand the reaction that occurs between the film components and the substrate. Annealing time for every used temperature was 5 min. AXIS SupraTM (Kratos Analytical Ltd, Manchester, UK) instrument was used to conduct this analysis, vacuum inside the chamber was around $2 \times 10^{-8}$ torr. This method has a sensitivity of ~5 nm. XPS spectra were acquired multiple times from both processed and unprocessed regions of the samples. Only an insignificant difference was observed in the proportion of the components, which can be a result of a non-homogenous distribution of delaminated regions and the bulk. The peak shapes indicate that the chemical bonding type remains unchanged across the entire surface. The dimension of the analyzed was $300 \times 700$ μm. Annealing time was around one minute. CasaXPS software with the Shirley background subtraction tool was used to provide a thorough characterization of the peaks. XPS spectra for before and after the temperature processing of the sample are given in Fig. 21.

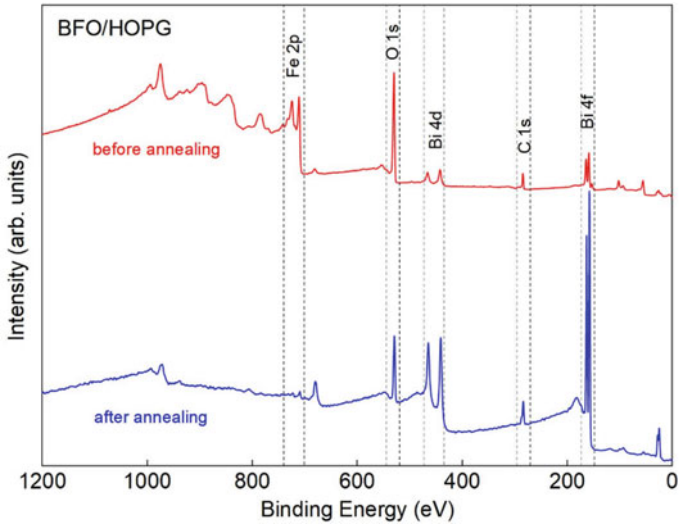


**Fig. 21** XPS spectra of the BFO/HOPG sample, at the bottom–before annealing, at the top–after annealing at the temperature of 923 K. The major peaks related to the compounds formed during the synthesis are designated

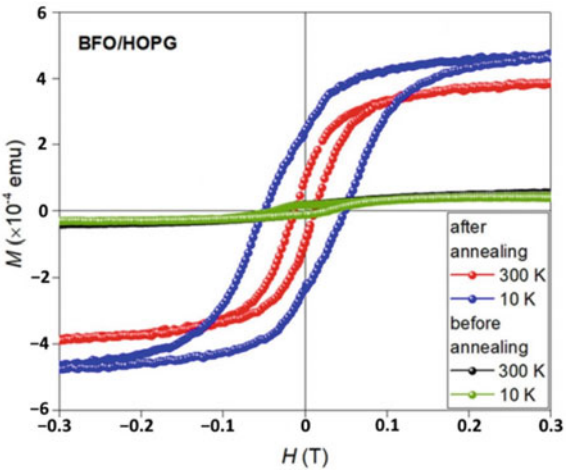


**Fig. 22** The hysteresis loop of the BFO/HOPG system of the as-deposited and annealed samples at 927 K, M–H dependencies are acquired at low (10 K) and room (300 K) temperatures

Vibrating magnetometer (Cryogen-Free High Field Measurement System from Cryogenic Limited, London, United Kingdom) was used to carry out the magnetic measurements. In this instrument, a sample is mounted on a rod and then vibrated by a linear magnetometer. A liquid helium superconducting magnet is used to create a magnetic field with an intensity of ~1 T. The frequency of sample oscillation is 21 Hz at the detector coil, where the created voltage is enhanced and detected, constant of the locking is 0.3 s. The measurements were conducted at two different temperatures: 300 K (room temperature) and 10 K. Hysteresis loops (M–H curves) were built to demonstrate the coercivity and magnetization of the samples. This is achieved through the measurements of the sample magnetization (M), which depends on the intensity of the applied magnetic field (H) at a constant temperature. The contributions of weak ferromagnetic (FM) and antiferromagnetic (AFM) types were considered during the plotting of the hysteresis loops. Figure 22 represents the magnetic hysteresis loops (M–H) for the BFO/HOPG sample with the magnetic field being applied in parallel to the surface of the sample; the measurements were carried out at 10 K and 300 K before and after temperature treatment. The fact that BFO demonstrates low-temperature ferromagnetic behavior and exhibits hysteresis is well known [49]. Measurements involving cooling at low temperatures (~10 K) can be carried out in order to confirm this observation. Weak magnetization behavior is common to all BFO systems, thin film, and bulk alike. The cause of this magnetization is the spin rotation resulting from the tilt in the oxygen octahedron, which is typical when the temperature decreases below Neel.

Consequently, it can be surmised that the large part of BFO/HOPG system magnetization occurs for two reasons: (1) exchange filed contribution at the superlattice's interface; (2) the redistribution of the $V_o$ charge. Strong hybridization at the substrate/film interface results in a creation of a novel magnetic configuration in the BFO system ($Fe^{3+}$–O–$Fe^{3+}$ sublattice). This magnetic configuration induces super exchange interaction with the superstructure of Fe–C [50]. Further amplification

of the FM state at the BFO/HOPG interface can be explained by electrons spin polarization in the carbon layer, which forms a bond between the electrons of both materials [51]. FM state magnetization from the acquired values can be calculated: room temperature saturation magnetization $M_s$ = V/M yields the value of $M_s$ ~120 emu/cm$^3$. With the use of the ALD method, it is possible to obtain ultrathin layers of BFO multiferroic on the surface of HOPG at relatively low temperatures. During the synthesis process, modification of the HOPG surface takes place which manifests in delamination and bubbles formation. TOF–SIMS results reveal that there is a good miscibility between $BiO_x$ and $FeO_x$ components on the HOPG surface. Self-organization and carbon reduction in the BFO film were detected during the annealing in vacuum. Such a two-stage approach (deposition and annealing) enables the design of the structures of high-quality using multiferroic materials with oxygen vacancies as the basis. Magnetic measurements detected a substantial increase in the sample magnetization, which can be attributed to superstructure properties occurring at the BFO/HOPG interface and oxygen vacancies. A novel magnetic configuration is created at the substrate/film interface of the BFO structure ($Fe^{3+}$–O–$Fe^{3+}$ sublattice). This magnetic configuration induces strong hybridization because of super exchange interaction with the reduced graphene FM sublattice where iron creates bonds with the –C = C sublayer dangling cores. The major benefit of using the ALD method is the possibility to grow thin films on the substrates of flexible polymers where low temperatures are required. The growth temperature for BFO phase formation was detected to be ~250 °C for the Kapton surface [52]. To grow an amorphous layer in the Bi–Fe–O structure, Kapton (poly (4,4'-oxydiphenylene-pyromellitimide)) was utilized as a substrate. It demonstrates stability over a wide range of temperatures (−273 up to +400 °C). Kapton was designed by the company known as DuPont and demonstrates a few attractive properties. Most commonly it takes shape of a thin film or a tape that is laminated/covered by other materials or has no lamination whatsoever. Kapton surface optical images before and after the formation of Bi–O and Fe–O are provided in Fig. 23. The acquired $BiO_x$–$FeO_x$ combined layer had a thickness of ~50 nm. Measurement of the layer thickness was performed using a contact mode, for this purpose a crack was created by intense bending of the sample as shown in Fig. 23.

The pulses proportion between the times of iron and bismuth precursor's introduction was $N_{Fe}/N_{Bi} \approx 5/3$ (First experiment). In the second experiment, the ratio between the precursor action times was $N_{Fe}/N_{Bi} = 1/1$ (Second experiment). The rest of the parameters for both experiments remained the same, this includes the number of cycles in the first and second experiments was ~500. That allows determining the pattern of self-organization of the oxide layer with a predominantly bismuth phase (segregation of metallic bismuth). The AFM method was used to study the surface morphology of the resulting film on the Kapton surface (Fig. 24).

According to AFM, it can be assumed that there is less oxidization of bismuth in the second case. Additionally, bismuth in the second case is self-organizing, agglomeration into metallic clusters can be observed. There is a relaxation of mechanical stresses in the film, similar to growth on a foreign substrate with a large mismatch of the crystal lattice parameters [53, 54]. The second sample demonstrates a larger

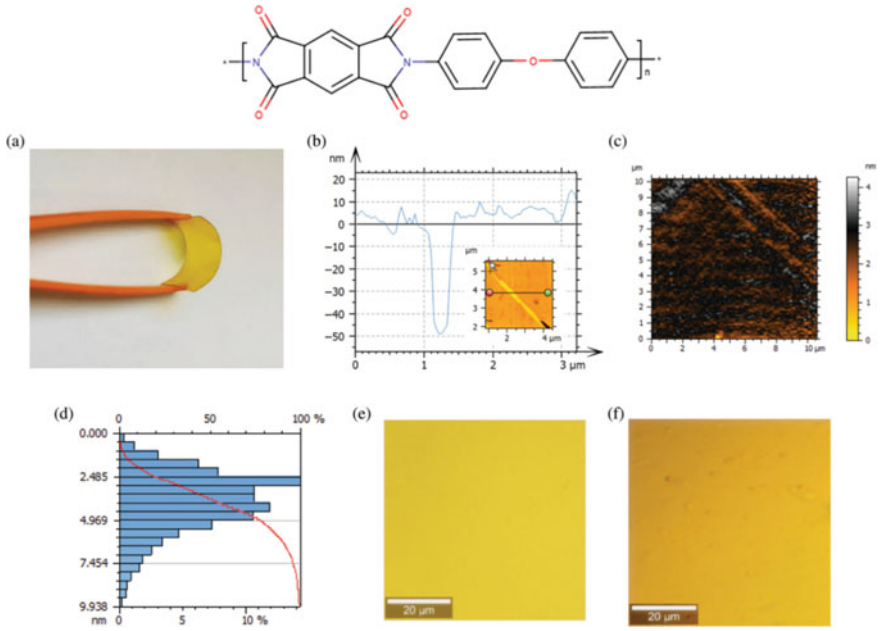


**Fig. 23** Chemical structure of polyimide Kapton, Kapton substrate (**a**), crack in the film created by strong bending (**b**), AFM scan of the pure substrate (**c**), Abbott curve (**d**), sample surface optical image before deposition (**e**), and after deposition of the Bi–Fe–O film (**f**)

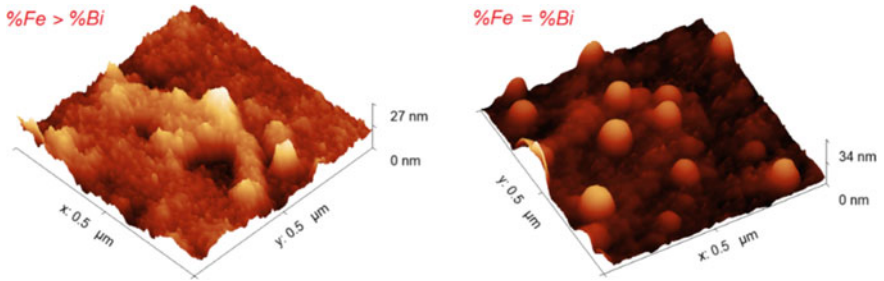


**Fig. 24** Image of the surface of the Bi–Fe–O/Kapton composite with a change in the ratio of the amount of the precursors

amount of oxygen dangling bonds, which implies a greater degree of amorphousness.This phenomenon results in a surplus of oxygen. Furthermore, the phase of Bi–O and Fe–O are also formed on the sample surface in the first case. This combination is more advantageous for the following emergence of the bismuth ferrite phase, considering the bismuth evaporation caused by heating and oxygen concentration decrease during thermal processing in vacuum. It has been noticed that at certain thicknesses and compositions it is possible to control the fracture toughness of the BFO/Kapton

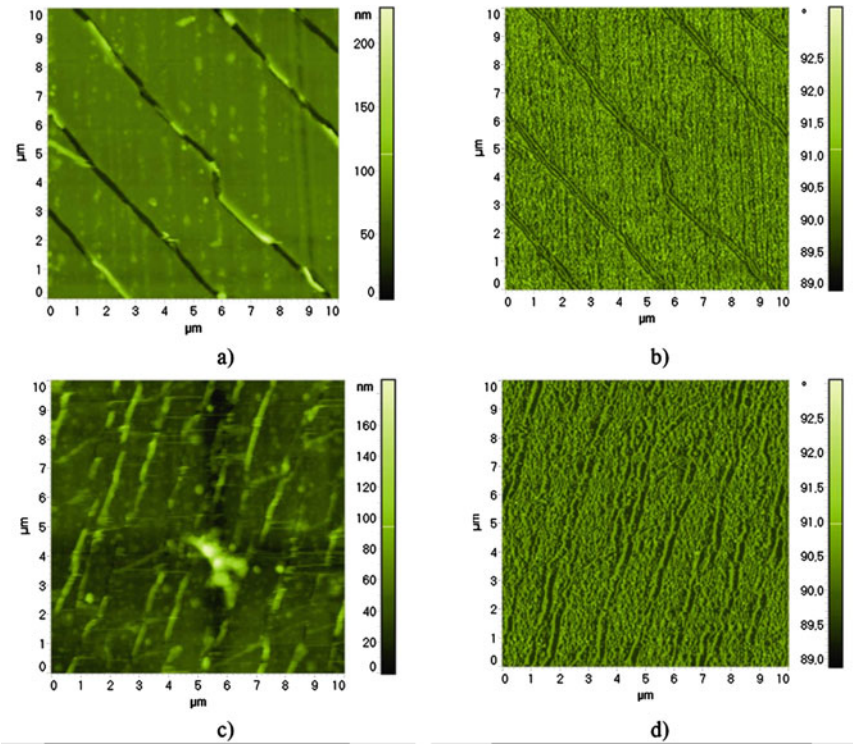


**Fig. 25** Topography and PFM phase contrast **a**, **b** first experiment and **c**, **d** second experiment

composite [55]. Figure 25 demonstrates topography and phase contrast at a bias voltage of 10 V.

As demonstrated by the AFM images, nanoscale features are present on the surface of the Bi–Fe–O/Kapton system. Bismuth organization on the surface is the main reason for the different topography. Among different techniques for surface imaging (optical methods, scanning electron microscopy, etc.) AFM proves to be the most reliable option when it comes to the 3D analysis of surface topography or surface modification with exact values of the Z-axis. Aside from the topographical analysis with actual height values, AFM has several different modes which facilitate the study of the mechanical and electrical properties of materials. Over the years these techniques have proven their reliability or surface characterization after various damaging or degradation processes. Such techniques as scanning microscopy of the piezoelectric response (PFM) can provide valuable data on how domains are organized on the surface. Scanning probe microscope NTEGRA Prima (NT-MDT, Russia) with a $W_2C$-coated conductive tip was utilized to perform PFM measurements. The probe utilized during the Force Modulation Mode measurement was the same as for PFM

measurements. Both samples exhibit a slight phase shift at the crack regions. Information on the qualitative distribution of the hardness can be obtained using this mode.

## 4 Solution Combustion Synthesis of Pure-Phase $BiFeO_3$

The solution combustion method is a unique technology for obtaining nanoscale materials (simple and complex oxides, metals, and sulfides). This method is of interest to researchers due to its low cost, simplicity, high energy efficiency, and purity of the final material. The main attention in this method is given to the combustion stage, since exothermic reactions between reactants are used, which, after reaching the ignition temperature, begin to react in a self-sustaining mode and therefore no additional contribution of external energy is required. Thus, the combustion method represents an attractive practical alternative to traditional technologies for the preparation of modern materials for a wide range of applications (catalysts, capacitors, fuel and solar cells, etc.). $BiFeO_3$ nanoparticles were obtained using a new synthesis method. The synthesis process is performed in the following manner: The initial reagents $Bi(NO_3)_3{\cdot}5H_2O$, $Fe(NO_3)_3{\cdot}9H_2O$ (molar ratio of $Bi_3{}^+$ and $Fe_3{}^+$ 1:1, chemically pure, «Nevareaktiv») were dissolved in distilled water. Glycine ($C_2H_5NO_2$, chemically pure, «Nevareaktiv») acted as an organic fuel providing a platform for the occurrence of redox reactions in the combustion process. Metal nitrates are known for their hygroscopicity, which is why they tend to form a suspension mixture when combined with glycine. The synthesis process consisted of three main stages: formation of a homogeneous solution→gel formation→gel combustion. The first stage in the synthesis process is to form the metal ions coordination complex with glycine, since the latter has complex-forming properties (Fig. 26).

$$\mathrm{Bi(NO_3)_3 \cdot 5H_2O + Fe(NO_3)_3 \cdot 9H_2O + NH_2CH_2COOH} \rightarrow \mathrm{Bi[Fe(NH_2CH_2COO)](NO_3)_3 \cdot H_2O + NO_2 + H_2O}$$

Nitrate ions existing in the complex itself supply the combustion process with the necessary oxygen. The complex, when heated, is reduced to bismuth and iron oxides: $Bi[Fe(NH_2CH_2COO)](NO_3)_3{\cdot}H_2O \rightarrow Bi_2O_3 + Fe_2O_3 + NO_2 + H_2O + CO_2$.

Bi and Fe oxides interact to form $BiFeO_3$:

$Bi_2O_3 + Fe_2O_3 \rightarrow BiFeO_3$.

It should be noted that the final characteristics of the obtained materials (morphology, phase composition, etc.) strongly depend on the synthesis parameters, namely: fuel, initial precursors, and the ratio of the reducing agent to the oxidizing agent ($\varphi$). The fuel chemistry concept was used to calculate the combustion reaction stoichiometry. Based on the stoichiometry calculation of the nitrate-glycine redox

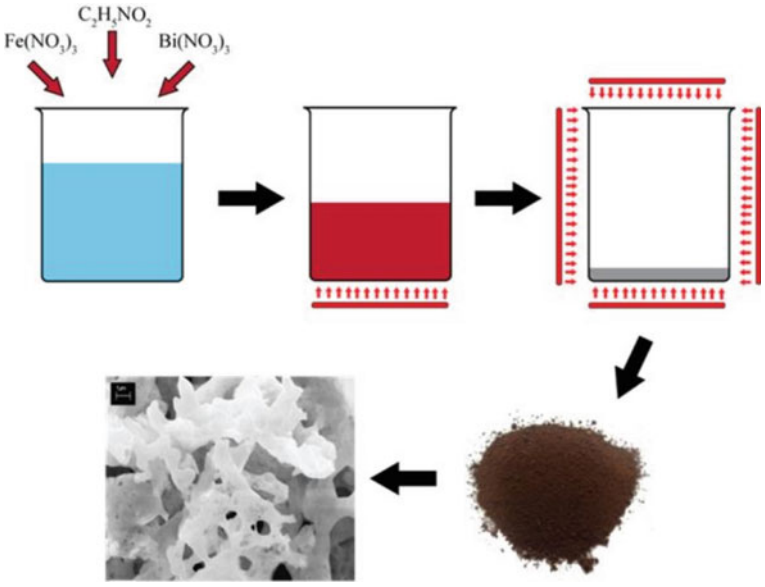


**Fig. 26** Technological scheme of nanopowder synthesis

mixture, it was established that 3.33 mol of glycine are required to obtain one mole of $BiFeO_3$. The reaction can be represented as follows:

$$Bi(NO_3)_3 \cdot 5H_2O + Fe(NO_3)_3 \cdot 9H_2O + 10/3NH_2CH_2COOH \rightarrow BiFeO_3 + 14/3N_2 + 67/3H_2O + 20/3CO_2$$

The results of X-ray diffraction analysis at room temperature for BFO nanopowders calcined at different temperatures are presented in Fig. 27. The main diffraction peaks are related to the rhombohedrally distorted perovskite structure *R3c* and are in good accordance with the standard reported values (ICSD # 98–010-9370, *R3c*).

As the calcination temperature increases, the BFO diffraction peaks grow sharper, and the splitting of the (104) and (110) peaks becomes more pronounced. This phenomenon confirms that the structure distortion of the rhombohedral type takes place. In addition to the main phase ($BiFeO_3$), peaks associated with impurity phases ($Bi_{25}FeO_{40}$ $2\theta \sim 28.1°$, $Bi_2Fe_4O_9$ $2\theta$ ~28.1°–29.1°), were observed in the diffraction patterns, which can be attributed to incomplete reactions between precursors during synthesis. As can be seen, an increase in the calcination temperature results in the peaks of the main phase becoming sharper and a decrease in the impurity phases proportion. The side phases proportion was around 7% in the synthesized powder; increase in the calcination temperature (450, 550, 600 °C) has led to a decrease in their concentration to 5, 3, and 1%, correspondingly. However, increasing temperature further (650 °C) results in an increase of the impurities phases concentration (up

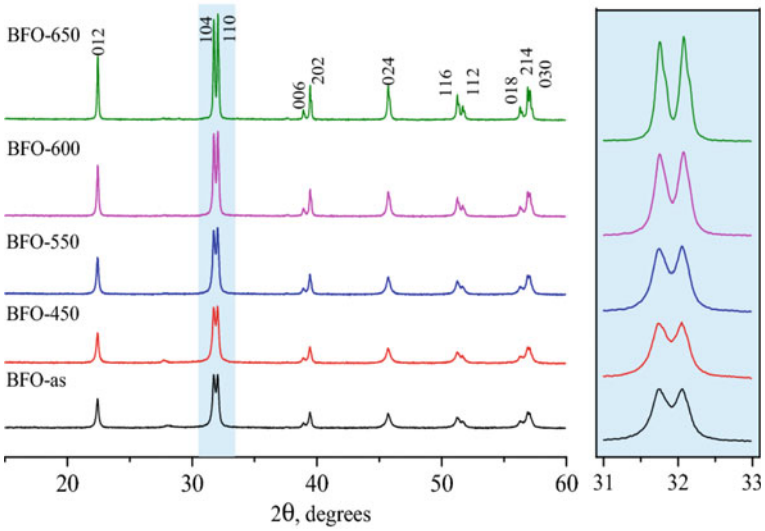


**Fig. 27** XRD spectra of BFO-as, BFO-450, BFO-550, BFO-600, and BFO-650 nanopowders [56]

to 10%). Furthermore, temperatures above 650 °C induce the main phase decomposition which in its turn leads to even higher values of impurity phases concentrations. The Scherrer formula was used to calculate the average crystallite size. The average crystallite sizes were approximately 40, 42, 46, 56, and 75 nm for the BFO-ref, BFO-450, BFO-550, BFO-600, and BFO-650 samples, correspondingly. An increase in the calcination temperature led to an increase in the average crystallite size due to recrystallization and particle clusters formation. The SEM scans of the BFO powders are shown in Fig. 28 a–g.

Highly porous structure has been detected in the samples. The shape of the pores is irregular, and the sizes range from several nanometers to submicron values. Release gases are the cause of the pore's formation during the synthesis process. It is also worth noting that an increase in the heat treatment temperature entails the aggregation of the nanopowder, which grows denser because of smaller particles being sintered. In the images, these regions are highlighted in yellow color. High-resolution image of BFO-as presented in Fig. 28c shows that non-crystallized amorphous areas surround the larger slightly crystallized particles. Energy-dispersive X-ray spectroscopy (EDX) was utilized to analyze the samples' chemical composition. EDX curves given in Fig. 28 h were acquired from a few selected regions of the sample. As expected, all these regions showed the existence of Bi, Fe, and O, and their contents were established to be in good agreement with the BFO stoichiometric composition. The existence of the carbon peak is attributed to the research methodology. The magnetic hysteresis loops (M–H) acquired for the synthesized BFO nanoparticles calcined at various temperatures are presented in Fig. 29. A strong ferromagnetic behavior has been observed for all samples, the values of which reach saturation.

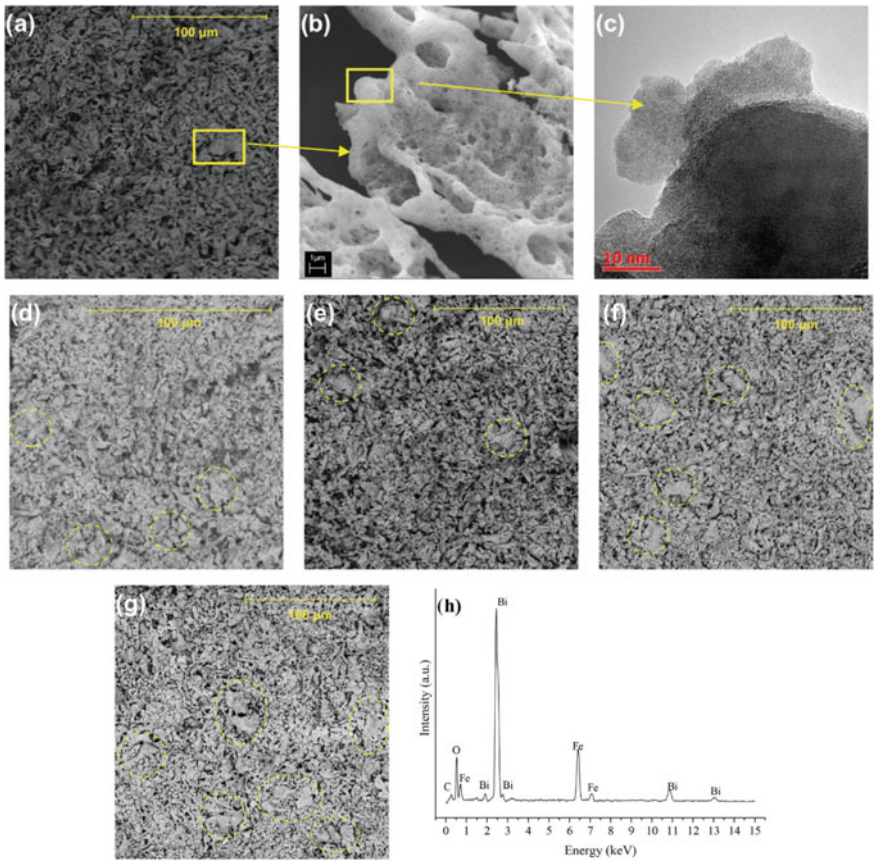


**Fig. 28** **a** **b** SEM scans for BFO-ref, **c** TEM image for BFO-as, **d** BFO-450, **e** BFO-550, **f** BFO-600, **g** BFO-650; **h** EDX spectrum of BFO-ref [56]

An increase in the size of the crystallites results in a sharp decrease in the saturation magnetization (*Ms*) from 1.908 emu/g to 0.236 emu/g.

There is a strong correlation between the crystallites sizes and the improvement in magnetic properties, which is the result of the BFO spiral spin structure modification. The following reasons can be responsible for the observed increase in the ferromagnetic response based on the results presented in this study:

- Suppression of the cycloidal type of spiral-spin structure with crystallites smaller than ~ <62 nm;
- The existence of uncompensated spins on the surface due to micro deformation resulting primarily from the oxygen vacancies leading to the $Fe^{2+}$ formation;
- The existence of magnetic impurity phases $Bi_{25}FeO_{40}$, $Bi_2Fe_4O_9$, which contents decrease as the heat treatment temperature increases.

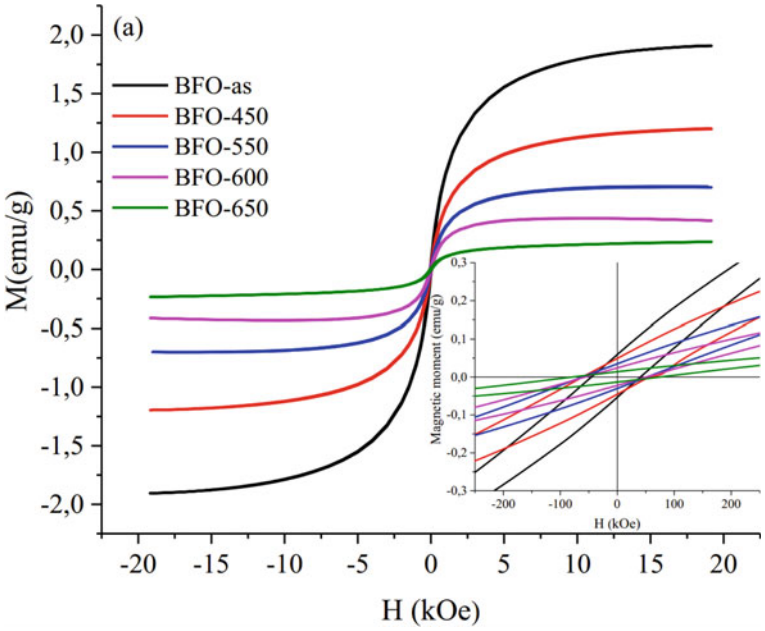


**Fig. 29** Magnetic hysteresis loops (M–H) of $BiFeO_3$ powders [56]

Piezo nanogenerators (PNGs) are electricity sources that demonstrate great promise for powering small electronics. Bismuth ferrite ($BiFeO_3$) with no lead content is a perovskite material that is among potential candidates for widespread use. This material has attracted a lot of practical interest thanks to its concurrent ferroelectric and antiferromagnetic states with exceptionally high ordering temperatures (Neel temperature $T_N = 370$ °C; Curie temperature $T_C = 830$ °C). Ferroelectric ordering presence results in the occurrence of spontaneous polarization.

The assembly process of the PNG model consisted of the following steps:

i. A curing catalyst was used to prepare the silicone solution (Super Mold M10, Guangzhou, China) (where the weight proportion of silicone to curing agent was 10:1);
ii. The prepared $BiFeO_3$ nanopowder was then dispersed into the mixture at different concentrations: 10, 30, and 50 mass%;
iii. The obtained composite was attached to an Al electrode using a double-sided tape on glass (2 × 2.5 cm) by ten-second spin-coating at 3000 rpm in a laboratory centrifuge (Liston C 2204 Classic, Liston, Zhukov, Russia);
iv. The curing of the samples was done in a drying oven (20 min at 50 °C);
v. An additional aluminum electrode was glued on top of the $BiFeO_3$–silicone composite layer, and then the material was left for 1 day to complete the curing process.

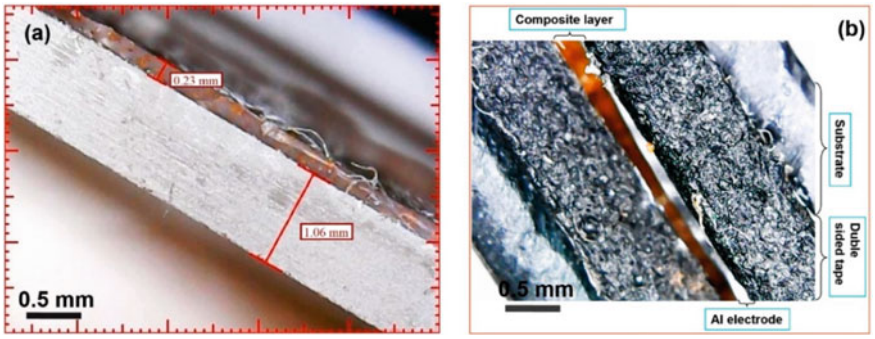


**Fig. 30** **a** An optical micrograph of the $BiFeO_3$–silicone composite film, 500 × times magnified; **b** an optical micrograph of the piezo nanogenerator (PNG) device, 500 × magnified [57]

Figure 30a contains a 500 × magnified optical micrograph of the cleavage of the $BiFeO_3$–silicone composite layer obtained using a centrifuge. The micrograph indicates the formation of a homogeneous layer with a thickness of around 230 μm. An optical 500 × magnified micrograph of the assembled PNG device cleavage is provided in Fig. 30b.

Figure 31 provides the characteristic dependencies of the output voltage on time. The measurements were carried out for different PNG loading concentrations (10, 30, and 50 mass%) with the following compression and relaxation. The output voltages generated by unpolarized PNG were acquired under vertical periodic compression and relaxation. The values of these voltages were around 0.028, 0.055, and 0.17 V for PNG with the $BiFeO_3$ loading concentrations of 10, 30, and 50 mass% correspondingly. An increase in $BiFeO_3$ nanoparticles content has also led to a gradual increase of the output voltage for the loading concentration of the composite up to

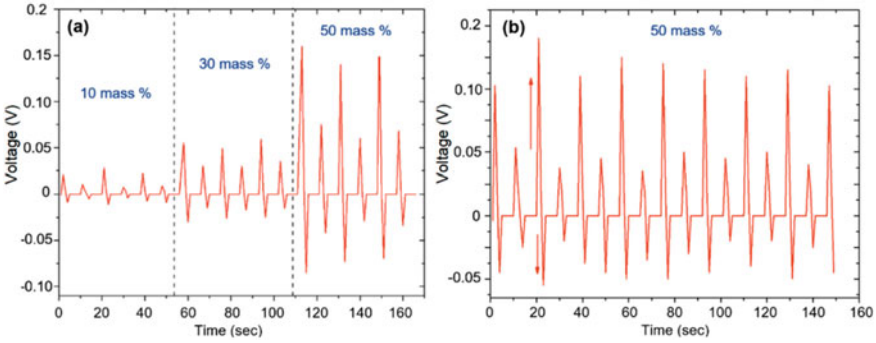


**Fig. 31** **a** Voltage occurring in the PNG circuit with various concentrations of $BiFeO_3$ loading; **b** the lower graph demonstrates the nature of the potential change in the composition for a longer time, where the increase in stress during compression and relaxation is observed [57]

50 mass%, and the maximum output voltage is reached at ~0.17 V. The obtained results suggest that the performance of the PNG model proposed in this study is comparable to that of other existing PNGs. The values difference of the peak stress between the states observed during compression and relaxation can be attributed to the PNG deformation rate difference in the course of compression and relaxation processes.

All the presented results from measurements demonstrate that the manufacturing process described produces an adequate piezoelectric material to be utilized in nanogenerators. The evaluation of the photocatalytic characteristics was done with the use of methyl orange (MO) photodegradation in a water solution (0.015 mmol/l) [58]. Photocatalytic experiments were performed inside a quartz cell with a volume of 100 ml. 250 W mercury lamp with high pressure was utilized as a light source. Air ventilation was used to maintain the temperature in the cell at a constant 26 °C, the thermometer was used for the temperature monitoring. 25 mg of photocatalyst were mixed with the MO water solution (0.015 mmol/l) for the photocatalytic reaction. Prior to switching the light on, the cell was kept in the darkness for 30 min to reach adsorption equilibrium. Ultrasonic treatment of the suspension was performed to achieve the photocatalyst degassing before the initiation of the experiment. Magnetic stirring was utilized throughout the entire process. 5 ml of the solution were taken every 10 min for sampling purposes. A magnetic separation tool equipped with a powerful neodymium magnet to avoid photocatalyst losses was used to separate nanopowder large particles. After the separation process, the suspension was centrifuged for 3 min at 14,000 rmp with the use of a high-speed refrigeration centrifuge MR23i JOUAN (Thermo Fisher Scientific) to achieve ultrafine particles deposition. UV/vis spectrophotometer (Beckman Coulter DU730 series UV/vis) was used to measure the MO concentration, the temperature remained constant at 26 °C during the measurement. Upon measurement, the solution was returned to the cell and the process was resumed. For comparative purposes, additional results were obtained by testing MO solution under identical conditions but with no photocatalyst. These results are provided in Fig. 32.

It can be observed in Fig. 32 that all samples demonstrate the discoloration and degradation processes that occur in the first 30 min. The most prominent photocatalytic activity was detected in bismuth ferrite annealed at 550 °C. Lesser activity was demonstrated by BFO annealed at 650 °C. Several reasons can be responsible for this effect. Firstly, the powder annealed at 650°c had large crystallite sizes and a high density. Given that photocatalysis is a surface process, the photocatalytic activity is limited by the reduction in specific surface area.Secondly, this may also be attributed to an increase in the bandgap optical width, which renders the photocatalytic process less effective.

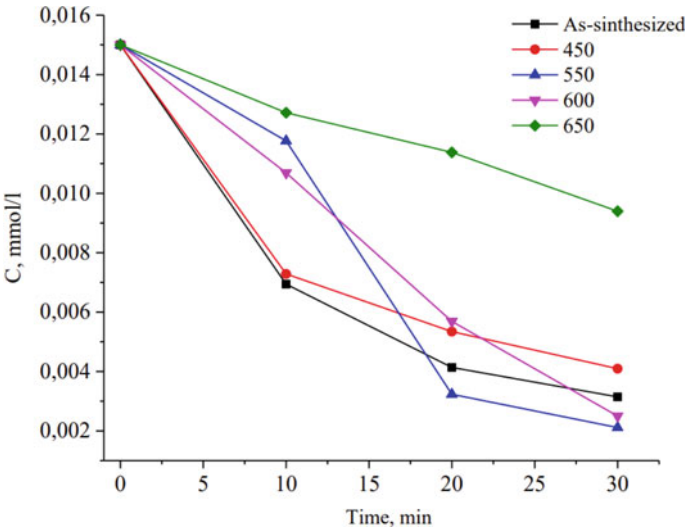


**Fig. 32** MO Photocatalytic oxidation under irradiation with UV–vis light on $BiFeO_3$ annealed at different temperatures

## 5 Conclusion

- The study of nanoscale structures as thin films and nanopowdes, in contrast to bulk materials, contributes to a deeper understanding of the fundamental laws and processes responsible for piezoelectric, electro- and magnetic ordering.The development of a scientific direction focused on the synthesis of multiferroics with given physical properties will make it possible to take a significant step forward in many areas of technology: ordered micro and nanostructures based on active materials, multilayer coatings for special purposes, etc.The research benefits the enhancement of existing sensing technology by using new design based on physical principles of low-dimension multifunctional materials. Further in-depth studies are needed to provide reliable application and spreading of multiferroics in electronics.

## References

1. Perejón A, Gil-González E, Sánchez-Jiménez PE, West AR, Pérez-Maqueda LA (2019) Electrical properties of bismuth ferrites: Bi2Fe4O9 and Bi25FeO39. J Eur Ceram Soc. https://doi.org/10.1016/j.jeurceramsoc.2018.09.008
2. Fujii T, Takano M, Katano R, Bando Y, Isozumi Y, Okuda T (1990) Conversion electron Mössbauer spectroscopy of a single crystalline Bi3Fe5O12 film. J Magn Magn Mater. https://doi.org/10.1016/0304-8853(90)90640-C

3. Qian-Jing R, Wei-De Z (2009) Tunable morphology of Bi2Fe4O9 crystals for photocatalytic oxidation. J Phys Chem C. https://doi.org/10.1021/jp810098f
4. Wang Y, Daboczi M, Mesa CA, Ratnasingham SR, Kim JS, Durrant JR, Dunn S, Yan H, Briscoe J (2019) Bi2Fe4O9 thin films as novel visible-light-active photoanodes for solar water splitting. J Mater Chem A. https://doi.org/10.1039/c8ta09583c
5. Yang H, Dai J, Wang L, Lin Y, Wang F, Kang P (2017) A novel approach to prepare Bi2Fe4O9 flower-like spheres with enhanced photocatalytic performance. Sci Rep. https://doi.org/10.1038/s41598-017-00831-3
6. Ramirez FEN, Espinosa EE, Pedroza LS, Souza JA (2016) Humidity sensing effect in Bi25FeO39 sillenite-like compound. J Mater Sci. https://doi.org/10.1007/s10853-016-0310-0
7. Flores Morales SS, León Flores JA, Pérez Mazariego JL, Marquina Fábrega V, Gómez González RW (2017) Synthesis of Bi25FeO39 by molten salts method and its mössbauer spectrum. Phys B Condens Matt. doi:https://doi.org/10.1016/j.physb.2016.10.019
8. Li J, Chen W (2019) Synthesis and characterization of Bi-Fe-O amorphous nanoparticles for Photocatalysis by Sol-Gel method. Integr Ferroelectr. https://doi.org/10.1080/10584587.2019.1592621
9. Suzuki K, Onodera H, Sakurai M, Masuda S, Matsumoto A, Sadamura H (1986) Structure and magnetic properties of Bi-Zn-Fe-O amorphous films. IEEE Trans Magn. https://doi.org/10.1109/tmag.1986.1064353
10. Krnel M, Vrtnik S, Jelen A, Koželj P, Jagličić Z, Meden A, Feuerbacher M, Dolinšek J (2020) Speromagnetism and asperomagnetism as the ground states of the Tb-Dy-Ho-Er-Tm "ideal" high-entropy alloy. Intermetallics. https://doi.org/10.1016/j.intermet.2019.106680
11. Quickel TE, Schelhas LT, Farrell RA, Petkov N, Le VH, Tolbert SH (2015) Mesoporous bismuth ferrite with amplified magnetoelectric coupling and electric field-induced ferrimagnetism. Nat Commun. https://doi.org/10.1038/ncomms7562
12. Singh A, Chen J (2019) Large vertical hysteretic shift and signature of exchange bias in BiFeO3/SrRuO3 heterostructure. Ceram Int. https://doi.org/10.1016/j.ceramint.2019.07.024
13. Liu H, Yang P, Yao K, Wang J (2011) Growth rate induced monoclinic to tetragonal phase transition in epitaxial BiFeO3 (001) thin films. Appl Phys Lett. https://doi.org/10.1063/1.3561757
14. Dong W, Guo Y, Guo B, Liu H, Li H, Liu H (2013) Photovoltaic properties of BiFeO3 thin film capacitors by using Al-doped zinc oxide as top electrode. Mater Lett. https://doi.org/10.1016/j.matlet.2012.10.031
15. Chen Z, Wang Y, Zheng D, Sun F, Deng X, Tan Z, Tian J, Zhang L, Zeng M, Fan Z et al (2019) Polarization tunable and enhanced photovoltaic properties in tetragonal-like BiFeO3 epitaxial films with graphene top electrode. J Alloys Compd. https://doi.org/10.1016/j.jallcom.2019.152013
16. Chu YH, Zhao T, Cruz MP, Zhan Q, Yang PL, Martin LW, Huijben M, Yang CH, Zavaliche F, Zheng H et al. (2007) Ferroelectric size effects in multiferroic BiFeO3 thin films. Appl Phys Lett, 90. doi:https://doi.org/10.1063/1.2750524
17. Sone K, Naganuma H, Ito M, Miyazaki T, Nakajima T, Okamura S (2015) 100-nm-sized magnetic domain reversal by the magneto-electric effect in self-assembled BiFeO<inf>3</inf>/CoFe<inf>2</inf>O<inf>4</inf> bilayer films. Sci Rep, 5. doi:https://doi.org/10.1038/srep09348
18. Gaikovich KP, Gribkov BA, Mironov VL, Treskov SA, Zhilin AV (2002) Image retrieval in scanning probe microscopy taking into account the probe-surface interaction non-locality. In Proceedings of the Physics of Low-Dimensional Structures
19. Glover CC, Killgore JP, Tung RC (2018) Scanning speed phenomenon in contact-resonance atomic force microscopy. Beilstein J Nanotechnol. https://doi.org/10.3762/bjnano.9.87
20. H Ki, PSM, JM (2002) Modelling of high-density laser–material interaction using fast level set method. J Phys D Appl Phys 34:364–372
21. Sobiestianskas R, Hardy A, Banys J, D'haen J, van B (2009) Microwave dielectric properties of BiFeO3 thin film prepared by aqueous chemical solution deposition method. Process Appl Ceram. doi:https://doi.org/10.2298/pac0904167s

22. George SM (2010) Atomic layer deposition: an overview. Chem Rev 110:111–131. https://doi.org/10.1021/cr900056b
23. Iatsunskyi I, Coy E, Viter R, Nowaczyk G, Jancelewicz M, Baleviciute I, Załeski K, Jurga S (2015) Study on structural, mechanical, and optical properties of Al2O3-TiO2 nanolaminates prepared by atomic layer deposition. J Phys Chem C. https://doi.org/10.1021/acs.jpcc.5b06745
24. Orudzhev F, Ramazanov S, Sobola D, Isaev A, Wang C, Magomedova A, Kadiev M, Kaviyarasu K (2020) Atomic layer deposition of mixed-layered aurivillius phase on tio2 nanotubes: synthesis, characterization and photoelectrocatalytic properties. Nanomaterials 10:1–16. https://doi.org/10.3390/nano10112183
25. Orudzhev FF, Ramazanov SM, Isaev AB, Alikhanov NMR, Sobola D, Presniakov MY, Kaviyarasu K (2019) Self-organization of layered perovskites on TiO2nanotubes surface by atomic layer deposition. In Proceedings of the Materials Today: Proceedings; Elsevier Ltd., vol. 36, pp. 364–367
26. Lomanova NA, Tomkovich MV, Osipov AV, Ugolkov VL (2019) Synthesis of nanocrystalline materials based on the Bi2O3-TiO2 system. Russ J Gen Chem 2019 8910 89, 2075–2081. doi:https://doi.org/10.1134/S1070363219100141
27. Lu CD, Chang LS, Lu YF, Lu FH (2009) The growth of interfacial compounds between titanium dioxide and bismuth oxide. Ceram Int. https://doi.org/10.1016/j.ceramint.2009.03.001
28. Lomanova NA, Ugolkov VL, Gusarov VV (2007) Thermal behavior of layered perovskite-like compounds in the Bi4Ti3O12-BiFeO3 system. Glas Phys Chem 2007 336, 33, 608–612. doi:https://doi.org/10.1134/S1087659607060120
29. Lomanova NA, Morozov MI, Ugolkov VL, Gusarov VV (2006) Properties of Aurivillius phases in the Bi 4Ti 3O 12-BiFeO 3 system. Inorg Mater. https://doi.org/10.1134/S0020168506020142
30. Morozov MI, Gusarov VV (2002) Synthesis of A m - 1Bi 2M mO 3m + 3 compounds in the Bi 4Ti 3O 12-BiFeO 3 system. Inorg Mater. https://doi.org/10.1023/A:1016252727831
31. Armstrong RA, Newnham RE (1972) Bismuth titanate solid solutions. Mater Res Bull. https://doi.org/10.1016/0025-5408(72)90154-7
32. Macak JM, Tsuchiya H, Ghicov A, Yasuda K, Hahn R, Bauer S, Schmuki P (2007) TiO2 nanotubes: self-organized electrochemical formation, properties and applications. Curr Opin Solid State Mater Sci 11:3–18. https://doi.org/10.1016/J.COSSMS.2007.08.004
33. Achary SN, Patwe SJ, Krishna PSR, Shinde AB, Tyagi AK (2008) Cation disorder and structural studies on Bi4-xNd xTi3O12 ($0.0 \leq \times \leq 2.0$). In Proceedings of the Pramana - Journal of Physics
34. Zhang ST, Lu MH, Wu D, Chen YF, Ming NB (2005) Larger polarization and weak ferromagnetism in quenched BiFeO3 ceramics with a distorted rhombohedral crystal structure. Appl Phys Lett. https://doi.org/10.1063/1.2147719
35. Ramazanov S, Ţălu Ş, Dallaev R, Ramazanov G, Škarvada P, Oulehla J, Sobola D, Nazarov D (2021) Surface morphology and X-ray photoelectron spectroscopy of BiFeO3 thin films deposited on top of Ta2O5/Si layers. E3S Web Conf 295, 04009. doi:https://doi.org/10.1051/E3SCONF/202129504009
36. Li X, Wang Y, Wang F, Liang A (2021) Ta2O5 in-situ composite Ta-based nanocrystalline coating with wonderful wear resistance and related wear mechanisms. Mater Lett 298:130000. https://doi.org/10.1016/j.matlet.2021.130000
37. Wang R, Pan L, Han Q, Zhu H, Wan M, Mai Y (2021) Reactively sputtered Ta2O5 solid electrolyte layers in all thin film electrochromic devices. J Alloys Compd 865:158931. https://doi.org/10.1016/j.jallcom.2021.158931
38. Das S, Singh VK (2021) The role of Ta2O5 thin film on a plasmonic refractive index sensor based on photonic crystal fiber. Photonics Nanostructures - Fundam Appl 44:100904. https://doi.org/10.1016/j.photonics.2021.100904
39. Knápek A, Sobola D, Burda D, Daňhel A, Mousa M, Kolařík V (2019) Polymer graphite pencil lead as a cheap alternative for classic conductive SPM probes. Nanomaterials 9. doi:https://doi.org/10.3390/nano9121756

40. Ţălu Ş, Marković Z, Stach S, Todorović Marković B, Ţălu M (2014) Multifractal characterization of single wall carbon nanotube thin films surface upon exposure to optical parametric oscillator laser irradiation. Appl Surf Sci 289:97–106. https://doi.org/10.1016/J.APSUSC.2013.10.114
41. Ţălu Ş, Morozov IA, Yadav RP (2019) Multifractal analysis of sputtered indium tin oxide thin film surfaces. Appl Surf Sci 484:892–898. https://doi.org/10.1016/J.APSUSC.2019.04.170
42. Ţălu Ş, Bramowicz M, Kulesza S, Dalouji V, Solaymani S, Valedbagi S (2016) Fractal features of carbon–nickel composite thin films. Microsc Res Tech 79:1208–1213. https://doi.org/10.1002/jemt.22779
43. Lesiak B, Kövér L, Tóth J, Zemek J, Jiricek P, Kromka A, Rangam N (2018) C sp 2 /sp 3 hybridisations in carbon nanomaterials – XPS and (X)AES study. Appl Surf Sci 452:223–231. https://doi.org/10.1016/j.apsusc.2018.04.269
44. Sobola D, Ramazanov S, Konečnỳ M, Orudzhev F, Kaspar P, Papež N, Knápek A, Potoček M (2020) Complementary SEM-AFM of swelling Bi-Fe-O film on HOPG substrate. Materials (Basel). https://doi.org/10.3390/ma13102402
45. Ramazanov S, Sobola D, Orudzhev F, Knápek A, Polčák J, Potoček M, Kaspar P, Dallaev R (2020) Surface modification and enhancement of ferromagnetism in BiFeO3 nanofilms deposited on HOPG. Nanomaterials 10:1–18. https://doi.org/10.3390/nano10101990
46. Sobola D, Papež N, Dallaev R, Ramazanov S, Hemzal D, Holcman V (2019) Characterization of nanoblisters on HOPG surface. J Electr Eng. 70. doi:https://doi.org/10.2478/jee-2019-0055
47. Ahmad M, Al-Hawat S, Akel M, Mrad O (2015) Characterization of bismuth nanospheres deposited by plasma focus device. J Appl Phys. https://doi.org/10.1063/1.4907579
48. Terajima H, Fujiwara S (1975) Temperature dependence of the surface diffusion distance of bismuth atoms adsorbed on mica, carbon and silicon monoxide surfaces. Thin Solid Films. https://doi.org/10.1016/0040-6090(75)90304-1
49. Albrecht D, Lisenkov S, Ren W, Rahmedov D, Kornev IA, Bellaiche L (2010) Ferromagnetism in multiferroic BiFeO3 films: a first-principles-based study. Phys Rev B – Condens Matter Mater Phys, 81, 140401. doi:https://doi.org/10.1103/PHYSREVB.81.140401/FIGURES/2/MEDIUM
50. Lee YH, Han TC, Huang JCA (2003) Magnetic properties of Fe3C nanograins embedded in carbon matrix. J Appl Phys 93:8462. https://doi.org/10.1063/1.1555852
51. Wang Z, Tang C, Sachs R, Barlas Y, Shi J (2015) Proximity-induced ferromagnetism in graphene revealed by the anomalous hall effect. Phys Rev Lett. https://doi.org/10.1103/PhysRevLett.114.016603
52. Ramazanov S, Sobola D, Ţălu Ş, Orudzev F, Arman A, Kaspar P, Dallaev R, Ramazanov G (2021) Multiferroic behavior of the functionalized surface of a flexible substrate by deposition of Bi2O3 and Fe2O3. Microsc Res Tech. https://doi.org/10.1002/JEMT.23996
53. Ramazanov SM, Ramazanov GM (2014) Relaxing layers of silicon carbide grown on a silicon substrate by magnetron sputtering. Tech Phys Lett 40:44–47. https://doi.org/10.1134/S1063785014010091X
54. Ştefan Ţ, Sebastian S, Shikhgasan R, Dinara S, Guseyn R (2017) Multifractal characterization of epitaxial silicon carbide on silicon. Mater Sci Pol 35:539–547. https://doi.org/10.1515/msp-2017-0049
55. Ramazanov S, Ţălu Ş, Sobola D, Orudzev F, Ramazanov G, Selimov D, Kaspar P, Macků R, Nazarov A (2021) Crack resistance of bismuth ferrite films obtained on a flexible substrate. E3S Web Conf 295, 04008. doi:https://doi.org/10.1051/E3SCONF/202129504008
56. Alikhanov NMR, Murlieva ZK, Sarnatskii VM, Palchaev DK, Sakhatskii AS, Murliev EK, Shevchenko EV (2016) Synthesis, structure and properties of nanostructured materials based on BiFeO3. AIP Conf Proc 1748:040011. https://doi.org/10.1063/1.4954363
57. Orudzhev F, Ramazanov S, Sobola D, Alikhanov N, Holcman V, Škvarenina L, Kaspar P, Gadjilov G (2020) Piezoelectric current generator based on bismuth ferrite nanoparticles. Sensors (Switzerland) 20:1–9

58. Orudzhev FF, Alikhanov N-R, Rabadanov MK, Ramazanov SM, Isaev AB, Gadzhimagomedov SK, Aliyev AS, Abdullaev VR (2018) Synthesis and study of the properties of magnetically separable Nanophotocatalyst BiFeO3. Chem Probl 16:484–495. https://doi.org/10.32737/2221-8688-2018-4-484-495

# Chapter 7
# Effect of $Mg_2Sn$ Alloy on Silicon Substrate and Its Mechanical Properties with Its Resistivity Measurement


**A. Ayeshamariam, S. Sivaranajani, S. Beer Mohamed, M. Ismail Fathima, M. Sivabharathy, M. Jayachandran, and K. Kaviyarasu**

## 1 Introduction

Metal oxide and semiconducting alloys can be synthesized efficiently using sonochemistry. Ultrasonic chemistry is a branch of study in which chemical reactions are triggered by waves with frequencies ranging from 20 kHz to 1 MHz Water is rapidly transformed to hydrogen peroxide in a sonication bath with a power of 0.3 W/cm,

A. Ayeshamariam (✉)
Department of Physics, Khadir Mohideen College (Affiliated to Bharathidasan University, Thiruchirappalli), Adirampattinam 614701, Tamil Nadu, India
e-mail: ayeshamariamkmc@gmail.com

S. Sivaranajani
Department of Physics, St. Antony's College of Arts and Sciences for Women, Thamaraipadi, Dindigul 624005, Tamil Nadu, India

S. Beer Mohamed
Department of Material Science, Central University of Tamil Nadu, Thiruvarur 610001, Tamil Nadu, India

M. Ismail Fathima
Department of Physics, Mangayarkarasi College of Arts and Science College for Women, Paravai Kanmai, Madurai 625402, Tamil Nadu, India

M. Sivabharathy
Department of Physics, Sethu Institute of Technology, Pulloor, Kariyapatti 62611, Tamil Nadu, India

M. Jayachandran
Department of Physics, Sethu Institute of Technology, Pulloor, Kariyapatti 62611, Tamil Nadu, India

K. Kaviyarasu
UNESCO-UNISA Africa Chair in Nanosciences/Nanotechnology Laboratories, College of Graduate Studies, University of South Africa (UNISA), Muckleneuk Ridge, P O Box 392, Pretoria, South Africa



K. Kasinathan et al. (eds.), *Nanomaterials for Energy Conversion, Biomedical and Environmental Applications*, Materials Horizons: From Nature to Nanomaterials,
https://doi.org/10.1007/978-981-19-2639-6_7

as is well known. In humans, tin oxide is a moderate irritant that has a pulmonary effect. Mild irritation of the eyes and skin has occurred because of exposure. Tin oxide should be kept in well-sealed containers in a cool, dry, well-ventilated location. Tin oxide containers should be kept away from acids and alkalies and should be protected against physical damage. To make magnesium tin alloys by using the electron beam evaporation process and coating the same precursor material on a glass substrate to make magnesium tin alloys. Such high heating rates favor reactions with large rate constant prefactors rather than based on their activation energies. Thus, the range of chemical phase space available to reactants can be expanded considerably as compared to more conventional methods of synthesis [1]. The morphological and structural analysis of magnesium tin composite oxides was presented by Feng Huang et al., Thermal gravimetric and differential thermal analyses were also used to investigate the precursor. In the form of Li/$MgSnO_3$ cells, the electrochemical performance of $MgSnO_3$ as anode materials for Li-ion batteries was investigated. The findings revealed that the samples were microporous materials, and that the charge capacity and cyclability of the electrode active materials were sensitive to their structure and surface [2]. $Mg_2SnO_4$ produced oxide material has already been described by Abdul-Masjeed Azad. The process for producing oxide ceramics from metallic precursors has been described in detail. $Mg_2SnO_4$, a promising contender for usage as a ceramic capacitor element in the high temperature, high frequency domain, was synthesized using metallic Tin and Magnesium powders. The traditional powder metallurgy process was used to create an alloy with the composition $Mg_2Sn$. This resulted in single phase inverse spinal type $Mg_2SnO_4$ after heating over air with specially planned ordinary and mild experimental conditions. The target oxide's schematic phase and powder shape are addressed and compared to those found in powders and generated by other methods [3]. The precursor magnesium tin alloy (Mg-Sn) synthesized and deposited on Silica substrate by deposition technique has been studied and confirmed by XRD. magnesium tin alloy (Mg-Sn) has been characterized for their structure, formation and growth process and surface morphology. The results are presented along with the discussions.

## 2 Experimental

As in liquid stage, the two dissimilar metals Mg and Sn are commonly miscible, merging to produce a single liquid solution. The particles of both metals are arranged on the same crystal structure, which is actually that of the basis metal, in the more common case of powder solution, though the dimensions may be altered and the structure distorted to some extent to accommodate the atoms of the second metal, if they are not of the same size as that of the basis metal. However, there is a limit to

Nanosciences African Network (NANOAFNET), Materials Research Group (MRG), iThemba LABS-National Research Foundation (NRF), 1 Old Faure Road, P O Box 722, Somerset West 7129, Western Cape, South Africa

the amount of accommodation that can be done. The essential atomic pattern of the basic metal is preserved during solid solubility, and the solutions are known to as primary solid solutions or terminal solid solutions. Mg alloys are usually melted in a crucible of heat-resisting material such as silica or alumina. On account of the ease with which molten magnesium and its alloy combine with the $O_2$ of the atmosphere, it is essential to protect the molten alloy with flux. The flux mixture contains $MgCl_2$ and KCl. The mixture should be melted and cast into ingots. The flux is heated in a furnace with temperature, control to a temperature till the flux is melted. The magnesium is added to the molten flux. Because of the difference in the density magnesium sink to the bottom of the crucible and melts once the temperature rises above its melting point, 650 °C. Then tin metal is added to the molten and thrusted into the melt with the help of ladles. The whole melt is maintained at a temperature of 900 °C for 3 h and stirred well to ensure complete miscibility of magnesium and tin. The melt with the flux is cooled and removed from the furnace. The solid contains flux as the top layer and Mg + Sn alloy as the bottom layer. The alloy is removed from the flux by washing it in the distilled water using magnetic stirrer. Now it is made ready to coat [4]. Under ultrasonic circumstances, Sn-doped Mg and Sn alloys were synthesized using the sol–gel technique. In the liquid stage, the two metals Mg and Sn are commonly miscible, merging to produce a single liquid solution. Silicon is chosen as the substrate to deposit the alloys as a thin film.

## *2.1 Electrolytic Deposition*

The deposition is governed by first and second law of electrolysis. The quantity of energy transmitted is proportional to the weight of the substance placed. The chemical equivalents ratio is the weight of the material deposited by a certain amount of power. The films must be produced on a metal cathode, and the wide range of electrolytic baths available are designed to produce a deposit with good adhesion, the right crystallite size for the job, and homogeneity. Another goal of the bath is to prevent secondary reactions from developing, however secondary reactions are usually what limit the pace of development that can be achieved. The type of growth can vary from single crystal or crystalline aggregates, right through fiber growth deposits to unoriented deposits of very fine grain sizes and disordered structure.

## *2.2 Electroless Deposition*

A chemical-reduction technique is being used to create electrolytic action without it being an external potential source. By reducing the chlorides of Ni, Co, and Pb employing sodium hypophosphite, this process is known as electroless deposition has been used to deposit Ni, Co, and Pb films. This might be essential to employ a

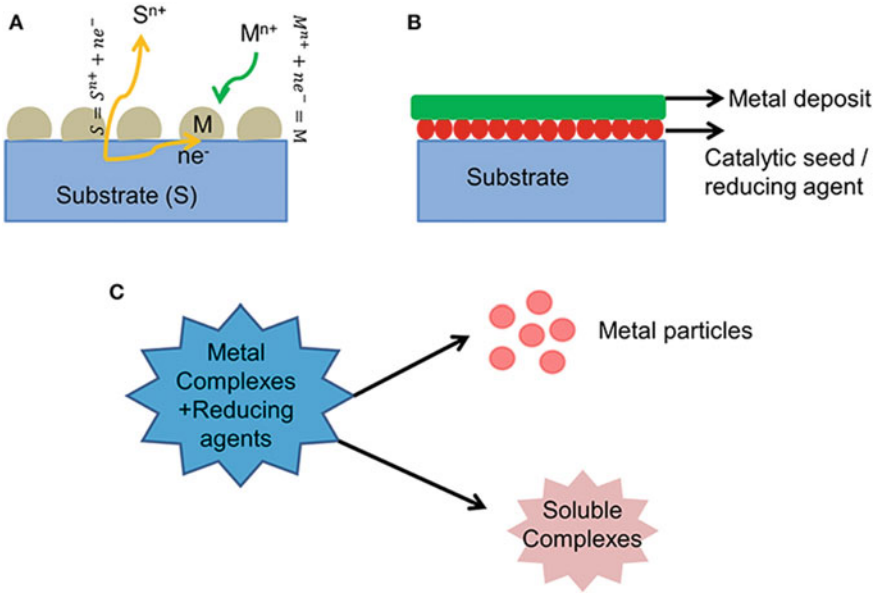


**Fig. 1** Electroless deposition process

sensitizer such as 0.1 percent stannous chloride on non-metallic surfaces. The rate at which this process produces film is highly dependent on the reaction temperature and is often difficult to control [5]. Electroless deposition is shown in Fig. 1.

## *2.3 Anodization*

Oxidation process is a method of producing oxide films that relies on the migration of oxygen ions to the electrode surfaces through a medium that is commonly made up of water but might also be made up of another material. such as fused sodium nitrite. At the anode, the most electronegative action will occur and in some cases this will mean that one will not produce the oxide of the metal anode. In other cases, although the oxide will be prepared, nevertheless it is non-adherent or too porous for any applications. Metal, including aluminium, tantalum, niobium, zirconium, titanium, and silicon, are common materials that can be anodized successfully. The films could be produced with either constant voltage or variable voltage growth. In both circumstances, the voltage developed from across film is being used to measure the thickness of the film.

There are some limits to the thickness of the film that one can obtain and one of these is that of voltage breakdown. This is an avalanche effect and some of the others are purity of foil, electrolytic treatment, conductivity and composition and temperature. It is possible to anodize in a glow discharge environment where the

specimen is placed in the discharge and is biased positive with respect to the anode of discharge. However, there is a limit to the amount of accommodation that can be made. The essential atomic pattern of the basic metal is preserved during solid solubility, and the solutions are referred to as primary solid solutions or terminal solid solutions. Mg alloys are usually melted in a crucible of heat-resisting material such as silica. Because of the ease with which molten magnesium and its alloy combine with the $O_2$ of the atmosphere it is essential to protect the molten alloy with flux. The flux mixture contains $MgCl_2$ and KCl. The mixture should be melted and cast into ingots. The flux is heated in a furnace with temperature, control to a temperature till the flux is melted. The magnesium is added to the molten flux. Because of the difference in the density magnesium sink to the bottom of the crucible and melts once the temperature rises above its melting point, 650 °C. Then tin metal is added to the molten and thrusted into the melt with the help of ladles. The whole melt is maintained at a temperature of 900 °C for 3 h and stirred well to ensure complete miscibility of magnesium and tin. The melt with the flux is cooled and removed from the furnace. The solid contains flux as the top layer and Mg + Sn alloy as the bottom layer. The alloy is removed from the flux by washing it in the distilled water using magnetic stirrer. XRD, SEM with EDAX, and Raman spectroscopy are often used to analyze the produced NPs. Seen from synthesis of modified heteroaryl thiols and 3-(aminomethyl) pyridine-2-amine, such heterogeneous catalyst was effectively used throughout the sonochemical synthesis of substituted-pyridopyrimidines in high returns.

## 3 Phase Transition

It is confirmed that the precursor which was coated as Mg-Sn alloy during annealing process as shown in Fig. 2. Table 1 shows the thickness of the film measured for different annealing temperature and different annealing duration. The values of strain and dislocation density are showing increasing trends. This is obvious for thin films with nano grains that once the size of the grain is in the nanometer range, there are more grain boundaries leading to higher strain between the grains and larger dislocation densities arising due to such boundaries [6]. The crystal lattice parameter values calculated are as follows: a = 5.3885 Å and c = 13.935 Å. These figures are extremely close to the normal figures, a = 5.2342 Å and c = 13.869 Å (Tables 2, 3 and 4).

## 4 Resistivity Measurement

Using the four probe resistivity method, the resistivity of $Mg_2Sn$ sheets annealed at 300 °C for 3 h was determined. It is seen that with increase in the annealing time the resistivity of the film is found to increase. It falls in the range between 0.02 and

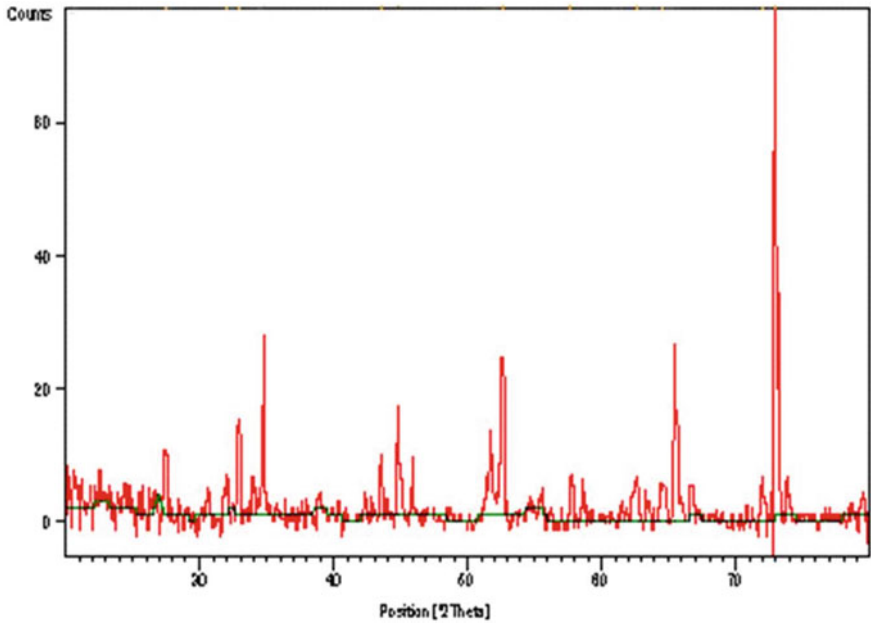


**Fig. 2** The precursor's XRD pattern ($Mg_2Sn$ annealed at 300 °C)

**Table 1** Thickness measurements

| S. No | As deposited thickness (μm) | Annealing temperature (°C) | Annealing duration (h) | Post annealing thickness (μm) |
|---|---|---|---|---|
| $Mg_2Sn$ | 0.23 | 300 | 3 | 0.34 |

0.001 Ω cm. The impedance of $Mg_2Sn$ coatings heated at various temperatures for varied annealing times is shown in Table 5. Two different trials of resistivity values were plotted here. The Arrhenius plot for the $Mg_2Sn$ alloys annealed at 300 ℃ at 3 h are shown in Figs. 3 and 4. The Arrhenius plot for the $Mg_2Sn$ alloys heated at 300 ℃ for 3 h are shown in Figs. 5 and 6 [7]. The pre-exponential, or frequency, factor corresponds to the quantity of times molecules will interact in the required orientation to begin a process. It's critical to understand that the Arrhenius equation is founded on collision theory. It implies that collision theory states properly oriented and with adequate power. We may use the Arrhenius equation [8] to solve for the rates constants at any temperature now that we have the acceleration and pre-exponential component from the Arrhenius plot. Plotting the logarithm of the rate constant, k, against the inverse temperature, 1/T, yields the Arrhenius plot. The resulting downward sloping line can be used to locate the missing Arrhenius equation components. The result for ln A is obtained by extrapolating the line back to the y-intercept [9]. The temperature-affected variable's experimental values, such as diffusivity and rate of reaction, are shown logarithmically versus 1/T. (K). The extremely nonlinear,

**Table 2** The precursor's XRD pattern ($Mg_2Sn$ annealed at 300 °C)

| S. No | Standard value | | | Observed value | |
|---|---|---|---|---|---|
| | d-spacing (Å) | Int (%) | (hkl) | d-spacing (Å) | Int (%) |
| 1 | – | – | – | 4.33262 | 2.72 |
| 2 | 3.1 | 40 | 112 | 3.24596 | 12.27 |
| 3 | 2.785 | 40 | – | 2.7972 | 5.57 |
| 4 | – | – | – | 2.72282 | 17.87 |
| 5 | 2.584 | 40 | 302 | 2.57959 | 33.95 |
| 6 | 2.098 | 40 | 331 | 2.08062 | 11.11 |
| 7 | 2.032 | 20 | 412 | 2.02575 | 20.64 |
| 8 | 1.793 | 40 | 403 | 1.76897 | 14.68 |
| 9 | – | – | – | 1.73975 | 31.14 |
| 10 | 1.593 | 20 | 701 | 1.59833 | 6.91 |
| 11 | – | – | – | 1.48279 | 7.24 |
| 12 | 1.436 | 60 | 630 | 1.44365 | 7.63 |
| 13 | 1.409 | 20 | 631 | 1.42679 | 34.08 |
| 14 | 1.301 | 20 | 722 | 1.31156 | 7.66 |
| 15 | 1.269 | 50 | 900 | 1.2959 | 100 |

**Table 3** XRD pattern of the $Mg_2Sn$ alloy annealed at 300 °C for 3 h

| S. No | Standard value | | | Observed value | |
|---|---|---|---|---|---|
| | d-spacing (Å) | Int (%) | (hkl) | d-spacing (Å) | Int (%) |
| 1 | 2.755 | 65 | 104 | 2.79168 | 32.64 |
| 2 | 2.619 | 100 | 110 | 2.69494 | 37.22 |
| 3 | 1.759 | 100 | 205 | 1.79955 | 18.49 |
| 4 | 1.67 | 30 | 122 | 1.65872 | 3.86 |
| 5 | 1.343 | 25 | – | 1.34221 | 1.7 |

**Table 4** Structural parameters of the $Mg_2Sn$ precursor material annealed at 300 ºC for 3 h

| 2θ degrees | Observed d(Å) | Standard d(Å) | (hkl) | D (nm) | $\varepsilon$ $lin^{-2}$ $m^{-4}$ ($10^{-4}$) | $\delta$ Lines/$m^2$ ($10^{14}$) |
|---|---|---|---|---|---|---|
| 34.7783 | 2.57954 | 2.584 | 302 | 39.997 | 9.051 | 6.251 |
| 57.6767 | 1.59833 | 1.593 | 701 | 28.326 | 12.781 | 12.463 |
| 64.5547 | 1.44365 | 1.436 | 630 | 24.454 | 14.805 | 16.722 |

**Table 5** Resistivity measurement by four probe method

| Samples | Condition of the sample | Resistivity (Ohm $cm^{-}$) |
|---|---|---|
| $Mg_2Sn$ | 300 °C, 3 h | 0.0018 |

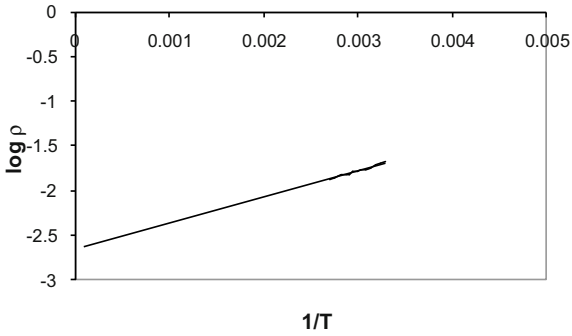


**Fig. 3** Arrhenius plot for the $Mg_2Sn$ alloy annealed at 300 °C for 3 h

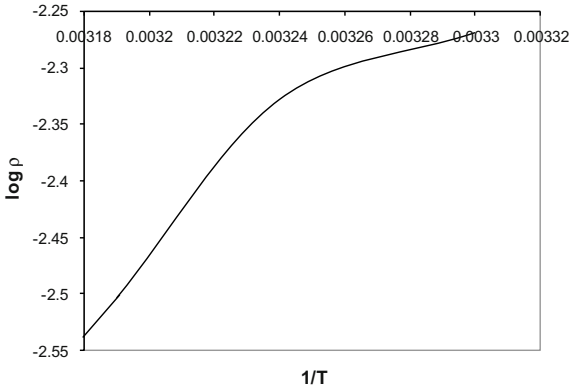


**Fig. 4** Arrhenius plot for the $Mg_2Sn$ alloy annealed at 300 °C for 3 h [10, 11]

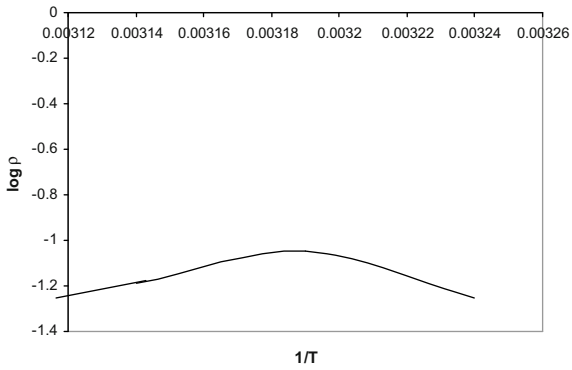


**Fig. 5** Arrhenius plot for the $Mg_2Sn$ alloy annealed at 300 °C for 3 h [12, 13]

thermally stimulated response is thereby linearized, making easy analysis possible. The diffusion coefficient of (interstitial) nitrogen in -iron is an example. Even though measured experimental values cover 16 orders of magnitude over a temperature range of around 1000 °C, Figs. 5 and 6, the data has an excellent linear fit. The negative

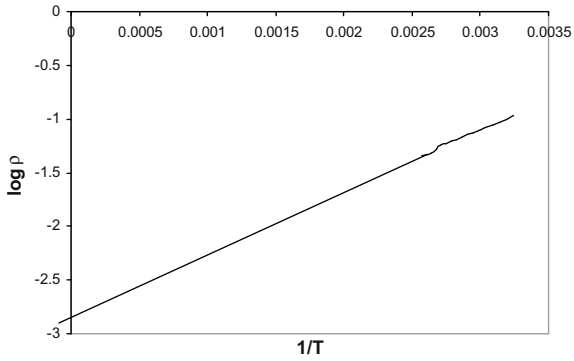


**Fig. 6** Arrhenius plot for the $Mg_2Sn$ alloy annealed at 300 °C for 3 h [14, 15]

activation energy divided by the gas constant, R, determines the line's slope. As a rule of thumb, the rate of most biological and chemical reactions doubles every 10 degrees Celsius increase in temperature [8]. The activation energy is calculated using two Arrhenius plots built on the same graph in this variant of the Arrhenius equation. The influence of temperature on numerous rate constants is shown in the equation above. This makes determining the rate constants' sensitivity to variations in activation energy and temperature simple. The rate constant is particularly sensitive if the activation energy is high for a given temperature range; temperature variations have a considerable effect on the rate constant [9].

## 5 Conclusion

Coating magnesium tin alloy prepared by the protective flux technique resulted in magnesium tin alloy as ($Mg_2Sn$) thin films. The ($Mg_2Sn$) thin films were found to increase with the increase in annealing temperature and annealing duration. The resistivity of the magnesium tin alloy films was measured using four probe resistivity measurement. It ranges from 0.02 $\Omega cm^{-1}$ to 0.001 $\Omega cm^{-1}$. Thus the ($Mg_2Sn$) thin films coated using electrodeposition technique shows high transparency, low resistivity and thus high conductivity, high crystallinity, and uniform surface morphology. Thus ($Mg_2Sn$) thin films are a more suitable novel alloy material for solar cell fabrication technology.

## References

1. Kim H, Kim YJ, Kim DG, Sohn HJ, Kang T (2001) Mechanochemical synthesis and electrochemical characteristics of $Mg_2Sn$ an anode material for Li-ion batteries. Solid State Ionics 144(1–2):41–49
2. Huang F, Yuan ZY, Zhan H, Zhou Y, Sun J (2004) Mater Chem Phys 83:16–22

3. Abdul-Majeed A (2001) Mater Res Bull 36:p755-765
4. Ikhe AB, Han SC, Prabakar SR, Park WB, Sohn KS, Pyo M (2020) 3Mg/ $Mg_2Sn$ anodes with unprecedented electrochemical performance towards viable magnesium-ion batteries. Journal of Mater Chem A 8(28):14277–14286
5. Chen HY, Savvides N (2009) Microstructure and thermoelectric properties of n-and p-type doped $Mg_2Sn$ compounds prepared by the modified bridgman method. J Electron Mater 38(7):1056–1060
6. Rashad MM, El-Shall H (2008) Effect of synthesis conditions on the preparation of $MgSnO_3$ powder via co-precipitation method. Powder Technol 183(2):161–168
7. Kalyane S (2017) Synthesis, characterization and AC conductivity study of polyaniline/$MgSnO_3$ composites. Int J Mater Sci 12(2):175–180
8. Kiruthiga G, Raguram T, Rajni KS, Selvakumar P, Nandhakumar E (2021) DSSCs: a facile and low-cost $MgSnO_3$-based transparent conductive oxides via nebulized spray pyrolysis technique. J Mater Sci: Mater Electron 32(18):22780–22791
9. Punitha K, Sivakumar R, Sanjeeviraja C (2012) Structural and surface morphological studies of magnesium tin oxide thin films. Energy Procedia 15:312–317
10. Yu R, Hojo H, Mizoguchi T, Azuma M (2015) A new $LiNbO_3$-type polar oxide with closed-shell cations: $ZnPbO_3$. J Appl Phys 118(9):094103
11. Rashad MM, Hessien MM, El-Midany A, Ibrahim IA (2009) Effect of synthesis conditions on the preparation of YIG powders via co-precipitation method. J Magn Magn Mater 321(22):3752–3757
12. Gonzalez-Nunez MA, Nunez lopez CA, Skeldon P, Lyon P, Wills TE (1995) Corros Sci 37(11):1763–1772
13. Conner PA, Irvine JTS (2001) J Power Sources 97–98:223–235
14. NamKim K, Jung H-K, Park HD, Kim D (2002) J Lumin 99:169–173
15. Huo H, Li Y, Wang F (2004) Corros Sci 46:1467–1477

# Chapter 8
# Metal Additive Manufacturing: Materials, Methods, Microstructure Evolution and Mechanical Properties via Post-processing Heat Treatments

**S. Beer Mohamed, C. Kaviarasu, A. Danielwillson, C. Velmurugan, R. Jayaganthan, and K. Kaviyarasu**

## 1 Introduction

The present scenario of global industries is continuously changing due to the impact of 4th industrial revolution so-called "Industry 4.0", for the betterment in data communications, geometry design, product development, product quality, and supply chains. Industry 4.0 relies on many pillars of technology among which the crucial one that has direct involvement in manufacturing is called additive manufacturing (AM)

S. Beer Mohamed (✉) · A. Danielwillson
Department of Materials Science, Central University of Tamil Nadu, Tamil Nadu, Thiruvarur 610005, India
e-mail: sbmohammed@cutn.ac.in

C. Kaviarasu
Department of Mechanical Engineering, Arasu Engineering College, Tamil Nadu, Kumbakonam 612501, India

C. Velmurugan
Department of Mechanical Engineering, Indian Institute of Information Technology, Tamil Nadu, Tiruchirappalli 620009, India

R. Jayaganthan
Department of Engineering Design, Indian Institute of Technology Madras, Tamil Nadu, Chennai 600036, India

K. Kaviyarasu
UNESCO-UNISA Africa Chair in Nanosciences/Nanotechnology Laboratories, College of Graduate Studies, University of South Africa (UNISA), Muckleneuk Ridge, PO Box 392, Pretoria, South Africa

Nanosciences African Network (NANOAFNET), Materials Research Group (MRG), iThemba LABS-National Research Foundation (NRF), 1 Old Faure Road, PO Box 722, Somerset West 7129, Western Cape, South Africa



K. Kasinathan et al. (eds.), *Nanomaterials for Energy Conversion, Biomedical and Environmental Applications*, Materials Horizons: From Nature to Nanomaterials,
https://doi.org/10.1007/978-981-19-2639-6_8

[1]. To date, worldwide industrial investment in additive manufacturing is figured as $16 billion and is expected to hike up to $40.8 billion by the year 2024 [2]. AM has been recognized as the new state-of-the-art manufacturing technology for producing parts that are design complex, lightweight and high performance in order to confront the expanding industrial demands. Notably, there is no need for cutting tools and components assembly when compared to conventional manufacturing technologies [3]. In AM, building a 3D part happens via a point-to-point, line-to-line or layer-after-layer fashion [4]. A broad spectrum of materials based on metals, polymers, ceramics and their composites can be processed to fabricate components successfully using AM [5]. However, only metals and alloys-based AM is emphasized in this article. In recent years, metal additive manufacturing techniques are gaining more interest among the manufacturers, materialists and researchers due to their dominance in automotive, aerospace, jewelry, energy and biomedical applications [6, 7]. Figure 1 represents the implementation of additive manufacturing in various domains [5].

A range of metal alloys have been witnessed for their usage in additive manufacturing that include aluminum alloys, steel alloys, titanium, nickel super alloys, cobalt chrome, and precious metals (gold, platinum, etc.) [8]. In metal additive manufacturing, all metal alloys are printed into components from a digital 3D design created via a CAD software, and so it is also labeled as 3D printing. A 3D printer uses the design data, preferably in stereolithography (STL) format and compute scan pattern via slicing for building each layer to complete part production. Recently, a new format has been developed called 3D Manufacturing Format (3MF) expanding the compatibility with respect to file transfer and accessibility among platforms, printers and other services [9, 10]. Referring to ISO/ASTM standards, metal additive manufacturing or 3D printing can be classified into powder bed fusion (selective

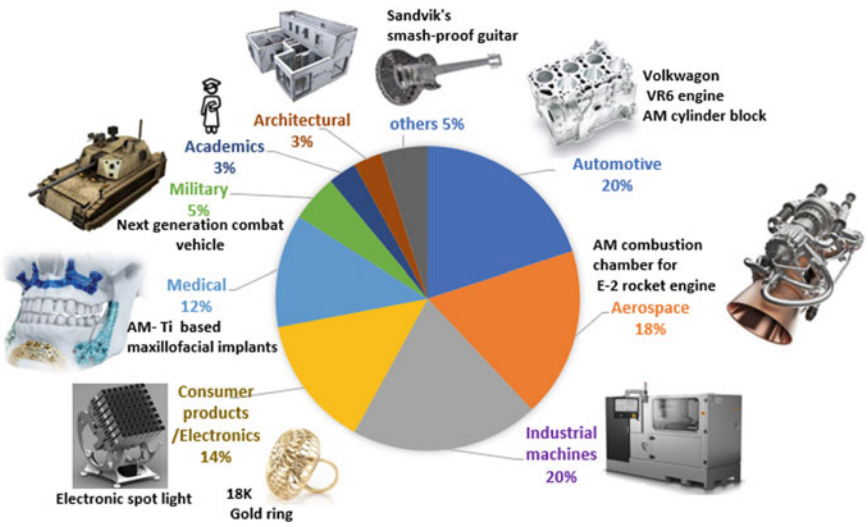


**Fig. 1** Implementation of additive manufacturing in various domains (Redrawn from Ref. [5])

laser melting, selective laser sintering, etc.), binder jetting, material extrusion, sheet lamination, and direct energy deposition (laser melt deposition, wire arc additive method, etc.) [11]. Though the additive manufacturing can be able to handle complex part designs, multiple metals and save materials by recycling, but the real picture in producing a top-notch component still lies with the post-processing steps. Post processing is inevitable in the process chain of additive manufacturing for producing products with desired quality. Post processing includes removal of support structures, micromachining for surface finish and heat treatments for improving the mechanical properties of the final product [12, 13]. In additive manufacturing, often the as-built products are prone to pores and internal cracks which are detrimental to the product quality and influence their mechanical properties adversely. Heat treatments play an effective role in eliminating these defects and also tune the microstructure to achieve better quality. By carefully adopting an appropriate heat treatment, the microstructure of the materials can be tailored to inherit remarkable mechanical properties like strength, hardness, toughness, ductility, resistance to creep, etc. [13]. A clear-cut understanding of microstructure in terms of phase distribution, structural defects, and residual stress is significantly essential in selecting a suitable thermo-mechanical treatment. However, the heat treatments for additive manufacturing are not the same as we do for conventional manufacturing technologies [14]. The existing information pertaining to metal alloy development and their subsequent heat treatments are inadequate for additive manufacturing. For comparison, there are 2,500 steel alloys that are qualified for conventional manufacturing whereas only two dozen available for additive manufacturing [15]. On the other hand, traditional heat treatments have been reported to be not suitable for components produced by additive manufacturing and so insisting modification in the heat treatment steps [16]. Hot Isostatic pressing (HIP) with slow cooling, homogenization with quenching, stress relief cycle followed by quenching, solution treatment with or without aging, annealing, tempering and peak hardening are some sets of heat treatments employed for additively manufactured components [17–19].

With this brief introduction to additive manufacturing in Sect. 1, this article proceeds with reviewing the availability of various materials for additive manufacturing in terms of metals, polymers and ceramics in Sect. 2. Raw materials production and their characteristics, specifically for metals are highlighted in Sect. 3. Various additive manufacturing techniques like powder bed fusion, binder jetting, and wire arc additive manufacturing are discussed in Sect. 4. In Sect. 5, some general defects and their root cause are highlighted. Post processing heat treatments like hot isostatic pressing (HIP), solution treatment (ST), annealing, tempering and peak hardening are emphasized in Sect. 6. The effect of post processing heat treatments on microstructural evolution and mechanical properties of the AM materials are discussed in Sect. 7 and Sect. 8, respectively. Issues and challenges with respect to feedstocks production, processing routes and post-processing heat treatments are reported in Sect. 9 along with possible solutions.

## 2 Materials for Additive Manufacturing

The processing capacity of additive manufacturing has been progressed over the years such that the feedstock of metals and alloys, polymers, ceramics or in combination as hybrid composite materials are utilized to print 3D products whose design are far from conventional thinking [20]. In this section, the aforementioned materials at their levels of technical readiness for use in AM process are highlighted with suitable examples.

### *2.1 Metals and Alloys*

Stainless steels are the leading candidates among other metals for being mostly processed by AM with respect to their figure of merit in mechanical properties [21]. Ferrite (409 SS, 403 SS, etc.), austenite (316 SS, 304 SS, etc.), austenite–ferrite (duplex 2205 SS, 2209 SS), and martensite (420 SS, 17–4 SS) steels have witnessed to showcase unique microstructure with tailored mechanical properties when processed by AM [22]. Aluminum-based alloys like Al-12Si [23], AlSi-10 Mg [24], AlSi-9Cu-3Fe [25], 5A06 [26], 4043 [27], 7075 [28], etc., have been reported to be qualified for AM. Titanium-based alloys qualified for processing via AM include Ti-6Al-4 V [29], Ti-3Al-10 V-Fe [30], Ti-Cr [31], γ-TiAl [32], etc., are widely used for biomedical and aerospace applications. Cobalt-chromium-molybdenum (Co-Cr-Mo) and cobalt-chromium-tungsten (Co-Cr-W) are successfully processed by AM for dental applications [33]. Nickle-based alloys typically Inconel 718 [34], Inconel 625 [35], Hastelloy -X [36] and RENE 108 [37] have shed light in making complex parts via AM for turbine blades and nuclear reactors owing to their strength, oxidation and corrosion resistance. Hight entropy alloys have also been found suitable for processing via AM. Some typical examples include Co-Cr-Fe-Mn-Ni [38], Mo-Nb-Ta-W [39], Al-Cr-Fe-Co-Ni [40], and Al-Cr-Fe-Mo-V [41] indicate the new milestones in processing capability of AM. Recent investigations spotlighted the ability of AM process in producing hybrid metal matrix composites by incorporating nanoparticles. TiC nanoparticles were reinforced in AlSi-10 Mg alloy to induce the phase strengthening for improving tensile strength and wear resistance [42]. TiC nanoparticles when added to H13 steels, reduced the friction and wear loss [43]. $TiB_2$ nanoparticles were incorporated into 316L steel metal matrix successfully for yielding high compressive strength and ductility at room temperature [44].

## 2.2 Polymers

Next to metals, materials that are utilized to the highest degree in AM process are polymers. Polymers like thermoplastics (polyamides, polyethylene, polypropylene, polystyrene, etc.), thermosets (phenolics, alkydes, epoxy, etc.), elastomers (polyetheresters, ALM TPE-210 s, etc.), hydrogels (chitosan, collagen, gelatin, etc.) and polymer composites have earned a descent pace in the AM for producing products [45]. Polystyrene [46], polymethylmethacrylate [47], polycarbonates [48], and styrene-acrylonitrile-copolymer [49] have been reported suitable for AM. Polyamides that have shown dominance in the AM market are PA – 12 (preferred for high strength), PA – 11 (preferred for high ductility) and PA – 6 (high melting point) [45]. Polymer composites especially with fiber as reinforcement are potential for making light weight product with reasonable strength. Glass fiber/propylene-co-ethylene [50], glass fiber/polyamide [51], glass fiber /polyester [52], carbon fiber/acrylonitrile butadiene styrene (ABS) [53], carbon fiber/polylactic acid (PLA) [54], and carbon fiber/nylon [55] are some eminent candidates successfully processed by AM. The processing window of AM have also been opened for design and development of nanocomposites. Carbon nanotubes (CNT) are widely used for incorporation in polymers like polyamide (PA-12) [56], polyvinylpyrrolidone (PVP) [57], polylactic acid (PLA) [58], and acrylonitrile butadiene styrene (ABS) [59]. Nanoparticles like iron oxide ($FeO_x$), alumina ($Al_2O_3$), boron nitride (BN) in PA-12 [60, 61], Barium titanium oxide ($BaTiO_3$) in PA-11 [62], and Hydroxyapatite (HA) in polyetheretherketone (PEEK) [63], have been successfully processed by the AM to produce polymer products with tailored properties.

## 2.3 Ceramics

Ceramics are often selected for producing parts that are subjected to high temperature and high stress applications like industrial furnace, rockets, and wear coating for tools. Various ceramics utilized in engineering applications include single oxides ($Al_2O_3$, $ZrO_2$, $SiO_2$, etc.), carbides (SiC, TiC, VC, WC, etc.), sulphides ($MoS_2$, $WS_2$, etc.), and nitrides (BN, $Si_3N_4$, etc.) [64]. In recent years substantial interest have grown in adopting ceramics for additive manufacturing. Alumina ($Al_2O_3$) and zirconia ($ZrO_2$) are processed by SLM to produce components that are crack-free with good flexural strength [65]. Carbide like silicon carbide (SiC) and titanium carbide (TiC) are processed by AM to produce structure with complex shapes [66, 67]. Bismuth molybdenum oxide ($Bi_2Mo_2O_9$) was successfully demonstrated to produce components for 3D radio frequency and microwave [68]. Barium titanate ($BaTiO_3$) have been employed as feedstock in binder jetting (BJ) to produce ceramic capacitors [69]. Lithium disilicate and tricalcium phosphate are used for dental and scaffold applications respectively [70, 71]. Multiphase ceramics like boron carbide and silicon carbide ($B_4C$–SiC) specimens having heterogeneous phase were prepared via AM

to inherit multifunctionality [72]. Silicon oxycarbide-based porous ceramic (SiOC) in a honeycomb structure was successfully processed by AM with high density, surface smooth and better compressive strength-to-weight ratio [73]. Molybdenum silicon boron titanium carbide (Mo-Si-B-TiC) was laser additively manufactured to produce refractory alloys that can withstand extreme temperature [74]. Nanorods of aluminum carbide ($Al_4C_3$) were dispersed homogeneously in Al matrix to form $Al_4C_3$/Al composite with enhanced mechanical performance for structural applications via AM [75]. Acid treated CNT was mixed with $Al_2O_3$ nanoparticle to form a colloid coating on Mo-Ti-Al metal matrix. This hybrid $Al_2O_3$-ATCNT/Mo-Ti-Al nanocomposite processed by LPBF has shown better hardness resulting from homogeneous dispersion of nanoparticles [76].

Among the metal, polymer and ceramic feedstock materials mentioned above, only the metal production techniques are briefed in the following section as the scope of this article lies within the metal additive manufacturing. Table 1 lists the palette of metal feedstocks utilized for AM in recent times.

## 3 Metal Feedstock: Production and Characteristics

Metal powders with high density, less porosity and flow ability to spread uniformly are essential for AM in building up the powder layer to print parts with supreme quality. These figures of merit concerned with the metal powders are achieved by adopting right powder production techniques. The production techniques can directly influence the characteristics of metal powder-like particle size, particle shape and their chemical nature [4]. Major group of metal elements are reported to be produced by atomization techniques (gas, water or plasma-assisted) [94]. The other techniques include hydride-dehydride method [95], rotating electrode process, mechanical alloying and oxide reduction chemical process [96]. Generally, the powder production via atomization technique occurs in three stages (melting, atomization, and solidification by cooling). Further, degassing and surface oxide reduction kind of post processing may yield powders with good quality [97]. In water atomization technique, mostly non-reactive metals like stainless steels (AISI 4130, 316L, etc.) are produced by atomizing a liquid metal using water jet. This method produces powders in size ranging from few micro meters to 500 μm, with non-spherical morphology leading to poor packing density [98–100]. Moreover, formation of oxide layers due to high oxygen consumption is a negative effect that will spoil the flow nature of powders and in turn affect the melt pool. This will deteriorate the mechanical properties of the AM product [101]. Gas atomization can reduce this oxidational hazard by employing inert gas typically argon or nitrogen. Microstructure and phase composition of the metal powders can be tuned by selecting a specific inert gas type. Different phase composition either austenitic or martensitic phase can be achieved for steels, when either argon or nitrogen is selected as inert gas in atomization process [102, 103]. Electron induction melting gas atomization (EIGA), a variant of gas atomization technique which involves induction melting of a metal rod followed by atomization

**Table 1** Palette of metal feedstocks for additive manufacturing

| S. No | Metal feedstocks | Key applications | | | | | | References |
|---|---|---|---|---|---|---|---|---|
| | | Aerospace | Automobile | Marine | Tools | Biomedical | Consumer products | |
| 1 | Stainless steels (316L SS, H13, etc.) | ⊗ | ⊗ | ⊗ | ⊗ | ⊗ | ⊗ | [77, 78] |
| 2 | Aluminum alloys (AlSi, AlSiMg, etc.) | ⊗ | ⊗ | ⊗ | – | – | ⊗ | [79, 80] |
| 3 | Nickel alloys (Inconel 625, 718, etc.) | ⊗ | ⊗ | ⊗ | ⊗ | – | – | [81–83] |
| 4 | Titanium alloys (TiAlV, TiCr, γ-TiAl, $TiB_2$, etc.) | ⊗ | ⊗ | ⊗ | ⊗ | ⊗ | ⊗ | [3, 29–32, 84, 85] |
| 5 | Cobalt-chrome (CoCrMo, CoCrW, etc.) | ⊗ | ⊗ | ⊗ | – | ⊗ | – | [33, 86] |
| 6 | High entropy alloys | ⊗ | ⊗ | ⊗ | ⊗ | ⊗ | – | [87–91] |
| 7 | Precious metals (Gold, Silver & Platinum) | – | – | – | – | ⊗ | ⊗ | [92, 93] |

* Note: ⊗ —suitable for application; (–)—not applicable

of fine metal droplet. Reactive metal powders especially titanium (Ti) and its alloy (Ti-Al-V) are obtained with high purity using EIGA [104]. Lately, plasma rotating electrode process (PREP) found to produce variety of metal alloys (examples include Ni-Al-Co-Cr, Ti-Al -V, 316-steel, Co-Cr-Mo, etc.) with good spherical morphology [105, 106]. In PREP, the key process parameter is the rotation speed that determines the final morphology of particle as either spherical, irregular or satellite. It was reported that for a maximum rotation speed of 14,000 rpm, the particle size was narrower down to 400 μm with spherical shape [107]. Table 2 presents some selective examples of processes, key parameters, powders produced, and their characteristics.

## 4 Methods for Metal Additive Manufacturing

In contrast to conventional subtractive manufacturing process where metals are subtracted from bulk volume, metal additive manufacturing performs metal addition to build part in a layer another layer passion with reference to a 3D CAD model design [114]. There are many streams of metal additive manufacturing are in practice today that include material extrusion (filament materials are melted and dispensed via a nozzle to build part), material jetting (involves in selective deposition of material droplets to build part), binder jetting (powders are joined using a liquid bonding agent to build part), sheet lamination (sheet materials are joined to form a part), powder bed fusion (heat energy by means of laser is applied to fuse powders in a bed to form part) and direct energy deposition (laser heat energy is directed to melt and fuse the depositing material) [115, 116]. In this section, more emphasis is given to powder bed fusion (selective laser melting), binder jetting and direct energy deposition (wire arc additive method) techniques of additive manufacturing.

### *4.1 Powder Bed Fusion*

Among the metal additive manufacturing methods, powder bed fusion is recognized as the most significant method for processing metals. In this technique, metal powders are uniformly spread over a builder plate upon which a specific spot will be hit by a laser source, thus melting and fusing the powders together to form a first layer. Following this, fresh raw powders are supplied and the same process is continued to build the second successive layer. This layer-by-layer passion is continued to complete the 3D part production. Powder bed fusion is also termed as selective laser melting (SLM), selective laser sintering (SLS), laser melt deposition (LMD), and direct electron beam melting (EBM) [117]. Recent powder bed fusion systems prefer SLM compare to others as they are outstanding in rapid prototyping, tool making and manufacturing complex structures [116, 118]. Table 3 provides some important factors to be considered for SLM and DLM.

**Table 2** Selective examples of processes, parameters, powders and their characteristics

| S. No | Production process | Key parameters | Powder produced | Powder characteristics | | | References |
|---|---|---|---|---|---|---|---|
| | | | | Size | Shape | Packing density | |
| 1 | Water atomization | Water pressure (280 bar), nozzle diameter (5,6 & 7 mm) | Low carbon steel, AISI 304 stainless steel, Copper | 56 μm | Non-spherical | – | [108] |
| 2 | Gas atomization | Gas pressure, velocity, metal flow velocity | SS 316 | 45–105 μm | Spherical | 63.87% | [109, 110] |
| 3 | Plasma rotating electrode process | Rotation speed, arc electric current | Al-Si-Cu-Mg | 203.68 μm | Spherical | – | [111] |
| 4 | Hydride-Dehydride | Hydration at 650 °C, Dehydration at 350 °C | Titanium (Ti) | 150–250 μm | Non-spherical | – | [112] |
| 5 | Mechanical alloying | Alloying time 10 h, Drum rotating speed 800 rpm | Co-Cr-Fe-Ni-Mn-W high entropy alloy | <45 μm | Spherical | – | [113] |

**Table 3** Important factors for SLM and DLM [116]

| AM method | Important factors | | | | | | |
|---|---|---|---|---|---|---|---|
| | Density (net shape) (%) | Complexity | Precision (mm) | Roughness (μm) | Building rate ($mm^3/s$) | Built on surface | Application |
| SLM | 100 | Hollow structures | <0.1 | 30–50 | 1–20 | Flat | New components |
| LMD | 100 | Limited | >0.3 | 60–100 | 3–140 | 3D surface | Surface repair |

Moussaoui et al. investigated the effect of SLM process parameters on Inconel 718 nickel-based alloy powder with 5–25 μm grain size. Process parameters like laser power (150–450 W), velocity (1000–1800 mm/s), scan distance (50–90 μm) and layer thickness (constant with 70 μm), have shown significant effect on microstructure and mechanical properties of the product developed [119]. Vanadium-based alloy V-6Cr-6Ti was selective laser melted with double zone scanning strategy to yield maximum compressive strength of 1078 MPa when compared to conventional manufacturing process [120]. CoCr powders were successfully processed by SLM to produce cardiovascular stents (2 mm diameter, 18.95 mm length, and 200 μm thickness) for biomedical applications [121]. Al-12Si powder alloy was processed successfully to produce a cylindrical specimen with diameter 5 mm and height 5 mm by pulsed SLM technique. Laser power (0.5–4.5 kW), speed (90–180 mm/min), spot size (150 μm), hatching distance (0.1 mm) and layer thickness (0.1 mm) are the process parameters associated with pulsed SLM [122]. Surface quality for AlSi10Mg alloy-based component was improved when the SLM was operated with optimized process parameters like laser power as 0.32 kW, scan speed as 0.60 m/s, hatching distance as 88.7 μm and overlap rate as 35% [123]. Composite development was also achieved by SLM. Silicon carbide (SiC) with size 7 μm was reinforced in AlSi10Mg matrix by SLM to improve the wear resistance of the composite [23]. The capability of SLM to alloy and reinforce metal oxide nanoparticles (zinc with size between 50 and 120 nm) in aluminum alloy Al6061 was also witnessed recently, thus promoting the SLM as a suitable candidate for developing composites with complex networks [24]. Figure 2 depicts the SLM process of AM with selective examples.

## *4.2 Binder Jetting*

Binder jetting (BJ) is one among the commercially expanding additive manufacturing technologies that produce parts by 3D printing. In principle, BJ uses powder materials that are bonded to one another with the help of a liquid binding agent being jetted on selective powder zone using inkjet printhead to print a first layer and then continuous to print successive layers to yield a greener part [125]. BJ manufacturing

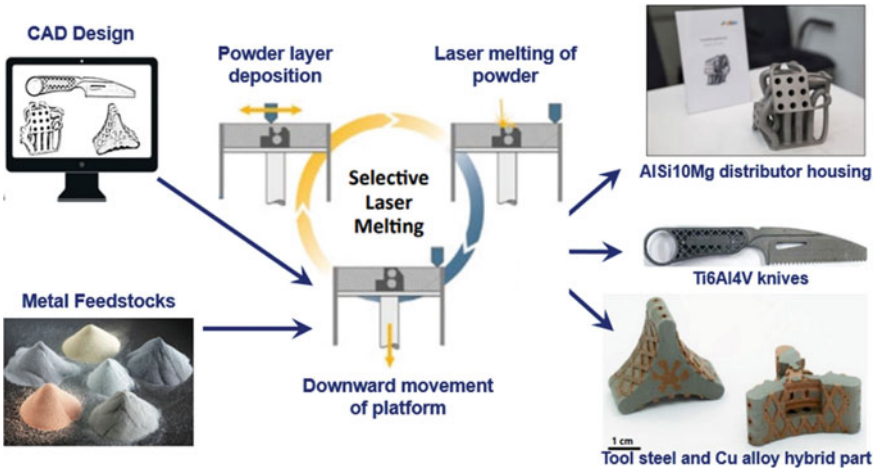


**Fig. 2** Schematic representation of SLM process with selective examples (Redrawn from Ref. [124])

process comprises seven sequential steps that starts with layering of powder, injection of binder phase into a selected powder zone, curing the binder, de-powdering and removing the loosen powders, sintering to improve the density and strength of greener part, infiltration of metal with low melting point, annealing heat treatment and ends with surface finishing [126, 127]. BJ can process a wide range of materials like metals, ceramics (alumina, silica, etc.), polymers (polyglycolic acid, polylactic acid, etc.) and biomaterials (hydroxyapatite, calcium silicate, etc.) [128]. A wide spectrum of metals and metal-alloy powders have been utilized by BJ to fabricate parts. Stainless steel 316L [129], 304L and 420 stainless steels [130], titanium (Ti) [131], copper (Cu) [132], nickel-based alloys Inconel 625 and Inconel 718 [133, 134], and cobalt-chromium alloys [135] are some exemplary works reported in recent years. Binder materials for BJ are typically based on any of the type like organics, inorganics, solvents, metal salts, phase change materials, etc., [136]. In modern metal BJ systems, metal binders are used either as suspended particles or metal-salt solutions. Nanoparticles can be used in BJ by incorporating with polymer binders to improve the properties of final product. Copper nanoparticles were binder jetted in steel powder and their effect on densification was revealed [137]. Metal salts dissolved in solvents (examples include copper sulfate, copper nitrate hydroxide, etc.) have been used as binders in printing conductive pattern structures [138, 139]. Recently, metal–organic decomposition (MOD) ink synthesized using copper metallorganic compound in 2-methoxyethanol biner solvent was successfully demonstrated for binder jetting of copper metal [140]. Figure 3 represents the principle of binder jetting process with selective examples. Table 4 presents the specification and process window of some binder jet machines available in the market.

Inconel 625 was binder jetted using ethylene glycol monobutyl ether (aqueous binder) to produce a green part in cylindrical shape (8 mm radius and height 90 mm)

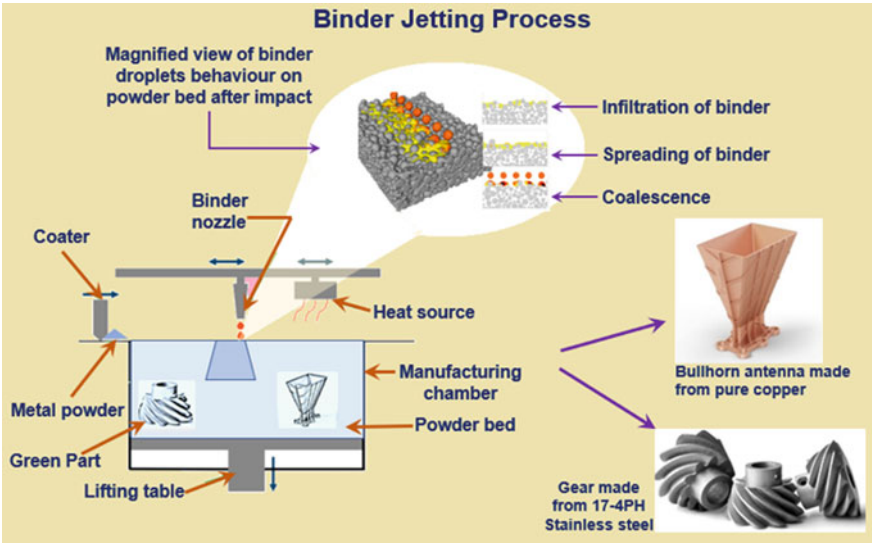


**Fig. 3** Schematic representation of Binder jetting process with selective examples (Redrawn from Ref. [19])

**Table 4** Specifications and process window of various binder jetting (BJ) systems [141]

| BJ system (ExOne) | Type of metals processed | Machine specifications | | | |
|---|---|---|---|---|---|
| | | Build box size (L × W × H) in 'mm' | Rate of deposition in 'cc/hr' | Resolution obtained in 'DPI' | Layer thickness in 'μm' |
| Innovent+ | 304L SS, 306L SS, Copper, Titanium, Inconel 625, 17–4 PH SS, Tungsten alloy, Aluminum 6061, Cobalt-Chrome | 160 × 65 × 65 | 166 | 800 × 800 | 30–200 |
| InnoventPrO 3L | | 3–5 L | 700 | | |
| X1160PRO | | 800 × 500 × 400 | 10,000 | – | |
| X125PRO | | 400 × 250 × 250 | 3,600 | – | |

with apparent density 96.5%. No support structures were involved in the binder jetting process [133]. P. Nandwana et al., investigated the binder jetting process of Inconel 718 and revealed that powder chemistry strongly influences the sintering process in achieving a near-net shape product. Impact of powder grain size on sintering kinetics was discussed [134]. In binder jetting of copper, the use of bimodal powder mixtures notably improved the flowability and packing density with 10.5% and 8.2% respectively. A 4% increase in the sinter density was witnessed with 6.4% reduction in the shrinkage [142]. Copper particles with fine grain size (5 μm) was successfully

binder jetted for the first time by Miyanaji et al., and observed to achieve a 9% increase in the sinter density when compared to coarse bimodal copper powder. Also, all those extra work and time associated in preparing bimodal powders (mixing ratio and blending) have got eliminated with the use of fine copper powder [143]. Recently, complex geometry like foam structures have also been developed by binder jetting using copper powder. The fabricated porous structure has shown 59% porosity and 5% volume shrinkage, indicated the expanding process capability of BJ [132]. Another interesting work reported recently in BJ, was the development of porous structured Co-Cr-Fe-Mn-Ni high entropy alloy. The high entropy alloy structure possessed homogenous distribution of pores with part porosity in the range 35–40% [144].

## *4.3 Wire Arc Additive Manufacturing (WAAM)*

For making large components with complex geometry at low cost in an environment friendly setup, wire arc additive manufacturing (WAAM) will be the prime choice among the direct energy deposition methods for all manufacturers in the world. In principle, WAAM uses the raw materials in wire form which is heated and melted via an electric arc leading to subsequent deposition of the melted droplet in a layer upon layer style to produce metal parts with near-net shape [145]. Figure 4 represents the WAAM process with selective examples. The heat source in the WAAM can be of any of the following: gas metal arc welding (GMAW), gas tungsten arc welding (GTAW), or plasma arc welding (PAW) [146]. WAAM can deal with distinct class

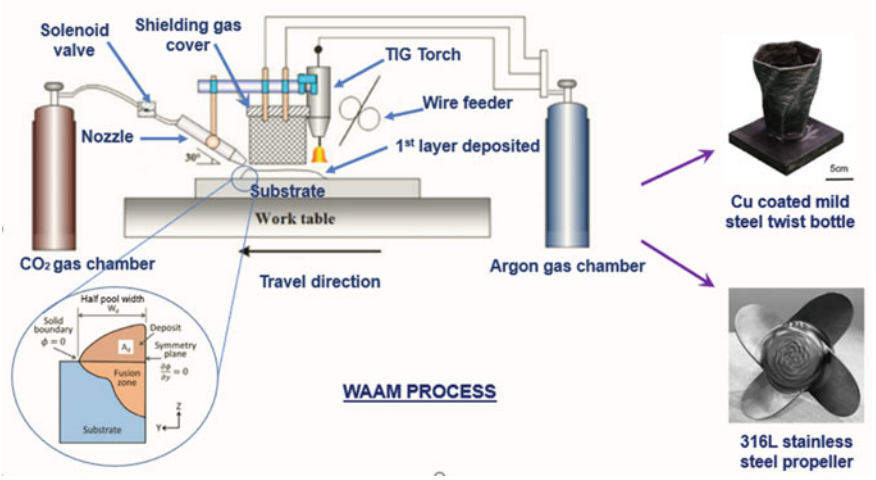


**Fig. 4** Schematic representation of WAAM process with selective examples (Redrawn from Ref. [148])

of metals and alloys by employing any of the aforementioned heat sources. Titanium alloys and nickel alloys can be processed by both GTAW and PAW. Steel alloys can be processed by using GMAW and PAW. Aluminum alloys can be processed by both GMAW and GTAW. Bronze can be processed by GMAW, whereas the functionally graded materials and intermetallics can be processed by GTAW [147]. Apart from the type of heat source, the other essential process preferences include welding parameters (voltage, wire feed rate, travel speed, etc.), wire (diameter, composition, single wire/dual wire, etc.), shield gas (flow rate, composition, etc.), motion system (accuracy, repeatability, etc.) and substrate (volume, composition, fixture, etc.) [145].

The metrics to measure the performance of the WAAM are geometrical properties (accuracy, surface waviness, and wall thickness), physical properties (micro-fissures, cracks, pores, and distortion), material properties (anisotropy, tensile strength, residual stress, corrosion resistance, etc.) and deposition rate (typically 1–10 kg/h) [145]. Table 5 summarizes the process details associated with WAAM.

## 5 General Defects and Their Root Cause in 3D Printed Parts

Despite the benefits attained from AM like reduced material volume and ability to handle complex design with no special tools for manufacturing, all the metal parts fabricated by AM are prone to some of the general defects that are grouped under four types like process flaws (lack of fusion, balling, and contaminations), microstructure based (segregation and banding), dimensional based (stair-stepping, distortion and surface condition), and porosity (voids, porosity due to gas and clusters) [3, 156]. Lack of fusion originates due to partial melting and fusion of metal into the base metal plate (substrate). Such a lack in the metal penetration may cause delamination in the deposited part. Sometimes when the lack of fusion of metal powders is caused by preformed thin oxide layers, it is termed as cold lap [3]. Inclusions are the formation of intermetallics (oxides and sulfides particles) in the fabricated part due to the chemical reaction between metals and process assisting gases [156]. Balling (formation of ball-bead shape melt) occurs as when the surface tension force dominates the wetting between melt droplet and metal substrate. Poor process parameters in terms of scan speed, power source, and layer thickness are the root cause for balling as well as stair stepping [157]. Local melting and solidification process results in the formation of shrinkage and distortion. Internal stresses buildup in the metal feed stock due to volume contraction induce shrinkage and distortion. Clear design, right material selection, and right process parameter can eradicate the defects [3]. Keyhole defects are observed in the surfaces and also in the bulk part produced from a thermal-based AM. Plasma generates a high penetration depth in which vapor bubbles get trapped and form keyhole porosity in the finished part [158]. Hydrogen gas entrapped in the molten pool upon cooling and solidification results in the formation of gas porosity. Aluminum is more prone to gas porosity. Argon gas during atomization gets trapped

**Table 5** Process details associated with WAAM

| S. No | WAAM process | Wire material | Substrate material ($l \times w \times h$) in $mm^3$ | Wire feed speed in m/min | Other parameters | Layer height/thickness in 'mm' | Part size ($l \times w \times h$) in 'mm' | References |
|---|---|---|---|---|---|---|---|---|
| 1 | Cold metal transfer GMAW | 2Cr13 martensitic stainless steel (Dia. 1.2 mm) | 2Cr13 martensitic stainless steel with size (150 × 150 × 8) | 5.2 | Deposition speed—0.4 m/min | 1.92 | 126.87 × 5.26 × 42.53 | [149] |
| 2 | PAW | Ti6Al4V (Dia. 1.14 mm) | Ti6Al4V with size (220 × 70 × 12) | 6.7 | Deposition rate—2 kg/hr | – | 210 × 15 × 105 | [150] |
| 3 | GMAW (Speed arc mode) | 316L stainless Steel (Dia.1.2 mm) | 316L stainless steel (250 × 100 × 5) | 4.5 | Deposition rate—2.4 kg/hr | 1.47 | 150 (l) | [151] |
| 4 | GMAW | NAB alloy (Dia. 1.2 mm) | NAB alloy (size not mentioned) | 5.4, 6.7, and 8 | Deposition rate—5 kg/hr | 2 | 100 × 40 ($l \times h$) | [152] |
| 5 | GTAW | ATI 718Plus (Dia. 1.6 mm) | Inconel 718Plus (12.5 × 110 × 45) | 0.4 | – | – | 70 ($l$) | [153] |
| 6 | GTAW | ER2219 (Dia. 1.2 mm) | Al6061 alloy (300 × 250 × 10) | 2 | – | – | 120 × 20 ($l \times h$) | [154] |
| 7 | GMAW | ER70S-6 (Dia. 0.889 mm) | ASTM A36 mild steel with 12 mm thickness | 6.24 | – | 3 | 135 × 22 × 150 | [155] |

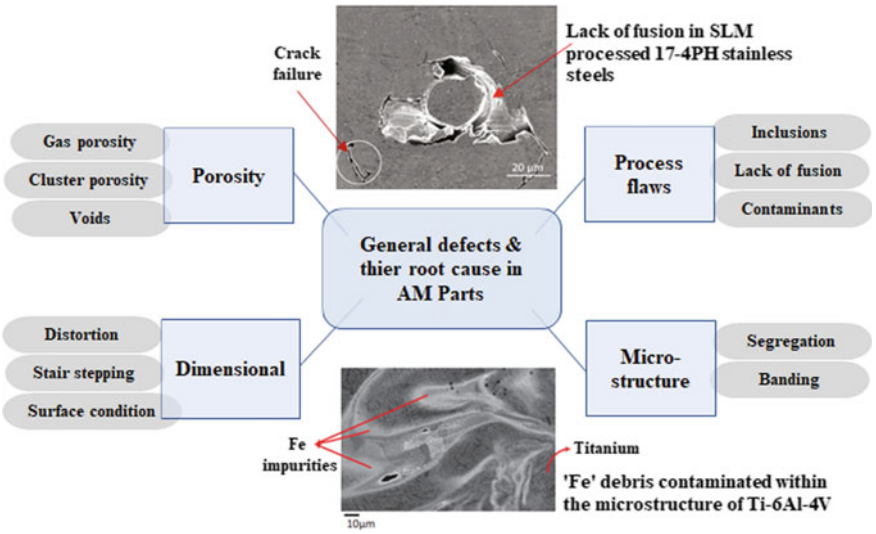


**Fig. 5** General defects occur in AM parts along with their root cause

into feed stock and arises as a major source for micro-porosity. Intense handling, safe storage and preprocessing may reduce the risk of porosity [3]. Lack of bonding between materials may result in crack formation. In AM, cracks occurring at the terminal of the deposition track are termed as crater cracks whereas hot cracks occur close to the solidification boundary upon cooling. Cracks that occur after several days of cooling are termed as cold cracks. Adjacent to the fusion boundary, hot tearing occurs when the metal is softened by heating below its melting temperature [3]. Through understanding on AM defects, their root cause, standardization of processes, parameters associated to AM type and framework on postprocessing may help in achieving defect-free products with high quality. Figure 5, shows the general defects formed in as-built AM parts.

## 6 Post Processing—Heat Treatments

Though the as-built 3D part produced by AM may possess equal quality compared to traditionally manufactured part, still there exist a need for post process heat treatments in order to eliminate the various defects like pores and internal cracks which are detrimental to product quality. The other critical-to-quality factors considered in AM include net density, material strength and hardness, surface quality and accuracy in dimension [159]. In general, heat treatments are performed for materials to achieve any of the following: grain size refinement, relieving internal stresses, improving the machinability, improving hardness to enhance wear resistance, improving surface hardness and microstructure development to achieve desired

properties [64]. However, as mentioned earlier heat treatments for additively manufactured parts are not the same as we perform in traditional manufacturing. In this section, heat treatments such as hot isostatic pressing (HIP), solution treatment (ST), annealing, tempering and peak hardening for AM parts are briefly discussed with some examples.

## *6.1 Hot Isostatic Pressing (HIP)*

Hot isostatic pressing (HIP) is used for compacting loose powders or to improve densification in already compacted parts by applying heat and pressure (inert gas as pressure medium) to remove structural defects like pores and inner cracks. The process involves applying high temperature and high gas pressure isostatically to densify the component. Densification process relies on three mechanisms (plastic deformation followed by creep and diffusion) to collapse the voids and results in pore closure, thus yielding a defect-free component [160]. Temperature (70% of materials solidus temperature), applied pressure (typically 100–200 MPa) and holding time (varies on component thickness and thermal conductivity) are the three ruling parameters in the HIP process cycle. The other parameters to be considered in the HIP cycle are the heating and cooling rate, which may not impact the densification process but do influence the final microstructure of product processed [160]. In binder jetting process of bimodal copper powders, 97.32% densification was achieved in printed part by using sinter-assisted HIP (sintering for 5 h at 1075 °C + HIPing at 1075 °C for 2 h held at 206.8 MPa). Porosity in the as-sintered part decreased from 2.9% to 0.37% after HIP. Tensile strength and ductility of the printed part have also been improved [161]. 316L steels processed by L-PBF were subjected to HIP (1125 °C held for 4 h at 137 MPa + furnace cool for 4 h) to reduce the porosity by 1% when compared to as-built 316L steel. Whereas the young modulus and yield strength of the sample increased by 3% and 3.4%, respectively after HIP [162]. SLM manufactured Ti6Al4V alloy have shown better fatigue property with moderate microhardness when subjected to a different heat treatment cycle (stress relieving at 704 °C + HIPing at 920 °C held for 2 h at 120 MPa + furnace cooling for 3.5 h) [163]. Interestingly, for the same Ti6Al4V alloy when processed by electron beam welding, a different heat treatment cycle (HIPing at 1120 °C held for 30 min at 100 MPa + rapid quenching) was employed. For Inconel 718, HIPing at 1120 °C held for 2 h with a pressure 100 MPa has influenced the microstructural development to achieve desired mechanical properties [164].

## *6.2 Solution Treatment (ST)*

Solution treatment (ST), a process where the metal alloy is heated to a specific temperature to form a solid solution in which the elemental constituents and intermetallics

get dissolved and diffused homogenously inside metal structure. The process ends by quenching to retain the metastable structure [165]. ST can play a vital role in material qualification process of gas atomized Al 6061 as a feedstock powder for AM. The chemistry and microstructure of Al 6061 powder was modified by solution treating for 60 min. A significant reduction in the secondary phase ($Mg_2Si$) improved the powder characteristics thus making it suitable for AM [166]. For SLM processed AlSi10Mg solution treatment (520 °C for 2 h) followed by water quenching and then artificial aging (160 °C for 10 h), have significantly improved the material hardness [167]. In contrast, a similar work performed by Aboulkhair et al., reported that the heat treatment has shown a negative effect in the SLM processed AlSi10Mg by reducing its tensile strength, compressive strength, nano and micro hardness of the material [16]. This indicates the existing gap in the knowledge of heat treatments for AM parts and calls for comprehensive research to develop heat treatment cycles. When solution treatment was applied to SLM processed SS 316 and laser direct energy deposited SS 316, the micro hardness value decreased with increase in the temperature was reported for both the cases. This is due to reduction in the dislocation density and increase in the grain size [109, 168]. WAAM processed Al6.3Cu alloy (referred as WAAM 2219) was subjected to solution treatment (535 °C for 90 min) followed by water quenching and then artificial aging (175 °C for 3 h) followed by furnace cooling. After heat treatment, due to precipitation hardening, the ultimate tensile strength and yield strength of the WAAM processed AL6.3Cu alloy have significantly improved [169]. In the case of 2024 aluminum alloy processed by WAAM, solution treatment was performed for three different temperatures (ST1-485 °C, ST2-498 °C, and ST3-503 °C) each with soaking time 90 min followed by water quenching and then subjected to natural aging for 2 days. Microhardness, tensile and elongation have increased with an increase in the temperature [170].

### *6.3 Annealing*

Annealing involves in softening of a metal by heating it to a specific temperature and holding it for a time period and then cooling down very slowly inside furnace to relieve internal stresses, to enhance ductility, to improve toughness and to tune the microstructure of material as desired [64]. Recovery (stress relieved as dislocations rearrange themselves with retaining the grain shape and alignment), recrystallization (new strain-free grains nucleates and grow to replace old grains) and grain growth (recrystallized grain continuous to grow due to long annealing which results in coarse grain microstructure) are the three processes of annealing [171]. In Ti6Al4V AM part, the modified annealing heat treatment (600 °C or 800 °C for 2 h in argon gas environment + furnace cooling) resulted in stress relieving from martensitic phase and enhanced the corrosion resistance by forming β-phase BCC structure [172]. 316L SS processed by SLM with low porosity was annealed (1095 °C for 1 h in argon gas environment + furnace cooling) and stress relieved (700 °C for 1 h). Annealing enhanced the ductility but showed an adverse effect in the ultimate tensile strength

and yield strength when compared to as-built SLM 316L SS [77]. Hardness variations due to the impact of dislocations evolved during annealing (1200 °C for 40 min in air filled furnace + natural cooling) was reported for SLM processed 316L SS. Geometrically necessary dislocations ruled the hardness of 316L SS sample indicating the dominance of dislocation strengthening [173]. AM Maraging steel when subjected to solution annealing (820 °C/1 h and 940 °C/2 h in argon gas environment + furnace cooling) and precipitation hardening (250–550 °C with soaking time 0–6 h), its hardness decreased by 11% while the elongation increased by 21% as compared to as-built [174]. In a feasibility study of producing $Ti_2AlNb$ alloy by binder jetting, the as-built greener part was sintered (1100 °C for 6 h in vacuum) and annealed (1400 °C for 2 h in vacuum). Annealing has significantly improved the densification by 40% and formed a microstructure consisting of B2-phase with needle-shaped $Ti_2AlNb$ precipitates [175]. AlCoCrFeNi high entropy alloy processed by binder jetting was annealed (1000 °C and 1200 °C for 2 h in air + water quenching). For higher annealing temperature (1200 °C), yield strength (1461 MPa) and fracture toughness (2272 MPa) significantly improved [176]. In a recent work, a hybrid AM (SLM/DED) was proposed to fabricate Inconel 718 where solution annealing (1010 °C for 1 h in argon atmosphere) prior to aging was applied to dissolve the lava phase for better mechanical properties [177].

## *6.4 Tempering*

Tempering heat treatment becomes essential after quench hardening in order to rule out the cracks and residual stresses developed in the hardened material. It improves the toughness of the hardened materials. There are three ranges of temperature at which tempering is usually carried out. Low temperature tempering (200 °C—hard martensite microstructure is retained), moderate temperature tempering (275 °C—transforms to troostite microstructure) and high temperature tempering (375 °C—transforms to sorbitic microstructure) [64]. H13 tool steel manufactured by AM, after stress relieving, was subjected to hardening (1020 °C for 75 min, nitrogen quench) and double tempering (585 °C for 3 h). The heat treatment has no effect in the porosity, but improved the yield strength by 25% and ultimate tensile strength by 26% with an elongation drop of 3.3% [178]. Hardness of H13 processed by SLM decreased with increase in tempering temperature when subjected to quenching and tempering heat treatment [179]. Performing an isothermal tempering (650 °C for 36 min) for maraging steel processed by SLM have achieved 78% martensite-austinite conversion with stability to promote ductility and toughness [180]. Plasticity of SLM processed Alsi10Mg was improved by 2.8 times with 40% decrement in strength when tempered at 200 °C for 5 h followed by air cooling for 5 h [181]. The anisotropic nature of as-built WAAM nickel aluminum bronze (NAB) alloy, after homogenization for 900 °C for 2 h, was water quenched and tempered at different temperatures (450, 550, 650 & 750 °C). Anisotropy modified while increasing tempering temperature. Precipitation strengthening is achieved till 650 °C, further any increase in temperature

shows adverse effect [182]. 9Cr steel processed by WAAM was subjected to normalizing (1050 °C for 40 min + air cooling) and at different tempering temperatures (710 °C, 760 °C and 810 °C for 2 h + air cooled). For high tempering temperature, precipitation hardening was dominated by solid solution and dislocation hardening and thus results in low hardness and strength value. However, the sample exhibits high toughness. It is suggested to go with 1050 °C and 760 °C for normalizing and tempering respectively for yielding good strength and ductility [183].

## *6.5 Peak Hardening*

Peak hardening also referred as T6 heat treatment which comprises three stages starting with solution heat treatment (ST) followed by quenching and then by aging, can be employed to the AM part in order to improve their mechanical properties. At first, the material is solution treated at high temperature (near to eutectic temperature) to dissolve all soluble phases (Cu, Mg, etc.,), to homogenize the alloying elements and spheriodize the silicon particles. Second stage involves quenching, which will retain the solutionized phase and resist the precipitation. In the third stage, aging either natural aging (at room temperature) or artificial aging (at 210 °C) is carried to achieve precipitation strengthening of alloys by even distribution of precipitates [184]. Fatigue resistance of AlSi10Mg alloy manufactured by SLM was improved by performing a combined heat treatment of peak hardening (T6) and heating the built plate to 300 °C. Post heat treatment effect (ST at 525 °C for 6 h + water quench + artificial aging at 165 °C for 7 h) was dominant than the built direction (0°, 45° and 90°) on fatigue resistance of the sample [185]. A modified T6 heat treatment (ST at 540 °C for 8 h + water quenching + tempering at 20 °C/1 day and 160 °C/10 h) was applied to SLM processed AlSi10Mg alloy and observed improvement in the fatigue resistance after peak hardening [186]. Additively manufactured A357 aluminum alloy was subjected to stress relieving and peak hardening heat treatment. Ductility improved by stress relieving (300 °C for 2 h) while peak hardening (ST at 530 °C for 5 h + aging at 170 °C for 3 h) improved the yield strength with comparable microhardness to the as-built sample [187]. T6 conditioned AlSiMg alloy have shown a good combo of strength and ductility resulting from precipitation strengthening caused by excessive Mg content irrespective of their loss in the course of SLM [188]. All the aforementioned post processing heat treatments have been witnessed to promote the quality of additively manufactured materials by eliminating the process-built defects like pores and cracks. In the following sections, more detailed investigation was provided on the effect of heat treatment with respect to microstructure and mechanical properties of additively manufactured materials.

## 7 Effects of Post Processing Heat Treatment on Microstructure Development of AM Materials

In general, for any metal, the phase transformation process plays a crucial role in yielding supreme mechanical properties by controlling the microstructure of the metal. Therefore, it's very essential to understand the microstructure development in AM material in the as-built condition and post heat treatment. The SLM processed Inconel 718 exhibits fine columnar dendritic microstructure in its as-built condition which resulted from high thermal energy and fast cooling rate (10 °C/s) during the process. After heat treatment (HIP + ST + double aging), all fine dendrites disappeared and resulted in formation of equiaxial columnar grain structure [119]. Figure 6 shows the SEM micrograph of Inconel 718 in as-built and post heat treatment.

For binder jetted Inconel 718, austenite phase microstructure with low porosity was obtained when fine feedstock powder (7 μm) was utilized. After sintering at 1290 °C and 1330 °C with holding time as 5 h for each, microstructure (for feedstock particle size 7 and 21 μm) with uniform equiaxed grains with boundary decorated with metal carbides and annealing twins was observed. For AM sample made from 70 μm particle size, the same heat treatment resulted in a different microstructure constituting carbides, δ and laves. This indicates that particle feedstock size affects the sintering process and thus influence the microstructure formation in binder jetting [134]. With the case of Inconel 625, a homogenous microstructure with large pore size was reported for the as-built binder jetted sample. After heat treatment (Sintering + HIP), an austenite phase microstructure with the presence of annealing twins was noticed with reduced pore size [133]. For WAAM processed Inconel 625, the microstructure of the as-built AM sample has shown brittle laves phases. After heat treatment (Annealing + water quenching), a phase transformation to Ni-Cr enriched γ-matrix was observed. Presence of metal carbides and undesired δ-phases were also reported and found to increase with increase in the heat treatment time [189]. Hard

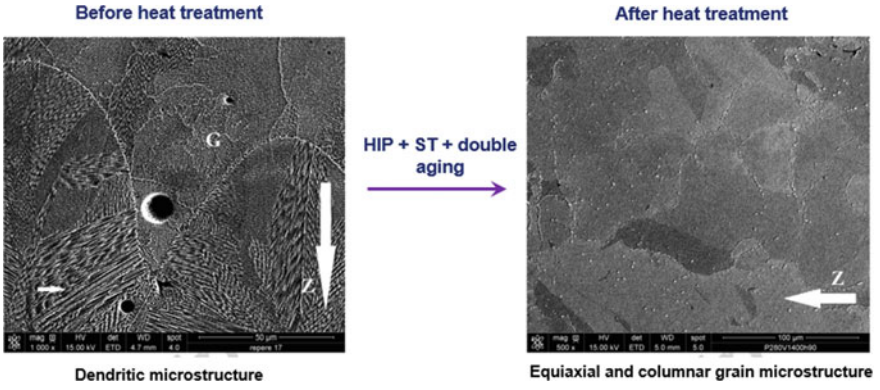


**Fig. 6** SEM micrographs of Inconel 718 before and after heat treatment (G—columnar cell structure, Z- built direction) [119]

to weld γ' nickel-based superalloy (RENE 108) has shown spherical pores in the sub-surface of the as-built AM sample indicated by the formation of primitive lines. The AM sample was subjected to HIP + ST + double aging heat treatment. After heat treatment, coarse γ' phase distribution in the microstructure was obtained for sub-solvus (1200 °C/2 h) and fine uniform & cuboidal γ' precipitates were obtained at super-solvus (1245 °C/2 h) temperature [37]. Figure 7 shows the microstructure of RENE 108 in as-built and post heat treatment condition.

The most commonly used 316L stainless steel has shown a coarsen microstructure with large grains in its as-built state when binder jetted. After sintering at 1300 °C for 90 min, a homogeneous microstructure with low porosity was attained [129]. In 316L steel processed by SLM, austenite phase is observed in both the as-built and annealed specimen indicating that the heat treatment has no influence in phase transformation. The typical cellular microstructure formed in the SLM component retained still 873 K and then vanishes with no trace at 1273 K. Further annealing to1673 K, microstructure coarsen and leads to pore formation (Refer to Fig. 8) [190].

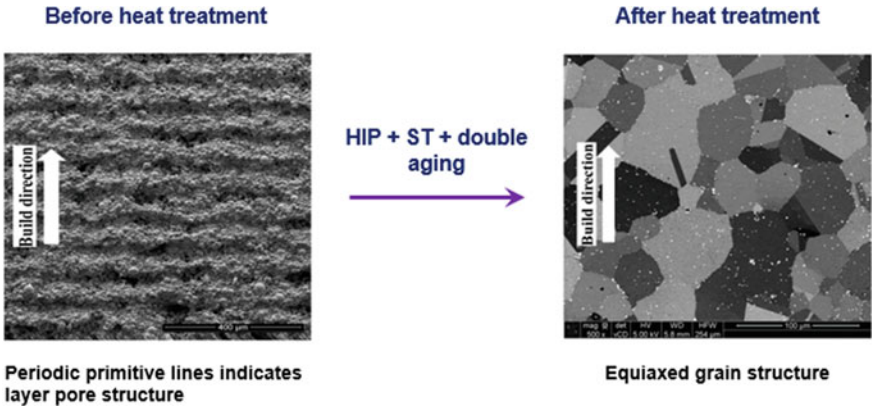


**Fig. 7** SEM micrographs of RENE 108 before and after heat treatment [37]

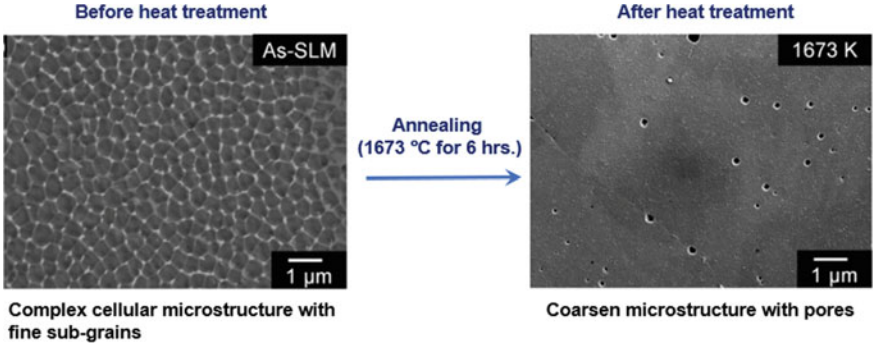


**Fig. 8** SEM micrographs of 316L steel before and after heat treatment [190]

Similarly, with H13 tool steel processed by SLM an austenite phase with an elongated grain structure having decorated with coarser carbides was observed in the as-built AM sample. Effect of heat treatment was investigated in two modes. First, stress relieving (SR) followed by hardening and tempering (HT) was performed in which a phase transformation from austenite to martensite with fine carbides was observed. Second heat treatment involves SR + HIP + HR. The microstructure was similar to the previous heat treatment indicating that HIP has no effect [178]. For maraging steel, the microstructure of as-built AM sample constitutes austenite phase with typical cellular structure when processed by SLM. From the substructure, polyhedral grains with high dislocations were observed. Further, the presence of finer spherical and sharp-edge particles was also confirmed. After annealing at 820 °C, austenite phase transformed into lath microstructure with 23% austenite retention when followed by precipitation hardening at 550 °C with 6 h hold time [174]. An investigation on microstructure evolution of WAAM processed 2Cr13 steel has revealed that the as-built AM sample contains a combination of martensite and ferrite microstructure instead of a complete martensite microstructure as observed in conventional 2Cr13 steels. Here, the formation of ferrite from martensite was induced by the in-situ micro-tempering phenomena of the deposition process in the WAAM [149]. Ti-6Al-4 V has observed to possess a martensite phase ($\alpha'$) with needle-shape structure in its as-built condition pertaining to quick solidification and cooling nature of the SLM process. This instable phase may weaken the material against corrosion and thus it should be heat treated. By annealing, a phase transformation from HCP martensite phase to BCC β phase occurs due to stress relieving and improves the resistance to corrosion [172]. Figure 9 shows the microstructure evolution of Ti-6AL-4 V in as-built and post heat treatment condition.

Notably, the same SLM processed Ti-6Al-4 V AM sample when subjected to a different heat treatment (SR + HIP + Furnace/air cooling), a similar phase transformation from martensite ($\alpha'$) into coarse-grain lamellar α + β microstructure (for furnace cooling) and $\alpha'$ + α combined microstructure (for air cooling) was reported [163]. The microstructure of binder jetted Ti-6Al-4 V exhibits lamellar, near-equiaxed α-phase and intergranular β-phase for a low sintering temperature. As

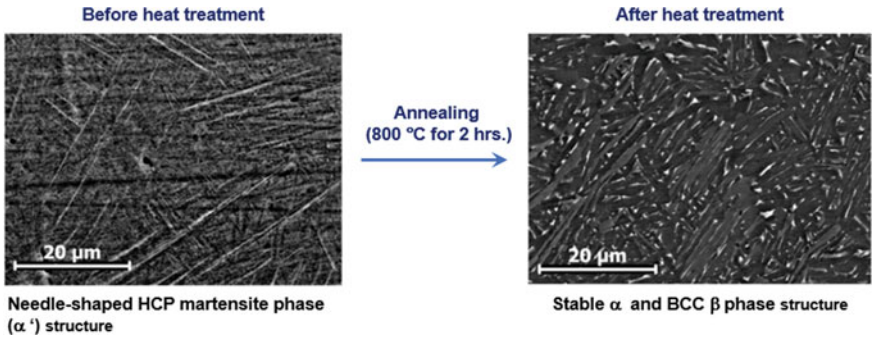


**Fig. 9** SEM micrographs of Ti-6Al-4 V before and after heat treatment [172]

the sintering temperature increases to 1460 °C, lamellar transforms to near-equiaxed α-phase microstructure with precipitates of 'V' and 'Al' rich elements was witnessed [191]. In WAAM processed nickel aluminum bronze (NAB) alloy, the microstructure of the as-built AM sample contains widmanstatten pattern of fine α and martensite phases. After heat treatment (annealing at 675 °C for 6 h) dissolves the existing widmanstatten α and martensite into fine homogeneous microstructure of α-phase and k precipitates. This refined microstructure will help in tailoring the mechanical properties [152]. Aluminum alloy 2024 when processed by WAAM, the microstructure of the as-built AM sample have shown the formation of predominant α-Al matrix along with θ phase and S phase. After solution treatment (ST) at 503 °C followed by natural aging, the microstructure exhibited α-Al matrix with θ eutectic phase, which significantly progress the mechanical properties. It was observed that the secondary phase distribution increased with increase in the ST temperature [170]. Al6.3Cu alloy when processed by WAAM has shown microstructure with α-Al and θ phase having fine dendritic and equiaxed grains. After heat treatment (ST followed by water quench + artificial aging followed by furnace cooling), dendrites were reduced and more equiaxed grains were observed. Similar to 2024 aluminum alloy, performing solution treatment for Al6.3Cu AM sample dissolved the secondary phases with distributing characteristics within the matrix [169].

## 8 Effects of Post Processing Heat Treatment on Mechanical Properties of AM Materials

AM materials with topnotch quality can be custom-made by tailoring their properties via heat treatments. Understanding the role of heat treatments in the evolution of mechanical properties become more important as they are inevitable in the process chain of additive manufacturing. In this section, the effect of heat treatments on mechanical properties of AM materials are discussed in detail. Heat treatments may not be the same as we handle with conventionally manufactured materials. Say for example, with the case of 316L steel processed by SLM, the as-built specimen has shown good strength and ductility than the annealed specimen. Further, annealing with high temperature has shown an adverse effect in the mechanical properties indicating that the conventional heat treatments need modifications when dealt with AM materials [190]. Binder jetted 316L steel when subject to sintering at 1300 °C for 90 min has shown good mechanical properties. The microhardness of the AM samples prepared by using fine powder and large powder are reported to be 90 HV and 30 HV respectively. Enhanced sintering kinetics observed in the green part with fine particles reduce the porosity and yield high microhardness. For large particles, weak sintering kinetics resulted in high porosity which ultimately reduced the microhardness [129]. WAAM processed 2Cr13 steel has shown betterment in ultimate tensile strength with a maximum value of 1450 MPa in the as-built state, which is nearly 61% higher than the conventionally produced 2Cr13 steel. The main reason

for such a remarkable result is due to the attainment of high densification between two deposited adjacent layers with no structural defects and martensite refinement inside ferrite matrix [149]. The microhardness of the SLM as-built Inconel 718 was measured in between 310 and 334 HV. Remarkably, the microhardness value improved and measured between 461 and 492 HV, by adopting a combination of heat treatment (HIP + Solution treatment + double aging). HIP reduced the porosity while the solution treatment and aging improved the hardness via precipitation hardening ($\gamma'$ phase & $\gamma''$ phase precipitates into the matrix) [119]. Binder jetted Inconel 625 alloy when built in the x-direction has shown mechanical properties that are equivalent to conventionally manufactured Inconel 625. The ultimate tensile strength, yield stress and young modulus of AM sample built in the x-direction are 0.707 GPa, 0.32 GPa and 0.524 GPa respectively. This suggests the opportunity for powder-bed technologies to integrate with manufacturing companies in metal fabrication in near future [133]. WAAM Inconel 625 alloy in its as-built condition has shown the tensile strength, yield strength and microhardness as 658 MPa, 373 MPa and 220 HV respectively. After annealing (980 °C/2 h), tensile strength and yield strength were significantly improved by 5% and 6.4% respectively. Grain-boundary precipitation of carbides and δ phases controlled the behavior of tensile strength in the AM sample [192]. Binder jetted RENE 108 nickel-based superalloy when subjected to heat treatment (HIP + ST + double aging), has shown 15% and 20% enhancement in yield strength and tensile strength respectively. Precipitation of carbides and oxides controls the grain refinement and thus influences the mechanical properties. For low temperature, the strength and ductility of BJ RENE 108 were higher with showing a transgranular mode of deformation [37]. The mechanical properties of as-built maraging steel are found superior than the heat-treated samples. Annealing at 820 and 940 °C followed by precipitation hardening at 540 °C with 6 h hold time, drastically reduced the strength of the material due to austenite retention. As an effect of hat treatment, hardness was reduced by 11% but elongation was improved by 23% [174]. For SLM processed H13 tool steel, the mechanical properties like hardness, young modulus, and yield strength are measured to be 894 ± 48 HV, 190 GPa, and 1236 ± 178 MPa respectively [193]. After heat treatments (SR + HT& SR + HIP + HT), yield strength and ultimate strength of the AM sample have improved by 25% and 26% respectively. However, the hardness value of the AM sample decreased after heat treatment. HIP has no effect in the porosity but improved the mechanical properties significantly [178]. With the case of Ti-6Al-4 V processed by SLM, the microhardness of the as-built measured to be 408 HV decreased to 364 HV when heat treated (SR + HIP + Air/Furnace cooling). However, the fatigue property of the heat-treated AM sample has shown betterment when compared to as-built pertaining to the presence of more ductile β phase [163]. For binder jetted Ti-6AL-4 V, the microhardness obtained was reported to be 316 HV after sintering at 1460 °C for 2 h. A maximum sintered density of 95.2% was achieved. The compressive strength and yield stress obtained for this binder jetted AM sample are reported to be 1021 MPa and 589 MPa respectively. Notably, the compressive strength obtained here is 4.5% higher than the conventionally casted titanium alloys [191]. WAAM processed nickel aluminum bronze (NAB) AM sample have shown poor mechanical properties like

microhardness, ultimate tensile strength, and yield strength as 181 HV, 35 MPa, and 26 MPa respectively. This is mainly due to insufficient heat input and cooling rate during the WAAM process. After heat treatment, a significant improvement in the mechanical properties was observed due to grain refinement and precipitation hardening. Microhardness, ultimate tensile strength, and yield strength were observed to be 210 HV, 342 MPa, and 653 MPa respectively [152]. Solution treatment (ST) followed by natural aging have significantly enhanced the mechanical properties of WAAM processed 2024 aluminum alloy. In as-built condition, the values of microhardness, ultimate tensile strength and yield strength are measured to be 95 HV, 284 MPa, and 177 MPa respectively. The microstructural modification after heat treatment especially for ST at 503 °C, has significantly enhanced the mechanical properties. Microhardness, ultimate tensile strength, and yield strength are obtained as 143 HV, 497 MPa, and 330 MPa respectively. Increase in ST temperature increased the secondary phase distribution within the microstructure [170]. When the ST + artificial aging heat treatment is applied to WAAM processed Al6.3Cu alloy, the microhardness improved from 68.3 HV to 144.5 HV. Tensile strength and yield strength were improved from 206 to 300 MPa and 125 MPa to 450 MPa respectively. However, the elongation has shown a decreasing trend upon heat treatment. Precipitation hardening is the main strengthening mechanism. Inter-layer rolling is recommended to further improve the mechanical properties as it causes grain refinement [169]. Table 6 presents the summary of AM methods, materials processed, choice of post-processing heat treatment, microstructure and mechanical properties along with research insights.

## 9 Challenges and Recommendations for Additive Manufacturing

Despite the potential benefits offered, there are still considerable challenges associated in additive manufacturing with respect to raw materials quality and suitability, processing methods to print 3D components, and appropriate heat treatments to configure the microstructure in order to attain the desired mechanical properties.

Powder feedstock characteristics (size, morphology, composition, flowability, etc.) should be accounted with utmost care while working on powder-bed-fusion technologies. Powder quality determines the product quality. Water atomization technique is not preferred for producing AM feedstocks, as it has certain limitations like only non-reactive materials can be used, produce irregular particles, and forms surface oxide contaminations. Hence, gas atomization is recommended as it has the ability to reduce oxidation risk, produce spherical particles, handle both reactive & non-reactive materials, and noticeably inert gas (argon/nitrogen) can tune the microstructure development to yield desired properties [4]. Powders with near-to-sphere morphology, monodispersed and agglomerate-free are highly recommended for use as AM feedstock since they can provide efficient energy absorbtion, stability

**Table 6** Summary of AM methods, material processed, choice of heat treatments, microstructure and mechanical properties

| S. No | AM Process | Material processed | Heat treatment type | Process profile | Microstructure | | Mechanical Property | | Research observations | References |
|---|---|---|---|---|---|---|---|---|---|---|
| | | | | | As-built | Post heat treatment | As-built | Post heat treatment | | |
| 1 | Selective laser melting (SLM) process | Nickel alloy Inconel 718 | Hot isostatic process (HIP) + Solution treatment (ST) + Double aging | **HIP:** 1160 °C, 102 MPa, 3 h & air cooling; **ST**: 980 °C, 1 h & air cooling; **Double aging:** 720 °C, 8 h & furnace cooling + 620 °C, 8 h & air cooling | Fine dendritic columnar microstructure was observed | Equiaxial columnar grains was observed | Microhardness was measured between 310 and 334 HV | Microhardness improved and measured between 461 HV and 492 HV | HIP reduced the porosity; Solution treatment & aging induced precipitation hardening | [119] |
| 2 | | 316L Stainless steel | Annealing in argon atmosphere followed by furnace cooling (FC) + stress relieving (SR) | **Annealing:** 1095 °C, 1 h & FC; **SR:** 700 °C for 1 h | Fine columnar dendritic microstructure was observed | Coarse grain microstructure was observed | Microhardness—325 HV; UTS 705 ± 15 MPa; Yield strength—590 ± 17 MPa | **After annealing:** Microhardness—200 HV, UTS—635 ± 17 MPa, Yield strength 375 ± 11 MPa **After SR:** Microhardness 300 HV | Porosity increases with increase in the scan speed, Annealing improved the ductility of the AM material but decreased its yield strength | [77] |
| 3 | | Maraging steel | Solution Annealing in argon atmosphere followed by furnace cooling (FC) + Precipitation hardening | **Annealing**: 820 °C, 1 h & FC; 940 °C, 2 h & FC; **Precipitation hardening:** 250 °C—550 °C for 0–6 h | Cellular microstructure with fine grain austenite phase was observed; Substructure shown polyhedral grains with dislocations; Fine spherical & sharp-edge particles were also seen | Lath microstructure was observed for annealing at 940 °C; Austenite phase reverted by 23% and 15% in AM sample for annealing at 820 °C & 940 °C with 6 h of precipitation hardening | Hardness—371 ± 2 HV, UTS—955 ± 7 MPa, YTS—815 ± 5 MPa | **Annealing at 820 °C** Hardness—330 ± 1 HV, UTS—943 ± 3 MPa, YTS—758 ± 7 MPa; **Annealing at 940 °C** Hardness—318 ± 3 HV, UTS—929 ± 5 MPa, YTS—729 ± 9 MPa | Hardness decreased by 11% and elongation improved by 21% for the heat-treated material | [174] |

(continued)

**Table 6** (continued)

| S. No | AM Process | Material processed | Heat treatment type | Process profile | Microstructure | | Mechanical Property | | Research observations | References |
|---|---|---|---|---|---|---|---|---|---|---|
| | | | | | As-built | Post heat treatment | As-built | Post heat treatment | | |
| 4 | | H13 tool steel | **Case 1:** Stress relieving (SR) + Hardening followed by tempering (HT) **Case 2**: Stress relieving (SR) + HIP + Hardening followed by tempering (HT) | **SR**: 650 °C for 8 h; **Hardening:** 1020 °C for 75 min nitrogen quenching; **Tempering:** 585 °C for 3 h **HIP:** 1130 °C, 100 MPa, 6 h | Austenite phase with elongated grains decorated with coarser carbides was observed | Martensite with fine carbides was observed | Hardness—894 ± 48 HV, Young modulus—190 GPa, Yield Strength—1236 ± 178 MPa | **SR + HT:** Hardness—515 HV, Young modulus—191 to 199 GPa, Yield Strength—1447 MPa **SR + HIP + HT**: Hardness—560 HV, Young modulus—191 to 199 GPa, Yield Strength—1502 MPa | Heat treatments have improved the yield strength and ultimate tensile strength by 25% and 26% respectively but reduced the hardness of the AM material, HIP has no effect in reducing the porosity | [178, 193] |

(continued)

**Table 6** (continued)

| S. No | AM Process | Material processed | Heat treatment type | Process profile | Microstructure | | Mechanical Property | | Research observations | References |
|---|---|---|---|---|---|---|---|---|---|---|
| | | | | | As-built | Post heat treatment | As-built | Post heat treatment | | |
| 5 | | Al-5Si-Cu-Mg aluminum alloy | Solution treatment (ST) followed by water quench (WQ) & Solution treatment (ST) followed by water quench (WQ) + artificial aging (AA) followed by air cooling (AC) | **ST:** 450 °C/6 h, 500 °C/6 h, 550 °C/6 h followed by WQ for each set **AA:** 180 °C/ 12 h followed by AC | Bimodal, columnar & equiaxed a-Al phase with grain boundary surrounded by eutectic Si-phases | Microstructure with Q-Al5Mg8Si6Cu2 phase & plate like β-Al5FeSi phase were found after ST; β" phase and C phase were observed after subsequent aging | UTS—223 MPa, Yield strength—99 MPa, Elongation—12.1% | UTS—416 MPa, Yield strength—316 MPa, Elongation—15.2% | Maximum tensile ductility (22.4%) was achieved for high ST temperature (550 °C) and also strength increased by precipitation hardening | [111] |
| 6 | | Ti-6Al-4 V alloy | Stress relieving (SR) + HIP + Furnace /Air cooling | **SR**: 704 °C for 2 h **HIP**: 920 °C, 120 MPa, 2 h **Furnace/Air cooling:** 3.5 h | Needle shaped martensite (α) microstructure was observed | Coarse-grain lamellar (α + β) microstructure (for furnace cooling) and (α' + α) mixed microstructure (for air cooling) was observed | Hardness—408 HV | Hardness—364 HV | Improved fatigue property with low microhardness due to the presence of ductile β phase | [163] |

(continued)

**Table 6** (continued)

| S. No | AM Process | Material processed | Heat treatment type | Process profile | Microstructure | | Mechanical Property | | Research observations | References |
|---|---|---|---|---|---|---|---|---|---|---|
| | | | | | As-built | Post heat treatment | As-built | Post heat treatment | | |
| 7 | Binder jetting (BJ) process | RANE 108—nickel based super alloy | HIP + Solution treatment (ST) + double aging | **HIP:** Not available **ST:** 1200 °C, 2 h (Sub-solvus), 1245 °C, 2 h (Super-solvus) **Double aging:** 1080 °C, 4 h & 870 °C, 4 h | Microstructure with spherical pores in sub-surface were observed (indicated by formation of primitive lines) | Coarse γ' phase distribution was observed for sub-solus heat treatment; For super-solvus, uniform & cuboidal γ' precipitates was observed | NA | Yield strength and tensile strength have improved by 15% and 20% respectively when compared to conventional alloy | HIP improved densification by 99.5%, Carbides (Ta) & oxides (HFO) precipitated in particle grain boundary and have influence in microstructure & mechanical properties | [37] |

(continued)

**Table 6** (continued)

| S. No | AM Process | Material processed | Heat treatment type | Process profile | Microstructure | | Mechanical Property | | Research observations | References |
|---|---|---|---|---|---|---|---|---|---|---|
| | | | | | As-built | Post heat treatment | As-built | Post heat treatment | | |
| 8 | | Inconel 625 nickel alloy | Sintering + HIP | **Sintering:** 1310 °C for 16 h **HIP:** 1163 °C, 102 MPa, 3 h | Homogenous microstructure with large pore size was noticed | Austenite phase microstructure with annealing twins was observed | NA | **UTS**—0.707 ± 0.012 GPa (X direction), 0.708 ± 0.022 GPa (Y direction); **Yield stress**—0.32 ± 0.014 GPa (X direction), 0.39 ± 0.002 GPa (Y direction); **Modulus of elasticity**—0.524 ± 0.047 GPa (X direction), 0.506 ± 0.051 GPa (Y direction) | Binder acted as the source for oxygen content and resulted in the formation of oxide layer; High chromium content resulted in the formation of surface oxide layer; No support structure is used for building parts | [133] |
| 9 | | 316L Stainless steel | Sintering + Furnace cooling | **Sintering:** 1300 °C for 90 min | Microstructure with coarse grain size was observed | Homogeneous microstructure with low porosity (for feedstock with fine particle) was observed | NA | Microhardness—90 HV (14 micron meter)—36 HV (78 micron meter) | Fine powder particles yielded good mechanical properties; Large powder particles favored the design accuracy and green sample density | [129] |

(continued)

**Table 6** (continued)

| S. No | AM Process | Material processed | Heat treatment type | Process profile | Microstructure | | Mechanical Property | | Research observations | References |
|---|---|---|---|---|---|---|---|---|---|---|
| | | | | | As-built | Post heat treatment | As-built | Post heat treatment | | |
| 10 | | Ti-6Al-4 V alloy | Sintering + air cooling | **Sintering:** 1460 °C for 2 h | Microstructure with lamellar, near-equiaxed α-phase and intergranular β-phase grains were observed | More near-equiaxed α-phase microstructure with V and Al rich precipitates was observed | NA | Microhardness—316 HV; Compressive stress—1021 MPa; Yield stress—589 MPa | Maximum sintered density of 95.2% was achieved; Compressive strength of green part increased with increase in the capillary force of powder bed | [191] |
| 11 | Wire arc additive manufacturing (WAAM) | Inconel 625 nickel alloy | Annealing + water quenching | **Annealing:** 980 °C for 30 min, 1 h, 2 h & water quenching | Brittle laves phase microstructure was observed | Microstructure constitutes of Ni-Cr enriched γ-matrix as major phase; Metal carbides & undesired d phase were also observed | Tensile strength—658 ± 4 MPa, Yield strength—373 ± 5 MPa, Microhardness—220 HV | Tensile strength—688 ± 4 MPa, Yield strength—397 ± 15 MPa, Microhardness—235 HV | Annealing (2 h) significantly improved the mechanical properties, Nb, No & secondary phase ruled the tensile strength, Ultimate tensile strength improved by 5% | [189, 192] |

(continued)

**Table 6** (continued)

| S. No | AM Process | Material processed | Heat treatment type | Process profile | Microstructure | | Mechanical Property | | Research observations | References |
|---|---|---|---|---|---|---|---|---|---|---|
| | | | | | As-built | Post heat treatment | As-built | Post heat treatment | | |
| 12 | | Nickel Aluminum Bronze alloy (NAB) | Annealing + air cooling | **Annealing:** 675 °C for 6 h | Widmanstatten α along with fine martensite was observed | Homogeneous microstructure of α-phase and k precipitates were formed | Microhardness—181 HV, UTS—35 MPa, Yield strength—26 MPa | Microhardness—210 HV, UTS—342 MPa, Yield strength—653 MPa | Widmanstatten pattern decomposes into homogeneous microstructure of fine α-phase and k precipitates | [152] |
| 13 | | Aluminum alloy 2024 | Solution treatment (ST) followed by water quench (WQ) + natural aging (NA) | Three set: ST1- 485 °C, ST2- 498 °C, and ST3- 503 °C each soaked for 90 min followed by WQ + NA for 48 h | Microstructure with predominant α-Al phase along with θ-phase and S phase was observed | Microstructure with α-Al with θ eutectic phase was observed | Microhardness—95 HV, UTS—284 MPa, Yield strength—177 MPa | Microhardness—143 HV, UTS—497 MPa, Yield strength—330 MPa | Solution treatment (at 503 °C) followed by natural aging have enhanced the hardness and tensile properties of WAAM 2024 | [170] |

(continued)

**Table 6** (continued)

| S. No | AM Process | Material processed | Heat treatment type | Process profile | Microstructure | | Mechanical Property | | Research observations | References |
|---|---|---|---|---|---|---|---|---|---|---|
| | | | | | As-built | Post heat treatment | As-built | Post heat treatment | | |
| 14 | | Al6.3Cu alloy | Solution treatment (ST) followed by water quench (WQ) + Artificial aging (AA) followed by furnace cooling (FC) | **ST:** 535 °C, 90 min followed by WQ **AA**: 175 °C, 3 h followed by FC | Microstructure with α-Al and θ-phase with fine dendrites and equiaxed grains was observed | Microstructure with reduced dendrites and more equiaxed grains were observed after heat treatment | Microhardness—68.3 HV, UTS—260 MPa, Yield strength—125 MPa, Elongation—16% | Microhardness—144.5 HV, UTS—300 MPa, Yield strength—450 MPa, Elongation—14% | Precipitation hardening is the main strengthening mechanism, inter rolling is recommended to improve tensile property via the formation of high-density dislocations and misaligned sub grains | [169] |

in melt-pool, increased layer thickness, fast scan speed (x–y horizontal direction), high built rate (z vertical direction), high production rate, and cutoff the production cost by nearly 50% [194]. For better flowability of powders, Hausner ratio (typical ratio value as 1) close to or less than one is recommended for AM feedstock [195]. Finer particles are pernicious to AM process as they tend to agglomerate easily and pose risk for safe handling. For SLM Inconel 625 and BJ Inconel 718, particle size less than 10 μm and 4 μm respectively, was not recommended for use [35, 134]. With the case of WAAM, using wire as additive will result in poor standard and low surface finish products. New wire materials should be developed by taking benefits from metal alloying for improved characteristics of wire feedstock. For a note Si and Mg elements, each with 4–5% by weight can be alloyed with aluminum wire. But, adding excess amount of alloy may invite hot cracking problem in the AM sample. This issue can be addressed by reinforcement of nanoparticles to wire feedstock which can possibly mitigate the crack formation and improves the strength of the as-built WAAM sample [196, 197]. Similarly in BJ, alloying of boron (0.5%) to 420 stainless steels can provide density enhancement. Also, adding nanoparticles of stainless steel to the powders of 410 SS and 316L steel can significantly improve the quality and density of the BJ AM sample [198, 199].

Process-related challenges are a major impediment that prevents AM from industrial implementation. Say, for example, the poor weldability nature in nickel-based alloys poses challenges when subjected to LPBF and direct energy deposition methods. To overcome this issue, binder jetting is recommended to process such hard-to-weld nickel-based alloys since the binder jetting process doesn't rely on heat source and liquid metal interaction for building a part [129]. This also indicates the presence of knowledge gap concerned with alloys development and their qualification for being processed by a particular AM technic. Whereas in binder jetting process, feedstock agglomeration with respect to splashing of binder (ink) and migration of excess ink beyond the predefined boundary, is a serious issue as this will deteriorate the quality of final part. Depowdering is another risky task that may cause surface damage to the printed part. Blended mode comprising of automation (pressurized air) and manual (soft brushes) could be a possible solution for handling mass and complex part production [200]. On the other hand, process parameters have shown a direct impact on part quality. For SLM, process parameters that include laser power source, part building direction, scan speed, scan hatch spacing, etc., are crucial for part quality. An insufficiency of laser power will cause poor melting of feedstock which will result in binding defect or balling. Laser power of 150 W, hatch distance of 0.07 mm, scan speed of 700 mm/s with build direction 45° (for maximum tensile strength) and 90° (for maximum elongation to failure) are recommended for 316L steel SLM AM sample [201]. Voids formation in the AM sample can be reduced by reducing the hatch distance, which in turn yields high densification, increased elongation, and high ultimate tensile strength [202]. In BJ process, position errors and saturation errors are observed to happen when there is a mismatch in droplet's exit angle and a volume shift in the droplet respectively. It is recommended to offset the position of the jet from layer after layer to eradicate the errors. The existence of knowledge gap in mapping out the dynamics behind the

binder droplet and powder interactions need to be addressed by developing computational simulations and experimental validations [128]. In WAAM process, the heat input is governed by supplied current, applied voltage and travel speed. Excess heat supplied may result in microstructure with coarse grain that leads to entrapment of gas and liquation. Also, porosity increases with increment in weld speed pertaining to elevated solidification rate [203]. Accumulation of heat in the AM sample during WAAM process is the root cause for structural failure. As the successive built layers increases, conduction of heat fluxes between them decreases which in turn enlarges the melt pool size and increases the interlayer temperature resulting in structural damage. To overcome this issue, convection mode of cooling via jet impingement is recommended to reduce the temperature built-up during WAAM process [204]. Also, the heat transfer in melt pool is ruled by convection mode of heat transfer. Reducing the heat input can yield rapid cooling rate. Solidification morphology can be figured by G/R ratio (thermal gradient to solidification rate). Selection of thick wire and maximal wire feeding rate are recommended for obtaining high deposition rate [196]. But high deposition rate in WAAM will arise undesired surface roughness and thus invites additional post-surface finishing operation which is time-consuming and not cost–benefit. It is recommended that the deposition rate should not exceed 4 kg/h and 1 kg/h for steels and aluminum/titanium alloys respectively to hold the buy-to-fly ratio below 1.5 [205].

Post-processing heat treatments are inevitable without which the process chain of AM would be incomplete. Most of the AM processed samples are prone to high porosity, process built internal stresses, anisotropic in behavior, and other structural defects. Though heat treatments became the prime choice to address many of these defects and improve the product quality, still there are certain challenges and knowledge gaps exist in adopting appropriate heat treatment for right material and right process. Say for example, annealing on SLM 316L AM sample has no influence in texture formation. Also, for high annealing temperature the strength of the AM sample decreased [190]. Instead of conventional annealing, it is recommended to perform intercritical annealing (IA) and/or deep cryogenic heat treatment (DCT) for 316L SLM AM sample to achieve homogeneous microstructure for better mechanical properties [206]. Post heat treatment have failed to retain the shape memory property of hard-to-process NiTi alloy processed by SLM via repetitive scanning strategy. When heat treated at high temperature (500–700 °C), NiTi elements agglomerated and resulted in coarser grain size along with poor martensite phase formation. To avoid particle agglomeration, dislocation formation, and strain-stimulated grain boundary movement, it is recommended to heat treat below 400 °C [207]. Stress relieving is not recommended for SLM processed AlSi material as it is witnessed to promote porosity pertaining to thermal softening occurred due to Si particles and $Mg_2Si$ particles precipitation [208]. Modifications in the existing heat treatments are essential for AM samples. For a note, traditional homogenization at 1050 °C will not be appropriate for WAAM process since it produces product with more heterogenous microstructure and anisotropic in nature. For P91 steel WAAM samples, modified homogenization (1200 °C for 2 h) is recommended to homogenize the microstructure and to eradicate the anisotropic effect for better mechanical properties [209].

Though sintering at high temperature can dramatically improve the part densification in BJ process, part deformation via volume shrinkage become a serious issue. Also, sintering process parameters will not be the same for all particle sizes. It is recommended to use bimodal and trimodal particle size distribution to belittle the volume shrinkage [142]. Numerical simulations and parametric optimization could provide solution to many existing issues by predicting phase composition, optimum parameters for AM process, microstructure evolution and mechanical properties. Discrete element method (DEM) and finite element method (FEM) can reasonably predict the powder behavior and part shrinkage respectively for LPBF technologies [210]. Calculation of phase diagrams (CALPHAD) in association with integrated computational materials engineering (ICME) could predict the phase composition leading to phase strengthening and microstructure development in HSLA steels [211]. COMSOL Multiphysics have proven to be capable to model the melt pool behavior and temperature effect to predict the influence on residual stress built on the AM sample [212]. However, the numerical models developed are capable for analyzing the thermo-mechanical behaviors of the AM processes, proper validation with the experimental results is mandatory.

## 10 Conclusion

In conclusion, the present scenario of additive manufacturing with respect to feedstock materials, processing methods in practice, and appropriate post processing heat treatments for microstructure evolution and mechanical properties was presented. Among the feedstocks, metals have been the most qualified and extensively utilized for 3D printing when compared to polymers and ceramics. The dominance of metallic materials in the AM was clearly witnessed via the escalating interest shown and the investment made by the industries in recent years for adopting metal additive manufacturing systems to produce parts. Powder quality and characteristics strongly influenced the 3D printed part quality. Metal powders produced via gas atomization, plasma rotating electrode and mechanical alloying have been revealed to be better in quality (high dense, less porosity, etc.) and in characteristics (fine size, spherical morphology, flowability, etc.). Selective laser melting, binder jetting and wire arc additive manufacturing have been reported to be the prime choice for processing most of the metals and alloys of aluminum, titanium, and nickel. The processing capacity of SLM, BJ and WAAM have also been extended for handling high entropy alloys and nanocomposites, and hence more industrial interest in recent days. Process parameters associated with each AM process that holds the key for achieving supreme quality and good surface finish were highlighted. Common defects occurred in the as-built AM parts and their root causes were also outlined. Post-processing heat treatments that are suitable for specific AM route and the corresponding processed metals were discussed with suitable examples. Importantly, thermal profile of all post-processing heat treatments and their effect in tunning the microstructure and in tailoring the mechanical properties of the AM parts were revealed. Modification in

microstructure and mechanical properties before and after post-processing heat treatments were mapped and presented along with the research insights for the benefit of the research community. Present challenges with respect to feedstocks, AM process implementations, and appropriate post-processing heat treatments for improving the product quality were addressed and possible solutions to overcome those issues were recommended.

**Declaration of Competing Interest** The authors declare that they have no competing financial interests or personal relationships that could have appeared to influence the work reported in this paper.

## References


1. Butt J (2020) Exploring the interrelationship between additive manufacturing and Industry 4.0. Designs 2020 4:13. https://doi.org/10.3390/designs4020013
2. Wohlers A (2020) Wohlers report 2020, 3D printing and additive manufacturing state of the industry. Annual Worldwide Progress Report, Wohlers Associates: Fort Collins, CO
3. Milewski JO (2017) Additive manufacturing of metals. In: From fundamental technology to rocket nozzles, medical implants, and custom jewelry. Springer Series in Materials Science, vol 258, 1st edn. Springer International Publishing AG, Cham, Switzerland, pp 134–157.
4. Herzog D, Seyda V, Wycisk E, Emmelmann C (2016) Additive manufacturing of metals. Acta Mater 117:371–392. https://doi.org/10.1016/j.actamat.2016.07.019
5. Wohlers T, Campbell I, Diegel O, Huff R, Kowen J (2017) 3D printing and additive manufacturing state of the industry. Annual Worldwide Progress Report, Wohlers Associates, Lund University, Lund, Sweden
6. Jasiuk I, Abueidda DW, Kozuch C, Pang S, Su FY, McKittrick J (2018) An overview on additive manufacturing of polymers. JOM 70:275–283. https://doi.org/10.1007/s11837-017-2730-y
7. Harrison N, Field JR, Quondamatteo F, Curtin W, McHugh PE, Mc Donnell P (2014) Preclinical trial of a novel surface architecture for improved primary fixation of cementless orthopaedic implants. Clin Biomech 29:861–868. https://doi.org/10.1016/j.clinbiomech.2014.07.007
8. Lewandowski JJ, Seifi M (2016) Metal additive manufacturing: a review of mechanical properties. Annu Rev Mater Res 46:151–186. https://doi.org/10.1146/annurev-matsci-070115-032024
9. Rindfleisch A, O'Hern M, Sachdev V (2017) The digital revolution, 3D printing, and innovation as data. J Prod Innov Manag 34:681–690. https://doi.org/10.1111/jpim.12402
10. Enabling the full potential of 3D printing. https://3mf.io/. Accessed 16 May 2021
11. ISO / ASTM52900-15 (2015) Standard terminology for additive manufacturing – general principles – terminology. ASTM International, West Conshohocken, PA. https://doi.org/10.1520/ISOASTM52900-15
12. Qian M, Xu W, Brandt M, Tang HP (2016) Additive manufacturing and postprocessing of Ti-6Al-4V for superior mechanical properties. MRS Bull 41:775–784. https://doi.org/10.1557/mrs.2016.215
13. Teixeira Ó, Silva FJG, Ferreira LP, Atzeni E (2020) A review of heat treatments on improving the quality and residual stresses of the Ti–6Al–4V parts produced by additive manufacturing. Metals 10:1006. https://doi.org/10.3390/met10081006
14. Liu S, Shin YC (2019) Additive manufacturing of Ti6Al4V alloy: a review. Mater Des 164:107552. https://doi.org/10.1016/j.matdes.2018.107552

15. Metal AM (2019) The magazine for metal additive manufacturing industry, vol 5(2). Inovar Communications Ltd, Cambrian Printers, Aberystwyth, UK. ISSN 2055-7183
16. Aboulkhair NT, Maskery I, Tuck C, Ashcroft I, Everitt NM (2016) The microstructure and mechanical properties of selectively laser melted AlSi10Mg: the effect of a conventional T6-like heat treatment. Mater Sci Eng A 667:139–146. https://doi.org/10.1016/j.msea.2016.04.092
17. Schneider J, Lund B, Fullen M (2018) Effect of heat treatment variations on the mechanical properties of Inconel 718 selective laser melted specimens. Addit Manuf 21:248–254. https://doi.org/10.1016/j.addma.2018.03.005
18. Karapuzha AS, Fraser D, Zhu Y, Wu X, Huang A (2022) Effect of solution heat treatment and hot isostatic pressing on the microstructure and mechanical properties of Hastelloy X manufactured by electron beam powder bed fusion. J Mater Sci Technol 2022(98):99–117. https://doi.org/10.1016/j.jmst.2021.04.059
19. Zhou L, Mehta A, Schulz E, McWilliams B, Cho K, Sohn Y (2018) Microstructure, precipitates and hardness of selectively laser melted AlSi10Mg alloy before and after heat treatment. Mater Charact 143:5–17. https://doi.org/10.1016/j.matchar.2018.04.022
20. Beaman JJ, Bourell DL, Seepersad CC, Kovar D (2020) Additive manufacturing review: early past to current practice. J Manuf Sci Eng 142:110812. https://doi.org/10.1115/1.4048193
21. Jin W, Zhang C, Jin S, Tian Y, Wellmann D, Liu W (2020) Wire arc additive manufacturing of stainless steels: a review. Appl Sci 10:1563. https://doi.org/10.3390/app10051563
22. Stützer J, Totzauer T, Wittig B, Zinke M, Jüttner S (2019) GMAW cold wire technology for adjusting the ferrite-austenite ratio of wire and arc additive manufactured duplex stainless steel components. Metals 9:564. https://doi.org/10.3390/met9050564
23. Chou R, Milligan J, Paliwal M, Brochu M (2015) Additive manufacturing of Al-12Si alloy via pulsed selective laser melting. JOM 67:590–596. https://doi.org/10.1007/s11837-014-1272-9
24. Majeed A, Ahmed A, Salam A, Sheikh MZ (2019) Surface quality improvement by parameters analysis, optimization and heat treatment of AlSi10Mg parts manufactured by SLM additive manufacturing. Int J Lightweight Mater Manuf 2:288–295. https://doi.org/10.1016/j.ijlmm.2019.08.001
25. Roudnická M, Molnárová O, Dvorský D, Křivský L, Vojtěch D (2020) Specific response of additively manufactured alsi9cu3fe alloy to precipitation strengthening. Met Mater Int 26:1168–1181. https://doi.org/10.1007/s12540-019-00504-y
26. Geng H, Li J, Xiong J, Lin X, Zhang F (2017) Geometric limitation and tensile properties of wire and arc additive manufacturing 5A06 aluminum alloy parts. J Mater Eng Perform 26:621–629
27. Miao Q, Wu D, Chai D, Zhan Y, Bi G, Niu F, Ma G (2020) Comparative study of microstructure evaluation and mechanical properties of 4043 aluminum alloy fabricated by wire-based additive manufacturing. Mater Des 186:108205. https://doi.org/10.1016/j.matdes.2019.108205
28. Griffiths RJ, Petersen DT, Garcia D, Yu HZ (2019) Additive friction stir-enabled solid-state additive manufacturing for the repair of 7075 aluminum alloy. Appl Sci 9:3486. https://doi.org/10.3390/app9173486
29. Bermingham MJ, StJohn DH, Krynen J, Tedman-Jones S, Dargusch MS (2019) Promoting the columnar to equiaxed transition and grain refinement of titanium alloys during additive manufacturing. Acta Mater 168:261–274. https://doi.org/10.1016/j.actamat.2019.02.020
30. Zhu Y-Y, Tang H-B, Li Z, Xu C, He B (2019) Solidification behavior and grain morphology of laser additive manufacturing titanium alloys. J Alloys Compd 777:712–716. https://doi.org/10.1016/j.jallcom.2018.11.055
31. Nagase T, Hori T, Todai M, Sun S-H, Nakano T (2019) Additive manufacturing of dense components in beta-titanium alloys with crystallographic texture from a mixture of pure metallic element powders. Mater Des 173:107771. https://doi.org/10.1016/j.matdes.2019.107771
32. Wimler D, Lindemann J, Reith M, Kirchner A, Allen M, Vargas WG, Franke M, Klöden B, Weißgärber T, Güther V et al (2021) Designing advanced intermetallic titanium aluminide

alloys for additive manufacturing. InterMet 131:107109. https://doi.org/10.1016/j.intermet.2021.107109
33. Hitzler L, Alifui-Segbaya F, Williams P, Heine B, Heitzmann M, Hall W, Merkel M, Öchsner A (2018) Additive manufacturing of cobalt-based dental alloys: analysis of microstructure and physicomechanical properties. Adv Mater Sci Eng 2018:8213023. https://doi.org/10.1155/2018/8213023
34. Popovich VA, Borisov EV, Popovich AA, Sufiiarov VS, Masaylo DV, Alzine L (2017) Functionally graded Inconel 718 processed by additive manufacturing: crystallographic texture, anisotropy of microstructure and mechanical properties. Mater Des 114:441–449. https://doi.org/10.1016/j.matdes.2016.10.075
35. Pleass C, Sathiskumar J (2018) Influence of powder characteristics and additive manufacturing process parameters on the microstructure and mechanical behaviour of Inconel 625 fabricated by selective laser melting. Addit Manuf 24:419–431. https://doi.org/10.1016/j.addma.2018.09.023
36. Han Q, Gu Y, Soe S, Lacan F, Setchi R (2020) Effect of hot cracking on the mechanical properties of Hastelloy X superalloy fabricated by laser powder bed fusion additive manufacturing. Opt Laser Technol 124:105984. https://doi.org/10.1016/j.optlastec.2019.105984
37. Martin E, Natarajan A, Kottilingam S, Batmaz R (2021) Binder jetting of "Hard-to-Weld" high gamma prime nickel-based superalloy RENÉ 108. Addit Manuf 39:101894. https://doi.org/10.1016/j.addma.2021.101894
38. Xu Z, Zhang H, Du X, He Y, Luo H, Song G, Mao L, Zhou T, Wang L (2020) Corrosion resistance enhancement of CoCrFeMnNi high-entropy alloy fabricated by additive manufacturing. Corros Sci 177:108954. https://doi.org/10.1016/j.corsci.2020.108954
39. Moorehead M, Bertsch K, Niezgoda M, Parkin C, Elbakhshwan M, Sridharan K, Zhang C, Thoma D, Couet A (2020) High-throughput synthesis of Mo-Nb-Ta-W high-entropy alloys via additive manufacturing. Mater Des 187:108358. https://doi.org/10.1016/j.matdes.2019.108358
40. Yang S, Liu Z, Pi J (2019) Microstructure and wear behavior of the AlCrFeCoNi high-entropy alloy fabricated by additive manufacturing. Mater Lett 261:127004. https://doi.org/10.1016/j.matlet.2019.127004
41. Gwalani B, Soni V, Waseem OA, Mantri SA, Banerjee R (2019) Laser additive manufacturing of compositionally graded AlCrFeMoVx (x = 0 to 1) high-entropy alloy system. Opt Laser Technol 113:330–337. https://doi.org/10.1016/j.optlastec.2019.01.009
42. Martin JH, Yahata BD, Clough EC, Mayer JA, Hundley JM, Schaedler TA (2018) Additive manufacturing of metal matrix composites via nanofunctionalization. MRS Commun 8:297–302. https://doi.org/10.1557/mrc.2018.95
43. AlMangour B, Grzesiak D, Yang J-M (2016) Nanocrystalline TiC-reinforced H13 steel matrix nanocomposites fabricated by selective laser melting. Mater Des 96:150–161. https://doi.org/10.1016/j.matdes.2016.02.022
44. AlMangour B, Kim Y-K, Grzesiak D, Lee K-A (2019) Novel TiB2-reinforced 316L stainless steel nanocomposites with excellent room-and high-temperature yield strength developed by additive manufacturing. Compos Part B Eng 156:51–63. https://doi.org/10.1016/j.compositesb.2018.07.050
45. Ligon SC, Liska R, Stampfl J, Gurr M, Mülhaupt R (2017) Polymers for 3D printing and customized additive manufacturing. Chem Rev 117:10212–10290. https://doi.org/10.1021/acs.chemrev.7b00074
46. Sathishkumar N, Arunkumar N, Balamurugan L, Sabarish L, Samuel Shapiro Joseph A (2020) Investigation of mechanical behaviour and surface roughness properties on copper electroplated FDM high impact polystyrene parts. In: Shunmugam M, Kanthababu M (eds) Advances in additive manufacturing and joining. Lecture notes on multidisciplinary industrial engineering. Springer, Singapore. https://doi.org/10.1007/978-981-32-9433-2_25
47. Riechmann S, Wunnicke O, Kwade A (2021) The effect of binder loading on the pore size of 3D printed PMMA. Materials 14:1190. https://doi.org/10.3390/ma14051190

48. Arai T, Kawaji M (2021) Thermal performance and flow characteristics in additive manufactured polycarbonate pulsating heat pipes with Novec 7000. Appl Therm Eng 197:117273. https://doi.org/10.1016/j.applthermaleng.2021.117273
49. Yan C, Shi Y, Yang J, Lin J (2010) Investigation into the selective laser sintering of styrene–acrylonitrile copolymer and postprocessing. Int J Adv Manuf Technol 51:973–982. https://doi.org/10.1007/s00170-010-2681-8
50. Kleijnen RG, Sesseg JPW, Schmid M, Wegener K (2017) Insights into the development of a short-fiber reinforced polypropylene for laser sintering. AIP Conf Proc 1914:190002. https://doi.org/10.1063/1.5016791
51. Lanzl L, Wudy K, Drummer D (2020) The effect of short glass fibers on the process behavior of polyamide 12 during selective laser beam melting. Polym Test 83:106313. https://doi.org/10.1016/j.polymertesting.2019.106313
52. İlhan R, Feyzullahoğlu E (2021) Investigation of adhesive wear properties of glass fiber reinforced polyester composites having different chemical compositions. In: Proceedings of the institution of mechanical engineers, part J: journal of engineering tribology 2021, p 13506501211005941. https://doi.org/10.1177/13506501211005941
53. Zhang W, Cotton C, Sun J, Heider D, Gu B, Sun B, Chou TW (2018) Interfacial bonding strength of short carbon fiber/acrylonitrile-butadiene-styrene composites fabricated by fused deposition modeling. Compos Part B Eng 137:51–59. https://doi.org/10.1016/j.compositesb.2017.11.018
54. Li N, Li YG, Liu ST (2016) Rapid prototyping of continuous carbon fiber reinforced polylactic acid composites by 3D printing. J Mater Proc Technol 238:218–225. https://doi.org/10.1016/j.jmatprotec.2016.07.025
55. Van Der Klift F, Koga Y, Todoroki A, Ueda M, Hirano Y, Matsuzaki R (2016) 3D printing of continuous carbon fibre reinforced thermo-plastic (CFRTP) tensile test specimens. Open J Compos Mater 6:18–27. https://doi.org/10.4236/ojcm.2016.61003
56. Bai J, Goodridge R, Yuan S, Zhou K, Chua C, Wei J (2015) Thermal influence of CNT on the polyamide 12 nanocomposite for selective laser sintering. Molecules 20:19041–19050. https://doi.org/10.3390/molecules201019041
57. Kim JH, Zhou H, Li BQ, Ding SJ (2016) Three-dimensional printing of highly conductive carbon nanotube microarchitectures with fluid ink. ACS Nano 10:8879–8887. https://doi.org/10.1021/acsnano.6b04771
58. Postiglione G, Natale G, Griffini G, Levi M, Turri S (2015) Conductive 3D microstructures by direct 3D printing of polymer/carbon nanotube nanocomposites via liquid deposition modeling. Compos Part A 76:110–114. https://doi.org/10.1016/j.compositesa.2015.05.014
59. Shofner ML, Rodriguez-Macias FJ, Vaidyanathan R, Barrera EV (2003) Single wall nanotube and vapor grown carbon fiber reinforced polymers processed by extrusion freeform fabrication. Compos Part A Appl Sci Manuf 34:1207–1217. https://doi.org/10.1016/j.compositesa.2003.07.002
60. Hupfeld T, Salamon S, Landers J, Sommereyns A, Doñate-Buendía C, Schmidt J, Wende H, Schmidt M, Barcikowski S, Gökce B (2020) 3D printing of magnetic parts by laser powder bed fusion of iron oxide nanoparticle functionalized polyamide powders. J Mater Chem C C8:12204–12217. https://doi.org/10.1039/D0TC02740E
61. Yuan Y, Wu W, Hu H, Liu D, Shen H, Wang Z (2021) The combination of Al2O3 and BN for enhancing the thermal conductivity of PA12 composites prepared by selective laser sintering. RSC Adv 11(4):984–1991. https://doi.org/10.1039/D0RA09775F
62. Qi FW, Chen N, Wang Q (2017) Preparation of PA11/BaTiO3, nanocomposite powders with improved processability, dielectric and piezoelectric properties for use in selective laser sintering. Mater Des 131:135–143. https://doi.org/10.1016/j.matdes.2017.06.012
63. Lai W, Wang Y, Fu H, He J (2020) Hydroxyapatite/polyetheretherketone nanocomposites for selective laser sintering: thermal and mechanical performances. e-Polymers 20(1):542–549. https://doi.org/10.1515/epoly-2020-0057
64. Jindal UC (2012) Material science and metallurgy. Pearson Education India

65. Wilkes J, Hagedorn Y-C, Meiners W, Wissenbach K (2013) Additive manufacturing of $ZrO_2$-$Al_2O_3$ ceramic components by selective laser melting. Rapid Prototyp J 19:51–57. https://doi.org/10.1108/13552541311292736
66. Zhang H, Yang Y, Hu K, Liu B, Liu M, Huang Z (2020) Stereolithography-based additive manufacturing of lightweight and high-strength Cf/SiC ceramics. Addit Manuf 34:101199. https://doi.org/10.1016/j.addma.2020.101199
67. Levy A, Miriyev A, Elliott A, Babu SS, Frage N (2017) Additive manufacturing of complex-shaped graded TiC/steel composites. Mater Des 118:198–203. https://doi.org/10.1016/j.matdes.2017.01.024
68. Gheisari R, Chamberlain H, Chi-Tangyie G, Zhang S, Goulas A, Lee C-K, Whittaker T, Wang D, Ketharam A, Ghosh A et al (2020) Multi-material additive manufacturing of low sintering temperature Bi2Mo2O9 ceramics with Ag floating electrodes by selective laser burnout. Virtual Phys Prototyp 15:133–147. https://doi.org/10.1080/17452759.2019.1708026
69. Gaytan SM, Cadena MA, Karim H, Delfin D, Lin Y, Espalin D, MacDonald E, Wicker RB (2015) Fabrication of barium titanate by binder jetting additive manufacturing technology. Ceram Int 41:6610–6619. https://doi.org/10.1016/j.ceramint.2015.01.108
70. Baumgartner S, Gmeiner R, Schönherr JA, Stampfl J (2020) Stereolithography-based additive manufacturing of lithium disilicate glass ceramic for dental applications. Mater Sci Eng C 116:111180. https://doi.org/10.1016/j.msec.2020.111180
71. Gorjan L, Reiff L, Liersch A, Clemens F (2018) Ethylene vinyl acetate as a binder for additive manufacturing of tricalcium phosphate bio-ceramics. Ceram Int 44:15817–15823. https://doi.org/10.1016/j.ceramint.2018.05.260
72. Pelz JS, Ku N, Shoulders WT, Meyers MA, Vargas-Gonzalez LR (2021) Multi-material additive manufacturing of functionally graded carbide ceramics via active, in-line mixing. Addit Manuf 37:101647. https://doi.org/10.1016/j.addma.2020.101647
73. Wang X, Schmidt F, Hanaor D, Kamm PH, Li S, Gurlo A (2019) Additive manufacturing of ceramics from preceramic polymers: a versatile stereolithographic approach assisted by thiol-ene click chemistry. Addit Manuf 27:80–90. https://doi.org/10.1016/j.addma.2019.02.012
74. Zhou W, Sun X, Tsunoda K, Kikuchi K, Nomura N, Yoshimi K, Kawasaki A (2019) Powder fabrication and laser additive manufacturing of MoSiBTiC alloy. Intermetallics 104:33–42. https://doi.org/10.1016/j.intermet.2018.10.012
75. Zhou WZ, Dong MQ, Zhou ZX, Sun XH, Kikuchi K, Nomura N, Kawasaki A (2019) In situ formation of uniformly dispersed $Al_4C_3$ nanorods during additive manufacturing of graphene oxide/Al mixed powders. Carbon 141:67–75. https://doi.org/10.1016/j.carbon.2018.09.057
76. Zhou W, Sun X, Kikuchi K, Nomura N, Yoshimi K, Kawasaki A (2018) Carbon nanotubes as a unique agent to fabricate nanoceramic/metal composite powders for additive manufacturing. Mater Des 137:276–285. https://doi.org/10.1016/j.matdes.2017.10.034
77. Carlton HD, Haboub A, Gallegos GF, Parkinson DY, MacDowell AA (2016) Damage evolution and failure mechanisms in additively manufactured stainless steel. Mater Sci Eng A 651:406–414. https://doi.org/10.1016/j.msea.2015.10.073
78. Narvan M, Al-Rubaie KS, Elbestawi M (2019) Process-structure-property relationships of AISI H13 tool steel processed with selective laser melting. Materials 12:2284. https://doi.org/10.3390/ma12142284
79. Hernandez FC, Ramírez JM, Mackay R (2017) Al-Si alloys: automotive, aeronautical, and aerospace applications, 1st edn. Springer International Publishing, Cham, Switzerland. ISBN 978-3-319-58379-2
80. Zhao L, Macías JGS, Ding L, Idrissi H, Simar A (2019) Damage mechanisms in selective laser melted AlSi10Mg under as built and different post-treatment conditions. Mater Sci Eng A 764:138210. https://doi.org/10.1016/j.msea.2019.138210
81. Kumar SP, Elangovan S, Mohanraj R, Ramakrishna JR (2017) A review on properties of Inconel 625 and Inconel 718 fabricated using direct energy deposition. Mater Today: Proc 2021 46:7892–7906. https://doi.org/10.1016/j.matpr.2021.02.566
82. Sivadasan P, Sharma GS, Rout IS, Pal Pandian P (2020) A review on influence of cutting fluid on improving the machinability of inconel 718. In: Praveen Kumar A, Dirgantara T, Krishna

PV (eds) Advances in lightweight materials and structures, vol 8. Springer proceedings in materials. Springer, Singapore. https://doi.org/10.1007/978-981-15-7827-4_50
83. Grzesik W, Nieslony P, Habrat W, Sieniawski J, Laskowski P (2018) Investigation of tool wear in the turning of Inconel 718 superalloy in terms of process performance and productivity enhancement. Tribol Int 118:337–346. https://doi.org/10.1016/j.triboint.2017.10.005
84. Oryshchenko AS, Gorynin IV, Leonov VP, Kudryavtsev AS, Mikhailov VI, Chudakov EV (2015) Marine titanium alloys: present and future. Inorg Mater Appl Res 6:571–579. https://doi.org/10.1134/S2075113315060106
85. Schirdewahn S, Spranger F, Hilgenberg K, Merklein M (2020) Localized laser dispersing of titanium-based particles for improving the tribological performance of hot stamping tools. J Manuf Mater Process 4:68. https://doi.org/10.3390/jmmp4030068
86. Oros AE, Vasile IM (2021) Microstructural and mechanical characterization of Co-Cr-Mo alloy components built by selective laser melting. UPB Sci Bull Ser D 83(3):217–226. ISSN 1454-2358
87. Dada M, Popoola P, Mathe N, Pityana S, Adeosun S, Aramide O, Lengopeng T (2020) Process optimization of high entropy alloys by laser additive manufacturing. Eng Rep 2(10):e12252. https://doi.org/10.1002/eng2.12252
88. Li W, Chen S, Liaw PK (2020) Discovery and design of fatigue-resistant high-entropy alloys. Scr Mater 187:68–75. https://doi.org/10.1016/j.scriptamat.2020.05.047
89. Gromov VE, Konovalov SV, Ivanov YF, Osintsev KA (2021) Prospects of high-entropy alloys application. in: structure and properties of high-entropy alloys. In: Advanced structured materials, vol 107. Springer, Cham. https://doi.org/10.1007/978-3-030-78364-8_4
90. Hua N, Wang W, Wang Q, Ye Y, Lin S, Zhang L, Guo Q, Brechtl J, Liaw PK (2020) Mechanical, corrosion, and wear properties of biomedical Ti-Zr-Nb-Ta-Mo high entropy alloys. J Alloys Compd 157997. https://doi.org/10.1016/j.jallcom.2020.157997
91. Zhou E, Qiao D, Yang Y, Xu D, Lu Y, Wang J, Smith JA, Li H, Zhao H, Liaw PK, Wank F (2020) A novel Cu-bearing high-entropy alloy with significant antibacterial behavior against corrosive marine biofilms. J Mater Sci Technol 46:201–210. https://doi.org/10.1016/j.jmst.2020.01.039
92. Korium M, Roozbahani H, Alizadeh M, Perepelkina S, Handroos H (2021) Direct metal laser sintering of precious metals for jewelry applications: process parameter selection and microstructure analysis. IEEE Access 9:126530–126540. https://doi.org/10.1109/ACCESS.2021.3112479
93. Hanawa T (2010) Overview of metals and applications. In: Niinomi M (ed) Metals for biomedical devices. Woodhead Publishing Limited, Cambridge, UK, pp 3–24. ISBN 9781845699246
94. Yolton CF, Fores FH(Sam) (2015) Conventional titanium powder production. In: Qian M, Froes FH (eds) Titanium powder metallurgy: science, technology and applications. Butterworth-Heinemann, Oxford, UK, pp 21–31
95. Moghadam MS, Fayyaz A, Ardestani M (2021) Fabrication of titanium components by low-pressure powder injection moulding using hydride-dehydride titanium powder. Powder Technol 377:70–79. https://doi.org/10.1016/j.powtec.2020.08.075
96. Kassym K, Perveen A (2020) Atomization processes of metal powders for 3D printing. Mater Today Proc 26:1727–1733. https://doi.org/10.1016/j.matpr.2020.02.364
97. Kaviarasu C, Ravichandran M (2020) Nanomaterials through powder metallurgy: production, processing, and potential applications toward energy and environment. In: Kharissova O, Martínez L, Kharisov B (eds) Handbook of nanomaterials and nanocomposites for energy and environmental applications. Springer, Cham
98. Fedina T, Sundqvist J, Powell J, Kaplan AF (2020) A comparative study of water and gas atomized low alloy steel powders for additive manufacturing. Addit Manuf 36:10165. https://doi.org/10.1016/j.addma.2020.101675
99. Riabov D, Hryha E, Rashidi M, Bengtsson S, Nyborg L (2020) Effect of atomization on surface oxide composition in 316L stainless steel powders for additive manufacturing. Surf Interface Anal 52(11):694–706. https://doi.org/10.1002/sia.6846

100. Dawes J, Bowerman R, Trepleton R (2015) Introduction to the additive manufacturing powder metallurgy supply chain. Johnson Matthey Technol Rev 59(3):243–256. https://doi.org/10.1595/205651315X688686
101. Herbert RJ (2016) Viewpoint: Metallurgical aspects of powder bed metal additive manufacturing. J Mater Sci 51:1165–1175. https://doi.org/10.1007/s10853-015-9479-x
102. Murr LE, Martinez E, Hernandez J, Collins S, Amato KN, Gaytan SM, Shindo PW (2012) Microstructures and properties of 17–4 PH stainless steel fabricated by selective laser melting. J Mater Res Technol 1:167–177. https://doi.org/10.1016/S2238-7854(12)70029-7
103. Starr T, Rafi H, Stucker B, Scherzer CM (2012) Controlling phase composition in selective laser melted stainless steels. University of Louisville: Louisville, KY, USA, pp 439–446
104. Guo RP, Xu L, Zong YP (2017) Characterization of prealloyed Ti–6Al–4V powders from EIGA and PREP process and mechanical properties of HIPed powder compacts. Acta Metall Sin 30:1–10. https://doi.org/10.1007/s40195-017-0540-4
105. Kaplanskii YY, Zaitsev AA, Sentyurina ZA, Levashov EA, Pogozhev YS, Loginov PA, Logacheva AI (2018) The structure and properties of pre-alloyed NiAl-Cr(Co, Hf) spherical powders produced by plasma rotating electrode processing for additive manufacturing. J Mater Res Technol 7:461–468. https://doi.org/10.1016/j.jmrt.2018.01.003
106. Nie Y, Tang JJ, Teng JW, Ye XJ, Yang BB, Huang JF, Yu S, Li YP (2020) Particle defects and related properties of metallic powders produced by plasma rotating electrode process. Adv Powder Technol 31:2912–2920. https://doi.org/10.1016/j.apt.2020.05.018
107. Tang JJ, Nie Y, Li Q, Li YP (2019) Characteristics and atomization behavior of Ti-6Al-4V powder produced by plasma rotating electrode process. Adv Powder Technol 30:2330–2337. https://doi.org/10.1016/j.apt.2019.07.015
108. Yenwiset S, Yenwiset T (2011) Design and construction of water atomizer for making metal powder. J Met Mater Miner 21(1):75–81
109. Benarji K, Kumar YR, Jinoop AN, Paul CP, Bindra KS (2021) Effect of heat-treatment on the microstructure, mechanical properties and corrosion behaviour of SS 316 structures built by laser directed energy deposition based additive manufacturing. Met Mater Int 27(3):488–499. https://doi.org/10.1007/s12540-020-00838-y
110. Do T, Bauder TJ, Suen H, Rego K, Yeom J, Kwon P Additively manufactured full-density stainless steel 316L with binder jet printing. In: Proceedings of the ASME 2018 13th international manufacturing science and engineering conference. Volume 1: additive manufacturing; bio and sustainable manufacturing. College Station, Texas, USA, 18–22 June 2018. V001T01A017. ASME. https://doi.org/10.1115/MSEC2018-6681
111. Li J, Cheng X, Li Z, Zong X, Zhang SQ, Wang HM (2018) Improving the mechanical properties of Al-5Si-1Cu-Mg aluminum alloy produced by laser additive manufacturing with post-process heat treatments. Mater Sci Eng A 735:408–417. https://doi.org/10.1016/j.msea.2018.08.074
112. McCracken CG, Barbis DP, Deeter RC (2011) Key characteristics of hydride–dehydride titanium powder. Powder Metall 54:180–183. https://doi.org/10.1179/174329011X13045076771849
113. Makhmutov T, Razumov N, Kim A, Ozerskoy N, Mazeeva A, Popovich A (2021) Synthesis of $CoCrFeNiMnW_{0.25}$ high-entropy alloy powders by mechanical alloying and plasma spheroidization processes for additive manufacturing. Met Mater Int 27:50–54. https://doi.org/10.1007/s12540-020-00747-0
114. Standard AJAI (2012) Standard Terminology for Additive Manufacturing Technologies. ASTM International: West Conshohocken, PA, USA
115. Wohlers TT (2017) Wohlers report 2014: additive manufacturing and 3D printing state of the industry annual worldwide progress report. Wohlers Associates, Inc., Fort Collins, CO, USA
116. Metal AM (2015) The magazine for metal additive manufacturing industry, vol 1(1). Inovar Communications Ltd, Cambrian Printers, Aberystwyth, UK. ISSN 2055-7183
117. Srivatsa S (2014) Additive Manufacturing (AM) design and simulation tools study. final report. Air Force Research Laboratory, Wright-Patterson Air Force Base, OH

118. King WE, Anderson AT, Ferencz RM, Hodge NE, Kamath C, Khairallah SA, Rubenchi AM (2015) Laser powder bed fusion additive manufacturing of metals; physics, computational, and materials challenges. Appl Phys Rev 2:041304. https://doi.org/10.1063/1.4937809
119. Moussaoui K, Rubio W, Mousseigne M, Sultan T, Rezai F (2018) Effects of selective laser melting additive manufacturing parameters of Inconel 718 on porosity, microstructure and mechanical properties. Mater Sci Eng A 735:182–190. https://doi.org/10.1016/j.msea.2018.08.037
120. Jialin Y (2017) Selective laser melting additive manufacturing of advanced nuclear materials V-6Cr-6Ti. Mater Lett 209:268–271. https://doi.org/10.1016/j.matlet.2017.08.014
121. Demir AG, Previtali B (2017) Additive manufacturing of cardiovascular CoCr stents by selective laser melting. Mater Des 119:338–350. https://doi.org/10.1016/j.matdes.2017.01.091
122. Gu D, Chang F, Dai D (2015) Selective laser melting additive manufacturing of novel aluminum based composites with multiple reinforcing phases. J Manuf Sci Eng 137:021010. https://doi.org/10.1115/1.4028925
123. Dadbakhsh S, Mertens R, Vanmeensel K, Vleugels J, Van Humbeeck J, Kruth J-P (2018) In situ alloying and reinforcing of Al6061 during selective laser melting. Procedia CIRP 74:39–43. https://doi.org/10.1016/j.procir.2018.08.009
124. Metal AM (2016) The magazine for metal additive manufacturing industry, vol 2(2). Inovar Communications Ltd, Cambrian Printers, Aberystwyth, UK. ISSN 2055-7183
125. Crane NB (2020) Impact of part thickness and drying conditions on saturation limits in binder jet additive manufacturing. Addit Manuf 33:101127. https://doi.org/10.1016/j.addma.2020.101127
126. Chen H, Zhao YF (2016) Process parameters optimization for improving surface quality and manufacturing accuracy of binder jetting additive manufacturing process. Rapid Prototyp J 22:527–538. https://doi.org/10.1108/RPJ-11-2014-0149
127. Do T, Kwon P, Shin CS (2017) Process development toward full-density stainless steel parts with binder jetting printing. Int J Mach Tools Manuf 121:50–60. https://doi.org/10.1016/j.ijmachtools.2017.04.006
128. Ziaee M, Crane NB (2019) Binder jetting: a review of process, materials, and methods. Addit Manuf 28:781–801. https://doi.org/10.1016/j.addma.2019.05.031
129. Miyanaji H, Momenzadeh N, Yang L (2019) Effect of powder characteristics on parts fabricated via binder jetting process. Rapid Prototyp J 25:332–342. https://doi.org/10.1108/RPJ-03-2018-0069
130. Gibson I, Rosen DW, Stucker B (2010) Design for additive manufacturing. In: Additive manufacturing technologies, 1st edn. Springer: New York, NY, USA, pp 283–316. https://doi.org/10.1007/978-3-030-56127-7
131. Wheat E, Vlasea M, Hinebaugh J, Metcalfe C (2018) Sinter structure analysis of titanium structures fabricated via binder jetting additive manufacturing. Mater Des 156:167–183. https://doi.org/10.1016/j.matdes.2018.06.038
132. Miyanaji H, Ma D, Atwater MA, Darling KA, Hammond VH, Williams CB (2020) Binder jetting additive manufacturing of copper foam structures. Addit Manuf 32:100960. https://doi.org/10.1016/j.addma.2019.100960
133. Gonzalez JA, Mireles J, Stafford SW, Perez MA, Terrazas CA, Wicker RB (2019) Characterization of Inconel 625 fabricated using powder-bed-based additive manufacturing technologies. J Mater Process Tech 264:200–210. https://doi.org/10.1016/j.jmatprotec.2018.08.031
134. Nandwana P, Elliott AM, Siddel D, Merriman A, Peter WH, Babu SS (2017) Powder bed binder jet 3D printing of Inconel 718: densification, microstructural evolution and challenges☆. Curr Opin Solid State Mater Sci 21:207–218. https://doi.org/10.1016/j.cossms.2016.12.002
135. Stoyanov P, Andre K, Prichard P, Yao M, Gey C (2016) Microstructural and mechanical characterization of Mo-containing stellite alloys produced by three dimensional printing. Procedia Cirp 45:167–170. https://doi.org/10.1016/j.procir.2016.02.358

136. Utela BR, Storti D, Anderson RL, Ganter M (2010) Development process for custom three-dimensional printing 3DP material systems. J Manuf Sci Eng 132:011008. https://doi.org/10.1115/1.4000713
137. Bailey A, Merriman A, Elliott A, Basti M (2016) Preliminary testing of nanoparticle effectiveness in binder jetting applications. In: 27th annual international solid freeform fabrication symposium, Austin, TX, 1 January 2016, pp 1069–1077
138. Petukhov DI, Kirikova MN, Bessonov AA, Bailey MJA (2014) Nickel and copper conductive patterns fabricated by reactive inkjet printing combined with electroless plating. Mater Lett 132:302–306. https://doi.org/10.1016/j.matlet.2014.06.109
139. Draper GL, Dharmadasa R, Staats ME, Lavery BW, Druffel T (2015) Fabrication of elemental copper by intense pulsed light processing of a copper nitrate hydroxide ink. ACS Appl Mater Interfaces 7:16478–16485. https://doi.org/10.1021/acsami.5b03854
140. Bai Y, Williams CB (2018) Binder jetting additive manufacturing with a particle-free metal ink as a binder precursor. Mater Des 147:146–156. https://doi.org/10.1016/j.matdes.2018.03.027
141. ExOne. (2021) https://www.exone.com. Accessed 6 June 2021
142. Bai Y, Wagner G, Williams CB (2017) Effect of particle size distribution on powder packing and sintering in binder jetting additive manufacturing of metals. J Manuf Sci Eng 139:081019. https://doi.org/10.1115/1.4036640
143. Miyanaji H, Rahman KM, Da M, Williams CB (2020) Effect of fine powder particles on quality of binder jetting parts. Addit Manuf 36:101587. https://doi.org/10.1016/j.addma.2020.101587
144. Xu Z, Zhu Z, Wang P, Meenashisundaram GK, Nai SML, Wei J (2020) Fabrication of porous CoCrFeMnNi high entropy alloy using binder jetting additive manufacturing. Addit Manuf 35:101441. https://doi.org/10.1016/j.addma.2020.101441
145. Cunningham CR, Flynn JM, Shokrani A, Dhokia V, Newman ST (2018) Invited review article: strategies and processes for high quality wire arc additive manufacturing. Addit Manuf 22:672–686. https://doi.org/10.1016/j.addma.2018.06.020
146. Wang Y, Chen X, Konovalov SV (2017) Additive manufacturing based on welding arc: a low-cost method. J Surf Investig X-ray Synchrotron Neutron Tech 11:1317–1328. https://doi.org/10.1134/S1027451017060210
147. Pan Z, Ding D, Wu B, Cuiuri D, Li H, Norrish J (2017) Arc welding processes for additive manufacturing: a review. In: Chen S, Zhang Y, Feng Z (eds) Transactions on intelligent welding manufacturing, vol 1, pp 3–24. Springer: Singapore. ISBN 978-981-10-5355-9
148. Metal AM (2020) The magazine for metal additive manufacturing industry, vol 6(3). Inovar Communications Ltd, Cambrian Printers, Aberystwyth, UK. ISSN 2055-7183
149. Ge J, Lin J, Chen Y, Lei Y, Fu H (2018) Characterization of wire arc additive manufacturing 2Cr13 part: process stability, microstructural evolution, and tensile properties. J Alloy Compd 748:911–921. https://doi.org/10.1016/j.jallcom.2018.03.222
150. Alonso U, Veiga F, Suárez A, Artaza T (2020) Experimental investigation of the influence of wire arc additive manufacturing on the machinability of titanium parts. Metals 10:24. https://doi.org/10.3390/met10010024
151. Wang L, Xue J, Wang Q (2019) Correlation between arc mode, microstructure, and mechanical properties during wire arc additive manufacturing of 316L stainless steel. Mater Sci Eng A 751:183–190. https://doi.org/10.1016/j.msea.2019.02.078
152. Ding D, Pan Z, Van Duin S, Li H, Shen C (2016) Fabricating superior NiAl bronze components through wire arc additive manufacturing. Materials 9(8):652. https://doi.org/10.3390/ma9080652
153. Asala G, Khan AK, Andersson J, Ojo OA (2017) Microstructural analyses of ATI 718Plus® produced by wire-ARC additive manufacturing process. Metall Mater Trans A 48:4211–4228. https://doi.org/10.1007/s11661-017-4162-2
154. Zhou Y, Lin X, Kang N, Huang W, Wang J, Wang Z (2020) Influence of travel speed on microstructure and mechanical properties of wire+ arc additively manufactured 2219 aluminum alloy. J Mater Sci Technol 37:143–153. https://doi.org/10.1016/j.jmst.2019.06.016

155. Rafieazad M, Ghaffari M, Nemani AV, Nasiri A (2019) Microstructural evolution and mechanical properties of a low-carbon low-alloy steel produced by wire arc additive manufacturing. Int J Adv Manuf Technol 105:2121–2134. https://doi.org/10.1007/s00170-019-04393-8
156. Gibson I, Rosen D, Stucker B, Khorasani M (2021) Materials for additive manufacturing. In: Additive manufacturing technologies, pp 379–428. Springer, Cham. https://doi.org/10.1007/978-3-030-56127-7_14
157. Kruth JP, Dadbakhsh S, Vrancken B, Kempen K, Vleugels J, Van Humbeeck J (2016) Additive manufacturing of metals via selective laser melting: process aspects and material developments. In: Srivatsan T, Sudarshan T (eds) Additive manufacturing: innovations, advances, and applications. CRC Press: Boca Raton, FL, USA, pp 69–99. ISBN 978-1-4987-1477-8
158. Khorasani AM, Gibson I, Ghaderi AR (2018) Rheological characterization of process parameters influence on surface quality of Ti-6Al-4V parts manufactured by selective laser melting. Int J Adv Manuf Technol 97:3761–3775. https://doi.org/10.1007/s00170-018-2168-6
159. Srivatsan TS, Sudarshan TS (2015) Additive manufacturing: innovations, advances, and applications. CRC Press, Boca Raton, FL, USA. ISBN 9781498714778
160. Metal AM (2015) The magazine for metal additive manufacturing industry, vol 1(4). Inovar Communications Ltd, Cambrian Printers, Aberystwyth, UK. ISSN 2055-7183
161. Kumar AY, Bai Y, Eklund A, Williams CB (2018) The effects of Hot Isostatic Pressing on parts fabricated by binder jetting additive manufacturing. Addit Manuf 24:115–124. https://doi.org/10.1016/j.addma.2018.09.021
162. Lavery NP, Cherry J, Mehmood S, Davies H, Girling B, Sackett E, Brown SGR, Sienz J (2017) Effects of hot isostatic pressing on the elastic modulus and tensile properties of 316L parts made by powder bed laser fusion. Mater Sci Eng A 693:186–213. https://doi.org/10.1016/j.msea.2017.03.100
163. Eshawish N, Malinov S, Sha W, Walls P (2021) Microstructure and mechanical properties of Ti-6Al-4V manufactured by selective laser melting after stress relieving, hot isostatic pressing treatment, and post-heat treatment. J Mater Eng Perform 30:5290–5296. https://doi.org/10.1007/s11665-021-05753-w
164. Peter WH, Nandwana P, Kirka MM, Dehoff RR, Sames W, Erdman I, Eklund A, Howard R (2015) Understanding the role of hot isostatic pressing parameters on the microstructural evolution of Ti-6Al-4V and Inconel 718 fabricated by electron beam melting, US Department of Energy (DOE) SciTech Connect. https://doi.org/10.2172/1209206, http://www.osti.gov/scitech/servlets/purl/1209206
165. Katgerman L, Eskin D (2003) Hardening, annealing and aging. In: Totten GE, Mackenzie DS (eds) Handbook of aluminum volume 1: physical metallurgy and processes. CRC Press, New York, pp 227–280
166. Walde C, Cote D, Champagne V, Sisson R (2019) Characterizing the effect of thermal processing on feedstock Al alloy powder for additive manufacturing applications. J Mater Eng Perform 28(2):601–610. https://doi.org/10.1007/s11665-018-3550-0
167. Kong D, Dong C, Ni X, Zhang L, Yao J, Man C, Cheng X, Xiao K, Li X (2019) Mechanical properties and corrosion behavior of selective laser melted 316L stainless steel after different heat treatment processes. J Mater Sci Technol 35:1499–1507. https://doi.org/10.1016/j.jmst.2019.03.003
168. Metal AM (2018) The magazine for metal additive manufacturing industry, vol 4(3). Inovar Communications Ltd, Cambrian Printers, Aberystwyth, UK. ISSN 2055-7183
169. Gu J, Ding J, Williams SW, Gu H, Bai J, Zhai Y, Ma P (2016) The strengthening effect of inter-layer cold working and post-deposition heat treatment on the additively manufactured Al–6.3 Cu alloy. Mater Sci Eng A 651:18–26. https://doi.org/10.1016/j.msea.2015.10.101
170. Qi Z, Cong B, Qi B, Zhao G, Ding J (2018) Properties of wire+ arc additively manufactured 2024 aluminum alloy with different solution treatment temperature. Mater Lett 230:275–278. https://doi.org/10.1016/j.matlet.2018.07.144
171. Handbook AM (1991) Heat treating, vol 4. ASM International. Materials Park, OH, USA
172. Ettefagh AH, Zeng C, Guo S, Raush J (2019) Corrosion behavior of additively manufactured Ti-6Al-4V parts and the effect of post annealing. Addit Manuf 28:252–258. https://doi.org/10.1016/j.addma.2019.05.011

173. Cui L, Jiang S, Xu J, Peng RL, Mousavian RT, Moverare J (2021) Revealing relationships between microstructure and hardening nature of additively manufactured 316L stainless steel. Mater Des 198:109385. https://doi.org/10.1016/j.matdes.2020.109385
174. Kučerová L, Burdová K, Jeníček Š, Chena I (2021) Effect of solution annealing and precipitation hardening at 250° C–550° C on microstructure and mechanical properties of additively manufactured 1.2709 maraging steel. Mater Sci Eng A 814:141195. https://doi.org/10.1016/j.msea.2021.141195
175. Polozov I, Sufiiarov V, Shamshurin A (2019) Synthesis of titanium orthorhombic alloy using binder jetting additive manufacturing. Mater Lett 243:88–91. https://doi.org/10.1016/j.matlet.2019.02.027
176. Karlsson D, Lindwall G, Lundbäck A, Amnebrink M, Boström M, Riekehr L, Schuisky M, Sahlberg M, Jansson U (2019) Binder jetting of the AlCoCrFeNi alloy. Addit Manuf 27:72–79. https://doi.org/10.1016/j.addma.2019.02.010
177. Godec M, Malej S, Feizpour D, Donik Č, Balažic M, Klobčar D, Pambaguian L, Conradi M, Kocijan A (2021) Hybrid additive manufacturing of Inconel 718 for future space applications. Mater Charact 172:110842. https://doi.org/10.1016/j.matchar.2020.110842
178. Åsberg M, Fredriksson G, Hatami S, Fredriksson W, Krakhmalev P (2019) Influence of post treatment on microstructure, porosity and mechanical properties of additive manufactured H13 tool steel. Mater Sci Eng A 742:584–589. https://doi.org/10.1016/j.msea.2018.08.046
179. Deirmina F, Peghini N, AlMangour B, Grzesiak D, Pellizzari M (2019) Heat treatment and properties of a hot work tool steel fabricated by additive manufacturing. Mater Sci Eng A 753:109–121. https://doi.org/10.1016/j.msea.2019.03.027
180. Conde FF, Escobar JD, Oliveira JP, Jardini AL, Bose Filho WW, Avila JA (2019) Austenite reversion kinetics and stability during tempering of an additively manufactured maraging 300 steel. Addit Manuf 29:100804. https://doi.org/10.1016/j.addma.2019.100804
181. Jiang X, Xiong W, Wang L, Guo M, Ding Z (2020) Heat treatment effects on microstructure-residual stress for selective laser melting AlSi10Mg. Mater Sci Technol 36(2):168–180. https://doi.org/10.1080/02670836.2019.1685770
182. Shen C, Pan Z, Ding D, Yuan L, Nie N, Wang Y, Luo D, Cuiuri D, van Duin S, Li H (2018) The influence of post-production heat treatment on the multi-directional properties of nickel-aluminum bronze alloy fabricated using wire-arc additive manufacturing process. Addit Manuf 23:411–421. https://doi.org/10.1016/j.addma.2018.08.008
183. Gao C, Chen X, Chen X, Su C (2019) Microstructure and mechanical properties of as-deposited and heat-treated additive manufactured 9Cr steel. Mater Sci Technol 35(18):2234–2242. https://doi.org/10.1080/02670836.2019.1668603
184. Sjölander E, Seifeddine S (2010) The heat treatment of Al–Si–Cu–Mg casting alloys. J Mater Process Technol 210(10):1249–1259. https://doi.org/10.1016/j.jmatprotec.2010.03.020
185. Brandl E, Heckenberger U, Holzinger V, Buchbinder D (2012) Additive manufactured AlSi10Mg samples using Selective Laser Melting (SLM): Microstructure, high cycle fatigue, and fracture behavior. Mater Des 34:159–169. https://doi.org/10.1016/j.matdes.2011.07.067
186. Ngnekou JND, Nadot Y, Henaff G, Nicolai J, Ridosz L (2017) Influence of defect size on the fatigue resistance of AlSi10Mg alloy elaborated by selective laser melting (SLM). Procedia Struct Integrity 7:75–83. https://doi.org/10.1016/j.prostr.2017.11.063
187. Lorusso M, Trevisan F, Calignano F, Lombardi M, Manfredi D (2020) A357 Alloy by LPBF for industry applications. Materials 13:1488. https://doi.org/10.3390/ma13071488
188. Aboulkhair NT, Everitt NM, Ashcroft I, Tuck C (2014) Reducing porosity in AlSi10Mg parts processed by selective laser melting. Addit Manuf 1:77–86. https://doi.org/10.1016/j.addma.2014.08.001
189. Tanvir ANM, Ahsan RU, Ji C, Hawkins W, Bates B, Kim DB (2019) Heat treatment effects on Inconel 625 components fabricated by wire + arc additive manufacturing (WAAM)—Part 1: microstructural characterization. Int J Adv Manuf Technol 103:3785–3798. https://doi.org/10.1007/s00170-019-03828-6
190. Salman O, Gammer C, Chaubey AK, Echert J, Scudino S (2019) Effect of heat treatment on microstructure and mechanical properties of 316L steel synthesized by selective laser melting. Mater Sci Eng A 748:205–212. https://doi.org/10.1016/j.msea.2019.01.110

191. Tang Y, Huang Z, Yang J, Xie Y (2020) Enhancing the capillary force of binder-jetting printing Ti6Al4V and mechanical properties under high temperature sintering by mixing fine powder. Metals 10:1354. https://doi.org/10.3390/met10101354
192. Tanvir ANM, Ahsan MR, Seo G, Kim JD, Ji C, Bates B, Lee Y, Kim DB (2020) Heat treatment effects on Inconel 625 components fabricated by wire+ arc additively manufacturing (WAAM)—part 2: mechanical properties. Int J Adv Manuf Technol 110(7):1709–1721. https://doi.org/10.1007/s00170-020-05980-w
193. Mertens R, Vrancken B, Holmstock N, Kinds Y, Kruth JP, Van Humbeeck J (2016) Influence of powder bed preheating on microstructure and mechanical properties of H13 tool steel SLM parts. Phys Procedia 83:882–890. https://doi.org/10.1016/j.phpro.2016.08.092
194. Metal AM (2021) The magazine for metal additive manufacturing industry, vol 7(1). Inovar Communications Ltd, Cambrian Printers, Aberystwyth, UK. ISSN 2055-7183
195. Pollak J, Bailly O, Dolbec R (2017) Production of spherical metallic powders for AM. In: Proceedings of international conference on powder metallurgy & particulate materials "PowderMet 2017," 13–16 June 2017, Las Vegas, USA
196. Horgar A, Fostervoll H, Nyhus B, Ren X, Eriksson M, Akselsen OM (2018) Additive manufacturing using WAAM with AA5183 wire. J Mater Process Technol 259:68–74. https://doi.org/10.1016/j.jmatprotec.2018.04.014
197. Fattahi M, Mohammady M, Sajjadi N, Honarmand M, Fattahi Y, Akhavan S (2015) Effect of TiC nanoparticles on the microstructure and mechanical properties of gas tungsten arc welded aluminum joints. J Mater Process Technol 217:21–29. https://doi.org/10.1016/j.jmatprotec.2014.10.023
198. Elliott A, Alsalihi S, Merriman AL, Basti MM (2016) Infiltration of nanoparticles into porous binder jet printed parts. Am J Eng Appl Sci 9:128–133. https://doi.org/10.3844/ajeassp.2016.128.133
199. Dahmen T, Henriksen NG, Dahl KV, Lapina A, Pedersen DB, Hattel JH, Christiansen TL, Somers MAJ (2021) Densification, microstructure, and mechanical properties of heat-treated MAR-M247 fabricated by Binder Jetting. Addit Manuf 39. https://doi.org/10.1016/j.addma.2021.101912
200. Mirzababaei S, Paul BK, Pasebani S (2020) Metal powder recyclability in binder jet additive manufacturing. JOM 72(9):3070–3079. https://doi.org/10.1007/s11837-020-04258-6
201. Liverani E, Toschi S, Ceschinim L, Fortunato A (2017) Effect of selective laser melting (SLM) process parameters on microstructure and mechanical properties of 316L austenitic stainless steel. J Mater Process Technol 249:255–263. https://doi.org/10.1016/j.jmatprotec.2017.05.042
202. Huang M, Zhang Z, Chen P (2019) Effect of selective laser melting process parameters on microstructure and mechanical properties of 316L stainless steel helical micro-diameter spring. Int J Adv Manuf Technol 104(5):2117–2131. https://doi.org/10.1007/s00170-019-03928-3
203. Thapliyal S (2019) Challenges associated with the wire arc additive manufacturing (WAAM) of aluminum alloys. Mater Res Express 6:112006. https://doi.org/10.1088/2053-1591/ab4dd4
204. Montevecchi F, Venturini G, Grossi N, Scippa A, Campatelli G (2018) Heat accumulation prevention in Wire-Arc-Additive-Manufacturing using air jet impingement. Manuf Lett 17:14–18. https://doi.org/10.1016/j.mfglet.2018.06.004
205. Williams SW, Martina F, Addison AC, Ding J, Pardal G, Colegrove P (2016) Wire + arc additive manufacturing. Mater Sci Technol 32:641–647. https://doi.org/10.1179/1743284715Y.0000000073
206. Zeng Q, Gan K, Wang Y (2021) Effect of heat treatment on microstructures and mechanical behaviors of 316L stainless steels synthesized by selective laser melting. J Mater Eng Perform 30(1):409–422. https://doi.org/10.1007/s11665-020-05330-7
207. Khoo ZX, An J, Chua CK, Shen YF, Kuo CN, Liu Y (2019) Effect of heat treatment on repetitively scanned SLM NiTi shape memory alloy. Materials 12:77. https://doi.org/10.3390/ma12010077

208. Mfusi BJ, Mathe NR, Tshabalala LC, Popoola PA (2019) The effect of stress relief on the mechanical and fatigue properties of additively manufactured AlSi10Mg parts. Metals 9:1216. https://doi.org/10.3390/met9111216
209. Li K, Klecka MA, Chen S, Xiong W (2021) Wire-arc additive manufacturing and post-heat treatment optimization on microstructure and mechanical properties of Grade 91 steel. Addit Manuf 37:101734. https://doi.org/10.1016/j.addma.2020.101734
210. Lee Y, Nandwana P, Simunovic S (2021) Powder spreading, densification, and part deformation in binder jetting additive manufacturing. Prog Addit Manuf. https://doi.org/10.1007/s40964-021-00214-1
211. Wang X, Xiong W (2020) Uncertainty quantification and composition optimization for alloy additive manufacturing through a CALPHAD-based ICME framework. NPJ Comput Mater 6:188. https://doi.org/10.1038/s41524-020-00454-9
212. Zhao X, Iyer A, Promoppatum P, Yao S-C (2017) Numerical modeling of the thermal behavior and residual stress in the direct metal laser sintering process of titanium alloy products. Addit Manuf 14:126–136. https://doi.org/10.1016/j.addma.2016.10.005

# Part II
# Biomedical and Environmental Applications

# Chapter 9
# In Vitro Degradation Behaviour of Chitosan-Based Blends by ATR-FTIR for Tissue Engineering Scaffolds: An Indirect Bioactivity Assay

**K. Kanimozhi, V. Sugantha Kumari, S. Khaleel Basha, and K. Kaviyarasu**

## 1 Introduction

Tissue engineering platforms performance an energetic part trendy reformative medication. This one not solitary offers brief 3-dimensional sustenance through flesh reparation, nonetheless, similarly controls the cell behaviour such as cell adhesion, proliferation besides variation [1–5]. Therefore, the goal in tissue engineering is on the way to mature efficient artificial or living alternates near healing otherwise exchange injured structures/matters trendy the physique based on silver or metal oxide nanoparticles [6–11]. Aimed at effective beneficial flesh industrial, these remains important fair previously reconstruct biomimetic cellular microenvironments that involve of extracellular matrix (ECM), compartments in place of fine equally living besides reminders near help flesh rebirth [12, 13]. Currently, a general variety of biomaterials in addition to treating performances permit the construction of platforms on behalf of various tenders

K. Kanimozhi (✉)
Department of Chemistry, Global Institute of Engineering and Technology, Melvisharam 632509, Tamil Nadu, India
e-mail: kanivlr8@gmail.com

K. Kanimozhi · V. S. Kumari
PG Research & Department of Chemistry, Auxilium College (Autonomous), Vellore, Tamil Nadu, India

S. K. Basha
Department of Chemistry, C. Abdul Hakeem College, Melvisharam 632509, Tamil Nadu, India

K. Kaviyarasu
UNESCO-UNISA Africa Chair in Nanosciences/Nanotechnology Laboratories, College of Graduate Studies, University of South Africa (UNISA), Muckleneuk Ridge, Pretoria, South Africa

Nanosciences African Network (NANOAFNET), Materials Research Group (MRG), iThemba LABS-National Research Foundation (NRF), 1 Old Faure Road, Somerset West 7129, Western Cape Province, South Africa



K. Kasinathan et al. (eds.), *Nanomaterials for Energy Conversion, Biomedical and Environmental Applications*, Materials Horizons: From Nature to Nanomaterials,
https://doi.org/10.1007/978-981-19-2639-6_9

happening growing back remedy [14]. Presently, fusion resources remain actuality comprehensively examined by means of the purpose of imitating the ECM microenvironment in the direction of stand talented just before grow threatening, price-efficient, bioactive platforms aimed at tissue engineering [15, 16]. In the platform, condition make after a solitary polymer, cannot communicate entirely these preferred belongings, then through attractive binary or additional polymers trendy mixture, it remains likely to modify a frame through the anticipated features [17, 18]. Mixtures prepared of together artificial as well as regular polymers can make available the varied choice of physicochemical belongings as well as treating performances of artificial polymers in place of fine as the biocompatibility then living connections of normal polymers. Chitosan remains a regular polymer resulting through deacetylation of chitin by means of stimulating belongings aimed at biomedical uses meanwhile the situation consumes a non-hazardous, recyclable, little provocative retort, and antimicrobial personality [19, 20]. Poly(vinyl alcohol) (P) stays a non-hazardous, aquatic-solvable, extremely glassy, biodegradable, and biocompatible polymer. The situation consumes motivating bodily and organic goods then decent flick-founding capability owing in the direction of the plenty of hydroxyl groups and, thus, development of intermolecular hydrogen bonding [21]. PVA remains a talented semi-crystalline polymer aimed at numerous submissions, such by way of medication distribution, wrapping, etc. Methyl cellulose (M) stands a polysaccharide resulting after fibre which stays extensively useful in pharmaceutics for medication and protein distribution, before by way of framework aimed at flesh manufacturing, taking a marvellous latent not completely broken until now. The takes certain extraordinary belongings such in place of little poisonousness, decent biocompatibility and biodegradability, a great-aquatic relationship aptitude besides a little price now judgement by extra normal polymers [22].

In the bodily belongings of Chitosan framework can remain improved through intercourse the situation through extra artificial before natural polymers, such as poly (vinyl alcohol), Collagen, Chitosan, then consequently onwards [23, 24]. In the direction of more enlarge that one request variety, though, plentiful further hard work remains unmoving mandatory just before incredulous certain inadequacies comprising little automatic asset then reduced high temperature fighting. Several of it meant next to refining the presentations of chitosan ought to remain conveyed. In the middle of these, joining together remains a positive technique owing in the direction of small price besides humble process. Subsequently, the amalgamation of artificial besides ordinary polymers possibly will improve the rate routine proportion of the compound flicks, that one stays a gifted tactic near merger PVA and CS just before gaining the shared belongings of together polymers. In the face of the PVA/CS mixture layers on condition that outstanding belongings, a nonexistence of elasticity remain motionless single of the chief limitations aimed at this one request. Methylcellulose possibly will stand charity fashionable merged resources consuming likewise crosslinking mediators in the direction of gain hydrogels through actual tall puffiness degree which might spread the requests of Methylcellulose by way of wound dressing before in place of great porous ingredients [25].

The proper scaffold selection depends on the selection of Humiliation performance of absorbent frameworks shows an significant part trendy the manufacturing method of a novel flesh and observing the situation possible behaviour when entrenched besides tolerate retrieval period [26]. The control degradation properties of scaffold play a critical role in the growth of degradable polymeric schemes, then a better understanding of this device would remain supportive for the success of the tissue-engineered construct. This method remains of countless attention aimed at experts employed trendy the arena, by way of that one allows the manufacture of resources which remain calm of the joint besides synergistic belongings of the dissimilar residents. Greatest of the poverty trainings stated trendy the works remain done through hatching the substantial popular phosphate buffer saline (PBS). Explanation. Now this way, this one stands predictable that lone poverty using usual hydrolysis resolve happen. Hooper and colleagues [27] originate that together PBS and simulated body fluid (SBF) explanations remained suitable incubation barriers aimed at a precise imitation of the in vivo squalor of tyrosine-resulting polymers. Non-buffered answers (aquatic, isotonic salty solutions) must remain too rummage-sale popular numerous dilapidation trainings, nevertheless these examinations consumed unnoticed the cushion volume of figure liquids. Moreover, several of the poverty trails fix not anticipate the regeneration of the squalor intermediate, and once more, such challenging procedures prepare not permit aimed at the clearing of squalor crops through watery movement, basic to in vivo circumstances [28]. This one remains supposed that the flawless in vivo degradation rate might remain comparable or somewhat fewer than the degree of flesh creation. Finally, the three-dimensional interplanetary engaged through permeable framework remains substituted through again shaped matters. Fourier transform infrared (FT-IR) attenuated total reflection (ATR)0 spectroscopy stands a humble nonetheless influential method, which consumes remained charity to portray the superficial of polymer flick framework models. That one delivers the material around the link coatings and superficial actions of the interior coatings of multilayer films, supercilious they container remain delaminated efficiently to depiction the interior coatings, and pretentious those coatings are dense sufficient near differentiate them after the subsurface coatings. In order to understand, a original CS/PVA/MC mixture frameworks remained ready finished a solution casting method founded on dissimilar scopes of methylcellulose extra. The invented frameworks showed to be an actual technique in the direction of delivering a atmosphere through similar permeable construction, manageable hole extent and mechanical properties to get desirable properties aimed at soft tissue engineering claims. Trendy this setting, the in-situ description of the deprivation performance development of ternary mixture frameworks requires remained methodically examined by Attenuated total reflection-Fourier transform infrared spectroscopy (ATR-FTIR) ready for 28 days in different biological media such as Phosphate Buffer Saline (PBS), Simulated Body Fluid (SBF) and Dulbecco's modified Eagle medium (DMEM) solution at 37 °C differing in $CO_2$ concentration, etc.

## 2 Materials and Methods

### 2.1 Materials

Chitosan (80% deacetylated, molecular weight: $5.3 \times 10^4$), Polyvinyl(alcohol) (molecular weight 14,000) then Methylcellulose (analytically pure) remained purchased from S&D fine Chemicals, Mumbai, India. Dulbecco's Modified Eagle Medium (DMEM) was purchased from SRL, India. All the chemicals were of the maximum pureness and used lacking more sanitisation.

### 2.2 Synthesis of Scaffolds

Scaffolds were prepared based on modifications of the process formerly testified through Kanimozhi et al. [29]. The preparation of the Chitosan beached cross ternary mixture frameworks continued prepared by a federation of flick casting and lyophilization methods. 1 g Chitosan (C) gunpowder was added into a 100 ml of 0.1 M acetic acid formerly the amalgamation stood motivated to arrangement a 1wt% pure chitosan solution. In the meantime, 1 g Poly (vinyl alcohol) (P) gunpowder was thrilling into 100 ml at 80 °C washed with water done exciting to form a 1% clear Poly(vinyl alcohol) clarification and methylcellulose (M) powder was inspiring into 100 ml rinsed water and inspired to form 1wt% methylcellulose solutions, similarly. The blend scaffolds, containing 25%, 50%, and 75% V/V solutions of methylcellulose of the total weight of chitosan and Poly(vinyl alcohol). The prepared hybrid blend scaffold samples were coded as CPM1, CPM2 and CPM3.

### 2.3 Scaffold Formation-Lyophilization Method

Popular technique a agenda each of the degassed merger (10 ml) continued elated bent on Teflon petri dishes, chilled at 4 °C, frosty at −20 °C in a profound freezer for 24 h. The frost-enclosed plates continued situated fashionable a lyophilizer at −40 °C though to come aimed at thirsty absorbent frameworks remained contracted. The following outlines (area 2 $cm^2$, width = 3.0 mm) continued responded in the way of removing acetate by plunging them in 10% NaOH shaded through washing through water whereas coming up aimed at responded, straggled over lyophilization.

### *2.4 In Vitro Degradation Studies by ATR-FTIR Method*

The scaffolds (10 mm × 20 mm) continued expurgated dependent toward a rectangular numeral meant by filth stimulating in vitro foulness hearings continued displayed done soaked the representations fashionable three different media: phosphate buffer saline (PBS: 0.13 M, NaCl:0.9%, $NaN_3$: 0.02%, pH: 7.4), simulated body fluid(SBF: which devours inanimate ion courtesies similar nearby folks of humanoid extracellular fluid, remained prepared over tender specific wholes of combination materials of NaCl, $NaHCO_3$, KCl, $K_2HPO_4$. $3H_2O$, $MgCl_2.6H_2O$, $CaCl_2$. $2H_2O$, and $Na_2SO_4$ into purified water, pH 7.25) and the Dulbecco's Modified Eagle Medium (DMEM: commercially purchased). The porous scaffolds were sterilized under UV irradiation for 2 h, enthusiastic close the covering quartz continued situated general 24-well plates by resources of tweezers, formerly later an aliquot (3 mL) of PBS, SBF and DMEM solution at 37 °C differing in $CO_2$ concentration.

The farming regular mounted relieved over the original clarification every 3 days. Three comparable frameworks of together offensiveness old mounted engaged available subsequent to different old-fashioned, rinse gone over sanitized fluid and cancelled desiccated obtainable meant on additional explanation by ATR-FTIR method. Attenuated Total Reflectance (ATR) -Fourier-transformed infrared spectroscopy (FTIR) (Schimadzu IR affinity-1S) was performed using an Assignment ATR ZnSe quartz compartment over size-up of 250 scans through a purpose of 4 $cm^{-1}$ and a wavenumber range of 4000−400 $cm^{-1}$ all spectrum continued educated smart transmission method after immersion in PBS, SBF and DMEM.

## 3 Results and Discussion

ATR-FTIR analysis using PBS and SBF was conducted to analyse the chemical structural changes in the samples by mimicking interactions in the body environment. PBS and SBF have ion concentrations comparable to those present in human blood plasma. Dulbecco's modified Eagle medium (DMEM) remainders assistance general mammalian compartment state close increase radio loyalty, reduce toxic ammonia character conscious then brand the greatest of cell performance. The ATR-FTIR studies are possibly an indication that the prepared films of chitosan, PVA and different ratios of methylcellulose scaffolds had undergone a chemical reaction in the different media of PBS, SBF and DMEM environment for four weeks. This study would be preferable to identify the degradation behaviour and the hazardous dated estimation intended by the frameworks grows fragile fashionable stabilities of polymer chains then subsequently convinced their covert fashionable flesh engineering application.

### 3.1 ATR-FTIR Spectra of CS/PVA, CPM1, CPM2 and CPM3 Scaffolds Before Immersion in Different Biological Media

ATR-FTIR spectroscopy is a simple but powerful method aimed at the investigation of chemical interactions of the compounds. The ATR-FTIR spectra of CS/PVA, CPM1, CPM2 and CPM3 scaffolds before involvement in PBS, SBF and DMEM solution are presented in Fig. 1. The spectrum of CS/PVA (Fig. 1) and band assignments are given in Table 1, exhibits a strong and broad absorption band at 3741 $cm^{-1}$ attributed to the OH group and a peak at 1032 $cm^{-1}$. The peak at 1643 $cm^{-1}$ (amide I) through a slight assume at 1556 $cm^{-1}$ (amide II) stands credited to acetylated amino group and checks that the model stands not completely deacetylated. The peak at 1032 $cm^{-1}$ was allocated to the free primary amino group (-$NH_2$) at C2 location of glucosamine. The fascination bands pragmatic at 1643 $cm^{-1}$ and at 1556 $cm^{-1}$ remained shifted near lower wave number owing to the contact among OH and NH bending vibration

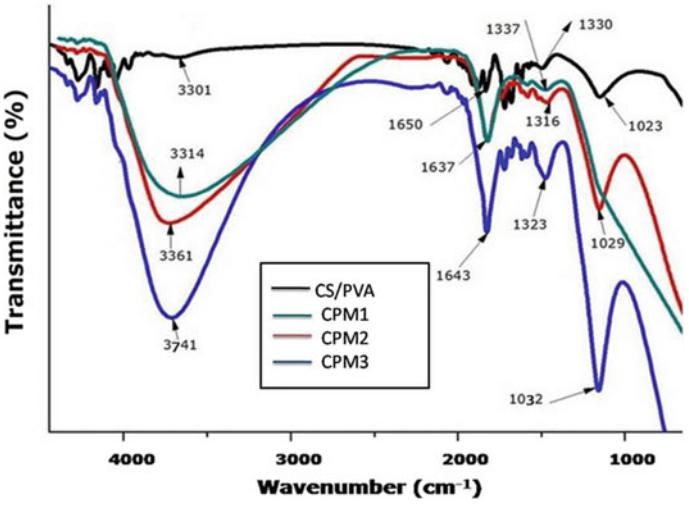


**Fig. 1** ATR-FTIR spectra of scaffolds before immersion in PBS, SBF and DMEM media

**Table 1** Assignments of ATR-FTIR bands of scaffolds before immersion in PBS, SBF and DMEM

| No. assignments | CPM1 | | CPM2 | CPM3 |
|---|---|---|---|---|
| | Band ($cm^{-1}$) | Band ($cm^{-1}$) | Band ($cm^{-1}$) | |
| 1 | 3314 | 3361 | 3741 | OH stretching |
| 2 | 1637 | – | 1643 | Amide I band |
| 3 | 1337 | 1316 | 1323 | C=C streching |
| 4 | – | 1492 | 1023 | C–0 streching |

of CS/PVA. Compared to the spectra of CS/PVA film, the bands by wave number 3361 $cm^{-1}$, 3314 $cm^{-1}$, 3301 $cm^{-1}$ and 1029 $cm^{-1}$ & 1023 $cm^{-1}$ in the CPM1, CPM2 and CPM3 frameworks remain lifted near lesser wavenumber morals. This change remained a consequence of the creation of intermolecular hydrogen bonds by the OH of PVAand OH or NH, and OH of methylcellulose. The intensity of the peak takes remained reduced and near is a shift in wavenumbers of the bands once attention enlarged since 25% to 75%.

## *3.2 ATR-FTIR Spectra of CPM1, CPM2 and CPM3 Scaffolds After Immersion in Different Biological Media*

### 3.2.1 Immersion of CPM1, CPM2 and CPM3 Scaffolds in Phosphate Buffer Solution (PBS)

The ATR-FTIR of CPM1 scaffold (Fig. 2) and band assignments are given in Table 2, after 7 days, 14 days and 28 days of immersion in PBS solution. A broad peak appears between 3500 $cm^{-1}$ and 3000 $cm^{-1}$ and additional peak everywhere at 1647 $cm^{-1}$. Trendy period peaks grow next to about 1042 $cm^{-1}$, 1036 $cm^{-1}$ and 1032 $cm^{-1}$ respectively. The band at 3364 $cm^{-1}$ is due to OH or NH stretching. In the spectra of the scaffold flick connections connecting normal besides artificial polymers at 1647 $cm^{-1}$ (amide I) and $NH_2$ in amino group at 1323 $cm^{-1}$ (amide II). These indicate the interaction among the polymeric scaffold; probably through the formation of hydrogen attachment among OH of PVA and OH or $NH_2$ of CS is obvious as of (Fig. 2a). The fascination peaks were found to be increased and decreased after 28 days degradation in PBS medium. The intensity of the bands around corresponding to around 1647 $cm^{-1}$ (amide I) and 1323 $cm^{-1}$ (amide II) remained nearly diminished later squalor in PBS medium. Figure 2a' demonstrations the transmission strength against the immersion period aimed at the transmission most at 3364, 1647 and 1042 $cm^{-1}$, consistent to the extending vibrations of PBS molecules and hydroxides. Throughout the leading 7 days of experience the quick strength growth of the group at 3364 $cm^{-1}$ might stand produced by phosphate buffer acceptance hooked on the polymer system. The reduction fashionable strength of the group at 1647 $cm^{-1}$ indicates the carriage kinetics interested in the polymer flick. Not at all continuous standards remained touched on extended contact periods and the strength rises of entire groups remained linear.

Figure 2b depicts the ATR-FTIR bands found subsequently dissimilar immersion periods for CPM2 scaffolds in contact with PBS solution. Next to smaller immersion periods, an extensive and strong band look as if trendy the ranges among 3500 and 3000 $cm^{-1}$, by a extreme everywhere 3367 $cm^{-1}$ might remain allocated near together symmetric and asymmetric extending vibrations arise from (-OH) group due to the polymer surface. Subsequently penetrating the polymer flick, PBS particles might remain obtainable by way of wholesale similar liquid next to the polymer

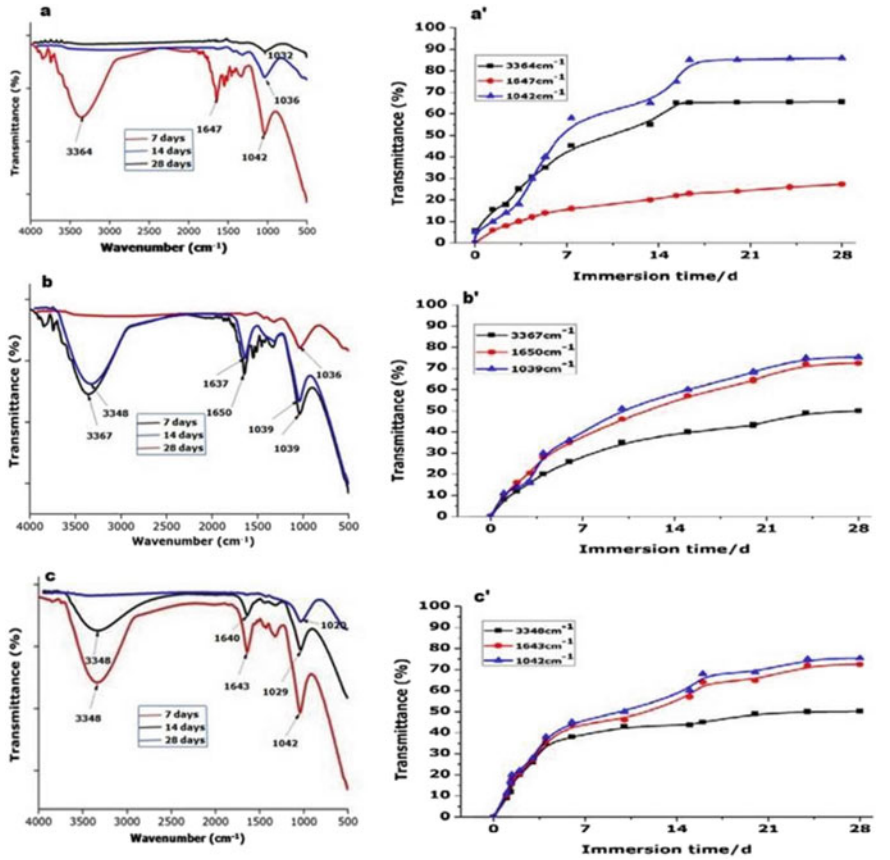


**Fig. 2** ATR-FTIR spectra of scaffolds after immersion in PBS and the corresponding transmittance intensities versus the immersion time of (i) (a & a') CPM1 (ii) (b & b') CPM2 and (iii) (c & c') CPM3

**Table 2** Assignments of ATR-FTIR bands of scaffolds in PBS

| No. assignments | CPM1 | | CPM2 | CPM3 |
|---|---|---|---|---|
| | Band ($cm^{-1}$) | Band ($cm^{-1}$) | Band ($cm^{-1}$) | |
| 1 | 3364 | 3364 | 3367 | OH stretching |
| 2 | 1647 | 1650 | 1643 | Amide I band |
| 3 | 1323 | – | – | C=C streching |
| 4 | – | 1042 | 1039 | C–0 streching |

border by means of tiny PBS-occupied holes and in place of combined inside the external close polymer system and the absorbent construction of the polymer flick [29]. Such combined PBS can be popular dissimilar methods, aimed at case, by means of powerfully hydrogen bonded, or broadsheets adsorbed against the hole. The peaks at 1650 $cm^{-1}$ remained due to the (amide I) band of the CPM2 scaffold. Although the extensive band under 1500 $cm^{-1}$ through an cumulative involvement period a comparatively shrill fascination peak look as if by about 1500–1000 $cm^{-1}$, through a extreme at 1039 $cm^{-1}$. This peak could remain allocated to longitudinal extending feelings of polymer and near bending vibrations of polymer which remain modifications owing near oxidation of the polymer superficial. Figure 2b' shows ATR-FTIR transmission intensities later dissimilar periods of immersion. A wide group seems next to everywhere 3367 $cm^{-1}$ owing near OH- stretching vibrations of CPM2. The peak at 1650 $cm^{-1}$ was due to the (amide I) band of the CPM2 scaffold present within the CPM scaffold. After 28 days of immersion periods added peaks remained got next to 1039 $cm^{-1}$. These peaks could both remain owing near tainted polymer material, though the peaks next to inferior wave statistics likewise tin remain owing near transformation of previously current M crops.

Figure 2c shows the ATR- FTIR spectra for scaffolds of CPM3 after 7, 14 and 28 days of involvement in PBS. A peak shift might remain experiential among 1042 $cm^{-1}$ & 1020 $cm^{-1}$. This consequence happens popular straight amount to the rise trendy the M proportion inside the flick, which resembles to the entrance of the C–O–C stretching vibration. The symmetry of M is lowered which in turn reflects interaction between M and the polymer in their system. The bands shift to even lower wavenumbers as more M is added as 75% of MC to CS/PVA. The transmission strengths against the immersion period aimed at transmission band greatest at 3348, 1643 and 1042 $cm^{-1}$ correspondingly remain shown in Fig. 2c. The intensity of altogether three transmission bands enlarged through the immersion while, nonetheless through dissimilar kinetics. The linear intensity rises of the P = O is elongating a shaking band through spell specifies that the buffer solution stimulated inside the polymer system through a dissimilar conveyance instrument than liquid and that ions stood nonstop accrued next to the border. The peaks at 1643 $cm^{-1}$ and 1042 $cm^{-1}$ reached the steady state level after 28 days of immersion indicating the MC incorporation in the scaffolds. The peak at 1650 $cm^{-1}$, the stable national equal touched inside 28 days of immersion time designates significant degradation behaviour of the polymer support.

### 3.2.2 Immersion of CPM1, CPM2 and CPM3 Scaffolds in Stimulated Body Fluid (SBF)

The contribution of *CPM1, CPM2 and CPM3* scaffold network was confirmed by ATR-FTIR subsequently involvement in SBF after 7, 14 and 28 days in Fig. 3 (a–c) and band assignments are given in Table 3. The wide-ranging bands experimental from 3200 $cm^{-1}$ to 3500 $cm^{-1}$ in the bands allocated to hydroxyls (OH) extending owing toward the robust hydrogen bond of intramolecular then the intermolecular

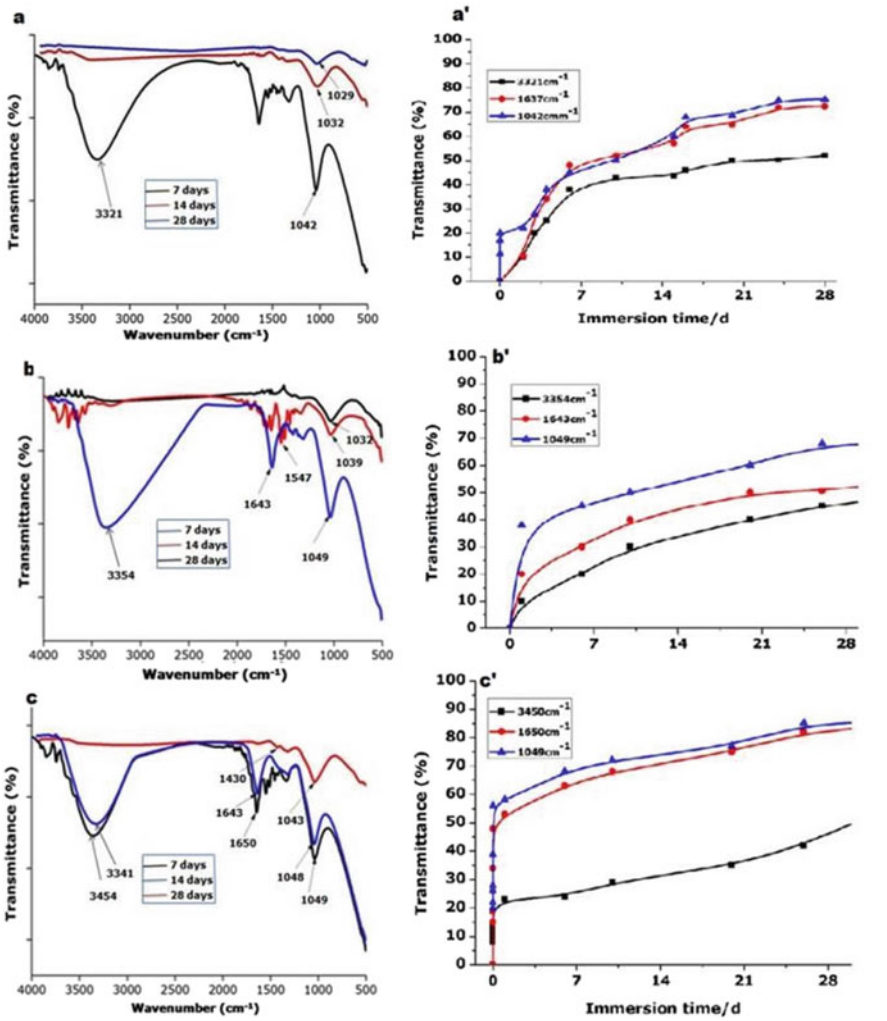


**Fig. 3** ATR-FTIR spectra of scaffolds after immersion in SBF and the corresponding transmittance intensities versus the immersion time of (i) (a & a') CPM1 (ii) (b & b') CPM2 and (iii) (c & c') CPM3

**Table 3** Assignments of ATR-FTIR bands of scaffolds in SBF

| No. Assignments | CPM1 | | CPM2 | CPM3 |
|---|---|---|---|---|
| | Band ($cm^{-1}$) | Band ($cm^{-1}$) | Band ($cm^{-1}$) | |
| 1 | – | 3321 | 3450 | OH stretching |
| 2 | 1650 | 1700 | 1650 | Amide I band |
| 3 | 1000 | 1042 | 1049 | C–O streching |

kind. The bands ranging from 1650 $cm^{-1}$ to 1700 $cm^{-1}$ and 1000 $cm^{-1}$ to 1200 $cm^{-1}$ ascend owing to the extending vibration carbonyl (C = O) correspondingly, after the vinyl acetate cluster originates trendy incompletely hydrolysed P-polymer. Near stands an overlying of the groups trendy the variety after 1650 to1700 $cm^{-1}$ resulting as of the CS/PVA/MC components. The scaffold development tips towards the expansion of the groups connected to vinyl group, which nearly vanish because of the hydrogen bonds in the scaffolds subsequently 28 days of involvement.

The spectrum of transmission intensities versus immersion time of *CPM1, CPM2 and CPM3* scaffolds after 7, 14 and 28 days of soaking in SBF in Fig. 3 (a', b' and c') displays bands in the range 3000–3500 $cm^{-1}$. They stand allocated towards extending vibrations of OH group through little strength owing to a greater binding attraction among CPM owing toward this detail a comparatively low response among CPM supports and SBF takes residence. As concentration increases transmission intensities also increase from 3321 $cm^{-1}$ to 3450 $cm^{-1}$ and 1042 $cm^{-1}$ to 1049 $cm^{-1}$. These indicate the interactions between the scaffolds and SBF and small changes in the degradation behaviours.

### 3.2.3 Immersion of CPM1, CPM2 and CPM3 Scaffolds in Dulbecco's Modified Eagle Medium (DMEM)

The attenuated total reflection-Fourier transform reflection (ATR-FTIR) spectra of *CPM1, CPM2 and CPM3* scaffolds in Dulbecco's modified Eagle medium (DMEM) after degradation for 7, 14 and 28 days remained shown in Fig. 4 (a, b & c) then band assignments are given in Table 4. ATR-FTIR ranges remained approved available to clarify the occurrence of CPM trendy the merged scaffolds then toward analyse the communication (hydrogen bonding) among them. The extensive peak at 3581 to 3730 $cm^{-1}$ designates extending vibrations of the hydroxyl collections owing to the intramolecular and intermolecular hydrogen bonds of the OH groups of CPM. The absorption peaks remained originate to be improved and diminished aimed at three types of scaffolds afterward 28 days filth in DMEM medium. The penetrating of absorption, designates a sturdier hydrogen bond looked inside the molecular cable of CPM scaffolds contributes to the slow squalor degree in DMEM solution. The strength of the groups around 2927 and 2942 $cm^{-1}$ agreed to $CH_2$ extending vibrations remained nearly diminished afterward squalor trendy DMEM average. In this consequence proposes the hydrolysis of CPM dim hooked on squalor average [30]. Trendy adding, the methylcellulose macromolecules suffer restraint scission then attaching toward the polymer support.

In Fig. 4 (a', b' and c') shows the transmission intensity versus immersion time of the scaffolds after 7, 14, 28 days of squalor. The range of existing key groups are 3581 and 1681 $cm^{-1}$, 3263 and 1630 $cm^{-1}$, 3730 and 1768 $cm^{-1}$. After immersion of the CPM in DMEM solutions, the absorption band intensities were decreased. These fascination groups describe -OH alcohol besides amide band then their decrement indicate that together amide then alcoholic groups donate toward the creation of scaffold surface of the membranes [31, 32]. The above results of transmission intensity

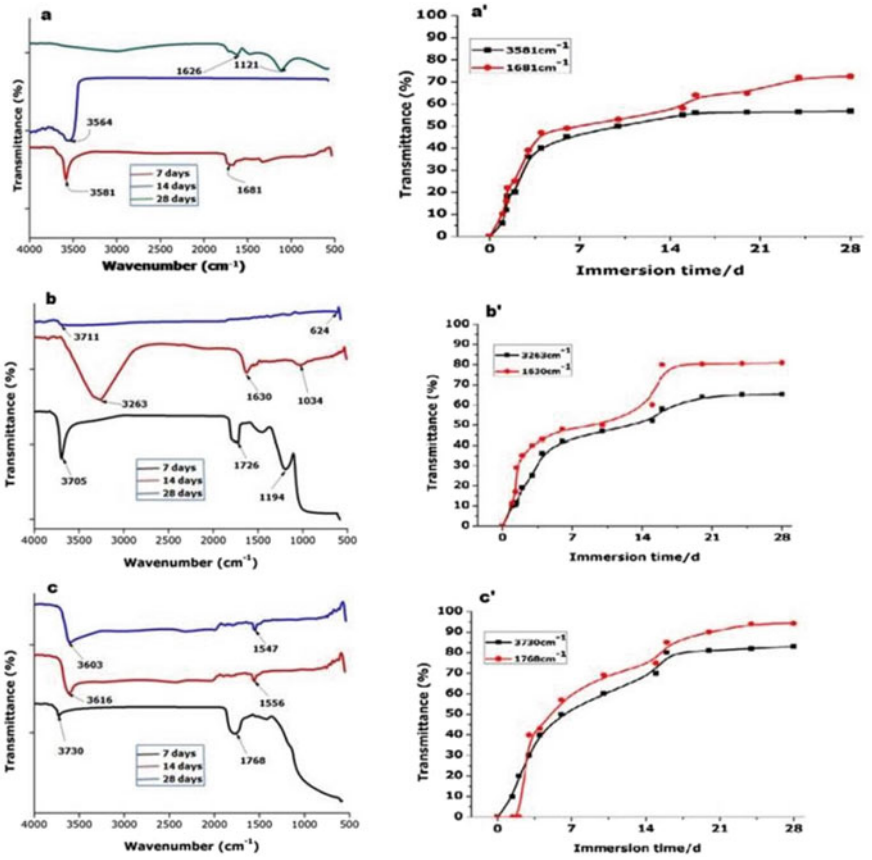


**Fig. 4** ATR-FTIR spectra of scaffolds after immersion in DMEM and the corresponding transmittance intensities versus the immersion time of (i) (a & a') CPM1 (ii) (b & b') CPM2 and (iii) (c & c') CPM3

**Table 4** Assignments of ATR-FTIR bands of scaffolds in DMEM

| No. assignments | CPM1 | | CPM2 | CPM3 |
|---|---|---|---|---|
| | Band ($cm^{-1}$) | Band ($cm^{-1}$) | Band ($cm^{-1}$) | |
| 1 | 3581 | 3263 | 3730 | OH stretching |
| 2 | 2927 | 2942 | – | C=H stretching |
| 3 | – | 1681 | 1630 | C=C streching |

changes attributed that the scaffolds had an insignificant degradation behaviour of the polymer backbone when compared to two biological media PBS and SBF.

## 4 Conclusion

The in vitro characterization of the degradation behaviour of the prepared hybrid polymeric scaffolds of *CPM1, CPM2 and CPM3* has been systematically investigated up to 28 days in PBS, SBF and DMEM at 37 ºC using ATR-FTIR spectroscopy. The effects of the methyl cellulose ratios on the characterization of the chemical structures of these hybrid porous scaffolds before and after degradation were also observed by ATR-FTIR. The visible observations of the hybrid scaffolds prepared in 7, 14 and 28 days showed significant differences in the absorption of bands and molecular interactions in the immersion time. During immersion in PBS and SBF solution, the fast-initial increases of the stretching and bending vibrations of PBS and SBF indicated the degrading behaviour of the polymer network and to the scaffold surface. The uptake effect of degradation behaviour of DMEM is insignificant in the presence of the methylcellulose in different concentration, due to the chain scission of the polymeric backbone compared to PBS and SBF. The results demonstrated that the degradation behaviour meets the requirements as a potentially degradable biomaterial for soft tissue engineering applications.

**Acknowledgements** The novelists remain appreciative to Auxilium College Management intended for providing that essential services intended for the investigational effort.

## References

1. Kanimozhi K, Basha SK, Kaviyarasu K, SuganthaKumari V (2019) Salt leaching synthesis, characterization and in vitro cytocompatibility of chitosan/poly (vinyl alcohol)/methylcellulose–ZnO nanocomposites scaffolds using L929 fibroblast cells. J Nanosci Nanotechnol 19:4447–4457
2. Nalini T, Basha SK, Sadiq AMM, Kumari VS, Kaviyarasu K (2019) Development and characterization of alginate/chitosan nanoparticulate system for hydrophobic drug encapsulation. J Drug Delivery Sci Technol 52:65–72
3. Siddhardha B, Pandey U, Kaviyarasu K, Pala R, Syed A, Bahkali AH, Elgorban AM (2020) Chrysin-loaded chitosan nanoparticles potentiates antibiofilm activity against Staphylococcus aureus. Pathogens 9(2):115
4. Kayalvizhi K, Alhaji NMI, Saravanakkumar D, Beer Mohamed S, Kaviyarasu K, Ayeshamariam A, Al-Mohaimeed AM, AbdelGawwad MR, Elshikh MS (2022) Adsorption of copper and nickel by using sawdust chitosan nanocomposite beads–a kinetic and thermodynamic study. Environ Res 203 (2022) 111814
5. Mani M, Harikrishnan R, Purushothaman P, Pavithra S, Rajkumar P, Kumaresan S, Al Farraj DA, Elshikh MS, Balasubramanian B, Kaviyarasu K (2021) Systematic green synthesis of silver oxide nanoparticles for antimicrobial activity. Environ Res 202:111627
6. Mani M, Pavithra S, Mohanraj K, Kumaresan S, Alotaibi SS, Eraqi ME, Gandhi AD, Babujanarthanam R, Maaza M, Kaviyarasu K (2021) Studies on the spectrometric analysis of metallic silver nanoparticles (Ag NPs) using Basella alba leaf for the antibacterial activities. Environ Res 199:111274
7. Mani M, Okla MK, Selvaraj S, Ram Kumar A, Kumaresan S, Muthukumaran A, Kaviyarasu K, El-Tayeb ME, Elbadawi YB, Almaary KS, Almunqedhi BMA, Elshikh MS (2021) A novel

biogenic Allium cepa leaf mediated silver nanoparticles for antimicrobial, antioxidant, and anticancer effects on MCF-7 cell line. Environ Res 198:111199
8. Valsalam S, Agastian P, Arasu MV, Al-Dhabi NA, Ghilan AKM, Kaviyarasu K, Ravindran B, Chang SW, Arokiyaraj S (2019) Rapid biosynthesis and characterization of silver nanoparticles from the leaf extract of Tropaeolum majus L. and its enhanced in-vitro antibacterial, antifungal, antioxidant and anticancer properties. J Photochem Photobiol B Biol 19:65–74
9. Badineni V, Maseed H, Arla SK, Yerramala S, Naidu BVK, Kaviyarasu K (2021) Effect of PVA/PVP protective agent on the formation of silver nanoparticles and its photocatalytic and antimicrobial activity. Mater Today Proc 36:121–125
10. Gandhi AD, Kaviyarasu K, Supraja N, Velmurugan R, Suriyakala G, Babujanarthanam R, Zang Y, Soontarapa K, Almaary KS, Elshikh MS, Chen TW (2021) Annealing dependent synthesis of cyto-compatible nano-silver/calcium hydroxyapatite composite for antimicrobial activities. Arab J Chem 14 (2021) 103404
11. Langer R, Vacanti J (1993) Tissue engineering. J Sci Commun 260:920–926
12. Sant S (2012) Tissue analogs by the assembly of engineered hydrogel blocks, biomimetic approaches for biomaterials development. Wiley-VCH Verlag GmbH & Co. KGaA, pp 471–493
13. Sant S, Hancock MJ, Donnelly JP, Iyer D, Khademhosseini A (2010) Biomimetic gradient hydrogels for tissue engineering. J Chem Eng 88:899–911
14. Hutmacher DW, Cool S (2007) Concepts of scaffold-based tissue engineering the rationale to use solid free-form fabrication techniques. J Cell Mol Med 11:654–669
15. Wang M (2003) Developing bioactive composite materials for tissue replacement. Biomat 24:2133–2151
16. Sachot N, Engel E, Castano O (2014) Hybrid organic-inorganic scaffolding biomaterials for regenerative therapies. Curr Org Chem 18:2299–2314
17. Gautam S, Chou CF, Dinda AK, Potdar PD, Mishra NC (2014) Fabrication and characterization of PCL/gelatin/chitosan ternary nanofibrous composite scaffold for tissue engineering applications. J Mat Sci 49(3):1076–1089
18. Dhandayuthapani B, Yoshida Y, Maekawa T, Sakthi Kumar D (2011) Polymeric scaffolds in tissue engineering application: a review. Inter J Polym Sci 19
19. Leceta I, Penalba M, Arana P, Guerrero P, de la Caba K (2015) Ageing of chitosan films: Effect of storage time on structure and optical, barrier and mechanical properties. J Europ Polym 66:170–179
20. Wang T, Zhu XK, Xue XT, Wu DY (2012) Hydrogel sheets of chitosan, honey and gelatin as burn wound dressings. Carbohyd Polym 88:75–83
21. Bonilla J, Fortunati E, Atares L, Chiralt A, Kenny JM (2014) Physical, structural and antimicrobial properties of poly vinyl alcohol-chitosan biodegradable films. Food Hydrocolloids 5:463–470
22. Kanimozhi K, KhaleelBasha S, SuganthaKumari V (2016) Fabrication of chitosan based hybrid porous scaffolds by salt leaching for soft tissue engineering. Surf Interfac 1–3:7–12
23. Vieira MGA, Silva MA, Santos LO, Beppu MM (2011) Natural-based plasticizers and biopolymer films: a review. J Eureo Polym 47:254–263
24. Boateng JS, Matthews KH, Stevens HN, Eccleston GM (2008) Wound healing dressings and drug delivery systems: a review. J Pharm Sci 97:2892–2923
25. Qiu X, Hu S (2013) Smart materials based on cellulose: a review preparations, properties, and applications. Materials 6:738–778
26. Pena J, Corrales T, Izquierdo-Barba I, Doadrio AL, Vallet-Regi M (2006) Long term degradation of poly(ε-caprolactone) films in biologically related fluids. Polym Degrad Stab 91:1424-1432
27. Hooper KA, Macon ND, Kohn J (1998) Comparative histological evaluation of new tyrosine-derived polymers and poly(L-lactic acid) as a function of polymer degradation. J Bio Mat Res 41:443
28. Agrawal CM, Athanasiou KA (1997) Technique to control pH in vicinity of biodegrading PLA-PGA implants. J Bio Mat Res 38:105
29. Kanimozhi K, Khaleel Basha S, Sugantha Kumari V (2016) Processing and characterization of chitosan/PVA and methylcellulose porous scaffolds for tissue engineering. Mat Sci Eng C 61:484–491

30. Zulkifli FH, Jahir Hussain FS, Abdull Rasad MSB, Yusoff MM (2014) In vitro degradation study of novel HEC/PVA/collagen nanofibrous scaffold for skin tissue engineering applications. Polym Degrad Stab 110:473–481
31. Chen Q, Roether JA, Boccaccini R (2008) Tissue engineering scaffolds from bioactive glass and composite materials. Topics Tissue Eng 4
32. Martin RA, Yue S, Hanna JV, Lee PD, Newport RJ, Smith ME, Jones JR (2012) Characterizing the hierarchical structures of bioactive sol-gel silicate glass and hybrid scaffolds for bone regeneration. Trans Math Phys Eng Sci 370:1422–1443

# Chapter 10
# Selenium Nanoparticles: Treatments in Tissue Engineering for Alcoholic Cardiomyopathy


**Suresh Naveenkumar, Narayanan Venkateshan, and Azhaguchamy Muthukumaran**

## 1 Introduction

Alcoholic cardiomyopathy (ACM) is a unique disease and more familiar to physicians as "*alcoholic heart disease"* coined by William Mackenzie. Alcohol addiction exists in most societies [42]. "*Tubingen Wine Heart*" described in 1877 and "*Munich Beer Heart"*, reported by German pathologist Otto Bollinger are two popular references to harmful consequences of alcohol intemperance identified during the early 20th century [42]. The progression of alcoholic cardiomyopathy is initiated by alcohol addiction. Alcohol-induced damage in the heart reduces blood pumping and increases myocardial apoptosis [83]. The latter half of the twentieth century witnessed a large meta-analysis of 34 studies comprising >1 million subjects and 10,000 deaths [54]. In epidemiology study of women and men (490,000) with middle age group, population group mortality increased with heavier drinking induced the risk of coronary heart diseases and stroke, including increased fibrinolysis, high-density lipoprotein (HDL) cholesterol, decreased fibrinogen, and decreased plasma viscosity and decreased platelet aggregation [56]. Alcoholic patients deformed in the cardiac structure and function change report consuming >90 g/d of alcohol for >5 years. It is imperative tos note potential damage to the heart with long-lasting alcohol [23, 39, 54]. Long-term studies have been conducted on rats that were fed 25% alcohol solution for seven months. The ventricular contractile force was decreased after four months of study. Controls remain normal and myocardial depression was identified in the rat

S. Naveenkumar · A. Muthukumaran (✉)
Department of Biotechnology, Kalasalingam Academy of Research and Education, Krishnankoil, Tamilnadu, India
e-mail: a.muthukumaran@klu.ac.in

N. Venkateshan
Department of Pharmaceutical Chemistry, Arulmigu Kalasalingam College of Pharmacy, Krishnankoil, Tamil Nadu, India



K. Kasinathan et al. (eds.), *Nanomaterials for Energy Conversion, Biomedical and Environmental Applications*, Materials Horizons: From Nature to Nanomaterials,
https://doi.org/10.1007/978-981-19-2639-6_10

administrated with vitamin supplementation. Recently another study was conducted on the rat fed an isocaloric liquid diet. During the study period (10 months), rats were fed 39% of the isocaloric liquid diet of their daily calories. The result showed no abnormalities found to occur in the isolated heart. However, the decreased response of left ventricular peak systolic pressure was observed in the rat fed by alcoholic solution [23, 39]. Alcohol has been affecting the myocardium's function and structure. Few studies also reported that increased myocyte loss was observed due to apoptosis when the hearts were exposed to a high amount of alcohol. Ethanol and its metabolites are toxic to the myocyte and unfavorable impacts were identified in cardiac myofibril shortening and myoprotein composition [34, 83]. Echocardiographic showed few abnormal functions such as decrease in fractional abnormalities, increased left atrial dimension, and left ventricular wall thickness in heavy alcohol drinkers [3]. Several researchers showed constant systolic dysfunction. The diastolic and systolic malfunctions have been seen in alcoholic cardiomyopathy in animal and human studies [31, 92, 109]. Potential mechanisms in the development of alcoholic cardiomyopathy are shown in Fig. 1. The patient who has alcoholic cardiac myopathy also develops magnesium deficiency in the blood serum. A lower amount of magnesium reduction was observed in the blood when the patient's blood ethanol levels

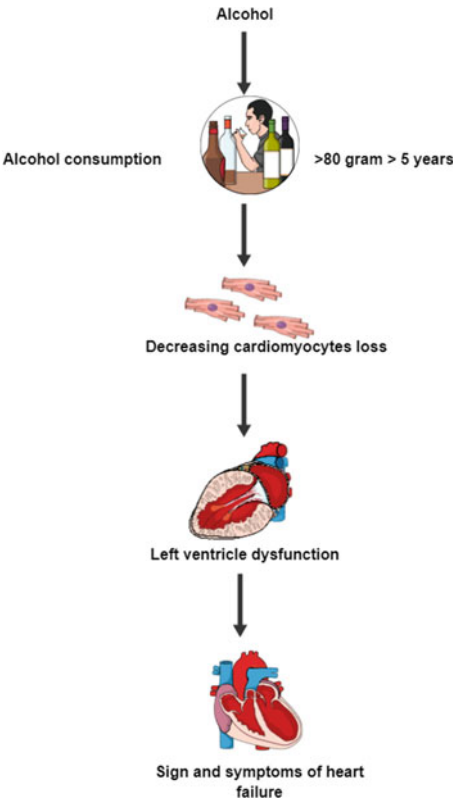


**Fig. 1** Potential mechanisms for the development of alcoholic cardiomyopathy

were above 80 mg/dL. These lead to cause arrhythmias and oxygen desaturation in the alcoholic patient [10].

## 2 Treatment for Alcoholic Cardiomyopathy

So far, there is no specific therapy available for ACM. ACE inhibitors, beta-blockers and diuretics are essential for the therapy at an advanced stage. However, the prognosis was dependent upon further alcohol abuse, causing the situation significantly worse. The mechanisms behind treatment for ACM are not well understood. So far, treating ACM relies on the general guidelines for heart failure, including diuretics, ACE-inhibitors/ARBs, β-antagonists, and cardiac glycosides. Presently, no treatment reports the pathology of ACM [83] explicitly.

## 3 Overview Glutathione Peroxidase

The free radicals are molecules or atoms with an unpaired electron in their outermost shell [46]. The presence of a free-electron gives these molecules a high reactivity and the ability to oxidize or reduce many compounds to stabilize their outer orbital. Reactive oxygen species (ROS) are free radicals consequential from molecular oxygen. They denote the largest class of generated reactive species in living organisms because of the importance of aerobic metabolism. Glutathione is a tripeptide (glutamic acid-glycine-cysteine) involved in many processes, including maintaining intercellular communications [4] and preventing oxidation of thiols group through its reducing power. It constitutes the majority of thiol intracellularly, where it is present mainly in reduced form. During aging, displacement of the balance between thiol shape and form disulfide has been highlighted and could be involved in cell dysfunction observed with age [26]. Glutathione, a direct hydrophilic chelator found in largish cellular compartments, is a cofactor for GPx and allows regenerating the vitamins C and E in their active form [66]. Glutathione also plays a vital role in the brain since the brain cells consume 20% of the oxygen in the body, while the brain is only 2% of body weight. Detoxification of ROS formed continuously during oxidative metabolism is therefore imperative. Glutathione can chelate cuprous ions and thus limit the Fenton-type reaction [47]. As an antioxidant, glutathione may intervene by two types of mechanisms, such as catch of radical species and participation in the activity of antioxidant enzymes. In 1973, Rotruck demonstrated the presence of selenium in the active site Glutathione peroxidase. Four isoforms have been identified, each having four selenium atoms as selenocysteine. These are essential antioxidant enzymes in the body. This feature helps reduce the spread of oxidative damage to noble biomolecules (lipids, lipoproteins, and DNA) and maintain membrane integrity. Enzyme activity is directly proportional to selenium intake [47].

## 4 Enzymes Acting on Peroxide

The hydrogen peroxide was destroyed by the enzyme glutathione peroxidases and cofactor selenium [104]. These enzymes can detoxify the hydrogen peroxide, the second substrate being reduced glutathione (GSH), on which they transfer oxygen, transforming it into oxidized glutathione (GSSG).

$$H_2O_2 + 2GSH \rightarrow GSSG + H_2O$$

Glutathione is regenerated by glutathione reductase (GSSG reductase) in the presence of a co-factor (selenium), NADPH.

$$GSSG + NADPH \rightarrow 2GSH + NADP$$

Glutathione peroxidases are not specific to hydrogen peroxide and hydroperoxides (ROOH) of the cell membrane are phospholipids, also possible substrates.

$$ROOH + 2GSH \rightarrow GSSG + ROH + H_2O$$

The detoxifying activity of glutathione peroxidases face hydroperoxides (ROOH) require the intervention of another enzyme, phospholipase A2. This releases the fatty acid peroxides cell membranes by hydrolyzing ester functions of membrane phospholipids. Glutathione peroxidases then convert peroxides released into the cytosol while the chain missing fatty acids is resynthesized [16]. Glutathione peroxidases are inhibited by superoxide ions [85]. They are five isoenzymes of glutathione peroxidase available, the most abundant are glutathione peroxidase 1 (cytoplasmic (90%) and mitochondrial (10%)). It is expressed in most cells, particularly in erythrocytes, kidneys, and liver. This is glutathione peroxidase 4, which can reduce directly under the action notification of a phospholipase A2, hydroperoxides phospholipids. So, it plays a fundamental role in keeping cell membranes against the toxic effects of lipid peroxidation. It is in the mitochondrion and cytoplasm. Human glutathione peroxidase may also reduce hydroperoxides thymine in DNA.

## 5 Selenium Dietary Intake

The amount of selenium in food depends on plants via by content and bioavailability of selenium in the soil on which it is grown, now and in animal foods from the selenium supply of animals via the feed [32, 33]. In accumulation to the supply of plants with selenium is another essential factor that influences the selenium content, to the ability of plants to capture and store the selenium. Plants can be in this regard are divided into three categories (i) non-selenium- accumulating

plants (100 μg Se/g dry wt), (ii) selenium-accumulating plants (accumulate selenium in direct proportion to the content of the soil in, ≤1.000 μg Se/g dry wt) and (iii) hyperaccumulating plants (up to 40,000 μg Se/g dry wt) [9, 86]. In addition, plants contain high protein higher selenium levels, as in the biosynthesis of proteins, sulphurous methionine can be replaced due to the structural and chemical properties similar by selenomethionine [74]. Therefore, fruits and most vegetables are due to the high-water content and the concomitant low protein content foods that only a small proportion of the daily selenium intakes contribute [73, 96]. Due to the world's different selenium content of soils, the content of these food groups varies greatly. When estimating the average recorded over the food selenium amount additionally been considered, can that be reduced in the preparation of food the selenium content by volatilization or loss (transfer to the cooking water) [48, 100]. Based on the described geographical conditions and regional and cultural-varying composition of the diet, the alimentary recorded selenium levels between different countries vary considerably. Table 1 summarizes the average per person per day recorded selenium amount for different countries together. The degree of reliability of such surveys is unstable due to varying methods and extensive inter-individual diet differences. However, the research shows the immense range of revenue worldwide. The example of Finland showed how strong the selenium content of the diet influences the people. In 1984, the Finnish Government decided the use of sodium selenate as the addition of fertilizers for cereals and animal feed. Increased within a short time, the concentrations in the food fourfold and below the selenium supply of the population has improved, so that in 1991, the amount of the additives was reduced again [2].

For the selenium supply of man is not only the quantity of the food contained but also the species contained crucial [38], since the different chemical compounds in their bioavailability and distribution processes in the body are different [33, 37]. In general, little information about the exact species composition of individual foods and their influence are known by their preparation. Selenium was detected in various foods [24]. Regarding the work on the identification of individual species, these are generally less well-developed in times of analytical instruments are developed, as they are available today. Therefore, further research is needed [86, 103]. Since selenium at elevated concentrations is also a toxic effect, it is useful also to define limits not covered by the selenium intake should not be exceeded. For adults, Yang et al. [110] recommended not to have a daily selenium intake of 750–800 mg cross as a safe upper limit was 400 mg of them selenium per day called.

The selenium status of the body-to-body fluids is determined from urine, blood, serum, plasma, and hair and toe or fingernails. The selenium content of selenium-containing shampoos hair and other cosmetic products can be influenced, and the selenium content of urine depends on renal function. Measurement of selenium concentration established in serum. This allows statements to be made via a medium persistent subnormal selenium status [79]. Recent studies are often the selenium concentrations determined in toenails. So are statements possible over the selenium supply over a more extended period. The selenium content in serum correlates with the concentration in the soft tissue organs and is independent of contrast to the concentration in whole blood. Which concentrations show an optimal supply has not

**Table 1** Level of Selenium intake in different countries

| S. No | Country | Absorbed amount of selenium (μg Se/person per day) | References |
|---|---|---|---|
| 1 | Australia | 57–87 | [35] |
| 2 | Belgium | 28–61 | [91] |
| 3 | Brazil | 28–37 | [63] |
| 4 | Germany | 38–47<br>30–42 | [71, 80] |
| 5 | Finland | Before 1984<br>25<br>1984–1990<br>110 from 1991<br>85 | [2] |
| 6 | India | 20–50 | [61] |
| 7 | Ireland | 50 | [70] |
| 8 | Japan | 104 | [87] |
| 9 | Canada | 113–220 | [44] |
| 10 | Croatia | 27 | [53] |
| 11 | New Zealand | 49–67 | [100, 101] |
| 12 | Poland | 30–40 | [107] |
| 13 | Portugal | 37 | [89] |
| 14 | Slovakia | 38 | [49] |
| 15 | Slovenia | 30 | [84] |
| 16 | Sweden | 38 | [6] |
| 17 | Switzerland | 55–70 | [45] |
| 18 | Spain | 35 | [21, 22] |
| 19 | Turkey | 44–51 | [43] |
| 20 | USA | 106 | [59] |
| 21 | Venezuela | 200–350 | [18] |
| 22 | United Kingdom | 29–39 | [69] |

yet been clarified. Frequently encountered selenium concentrations in serum range from 70 and 80 μg/L. Selenium concentrations in serum of less than 50 μg/L may be selenium deficiency [79].

## *5.1 Selenium*

The immunomodulatory effects by maintaining a pool reduced glutathione intra-lymphocytaire, which protects the membrane and allows immunocompetent cells to maintain their response [94]. It is important in protecting cells and their constituents against free radicals. This is due to its location in the active site enzymes glutathione

peroxidases selenodependent and the anti-radical activity selenoproteins, the main in carnivores being selenocysteine. The activity glutathione peroxidases are directly proportional to the selenium intake and thus, there is a strong link between selenium deficiency and oxidative stress. Thus, the protective role is complemented by other essential functions, such as its role in detoxifying heavy metals (cadmium, mercury, and lead) or effect activator of the metabolism of organic xenobiotics [20, 94]. Selenium deficiency increases the risk of oxidative damage if other antioxidants are concurrently exhausted (especially vitamin E). However, selenium deficiency is nonexistent in animals fed with industrial foods by conventional nutritional recommendations. The use of selenium as an antioxidant does not make sense in dogs' liver disease unless they have been fed rations unbalanced or have presented a very long period of anorexia [11]. Selenium deficiency could be the source of two serious diseases, Keshan disease and Kashin-Beck [42]. Subsequently, it was shown that selenium deficiencies were associated with instances of mental retardation, male infertility, immune deficiency, cardiovascular disease, as well as myopathies and/or cardiomyopathies. These same deficiencies are also involved in the development of several types of cancer in the recrudescence of certain viral infections and in accelerating the process of aging. Selenium appears to be essential for life and fourteen other essential trace elements. The daily requirement of selenium necessary for man adults was estimated to be 50–200 mg. The maximum daily intake before the toxicity threshold is valued at 450 mcg. The dietary intake of selenium is mainly provided by cereals, starchy foods, mushrooms, red meat, offal fish and eggs whose selenium contents vary depending on the availability and abundance of the trace element in the original environment. However, the minimum dose and especially the forms in which they are made are the subject of much debate, particularly for food supplementation [87].

## *5.2 Selenium and Heart*

Several studies have shown that plasma or serum levels of selenium are significantly lower in patients with various heart diseases. For example, [67] observed lower plasma selenium levels in hypertensive subjects and those with chronic heart problems compared with subjects "control" [67]. In myocardial infarction, the EURAMIC study has shown a correlation reverse between increased selenium levels in the big toenail and decreased risk of myocardial infarction. In a prospective study, Nawrot et al. showed that increased plasma selenium concentration was associated with a lower risk of developing hypertension but only in men [75]. Selenium is essential for the proper functioning of the body. A supply of at least 20 μg/L appears to be necessary to prevent Keshan disease [101]. In France, the recommended dietary intakes are between 50 and 80 μg/L in adolescents and adult subjects and although the optimal intake is difficult to define, the dose of 1 μg/L/kg of body weight can be considered as an adequate dose [64].

## 5.3 Emerging Trends: Selenium Nanoparticles Preparations

Selenium nanoparticles have potential catalytic applications in biology, medicine, material science, physics, chemistry, and other interdisciplinary fields [72, 93]. Selenium-containing nanomaterials provide some of the primary materials used in the electronics photo manufacture of photocopiers solar cells. The chemical element has with its extensive, highly diverse forms (trigonal, monoclinic, rhombohedral, and amorphous) a sizeable structural diversity, which in is made the field of application-oriented research to use [1, 36, 41]. Trigonal selenium has photoelectric as p-type semiconductor very good properties, which is also used in medical diagnostics [41]. Different experimental strategies generate the reinforced selenium-containing nanowires and nanotubes with the help of the hydrothermal method [14, 15, 60]. There are physical and chemical methods available to synthesize metallic nanoparticles [28, 50–52]. Nowadays, the biological synthesis of nanomaterials has gained significant interest. To its fullest potential, this eco-friendly technique could present extra advantages over chemical methods such as higher productivity and lower cost. The synthesis of selenium nanoparticles has been reported from bacteria, fungi, phage, and other biological sources [50, 52].

The applicability of safer formulas in pursuit of new researchers and new technology development spurs. The latest trend of Se nanoparticles currently produces two methods: the first chemical synthesis [111], the so-called second. The medium of adding many bacteria used in the electron selenite Se oxyanions bacteria during metabolism, and then selecting the form of nano-scale culture environment (50–500 nm) elemental Se pellets ($Se^0$). A bacterium can reduce into selenium. In contrast to the chemical synthesis, this method is much more efficient because single-size, high purity selenium particles fit dietary supplement expectations. The production of 100–500 nm diameter nanospheres was published [30] neither the source of the inoculums (probiotic bacteria in yogurt) was 1 L MRS medium (Oxoid Ltd., Hampshire, United Kingdom). Selenium as a source of sodium hidroselenite ($NaHSeO_3$) 10 g/l stock solution was used. 20 mL selenite stock solution was 980 ml MRS medium to a final concentration of 0.2 g/L. The 10 ml of the inoculum, *Lactobacillus acidophilus, Streptococcus thermophilus*, and *Lactobacillus casei contain* a mixture of bacterial species. After adding the inoculum, selenium source and started the mixer at 37 °C in 48 h of fermentation. After 7 days at room temperature, it was treated with concentrated hydrochloric acid. The product was lysed by bacteria and was free from selenium pellets. Repeated washing with water centrifugation, these Se nanoparticles were clearly separable.

## 5.4 Anti-Oxidative Properties of Selenium Nanoparticles

Based on the already well-known pro- and antioxidant properties of elemental selenium were, first trials of selenium-containing nanoparticles in various biological

Models (e.g. cancer cells and bacteria) conducted [102, 111]. The mouse model was able to, for example, be shown that the selenium nanoparticles (~40–60 nm) compared with sodium selenite ($Na_2SeO_3$) a seven times lower acute toxicity show (LD50 113 and 15 mg Se/kg body weight) [111]. Moreover, exhibit selenium-containing nanoparticles (7.8, 15.5 and 31 μg/ml) with an average size of about 40–60 nm significant antibacterial activity against Gram-positive *Staphylococcus aureus* [102]. Recently, selenium nanoparticles (SeNPs) as an antioxidant supplement in treating arthritis. Arthritis-induced Wistar Rats were fed orally for up to 21 days. The concentration of SeNPs at 500 μg/ kg body weight acted as a potent anti-oxidative agent.

## *5.5 Tissue Engineering*

The specialist TE is considered one of the youngest in medicine. Anfang 90 s appeared the Term for the first time and literally means "tissue engineering" Some more broadly could synthesis and processing of organic tissue describe in tissue engineering (TE) is a research field in which engineers, Biologists, and physicians to work together interdisciplinary. The concept of tissue engineering (tissue engineering) integrates all technologies using living cells or biomaterials (natural or synthetic) to rebuild or regenerate human tissue and organs or replacing a defective body [76]. Thus, tissue-engineered can be defined as "the application of the principles of tissue ingrowth to produce a replacement tissue practical for clinical use" [88]. The tools currently available for valve-a-path cardiac output have certain limitations. This is illustrated particularly in the field of reconstruction of the right channel output of the heart in patients suffering from heart disease Congenital. The duct should present ideal valved of the following: biocompatibility, permeability long term availability in terms of number and size, ease handling, long-term valve competence, low cost, low risk of infection, non-thrombogenicity, good hemostatic qualities and growth potential. In the literature are numerous find overview articles about TE, the detail on the concept itself and the possibilities enter and limit this area [77]. Tissue Engineering is based on 3 pillars: scaffolds, cells, and culturing techniques. The scaffolds represent the support structure, which is colonized with cells. In the end, only the patient's tissue should remain in the body. By this approach, there are no additional donor needs and the rejection of the transplant or a strong inflammatory response by using the body's own cells to construct the replacement structure are avoided or minimized [7, 19]. The following are briefly some properties be addressed by scaffolds that have a material impact on its functionality [40, 106].

## 6 Biocompatibility

The scaffold material used must be biocompatible and should not be absorbable. Neither the material itself nor its degradation products may be toxic to cells. The degradation should optimally by an adjustable degradation rate of scaffolds, which at the reconstruction of the fabric is adjusted by the cells to be controlled. The various type of biocompatibility material is shown in Table 2.

### *6.1 Porosity*

A second important feature is porosity. The pores in a scaffold should be big enough and be interconnected, i.e. they should have a high interconnectivity exhibit. This is necessary to provide a homogeneous population of scaffolds with cells and to allow their migration into the scaffold. In addition, the pores provide the care of the scaffold cells with nutrients and oxygen, and the removal of metabolic products of the cells from the scaffold safe [17].

**Table 2** Types of material employed in cardiac tissue engineering

| Scaffold material | Type of cell | Mechanical properties | Electrical properties | Result | References |
|---|---|---|---|---|---|
| Chitosan–carbon scaffold | Rat cardiomyocyte | 25 kPa | $0.04 \pm 0.02$ S/m | Expression of cardiac-specific genes involved in muscle contraction and electrical coupling | [65] |
| Alginate or poly(lactic acid) (PLA)/gold | Rat cardiomyocyte | 3.5–0.2 kPa | Electrical conductivity | Proteins involved in muscle contraction and electrical coupling are detected | [29] |
| Polypyrrole (PPy)-chitosan hydrogel | Rat smooth muscle cells | No | $25 \times 10^{-5}$ S/cm | Increases biological conduction in vitro and in vivo | [68] |

## 6.2 Surface Finish

The scaffolds' surface allows cell adhesion and the proliferation and migration of cells into the scaffold support. In addition to the adhesion and proliferation should also promote differentiation of the cells, or at least not be hindered [58, 112].

## 6.3 Mechanical Characteristics

Ideally, a scaffold should have mechanical properties to those of the target tissue match, but at least an initial mechanical stability brings that makes it possible to colonize the scaffolds in cell culture and bend to implant. The cells gradually build their own ECM to stabilize the newly formed tissue. Generally, maximum at Scaffolds Porosity is sought while maintaining the mechanical stability [97].

## 6.4 Preparation

The scaffold was cost-effectively and in a wide variety of shapes to be produced with the simplest possible methods. For the preparation of scaffolds come, various materials are used. In addition to the natural polymers (biopolymers), collagen, hyaluronic acid, alginate, gelatin, chitosan, or cellulose, synthetic polymers, e.g. as polylactic acid (PLA), polyglycolic acid (PGA), and their copolymer or PLGA and polycaprolactone (PCL) are used. In the development of substitute materials for mineralized tissues such as bone, ceramics such as hydroxyapatite (HAp) or tricalcium phosphate (TCP) are used. Frequently provided scaffolds are composite, i.e. they consist of several of the components above. In bone substitute material, scaffolds can make collagen and HAp [82]. As varied as the materials are the methods for preparing scaffolds for the TE. The choice of the fabrication process while significantly influenced the properties of the scaffolds and limits usually also applicable to produce biomaterials.

## 6.5 Kinetics and Metabolism Selenium in Humans

The route of entry of pulmonary absorption in this way, the contribution is estimated at 4.2 ng/L, which is negligible [62]. However, this path can become important [108]. Skin absorption, as in the previous case, is not a major route of exposure apart from occupational exposure contacts. However, topical application of selenium preparations is used for the treatment of dermatoses. For example, the thermal water from La Roche-Posay [Se]", 50–60 μg/L), whose properties arise in part from the high

concentration of selenium, affects atopic dermatitis and psoriasis [90]. Moreover, specific topical preparations containing selenium sulfide (Selsun 2.5% Selsun Blue ® and 1% ®) are used as an antifungal in case of infections, pityriasis Versicolor seborrheic dermatitis or dandruff of scalp [25].

## 6.6 Digestive Absorption

Selenium absorption efficiency is high (50–95%) and appears to be subject to a homeostatic control [27, 64]. It depends on the chemical form, which involves different absorbing mechanisms [32].

- Elemental selenium is not absorbed, it is irritating to mucous membranes [12].
- Selenomethionine is absorbed in the small intestine by an active mechanism like methionine.
- The selenate is absorbed in the selenium by an active transport mechanism identical to the sulphates [64].
- The selenite is absorbed by simple diffusion, but the presence of thiol groups stimulates its absorption. Indeed, selenite could react with the glutathione or cysteine to form compounds of the type sélénosulfures (selenotrisulfure selenodiglutathion), which would be resolved after the intervention of an enzymatic system [64, 95].
- Regarding the absorption mechanism of selenocysteine, no details have been found in the bibliography explored. It seems that the organic selenium is absorbed better (75–90%) as selenium inorganic (45–70%) [12, 13, 98]. Among the mineral selenium, absorption of selenate would be greater than that of selenite [98]. Absorption is also dependent on age; according to [105], the absorption of selenite is about 70% in adults while it would be 50% in children. Their difference in absorption for the selenate is lower (about 91% in adults and 97% in the child).

## 6.7 Distribution

The selenium content of the human body of an adult varies between 3 and 15 mg [27]. After intestinal absorption, selenium is picked up by the liver and red blood cells. In erythrocytes, selenium is reduced and released into the plasma in different form (selenidiglutathion or selenide) where it binds to proteins not specifically. Three entities transporting plasma selenium are distinguished today: non-specific selenoproteins, selenoprotein P (over 50%) (76), and glutathione peroxides (12–15%) [27]. In the body, selenium is mainly localized in the following organs [27, 64, 95].

- The liver contains about 30% of the total selenium and plays a leading role in selenium metabolism. It provides a quick exchange zone with blood. Their half-life of hepato-pancreatic selenium is 2–45 days.

- The kidneys have the highest selenium concentration (principal place of synthesis of glutathione peroxidase plasma). Skeletal muscles, which are an important place of storage due to their proportion in the body (about 50% of total body selenium). Selenium is slowly exchanged with the blood. It also seems necessary for their function. The half-life of muscle selenium is 150 days. Note that selenium concentration was greater in cardiac muscle than in skeletal muscles.
- The endocrine glands (the testes have the third most concentration high after kidney and liver).

## *6.8 Metabolism*

Selenium can be metabolized by various routes selenide. Se-Met may be metabolized by the route analogous to that of the methionine or by trans-sulfuration via selenocystathionine training and selenocysteine. Se-Cys is metabolized selenide by b-lyase. Selenates are reduced selenites which are then metabolized selenide via selenodigutothione training. This can be transformed into selenide selenophosphate and incorporated into the polypeptide selenoproteins as selenocysteine. Note that, unlike plants, animals and humans cannot synthesize Se-Met [5, 99]. There are three types of selenoproteins [8, 57]. The proteins in which selenium is incorporated non-specifically: Se-Cys and Se- Met can take the place of their sulfur counterparts, respectively cysteine and methionine. The physiological consequences of this non-incorporation specific are unclear [81].

## *6.9 Elimination*

Unabsorbed or selenium from the digestive secretions is excreted in the feces. This route accounts for approximately 35% of the removed selenium levels. The urinary tract is the main route of excretion (about 60% of selenium Total eliminated) [64]. Homeostasis selenium is also partially regulated by the excretion kidney: it has been shown that man can adapt to low intakes by reducing excretion [13, 64, 78] and conversely a higher intake conduit at a concentration higher urinary [55]. This removal occurs after sorting ion methylation methyl selenonium (TMSE) soluble (by methyltransferases localized in the cytosol of liver cells and kidney) [13, 78]. Some authors have identified a sélénoglucide (methyl seleno N-acetyl D galactosamine) derived from the reaction between the conjugate selenide glutathione and an activated sugar followed by methylation [55]. These authors suggest that this metabolite is essential for proper body selenide rate while the TMSE is excreted in case of excess selenide. However, Suzuki et al. have shown that, in rats, this observation depends on age [98]. The formation of TMSE is saturable: high concentrations saturate the way urinary excretion. The diméthylséléniure and volatile dimethyl diselenide are then formed and excreted through the lungs giving a garlic odor in the

breath [13, 78]. Thus, under normal conditions, excretions by exhalation, and saliva Sweating increases are negligible but if important contribution.

## 7 Conclusion

The heart is needed to restore the damaged tissue after injury. The challenge in the construction of cardiac tissue engineering demands special mechanical and electrical properties from the utilized scaffold film. Electrical conductivity has been beneficial as electrical stimulation can advance the growth of electro-responsive cells such as heart cells. Cardiac tissue engineering develops suitable scaffold film to support cardiac cell attachment and differentiation. In recent years, hydrogel has shown excellent properties as a biomaterial in cell adhesion, migration, differentiation, and proliferation of cardiomyocytes. These properties make it an ideal candidate material for generating contractile tissue like cardiac patches. The heart cell growth, and electrical properties of some films show enhanced proliferation and differentiation. The electrical conductivity studies have demonstrated that cardiomyocytes cultured on different nanoparticles supplemented hydrogels. The critical challenge in cardiac tissue engineering is fabricating a nonimmunogenic scaffold that avoids an adverse immune response after transplantation.

## References

1. Abdelouas A, Gong WL, Lutze W, Shelnutt JA, Franco R, Moura I (2000) Using cytochrome c 3 to make selenium nanowires. Chem Mater 12(6):1510–1512
2. Aro A, Alfthan G, Varo P (1995) Effects of supplementation of fertilizers on human selenium status in Finland. Analyst 120:841–843
3. Bär KJ, Boettger MK, Koschke M, Boettger S, Grotelüschen M, Voss A, Yeragani VK (2007) Increased QT interval variability index in acute alcohol withdrawal. Drug Alcohol Depend 89(2):259–266
4. Barhoumi R, Bowen JA, Stein LS, Echols J, Burghardt RC (1993) Concurrent analysis of intracellular glutathione content and gap junctional intercellular communication. Cytometry 14(7):747–756
5. Beaulieu M (2005) Sélénium et chimioprévention du cancer. Annales de biologie clinique du Québec 42(1):15–20
6. Becker W, Kumpulainen J (1991) Contents of essential and toxic mineral elements in Swedish Market-basket diets in 1987. Braz J Nutr 66:151–160
7. Bose S, Roy M, Bandyopadhyay A (2012) Recent advances in bone tissue engineering scaffolds. Trends Biotechnol 30(10):546–554
8. Brenneisen P, Steinbrenner H, Sies H (2005) Selenium, oxidative stress, and health aspects. Mol Aspects Med 26(4–5):256–267
9. Broadley MR, White PJ, Bryson RJ, Meacham MC, Bowen HC, Johnson SE, Tucker M (2006) Biofortification of UK food crops with selenium. Proc Nutr Soc 65(2):169–181
10. Brown RA, Crawford M, Natavio M, Petrovski P, Ren J (1998) Dietary supplementation attenuate ethanol-induced myocardial dysfunction. Alcohol Clin Exp Res 22(9):2062–2072

11. Center SA, Randolph JF, Warner K, Hoffman WE, McCabe J, Foureman P (2000) Influence of SAMe on erythrocytes and liver tissue in healthy cats. J Vet Intern Med 14:357
12. Césarini JP (2004) Le sélénium: actualités, Édition John Libbey Eurotext, Collection pathologie science formation, Montrouge
13. Chappuis P (1991) Les oligoéléments en médecine et biologie
14. Chen J, Berry MJ (2003) Selenium and selenoproteins in the brain and brain diseases. J Neurochem 86(1):1–12
15. Chen YT, Zhang W, Zhang FB, Zhang ZX, Zhou BZ, Li HL (2004) A novel route to controlled synthesis of selenium nanowires. Mater Lett 58(22):2761–2763
16. Clausse F (2001) Radicaux libres et molécules à activité anti-oxydante. Those Doct. Vet.–Alfort
17. Collins MN, Birkinshaw C (2013) Hyaluronic acid based scaffolds for tissue engineering—a review. Carbohyd Polym 92(2):1262–1279
18. Combs GF Jr, Combs SB (1986) The biological availability of Se in foods and feeds. The role of Se in nutrition. Academic Press, New York, pp 127–177
19. Croisier F, Jérôme C (2013) Chitosan-based biomaterials for tissue engineering. Eur Polymer J 49(4):780–792
20. Delattre J, Beaudeux J-L, Bonnefont-rousselot D (2005) Radicaux libres et stress oxydant: aspects biologiques et pathologiques. Lavoisier, Paris, p 549
21. Diaz-Alarcon JP, Navarro-Alarcón M, de la Serrana HLG, Lopez-Martinez MC, (1996) Determination of selenium in cereals, legumes and dry fruits from southeastern Spain for calculation of daily dietary intake. Sci Total Environ 184(3):183–189
22. Diwadkar-Navsariwala V, Prins GS, Swanson SM, Birch LA, Ray VH, Hedayat S, Lantvit DL, Diamond AM (2006) Selenoprotein deficiency accelerates prostate carcinogenesis in a transgenic model. Proc Natl Acad Sci 103(21):8179–8184
23. Djoussé L, Levy D, Benjamin EJ, Blease SJ, Russ A, Larson MG, Massaro JM, D'Agostino RB, Wolf PA, Ellison RC (2004) Long-term alcohol consumption and the risk of atrial fibrillation in the Framingham Study. Am J Cardiol 93(6):710–713
24. Dodig S, Cepelak I (2004) The facts and controverses about selenium. Acta Pharm 54:261–276
25. Dorosz P (2002) Guide pratique des médicaments, Éditions Maloine, Paris
26. Dröge W (2002) Free radicals in the physiological control of cell function. Physiol Rev 82(1):47–95
27. Ducros V, Favier A (2004) Métabolisme du sélénium. EMC-Endocrinologie 1(1):19–28
28. Durán N, Marcato PD, Durán M, Yadav A, Gade A, Rai M (2011) Mechanistic aspects in the biogenic synthesis of extracellular metal nanoparticles by peptides, bacteria, fungi, and plants. Appl Microbiol Biotechnol 90(5):1609–1624
29. Dvir T, Timko BP, Kohane DS, Langer R (2011) Nanotechnological strategies for engineering complex tissues. Nat Nanotechnol 6(1):13–22
30. Eszenyi P, Sztrik A, Babka B, Prokisch J (2011) Elemental, Nano-sized (100–500 nm) selenium production by probiotic lactic acid bacteria. Int J Biosci, Biochem Bioinform 1(2):148
31. Evans W (1959) The electrocardiogram of alcoholic cardiomyopathy. Br Heart J 21:445–456
32. Fairweather-Tait S, Hurrell RF (1996) Bioavailability of minerals and trace elements. Nutr Res Rev 9:312–315
33. Fairweather-Tait SJ, Bao Y, Broadley MR, Collings R, Ford D, Hesketh JE, Hurst R (2011) Selenium in human health and disease. Antioxid Redox Signal 14(7):1337–1383
34. Fakanya WM, Tothill IE (2014) Detection of the inflammation biomarker C reactive protein in serum samples: towards an optimal biosensor formula. Biosensors 4(4):340–357
35. Fardy J, McOrist G, Farrar Y (1989) The determination of selenium status in the Australian diet using neutron activation analysis. J Radioanal Nucl Chem 133(2):397–405
36. Fernández-Ujados M, Trapiella-Alfonso L, Costa-Fernández JM, Pereiro R, Sanz-Medel A (2013) One-step aqueous synthesis of fluorescent copper nanoclusters by direct metal reduction. Nanotechnology 24(49):495601
37. Finley JW (2005) Selenium accumulation in plant foods. Nutr Rev 63(6):196–202

38. Fordyce FM (2013) Selenium deficiency and toxicity in the environment. Springer, Netherlands, pp 375–416
39. Frost L, Vestergaard P (2004) Alcohol and risk of atrial fibrillation or flutter: a cohort study. Arch Intern Med 164(18):1993–1998
40. Gao X, Wang Y, Chen J, Peng J (2013) The role of peripheral nerve ECM components in the tissue engineering nerve construction. Rev Neurosci 24(4):443–453
41. Gates B, Yin Y, Xia Y (2000) A solution-phase approach to the synthesis of uniform nanowires of crystalline selenium with lateral dimensions in the range of 10–30 nm. J Am Chem Soc 122(50):12582–12583
42. George A, Figueredo VM (2011) Alcoholic cardiomyopathy: a review. J Cardiac Fail 17(10):844–849
43. Giray B, Hincal F (2004) Selenium status in Turkey: possible link between status of selenium, iodine, antioxidant enzymes and oxidative DNA damage. J Radioanal Nucl Chem 259:447–451
44. Gissel-Nielsen G (1998) Effects of selenium supplementation of field crops. Environ Chem Selenium 99–112
45. Haldimann M, Venner TY, Zimmerli B (1996) Determination of selenium in the serum of healthy Swiss adults and correlation to dietary intake. J Trace Elem Med Biol 10(1):31–45
46. Halliwell B (1999) Establishing the significance and optimal intake of dietary antioxidants: the biomarker concept. Nutr Rev 57(4):104–113
47. Hanna PM, Mason RP (1992) Direct evidence for inhibition of free radical formation from Cu (I) and hydrogen peroxide by glutathione and other potential ligands using the EPR spin-trapping technique. Arch Biochem Biophys 295(1):205–213
48. Higgs DJ, Morris VC, Levander OA (1972) Effect of cooking on selenium content of foods. J Agric Food Chem 20(3):678–680
49. Kadrabová J, Mad'arič A, Ginter E (1998) Determination of the daily selenium intake in Slovakia. Biol Trace ElemT Res 61(3):277–286
50. Kalimuthu K, Babu RS, Venkataraman D, Bilal M, Gurunathan S (2008) Biosynthesis of silver nanocrystals by *Bacillus licheniformis*. Colloids Surf B Biointerfaces 65(1):150–153
51. Kalishwaralal K, BarathManiKanth S, Pandian SRK, Deepak V, Gurunathan S (2010) Silver nanoparticles impede the biofilm formation by *Pseudomonas aeruginosa* and *Staphylococcus epidermidis*. Colloids Surf B Biointerfaces 79(2):340–344
52. Kalishwaralal K, Deepak V, Pandian SRK, Kottaisamy M, BarathManiKanth S, Kartikeyan B, Gurunathan S (2010) Biosynthesis of silver and gold nanoparticles using *Brevibacterium casei*. Colloids Surf B Biointerfaces 77(2):257–262
53. Klapec T, Mandić ML, Grgić J, Primorac L, Ikić M, Lovrić T, Grgić Z, Herceg Z (1998) Daily dietary intake of selenium in eastern Croatia. Sci Total Environ 217(1):127–136
54. Kloner RA, Rezkalla SH (2007) To drink or not to drink? That is the question. Circulation 116(11):1306–1317
55. Kobayashi Y, Ogra Y, Ishiwata K, Takayama H, Aimi N, Suzuki KT (2002) Selenosugars are key and urinary metabolites for selenium excretion within the required to low-toxic range. Proc Natl Acad Sci 25(99):15932–15936
56. Kuppari MKM (2007) Alcohol and Cardiovascular disease. Wiley
57. Li N, Gao Z, Luo D, Tang X, Chen D, Hu Y (2007) Selenium level in the environment and the population of Zhoukoudian area, Beijing China. Sci Total Environ 381:105–111
58. Li X, Wang L, Fan Y, Feng Q, Cui FZ, Watari F (2013) Nanostructured scaffolds for bone tissue engineering. J Biomed Mater Res Part A 101(8):2424–2435
59. Longnecker MP, Taylor PR, Levander OA, Howe M, Veillon C, McAdam PA, Patterson KY, Holden JM, Stampfer MJ, Morris JS (1991) Selenium in diet, blood, and toenails in relation to human health in a seleniferous area. Am J Clin Nutr 53(5):1288–1294
60. Lu W, Lieber CM (2006) Semiconductor nanowires. J Phys D: Appl Phys 39(21):R387
61. Mahalingam TR, Vijayalakshmi S, Prabhu RK, Thiruvengadasami A, Wilber A, Mathews CK, Shanmugasundaram KR (1997) Studies on some trace and minor elements in blood. Biol Trace ElemT Res 57(3):223–238

62. Mahapatra S, Tripathi RM, Raghunath R, Sadasivan S (2001) Daily intake of Se by adult population of Mumbai, India. Sci Total Environ 277:217–233
63. Maihara VA, Gonzaga IB, Silva VL, Fávaro DIT, Vasconcellos MBA, Cozzolino SMF (2004) Daily dietary selenium intake of selected Brazilian population groups. J Radioanal Nucl Chem 259(3):465–468
64. Martin A (2000) Apports nutritionnels conseillés pour la population française, ÉditionsTec&Doc, 3 ème éd. Paris
65. Martins AM, Eng G, Caridade SG, Mano JF, Reis RL, Vunjak- Novakovic G (2014) Electrically conductive chitosan/carbon scaffolds for cardiac tissue engineering. Biomacromolecules 15(2):635–643
66. Masella R, Di Benedetto R, Varì R, Filesi C, Giovannini C (2005) Novel mechanisms of natural antioxidant compounds in biological systems: involvement of glutathione and glutathione-related enzymes. J Nutr Biochem 16(10):577–586
67. Mihailovic MB, Avramovic DM, Jovanovic IB, PesŒut OJ, Matic DP, Stojanov VJ (1998) Blood and plasma selenium levels and GSH-Px activities in patients with arterial hypertension and chronic heart disease. J Environ Pathol Toxicol Oncol 17(3–4):285–289
68. Mihic A, Cui Z, Wu J, Vlacic G, Miyagi Y, Li SH, Lu S, Sung HW, Weisel RD, Li RK (2015) A conductive polymer hydrogel supports cell electrical signaling and improves cardiac function after implantation into myocardial infarct. Circulation 132(8):772–784
69. Ministry of Agriculture, Fisheries and Food (1997) Ministry of Agriculture, fisheries and food. Food surveillance information sheet, no 126. Dietary intake of Se. Joint Food Safety and Standards Group, London
70. Murphy J, Hannon EM, Kiely M, Flynn A, Cashman KD (2002) Selenium intakes in 18–64y-old Irish adults. European J Clin Nutr 56(5)
71. Nagueh SF, Shah G, Wu Y, Torre-Amione G, King NM, Lahmers S, Granzier HL (2004) Altered titin expression, myocardial stiffness and left ventricular function in patients with dilated cardiomyopathy. Circulation 110(2):155–162
72. Narmato K (1997) Infrared and Raman spectra of inorganic and coordination compounds. Wiley, New York, pp 296–346
73. Navarro-Alarcon M, de la Serrana HLG, Perez-Valero V, López- Martınez C (1999) Serum and urine selenium concentrations as indicators of body status in patients with diabetes mellitus. Sci Total Environ 228(1):79–85
74. Navarro-Alarcon M, Lopez-Martinez MC (2000) Essentiality of selenium in human body: relationship with different diseases. Sci Total Environ 249(1–3):347–371
75. Nawrot TS, Staessen JA, Roels HA, Den Hond E, Thijs L, Fagard RH, Dominiczak AF, Struijker-Boudier HA (2007) Blood pressure and blood selenium: a cross-sectional and longitudinal population study. Eur Heart J 28(5):628–633
76. Nerem RM, Sambanis A (1995) Tissue engineering: from biology to biological substitutes. Tissue Eng 1(1):3–13
77. Nettles DL, Elder SH, Gilbert JA (2002) Potential use of chitosan as a cell scaffold material for cartilage tissue engineering. Tissue Eng 8(6):1009–1016
78. Nève J (1997) Selenium in nutrition and therapeutics. Princ Med Biol Mol Cell Pharmacol 8(50):985–994
79. Oster O, Prellwitz W, Kasper W, Meinertz T (1983) Congestive cardiomyopathy, and the selenium content of serum. Clin Chim Acta 128(1):125–132
80. Oster O, Dahm M, Oelert H, Prellwitz W (1989) Concentrations of some trace elements (Se, Zn, Cu, Fe, Mg, K) in blood and heart tissue of patients with coronary heart disease. Clin Chem 35(5):851–856
81. Papp LV, Lu J, Holmgren A, Khanna KK (2007) From selenium to selenoproteins: synthesis, identity and their role in human health. Antioxid Redox Signal 9:776–805
82. Patrick CW Jr, Chauvin PB, Hobley J, Reece GP (1999) Preadipocyte seeded PLGA scaffolds for adipose tissue engineering. Tissue Eng 5(2):139–151
83. Piano MR (2002) Reviews—alcoholic cardiomyopathy: incidence, clinical characteristics, and pathophysiology. Chest 121(5):1638–1650

84. Pokorn D, Stibilj V, Gregorič B, Dermelj M, Štupar J (1998) Elemental composition (Ca, Mg, Mn, Cu, Cr, Zn, Se, and I) of daily diet samples from some old people's homes in Slovenia. J Food Compos Anal 11(1):47–53
85. Rahman K (2007) Studies on free radicals, antioxidants, and co-factors. Clin Interv Aging 2(2):219
86. Rayman MP (2008) Food-chain selenium and human health: emphasis on intake. Br J Nutr 100(2):254–268
87. Rayman MP (2004) The use of high-selenium yeast to raise selenium status: how does it measure up? Br J Nutr 92(4):557–573
88. Reddi AH (2000) Morphogenesis and tissue engineering of bone and cartilage: inductive signals, stem cells, and biomimetic biomaterials. Tissue Eng 6(4):351–359
89. Reis MF, Holzbecher J, Martinho E, Chatt A (1990) Determination of selenium in duplicate diets of residents of Pinhel, Portugal, by neutron activation. Biol Trace Elem Res 26(1):629–635
90. Renaudin C (1999) Sélénium: action, toxicité et utilisation en thérapeutique, Thèse pour le doctorat de Pharmacie de l'Université de Poitiers
91. Robberecht HJ, Hendrix P, Van Cauwenbergh R, Deelstra HA (1994) Actual daily dietary intake of selenium in Belgium, using duplicate portion sampling. Zeitschrift fuÈr Lebensmittel-Untersuchung und Forschung 199(4):251–254
92. Rossinen J, Viitasalo M, Partanen J, Koskinen P, Kupari M, Nieminen MS (1997) Effects of acute alcohol ingestion on heart rate variability in patients with documented coronary artery disease and stable angina pectoris. Am J Cardiol 79(4):487–491
93. Salata OV (2004) Applications of nanoparticles in biology and medicine. J Nanobiotechnol 2(1):3
94. Siliart B (2007) Rôle des oligo-éléments dans le stress oxydatif. Bull Group Tech Vét 38:44–50
95. Simonoff M, Simonoff G (1991) Le sélénium et la vie. Éditions Masson, Paris
96. Sirichakwal PP, Puwastien P, Polngam J, Kongkachuichai R (2005) Selenium content of Thai foods. J Food Compos Anal 18(1):47–59
97. Song MJ, Dean D, Tate MLK (2013) Mechanical modulation of nascent stem cell lineage commitment in tissue engineering scaffolds. Biomaterials 34(23):5766–5775
98. Suzuki KT, Kurasaki K, Okazaki N, Ogra Y (2004) Selenosugar and trimethylselenonium among urinary Se metabolites: dose- and age-related changes. Toxicol Appl Pharmacol 206(1):1–8
99. Taylor EW, Nadimpalli RG, Ramanathan CS (1997) Genomic structures of viral agents in relation to the biosynthesis of selenoproteins. Biol Trace ElemT Res 56(1):63–91
100. Thomson CD, Robinson MF (1990) Selenium content of foods consumed in Otago, New Zealand. N Z Med J 103(886):130–135
101. Thomson CD (2004) Assessment of requirements for selenium and adequacy of selenium status: a review. Eur J Clin Nutr 58:391–402
102. Tran PA, Webster TJ (2011) Selenium nanoparticles inhibit *Staphylococcus aureus* growth. Int J Nanomed 6:1553–1558
103. Tsongas TA, Ferguson SW (1977) Human health effects of selenium in a rural Colorado drinking water supply. In: Proceedings of University of Missouri's 11th annual conference on trace substances in environmental health, Edité par D.D. Hemphill.
104. Van Bakel MM, Printzen G, Wermuth B, Wiesmann UN (2000) Antioxidant and thyroid hormone status in selenium-deficient phenylketonuric and hyperphenylalaninemic patients. Am J Clin Nutr 72(4):976–981
105. Van Dael P, Lewis J, Barclay D (2004) Stable isotope-enriched selenite and selenate tracers for human metabolic studies: a fast and accurate method for their preparation from elemental selenium and their identification and quantification using hydride generation atomic absorption spectrometry. J Trace Elem Med Biol 18(1):75–80
106. Wade RJ, Burdick JA (2012) Engineering ECM signals into biomaterials. Mater Today 15(10):454–459

107. Wasowicz W, Gromadzinska J, Rydzynski K, Tomczak J (2003) Selenium status of low-selenium area residents: polish experience. Toxicol Lett 137(1):95–101
108. Weast RC (1980–1981) Handbook of chemistry and physics, 61st edn, CRC Press Inc., Boca Raton, Florida
109. Weise F, Krell D, Brinkhoff N (1986) Acute alcohol ingestion reduces heart rate variability. Drug Alcohol Depend 17(1):89–91
110. Yang GQ, Chen JS, Wen ZM, Ge KY, Zhu LZ, Chen XC, Chen XS (1983) The role of selenium in Keshan disease. Adv Nutr Res 6:203–231
111. Zhang JS, Gao XY, Zhang LD, Bao YP (2001) Biological effects of a nano red elemental selenium. BioFactors 15(1):27–38
112. Zheng C, Wang J, Liu Y, Yu Q, Liu Y, Deng N, Liu J (2014) Functional selenium nanoparticles enhanced stem cell osteoblastic differentiation through BMP signaling pathways. Adv Func Mater 24(43):6872–6883

# Chapter 11
# Nanomaterials as Drug Carriers in Diagnosis and Treatment of Various Cancers


**Rathi Muthaiyan Ahalliya, Girisan Elliangal Kunhappa, Gopalakrishnan Velliyur Kanniappan, Meenakshi Periasamy, and Guru Kumar Dugganaboyana**

## 1 Introduction

Nanotechnology boomed into the world from last century onwards and produced various revolutionary developments in the field of science and technology. Richard Feynman, physicist was the recipient of American Nobel prize who innovate nanotechnology and its applications. '*Nano*' means dwarf derived from a Greek Word. Physical, chemical, and biological methods are used for the synthesis of metal nanoparticles. Synthesis of nanoparticles by physical and chemical methods need high temperature, high pressures and chemicals which may cause many disadvantages this can be overcome by relaying on biological methods of synthesis. European commission demonstrated that nanomaterial is outlined as natural, incidental, or factory-made material consists of particle in unbound or clustered, about 50% of

M. A. Rathi (✉)
Department of Biochemistry, FASCM and Karpagam Cancer Research Center, Karpagam Academy of Higher Education, Coimbatore, Tamil Nadu 641021, India
e-mail: rathi.muthaiyan@kahedu.edu.in

E. K. Girisan
Department of Computer Applications, Sree Narayana Guru College, Coimbatore, Tamil Nadu 641105, India

V. K. Gopalakrishnan
School of Medicine, Bule Hora University Institute of Health, Bule Hora University, Bule Hora, Ethiopia

P. Meenakshi
Department of Biochemistry, Tamil Nadu Agricultural University, Coimbatore, Tamil Nadu 641003, India

D. Guru Kumar
Division of Biochemistry, School of Life Sciences, JSS Academy of Higher Education and Research, Mysuru, Karnataka 570015, India



K. Kasinathan et al. (eds.), *Nanomaterials for Energy Conversion, Biomedical and Environmental Applications*, Materials Horizons: From Nature to Nanomaterials,
https://doi.org/10.1007/978-981-19-2639-6_11

particles are range in size 1–100 nm [22]. The cells present in the biological system are very small as 10 μm. Nevertheless, the cell organelles are much smaller. The dimension of synthesized nanomaterials is smallest than it. Thus, it can easily enter the pores present in the call membrane without causing any interference [68]. Nanomaterials are broadly categorized into organic, and inorganic based on the components that construct the structure. Organic nanomaterials are dendrimers, liposomes, polymeric micelle, and nanocapsule. Inorganic nanomaterials such as silica nanoparticles, carbon nanotubes, iron oxide nanoparticles and gold nanoparticles [57]. Nanomaterials are broadly classified into (i) carbon-based, (ii) metal-based. Carbon-based nanoparticles are fullerenes and carbon nanotubes. Carbon nanotubes and carbon quantum dots have turned outstanding attraction, owed on the specific properties of carbon. Metal nanoparticles such as silver, gold, nickel, platinum, iron oxide, zinc oxide, gadolium, silica and titanium oxide possess different colors and specific characteristics. They are classified into Fullerenes, graphene, carbon nanotubes, carbon nanofibers and carbon black containing nanomaterials are made up of globular hollow cage such as allotropic forms of carbon. [4]. Fullerenes is spherical in shape consists of 28–1500 carbon atoms with a diameter upto 8.2 nm. Graphene is hexagonal like honeycomb made up of carbon atom. the thickness of graphene atom is 1 nm. Carbon nanotubes is a graphene nanofoil with a honeycomb lattice of lattice of carbon atoms wound into hollow cylinder to form nanotubes of diameter as low as 0.7 nm. Carbon nanofiber is a graphene nanofoils that are used to produce carbon nanofiber wound into a cone or cup shape. Carbon black is generally spherical in shape with a diameter from 20 to 70 nm [21].

*Metal-based nanoparticles*: Silver, gold, copper, iron, zinc platinum are some of the metal-based nanoparticles used for diagnosis and therapeutics of various diseases. The noble metal nanoparticles can be able to target different cells along with polymers and bind numerous functional groups such as peptide molecules, antibodies, RNA and DNA. [23]. Copper based nanoparticles were used as a potent antibacterial activity against gram negative and gram-positive bacteria [73]. Gold nanoparticles are used in tumor cell imaging and diagnosis [19]. In ancient period itself, gold is used as medicine to enhance the mental fitness of a baby. Silver nanoparticles were predominantly used in imaging of cells, cancer therapy, delivery of gene and drug [42]. Nanotechnology the emerging field of the present scenario promotes a wide application in food processing, cloth viewing, cosmetics, renewable energy and enormously in treatment and diagnosis of various diseases. Apart from this, it plays a very important role in purification, production of nanowires, water filtration and remediation of environmental pollution. It is also considered as a revolutionary technology of twenty-first century. Nanoparticles possess a potent role in the development of biotechnological and biomedical applications. The transplantation of organs can be replaced by regeneration and repair of damaged tissues with the help of tissue nanotechnology. The reformation of bones can be done with the help of carbon nanotube scaffolds [47].

Cancer is one of the unpardonable ailments putting to death millions of people every year [66] among cancer related deaths in 2020 were resist of lung (1.8 million death), colorectal (935,000 deaths), liver (830,000 deaths), stomach (769, 000 deaths)

and breast (685,000 deaths) [26]. The cancer cell proliferates and divide uncontrollably, and metastasis occurs by spreading the cancer cells into surrounding tissues, cells can also travel through blood stream to distant locations of the body. The apoptosis pathway can be disrupted by mutation, due to this genetic instability and molecular alterations; the normal cell is converted into cancerous cells [16]. To destroy the fast-growing cells, physicians decide on chemotherapy and radiation therapy to treat cancer patients. But the fast-growing cells such as blood and hair cells also can also damage along with this. These non-cancerous cells should be saved while destroying the cancerous cell is one of the greatest challenges [41]. To rectify these issues nanotechnology played an eminent role in early diagnosis and treatment of cancer. Nano-sized formulation was prepared and delivered toward the targeted cancerous cells for providing significant cytotoxicity activity [74]. The nanoparticles synthesized from chemical and physical methods are more expensive and produce toxic byproducts in nature [1].

## *1.1 Mechanism of Cancer Cell Invasion*

Tumors are abnormal growth of the body. They can be classified into benign or malignant. Benign tumor is a mass of cells tend to stay in their primary location. The malignant tumor cells migrated from the tissue of origin, enter the circulation, and are implanted in neighboring tissues is the most dangerous aspect of this deathly disease. This process is called metastasis [29]. The incapability of cell–cell adhesion discharge the cancerous tumor cells to detach from the primary tumor mass and enter into the circulatory system and occupy the surrounding area, is known as intravasation [10, 27]. Diagnosis and therapeutic approaches to cancer are performed at the earliest. Some of the early diagnostic tools include PET, MRI, CT, and ultrasound.

## *1.2 Role of Nanomaterials to Treat Cancer*

Cancer frequency, preponderance, and mortality retain on at exceedingly high levels, thus the urgency for a modern technology in cancer treatment is required for the hour [33]. Materials on the nanoscale are increasingly being used to target the cancer cells. Nanomaterials are prepared from biological components such as albumin, gelatin, and phospholipids for liposomes and from chemical components such as polymers and solid metals [17]. Semiconductors, quantum dots and iron oxides nanocrystals [54] and biomolecules such as peptides, antibiotics, anticancer drugs are used for early detection of cancer [64]. Quantum dots emit fluorescence are more suitable for imaging CRC, liver cancer, PC, and lymphoma [20, 53]. By early detection of cancer, the patients can gain half of their battle. Nanoshells, size is between 10 and 300 nm is made up of silicon and coated with thin gold metal shell [46] is also used in the application of cancer detection.

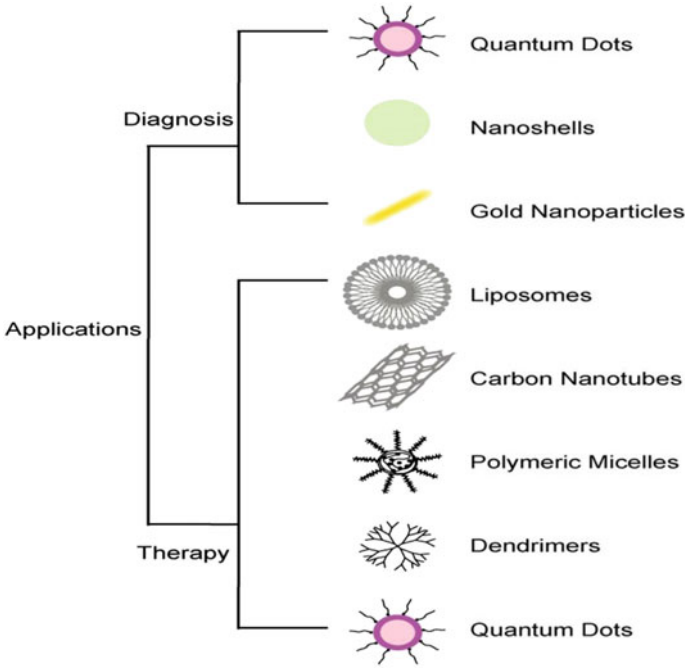


**Fig. 1** List of nanoparticles used in detection and treatment of cancer

Figure 1 demonstrated the nanomaterials used in cancer therapy and diagnosis [39].

## 2 Overview About Liver Cancer

Liver cancer or hepatocellular cancer is one of the third most global health challenge disease, [70, 73]. It is figured that by 2025 greater than one million individuals will be affected by hepatocellular cancer annually worldwide [9]. Causative factors for the development of liver cancer include injection with hepatitis (B and C), inflammation, consumption of alcohols and aflatoxins [51]. About fifty percentage of liver cancer are caused by and hepatitis B infection (Akinyemiji et al. 2015). It was reported that only 25% of patients are diagnosed with liver cancer at the early stage. Early detection of this disease can remarkably prevent the mortality rate [25, 69]. Moreover, the detection of liver cancer at the final stage remains the patients under palliative care and thus increases the high mortality rate (Stewart et al. 2014).

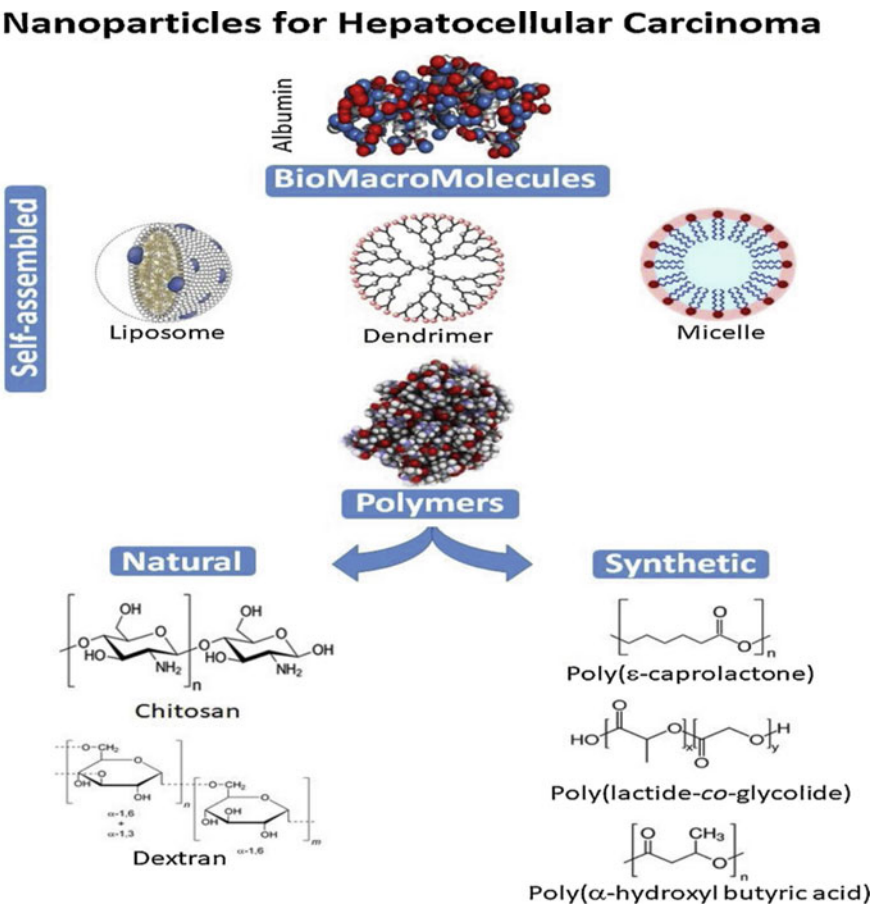


**Fig. 2** Macromolecular nanoparticles used for hepatocellular cancer treatment [24]

## *2.1 Nanoparticles in Treatment of Liver Disease*

Nanoparticles such as organic and inorganic materials like metal and ceramic are prepared for drug delivery to liver cells [31]. Liver is the major site involved in the clearance of nanoparticles. About 99% of the nanoparticles injected in the blood stream are cleared by the liver. Macromolecules such as liposomes, albumin, dendrimers, micelles, polysaccharides such as chitosan, dextran and poly hydroxy esters are used to deliver the drugs in targeted area and enhance the intracellular penetration [45]. Albumin coupled within sulfide nanoparticles inhibit the growth of hepatocytes at a very low concentration [11]. It also possesses excellent lyoprotectant for

the development of nanomedicine. Albumin bound with paclitaxel possesses prominent efficacy in liver cancer xenograft models [75]. Gold nanoparticles as antiangiogenic agent down regulate VEGF activity and disrupt the cellular morphology [48].

### *2.2 Role of Nanoparticles in Liver Cancer*

There are many nanoparticles are used to identify liver abnormalities. CT has shown the capability to identify the liver diseases by using various nanoparticles. Among this, most used nanoparticle in MRI and micro-CT imaging are SPION. Imaging of liver by nanoparticles facilitates the earliest diagnosis of liver cancer (Table 1).

## 3 Overview About Lung Cancer

Lung cancer is a common leading disease of men and women of multiple aetiologies that arise because of neoplastic metamorphosis of epithelial cells in lung. The aromatic mutagens present in tobacco smoke are the major cause of lung cancer [72]. The respiratory malignancy is classified into non-small cell lung cancer (NSCLC)

**Table 1** List of nanoparticles used for liver imaging [24]

| S. no | Nanoparticles | Size | Properties | Applications |
|---|---|---|---|---|
| 1 | Supermagnetic iron oxide nanoparticle (SPION) | Less than 50 nm | High transverse relaxation<br>Detection of some pathogens | Magnetic resonance imaging (MRI) of liver and spleen |
| 2 | Ultra-small superparamagnetic iron oxide (USPIO) | Less than 50 nm | Short T2 time<br>Less uptake in liver than SPIO | MRI of liver |
| 3 | SPIO + Quantum dots (QD) $Ag_2S$ | – | Great luminescence<br>Non invasive<br>Good response to magnetic field<br>Correct diagnosis and anatomical information | Molecular imaging |
| 4 | Iron oxide nanoparticles (IONPs) | 10–30 nm | Effective agent | MRI of liver |
| 5 | Gold nanoparticles (Au NPS) | Smaller or larger than 25 nm | Cost effective<br>Greater contrast agent for imaging | Liver imaging with computed tomography (CT) |

and small cell lung cancer (SCLC). Ramalingam et al. [55] in 2011, reported that the survival rate of lung cancer in worldwide is 15%. 85% of 220,000 lung cancer subjects involve non-small cell type, while the remaining 15% are categorized in small cell type. The rapid spreading and early metastasis the survival rate of the small cell lung carcinoma is only four months if not treated [14]. In the present scenario lung cancer accounts 23% [2, 37] of mortality because of late in early detection, only 50% of disease are diagnosed at stage IV [49]. The adenocarcinoma is one of the subclasses of lung cancer caused due to occupational exposure to carcinogenic agents such as radon, asbestos, and other types of radiations. *Helicobacter pylori* infection can cause major risk factor for colorectal cancer. also causes minor class of lung cancer [36, 38]. Lung cancers are diagnosed by physical examination, medical imaging techniques such as X-ray, computed tomography, magnetic resonance imaging (MRI), positron emission tomography (PET) [58].

### *3.1 Role of Nanoparticle in Lung Cancer*

In lung cancer, lipid-based nanocarriers may be a promising delivery system for drugs and genes. Boulikas et al. [8] in 2004 developed a liposome-based cisplatin drug named lipoplatin were used for the treatment of lung cancer. Apart from this magnetic nanoparticle (MNPs) plays a potential role in diagnosis and treatment of lung cancer. The main advantage of using MNPs is its potential deposition of drugs in tumor and possess a minimum detrimental effect in healthy tissues [60]. The biocompatibility of this particle relies on factors such as size, architecture concentration, ability to undergo biodegradation. Polymers, liposomes, proteins, and inorganic materials are used as the biocompatible coating materials (Singh et al. 2010). Paclitaxel liposome significantly enhances the cellular uptake of drug and induces mitochondria-mediated apoptotic cell death in A549 cell lines [44]. Hybrid nanostructure that links $Fe_3O_4$ MNPs with polyelectrolyte layers and doxorubicin hydrochloride showed cytotoxicity toward A549 cells [76]. It was demonstrated that polylactic acid nanoparticles filled with taxanes importantly improved the effectiveness of chemoradiation therapy in A549 cell lines and tumor xenograft model [40]. Metal-based nanomaterials such as gold and silver have been significantly used in imaging, detecting and classification of lung cancer [15].

## 4 Overview of Breast Cancer

Breast cancer is one of the most common gynecological malignancies in Worldwide. About 1.7 million women are diagnosed in worldwide which lead to 45,000 deaths per year [62]. Generally, breast cancer developed in both women but rarely less than 1% of all breast cancer cases occur in men [12, 32]. The overall five years survival rate for women with breast cancer was significantly improved from 75% (1975–1977)

to 91% (2005–2011) due to the advanced techniques in diagnosis and treatment [63]. The risk factors of breast cancer include sex, genetic factors, usage of hormone therapy, dietary and lifestyle habits [30]. Breast can be detected by mammography, ultrasound, and magnetic resonance imaging.

### *4.1 Role of Nanomaterials in Breast Cancer*

Nanomaterials are promising aid that has been developed for the early diagnosis and treatment of breast cancer. The limitation in cancer immunotherapy can be overcome by the development of nanomaterials [34]. Genexol—PM, paclitaxel doped poly (D,L-lactid acid) is apolymeric nanomedicine used in clinical trials for breast cancer treatment [43]. Nab-paclitaxel (Abraxane) is approved by FDA in 2005 to treat metastatic breast cancer [35]. Overexpression HER2 a transmembrane receptor possesses tyrosin kinase activity and increases the progression of breast cancer. Trastuzumab (Herceptin) which can bind to HER2, preventing the activation of tyrosin kinase and reduce the breast cancer [52]. Graphene is a bidimensional carbon nanomaterial used for drug delivery in breast cancer [50]. Thus, nanomaterials help in the delivery of active pharmaceutical molecule to the targeted site for improved treatment (Tables 2 and 3).

## 5 Overview of Ovarian Cancer

Ovarian cancer is one of the most common types of gynecological cancer [7]. Since there is no any symptoms noticed by the patients, it is diagnosed at the advance stage. It is estimated that more than 60% of ovarian cancer subjects are diagnosed during third stage or final stage, so for the past thirty years, the survival stage has not increased tremendously. This may be because of the limitation in application of imaging technologies foster complicate in diagnosis [59]. This silent killer can be treated by removing the cancerous tissues by surgery, and it is effective only at the first stage for the other stages chemotherapy is required [3].

### *5.1 Role of Nanomaterials in Ovarian Cancer*

The metal nanoparticle such as gold, iron silver and metal oxides showed more attention recently for treating ovarian cancer. Among these, iron-oxide nanoparticles ($Fe_2O_3$ NPs) play a potential role in ovarian cancer treatment [67]. $Fe_2O_3$ NPs showed noticeable cytotoxic activity by elevating the reactive oxygen species (ROS), altering the mitochondrial membrane potential and promote the apoptosis in ovarian cancer cell lines (PA-1). Nanomaterial such as poly (lactic-co-glycolic) and chitosan-based

**Table 2** Nanoparticles support immunotherapy in breast cancer [24]

| S. no | Biomaterial | Action | References |
|---|---|---|---|
| 1 | Lipid based liposome<br>Urosolic acid | STAT5<br>Phosphorylation inhibition and IL -10 secretion | Zhang et al. (2020) |
| 2 | Liposome with PEG (modified) | Increased number of NK cells and APCs | Atukorale et al. (2019) |
| 3 | Liposome<br>cGAMP | Conversion of phenotype, enhancement of MHC and costimulatory molecules | [13] |
| **4** | Lamda phage coat protein gpD AE37 | Generation of robust immune responses peptide in breast cancer | [38] |
| 5 | EVs from NK -92 MI cells<br>IL 15 | Cytotoxicity | [6] |
| 6 | Cationic lipid assisted nanoparticles<br>Lactate dehydrogenase A-siRNA | Increased migration of TC and NK cells and neutralized tumor environment | [71] |
| 7 | Polymer based protein<br>CRISPR—Cas9-cyclin dependent kinase | Down regulation of PD L1 expression | [18] |
| 8 | Albumin coated with aluminum hydroxide<br>Melittin and chlorin e6 | Increased reactive oxygen species | Wang et al. (2019) |
| 10 | Lipid nanoparticle<br>Colony—stimulating factor 1 receptor and mitogen activated protein kinase inhibitors | Increased MI like phenotype at tumor microenvironment | [56] |

**Table 3** Nanomaterials for breast cancer treatment [5, 24]

| S. no | Nanocarriers | Advantages—drug therapy |
|---|---|---|
| 1 | Solid lipid nanoparticles | Potent solubility and bioavailability due to organic makeup |
| 2 | Liposome | Broad range of drug delivery |
| 3 | Polymeric | Versatile in terms of chemical composition |
| 4 | Magnetic nanoparticles | Imaging and drug delivery |
| 5 | Quantum dots | Possess fluorescent properties for drug tracking and imaging |
| 6 | Carbon nanotubes | Penetrate and localize the drug to cellular level |

biocompatible component increased the cytotoxic and antitumor efficacy against SKOV-3 cells [61]. Cannabidiol (CBD) were incorporated in a polymer nanoparticle to suppress the survival of ovarian cancer cells. Targeted delivery of paclitaxel using liposomal nanoformulation (PL-PTX) remarkably suppressed the proliferation of ovarian tumor growth by enhancing the TNF mediated ERK/AKT signaling

**Table 4** Nanoparticles for ovarian cancer approved by FDA—under clinical trials [24]

| S. no | Drug product | Active ingredient |
|---|---|---|
| 1 | Abraxane | Albumin-bound PTX nanosphere |
| 2 | Doxil | PEGylated doxorubicin |
| 3 | OSI—211 | Liposomal, Lutotecan |
| 4 | Paclical | PTX micelles |
| 5 | LEP-ETU | Liposomal PTX |

mechanism [28]. Staffhorst et al. [65] reported that the effects of cisplatin were enhanced when used as conjugated nanocapsules during ovarian growth inhibition in a humanized model system (Table 4).

Anticancer drugs are targeted to tumors through the conjugation of tumor-specific antibody by polymer micelle nanotechnology. Ovarian cancer therapy was remarkably improved by the development of multifunctional polymer micelles such as nanogels, magnetic-based micelles. These formulations have the ability of MRI targeting, targeted photodynamic therapy, thermosensitive therapy and luminescence, model imaging properties, which will monitor the nanoformulation and accumulated drugs at the tumor site.

## 6 Conclusion

Nanomaterial-based medicine has a promising novel application being in detection, diagnosis, imaging, therapeutics, and prognosis of various types of cancers. Some of the nanomaterials and are on the sensible horizon alleviate personalized and customized in cancer treatment. The best outcome of nanomaterial should possess correct selection, reliability, uncomplicated preparation methods, cheap cost, conditions, and efficacy of nanomaterials must be tested in clinical trials. By their improvement pharmacodynamic and pharmacokinetic properties, nanomaterials are widely used to enhance diagnosis and treatment of cancer with immensely reduced side effects.

## References

1. Ahamed M, Khan M, Siddiqui M et al (2011) Green synthesis, characterization and evaluation of biocompatibility of silver nanoparticles. Phys E Low Dimens Syst Nanostruct 43:1266–1271
2. American Lung Association: trends in lung cancer morbidity and mortality, epidemiology and statistics unit: research and scientific affairs. http://www.lung.org/lung-disease/lung-cancer/learning-more-about-lung-cancer/understanding-lung-cancer/. Accessed 28 Feb 2013
3. Armstrong DK (2002) Relapsed ovarian cancer: challenges and management strategies for a chronic disease. Oncologist 7:20–28

4. Astefanei A, Nunez O, Galceran MT (2015) Characterisation and determination of fullerenes: a critical review. Anal Chim Acta 882:1–21
5. Bahreyni A, Mohamud Y, Luo H (2020) Emerging nanomedicines for effective breast cancer immunotherapy. J Nanobiotechnol 18:180
6. Barati N, Razazan A, Nicastro J, Slavcev R, Arab A, Mosafa F, Nikpoor AR, Badiee A, Jaafari MR, Behravan J (2018) Immunogenicity and antitumor activity of the superlytic lambdaF7 phage nanoparticles displaying a HER2/neu-derived peptide AE37 in a tumor model of BALB/c mice. Cancer Lett 424:109–116
7. Bhatt P, Vhora I, Patil S, Amrutiya J, Bhattacharya C, Misra A, Mashru R (2016) Role of antibodies in diagnosis and treatment of ovarian cancer: basic approach and clinical status. J Control Release 226:148–167
8. Boulikas T (2004) Low toxicity and anticancer activity of a novel liposomal cisplatin (Lipoplatin) in mouse xenografts. Oncol Rep 12(1):3–12
9. Bray F, Ferlay J, Soerjomataram I, Siegel RL, Torre LA, Jemal A (2018) Global cancer statistics 2018: GLOBOCAN estimates of incidence and mortality worldwide for 36 cancers in 185 countries. CA Cancer J Clin 68:394–424
10. Brooks PC (1996) Cell adhesion molecules in angiogenesis. Cancer Metastasis Rev 15:187–194
11. Cao Y, Wang HJ, Cao C et al (2011) Inhibition effects of protein-conjugated amorphous zinc sulfide nanoparticles on tumor cells growth. J Nanoparticle Res 13:2759–2767
12. Chavez-Hernandez NH, Salamanca-Garcıa M (2014) Epidemiolog´ıa del cancer de mama en hombres atendidos en el Centro´ Medico Nacional 20 de noviembre. Revista de Especialidades Medico Quirurgicas 19:267–71
13. Cheng N, Watkins-Schulz R, Junkins RD, David CN, Johnson BM, Montgomery SA, Peine KJ, Darr DB, Yuan H, McKinnon KP et al (2018) A nanoparticle-incorporated STING activator enhances antitumor immunity in PD-L1-insensitive models of triple-negative breast cancer. JCI Insight 3:e120638
14. Cochrane Database of Systematic Reviews Non-small Cell Lung Cancer Collaborative Group: Chemotherapy can improve survival rates for nonsmall cell lung cancer. http://summaries.cochrane.org/CD002139/chemotherapy-can-improve-survival-rates-for-non-small-cell-lung-cancer (2010). Accessed 28 Feb 2013
15. Conde J, Doria G, Baptista P (2012) Noble metal nanoparticles applications in cancer. Journal of Drug Delivery, Cooper GM. The Cell: A Molecular Approach. 2nd edition. Sunderland, delivery of Ursolic-acid for modulating tumor microenvironment and regulatory T cell activities in cancer immunotherapy. J Control Release 320:168–78
16. Cooper GM (2000) The cell: a molecular approach. 2nd edn. Sinauer Associates, The Development and Causes of Cancer, Sunderland (MA). https://www.ncbi.nlm.nih.gov/books/NBK9963/
17. De Jong WH, Borm PJA (2008) Drug delivery and nanoparticles: applications and hazards. Int J Nanomedicine 3:133–149
18. Deng H, Tan S, Gao X, Zou C, Xu C, Tu K, Song Q, Fan F, Huang W, Zhang Z (2020) Cdk5 knocking out mediated by CRISPR-Cas9 genome editing for PD-L1 attenuation and enhanced antitumor immunity. Acta Pharm Sin B 10:358–373
19. Dreaden EC, Alkilany AM, Huang X, Murphy CJ, El-Sayed MA (2012) The golden age: gold nanoparticles for biomedicine. Chem Soc Rev 41:2740–2779
20. Dubertret B, Skourides P, Norris DJ, Noireaux V, Brivanlou AH, Libchaber A (2002) In vivo imaging of quantum dots encapsulated in phospholipid micelles. Science (New York, NY) 298:1759–1762
21. Ealias AM, Saravanakumar MP (2017) A review on the classification, characterisation, synthesis of nanoparticles and their application. IOP Conf Ser Mater Sci Eng 263:032019
22. European Commission (2016) Recommendation on the definition of a nanomaterial. http://data.europa.eu/eli/reco/2011/696/oj
23. Fan G, Dundas CM, Zhang C, Lynd NA, Keitz BK (2018) Sequence-dependent peptide surface functionalization of metal–organic frameworks. ACS Appl Mater Interfaces 10:18601–18609

24. Farideh FM (2017) Using nanoparticles in medicine for liver cancer imaging. Oman Med J 32:269–274
25. Farinati F, Sergio A, Baldan A et al (2009) Early and very early hepatocellular carcinoma: when and how much do staging and choice of treatment really matter? A multi-center study. BMC Cancer 9:33
26. Ferlay J, Ervik M, Lam F, Colombet M, Mery L, Pineros,M et al (2020) Global cancer observatory: cancer today. Lyon: International Agency for Research on Cancer
27. Folkman J (1996) Fighting cancer by attacking its blood supply. Sci Am 275:150–154
28. Fraguas AI, Torres-Suarez AI, Cohen MD, Bastida F, Yart D, Martin- L, Fernandez- CA (2020) PLGA nanoparticles for the Intraperitoneal administration of CBD in the treatment of ovarian cancer: in vitro and in Ovoassessment. Pharmaceutics 12:439
29. Friedl P, Wolf K (2003) Tumour-cell invasion and migration: diversity and escape mechanisms. Nat Rev Cancer 3:362–374
30. Garcia-Aranda M, Redondo M (2019) Immunotherapy: a challenge of breast cancer treatment. Cancers 11:1822
31. Ghosh D, Choudhury ST, Ghosh S et al (2012) Nanocapsulated curcumin: oral chemopreventive formulation against diethylnitrosamine induced hepatocellular carcinoma in rat. Chem Biol Interact 195:206–214
32. Girish PV, Mentham R, Rao CB, Nama S (2014) A review on breast cancer. Int J Pharm Bio Sci 4:47–54
33. Gmeiner WH, Ghosh S (2015) Nanotechnology for cancer treatment. Nanotechnol Rev 2:111–122
34. Goldberg MS (2019) Improving cancer immunotherapy through nanotechnology. Nat Rev Cancer 19:587–602
35. Hawkins MJ, Soon- P, Desai N (2008) Protein nanoparticles as drug carriers in clinical medicine. Adv Drug Del Rev 60:876–885
36. Henschke CI, McCarthy P, Wernick S (2002) Lung cancer myths, facts, choices and hope. W.W. Norton and Company, New York
37. Jemal A, Bray F, Center MM, Ferlay J, Ward E, Forman D (2011) Global cancer statistics. CA Cancer J Clin 61:69–90
38. Jimenez-Chavez AJ, Moreno- L, Bustos- I (2019) Therapy with multi-epitope virus-like particles of B19 parvovirus reduce tumor growth and lung metastasis in an aggressive breast cancer mouse model. Vaccine 37:7256–7268
39. Jin J, Krishnamachary B, Barnett JD, Chatterjee S, Chang D, Mironchik Y, Wildes F, Jafee EM, Nimmagadda S, Bhujwalla ZM (2019) Human cancer cell membrane-coated biomimetic nanoparticles reduce fbroblastmediated invasion and metastasis and induce T-cells. ACS Appl Mater Interfaces 11:7850–7861
40. Jung J, Park SJ, Chung HK et al (2012) Polymeric nanoparticles containing taxanes enhance chemoradiotherapeutic efficacy in non-small cell lung cancer. Int J Radiat Oncol Biol Phys 84:e77–e83
41. Karmous I, Pandey A, Ben K, Haj KB, Chaoui A (2020) Efficiency of the green synthesized nanoparticles as new tools in cancer therapy: insights on plant-based bioengineered nanoparticles, biophysical properties, and anticancer roles. Bio Tra Ele Res 196:330–342
42. Keat CL, Aziz A, Eid AM, Elmarzugi NA (2015) Biosynthesis of nanoparticles and silver nanoparticles. Bioresour Bioproc 2:47–58
43. Kim TY, Kim DW, Chung JY et al (2004) Phase I and Pharmacokinetic study of Genexol-PM a cremophor—free, polymeric micelle formulated paclitaxel in patients with advanced malignancies. Clin Cancer Res 10:3708–3716
44. Koudelka S, Turanek J (2012) Liposomal paclitaxel formula tions. J Control Release 163(3):322–334
45. Kumari A, Yadav SK, Yadav SC (2010) Biodegradable polymeric nanoparticles-based drug delivery systems. Colloids Surf B Biointerfaces 75:1–8
46. Loo C, Lin A, Hirsch L, Lee MH, Barton J, Halas N et al (2004) Nanoshell-enabled photonics-based imaging and therapy of cancer. Technol Cancer Res Treat 3:33–40. Masood F (2016)

Polymeric nanoparticles for targeted drug delivery system for cancer therapy. Mater Sci Eng 1:569–578
47. Mudshinge SR, Deore AB, Patil S, Bhalgat CM (2011) Nanoparticles: emerging carriers for drug delivery. Saudi Pharm J 19:129–141
48. Mukherjee P, Bhattacharya R, Wang P, Wang L, Basu S, Nagy JA, Atala A, Mukhopadhyay D, Soker S (2005) Antiangiogenic properties of gold nanoparticles. Clin Cancer Res 11:3530–3534
49. National Cancer Institute: SEER Stat Fact Sheet: Lung and Bronchus. http://seer.cancer.gov/statfacts/html/lungb.html (2002–2008). Accessed 19 Dec 2012
50. Novoselov KS, Geim AK, Morozov SV et al (2004) Electric feld in atomically thin carbon flms. Science 306:666–669
51. Parikh S, Hyman D (2007) Hepatocellular cancer: a guide for the internist. Am J Med 120:194–202
52. Park S, Jiang Z, Mortenson ED et al (2010) The therapeutic effect of anti—HER/neu antibody depends on both innate and adaptive immunity. Cancer Cell 18:160–170
53. Parungo CP, Ohnishi S, De Grand AM, Laurence RG, Soltesz EG, Colson YL et al (2004) In vivo optical imaging of pleural space drainage to lymph nodes of prognostic significance. Ann Surg Oncol 11:1085–1092
54. Popescu RC, Fufa MO, Grumezescu AM (2015) Metal-based nanosystems for diagnosis. Roman J Morphol Embryol = Revue roumaine de morphologie et embryologie 56:635–649
55. Ramalingam SS, Owonikoko TK, Khuri FR (2011) Lung cancer: new biological insights and recent American Lung Association therapeutic advances. CA Cancer J Clinic 61:91–112
56. Ramesh A, Brouillard A, Kumar S, Nandi D, Kulkarni A (2020) Dual inhibition of CSF1R and MAPK pathways using supramolecular nanoparticles enhances macrophage immunotherapy. Biomaterials 227:119559
57. Richards DA, Maruani A, Chudasama V (2017) Antibody fragments as nanoparticle targeting ligands: a step in the right direction. Chem Sci 8:63–77
58. Rivera MP, Mehta AC, Wahidi MM (2013) Establishing the diagnosis of lung cancer: diagnosis and management of lung cancer: American college of chest physicians evidence-based clinical practice guidelines. Chest J 143:e142S – e165
59. Russell MR, Graham CD, Amato A, Gentry- A, Ryan A, Kalsi JK, Ainley C, Whetton AD, Menon U, Jacobs I et al (2017) A combined biomarker panel shows improved sensitivity for the early detection of ovarian cancer allowing the identification of the most aggressive type II tumours. Br J Cancer 117:666–674
60. Saadat M, Manshadi MK, Mohammadi M, Zare MJ, Zarei M, Kamali R et al (2020) Magnetic particle targeting for diagnosis and therapy of lung cancers. J Control Release 328:776–791
61. Sanchez-Ramirez R, Domínguez-Ríos R, Juarez J, Valdés, M. Hassan N, Quintero-Ramos A, del Toro-Arreola A, Barbosa S, Taboada P, Topete A (2020) Iodegradable photoresponsive nanoparticles for chemo-, photothermal-and photodynamic therapy of ovarian cancer. Mater Sci Eng 111196
62. Siegel JM, Zou Z, Jemal A (2014) Cancer statistics, 2014. CA Cancer J Clin 64: 9–29
63. Siegel RL, Miller KD, Jemal A (2016) Cancer statistics, 2016. CA Cancer J Clin 66:7–30
64. Singh R (2019) Nanotechnology based therapeutic application in cancer diagnosis and therapy. 3 Biotech 9:415
65. Staffhorst RW, Van der Born K, Erkelens CA, Hamelers IH, Peters GJ, Boven E, De Kroon AI (2008) Antitumor activity and biodistribution of cisplatin nanocapsules in nude mice bearing human ovarian carcinoma xenografts. AntiCancer Drugs 19:721–727
66. Sutradhar KB, Amin ML (2014) Nanotechnology in cancer drug delivery and selective targeting. ISRN Nanotechnology
67. Taghavi F, Saljooghi AS, Gholizadeh M, Ramezani M (2016) Deferasirox-coated iron oxide nanoparticles as a potential cytotoxic agent. Med Chem Comm 7:2290–2298
68. Taton TA (2002) Nanostructures as tailored biological probes. Trends Biotechnol 20:277–279
69. Tsuchiya N, Sawada Y, Endo I, Saito K, Uemura Y, Nakatsura T (2015) Biomarkers for the early diagnosis of hepatocellular carcinoma, World J. Gastroenterol WJG 21:10573

70. Villanueva A (2019) Hepatocellular carcinoma. N Engl J Med 380:1450–1462
71. Whang YX, Zhao YY, Shen J, Sun X, Liu Y, Liu H, Wang Y, Wang J (2019) Nanoenabled modulation of acidic tumor microenvironment reverses anergy of infltrating T cells and potentiates anti-PD-1 therapy. Nano Lett 19:2774–2783
72. Witschi H (2001) A short history of lung cancer. Toxicol Sci 64:4–6
73. Xiong J, Wang Y, Xue Q, Wu X (2011) Synthesis of highly stable dispersions of nanosized copper particles using L-ascorbic acid. Green Chem 13:900–904
74. Yesilot S, Aydin C (2019) Silver nanoparticles; a new hope in cancer therapy? East J Med 24:111–116
75. Zhou Q, Ching AK, Leung WK et al (2011) Novel therapeutic potential in targeting microtubules by nanoparticle albumin-bound paclitaxel in hepatocellular carcinoma. Int J Oncol 38:721–731
76. Zhao J, Li X, Wang X, Wan X (2019) Fabrication of hybrid nanostructures based on $Fe_3O_4$ nanoclusters as theranostic agents for magnetic resonance imaging and drug delivery. Nanoscale Res Lett 14:200

# Chapter 12
# Green Synthesis of Metallic Nanoparticles and Applications in Biomedical and Environmental Research


**Mariadhas Valan Arasu**

## 1 Introduction

Nanotechnology is one of the emerging fields used to produce interatomic structural particles. Nanoparticles are small in size (1–100 nm) and these particles exhibited wide application in medical, agriculture, chemical electronic, and pharmaceutical fields. The synthesis of NPs with predetermined morphology is the important objective in the fields of chemistry that can be used for the preparation of biosensor, biomedical, catalysis, and lower cost electrode. Nanoparticles have unique functional properties, and these NPs have specific characteristics of bulk materials. Hence NPs are the ideal materials for various uses in biotechnology, medicine, wastewater treatment, and preparation of health care products. Many methods have been applied for the fabrication of NPs with predetermined properties. Although these methods have resulted in NPs with desired properties, still a basic knowledge of the high-quality fabrication is essential that could be effectively utilized at industrial levels for bulk manufacturing. To prepare NPs, two basic approaches (bottom-ups and top-down) are used. Conventionally, NPs are prepared by using various methods, such as sputtering, etching, ball milling, and lithographic techniques [4, 10]. The use of the bottom-up approach method involves many steps, including, sol–gel process, atomic condensation, vapor protocols, and spray pyrolysis. Green synthesis methods of NPs preparation attained much more attention in recent years and are presently used in current research and development on materials science. These green synthesized NPs reduce environmental pollution; reduce the utilization of toxic-solvents, prevention of waste, and eco-friendly. Biosynthesis is one of the important approaches to use biological materials and avoid toxic by-products using sustainable and eco-friendly

M. Valan Arasu (✉)
Department of Botany and Microbiology, College of Science, King Saud University, P.O. Box 2455, Riyadh 11451, Saudi Arabia
e-mail: mvalanarasu@gmail.com



K. Kasinathan et al. (eds.), *Nanomaterials for Energy Conversion, Biomedical and Environmental Applications*, Materials Horizons: From Nature to Nanomaterials,
https://doi.org/10.1007/978-981-19-2639-6_12

method. Green synthesis of metal and metal oxide NPs has been adopted to accommodate many sources, including, bacteria, algae, and plant extract [24]. The application of plant extract is a simple, rapid, and easy method to obtain NPs in large quantities than bacteria, plant, and fungi-based NPs synthesis. Biosynthesized NPs have several applications in the pharmaceutical industries such as synthesis of functional nanodevices, drug delivery personification procedure. These NPs have various applications in industries, including wastewater treatment, in the preparation of pharmaceuticals, synthesis of functional nanodevices, and drug delivery personification procedure [17, 23]. In this chapter we summarize the present research on the green synthesis of ZnO NPs and their applications. The main objective of this chapter was to promote green synthesis of ZnO NPs using plant extracts form biomedical and environmental applications.

## 2 Green Chemistry in Nanoparticles Biosynthesis

Green chemistry is widely used to produce NPs using biological samples. Chemical synthesis of NPs was achieved with the generation of hazard materials and many methods have been suggested to reduce the hazards to the environment. The sustainable and safe approaches and analysis support to reduce health hazard to the animals and the environment. Green chemistry is one of the newly emerged fields in chemistry. Green chemistry has potential role in the sustainable development that emerged for the fulfillment of present-day requirements and for future generations [46]. Green chemistry has specific role in sustainable development and has unique importance because of its application in pollution control and the application of naturally available resources [1].

## 3 Green Synthesis of Metal and Metal Oxide Nanoparticles

Plants, fungi, bacteria, actinomycetes, and algal samples are commonly applied for the biosynthesis of NPs. These extracts/samples have novel therapeutic properties and are applied for the biosynthesis of NPs with desired biological properties. In biological synthesis, both unicellular and multicellular organisms are applied in green chemistry [36]. Among various natural sources, plants are one of the major bioresources of natural environment that are eco-friendly and inexpensive. Algae, fungi, bacteria, and actinomycetes extracts are used for the green synthesis of NPs, moreover, the application of plant extract to produce NPs has several advantages. In plants, root, fruit, leaf, stem, bark, flower, and seeds have various phytochemicals, and these phytochemicals have the ability to reduce NPs. The selected plant parts are processed using sterile water and used as a reducing agent. The color of the salt solutions begins to change after the addition of plant extract and this color change reveals the synthesis of NPs.

## 4 Plant Extract is a Natural Capping Agent

Plant extract is widely used as the natural capping agent for the biosynthesis of NPs production. These natural capping agents are applied to maintain functional properties and to stabilize NPs. Capping agents are used to produce NPs with desired morphology. Generally, surfactants have used as the capping agent to achieve desired properties. However, these chemical capping agents are highly toxic to the environment and very difficult to remove. Due to these drawbacks, alternate capping agents are essential to form NPs with desired particle sizes. The phytochemicals of the medicinal plants serve as stabilizing agent and some of the phytocompounds acting as capping agent. In recent years, plant-mediated NPs synthesis was performed using various medicinal plants [29]. Plant phyto-components such as terpenoids, flavonoids, phenolic compound, protein, and amino acid are used for the biosynthesis of NPs. Isoprenoids or terpenoids have applied for the biosynthesis of iron NPs. These terpenoids are important secondary metabolites of the terrestrial plants. Terpenoids are also used for the preparation metal NPs [58]. Sesquiterpenoids and monoterpenoids are the two important terpenoids used for the biosynthesis of silver NPs [54]. Flavonoid is one of the phytochemicals in plants and this pigment is widely distributed among plants. About 7000 flavonoids are reported and are available in various forms such as, isoflavones, flavanol, flavones, anthocyanidins, flavanones, and flavan3-ol. Flavonoids are primarily considered as one of the widely distributed plants based reducing substances and their bio-reducing property and donate electrons. Phenolic acid including gallic acid, ellagic acid and protocatechuic acid are used as reducing agent for the green synthesis of NPs [3]. Polysaccharides are used as the reducing agents and widely used in green chemistry. These polysaccharides modify the shape, size, and structure of $TiO_2$ and induced various phases. For example, rutile phase is obtained in the presence of chitosan in the medium and starch is used to generate anatase phase. Green synthesis offers the use of non-toxic substances for the extraction of phytochemicals [16]. Natural polysaccharides improve the kinetics of sol–gel methods because of their potent catalytic properties and have been reported previously [9]. Amino cellulose is used for the synthesis of gold nanoparticles and acted as reducing and capping agent. Amino acids are useful for the preparation of NPs with smaller particle size (4–7 nm). L-histidine is used for the preparation of gold NPs and the concentration of amino acid decides the particle sizes [35].

## 5 Synthesis of ZnO Nanoparticles Using Plant Extract

Root, bark, seed, peel, stem, and leaves are applied for the preparation of ZnO NPs. Walnut extract has been recently used to produce ZnO NPs [48]. The phytochemicals extracted from *Cayratia pedata* are used to produce ZnO NPs [26]. Plant phytochemicals extracted from the root are used in the preparation of ZnO NPs.

Dimethyl sulfoxide extract of *Rubus fairholmianus* has the potential to produce ZnO NPs and the average particle size was approximately 10–12 nm [44]. *Phoenix dactylifera* is applied for the green synthesis of ZnO NPs [39]. Flower contains various pigments and the biological action of these pigments mediated ZnO NPs. *Cassia auriculata* extract is applied for the generation of flake structured ZnO NPs [61]. *Punica granatum* flower synthesized ZnO nanoparticles with excellent properties [41]. The aqueous flower extract of *Moringa oleifera* is evident in the presence of bioactive secondary metabolites and these compounds mediated ZnO NPs with 13–14 nm [45]. A hexagonal and triangular-shaped ZnO NPs with 30–40 nm size was obtained with *Syzygium aromaticum* extract [60].

## 6 Antibacterial Activity of ZnO Nanoparticles Against Drug Resistant Bacteria

Zinc oxide NPs have antibacterial activities and the NPs caused ROS-mediated cellular toxicity and membrane damage. They are bioactive potential against drug resistant bacteria, including, *Pseudomonas aeruginosa*, *Staphylococcus aureus*, *Klebsiella pneumoniae*, *Pseudomonas aeruginosa*, *Bacillus megaterium*, *Bacillus subtilis*, *Sarcina lutea*, *Aspergillus niger,* and *Candida albicans* [27, 34, 50]. Walnut aqueous leaf extract mediated ZnO nanoparticles showed activity against multi-drug resistant *E. coli*, *S. aureus,* and *E. coli* [48]. The aqueous extract of leaves from *Lippia adoensis* mediated ZnO NPs was effective against bacteria such as *Escherichia coli*, *Klebsiella pneumonia*, *Staphylococcus aureus,* and *Enterococcus faecalis* [14]. Piper betle-mediated ZnO NPs show potential antibacterial activity against *S. aureus* and *E. coli* [56]. *Arthrospira platensis* leaves extracted with fabricated ZnO was effective against bacterial strains such as *S. aureus*, *B. subtilis* and the increased activity was observed at higher concentrations. At lower concentrations of ZnO antibacterial activity decreased [18]. The ethanol extract of *Sambucus ebulus* mediated ZnO nanoparticles have antibacterial activity against various human bacteria. *Anacardium occidentale* mediated ZnO nanoparticles showed activity against drug resistant pathogens such as *A. Baumanii*, *E. coli*, *K. pneumoniae*, *E. aquaticum,* and *S. aureus* [15]. *Punica granatum* flower extract has effectively mediated ZnO NPs biosynthesis and was effective against bacteria such as *K. pneumoniae*, *P. aeruginosa*, *B. cereus*, *S. aureus*, *S. diarizonae*, *E. faecalis*, *E. coli*, *L. monocytogenes*, *A. hydrophila*, *E. faecium*, *M. catarrhalis,* and *A. hydrophila* [25].

## 7 Mechanism of Action of ZnO on Microorganisms

ZnO materials have antimicrobial properties, and the mechanism of action is based on adsorption, $Zn^{2+}$ ion release, generation of reactive oxygen species, and intracellular energy metabolism inhibition, cell membrane damage, lipid peroxidation, DNA breakage, and DNA replication disruption [32]. ZnO NPs/MPs release $Zn^{2+}$ ions and it induced an antimicrobial response against various pathogenic bacteria due to inhibitory effect in enzyme system and in metabolic processes. The surface of ZnO NPs/MPs (positively charge) effectively interacted with the bacterial cell wall (negatively charge) [22]. After adsorption, the microorganism losses its integrity, membrane rupture or cell wall, and induced oxidative stress owing to lipid peroxidation reaction and damage DNA. ZnO NPs have different specificity against bacterial pathogens, influenced by their physicochemical properties such as porosity, morphology, surface charge, and particle size [22]. ZnO NPs/MPs have multiple functions than other NPs prepared from metals. The antibiotic metals namely, gold and silver NPs have the principal function of membrane adsorption, and metal ion release. The other particles such as cupric oxide, titanium dioxide, and magnesium oxide NPs show NP internalization, ROS generation, and induce damage to bacteria. ZnO NPs/MPs effectively combat bacterial growth and prevent the development of antibiotic resistance and NPs penetrate the bacterial cell [28].

ZnO NPs combined with other metal NPs showed considerable antibacterial activity against virulence hospital pathogens. The synergistic bioactive materials improve sustainability and have repeat usability in various biomedical applications, then ZnO NPs alone. These particles combined with ZnO NPs/MPs improved activity against bacterial strains and overcome antibiotic resistance. Metals doped with polymers, polyhydroxyapatite, carbon-based material, graphene oxide, quantum dots, and reduced graphene oxide [51]. They improved synergistic microbial inhibition or involved the antibacterial pathways of ZnO NPs in bacteria to inhibit bacterial growth or create synergistic properties.

## 8 Antifungal Activity of ZnO Nanoparticles

ZnO NPs are ionic metal oxides that have unique properties such as unusual crystal structures and high surface area. Inorganic materials such as ZnO show greater selectivity, superior durability, and heat resistance. However, zinc is one of the important mineral elements required for human health in the form of ZnO [21]. ZnO NPs have antifungal properties and zinc compounds are widely used as fungicides. The antifungal activities of ZnO NPs are based on the development of free radicals on the surface of the ZnO NPs and break down of the cell membranes. Zinc oxide NPs induced ROS-mediated cellular changes and membrane damage. They are highly effective against fungal species such as *Aspergillus niger* and *Candida albicans.*

The commercially available antifungal agents have very limited applications. Consequently, the inorganic antifungal agents cause serious side effects such as renal failure, liver damage, diarrhea, nausea, increased body temperature after drug consumption. The plant-mediated iron or iron oxides NPs can damage fungal hyphae and effective against spore-forming fungal strains. The metal and metal oxide NPs interact with fungi cell membrane and structure and affect membrane structure and function [30].

## 9 Antioxidant Activity

Nanoparticles have antioxidant activity and these NPs involved in various biochemical reactions. These antioxidants have scavenging of free radicals, production of reactive oxygen species, and changing intracellular redox state [20]. Reactive oxygen species generation is involved in various diseases including, Alzheimer's-, Parkinson's-disease, and various neurodegenerative disorders. The generated free radicals in the biological system effectively cleave hydrogen bonds in DNA macromolecule and affect the base pairs of DNA, which can mediate in the development of types of cancers. Cancer disease is one of the leading causes of death throughout the world and the current radiation therapy and drugs affect the normal cells. Antioxidant molecules have potential anticancer activities and may effectively reduce various types of toxicity linked with chemotherapy treatment [31]. Hence, the application of antioxidant from natural sources during treatment shows an adjunct for the treatment of various types of cancers. There are various drugs used to treat cancer, moreover, these drugs involved unexpected side effects [12]. ZnO NPs are applied in the textile and rubber industries [57]. ZnO nanoparticles show 1-diphenyl-2-picryl-hydrazyl (DPPH) free radical scavenging antioxidant activity [12]. Medicinal plants extract mediated NPs have antioxidant potentials. *Polygala tenuifolia* root extract mediated ZnO nanoparticles show antioxidant activity [40, 52].

## 10 Anticancer Activity

Cancer disease is the emerged diseases and consists of about 100 types of cancers. Cancer cells are characterized by unrestricted cell division of cells with abnormal characters. The number of cancer cases increased in recent years. It is estimated about $150 billion in 2020 [6]. Nanomedicine is one of the emerging fields and attained much more attention for the treatment and diagnosis of cancers. Nanomedicine shows potential characteristics based on phytochemicals involved in the formulations of metal nanoparticles. The plant-mediated NPs have attracted increased attentions for cancer treatment. The NPs have unique physical, optical, electrical, and the properties may vary based on the surface volume, charge, particle size, and other functional properties. Nanomedicine is one of the fast-expanding research areas of

nanoscience and mainly metallic NPs have applications in the synthesis of nanoplatform drugs because of unique physicochemical activities. Moreover, the biogenic metallic nanoparticles have potential applications in the treatment of cancer. Medicinal plant extract has been applied for the preparation of anticancer ZnO NPs [30]. These metallic NPs have fluorescent properties when exposed to X-rays. It can be used to diagnose cancer cells in the human body. In recent years, various therapeutic molecules and strategies were applied for the treatment of cancer at various stages of development. Moreover, most of the commercial drugs have least specificity against cancer cells and induced toxicity to the normal cells. These drugs show least stability, low degradation potential from the biological system, and poor targeting ability. FDA approved nanomedicine for the preparation of cancer treatment. Onivyde (80 and 140 nm), NanoTherm iron oxide NPs (20 nm) are used to treat metastatic pancreatic cancer and for thermal ablation of glioblastoma.

Anticancer properties of ZnO NPs (10 nm) Hela cell lines were studied at various NPs concentrations. ZnO NPs showed dose-dependent anticancer activity and the cell viability reduction was 5–50% in HeLa cells. Fe-doped ZnO NPs and ZnO NPs are quasi-spherical in shape and the synthesized particle size was approximately 10–20 nm in size and showed anticancer activities [42]. The chitoson-coated NPs are spherical shaped and 100 nm in diameter. These chitosan-coated and uncoated materials were tested against Hela cells at various concentrations [11]. The chitosan-coated Hela cells improved cytotoxicity through cellular internalization, formation of ROS, apoptosis, and cell death at 75 μg/mL concentrations. The green synthesized ZnONPs mediated by the aqueous extract of *Gracilaria edulis* showed cytotoxicity [19].

## 11 Pesticidal Properties

Nanoparticles penetrate through plants cells hence they become to act as nanocarriers making them more efficient in targeting the plant pests. The nanoparticles such as CuO, Ag, ZnO, and MgO have potent insecticidal activity against various pests. ZnO has a lot of potential against various pests than other oxides. Metal NPs have toxic effects, and it effects on crustaceans, plant pests, and bacteria. NPs are effective against pests from different orders including, *Lepidoptera*, *Coleoptera*, *Diptera*, *Hemiptera*, Nanoparticles such as gold, silver, aluminum, zinc, silica, zinc oxide, metal oxide, and titanium dioxide are useful to control pests [47, 55]. Silica nanoparticles are also applied to control insect pests [13]. Nanoparticles induce desiccation in larvae and decreased cell viability. Silica microparticles affect *T. molitor* larvae and induced mortality and the mortality rate was about 70%. Silica microparticles damage dermal and epidermal cells of larvae which lead to dehydration of the larvae and become dark [7].

## 12 Photocatalytic Degradation of Organic Dyes

Organic dyes are one of the important pollutants causing negative effects on the environment. Organic dyes are very stable, toxic, resistant, and carcinogenic compounds. These are applied in the food, plastic, textile, and leather industries. The textile industry involves the maximum levels of water pollution due to organic dyes. The existence about 10,000 colorants has been introduced, of which about 700,000 tons are discharged in every year [49]. The methods such as adsorption, reductive reaction, Fenton reaction, and biodegradation are useful [43]. Moreover, some of these described methods are highly expensive, required toxic chemicals, and affect the eco-system and the environment. Among these techniques, photocatalytic method is a low-cost, simple degradation, and harmless. This method is useful in removing various pollutants in wastewater and aquatic system using UV energy or solar energy. The green synthesized silver NPs and zinc oxide nanorods composite was effective to degrade 92% of paracetamol in water within 4 h of incubation [2]. Photocatalyst is used in photocatalytic process, and this is generally a semiconductor substance that, by effectively absorbing photons from the water, is generally activated to generate hydroxyl radicals and thus uses the complete organic dye degradation [59]. The semiconductors such as, tin dioxide ($SnO_2$), titanium dioxide ($TiO_2$), iron oxide (III) ($Fe_2O_3$), copper oxide (CuO), and ZnO are widely used as photocatalysts [8, 37]. ZnO is widely applied in sensor, batteries, solar cells, and ZnO is considered as one of the super catalysts in the removal of pollutants from the wastewater. ZnO NPs have good oxidizing potential and show a bandgap of approximately 3.37 eV, excellent mechanical and chemical stability, photosensitive property, leading to various environmental applications [53]. *Camellia sinensis* extract is useful for the green synthesis of $SnO_2$ NPs with the particle size between 4 and 5 nm [33]. Lemon peel extract was used to green synthesize $TiO_2$ NPs and it was quasi-spherical shape, and the size was between 80 and 140 nm [38]. *Allium sativum* extract was used for the green synthesis of CuO NPs and the particle size ranged between 20 and 40 nm [33]. These green synthesized NPs have potential application in the degradation of various organic dyes. The NPs prepared using Jasmine powder showed MB degradation activity and 78% degradation was achieved within 2 h [5]. Camellia sinensis extract was used for the synthesis of iron NPs and is applied for the degradation of MO from the wastewater.

## 13 Conclusion

Metal and metal oxide NPs have been widely used in the field of environment and health sciences. Thus, the chemistry of green synthesis and the application of the synthesized NPs are important for various applications. Green synthesis uses extracts from bacteria, fungi, algae, and plants. Moreover, plant extracts have remarkable efficiency in reducing, capping, and stabilizing agents than other sources for the

preparation of nanoparticles with desired molecular properties due to the presence of capping agents and reducing power. This chapter shows the use of plants for the green synthesis of nanoparticles and covers the application of nanoparticles for biomedical and environmental applications. The antibacterial, antifungal, anticancer, and antioxidant power of the nanoparticles were described. ZnO is a semiconductor that has excellent thermal stability and is widely used as sensor, luminescent material, batteries, solar cells, optoelectronic applications and is considered as one of the super catalysts in the removal of pollutants from the wastewater.

## References

1. Al Ansari MS (2012) A review of optimal designs in relation to supply chains and sustainable chemical processes. Mod Appl Sci 6(12):74
2. Al-Gharibi MA, Kyaw HH, Al-Sabahi JN, Myint MTZ, Al-Sharji ZA, Al-Abri MZ (2021) Silver nanoparticles decorated zinc oxide nanorods supported catalyst for photocatalytic degradation of paracetamol. Mater Sci Semicond Process 134:105994
3. Ali M, Khan T, Fatima K, Ali QUA, Ovais M, Khalil AT, Ullah I, Raza A, Shinwari ZK, Idrees M (2018) Selected hepatoprotective herbal medicines: Evidence from ethnomedicinal applications, animal models, and possible mechanism of actions. Phytother Res 32(2):199–215
4. Arasu MV, Arokiyaraj S, Viayaraghavan P, Kumar TSJ, Duraipandiyan V, Al-Dhabi NA, Kaviyarasu K (2019) One step green synthesis of larvicidal, and azo dye degrading antibacterial nanoparticles by response surface methodology. J Photochem Photobiol, B 190:154–162
5. Aravind M, Ahmad A, Ahmad I, Amalanathan M, Naseem K, Mary SMM, Parvathiraja C, Hussain S, Algarni TS, Pervaiz M, Zuber M (2021) Critical green routing synthesis of silver NPs using jasmine flower extract for biological activities and photocatalytical degradation of methylene blue. J Environ Chem Eng 9(1):104877
6. Barabadi H, Ovais M, Shinwari ZK, Saravanan M (2017) Anti-cancer green bionanomaterials: present status and future prospects. Green Chem Lett Rev 10(4):285–314
7. Barik TK, Kamaraju R, Gowswami A (2012) Silica nanoparticle: a potential new insecticide for mosquito vector control. Parasitol Res 111(3):1075–1083
8. Belaidi, S., Sangare, S., Felahi, A., Remache, W., Belattar, S. and Sehili, T., 2021. Synthesis of metal and non-metal doping hematite nanoparticles for adsorption and photocatalytic degradation of acid red 14 in aqueous solutions. *International Journal of Environmental Analytical Chemistry*, pp.1–14.
9. Boury B, Plumejeau S (2015) Metal oxides and polysaccharides: an efficient hybrid association for materials chemistry. Green Chem 17(1):72–88
10. Cao G (2004) Nanostructures & nanomaterials: synthesis, properties & applications. Imperial college press, London, UK
11. Chen X, Cai K, Fang J, Lai M, Hou Y, Li J, Luo Z, Hu Y, Tang L (2013) Fabrication of selenium-deposited and chitosan-coated titania nanotubes with anticancer and antibacterial properties. Colloids Surf, B 103:149–157
12. Das A, Wang DY, Leuteritz A, Subramaniam K, Greenwell HC, Wagenknecht U, Heinrich G (2011) Preparation of zinc oxide free, transparent rubber nanocomposites using a layered double hydroxide filler. J Mater Chem 21(20):7194–7200
13. Debnath N, Mitra S, Das S, Goswami A (2012) Synthesis of surface functionalized silica nanoparticles and their use as entomotoxic nanocides. Powder Technol 221:252–256
14. Demissie MG, Sabir FK, Edossa GD, Gonfa BA (2020) Synthesis of zinc oxide nanoparticles using leaf extract of lippia adoensis (koseret) and evaluation of its antibacterial activity. J Chem 2020:7459042

15. Droepenu, E.K., Wee, B.S., Chin, S.F., Kok, K.Y. and Maligan, M.F., 2021. Zinc Oxide Nanoparticles Synthesis Methods and its Effect on Morphology: A Review. http://ugspace.ug.edu.gh/handle/123456789/37152.
16. Duan H, Wang D, Li Y (2015) Green chemistry for nanoparticle synthesis. Chem Soc Rev 44(16):5778–5792
17. El Shafey AM (2020) Green synthesis of metal and metal oxide nanoparticles from plant leaf extracts and their applications: A review. Green Processing and Synthesis 9(1):304–339
18. El-Belely EF, Farag M, Said HA, Amin AS, Azab E, Gobouri AA, Fouda A (2021) Green synthesis of zinc oxide nanoparticles (ZnO-NPs) using Arthrospira platensis (Class: Cyanophyceae) and evaluation of their biomedical activities. Nanomaterials 11(1):95
19. Fakhroueian Z, Vahabpour R, Assmar M, Massiha A, Zahedi A, Esmaeilzadeh P, Katouzian F, Rezaei S, Keyhanvar P, Mozafari Dehshiri A (2018) ZnO Q-dots as a potent therapeutic nanomedicine for in vitro cytotoxicity evaluation of mouth KB44, breast MCF7, colon HT29 and HeLa cancer cell lines, mouse ear swelling tests in vivo and its side effects using the animal model. Artificial cells, nanomedicine, and biotechnology 46(sup2):96–111
20. Finkel, T. and Holbrook, N.J., 2000. Oxidants, oxidative stress and the biology of ageing. *nature*, *408*(6809), 239–247.
21. Gur T, Meydan I, Seckin H, Bekmezci M, Sen F (2022) Green synthesis, characterization and bioactivity of biogenic zinc oxide nanoparticles. Environ Res 1(204):111897
22. Hajipour MJ, Fromm KM, Ashkarran AA, de Aberasturi DJ, de Larramendi IR, Rojo T, Serpooshan V, Parak WJ, Mahmoudi M (2012) Antibacterial properties of nanoparticles. Trends Biotechnol 30(10):499–511
23. Haritha E, Roopan SM, Madhavi G, Elango G, Al-Dhabi NA, Arasu MV (2016) Green chemical approach towards the synthesis of SnO2 NPs in argument with photocatalytic degradation of diazo dye and its kinetic studies. J Photochem Photobiol, B 162:441–447
24. Helan V, Prince JJ, Al-Dhabi NA, Arasu MV, Ayeshamariam A, Madhumitha G, Roopan SM, Jayachandran M (2016) Neem leaves mediated preparation of NiO nanoparticles and its magnetization, coercivity and antibacterial analysis. Results in physics 6:712–718
25. Ifeanyichukwu UL, Fayemi OE, Ateba CN (2020) Green synthesis of zinc oxide nanoparticles from pomegranate (Punica granatum) extracts and characterization of their antibacterial activity. Molecules 25(19):4521
26. Jayachandran A, Aswathy TR, Nair AS (2021) Green synthesis and characterization of zinc oxide nanoparticles using Cayratia pedata leaf extract. Biochemistry and Biophysics Reports 26:100995
27. Jin SE, Jin JE, Hwang W, Hong SW (2019) Photocatalytic antibacterial application of zinc oxide nanoparticles and self-assembled networks under dual UV irradiation for enhanced disinfection. Int J Nanomed 14:1737
28. Jin SE, Hwang W, Lee HJ, Jin HE (2017) Dual UV irradiation-based metal oxide nanoparticles for enhanced antimicrobial activity in Escherichia coli and M13 bacteriophage. Int J Nanomed 12:8057
29. Khalil, A.T., Ovais, M., Ullah, I., Ali, M., Shinwari, Z.K., Khamlich, S. and Maaza, M., 2017. Sageretia thea (Osbeck.) mediated synthesis of zinc oxide nanoparticles and its biological applications. *Nanomedicine*, *12*(15), pp.1767–1789.
30. Khan R, Inam MA, Park DR, Zam Zam S, Yeom IT (2018) Taguchi orthogonal array dataset for the effect of water chemistry on aggregation of ZnO nanoparticles. Data 3(2):21
31. Labriola D, Livingston R (1999) Possible interactions between dietary antioxidants and chemotherapy. Oncology (Williston Park) 13(7):1003–1008
32. Lemire JA, Harrison JJ, Turner RJ (2013) Antimicrobial activity of metals: mechanisms, molecular targets and applications. Nat Rev Microbiol 11(6):371–384
33. Luque PA, Chinchillas-Chinchillas MJ, Nava O, Lugo-Medina E, Martínez-Rosas ME, Carrillo-Castillo A, Vilchis-Nestor AR, Madrigal-Muñoz LE, Garrafa-Gálvez HE (2021) Green synthesis of tin dioxide nanoparticles using Camellia sinensis and its application in photocatalytic degradation of textile dyes. Optik 229:166259

34. Martínez-Carmona M, Gun'Ko Y, Vallet-Regí M (2018) ZnO nanostructures for drug delivery and theranostic applications. Nanomaterials 8(4):268
35. Maruyama T, Fujimoto Y, Maekawa T (2015) Synthesis of gold nanoparticles using various amino acids. J Colloid Interface Sci 447:254–257
36. Mohanpuria P, Rana NK, Yadav SK (2008) Biosynthesis of nanoparticles: technological concepts and future applications. J Nanopart Res 10(3):507–517
37. Molkenova A, Sarsenov S, Atabaev S, Khamkhash L, Atabaev TS (2021) Hierarchically-structured hollow CuO microparticles for efficient photo-degradation of a model pollutant dye under the solar light illumination. Environmental Nanotechnology, Monitoring & Management 16:100507
38. Nabi, G., Ain, Q.U., Tahir, M.B., Nadeem Riaz, K., Iqbal, T., Rafique, M., Hussain, S., Raza, W., Aslam, I. and Rizwan, M., 2020. Green synthesis of TiO2 nanoparticles using lemon peel extract: their optical and photocatalytic properties. *International Journal of Environmental Analytical Chemistry*, pp.1–9.
39. Naser R, Abu-Huwaij R, Al-khateeb I, Abbas MM, Atoom AM (2021) Green synthesis of zinc oxide nanoparticles using the root hair extract of Phoenix dactylifera: antimicrobial and anticancer activity. Appl Nanosci 11(5):1747–1757
40. Nethravathi PC, Shruthi GS, Suresh D, Nagabhushana H, Sharma SC (2015) Garcinia xanthochymus mediated green synthesis of ZnO nanoparticles: photoluminescence, photocatalytic and antioxidant activity studies. Ceram Int 41(7):8680–8687
41. OECD. Physical-Chemical Decision Framework to Inform Decisions for Risk Assessment of Manufactrued Nanomaterials; Organization for Economic Co-operation and Development: Paris, France, 2019; Volume 90.
42. Pandurangan M, Enkhtaivan G, Kim DH (2016) Anticancer studies of synthesized ZnO nanoparticles against human cervical carcinoma cells. J Photochem Photobiol, B 158:206–211
43. Rabbani F, Shaikh AJ, Khan J, Ajaz H, Rafique M, Khan ZUH, Ali Z, Hussain H, Gillani MM, Aslam K, Shah GM (2019) Removal of Organic Colorants Using Nano Copper Antimony Oxychloride Synthesized by Non-solvated System. J Inorg Organomet Polym Mater 29(3):893–900
44. Rajendran NK, George BP, Houreld NN, Abrahamse H (2021) Synthesis of Zinc Oxide Nanoparticles Using Rubus fairholmianus Root Extract and Their Activity against Pathogenic Bacteria. Molecules 26(10):3029
45. Rasmussen K, Rauscher H, Mech A, Sintes JR, Gilliland D, González M, Kearns P, Moss K, Visser M, Groenewold M, Bleeker EA (2018) Physico-chemical properties of manufactured nanomaterials-Characterisation and relevant methods. An outlook based on the OECD Testing Programme. Regul Toxicol Pharmacol 92:8–28
46. Robert, K.W., Parris, T.M. and Leiserowitz, A.A., 2005. What is sustainable development? Goals, indicators, values, and practice. *Environment: science and policy for sustainable development*, *47*(3), pp.8–21.
47. Sabbour MM (2012) Entomotoxicity assay of two nanoparticle materials 1-(Al2O3and TiO2) against Sitophilus oryzae under laboratory and store conditions in Egypt. J Nov Appl Sci 1(4):103–108
48. Saemi R, Taghavi E, Jafarizadeh-Malmiri H, Anarjan N (2021) Fabrication of green ZnO nanoparticles using walnut leaf extract to develop an antibacterial film based on polyethylene–starch–ZnO NPs. Green Processing and Synthesis 10(1):112–124
49. Shim YJ, Soshnikova V, Anandapadmanaban G, Mathiyalagan R, Perez ZEJ, Markus J, Kim YJ, Castro-Aceituno V, Yang DC (2019) Zinc oxide nanoparticles synthesized by Suaeda japonica Makino and their photocatalytic degradation of methylene blue. Optik 182:1015–1020
50. Siddiqi KS, ur Rahman, A. and Husen, A. (2018) Properties of zinc oxide nanoparticles and their activity against microbes. Nanoscale Res Lett 13(1):1–13
51. Singh AK, Pal P, Gupta V, Yadav TP, Gupta V, Singh SP (2018) Green synthesis, characterization and antimicrobial activity of zinc oxide quantum dots using Eclipta alba. Mater Chem Phys 203:40–48

52. Siripireddy B, Mandal BK (2017) Facile green synthesis of zinc oxide nanoparticles by Eucalyptus globulus and their photocatalytic and antioxidant activity. Adv Powder Technol 28(3):785–797
53. Siva N, Sakthi D, Ragupathy S, Arun V, Kannadasan N (2020) Synthesis, structural, optical and photocatalytic behavior of Sn doped ZnO nanoparticles. Mater Sci Eng, B 253:114497
54. Song JY, Kim BS (2009) Rapid biological synthesis of silver nanoparticles using plant leaf extracts. Bioprocess Biosyst Eng 32(1):79–84
55. Stadler T, Buteler M, Weaver DK (2010) Novel use of nanostructured alumina as an insecticide. Pest Management Science: formerly Pesticide Science 66(6):577–579
56. Thi Tran QM, Thi Nguyen HA, Doan VD, Tran QH, Nguyen VC (2021) Biosynthesis of Zinc Oxide Nanoparticles Using Aqueous Piper betle Leaf Extract and Its Application in Surgical Sutures. J Nanomater 2021:8833864
57. Vigneshwaran N, Kumar S, Kathe AA, Varadarajan PV, Prasad V (2006) Functional finishing of cotton fabrics using zinc oxide–soluble starch nanocomposites. Nanotechnology 17(20):5087
58. Vilas V, Philip D, Mathew J (2014) Catalytically and biologically active silver nanoparticles synthesized using essential oil. Spectrochim Acta Part A Mol Biomol Spectrosc 132:743–750
59. Yusoff N, Ho LN, Ong SA, Wong YS, Khalik W (2016) Photocatalytic activity of zinc oxide (ZnO) synthesized through different methods. Desalin Water Treat 57(27):12496–12507
60. Zheng X, Shen G, Wang C, Li Y, Dunphy D, Hasan T, Brinker CJ, Su BL (2017) Bio-inspired Murray materials for mass transfer and activity. Nat Commun 8(1):1–9
61. Zukas BG, Gupta NR (2017) Interphase Synthesis of Zinc Oxide Nanoparticles in a Droplet Flow Reactor. Ind Eng Chem Res 56(25):7184–7191

# Chapter 13
# In Vitro Studies of Chitosan/PVA/Methylcellulose—Silver Nanocomposites Scaffolds Using L929 Fibroblast Cells

**K. Kanimozhi, V. Sugantha Kumari, S. Khaleel Basha, and K. Kaviyarasu**

## 1 Introduction

Popular fresh ages, silver nanoparticles must involve substantial benefits since of their latent requests. Numerous approaches must be remained advanced aimed at the mixture of silver nanoparticles [1–3]. These approaches remain predictable near outcome trendy an actual thin atom scope delivery then atoms of even figure. Scaffold remains unique of the greatest significant matters trendy skin manufacturing then renewing drug [4–7]. Exploiting automatically strong nano-sized supports, designed for instance carbon nanotubes, nanoclays, graphite and inorganic nanoparticles, addicted to polymer crowds in the direction of improve polymers possessions consumes remained extensively subjugated [8–11]. Several reviews have been published on salt leaching and the use of varies size of sodium chloride salt particles of nanocomposites [4]. Biopolymers related to salt leaching nanocomposites, including

K. Kanimozhi (✉)
Department of Chemistry, Global Institute of Engineering and Technology, Melvisharam, Tamil Nadu 632509, India
e-mail: kanivlr8@gmail.com

K. Kanimozhi · V. S. Kumari
PG Research & Department of Chemistry, Auxilium College (Autonomous), Vellore, Tamil Nadu, India

S. K. Basha
Department of Chemistry, C. Abdul Hakeem College, Melvisharam, Tamil Nadu 632509, India

K. Kaviyarasu
UNESCO-UNISA Africa Chair in Nanosciences/Nanotechnology Laboratories, College of Graduate Studies, University of South Africa (UNISA), Muckleneuk Ridge, Pretoria, South Africa

Nanosciences African Network (NANOAFNET), Materials Research Group (MRG), iThemba LABS-National Research Foundation (NRF), 1 Old Faure Road, Somerset West 7129, Western Cape Province, South Africa



K. Kasinathan et al. (eds.), *Nanomaterials for Energy Conversion, Biomedical and Environmental Applications*, Materials Horizons: From Nature to Nanomaterials,
https://doi.org/10.1007/978-981-19-2639-6_13

processing, structure and property characterization, applications as well as modelling and simulations [5]. The silver nanoparticles remain of attention as of the single belongings scope besides form liable visual, electrical, then attractive belongings which tin remain combined interested in antimicrobial claims, biosensor resources, compound threads, cryogenic superconducting resources, beautifying crops, then microelectronic workings [6, 12–14]. Chitosan, the deacetylated creation of chitin, remains answerable popular thinned acids such by means of acetic acid besides formic acid. Lately the termination of chitosan trendy N-methyl morpholine-N-oxide/H2O consumes stood conveyed [7, 15]. The hydrolysis of chitosan through focused acids below dangerous situations crops comparatively the unadulterated amino sugar, D-glucosamine [8, 16]. Poly(vinyl alcohol) (PVA) remains a polymer through carbon cable mainstay devoted through hydroxyl collections. PVA remains a artificial polymer that remains non-poisonous, biocompatible, recyclable, humble toward make, consumes outstanding powered asset besides remains chemically besides thermally steady [9, 17]. Poly(vinyl alcohol) (PVA) goes toward the collection of polymers which container remain charity trendy mixture through silver nitrate [7, 18]. PVA remains unique of the artificial, recyclable, biocompatible, aquatic-solvable polymers exploited trendy therapeutic requests such by way of twisted coverings, synthetic coating, coverings, transdermal reinforcements, circulatory strategies, then medication distribution schemes [5, 10]. Methylcellulose [MC] a unoriginal of normal polysaccharides performs thermo adjustable sol–gel changeover trendy aqueous explanation in place of healthy. Methylcellulose offerings an growth trendy permeability besides solubility popular liquid related by means of the rise of the inflammation gradation, which advance the profitable applicability of the polymer [11].

Silver nitrate ($AgNO_3$) remains unique of the springs of silver ions. The situation remains resolvable trendy liquid besides for of the situation bright understanding, the situation remains charity trendy work of clear the flicks, looking glass silvering, shock coloring, gray gilding as per fine such as trendy drug in place of cautery besides sterile antiseptic movement (against Staphylococcus aureus and Escherichia coli) remained showed [12, 19, 20]. The goal of the current effort consumed exposed that CS/PVA/MC3 through AgNps nanocomposites ready through salty filtering method near improve the belongings of CS/PVA/MC3 medium. The cytocompatibility besides suitable physicochemical belongings of CS/PVA/MC3-AgNps frameworks specified the talented habit trendy more schoolwork aimed at casing flesh manufacturing submission [21–23].

## 2 Materials and Methods

### *2.1 Materials*

Chitosan (CS) through a 92% grade of deacetylation, Polyvinyl alcohol (PVA) 88% of gradation of hydrolysis, Methyl Cellulose (MC), (Logical score) acetic acid (AA), and Sodium chloride (NaCl) remained acquired after (Sigma-Aldrich) logical rating. The Silver nitrate Nanopowder ($AgNo_3$) (>99%) remained acquired since Sisco Research Laboratories Pvt. Ltd. (SRL) besides molecular heaviness of $AgNo_3$ stayed 81.38. Completely the extra substances rummage-sale remained of logical score, besides stayed charity minus some more sanitization.

### *2.2 Synthesis of Silver Nanoparticle*

The silver nanoparticles remained ready through by means of biochemical decrease technique. 50 ml of 0.001 M Silver Nitrate stood animated near spot. Just before the overhead solution 5 ml of 1% trisodium citrate remained additional drip by drip. Throughout the course, clarifications stood miscellaneous strongly besides fiery while waiting for alteration of colour stayed obvious. Formerly the situation remained detached starting the boiler expedient and stimulated awaiting chilled near chamber fever.

### *2.3 Preparation of CS/PVA/MC3-AgNps Nanocomposites*

Chitosan and PVA remained mixed through socializing a 1% explanation of chitosan trendy 1% aqueous acetic acid besides 1% solution of PVA in earnest aquatic. 1% Chitosan and 1% PVA solutions stood gradually supplementary to 0.9% MC solutions to obtain blends of 75% MC. AgNps Nanocomposite films were prepared by casting composite solution (CS/PVA/MC3- AgNps1 CS/PVA/MC3- AgNps2, CS/PVA/MC3- AgNps3) containing 0.5%, 1%, and 2% AgNps, correspondingly. The combinations stayed ready in 6 h attractive thrilling by chamber temperature near get similar solution. Then, 4 g of grainy sodium chloride were sieved (NaCl, 200 μm-600 μm) and homogeneously added into the nano composite solutions and stirred for 4 h. The resolution stood leftward by chamber temperature aimed at 3 days near agree gelation, previous near wash through deionized aquatic trendy directive toward filter ready the saline rocks. After leaching, the frameworks remained leftward near thirsty aimed at 24 h besides the saline-filtered CS/PVA/MC3-AgNps frameworks stayed gained.

## 2.4 Salt Leaching—Scaffold Preparation

The spongy framework container remains gained through torrential combination hooked on the petri plates. NaCl atoms (200-500 μm) remained filtered besides formerly further interested in the CS/PVA/MC3-AgNps combination besides stimulated aimed at 4 h. The examples stood in-flight-desiccated through ordinary vanishing on behalf of 24 h. The saline elements stayed filtered obtainable through submerging the tasters popular deionized aquatic aimed at 72 h by 37 °C. In the marine remained rested 3 periods a time toward favour the whole closure of the salty. Subsequently leakage, the frameworks remained gotten thru air-dried aimed at 24 h.

## 2.5 Characterization

### 2.5.1 Attenuated Total Reflectance-Fourier Transform Infrared Spectroscopy (ATR-FTIR)

The substance construction of the arranged permeable framework remained considered by means of an attenuated total reflectance Fourier trans method (ATR-FTIR) spectrophotometer (Shimadzu IR affinity—1S). Both ranges stayed developed trendy diffusion style happening a Quest ATR ZnSe crystal lockup through buildup of 250 scans by a resolve of 4 $cm^{-1}$ and a wavenumber variety of 4000–500 $cm^{-1}$.

### 2.5.2 X-ray Diffraction (XRD)

X-ray diffraction designs of CS/PVA/MC3-$AgNo_3$ frameworks remained chronicled through an X-ray diffractometer (XRD; Rigaku Co, model; DMAX—2200, Japan). The energy and then current used were 40 kV and 36 mA, correspondingly. X-rays of 1.5406 Å wavelengths remained generated by a CuKα basis and the 2θ viewpoint stood diverse after 5° to 80°.

### 2.5.3 Scanning Electron Microscopy (FE-SEM)

The morphology of the frameworks remained examined consuming Field emission Scanning Electron Microscope (FE-SEM) examination remained approved available aimed at the disinfected JEOL-JSM6390 (Japan). The framework microstructures remained assessed after geometrical capacities happening the scanning electron micrographs.

### 2.5.4 Raman Spectroscopy (RS)

Raman ranges remained too chronicled aimed at covered Ti substrates by means of a confocal Raman microscope (RENISHAW) by an excitation wavelength of 795 nm.

### 2.5.5 Atomic Force Microscopy (AFM)

Atomic force microscopy (AFM, BRUKER MM8, SOUTH AFRICA) remained charity toward asses the superficial unevenness and landscape of the coverings in 2 $\times$ 2 μm areas. Root mean square (RMS) unevenness standards stood busy after 15 capacities achieved scheduled dissimilar places finished every taster. High resolution (618 $\times$ 618 pixel) image remained completed toward and the consequences remained investigated.

### 2.5.6 Transmission Electron Microscopy (TEM)

Transmission electron microscopy (TEM) capacities remained approved available on Phillips CM100 and JEOL 2010F electron microscope tools through working energies of 150 kV. The tasters remained ready through conveying a drip of the CS/PVA/MC3-$AgNo_3$ nanocomposite explanation onto a carbon-covered copper lattice.

### 2.5.7 Porosity

The permeability of invented frameworks remained intended by Eq. (1).

$$Porosity = \frac{Wt - Wd}{Wd} \text{ X } 100(\%) \tag{1}$$

Anywhere $W_t$ remained the heaviness of the enflamed framework on period t and $W_d$ remained early heaviness of the framework.

### 2.5.8 Swelling Degree

The bulge behavior of frameworks remained examined by area high temperature through revealing them near phosphate buffer solution (PBS). A recognized bulk of framework sensible remained located trendy PBS explanation aimed at 30 days. The wet heaviness of the framework remained gritty through major tarnishing the framework external through sieve tabloid, near eradicate additional external aquatic besides before considered directly. The fraction of water preoccupation thru framework remained intended after the appearance.

$$W_{sw} = W_w - W_d / W_d \times 100 \quad (2)$$

Where $W_w$ signify the wet weight of frameworks submerged trendy the PBS specific period break, $W_d$ is the thirsty showery of frameworks, and $W_{sw}$ is the gradation of bulge [22].

### 2.5.9 Mechanical Properties

The motorized belongings of flicks remained largely estimated through the ductile examination. This remained achieved consuming difficult device (MTS Criterion 5 KN) trendy agreement by normal approaches (ASTM D638-2010). The tasters remained censored hooked on floorings through 70 mm distance then 25 mm thickness per an exactness of ±5 μm. The comparative moistness and crosshead rapidity remained 50% and 50 mm/min, individually. Altogether varieties remained strained on ambient infection then final tensile strength besides stood intended trendy triplicate by means of elongation besides rapidly noted by means of a processor. Near gain the mechanical properties of the flick's trendy the drizzly national, the flicks remained saturated in marine aimed at 20 min on room temperature previously challenging. By smallest five samples remained leisurely intended for every taster.

### 2.5.10 Screening of Antibacterial Activity of the Synthesized Bionanocomposites

The antimicrobial exam remained approved ready by means of *Staphylococcus aureus* Gram-positive, *Bacillus cereus* Gram-positive, *and Escherichia coli* Gram-negative. The frameworks remained pasteurized through submerging trendy 70% (v/v) ethanol, formerly eroded through disinfected PBS explanation and midair desiccated beneath Laminar air movement (LAF) toward decrease bacterial infection. The extent of the region of hang-up events the efficiency of the mixtures: a extra real multiple crops a greater strong extent about the sieve floppy. Altogether examinations must remained complete underneath laminar movement cover. Lastly, altogether Petri plates limited bacteria and antibacterial substances remained hatched and preserved at 37 °C aimed at 24 h. Afterward this historical, the distances of the reserve regions molded about all floppy remained strong-minded and obtainable in mm.

## *2.6 Cell Experiment*

### 2.6.1 Cell Culture

The L929 fibroblast compartment streak remained rummage-sale trendy the examine. Booths remained hatched in Dulbecco's modified eagle medium (DMEM)

comprising 10% fetal bovine serum 1% penicillin and streptomycin. L929 fibroblast chambers stood before sowed by a thickness of $2\times10^4$ cells/ml against the dissimilar sorts of frameworks. Collagen stayed exploited in place of switch. The booth-framework concepts remained hatched trendy an incubator by 37 °C through 5% $CO_2$, besides the average stayed altered each 2 beings.

### 2.6.2 Cell Seeding

Near regulate cytocompatibility of the CS/PVA/MC3-$AgNo_3$ frameworks, spherical frames ($\phi$ =15 mm) stood gilded trendy a 24-fine values plate besides then occupied hip a DMEM standard holding 10% fetal bovine serum 1% penicillin and streptomycin. L929 fibroblast cells stood before planted by a thickness of $2\times10^4$ cells/ml against the dissimilar brands of platforms. Collagen stayed exploited by way of regulator. The booth-framework concepts remained hatched now an incubator at 37 °C through 5% $CO_2$. The intermediate remained altered each 2 days.

### 2.6.3 Cell Proliferation

Sustainability of booths happening supports stood assessed. The antiseptic supports stood located addicted to 96 glowing crystal platters. $1\times10^4$ lockups/glowing of fibroblast lockups stayed planted happening the ready framework and formerly hatched by the side of 37 °C through 5% $CO_2$. Subsequently 1, 3, and 5 days, the capability of booths be situated strong-minded through consuming fluorescence microscope.

### 2.6.4 Cell Viability Assay

Compartment feasibility stood examined via 3-(4,5-dimethylthiazol-2-yl)-2,5-diphenyltetrazolium bromide MTT assay. The salty filtered merged framework consumes presentation corresponding to collagen frameworks by deference near the compartment relocation and propagation amount happening the framework. The passaged compartments stayed sowed happening the collagen and CPM merged supports next to a thickness of $1 \times 10^5$ compartments/thriving. The structures remained nurtured by the side of 37 °C through 5% $CO_2$ aimed at 3 h. Dulbecco's Modified Eagle Medium (Sigma Aldrich) covering 10% fetal bovine serum (Invitrogen), penicillin (50unit/ml), and streptomycin (50 unit/ml) remained supplementary besides hatched by the side of 37 °C through 5% $CO_2$. This average stayed exploited near produce L929 fibroblast cubicles remained measured by MTT assay. The intermediate was altered each 2 days besides the frameworks remained experiential below a microscope. Collagen framework remained occupied by means of switch. Subsequently 1, 3, and 5 days of philosophy, booth feasibility remained leisurely quantitatively MTT assay, which remains a colorimetric method aimed

at defining the quantity of feasible cubicles, that trusts taking place the adaptation of MTT-to-MTT formazan via the enzyme mitochondrial reductase of the feasible compartments. The cubicle excerpts after the framework remained varied through MTT explanation besides the absorbance by 550 nm stood unhurried happening a microplate reader.

### 2.6.5 Cell Morphology

The morphology of fibroblast lockups arranged the frameworks stood experiential happening days 1, 3, and 5 by SEM. The tasters remained sweep away through PBS besides then secure through 3.0% glutaraldehyde at 4 °C aimed at 4 h. Subsequently, they remained dry finished a sequence of categorized ethanol, inflight-dehydrated instant, and sputtered through gold-plated for SEM statement.

### 2.6.6 In Vivo Wound Healing Analysis

In vivo bodily education remained approved available by means of sturdy manly albino rats (150−200 g, 8.5 months) stood detached addicted to three clusters through three rats all. Happening the jump of the challenging rats remained contained in a infection unhurried site apartment through allowed admittance towards blow aquatic besides normal nourishment. Altogether procedures of this schoolwork counting faunas stayed accepted thru the Institutional Animal Ethical Committee, KMCH College of Pharmacy, Coimbatore, Tamilnadu, India. The dorsal mane of the rats remained detached, and the covering stayed gutted by means of malt. The rats remained under through a ether and 2 cm × 2 cm exposed editing-kind coiled was shaped near the complexity of movable hypodermal flesh. The injuries remained enclosed via Povidone-iodine ointment (control), CS/PVA/MC3-AgNps bionanocomposites. Subsequently spread over the bionanocomposites, the rats remained contained independently in crates below standard chamber disease. The bionanocomposites stayed different next to 3 and 5th days. By the diurnal of varying the bionanocomposites the coiled zone stayed unrushed on 0, 1, 3, and 5 days.

The degree of looped finish remained resolute through the subsequent comparison:

$$\text{Wound area} = A_0 - A/A_0 \times 100\,(5) \tag{3}$$

Where $A_0$ remains the looped zone on the period of twisted designed and A stands the twisted part on the time of varying the bionanocomposites.

### 2.7 Statistical Analysis

Altogether statistics stood obtainable by way of resources ± typical aberrations. Judgments between the three clusters remained complete through unique-technique examination of alteration.

## 3 Results and Discussion

### 3.1 Attenuated Total Reflectance-Fourier Transform Infrared Spectroscopy (ATR-FTIR)

The typical functional groups remained examined over ATR-FTIR ranges of the pure CS, CS/PVA, CS/PVA/MC3, CS/PVA/MC3-AgNps1, CS/PVA/MC3-AgNps2, and CS/PVA/MC3-AgNps3 frameworks Fig. 1. The range of pure CS displays the preoccupation peaks on everywhere 3406 $cm^{-1}$ aimed at the OH group next to everywhere 1639 $cm^{-1}$ NHCOCH3 (amide I band) then by near 1585 $cm^{-1}$ designed for the NH2 group (amide II band). The spectrum of CS/PVA exhibited a extensive group at 3449 $cm^{-1}$. The fascination gang's pragmatic by the side of 1642 $cm^{-1}$ stood lifted near developed wave number outstanding to the contact among OH and NH twisting shaking of CS/PVA. The band of CS/PVA/MC3 displays the

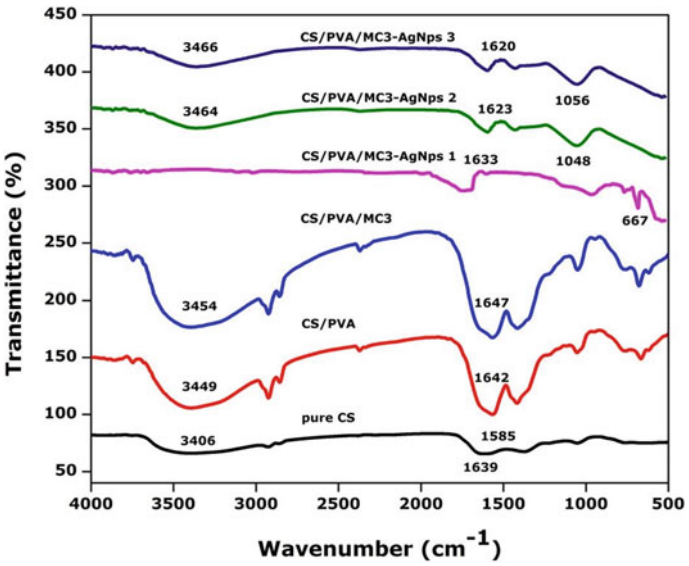


**Fig. 1** ATR-FTIR spectra of pure CS, CS/PVA, CS/PVA/MC3, CS/PVA/MC3-AgNps1, CS/PVA/MC3-AgNps2 and CS/PVA/MC3-AgNps3 porous scaffolds

fascination crests at everywhere 3454 $cm^{-1}$ OH collections next to from place-to-place 1647 $cm^{-1}$ amide I band. Associated to the bands of pure CS, CS/PVA, and CS/PVA/MC3 supports the groups next to wavenumber at 3466 $cm^{-1}$ and 1625 $cm^{-1}$ in the CS/PVA/MC3-AgNps1, CS/PVA/MC3-AgNps2, and CS/PVA/MC3-AgNps3 frameworks stand lifted near lesser wavenumber standards. As soon as AgNps stayed merged obsessed by the frames, the crests stood distended in its place of a piercing top in AgNps. The rise in strength of fascination summits remained experiential when AgNps stood charity, which showed the development of sure relations among AgNps and CS/PVA/MC3 frameworks.

## *3.2 X-ray Diffraction (XRD)*

X-ray diffraction designs of the frameworks remain characterized in Fig. 2. The X-ray diffraction of CS/PVA/MC3 frameworks displays same thin dump everywhere $2\theta = 10°$. In the case of a CS/PVA/MC3-AgNps1, CS/PVA/MC3-AgNps2, and CS/PVA/MC3-AgNps3 nanocomposites the XRD design displays the peaks that resemble to the $2\theta = 26°$, $2\theta = 28°$, and $2\theta = 31°$ planes of hexagonal AgNps and the strength of crests remain realized marginally cumulative by way of the totaling of AgNps besides the strength of crests remain realized a little swelling by means of the totaling of AgNps nanoparticles trendy the intermingling of CS/PVA/MC3. The

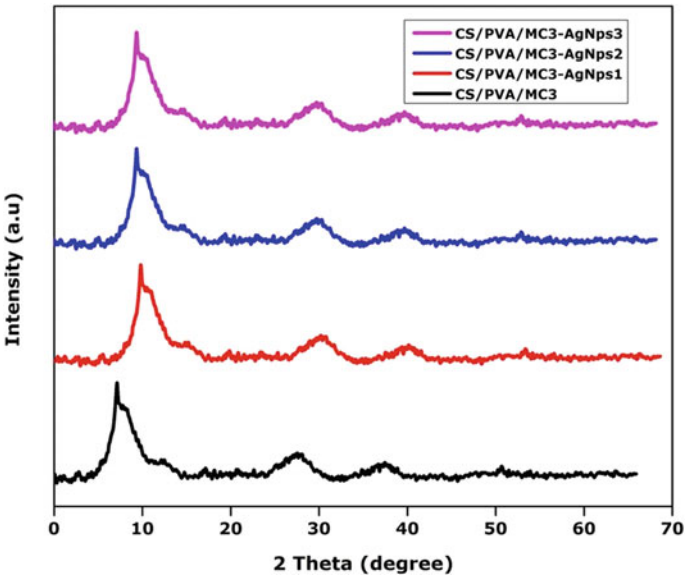


**Fig. 2** XRD of pure CS, CS/PVA, CS/PVA/MC3, CS/PVA/MC3-AgNps1, CS/PVA/MC3-AgNps2 and CS/PVA/MC3-AgNps3 porous scaffolds

original shrill summits trendy the deflection design can stand payable to the creation of fresh covalent pledges molded among CS/PVA/MC3-AgNps3 nanoparticles too CS/PVA/MC3.

## 3.3 *Field Emission-Scanning Electron Microscopy (FE-SEM)*

The field emission-perusing electron microscopy imageries obtainable actual alike morphological features aimed at the CS/PVA/MC3, CS/PVA/MC3-AgNps1, CS/PVA/MC3-AgNps2, and CS/PVA/MC3-AgNps3 nanocomposites viewing the development of unvarying then nonstop frameworks as shown in Fig. 3. CS/PVA/MC3 the merged frameworks showed require actual minor holes remained display. CS/PVA/MC3-AgNps1 followed happening the internal superficial of the interconnected pore construction of CS/PVA/MC3 scaffolds. The CS/PVA/MC3-AgNps2 nanoparticles remained fine remote some pores was exhibited. The CS/PVA/MC3-AgNps3 nanoparticles remained healthy remote inside the mixture framework subsequent in the entrance of pores. The size and shape of CS/PVA/MC3-AgNps3 nanoparticles was more pores and were regular cubic. The rise trendy

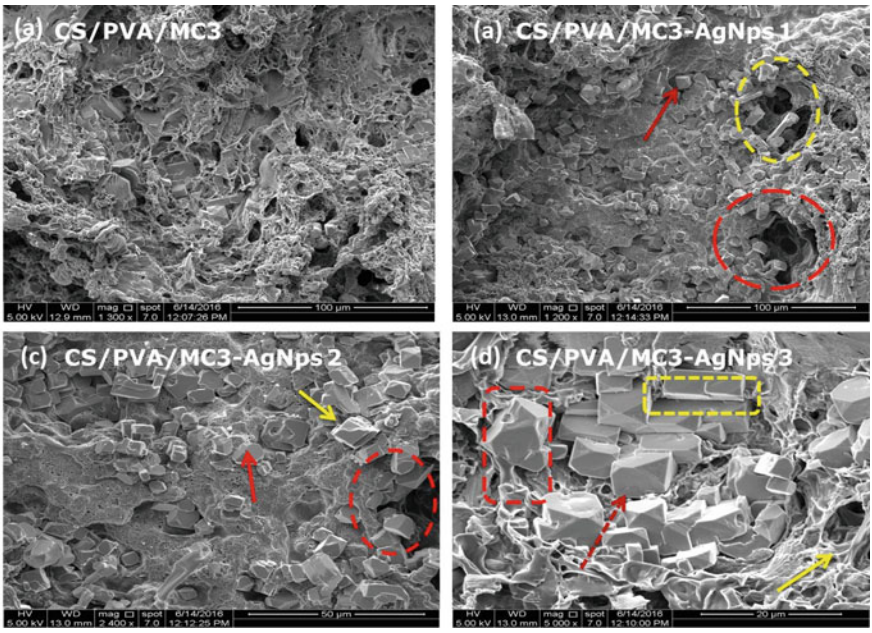


**Fig. 3** FE-SEM images of CS/PVA/MC3, CS/PVA/MC3-AgNps1, CS/PVA/MC3-AgNps2, and CS/PVA/MC3-AgNps3 porous scaffolds

the absorbency composed through the discount in the interatomic pores structure. Furthermore, a porous surface with pore size distribution which container simplify infiltration of cellular harvests besides helpful compartment evolution.

## *3.4 Transmission Electron Microscopy (TEM)*

The transmission electron microscopy (TEM) images of the CS/PVA/MC3-AgNps1, CS/PVA/MC3-AgNps2, and CS/PVA/MC3-AgNps3 frameworks stand presented in Fig. 4. The transmission of CS/PVA/MC3-AgNps1 has a less cubic shape exhibit and SAED images due to also less crystallinity nature appeared. CS/PVA/MC3-AgNps2 has a depicts cubic with uniform shape and good crystallinity. The CS/PVA/MC3-AgNps3 micrographs more cubic shape and more good crystallinity images was

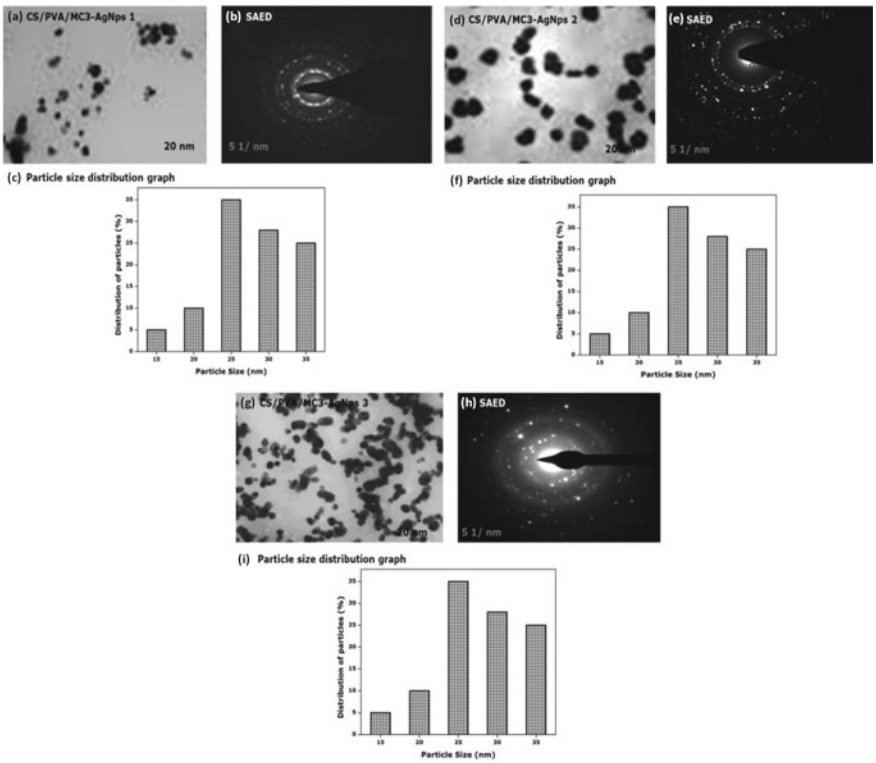


**Fig. 4** **a** TEM image of CS/PVA/MC3-AgNps1 **b** SAED pattern of nanocomposite and **c** Particle size distribution graph **d** TEM images of CS/PVA/MC3-AgNps2 **e** SAED pattern of nanocomposites and **f** Particle size distribution graph and **g** TEM images of CS/PVA/MC3-AgNps3 **h** SAED pattern of nanocomposites and **i** Particle size distribution graph

exhibited, and the average cube size was exhibited. It was shown that CS/PVA/MC3-AgNps frameworks near accept a well-ordered conformation finished trendy the AgNps nanocrystal growing near the experiential the cubic morphology. The subdivision extent delivery of the AgNps nanoparticles in the CS/PVA/MC3-AgNps framework remains signified through the histogram, presentation a wide-ranging of nano particles in the 25 nm variety.

## *3.5 Atomic Force Microscopy (AFM)*

The CS/PVA/MC3 polymeric scaffold dopped with AgNps nanoparticles exteriors showed a lesser besides fewer rough nanostructured in comparison through CS/PVA/MC3-AgNps. AFM descriptions of nanocomposite frameworks remained examined towards measure the exterior landscape structures of CS/PVA/MC3, CS/PVA/MC3-AgNps1, CS/PVA/MC3-AgNps2 and CS/PVA/MC3-AgNps3 nanocomposites frameworks as shown in Fig. 5. The AFM construction examination revealed that the shallow of CS/PVA/MC3 remained homogeneous without nano structure of AgNps. The width of the CS/PVA/MC3-AgNps1 platform

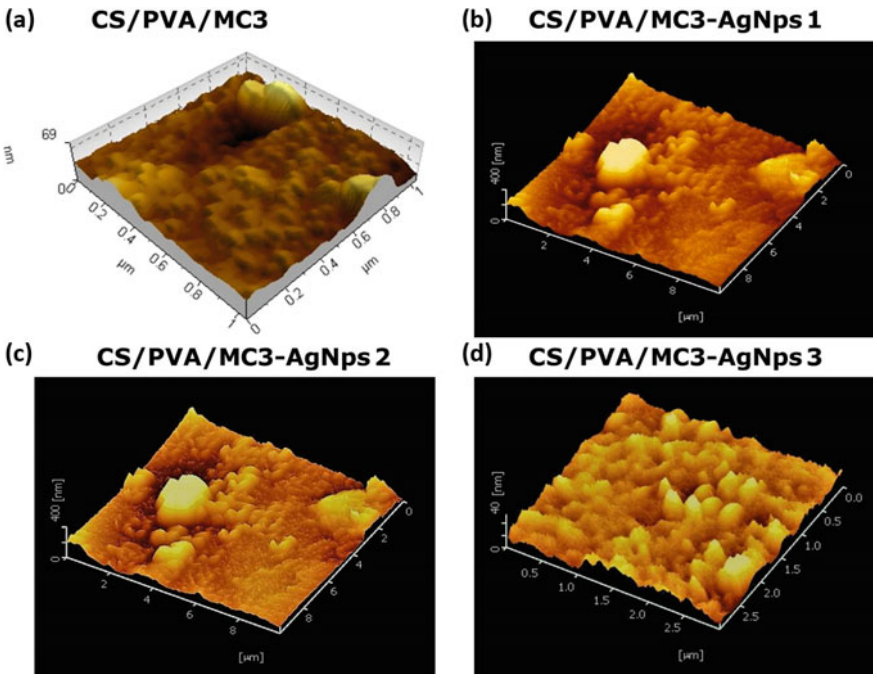


**Fig. 5** AFM images of CS/PVA/MC3, CS/PVA/MC3-AgNps1, CS/PVA/MC3-AgNps2 and CS/PVA/MC3-AgNps3 porous scaffolds

remained projected after the AFM image, remained near 10–20 nm besides a unevenness similar construction stayed experiential. On the other hand, the CS/PVA/MC3-AgNps2 scaffold exhibited the thickly dispersed minor adverts and the width was observed. The CS/PVA/MC3-AgNps3 polymeric scaffold was more bunches exhibited. The superficial descriptions depiction extent lots through calmly dispersed nanosized grains. These descriptions demonstrate the dopped stand molded thru nanometer sized regularly spread during the exteriors. Obviously, the compartments meeting a uneven superficial through the CS/PVA/MC3 frameworks, as soon as likened near the CS/PVA/MC3-AgNps nanocomposites. Certain times need exposed an improvement trendy cell union through enlarged superficial unevenness.

## *3.6 Raman Spectroscopy (RS)*

Raman spectra analysis were also used near safeguard the reproducibility of Raman shift spectrum stayed collect after diverse spot of every model. Aimed at the bionanocomposites of AgNps strengthened happening CS/PVA/MC3 framework aimed at a assumed example the strength of Raman summits tin differ after unique advert towards extra owing towards difference trendy AgNps insides the result remained reproducible. The Raman spectrum of CS/PVA/MC3 support displayed on 349 $cm^{-1}$ extending shakings allocated intended for C-N extending of a main amine stood reduced as the AgNps satisfied enlarged besides vanished trendy AgNps. Compared toward the ranges of CS/PVA/MC3-AgNps1, CS/PVA/MC3-AgNps2 and CS/PVA/MC3-AgNps3 frameworks the strength groups by 316 $cm^{-1}$, 318 $cm^{-1}$ and 328 $cm^{-1}$ trendy the frameworks remain lifted near developed concentration morals. When AgNps stayed incorporated interested in the supports, the projecting crests stayed enflamed instead of a sharp peak in AgNps. The strength of Raman topmost next to 484 $cm^{-1}$ dispensed near C–OH stayed meaningfully improved per growing AgNps nanocomposites insides trendy the scaffolds besides converted the bulging crowning popular CS/PVA/MC3-AgNps3 as shown in Fig. 6. This result proves the cumulative the dipolar connections connecting through swelling CS/PVA/MC3-AgNps nanocomposites content.

## *3.7 Mechanical Properties*

To investigate the influence of pure CS, CS/PVA, CS/PVA/MC3, CS/PVA/MC3-AgNps1, CS/PVA/MC3-AgNps2, and CS/PVA/MC3-AgNps3 on the mechanical properties of the scaffolds their tensile strength and elongation at break are displayed in Fig. 7. From the tensile strength for pure CS was 40%, CS/PVA 50%, CS/PVA/MC3 73%, CS/PVA/MC3-AgNps1 38%, CS/PVA/MC3-AgNps2 60%, and CS/PVA/MC3-AgNps3 70% displayed advanced morals of tensile strength sizes. Elongation at break of pure CS was 29%, CS/PVA 19%, CS/PVA/MC3 15%,

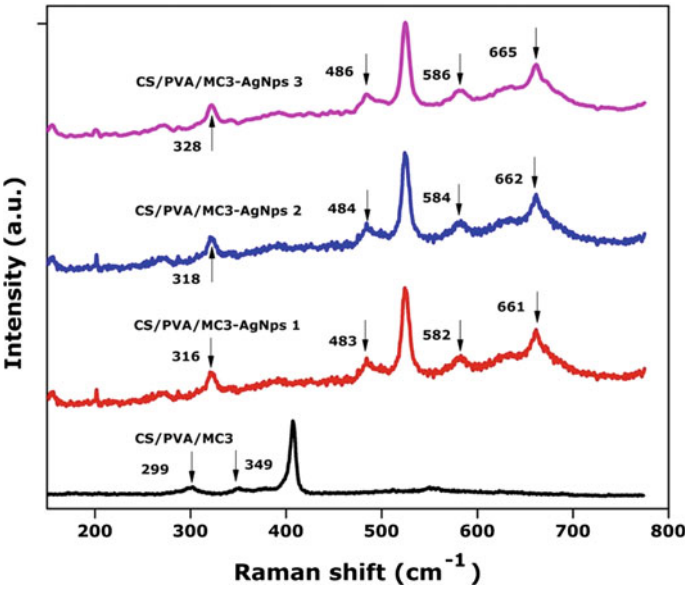


**Fig. 6** Raman spectra of CS/PVA/MC3, CS/PVA/MC3-AgNps1, CS/PVA/MC3-AgNps2 and CS/PVA/MC3-AgNps3 porous scaffolds

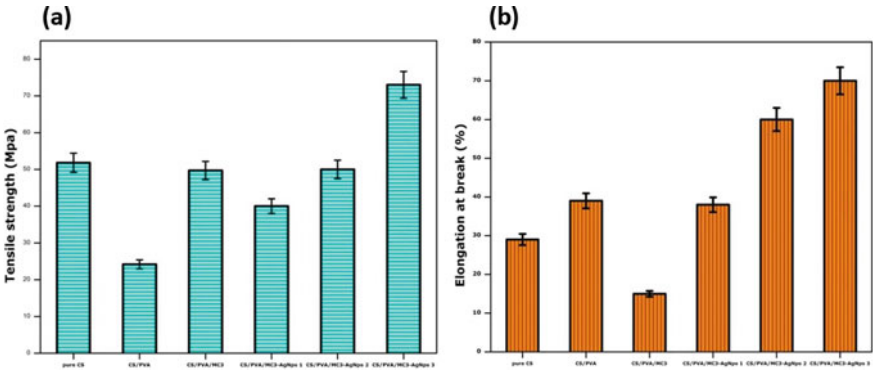


**Fig. 7** Mechanical properties of pure CS, CS/PVA, CS/PVA/MC3, CS/PVA/MC3-AgNps1, CS/PVA/MC3-AgNps2 and CS/PVA/MC3-AgNps3 porous scaffolds

CS/PVA/MC3-AgNps1 31%, CS/PVA/MC3-AgNps2 55%, and CS/PVA/MC3-AgNps3 60% exhibited lesser standards. The mechanical performance of the CS/PVA/MC3-AgNps3 supports nearby stood a reduction trendy the elongation at break although the tensile strength augmented, perhaps owing to the enlarged trendy the interatomic detachment, although the elongation at break lessened aimed at the CS/PVA/MC3-AgNps3 frameworks. There mechanical properties are due to the CS/PVA/MC3 scaffolds results in strong interactions due to AgNps. The tensile test

outcomes designated that the CS/PVA/MC3-AgNps3 frameworks converted extra elastic through added gift besides painfulness later the creation of AgNps nanocomposites. The variations trendy tensile belongings recommend that amalgamation of AgNps nanoparticles keen on CS/PVA/MC3 scaffolds consumes persuaded physical deviations trendy the polymer matrix.

## *3.8 Swelling Studies*

The bulge of the polymeric frameworks trendy (PBS) Phosphate buffer solution remains obtainable in Fig. 8. By way of each the bulge grade of pure CS, CS/PVA/MC3-AgNps1, CS/PVA/MC3-AgNps2 and CS/PVA/MC3-AgNps3 frameworks. The bulge grade of the pure CS, CS/PVA/MC3, and CS/PVA/MC3-AgNps scaffolds to increase with addition of AgNps nanoparticles. Bulge training presented that polymer flick tasters displayed least bulge aimed at uncontaminated CS, CS/PV/MC3. The swelling of scaffolds increased with the addition of AgNps nanoparticles when the CS/PVA/MC3-AgNps3 was increased in the blend due to high hydrophilicity of AgNps nanoparticles. CS/PVA/MC3-AgNps3 in the blend scaffold acting an significant part as the situation tin can recover together of the mechanical properties besides swelling capacity of supports. It can remain experiential that CS/PVA/MC3-AgNps3 frameworks outcome trendy advanced percentages of poverty then swelling degree. By the totaling of AgNps nanoparticles near the

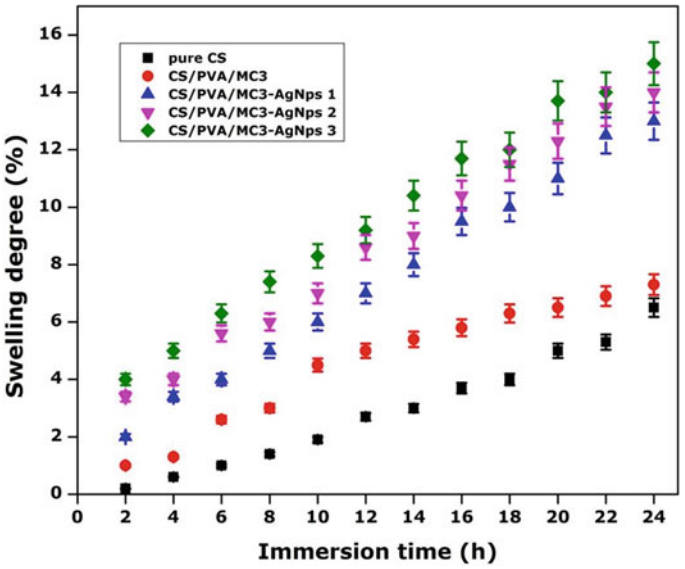


**Fig. 8** The swelling behavior of pure CS, CS/PVA/MC3, CS/PVA/MC3-AgNps1, CS/PVA/MC3-AgNps2 and CS/PVA/MC3-AgNps3 porous scaffolds

flicks and rise trendy the poverty then bump remained established. At the same time, the swelling degree remained powerfully partial through the general hydrophilicity of the subsequent scaffolds. Through attractive the addition of AgNps nanoparticles the frameworks networks converted additional hydrophilic then therefore fascinated extra PBS subsequent fashionable and development of bulge degree.

## *3.9 Porosity*

The porosity is a vital role for the tissue engineering scaffolds. The porosity (%) of pure CS, CS/PVA, CS/PVA/MC3, CS/PVA/MC3-AgNps1, CS/PVA/MC3-AgNps2, and CS/PVA/MC3-AgNps3 samples displayed trendy Fig. 9. The porosity of pure CS scaffolds remained around 24% and 32% popular thirsty then drizzly conditions correspondingly, though significantly the porosity (%) increased for CS/PVA scaffolds of about 28%, and 42% CS/PVA/MC3 scaffolds of about 36% and 57% and CS/PVA/MC3-AgNps1, CS/PVA/MC3-AgNps2, and CS/PVA/MC3-AgNps3 nanocomposites scaffolds due to in the wet state, however in dry state these scaffolds have 58%, 69% and 65%, 75% and 72%, 90% in wet state which is marginally increased in wet state specifying that the doped of AgNps nanoparticles of CS/PVA/MC3 scaffolds increased the porosity of the scaffolds. Nevertheless, the superficial morphology of CS/PVA/MC3-AgNps3 stood actual dissimilar after individuals of pure CS, CS/PVA, CS/PVA/MC3, CS/PVA/MC3-AgNps1, and CS/PVA/MC3-AgNps2 scaffolds the permeability displayed more alteration aimed

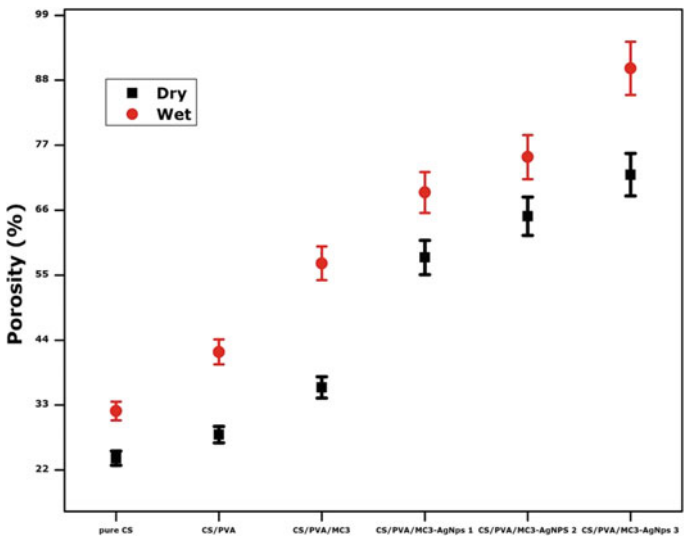


**Fig. 9** The Porosity of pure CS, CS/PVA, CS/PVA/MC3, CS/PVA/MC3-AgNps1, CS/PVA/MC3-AgNps2, and CS/PVA/MC3-AgNps3 absorbent supports

at the AgNps nanoparticles further scaffolds. Commonly, the appropriate opening great permeability remain the features on behalf of the ultimate permeable scaffold charity popular flesh manufacturing.

## *3.10 Antibacterial Activity*

The antiseptic movement of the ready CS/PVA/MC3-AgNps1, CS/PVA/MC3-AgNps2, and CS/PVA/MC3-AgNps3 nanocomposites tasters stood tried alongside Staphylococcus aureus (S.aureus) and Escherichia coli (E. coli) owing near disk diffusion method Fig. 10. Antibiotic amoxicillin stayed reserved by way of the regulator aimed at difficult the antiseptic movement of numerous scaffolds of CS/PVA/MC3-AgNps1, CS/PVA/MC3-AgNps2, and CS/PVA/MC3-AgNps3 nanocomposites. Both CS/PVA/MC3-AgNps1, CS/PVA/MC3-AgNps2, and CS/PVA/MC3-AgNps3 trials showed strong antibacterial activity. The inhibitory region of CS/PVA/MC3-AgNps3 nanocomposites experiential must sturdy antiseptic movement in contradiction of S. aureus and E. coli than CS/PVA/MC3-AgNps1 and CS/PVA/MC3-AgNps2. The antiseptic doings need stayed improved through swelling the gratified of AgNps nanoparticles. Antibacterial of AgNps nanoparticles usually believed that AgNps nanoparticles interrelate through booth crust allowed near harvest the enlarged attention of reactive oxygen species (ROS). In our outcomes exposed around stayed durable antibacterial activity of CS/PVA/MC3-AgNps nanocomposites. The microbes of the S. aureus and E. coli continued feasible

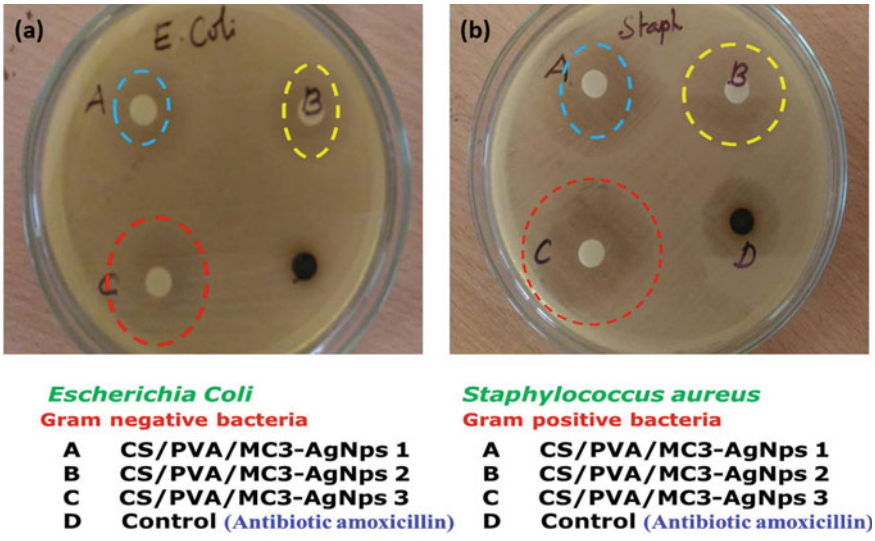


**Fig. 10** Antibacterial activity of **a** CS/PVA/MC3-AgNps1, **b** CS/PVA/MC3-AgNps2, and **c** CS/PVA/MC3-AgNps3 porous scaffolds

in the scaffolds deprived of the doped the combination of AgNps nanoparticles slightly inhibition zone was formed. Once accumulation the AgNps nanoparticles together microbes remained actual decent inhibition zone stood gotten. The results display that CS/PVA/MC3-AgNps nanocomposites frameworks shows non-poisonousness aimed at mutual besides together Gram-positive and Gram-negative bacteria.

## *3.11 In Vitro Cytocompatibility Studies*

The biocompatibility, cytotoxicity of the ready CS/PVA/MC3 by way of nanocomposite support aimed at flesh manufacturing remained measured finished cell culture besides MTT assay Fig. 11. displays the feasibility of L929 cells later an gestation retro of 1, 3 and 5 days. The outstanding cell feasibility of the compound scaffold remained credited to the decent biocompatibility of the CS/PVA/MC3-AgNps3 by way of fine as lime construction procedure of the frameworks. The quantity of cells performs the wonder of slow surge through philosophy period, signifying the scaffolds tin provision the growing then propagation of the booths. On the commencement, altogether booths be by way of solitary cubicles then discrete calmly during the medium. The ready CS/PVA/MC3-AgNps nanocomposites framework consumes presentation corresponding near collagen scaffold through deference towards the cell immigration besides propagation amount happening

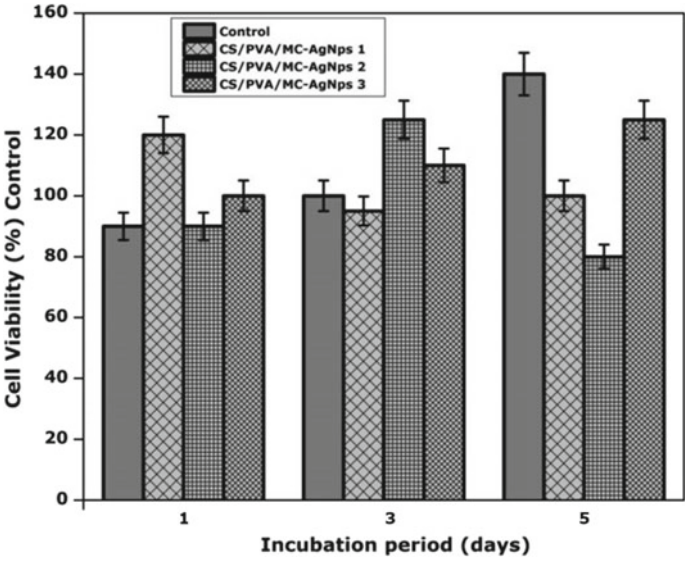


**Fig. 11** MTT results of L929 fibroblast cultured on collagen as a control, CS/PVA/MC3-AgNps1, CS/PVA/MC3-AgNps2, and CS/PVA/MC3-AgNps3 porous scaffolds after 1, 3, and 5 days

the framework. CS/PVA/MC3-AgNps3 takes advanced feasibility associated to CS/PVA/MC3-AgNps1 and CS/PVA/MC3-AgNps2 frameworks.

## 3.12 Fluorescence Image

The fluorescence descriptions of L929 on CS/PVA/MC3-AgNps1, CS/PVA/MC3-AgNps2 then CS/PVA/MC3-AgNps3 frameworks subsequently 1, 3, and 5 days of philosophy by way of exposed in Fig. 12. Since the descriptions we can get that L929 might assign then cultivate fine happening the frameworks, live cells (stained green) arranged entirely frameworks displayed cube similar morphology remained perceived, representative that the totaling of AgNps displays probable biocompatibility. This one stand understandable that nearby stand further aware cells arranged CS/PVA/MC3-AgNps3 support than CS/PVA/MC3-AgNps1 and CS/PVA/MC3-AgNps2.

## 3.13 In Vivo Wound Healing Analysis

In vivo study remained done by mature Albino rats toward training the twisted remedial competence of ready unequal chitosan founded bionanocomposite. Photographic

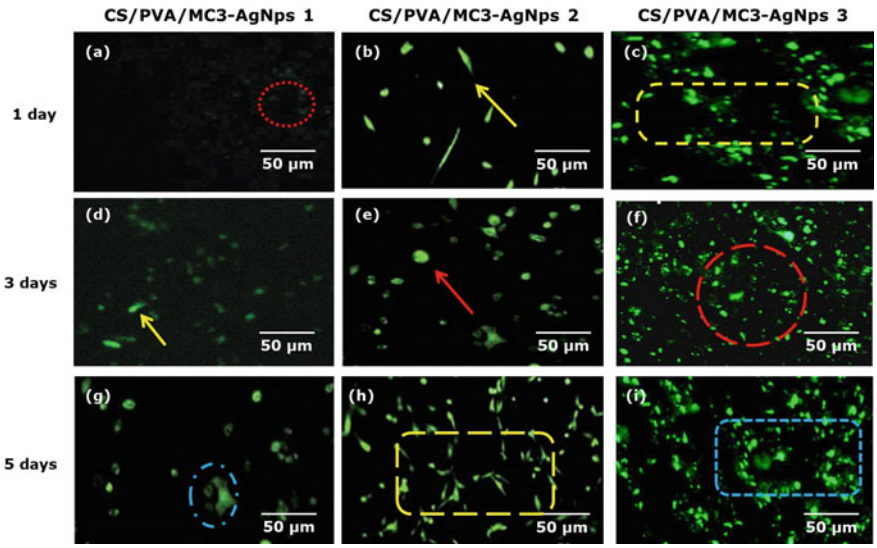


**Fig. 12** Fluorescence images of CS/PVA/MC3-AgNps1, CS/PVA/MC3-AgNps2, and CS/PVA/MC3-AgNps3 porous scaffolds after 1, 3, and 5 days

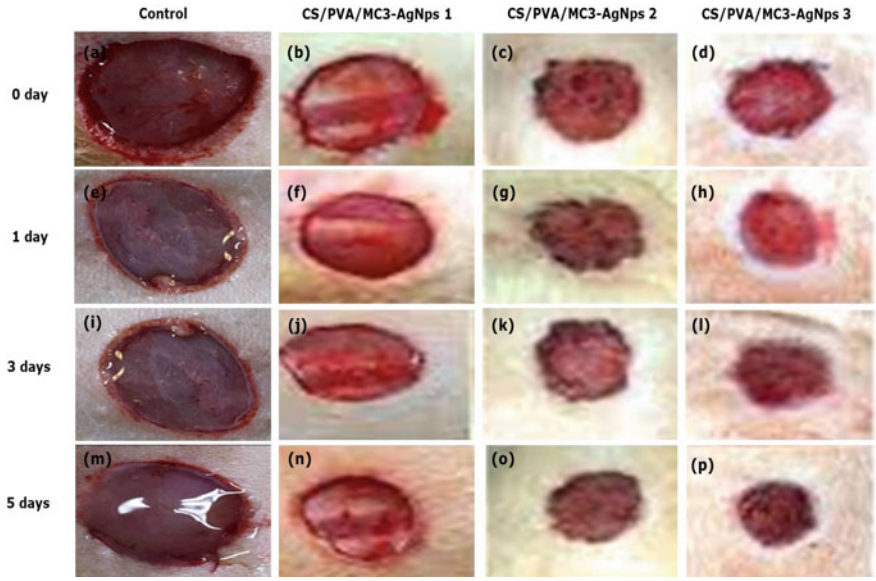


**Fig. 13** Photographic representation of wounds treated with control, CS/PVA/MC3-AgNps1, CS/PVA/MC3-AgNps2, and CS/PVA/MC3-AgNps3 porous scaffolds after 1, 3 and 5 days

depiction of working of povidone-iodine as a control, CS/PVA/MC3, CS/PVA/MC3-AgNps1, CS/PVA/MC3-AgNps2, and CS/PVA/MC3-AgNps3 bionanocomposite remained revealed in Fig. 13. Arranged the diurnal of hurtful near stands not at all alteration trendy the entrance of helical aimed at entirely three clusters. Arranged day 1, the spiral part of entirely clusters stayed nearly similar besides degree of remedial was 10% of regulator and CS/PVA/MC3-AgNps1 groups whereas 18%. The spiral zone stayed suggestively condensed on behalf of CS/PVA/MC3-AgNps1 once likened to regulator and CS/PVA/MC3 bionanocomposite arranged the 3 day and remedial frequency stayed advanced aimed at the twisted preserved through CS/PVA/Mc3-AgNps2 bionanocomposite. The twisted stayed entirely preserved arranged 5 days by the CS/PVA/MC3-AgNps3 bionanocomposite than the regulator and CS/PVA/MC3 bionanocomposite.

As shown in Fig. 14 the degree of remedial stood extra improved near 87% on behalf of CS/PVA/MC3-AgNps bionanocomposite. The occurrence of silver nanoparticles augments the curative speed then that one strength remains owing in the direction of the relocation besides propagation of keratinocytes then fibroblasts arranged the looped place. The silver nanoparticles trendy the looped bandage substantial improved the development of novel casing flesh besides constrains the infectious explosion then hereafter the situation hurries coiled remedial movement.

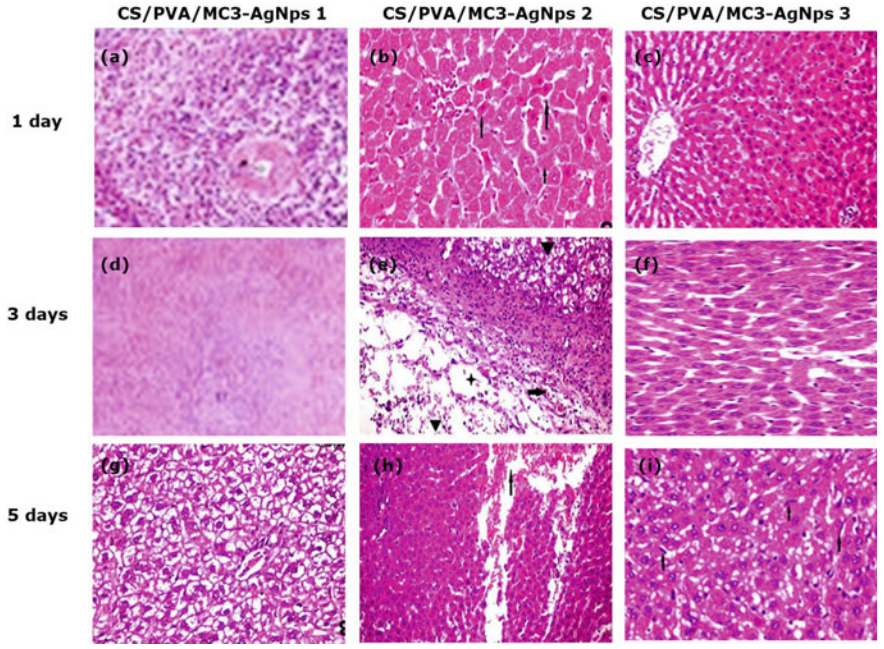


**Fig. 14** Optical images of cell viability of CS/PVA/MC3-AgNps1, CS/PVA/MC3-AgNps2 and CS/PVA/MC3-AgNps3 porous scaffolds after 1, 3 and 5 days

## 4 Conclusion

Trendy this exertion, an original CS/PVA/MC3-AgNps1, CS/PVA/MC3-AgNps2, and CS/PVA/MC3-AgNps3 nanocomposites frameworks through unified holes remained invented by means of salt leaching technique. The features of pure CS, CS/PVA, CS/PVA/MC3, CS/PVA/MC3-AgNps1, CS/PVA/MC3-AgNps2, and CS/PVA/MC3-AgNps3 nanocomposites frameworks remained endangered near thorough examination by ATR-FTIR, XRD, and FE-SEM. The FE-SEM research presented that the morphology of the supports can remain tailor-made thru the AgNps nanoparticles gratified. Fashionable judgment near the pure CS frameworks showed a plane besides similar shallow representative that not at all holes. Consequences after XRD exposed those amorphous areas of the frameworks remained rest on arranged the gratified of the AgNps nanoparticles.

By the rise of the AgNps nanoparticles percentage the crystallinity of the trials reduced dramatically. ATR-FTIR ranges more established the attendance of the connections, such equally hydrogen promises among the polymers and AgNps nanoparticles. The bulge dimensions of the cross frameworks remained projecting through the totaling of CS/PVA/MC3 trendy the system. The powered constancy of the frameworks remained improved the ductile trial consequences designated that the CS/PVA/MC3-AgNps frameworks converted extra supple through

extra power besides difficulty subsequently the creation of AgNps nanocomposites. The sterile movement designated that the permeable framework demonstration that CS/PVA/MC3-AgNps nanocomposites frames displays non poisonousness aimed at mutual also together Gram-positive and Gram-negative bacteria Staphylococcus aureus (*S. aureus*) and Escherichia coli (*E. Coli*). The MTT assay trials besides SEM pictures established the aptitude of the supports, by unified holes, near provision besides produce fibroblast L929 cells. In vivo helical remedial training of CS/PVA/MC-AgNps by way of a provisional organic twisted remedial substantial arranged the investigational effort of albino rats consumes exposed that the new injuries whole earlier than the regulator injuries. The uncultured comments need exposed that the whole final of injuries remained experiential through 5 days aimed at the faunae preserved by stearic acid covered porous scaffolds CS/PVA/MC3-AgNps3. Furthermore, these CS/PVA/MC3-AgNps nanocomposites frameworks can care cell adhesion. Associated to CS/PVA/MC3-AgNps3 nanocomposites frameworks the cell adhesion recovers decidedly after extra two nanocomposites of CS/PVA/MC3-AgNps1 besides CS/PVA/MC3-AgNps2. These nanocomposites frameworks suggestion a original possible aimed at biomedical claims particularly trendy cell adhesion also casing flesh manufacturing.

## References

1. Mani M, Harikrishnan R, Purushothaman P, Pavithra S, Rajkumar P, Kumaresan S, Al Farraj DA, Elshikh MS, Balasubramanian B, Kaviyarasu K (2021) Systematic green synthesis of silver oxide nanoparticles for antimicrobial activity. Environ Res 202:111627
2. Mani M, Pavithra S, Mohanraj K, Kumaresan S, Alotaibi SS, Eraqi ME, Gandhi AD, Babujanarthanam R, Maaza M, Kaviyarasu K (2021) Studies on the spectrometric analysis of metallic silver nanoparticles (Ag NPs) using Basella alba leaf for the antibacterial activities. Environ Res 199:111274
3. Mani M, Okla MK, Selvaraj S, Ram Kumar A, Kumaresan S, Muthukumaran A, Kaviyarasu K, El-Tayeb MA, Elbadawi YB, Almaary KS, Almunqedhi BMA, Elshikh MS (2021) A novel biogenic Allium cepa leaf mediated silver nanoparticles for antimicrobial, antioxidant, and anticancer effects on MCF-7 cell line. Environ Res 198:111199
4. Kanimozhi K, Basha SK, Kumari VS, Kaviyarasu K (2018) Development of biomimetic hybrid porous scaffold of chitosan/polyvinyl alcohol/carboxymethyl cellulose by freeze-dried and salt leached technique. J Nanosci Nanotechnol 18:4916–4922
5. Kanimozhi K, Basha SK, Kumari VS, Kaviyarasu K, Maaza M (2018) In vitro cytocompatibility of chitosan/PVA/methylcellulose–Nanocellulose nanocomposites scaffolds using L929 fibroblast cells. Appl Surf Sci 449:574–583
6. Kanimozhi K, KhaleelBasha S, SuganthaKumari V, Kaviyarasu K (2019) Development and characterization of sodium alginate/poly (vinyl alcohol) blend scaffold with ciprofloxacin loaded in controlled drug delivery system. J Nanosci Nanotechnol 19:2493–2500
7. Kanimozhi K, Basha SK, Kaviyarasu K, SuganthaKumari V (2019) Salt leaching synthesis, characterization and in vitro cytocompatibility of chitosan/poly (vinyl alcohol)/methylcellulose–ZnO nanocomposites scaffolds using L929 fibroblast cells. J Nanosci Nanotechnol 19:4447–4457
8. Nalini T, Basha SK, Sadiq AMM, Kumari VS, Kaviyarasu K (2019) Development and characterization of alginate/chitosan nanoparticulate system for hydrophobic drug encapsulation. J Drug Delivery Sci Technol 52:65–72

9. Siddhardha B, Pandey U, Kaviyarasu K, Pala R, Syed A, Bahkali AH, Elgorban AH (2020) Chrysin-loaded chitosan nanoparticles potentiates antibiofilm activity against Staphylococcus aureus. Pathogens 9(2):115
10. Kayalvizhi K, Alhaji NMI, Saravanakkumar D, Beer Mohamed S, Kaviyarasu K, Ayeshamariam A, Al-Mohaimeed AM, AbdelGawwad MR, Elshikh MS (2022) Adsorption of copper and nickel by using sawdust chitosan nanocomposite beads–a kinetic and thermodynamic study. Environ Res 203:111814
11. Afzali M, Mostafavi A, Shamspur T (2016) Electrospun composite nanofibers of poly vinyl pyrrolidone and zinc oxide nanoparticles modified carbon paste electrode for electrochemical detection of curcumin. Mater Sci Eng C 68:789–797
12. Badineni V, Maseed H, Arla SK, Yerramala S, Naidu BVK, Kaviyarasu K (2021) Effect of PVA/PVP protective agent on the formation of silver nanoparticles and its photocatalytic and antimicrobial activity. Mater Today Proc 36:121–125
13. Gandhi AD, Kaviyarasu K, Supraja N, Velmurugan R, Suriyakala G, Babujanarthanam R, Zang Y, Soontarapa K, Almaary KS, Elshikh MS, Chen TW (2021) Annealing dependent synthesis of cyto-compatible nano-silver/calcium hydroxyapatite composite for antimicrobial activities. Arab J Chem 14:103404
14. Valsalam S, Agastian P, Arasu MV, Al-Dhabi NA, Ghilan AKM, Kaviyarasu K, Ravindran B, Chang SW, Arokiyaraj S (2019) Rapid biosynthesis and characterization of silver nanoparticles from the leaf extract of Tropaeolum majus L. and its enhanced in-vitro antibacterial, antifungal, antioxidant and anticancer properties. J Photochem Photobiol B Biol 19 (2019):65–74
15. Dutta PK, Dutta J, Chattopadhyaya MC, Tripathi VS (2004) Chitin and chitosan: novel biomaterials waiting for future development. J Polym Mater 21:321–333
16. Jayakumar R, Prabaharan M, Nair SV, Tokura S, Tamura H, Selvamurugan N (2010) Novel carboxymethyl derivatives of chitin and chitosan materials and their biomedical applications. Progress Mater Sci 55:675–709
17. Hussain F, Hojjati M, Okamoto M, Gorga RE (2006) Review article: Polymer–matrix nanocomposites, processing, manufacturing, and application: An overview. J Compos Mater 40:1511–1575
18. Zhang L, Webster TJ (2009) Nanotechnology and nanomaterials: Promises for improved tissue regeneration. Nano Today 4:66
19. Renuka R, Renuka Devi K, Sivakami M, Thilagavathi T, Uthrakumar R, Kaviyarasu K (2020) Biosynthesis of silver nanoparticles using Phyllanthus emblica fruit extract for antimicrobial application. Biocatal Agric Biotechnol 24:101567
20. Nagasundari SM, Muthu K, Kaviyarasu K, Al Farraj DA, Alkufeidy RM (2021) Current trends of Silver doped Zinc oxide nanowires photocatalytic degradation for energy and environmental application. Surf Interfaces 23:100931
21. Ezequiel Costa-Junior S, Edel Barbosa- Stancioli F, Alexandra Mansur AP, Wander Vasconcelos L, Herman Mansur S (2009) Preparation and characterization of Chitosan/poly (vinyl alcohol) chemically crosslinked blends for biomedical applications. Carbohyd Poly 7:472–481
22. Jayakumar R, Prabaharan M, Nair SV, Tokura S, Tamura H, Selvamurugan N (2010) Novel carboxymethyl derivatives of chitin and chitosan materials and their biomedical applications. Prog Mater Sci 55:675–709
23. Kumara A, Negia YS, Bhardwaja NK, Choudhary V (2012) Synthesis and characterization of methylcellulose/PVA based porous composite. Carbohyd Polym 88:13641372

# Chapter 14
# Role of Nanodiagnostics in Health Sciences


**Vijaya Chitra Arumugam, Selvajeyanthi Selvaraj, Ayyasamy Pudukkadu Munusamy, Nanthakumar Kuppanan, and Karthikeyan Kannan**

## 1 Introduction

Diagnosis of infectious and non-infectious diseases is gaining utmost importance as each day new diseases arrive in today's world. The detection of disease in a timely and quick manner, the sensitivity and accuracy of the test, and reproducibility of the results help the diseased to get appropriate treatment. Nanotechnology, the emerging field, has opened various possibilities in many fields exclusively in the medical field. Nanodiagnostics, an application of nanotechnology, are used in the medical field in the diagnosis and in treatment of diseases. The COVID-19 pandemic has clearly indicated the need for a robust diagnostic tool for early detection of the disease. Diagnosis of disease aids the doctors to move in the correct treatment procedures instead of varying different types of drugs for the treatment.

A. Vijaya Chitra (✉)
Department of Microbiology, Sri Ramakrishna College of Arts and Science for Women, Coimbatore, India
e-mail: vijayamicro@srcw.ac.in

S. Selvaraj
Department of Microbiology, Shri Nehru Maha Vidyalaya College of Arts and Science, Coimbatore, India

A. P. Munusamy
Department of Microbiology, Periyar University, Salem, India

N. Kuppanan
The Energy and Resources Institute (TERI), New Delhi, India

K. Kannan
Gujarat Institute of Desert Ecology, Gujarat Bhuj, India



K. Kasinathan et al. (eds.), *Nanomaterials for Energy Conversion, Biomedical and Environmental Applications*, Materials Horizons: From Nature to Nanomaterials,
https://doi.org/10.1007/978-981-19-2639-6_14

## 2 Why Nanodiagnostics?

Conventional treatment methods were used till nineteenth century for testing of biological samples and analysis which were time-consuming and less sensitive. In a slow pace, immunological methods started to occupy the place of conventional methods providing immediate results especially for infectious diseases. The enzyme-linked immunosorbent assay (ELISA), fluorescent immunoassays, magnetic immunoassays, radioimmunoassays (RIA), and lateral flow immunoassays are some of the most often used diagnostic procedures for infectious disorders. But these techniques too face limitations as they target specific carbohydrates or proteins moieties unique to the pathogen and could not trace out the presence or metabolic state of the microorganism in the sample. With the development of Polymerase Chain Reaction (PCR), this molecular-based diagnosis tool is adopted that exclusively looks for genes and proteins associated for virulence and disease pattern [1]. Multiplex PCR, reverse transcriptase PCR, and real-time PCR are among the PCR-based techniques used to diagnose infectious diseases, with real-time PCR leading the others due to its high speed, accuracy, and reliability.

## 3 Nanodiagnostic Technologies

Nanomaterials have a substantial benefit in nanodiagnostics since most biological molecules and structures are similar in size to nanomaterials, making them suitable for in *vivo* and in vitro biomedical research and applications [2]. The nanodiagnostic tools use signal transduction as a means of detection and molecular characterization by using a nanodevice or a nanoscale tool that uses systems such as micro- and nanofluidics devices, microgravimetric and miniaturized piezoelectric transducers, nanotubes, nanoparticles [3], diagnostic magnetic resonance platform (DMRP), magnetic barcode assay system (MBAS), cellphone-based polarized light microscopy platform, cellphone dongle platform, and paper-based POCT platform. Many such nanodiagnostics tools have been developed by many researchers that find major application in the medical field (Table 1).

## 4 Diagnosis of Cancer Cells

Quantum dots have a lot of potential in cancer diagnosis. Quantum dots are semiconductor nanoparticles with unusual physical and chemical properties that can be used to mark biomolecules fluorescently. The size of these nanocrystals ranges from 1 to 10 nm. QDs are employed for colorful imaging of molecular, cellular, and in vivo processes in living beings because of their high photostability. Different types of QDs are available depending on their chemical makeup, with binary QDs made up

**Table 1** Nanodiagnostic tools and applications

| Nanodiagnostic tools/devices | Application |
|---|---|
| BioMEMs—biomicroelectromechanical system-based microdiagnostic kit | Tuberculosis |
| Cantilevers | Sensitive detection of various disease-specific molecules, sensitive screening of protein biomarkers detections, SNPs for mutation detection, gene expression detection |
| Carbon nanotubes | Disease protein and gene biomarkers detection |
| Dendrimers | Image contrast agents, thyroid profile, panel of steroid hormones, and inflammatory cytokines |
| DNA-coated gold nanoparticles, nano-i-PCR, magnetic microparticles (MMPs), DNA-labeled magnetic nanobeads | Cancer biomarker detection |
| DNA-based electrochemical sensors | Detection of mutated genes associated with human disease; hyper coagulation disorders |
| Fluid magnetic ceramic nanospheres, nanolithography | Infectious agent detection |
| Linear padlock probes | Detect target DNA |
| Magnetic iron oxide nanoparticles | Detection of cancer cells and biomedical imaging of cancer |
| Multilayer films/DNA capsules | To know specific biomarkers |
| Microfluidic system | For inspecting disease staging and monitoring |
| Nanobeads | Genetic disorders, detect altered DNA sequence, clinical detection of viruses and bacteria |
| Nanobased SNP analysis | CVD, diabetes mellitus, HTN |
| Nanoclinics with marker-specific monoclonal abs coated with polyethylene glycol | Immune system detection |
| Nanodevices | In vitro and in vivo diagnosis |
| NanoLogix's "Identikit" | Detection of mycobacterium avium complex (MAC) infection |
| Nanoshells | Tumor-specific imaging |
| Nanospheres | Detect multiple SNPs at the same time |
| Nanoparticle intravascular/cellular probes | Imaging purpose |
| Nanowires | Pinpoint the genetic changes |
| Optical tweezers | Differential diagnosis of tissue growth, calculi, cysts, abscess, hepato and splenomegaly |

(continued)

**Table 1** (continued)

| Nanodiagnostic tools/devices | Application |
|---|---|
| Optical nanosensor-based glucose sensing | Monitoring of glucose level |
| Quantum dots | Tumor and optical detection |
| Photodynamic sensitizers | Detect malignant and abnormal cells |
| Proteolytic cascades with nanosensor | Understanding the biological alteration of diabetes, asthma, cardiovascular disease, cancer |

of elements in Groups II–VI being the most frequent. CdSe, CdS, CdTe, ZnSe, ZnS, ZnTe, HgS, HgSe, HgTe, and ZnO are the most utilized QDs [4]. In the qualitative and quantitative study of Ramos cells, which typically causes human Burkitt's lymphoma, a DNA quantum dot composed of CdTe QDs sheath is utilized [5]. Chen et al. [6] used an aptamer-based fluorescence QD to detect Mucin 1 (MUC1), and a glycoprotein that is overexpressed in epithelial malignancies. Fluorescence intensity is used to determine the presence of MUC1 peptide. The presence of MUC1 peptide resulted in reduced fluorescence, whereas the lack of MUC1 resulted in high fluorescence, indicating that this QD-based technique can detect MUC1 at nanomolar concentrations.

The first application of iron oxide nanoparticles was in an MRI (magnetic resonance imaging) system that provides 3D images and detailed information on normal and cancerous hepatocytic cells. Use of Fe/$Fe_3O_4$ core/shell nanoparticles and two tethered fluorescent dyes in liquid biopsies and early-stage breast cancer, TCPP (Tetrakis(4-carboxyphenyl) porphyrin) and cyanine 5.5 are used to diagnose pancreatic cancer. The urokinase plasminogen activator, matrix-metalloproteinases, and cathepsins (CTS) protease activity in serum samples from stage 0 and stage 1 breast cancer patients may be recognized using Fe/$Fe_3O_4$ core/shell nanoparticles [7]. Similarly, the activity of the proteases mentioned above can be utilized to detect pancreatic cancer [8]. Nanoparticles of copolymers poly(lactic-co-glycolic acid)-b-poly-l-lysine and poly(lactic acid)-b-poly(ethylene glycol) loaded with Doxarubicin were used as theranostic nanoparticles for diagnosis and treatment of breast cancer [9].

Nanostructure-based MRI contrast agents are used in colorectal cancer imaging. These nanostructure-based MRI contrast agents significantly benefit in vivo imaging and diagnosis of colon or rectum cancer. By changing standard contrast agents like gadolinium or imaging agents like iron oxide, nanostructures could be employed to increase the diagnostic power of clinical imaging. These nanostructures have the potential to transform how colorectal cancer is identified and handled, in addition to improving the features visible in regular MRI imaging. Better endoscopic visualization techniques using near-infrared fluorescence imaging agents, such as tunable quantum dots, may improve the standard of care. A NIRF agent has been used to study a murine model of colon cancer [10]. A model developed by [11] for imaging of liver lesions using MRI and CT was found to be accurate and sensitive in diagnosis of liver metastatic CRC. Nanotheranostics is an upcoming technology for colorectal

cancer that uses the blending of both diagnosis and therapy in a single nanoplatform that uses a combination of any form of therapy as well nanotechnology.

Nanodiagnosis is also applied in the detection of oral cancer. Exosome, a membrane-bound secretory vesicle that contains malignancy-related proteomic and genomic signature, was used as marker to detect oral cancer using nanoparticles and atomic force microscopy. The nanoelectromechanical system, oral fluid nanosensor test, and optical nanobiosensor can also be used to detect oral cancer. Nanodentistry will give near-perfect oral health by combining nanomaterials and biotechnologies such as tissue engineering and nanorobots. Digital dental imaging processes are also likely to benefit from nanotechnology. Use of nanophosphor scintillators, for digital radiography, has the advantage of reduced radiation dose and high-quality images. Dentifrobots, also called nanorobotic dentifrice, can eliminate organic residues by moving through supragingival and subgingival surfaces, metabolizing trapped organic matter into odorless vapors, and performing continuous calculus debridement on the occlusal surface of teeth with mouthwash or toothpaste. These nanorobots can move at speeds ranging from 1 to 10 times per second and will deactivate if consumed [12]. Oral Fluid NanoSensor Test (OFNASET) uses proteomic and salivary biomarkers to detect oral cancer [13].

## 5 Diagnosis of Gastrointestinal Disease

Nanotechnology has a vivid role in the field of gastroenterology. In Lamprecht et al. [14] investigated the interaction of micro- and nanoparticles with inflamed intestinal mucosa in greater depth. From the study, the authors were able to analyze the aggregation of poly(lactic-co-glycolic acid) nanoparticles preferentially in the thicker mucus layer surrounding colitis ulcers, as opposed to the mucus layers of healthy tissue. Kirui et al. [15] developed multifunctional gold-iron oxide nanoparticles for imaging and targeting gastrointestinal disorders. Application of capsule endoscopy with nanoparticles involves the application of a small capsule, containing wireless camera and nanoparticles permits the identification and detection of small bowel lesions. The nanobased capsule endoscopy with molecular imaging and optical biopsy (NEMO), A European FP6 project targets the deployment of optical technology with nanotechnology for detection of disorders. Camera pills are like nanorobots capable of diagnostic and therapeutic activities [16].

## 6 Diagnosis of Alzheimer's Disease

The detection of Alzheimer's disease biomarkers is critical for both early and late diagnosis. Amyloid precursor protein (APP) gene mutations, as well as Presenilin 1 (PS1) and Presenilin 2 (PS2) gene mutations, cause extracellular sensile plaques and hyperphosphorylation of microtubule-associated protein tau (Tau), resulting in

neurofibrillary tangles and cortical damage, as well as the loss of cholinergic neurons in the basal forebrain [17]. One of the most important aspects of early AD pathogenesis is the examination of amyloid protein. Nanotechnology opens new possibilities for detecting the A-peptide with nanoparticles. Nanotechnology is utilized to diagnose Alzheimer's disease via amyloid imaging. Cheng et al. [18] employed MRI to visualize amyloid plaques using curcumin-conjugated magnetic nanoparticles (Cur-MNPs) made of polyethylene glycol-polylactic acid block copolymer and polyvinylpyrrolidone. Cur-MNPs revealed no cytotoxicity and might be used to make a non-invasive Alzheimer's disease diagnosis using MRI. Zeng et al. [19] used $Mn_{0.6}Zn_{0.4}Fe_2O_4$ (MZF) modified by Pittsburgh compound B (PiB) to create PiB-MZF nanoparticles that particularly bind to amyloid plaques and aid in the detection of Alzheimer's disease. In 2016, Lai et al. devised a fluorescence bioimaging approach for AD-infected mice that involves intravenous injection of aqueous $HAucl_4$ with the ability to cross the blood–brain barrier. In situ biosynthesis of gold nanoclusters occurs, allowing fluorescence labeling to be used to observe the location of damaged brain regions.

## 7 Diagnosis of Cardiovascular Disease

The cardiac troponin proteins, troponin I (cTnI) and troponin T (cTnT), which are released into the bloodstream when cardiomyocytes are damaged serve as biomarkers for the diagnosis of acute myocardial infarction. Cardiovascular disease biomarkers are detected using electrochemical immunosensors, amperometric sensors, and potentiometric sensors. An electrochemical sensor is made up of a bioreceptor molecule that detects and binds to a certain antigen. The binding events are converted into electric impulses via a transducer. Brondani et al. [20] developed an immunosensor for cardiac troponin T-detection based on an ionic organic compound ((E)-4-[(4-decyloxy phenyl) diazenyl]-1-methylpyridinium iodide) and chitosan-stabilized gold nanoparticles (CTS-AuNPs) (cTnT). Gomes-Filho et al. [21] developed a nanostructured immunosensor based on carbon nanotubes with conductive polymer, polyethyleneimine film support for detection of cardiac Troponin-T (cTnT). The Supraja Group developed a $ZnSnO_3$ perovskite nanomaterial for electrochemical detection of the cardiac biomarker Troponin-T using a glassy carbon electrode (GCE) and indium tin oxide-coated polyethylene terephthalate (ITO/PET) [22]. Bhalla et al. [23] employed citrate-capped gold nanoparticles on screen-printed electrodes immobilized with anti-cTnI antibodies to detect cTnI, and electrical capacitance variations were used to evaluate the interaction between cTnI and anti-cTnI. Nanoparticles are also employed for cardiovascular disease imaging. Rouleau et al. [24] employed gold nanoshells and photoacoustic imaging to visualize atherosclerotic plaque. Optical coherence tomography was used by Adhi et al. [25] to envision cardiovascular imaging with gold nanoparticles.

# 8 Diagnosis of Infectious Diseases

## *8.1 Diagnosis of SARS-COVID*

Alafeef et al. [26] developed a colorimetric assay based on gold nanoparticles for detecting COVID-19 from patient RNA samples. They used gold nanoparticles bound with antisense oligonucleotides as part of a nanoamplified colorimetric test (NACT) for naked-eyed detection of SARS-CoV-2 (ASOs). Moitra et al. [27] have produced N Gene targeted Antisense Oligonucleotide capped plasmonic nanoparticles for SARS-CoV-2 detection.

## *8.2 Diagnosis of Viral Infections*

In serum samples, bloodborne infectious agents such as HIV and HBV can also be detected utilizing an integrated nanodevice that combines quantum dots and microfluidics for high-throughput detection [28]. Cheng et al. [29] developed an HIV detection system based on the envelope glycoprotein gp120 and a mesoporous silica-based nanodevice. The team created sCD4, a fragment that mimics the gp120 binding region and is bound to mesoporous silica particles. It actively recognizes HIV-gp120 and has a high binding affinity for it. A gold nanoparticle pseudopathogen is created by using citrate gold nanoparticles coated with a Zika virus lysate [30]. Patients with zika infection have active immune molecules, such as antibodies, which react with the pseudovirus, causing nanoparticle aggregation and a color shift due to a change in surface plasmon resonance wavelength, which may be measured using a UV–vis spectrophotometer.

## *8.3 Diagnosis of Bacterial Infections*

Cihalova et al. [31] developed a magnetic barcode system that uses magnetic particles and CdTe-based quantum dots to detect *Staphylococcus aureus*, MRSA, and *Klebsiella pneumoniae*. Even at low concentrations, the system precisely targets genes including fnbA, wcaG, and mecA. Cheng et al. [32] used functionalized four-layer magnetic nanoparticles to develop an amperometric immunosensor for the detection of *E. coli* (O157:H7). Magnetic $Fe_3O_4$, Prussian blue, N-(2-aminoethyl)-3-aminopropyltriethoxysilane, and a gold nanoparticle shell containing antibodies specific for O157:H7 are among the layers. For the detection of E.Coli O157:H7, [33] developed a DNA biosensor using graphene oxide (GOx) as a nanocarrier to encapsulate thionine and gold nanoparticles coated with $SiO_2$ nanocomposites. Luo et al. [34] created a microfluidic multiplex electrochemical LAMP (ME-LAMP) system

for real-time bacterial differentiation, including loop-mediated isothermal amplification (LAMP) of nucleic acid integrated on an indium tin oxide (ITO) electrode. In this study, they qualitatively and quantitatively separated and evaluated various genes of Mycobacterium TB, Haemophilus influenzae, and Klebsiella pneumonia within 45 min and discovered that this method may be used for clinical identification of bacteria.

### *8.4 Diagnosis of Protozoan Infections*

A colorimetric aptasensor for detection of plasmodium lactate dehydrogenase enzyme has been constructed using gold nanoparticles and cationic polymers with pL1 apatmer [35]. The aptasensor has the potential to be used as a diagnostic tool for *Plasmodium vivax* and *Plasmodium falciparum.* Pirnstill et al. [36] created a cellphone-based transmission polarized light microscope to detect hemozoin for malaria detection. A nanodiagnostic colorimetric assay was devised employing gold nanorods for the detection of Leishmania pathogens' 18S rRNA using nucleic acid sequence-based amplification [37].

## 9 Conclusion

Nanotechnology holds enormous promise for medical diagnosis, treatment in the future. Nanoparticles can be used to detect pathogens as well as for other medicinal purposes such as cancer diagnostics and real-time monitoring. Nanodevices can be implanted into the body to collect human fluids or tissue samples and undertake a variety of subcellular research, such as diagnosing disease in its early stages or finding and measuring dangerous substances and tumor cells. Nanotechnology's exceptional applications and attributes provide promising goals to researchers to experiment with new concepts to improve miniature devices, for early intervention as well for appropriate treatment, which are the key goals of medical sciences.

## References

1. Salyers AA, Whitt DD (2002) Bacterial pathogenesis: a molecular approach, 2nd edn. ASM Press, Washington, D.C.
2. Curtis A, Wilkinson C (2001) Nanotechniques and approaches in biotechnology. Trends Biotechnol 19:97
3. Baptista PV, Koziol-Montewka M, Paluch-Oles J, Doria G, Franco R (2006) Gold-nanoparticle-probe-based assay for rapid and direct detection of Mycobacterium tuberculosis DNA in clinical samples. Clin Chem 52:1433–1434

4. Bhagyaraj SM, Oluwafemi O (2018) Applications of nanomaterials: advances and key technologies
5. Zhong H, Zhang Q, Zhang S (2011) High-intensity fluorescence imaging and sensitive electrochemical detection of cancer cells by using an extracellular supramolecular reticular DNA-quantum dot sheath. Chem Eur J 17:8388–8394
6. Cheng A, Su H, Wang Y, Yu H-Z (2009) Aptamer-based detection of epithelial tumor marker mucin 1 with quantum dot-based fluorescence readout. Anal Chem 81:6130–6139
7. Udukala DN, Wang H, Wendel SO, Malalasekera AP, Samarakoon TN, Yapa AS, Abayaweera G, Basel MT, Maynez P, Ortega R, Toledo Y, Bossmann L, Robinson C, Janik KE, Koper OB, Li P, Motamedi M, Higgins DA, Gadbury G, Zhu G, Troyer DL, Bossmann SH (2016) Early breast cancer screening using iron/iron oxide-based nanoplatforms with sub-femtomolar limits of detection. Beilstein J Nanotechnol 7(7):364–373
8. Kalubowilage M, Covarrubias-Zambrano O, Malalasekera AP, Wendel SO, Wang H, Yapa AS, Chlebanowski L, Toledo Y, Ortega R, Janik KE, Shrestha TB, Culbertson CT, Kasi A, Williamson S, Troyer DL, Bossmann SH (2018) Early detection of pancreatic cancers in liquid biopsies by ultrasensitive fluorescence nanobiosensors. Nanomedicine 14(6):1823–1832
9. Yildiz T, Gu R, Zauscher S, Betancourt T (2018) Doxorubicin-loaded protease-activated near-infrared fluorescent polymeric nanoparticles for imaging and therapy of cancer. Int J Nanomed 13:6961–6986
10. Weissleder R, Tung CH, Mahmood U et al (1999) In vivo imaging of tumors with protease-activated near-infrared fluorescent probes. Nat Biotechnol 17:375–378
11. Saing S, Haywood P, Duncan JK, Ma N, Cameron AL, Goodall S (2018) Cost-effective imaging for resectability of liver lesions in colorectal cancer: an economic decision model. ANZ J Surg 88(6):E507–E511
12. Abiodun-Solanke I, Ajayi D, Arigbede A (2014) Nanotechnology and its application in dentistry. Ann Med Health Sci Res 4(3):S171–S177
13. Gau V, Wong D (2007) Oral fluid nanosensor test (OFNASET) with advanced electrochemical-based molecular analysis platform. Annals New York Acad Sci 1098(1):401–410
14. Lamprecht A, Ubrich N, Yamamoto H, Schafer U, Takeuchi H, Maincent P, Kawashima Y, Lehr CM (2001) Biodegradable nanoparticles for targeted drug delivery in treatment of inflammatory bowel disease. J Pharmacol Exp Ther 299:775–781
15. Kirui DK, Rey DA, Batt CA (2010) Gold hybrid nanoparticles for targeted phototherapy and cancer imaging. Nanotechnology 21:105105
16. Laroui H, Wilson DS, Dalmasso G, Salaita K, Murthy N, Sitaraman SV, Merlin D (2011) Nanomedicine in GI. Am J Physiol Gastrointest Liver Physiol 300(3):G371–G383
17. Sahni JK, Doggui S, Ali J, Baboota S, Dao L, Ramassamy C (2011) Neurotherapeutic applications of nanoparticles in Alzheimer's disease. J Control Release 152(2):208–231. https://doi.org/10.1016/j.jconrel.2010.11.033
18. Cheng KK, Chan PS, Fan S, Kwan SM, Yeung KL, Wáng YX, Chow AH, Wu EX, Baum L (2015) Curcumin-conjugated magnetic nanoparticles for detecting amyloid plaques in Alzheimer's disease mice using magnetic resonance imaging (MRI). Biomaterials 44:155–172
19. Zeng J, Wu J, Li M, Wang P (2018) A novel magnetic nanoparticle for early detection of amyloid plaques in Alzheimer's disease. Arch Med Res 49(4):282–285
20. Brondani D, Piovesan JV, Westphal E, Gallardo H, Dutra RA, Spinelli A, Vieira IC (2014) A label-free electrochemical immunosensor based on an ionic organic molecule and chitosan-stabilized gold nanoparticles for the detection of cardiac troponin T. Analyst 139(20):5200-5208
21. Gomes-Filho SLR, Dias ACMS, Silva MMS, Silva BVM, Dutra RFA (2013) A carbon nanotube-based electrochemical immunosensor for cardiac troponin T. Microchem J 105:10-14
22. Supraja P, Sudarshan V, Tripathy S, Agrawal A, Singh SG (2019) Label free electrochemical detection of cardiac biomarker troponin T using ZnSnO3 perovskite nanomaterials. Anal Methods 11:744–751
23. Bhalla V, Carrara S, Sharma P, Nangia Y, Suri CR (2012) Gold nanoparticles mediated label-free capacitance detection of cardiac troponin I. Sensors Actuators B Chem 161(1):761–768

24. Rouleau L, Berti R, Ng VW, Matteau-Pelletier C, Lam T, Sabourał P, Kakkar AK, Lesage F, Rheaume E, Tardif JC (2013) Contrast Media Mol Imaging 8:27–39
25. Adhi M, Duker JS (2013) Curr Opin Ophthalmol 24:213–221
26. Alafeef M, Moitra P, Dighe K, Pan D (2021) RNA-extraction-free nano-amplified colorimetric test for point-of-care clinical diagnosis of COVID-19. Nat Protoc 16:3141–3162
27. Moitra P, Alafeef M, Dighe K, Frieman MB, Pan D (2020) Selective naked-eye detection of SARS-CoV-2 mediated by N gene targeted antisense oligonucleotide capped plasmonic nanoparticles. ACS Nano 14(6):7617–7627
28. Klostranec JM, Xiang Q, Farcas GA et al (2007) Convergence of quantum dot barcodes with microfluidics and signal processing for multiplexed high-throughput infectious disease diagnostics. Nano Lett 7(9):2812–2818
29. Cheng K, El-Boubbou K, Landry CC (2012) Binding of HIV-1 gp120 glycoprotein to silica nanoparticles modified with CD4 glycoprotein and CD4 peptide fragments. ACS Appl Mater Interfaces 4(1):235–243
30. Zheng T, Huo Q (2020) A nanoparticle pseudo pathogen for rapid detection and diagnosis of virus infection. Sensors Int 1 (Article ID: 100010)
31. Cihalova K, Hegerova D, Jimenez AM et al (2017) Antibody-free detection of infectious bacteria using quantum dots-based barcode assay. J Pharm Biomed Anal 134:325–332
32. Cheng P, Huang ZG, Zhuang Y, Fang LC, Huang H, Deng J et al (2014) A novel regeneration-free E. coli O157:H7 amperometric immunosensor based on functionalised four-layer magnetic nanoparticles. Sensors Actuators B 204:561–56
33. Li Y, Deng J, Fang L, Yu K, Huang H, Jiang L, Liang W, Zheng J (2015) A novel electrochemical DNA biosensor based on HRP-mimicking hemin/G-quadruplex wrapped GOx nanocomposites as tag for detection of Escherichia coli O157: H7. Biosensors Bioelectron15;63:1–6
34. Luo J, Fang X, Ye D, Li H, Chen H, Zhang S, Kong J (2014) A real-time microfluidic multiplex electrochemical loop-mediated isothermal amplification chip for differentiating bacteria. Biosens Bioelectron 60:84–91
35. Jeon W, Lee S, Manjunatha D, Ban C (2013) A colorimetric aptasensor for the diagnosis of malaria based on cationic polymers and gold nanoparticles. Anal Biochem 439:11–16
36. Pirnstill CW, Coté GL (2015) Malaria diagnosis using a mobile phone polarized microscope. Sci Rep 5:13368
37. Niazi A, Jorjani ON, Nikbakht H, Gill P (2013) A nanodiagnostic colorimetric assay for 18S rRNA of Leishmania pathogens using nucleic acid sequence-based amplification and gold nanorods. Mol Diagn Ther 17(6):363–370

# Chapter 15
# Mycosynthesis of Nanoparticles from Basidiomycetes Mushroom Fungi: Properties, Biological Activities, and Their Applications

**C. Pothiraj, M. Kumar, M. Eyini, and P. Balaji**

## 1 Introduction

Nanoparticles (NPs) can have a variety of forms, sizes, and chemical characteristics. They are zero-dimensional nanostructures. Due to the occurrence of "quantum confinement," where electrons are confined within molecules that have a shorter electron scattering range than the bulk electron scattering range, this unusual form of material displays amazing physicochemical and optoelectronic properties [1]. As a result, nanoparticles are found in many different of applications in diagnostics, medicines, catalysts, semiconductors, and a multitude of other fields, and a huge range of financial goods comprise designed nanomaterials [2, 3]. Nanoparticles are synthesized using a variety of methods, however, to develop ecologically friendly techniques for producing nanoparticles, scientists have redirected their focus away from chemical processes and toward biological systems [4]. Several published papers, investigations, and research recently started to examine the possibility of synthesising nanomaterial from several species of medicinal and culinary mushrooms due to their plethora of bioactive compounds with pharmacological properties. Amongst fungi, basidiomycetous fungi, or mushrooms exhibit considerable effects on a variety of habitats and morphologies. Several fungi occur naturally and also grow on fields

C. Pothiraj
Department of Botany, Government Arts College, Melur, Tamil Nadu, India

M. Kumar
Department of Plant Biology and Plant Biotechnology, Madras Christian College (Autonomous), Tambaram, Tamil Nadu, India

M. Eyini
PG and Centre for Research in Botany, Thiagarajar College, Madurai, Tamil Nadu, India

P. Balaji (✉)
PG and Research Centre in Biotechnology, MGR College, Hosur, Tamil Nadu, India
e-mail: balaji_paulraj@yahoo.com



K. Kasinathan et al. (eds.), *Nanomaterials for Energy Conversion, Biomedical and Environmental Applications*, Materials Horizons: From Nature to Nanomaterials,
https://doi.org/10.1007/978-981-19-2639-6_15

for their nutritive value due to its abundance of bioactive substances varying from carbohydrates and peptides to intricate phytochemicals [5]. The immunomodulatory and immunostimulatory properties of therapeutic mushrooms contribute to the nutritious content of mushroom extracts, reduction, and combinations. Currently, the emphasis of nanomaterials' research has switched to the prospect of synthesising nanoparticles that used a range of medicinal and culinary mushroom genera [6]. The quantity of bioactive compounds found in mushrooms creates a great possibility for nanoparticle synthesis. Numerous peptides and carbohydrates isolated from mushrooms have been used to synthesize organic and inorganic nanoparticles on both the intracellular and extracellular levels. On an endogenous and environmental scale, a multitude of peptides, and carbohydrates present in mushrooms have been employed to produce various metal nanoparticles [7]. Due to the composites produced by edible and therapeutic mushrooms, nanomaterials with a significant level of consistency and distribution are formed [8]. Therefore, nano-tests involving macrofungi (mushrooms) look to be highly encouraging and pave the way for a new field of sustainable and environment, and durable nanoparticle mycosynthesis via a variety of approaches (Fig. 1). As a result, our knowledge as to how mushrooms make nanomaterials keeps expanding.

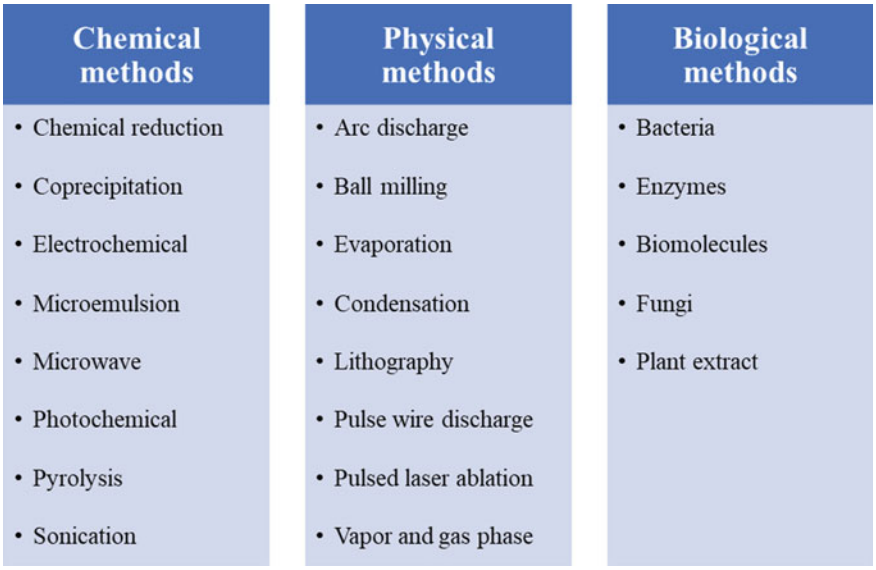


**Fig. 1** Various methods of synthesis of nanoparticles

## 2 Bioactive Compounds of Mushroom and Its Therapeutical Properties

Mycophagy is the practice of consuming mushrooms as a part of the diet. Mushrooms are very popular macrofungal with a unique basidiocarp or cap, which shows hypogeal or epigeal growth in nature. Mushrooms come from a variety of traditional foods, and in several nations, both raw and stored mushroom species are considered delicacies, owing to their exact fragrance and consistency. Approximately around ~2 million species of mushrooms thrive on the mycelium, a output of vegetative growth, that transports food and promotes growth [9]. Three thousand of the 14,000 mushroom species discovered are edible, and 270 are believed to have therapeutic properties that aid in human well-being [10]. Mushrooms deemed edible are a nutrient-dense food with a high physiological benefit [11]. The primary nutrient in mushroom dry mass is polysaccharides, which include both digestible (trehalose, glycogen, mannitol, and glucose) and indigestible (chitin, mannans, and -glucan) carbs. Compounds have been identified all essential nutrients and a substantially larger ratio of polyunsaturated fatty acids (PUFA) than saturated fatty acids. Mushrooms are indeed the sole vegetal source of nutrient and are high in B-complex vitamins and a variety of nutrients necessary for human biological mechanisms [12–14]. In count to this nutrient content, mushrooms include a variety of bioactive chemicals, including carbohydrates, polypeptide, amino acids, extracellular matrix, polyphenols, terpene, and lectins. Humans consume a wide variety of mushrooms for their health advantages, which increases demand for commercial production and globalization. As a result, there has been a significant growth in the variety of edible mushroom production [9], with roughly 30 mushroom species now commercially available [15]. *Agaricus bisporus, Flammulina velutipes, Lentinula edodes*, and *Pleurotus* species seem to be the most widely farmed mushrooms worldwide. Mushrooms have been used therapeutically for their anti-tumour, antioxidants, immunomodulatory, radicals scavenging, cholesterol-lowering, cardiovascular, antibacterial, wound healing, liver protective, among others. They can be ingested whole or in portions to enhance healthy and quality of life [16, 17]. Recently, indigenous basidiomycetes fungi such as *Laetiporus sulphureus* and *Grifola frondosa* have gained popularity due to their high nutritive value, palatable sensory characteristics, and various medicinal effects [13]. According to statistics sources, global mushroom production climbed from 7 to 10 million metric tonnes in the 10 years between 2008 and 2017 [18]. Additionally, human consumption of edible basidiomycetes mushroom fungi increased dramatically from 1 to 4.7 kg per capita between 1997 and 2013 and continues to grow as consumers become more aware of the nutritional and medicinal benefits of mushrooms [9, 19]. Nonetheless, mushrooms remain a relatively untapped resource of potential therapeutic chemicals.

Since a significant period, consumable mushrooms have been widely utilized for mankind nutrition and, therefore, are renowned for its attractive consistency, flavour, and therapeutic properties. Except for the rigid, naked fruiting body of *Ganoderma lucidum*, mushroom fruiting bodies typically contain roughly 90% moisture. Their

dried mass is primarily composed of carbohydrate and proteins, with a trace of fat [13]. Mushrooms, on the other hand, have an attractive nutrient quality from a feeding standpoint. Mushrooms are a highly nutritious, fibre, micronutrients, and lipids, and their nutrient benefits vary considerably between species. Fatty acids (polyunsaturated) make for >75% of total lipids in mushrooms, which mostly contains oleic and linoleic acids. Mushroom protein consists all the essential nutrients necessary to adult growth [20]. Mushrooms are regarded a prospective vitamin supplementation due to their high B vitamin content [13]. Additionally, they are the sole vegetarian source of vitamin D [12]. Additionally, mushrooms are an excellent source of different of elements, including K, $PO_4$, Mg, Fe, Zn, Cu and are a rich resource of calcium [13]. Mushrooms are beneficial from a nutritional standpoint since they are gluten-free, cholesterol-free and include polyunsaturated fats [21]. While exotic mushroom variants contain more protein, α-tocopherol, polyunsaturated fatty acids, and phenolic compounds than commercial mushroom cultivar, commercially cultivated species probably contain elevated levels of antioxidant compounds, as the key element [13]. The constitution of biomolecules and associated nutrient intake all have an influence on the development, production, taste, and nutritive values of mushrooms. Utilizing the substratum on which mushrooms were formerly grown can help increase the concentration of bioactive chemicals, aid in waste breakdown, and promote the mushroom industry's supply chain [10]. It has been shown that effective biotransformation of starch-based agricultural industry waste material to *Morchella* species biomass and mycelium results in a high nutritional content and biological properties [22].

Despite of its rich heritage of eating, the mushroom has indeed been grossly underutilized and subjugated from a practical perception. Mushrooms are recognized as quality food stuffs due to its nutritious and therapeutic purposes and are appreciated as a wellspring of vitality including for their medicinal benefits in both conventional oriental and western medicine traditions [23]. Mushrooms are a source of various biologically active nutritional supplements which could be used as an active substance in the order to prepare functional ingredients that may improve health by boosting the immune system, preventing and/or reducing cancer risks, and protecting the nervous system from impairment, among other benefits. Nevertheless, future studies should concentrate on the improvement of fabrication of functional foodstuffs and associated shelf-life enhancement by non-thermal technology. Mushrooms are said to accumulate more useful components when grown on agricultural residues [24]. Thus, the usage of diverse agriculture waste for mushroom cultivation should be pushed as a much more cost-effective and ecologically responsible method of meeting the world's ever-growing population's nutrition and agriculture demands while also supporting the mushroom industry in terms of value chain. The vast quantities of trash feedstock generated as a by-product of mushroom growth have aroused scientists' interest in the possibility of converting it into profitable items [25]. As a result, additional research is required to improve resource productivity, reduce waste output, and reduce resource overexploitation.

Number of researchers had already confined numerous bioactive molecules from mushrooms that are thought to be accountable for their medicinal potential; nevertheless, the efficiency of most of these elements has not even been affirmed in clinical studies [26, 27]. Additional investigation is warranted to enhance the biological efficiency of existing nutrient content throughout many mushroom cultivars via structural modifications, as it was disclosed recently that all those naturally occurring substances exhibit only a negligible level of biological activity, which can be enhanced through certain chemical alterations [28]. While several medicinal benefits were recognized for mushrooms, there is a dearth of study on their pharmacological compounds and the mechanisms global health problems. Additionally, scientists worldwide have recently concentrated on mushroom-derived prebiotics, particularly in relation to the relationship among intestinal flora control and host well-being. However, new research is required to comprehend the pathways of activities of various mushroom biochemicals in therapy and illness prevention, and further strengthen medical and biological proof depending on the known data in efforts to progress their curing value. Currently, the engagement of bacteria, viruses, fungus, and plant, as well as their cellular constituents, has been proposed as a means of decreasing emissions and providing a more environmentally friendly, durable, and feasible method. As eukaryotes, basidiomycetes mushroom fungi produce a multitude of bioactive components. The more of these metabolites produced, the higher possibility for metallic reductions. Numerous fungi from distinct classifications, most notably Ascomycota and Basidiomycota, showed to be accomplished of synthesising different metal nanomaterials [29, 30]. Mushroom produce huge quantities of enzymes and proteins that aid in increasing the output of nanoparticles. Additionally, it provides benefits such as safe separation process and easy handling that are suited for biological procedures. As a result, this chapter discusses the utilization of basidiomycetes mushroom fungi in the manufacture of metal nanoparticles.

## 3 Importance of Nanoparticles in Healthcare

Nanotechnology is a boon to mankind. They are derived from natural sources in molten rock, peptides, and biopolymers, but these could simply be synthesized. Every form of nanoparticles has an influence on public health and the environment, and current research has focused exclusively on these concerns. Additionally, the Ayurvedic and Siddha systems have various nanomaterials. However, owing to the nanoscale variations in the structural, chemical, and biological features, the use of nanostructures raises safety concerns. As a result, the requirement and relevance of rules are self-evident. Many agencies throughout the world are regulating nanotechnology-based components in compliance with established norms and regulations. Regulations are necessary, particularly for goods containing nanoparticles, and regulations addressing essential issues shall be established and implemented. Figure 2 depicts the timeline of nanomaterials' effects. Several of the immediate and

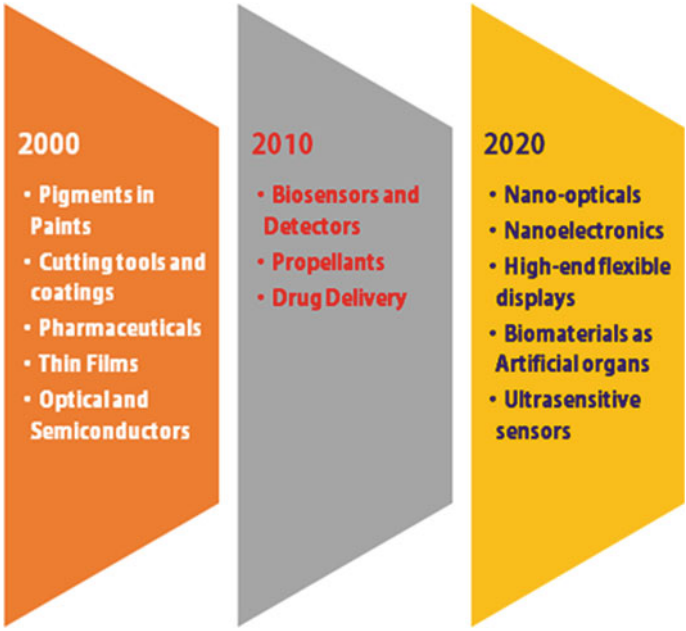


**Fig. 2** Timeline and application of nanomaterials

projected long-term consequences of the technical revolution brought in by nanoscale science and technology are described in greater detail below.

Nanoparticles, or nanomedicine, are the most utilized and economically viable technology for boosting the performance of the healthcare solutions. Although nanomaterials do have some limits, various pharmaceutical and biotechnology companies have already adopted it for medicinal applications. Nanotechnology permits the delivery of pharmaceuticals with a high potential for toxic effects, such as chemo treatments, with a more safety and tolerability profile in specific conditions. Keep in mind that living cells are small virtualization technology that engage in all bioactivities, including signalling, metabolic functions, power generation, and nutrition intake. As such, it is a perfect candidate technique for clinical uses including biomedicine [31]. Using biomaterials as medicine is a significant and important advance in the contemporary day, with a particular emphasis on producing tiny therapeutic solutions to aid in the implementation of an appropriate medical system. This technique helps us to gain a deeper knowledge of human metabolism and, as a significance, to combat a variability of deadly diseases, with cancer and heart disease. Nanomedicine's importance is mainly in image analysis, analysis of illnesses, regeneration of cells, and designing and developing added effectual, cheap, and harmless medication transport to achieve medications exactly to goal positions, thereby speeding up therapies outcomes and reduce off-target impacts and adverse reactions [32]. Nanotechnology does have the ability to substantially speed advancements in healthcare, information technology, genomics, and global health robotic


**Fig. 3** Application of nanotechnology in healthcare

devices, resulting in significant clinical benefits. Examining and examining the full application of nanoparticles is wide and diverse [33]. However, the primary advantage of nanotechnology techniques and equipment is that they could have significant health advantages in global contexts (Fig. 3).

## 4 Nanoparticles Synthesized from Mushrooms

Mushrooms are grown widely for its flavour, delectability, and nutritive quality. The mushroom fungus is vital in environment since it recycles carbohydrates via white rot lignin degradation. Nanoparticles were synthesized using both the basidiocarp and mycelial component of mushrooms. Mushrooms of therapeutic potential that are edible have indeed been utilized to generate a variety of nanomaterials by employing metallic constituents including such trace minerals (Fig. 4). Silver nitrate,

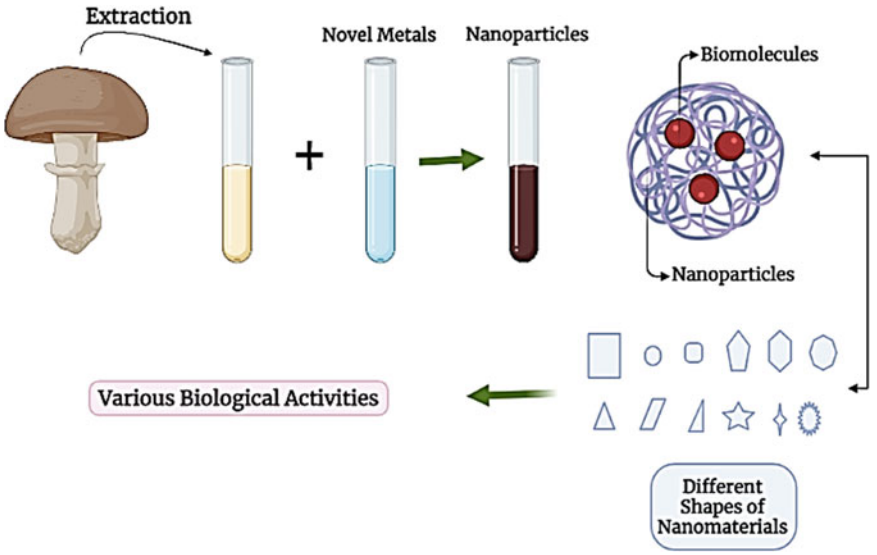


**Fig. 4** Synthesis of nanoparticles from basidiomycetes mushroom fungi

chloroauric acid, zinc oxide, titanium oxide, lead oxide, zinc sulphide, cadmium sulphide, iron oxide, aluminium, and palladium are just a few examples [34]. The technique is complete when the basidiocarps are carefully cleaned using deionized water to remove any impurities. The combination is next mixed or crushed, and the resulting paste is suspended in a specific volume of pure water. By filtration or centrifuging the solution, cell fractions could be generated automatically. By incorporating the filtrate/supernatant with metal salt solution and incubation with and without exposure to electric radiation, nanoparticles can be generated. Certain processes for the synthesis of metallic particles can be recognized through a shift in appearance of the reaction medium whenever the metal is added [35]. Numerous papers on mycogenesis-derived NPs have indeed been described in past few decades [36]. Nevertheless, the exact mechanism of mycogenic nanoparticle creation with varying size dimensions and morphologies remain unknown (yet). Numerous heterotrophic multicellular eukaryotic organisms can be classified as constituents of the fungus kingdom. These bacteria are critical in a variety of habitats, most notably in nutrient cycle models. Organisms reproduce sexually and asexually and have demonstrated mutualistic relationship with bacteria and plants. Mildew, mould, rust, yeast, and mushrooms are the most common fungi [37].

The benefits and practical utility of fungal cell wall are ascribed toward the secretion of substantial quantities of enzymes secreted outside the cell that operate as reducing and stabilising factors for nanoparticle production. Additionally, nanoparticles derived from fungi are superior to bacteria-derived nanoparticles. Components that are produced by cells of the fungi are critical in the generation of nanoparticles, which lower the toxicity of chemicals [38]. Ions are typically damaging, and

when injected into prokaryotic cells, they spread evenly across the microbial cell's environment, with no localization. By contrast, nanoparticles that interact therewith the bacterial membrane provide a concentrated supply of ions through continuous ion discharge, increasing the cytotoxicity of the organisms [39]. Fungi have a higher capacity for metal binding than bacteria, and as a result, fungal biomass has attracted researchers' attention for the large-scale generation of NPs. Numerous metal nanoparticles can be manufactured utilizing fungal biomasses [30]. Nanoparticle obtained from fungal organic matter displays good optical, structural, and chemical characteristics, including enhanced properties, biocompatible, and sufficient infrared photo-absorption potential, that enables their use in a range of biochemical and health sectors, including detecting, pharmaceutics, catalyst supports, and packaged food [40–42]. Mushrooms synthesize myco-NPs in a variety of locations, and their medical significance is summarized in Table 1.

## 5 Biological Activity of Different Nanoparticles Prepared by Mushrooms

The rationale nanoscience is such a potential sector in the pharmaceutical field, and current healthcare system is important for biological functional properties and ability to work in harmony with our bodies' natural system. As previously stated, live cells exist on the nanoscale. As a result, it was speculated that the world of nanotechnology is an appealing subject of biology and medicine. Currently, nanotechnology's application in healthcare is increasing at a rapid pace because of its targeted transport and properties. Too far, numerous nanoscale materials are developed for a variety of therapeutic use, together with illness detection, drug delivery, and molecular medical imaging, followed by the development of several products currently undergoing clinical trials. Mycosynthesis is a method for synthesizing nanoparticles that utilizes several kinds of fungi especially their enzymes that act as catalyst in the reduction reactions. Additionally, mushrooms are easy to manage and generate a substantial quantity of biomass when employed in substantial manufacture of a variety of nanoparticles. Out of many metallic nanoparticles synthesized, silver nanoparticles were synthesized in enormous numbers, trailed by gold, selenium, zinc sulphide, cadmium and many. Iron nanoparticles and other bimetallic nanoparticles were least to be synthesized and studied for their potent biological activities. Many nanoparticles apart from metallic nanoparticles were also synthesized from mushrooms [64], which were utilized in biosorption process [65]. Nonetheless, *A. bisporus* mushroom microorganisms were induced to produce irregular silver nanoparticles ranging in size from 500 nm to 10 m. [66].

**Table 1** Applications of nanoparticles derived from basidiomycetes mushroom

| Mushroom | Application | References |
|---|---|---|
| *Agaricus bisporus* | Antibacterial effects | Mirunalini et al. [36], Sudhakar et al. [43] |
| *Flammulina velutipes* | Bioremediation | Narayanan et al. [44] |
| *Ganoderma lucidum* | Antibacterial effects | Mirunalini et al. [36] |
| | Anticancer effects | Paul et al. [45] |
| *Hericium erinaceus* | Anticancer effects | Raman et al. [46] |
| *Hypsizygus ulmarius* | Antimicrobial effects | Shivashankar et al. [47] |
| *Lentinula edodes* | Antibacterial effects | Sujatha et al. [48] |
| *Phellinus igniarius* | Antioxidant effects | Paul et al. [45] |
| *Pleurotus ostreatus* | Antibacterial effects | Mirunalini et al. [36] |
| | Anticancer effects/ Anticandidal effects | Yehia and Al-Sheikh [49] |
| | Dye decolourization | Karthikeyan et al. [50] |
| *Pleurotus florida* | Antibacterial effects | Bhat et al. [51], Sen et al. [52], Sujatha et al. [53] |
| *Pleurotus citrinopileatus* | Antibacterial effects | Bhardwaj et al. [54] |
| | Anticandidal effects | Owaid [55] |
| *Pleurotus sajor caju* | Antimicrobial effects | Nithya and Ragunathan [56] |
| | Dye Decolourization | Nithya [57] |
| | Anticandidal effects | Musa et al. [58] |
| *Pleurotus djamor* | Antimicrobial effects | Shivashankar et al. [47] |
| | Anticancer effects | Raman et al. [59] |
| *Polyporus rhinoceros* | Cellular uptake/ Anticancer effects | Wu et al. [60] |
| *Pycnoporus sanguineus* | Antibacterial effects | Chan and Don [61] |
| *Schizophyllum commune* | Antibacterial effects | Chan and Don [61] |
| | Antifungal and Antibacterial effects | Arun et al. [62] |
| | Novel protein composites designing | Numata et al. [63] |

## *5.1 Silver Nanoparticles*

Silver nanoparticles synthesized from oyster mushroom species have been used in vitro to combat pathogens. Antibacterial properties of oyster mushroom species were reported previously [67]. Metallic nanoparticles have been mycosynthesized using microfungi and macrofungi. Because silver nanoparticles are recognized to be effective wound healing and antimicrobial agents, they are utilized in therapeutic application [68]. Accordingly, silver nanoparticles from various *Pleurotus* species

were used as antibacterial agents [47, 51, 54, 69–71]. However, when compared to antifungal medications, the fungicidal effect of silver nanoparticles against yeast fungi was found to be stronger. The effects of AgNP on *C. albican* sexual dimorphism transformation were examined [49]. AgNPs are particularly beneficial when used in external lotions to avoid skin disease in exposed wound infections. The antifungal activity of AgNPs demonstrates nanosilver's utility in bio-stabilization of footwear materials [43]. Owaid et al. [67] investigated the effectiveness in controlling various *Candida* species by biologically synthesized silver nanoparticles in vitro using the agar well diffusion technique. *Pleurotus cornucopiae* aqueous fractions demonstrated no inhibition efficacy against every *Candida* species. However, the AgNPs produced by *Pleurotus cornucopiae* displayed an effective inhibitory activity towards *Candida* sp. According to a few research findings, the charge density of $Ag^+$ plays a critical role in its fungicidal efficacy via cellular proliferation and accelerated discharge of cell wall components [72], oxygen radicals' production [73], and electrostatic interaction (Janga et al. 2011) [74]. Thus, the anti-fungal efficacy of AgNP versus *Candida* sp. is modest in vitro infections [67].

Considering mycosynthesized AgNPs using native mushroom extraction has a higher anticancer efficacy and a lesser side effect to native cells in vivo than chemo synthesized AgNPs, they are being used in therapeutic formulations. AgNP produced by mushrooms might be a promising anti-cancer agent [75]. AgNPs from *Pleurotus sanguineus* with 20 nm diameter have been shown to induce apoptosis more effectively than bigger AgNPs in the Mc3T3-E1 cell line. As a result, the size of nanoparticles must be specifically chosen for biological and pharmacological purposes [61]. The anti-tumour property of AgNPs has been demonstrated in breast carcinoma cells (MCF7 cells), which resulted in a reduced cell proliferation in MCF7 cell lines in a dose-dependent manner [49]. Silver nanoparticles readily penetrate the nuclear envelope and interact with DNA and intracellular biomolecules and produce oxidative stress. Cells that are harmed lead to the decrease of membrane stability, oxidative stress, and programmed cell death. Numerous parameters, such as the size, duration, and dose of AgNPs, contribute to their toxicity. AgNPs create considerable morphological alterations, such as coiling as well as shrinkage, as compared to the reference cell [76–78].

## *5.2 Gold Nanoparticles*

Au-NPs from mushrooms are round, triangle, or polygonal in structure and vary in diameter (>100 nm), while in the mushrooms *Flammulina velutipes,* they are <25 nm in size [44]. Previously, a green chemical strategy to the manufacture of Au-NPs utilising *P. florida* extract or glucan was discovered [52, 79]. A unique approach was used to create *Volvariella volvacea* Au-NPs with a range of sizes (20–150 nm) and morphologies, ranging from triangular nanoprisms to nearly spherical and hexagonal geometries [80]. The spectrum matching to surface plasmon resonance is found at a wavelength of 540 nm, indicating the creation of Au-NP in the reaction medium.

Au-NPs produced by mycobacteria are spherical or triangular in form and range in size from 10 to 50 nm [79]. The mycosynthesis of Au-NPs in an aqueous medium employing *P. sapidus* culture supernatant as a reducing and stabilising agent resulted in NPs ranging in size from 15 to 100 nm with a mean size of 65 nm [81]. Additionally, Au-NPs were synthesized using chloroauric acid and *P. florida* glucan, which tends to produce circular shapes with rougher surfaces and aggregation sizes of approximately 20 nm [52], where the variation in dimensions of Au-NPs is due to the fluctuating temperature of extract [80]. The functional AuNPs displayed impressive anticancer activity towards a diversity of cancer cells [79].

## 5.3 Zinc Nanoparticles

The source element for the ZnS NPs was *P. ostreatus* extract, $ZnCl_2$, and $Na_2S$ solution [82]. To begin, tiny mushroom pieces were cooked and strained. The obtained filtrate was then combined with aqueous phase of $ZnCl_2$ and $Na_2S$, and the resultant mixtures then dehydrated at 120 °C for 2 h. The resulting filtrate was used to stabilize spherical ZnS NPs during their preparation. The generated ZnS NPs were extremely crystalline, varying in length from 2.30 to 4.04 nm. The authors observed a decrease in the size of the ZnS nanoparticles while the extract concentration is increased. ZnO NPs were produced by adding *P. djamor* extract to Zn $(NO_3)_2$. Constant mixing of the $H_2O$ (5 mM) solutions at ambient temperature for 24 h validated the formation of ZnO NPs [83].

## 5.4 Other Nanoparticles

ZnS-NPs from mushrooms ranged in dimensions between 3 and 201 nm [84, 85]. It's noteworthy that iron nanoparticles were identified within the cellular structures. Nevertheless, the quantity of metal nanoparticles found within *Pleurotus* spp. cells was much less than the quantity found in extracellular depositions. The conversion of $Fe^{+3}$ to $Fe^{+2}$ occurs during the absorption of Fe-NPs via cytoplasmic membrane. Indeed, iron NPs may be found within the cell because of metal ion conversions. Although all metal absorption by fungi occurs via two pathways: uptake of siderophore iron (among the subdivisions of the Kingdom of fungi) and an iron uptake process in 2 of such subcategories, Basidiomycota and Ascomycota [86]. Additionally, non-metallic NPs were generated, for example, by reacting *P. tuberregium* cell wall polysaccharides with $D_2O$ water, resulting in spherical NPs with such a diameter of 38.5 nm [87]. Additionally, HENIG was employed to biosynthesize *P. ostreatus* nanoparticles ranging in size from 1 to 299 nm [88]. Fungi have been employed to synthesize Cd-NPs via mycosynthesis [89]. Merely 2 types (*Coriolus versicolor* and *P. ostreatus*) are often used in mushroom research to synthesize

CdS-NPs and have been utilized in industry applications. *Coriolus versicolor*-CdS-NPs were effectively formed using a mixture of exogenous biomass and cadmium sulphide,the NPs range in size from 100 to 200 nm and had a spherical morphology [73]. Extracellular environment produced spherical nanoparticles of C. versicolor CdS-NPs with a diameter of approximately 100–3000 nm [87]. While in *P. ostreatus*, the Cd-NPs were approximately 4–5 nm in diameter and circular [90], which are used in a variety of commercial processes.

## 6 Advantages of Mushroom Nanoparticles

In comparison to other microorganisms, greener nanotechnology employing a mushroom as a bioprocessing component leads in the development of smaller, better, safer, cheaper, more renewable, and more exact goods. It enables the production of nanoparticles with various sizes, forms, chemical makeup, and dispersion under controllable circumstances without using harmful agents. Production of metals from biological agents, such as employing AgNPs and microorganisms, is regarded to be ecologically responsible and is acquiring status due to the suitable solvent, reductants, and non-toxic substance used to stabilize the nanoparticles [91]. Metallic nanoparticles generated by basidiomycetes mushrooms are more persistent and ecofriendly than those derived from plants as well as other life forms [92, 93]. Mushrooms could be utilized to manufacture enormous quantities of nanoparticles due to its capacity to synthesize significant levels of protein, which subsequently increase nanoparticle creation. Due to their resilience to circulation, turbulence, and severe conditions seen in compartments such as bioreactors, fungus or mushrooms make good biological catalysts for pilot-scale manufacturing. Utilizing these organisms in a bioreactor result in the production of extracellular reducing proteins that are beneficial in following processing steps, and the cells itself could be controlled in a variety of material sciences and nanotechnology-related ways. Additionally, mushroom extracts are extremely good sources of protein, amino acids, carbohydrates, and minerals, including those that serve as reducing, stabilising, and encapsulating elements for the nanoparticle manufacturing process when compared to previously documented biosynthesis pathways [80]. Current research has established a stronger correlation among mushroom manufacturing of metallic nanoparticles and antibacterial activity. The formation of synthesized nanoparticles from biological molecules found in various microorganisms prevents the development and proliferation of a variety of bacteria. Nanoparticles are hypothesized to create free radicals and oxidative stress, whereby induce apoptosis, ultimately preventing its multiplication [94]. Due to such novel, unexpected various physicochemical characteristics, and pharmacological activity, they are being used in various medical applications [38].

Despite mushrooms can produce nanoparticles with appropriate sizes, especially in monodispersity [95], their influence of nanoparticles varies from mushrooms to

mushrooms, and underlying pathway is unknown, consequently, that there is much more to learn further about circumstance [96]. Nevertheless, as a well-established scientific area of research, a conceptual framework will develop.

# 7 Application of Mushroom Nanoparticles

## *7.1 Biomedical Applications*

It has historically been established that edible mushrooms possess therapeutic effects. Numerous bioactive components containing immunomodulatory properties have already been identified and more study is underway. Carbohydrates, proteoglycans, triterpenoids, and mushroom immuno stimulators are all contained in the mushrooms [21, 97]. The mushroom within the entirety or their extracts has shown to be advantageous because of its bioactive polymers and capacity to assist to antimicrobial, antivirus, antitumor, antioxidants, haematological, and cytotoxic effects. Metallic nanoparticles are now getting generated from a variety of important medicinal genera and its therapeutic potential is now being investigated.

### 7.1.1 Antimicrobial Potential

The pharmacological efficacy of mycosynthesized nanoparticles has been extensively investigated for pharmaceutical applications, most notably in bactericidal, fungicidal, antitumor, and biosensor uses. Silver nanoparticles constitute sources of bioactive compounds of exceptional efficacy. Silver nanoparticles derived from crude polysaccharide aqueous extracts *A. bisporus*, *A. brasiliensis*, and *Phellinus linteus* have been evaluated against pathogenic organisms and found to have a substantially lower minimum inhibitory concentration than the reference amoxicillin, indicating that all these ecofriendly biomaterials may be used as prospective antibacterial drugs [98]. Furthermore, iron nanomaterials derived from *P. florida* have been evaluated against a range of human infections and shown equal antibacterial effectiveness towards the pathogenic microbes while exhibiting a greater diameter of resistance region towards the reference antibiotic, ampicillin [99]. A graphene oxide composite derived from *G. lucidum* displayed a species-specific bactericidal effect against gram-positive and gram-negative organisms [100]. *P. ostreatus* similarly displayed antibacterial and α-amylase inhibition effect when coated with silver nanomaterials [101, 102]. Additionally, nanomaterials derived from G. lucidum displayed antioxidant and antibacterial properties [103, 104]. These studies reveal that mushroom-derived nanoparticles as possible antimicrobial drugs do have a lot of promise for pharmaceutical formulation. Another intriguing topic for medicinal uses is the anti-fungal capability of mushroom-based nanoparticles. Gold nanoparticles generated through hydrothermal technique

from A. bisporus extraction and nanomaterials synthesized from Inonotus hispidus exhibited exceptional anti-fungal efficacy towards *Aspergillus flavus, A. niger*, and *A. terreus* [105, 106].

### 7.1.2 Anti-tumour Potential

The mushroom polysaccharide alteration enhanced the therapeutic effects of Se-nanoparticles. This alteration increased Se-nanoparticles' accessibility, durability, bio-compatibility, and malignant specificity. By activating caspase- and mitochondria-mediated apoptosis, the altered Se-nanoparticles demonstrated improved carcinogenic activity in vivo, and hence ultimate antiproliferative effectiveness [107]. $TiO_2$ nanoparticles derived from *P. djamor* exhibited antitumor effect towards A549 cancerous cells [83]. The in vitro study of Au–Pt nanoparticles on human colon cancer cell lines (HCT 116) revealed dose-dependent apoptotic efficacy [108]. A graphene oxide nanoparticle with outstanding antitumor characteristics was produced using *G. lucidum* mushrooms extraction [109] that demonstrated cytotoxicity to cancerous cells while remaining nontoxic with healthy cell cultures. Additional cancer treatment approach was established by synthesising palladium (Pd) nanomaterials from chaga mushroom (*I. obliquus*) extracts. Despite their anticancerous properties, these nanomaterials were used to distribute anticancer drug in a regulated manner via electrostatic contact and photothermal transformation utilising 808 nm lasers. The synergy of mushroom bioactive compounds with nanoparticles can change cancer treatment in the long term [110].

## *7.2 Other Industrial Applications*

Nutrition, beauty, sensing, and water purification are just a few of the commercial processes for mycosynthesized nanoparticles. The phytochemical and pharmacological properties of mushroom-based nanoparticles can promote value and safety of food and quality, as well as shelf life [111]. Myogenic ZnO nanoparticles inhibited the growth of infectious and pathogenic microbes effectively [112]. Additionally, determining the substance of food is yet another method for determining the nutritional values,thus, myconanomaterials have been used as detectors to detect harmful metallic ions in food and supplies [113]. Due to the antioxidants, antimicrobial characteristics of mushroom-based nanoparticles, they are attractive as cosmetics and personal care products. Due to their high antioxidant content and ability to reduce oxidative stress, mushroom-derived biological molecules have a high economic value. In comparison to the conventional samples, antioxidant derived from diverse mushroom demonstrated superior antioxidants capabilities, rendering them desirable aesthetic ingredients [114].

Indigo dyes are one of the most widely used chemical dye in the textile manufacturing, as they contain aromatic molecules having complicated poisonous and

harmful properties. The elimination of indigo dyes is a critical stage in treating wastewater in which these biodegradable Ag nanoparticles are used [115]. Methylene blue is a hazardous contaminant that has a negative impact on public health. Since methylene blue degradation is a kinetically undesirable process, sorption process using nanocatalysts is a possible option in this field [116]. Adsorption activity was observed for green biosynthesized Ag-nanoparticles from Agaricus species. Ag-nanoparticles were employed to decrease methylene blue using NaBH4, which resulted in a 5-min reduction [117]. Au-nanoparticles produced from Portabello mushrooms and A. bisporus basidiocarp demonstrated outstanding breakdown of methylene blue dye, with a decolourization rate of ~98% [118]. Nanotubes derived from culinary or therapeutic mushroom have also been explored for use in treating wastewater [7]. Au-nanoparticles synthesized from the *Flammulina* sp. demonstrated high catalytic activity for decolourizing methylene blue dye, with the best decolourization rate of ~75% with a incubation time of 4 h [119]. Furthermore, Au-nanoparticles produced intracellularly using *F. velutipes* mycelia exhibited varied catalytic performance in the reduction of a variety of organic contaminants, including methylene blue and 4-nitrophenol, exhibiting pseudo-first-order kinetics [44].

The gold-silver composites prepared from *Ramaria botrytis* mushroom polysaccharides were assessed for its catalytic properties in degrading p-nitrophenol [120]. To measure zinc ($Zn^{2+}$) atoms in Ag-nanoparticles synthesized from *Tricholoma* mushroom polysaccharide, a highly precise electroanalytical device has been devised. Even at concentrations less than 1 nM, this biosensor demonstrated a specific and sensitive responsiveness to aqueous Zn ions. Furthermore, additional biosensor was constructed using a grafting copolymer–CuO composites derived from *Tricholoma* mushroom polysaccharides in detection of thorium ($Th^{4+}$) ions in an aqueous medium through optically, spectrophotometric, and electrolytic approaches [121]. Similarly, Ag-nanoparticles derived from *A. bisporus* demonstrated excellent electronic and optoelectronic detection capabilities for identifying mercury (Hg (II) ions) in samples collected [122]. Nanomaterials are also employed for packaged foods and coatings due to their exceptional capabilities in reducing respiratory and enzymatic browning [123] and a comparable investigation with chitosan has indeed been published [124].

## 8 Conclusion and Future Perspectives

Metallic nanomaterials have indeed been created in a sustainable way from a variety of fungus, most notably the basidiomycetes mushroom, in recent times. Mushrooms have been used to produce nanoparticles as a comparatively recent effort in nanobiotechnology. However, the concept has gained momentum due to several benefits, including ease of extraction processes, protein-rich contents in mushroom, relatively inexpensive, and simple scaling up of production. Extracellular and intracellular reductases have indeed been implicated in the creation of nanomaterials. Mushrooms offer an innovative and low-cost approach for recycling agricultural

residues and by-products creating renewable biomaterials. Studies give pertinent data regarding the effect of each processing parameter on the synthesized material's qualities. The mushroom-based composites' primary structure is deduced from three basic frames: (a) constituents including such fungal species and medium, (b) operating factors, and (c) applicability. Mushrooms, as a conventional resource of natural bioactive chemicals, could be used to create biocomposites for use in the pharmaceutical, biotechnology, and cosmetics applications. While mushroom-derived nanomaterials have already been gaining uses in pharmaceuticals and bioengineering, it emerges as though we have just scraped the surface. In the future, mushrooms could be genetically manipulated to generate much of the enzymes responsible for nanoparticle generation. The improved understanding of the processes underlying in the mycosynthesis of nanoparticles is crucial at this phase because variability in the process across mushroom species can aid in identifying alternative biosynthetic approaches and in modulating the dimensions, form, and gain of nanoparticles for use in healthcare, farming, and future technologies.

**Acknowledgements** The authors thankfully recognize the support of the management of MGR College in Hosur, Tamilnadu, India.

**Conflicts of Interest** None to declare.

## References

1. Foldbjerg R, Jiang X, Miclăuş T, Chen C, Autrup H, Beer C (2015) Silver nanoparticles–wolves in sheep's clothing? Toxicol Res 4(3):563–575
2. Matsoukas T, Desai T, Lee K (2015) Engineered nanoparticles and their applications. J Nanomater 2015
3. Zhang Y, Leu YR, Aitken RJ, Riediker M (2015) Inventory of engineered nanoparticle-containing consumer products available in the Singapore retail market and likelihood of release into the aquatic environment. Int J Environ Res Public Health 12(8):8717–8743
4. Khan AU, Malik N, Khan M, Cho MH, Khan MM (2018) Fungi-assisted silver nanoparticle synthesis and their applications. Bioprocess Biosyst Eng 41(1):1–20
5. Atkins FC, Haycraft WC (2014) Mushroom growing today. Read Books Ltd
6. Cheung PCK (2010) The nutritional and health benefits of mushrooms. Nutr Bull 35(4):292–299
7. Owaid MN, Ibraheem IJ (2017) Mycosynthesis of nanoparticles using edible and medicinal mushrooms. Eur J Nanomed 9(1):5–23
8. Moghaddam BA, Namvar F, Moniri M, Azizi S, Mohamad R (2015) Nanoparticles biosynthesized by fungi and yeast: a review of their preparation, properties, and medical applications. Molecules 20(9):16540–16565
9. Carrasco J, Zied DC, Pardo JE, Preston GM, Pardo-Giménez A (2018) Supplementation in mushroom crops and its impact on yield and quality. AMB Express 8(1):1–9
10. El Sheikha AF, Hu DM (2018) How to trace the geographic origin of mushrooms? Trends Food Sci Technol 78:292–303
11. Upadhyaya J, Raut JK, Koirala N (2017) Analysis of nutritional and nutraceutical properties of wild-grown mushrooms of Nepal. EC Microbiol 2(3):136–145
12. Cardwell G, Bornman JF, James AP, Black LJ (2018) A review of mushrooms as a potential source of dietary vitamin D. Nutrients 10(10):1498

13. Rathore H, Prasad S, Sharma S (2017) Mushroom nutraceuticals for improved nutrition and better human health: a review. PharmaNutrition 5(2):35–46
14. Samsudin NIP, Abdullah N (2019) Edible mushrooms from Malaysia; a literature review on their nutritional and medicinal properties. Int Food Res J 26(1):11–31
15. Li H, Tian Y, Menolli N Jr, Ye L, Karunarathna SC, Perez-Moreno J, Rahman MM, Rashid MH, Phengsintham P, Rizal L, Kasuya T (2021) Reviewing the world's edible mushroom species: a new evidence-based classification system. Compr Rev Food Sci Food Safety 20(2):1982–2014
16. Rathore H, Sehwag S, Prasad S, Sharma S (2019) Technological, nutritional, functional and sensorial attributes of the cookies fortified with Calocybe indica mushroom. J Food Measure Charact 13(2):976–987
17. Roncero-Ramos I, Mendiola-Lanao M, Pérez-Clavijo M, Delgado-Andrade C (2017) Effect of different cooking methods on nutritional value and antioxidant activity of cultivated mushrooms. Int J Food Sci Nutr 68(3):287–297
18. FAOSTAT (2019) Mushrooms and truffles. http://www.fao.org/faostat/en/#data/QC. Accessed 12 Aug 2019
19. Royse DJ, Baars J, Tan Q (2017) Current overview of mushroom production in the world. Edible and medicinal mushrooms: technology and applications, pp 5–13
20. Kayode RMO, Olakulehin TF, Adedeji BS, Ahmed O, Aliyu TH, Badmos AHA (2015) Evaluation of amino acid and fatty acid profiles of commercially cultivated oyster mushroom (Pleurotus sajor-caju) grown on gmelina wood waste. Niger Food J 33(1):18–21
21. Valverde ME, Hernández-Pérez T, Paredes-López O (2015) Edible mushrooms: improving human health and promoting quality life. Int J Microbiol 2015:1–14
22. Papadaki A, Diamantopoulou P, Papanikolaou S, Philippoussis A (2019) Evaluation of biomass and chitin production of Morchella mushrooms grown on starch-based substrates. Foods 8(7):239
23. Illuri R, Kumar M, Eyini M, Veeramanikandan V, Almaary KS, Elbadawi YB, Biraqdar MA, Balaji P (2021) Production, partial purification and characterization of ligninolytic enzymes from selected basidiomycetes mushroom fungi. Saudi J Biol Sci 28(12):7207–7218
24. Pothiraj C, Balaji P, Eyini M (2006) Enhanced production of cellulases by various fungal cultures in solid state fermentation of cassava waste. Afr J Biotechnol 5(20)
25. Madhanraj R, Ravikumar K, Maya MR, Illuri R, Venkatakrishna K, Rameshkumar K, Veeramanikandan V, Eyini M, Paulraj B (2019) Evaluation of anti-microbial and anti-haemolytic activity of edible basidiomycetes mushroom fungi. J Drug Deliv Ther 9(1):132–135
26. Balaji P, Madhanraj R, Rameshkumar K, Veeramanikandan V, Eyini M, Arun A, Thulasinathan B, Al Farraj DA, Elshikh MS, Alokda AM, Mahmoud AH (2020) Evaluation of antidiabetic activity of Pleurotus pulmonarius against streptozotocin-nicotinamide induced diabetic wistar albino rats. Saudi J Biol Sci 27(3):913–924
27. Madhanraj R, Eyini M, Balaji P (2017) Antioxidant assay of gold and silver nanoparticles from edible basidiomycetes mushroom fungi. Free Radicals Antioxid 7(2):137–142
28. Boobalan T, Sethupathi M, Sengottuvelan N, Kumar P, Balaji P, Gulyás B, Padmanabhan P, Selvan ST, Arun A (2020) Mushroom-derived carbon dots for toxic metal ion detection and as antibacterial and anticancer agents. ACS Appl Nano Mater 3(6):5910–5919
29. Dhillon GS, Brar SK, Kaur S, Verma M (2012) Green approach for nanoparticle biosynthesis by fungi: current trends and applications. Crit Rev Biotechnol 32(1):49–73
30. Gade A, Ingle A, Whiteley C, Rai M (2010) Mycogenic metal nanoparticles: progress and applications. Biotech Lett 32(5):593–600
31. Sahu T, Ratre YK, Chauhan S, Bhaskar LVKS, Nair MP, Verma HK (2021) Nanotechnology based drug delivery system: current strategies and emerging therapeutic potential for medical science. J Drug Delivery Sci Technol 63:102487
32. Dobrovolskaia MA (2015) Pre-clinical immunotoxicity studies of nanotechnology-formulated drugs: Challenges, considerations and strategy. J Control Release 220:571–583
33. El-Sayed A, Kamel M (2020) Advances in nanomedical applications: diagnostic, therapeutic, immunization, and vaccine production. Environ Sci Pollut Res 27(16):19200–19213

34. Vaseghi Z, Nematollahzadeh A, Tavakoli O (2018) Green methods for the synthesis of metal nanoparticles using biogenic reducing agents: a review. Rev Chem Eng 34(4):529–559
35. Kalia A, Kaur G (2018) Biosynthesis of nanoparticles using mushrooms. In: Biology of Macrofungi, pp 351–360. Springer, Cham
36. Mirunalini S, Arulmozhi V, Deepalakshmi K, Krishnaveni M (2012) Intracellular biosynthesis and antibacterial activity of silver nanoparticles using edible mushrooms. Notulae Scientia Biologicae 4(4):55–61
37. Duhan JS, Kumar R, Kumar N, Kaur P, Nehra K, Duhan S (2017) Nanotechnology: the new perspective in precision agriculture. Biotechnol Rep 15:11–23
38. Owaid MN, Al-Saeedi SSS, Abed IA (2017) Biosynthesis of gold nanoparticles using yellow oyster mushroom Pleurotus cornucopiae var. citrinopileatus. Environ Nanotechnol Monitor Manag 8:157–162
39. McQuillan JS, Groenaga Infante H, Stokes E, Shaw AM (2012) Silver nanoparticle enhanced silver ion stress response in Escherichia coli K12. Nanotoxicology 6(8):857–866
40. Kreibig U, Vollmer M (1995) Optical properties of metal clusters. Springer Series in Material Science, 25
41. Narayanan R, El-Sayed MA (2003) Effect of catalytic activity on the metallic nanoparticle size distribution: electron-transfer reaction between Fe (CN) 6 and thiosulfate ions catalyzed by PVP− platinum nanoparticles. J Phys Chem B 107(45):12416–12424
42. Owaid MN (2020) Biomedical applications of nanoparticles synthesized from mushrooms. In: Patra J, Fraceto L, Das G, Campos E (eds) Green nanoparticles, pp 289–303.
43. Sudhakar T, Nanda A, Babu SG, Janani S, Evans MD, Markose TK (2014) Synthesis of silver nanoparticles from edible mushroom and its antimicrobial activity against human pathogens. Int J PharmTech Res 6(5):1718–1723
44. Narayanan KB, Park HH, Han SS (2015) Synthesis and characterization of biomatrixed-gold nanoparticles by the mushroom Flammulina velutipes and its heterogeneous catalytic potential. Chemosphere 141:169–175
45. Paul S, Singh AR, Sasikumar CS (2015) Green synthesis of bio-silver nanoparticles by Parmelia perlata, Ganoderma lucidum and Phellinus igniarius & their fields of application. Indian J Res Pharm Biotechnol 3(2):100
46. Raman J, Reddy GR, Lakshmanan H, Selvaraj V, Gajendran B, Nanjian R, Chinnasamy A, Sabaratnam V (2015) Mycosynthesis and characterization of silver nanoparticles from Pleurotus djamor var. roseus and their in vitro cytotoxicity effect on PC3 cells. Process Biochem 50(1):140–147
47. Shivashankar M, Premkumari B, Chandan N (2013) Biosynthesis, partial characterization and antimicrobial activities of silver nanoparticles from pleurotus species. Int J Integ Sci Innov Technol 2:13–23
48. Sujatha S, Kanimozhi G, Panneerselvam A (2015) Synthesis of silver nanoparticles from Lentinula edodes and antibacterial activity. Int J Pharm Sci Rev Res 33:189–191
49. Yehia RS, Al-Sheikh H (2014) Biosynthesis and characterization of silver nanoparticles produced by Pleurotus ostreatus and their anticandidal and anticancer activities. World J Microbiol Biotechnol 30(11):2797–2803
50. Karthikeyan V, Ragunathan R, Johney J, Kabesh K (2019) Green synthesis of silver nanoparticles and application in dye decolorization by Pleurotus ostreatus (MH591763). J Biosci Biotechnol 8(1):80–86
51. Bhat R, Deshpande R, Ganachari SV, Huh DS, Venkataraman A (2011) Photo-irradiated biosynthesis of silver nanoparticles using edible mushroom Pleurotus florida and their antibacterial activity studies. Bioinorg Chem Appl 2011
52. Sen IK, Maity K, Islam SS (2013) Green synthesis of gold nanoparticles using a glucan of an edible mushroom and study of catalytic activity. Carbohyd Polym 91(2):518–528
53. Sujatha S, Tamilselvi S, Subha K, Panneerselvam A (2013) Studies on biosynthesis of silver nanoparticles using mushroom and its antibacterial activities. Int J Curr Microbiol App Sci 2(12):605–614

54. Bhardwaj AK, Shukla A, Maurya S, Singh SC, Uttam KN, Sundaram S, Singh MP, Gopal R (2018) Direct sunlight enabled photo-biochemical synthesis of silver nanoparticles and their Bactericidal Efficacy: photon energy as key for size and distribution control. J Photochem Photobiol B Biol 188:42–49. https://doi.org/10.1016/j.jphotobiol.2018.08.019
55. Owaid MN (2013) Testing efficiency of different agriculture media in growth and production of four species of oyster mushroom Pleurotus and evaluation the bioactivity of tested species. Doctoral dissertation, Ph. D. Dissertation. University of Anbar, Ramadi, Iraq
56. Nithya R, Ragunathan R (2009) Synthesis of silver nanoparticle using Pleurotus sajor caju and its antimicrobial study. Dig J Nanomater Biostruct 4(4):623–629
57. Nithya R (2012) A novel biological approach for the synthesis of silver nanoparticles using Brevibacterium linens, Pleurotus Sajor Caju and Aspergillus niger—a comparative study and their applications. Shri Nehru Maha Vidhyalaya College of Arts and Science, Institute of Management Studies and Bioscience Research Center, Bharathiar University, India
58. Musa SF, Yeat TS, Kamal LZM, Tabana YM, Ahmed MA, El Ouweini A, Lim V, Keong LC, Sandai D (2018) Pleurotus sajor-caju can be used to synthesize silver nanoparticles with antifungal activity against Candida albicans. J Sci Food Agric 98(3):1197–1207
59. Raman J, Hariprasath Lakshmanan PAJ, Zhijian C, Periasamy V, David P, Naidu M, Sabaratnam V (2015) Neurite outgrowth stimulatory effects of myco synthesized auNPs from Hericium erinaceus (Bull.: Fr.) Pers. on pheochromocytoma (Pc-12) cells. Int J Nanomed 10:5853
60. Wu H, Zhu H, Li X, Liu Z, Zheng W, Chen T, Yu B, Wong KH (2013) Induction of apoptosis and cell cycle arrest in A549 human lung adenocarcinoma cells by surface-capping selenium nanoparticles: an effect enhanced by polysaccharide–protein complexes from Polyporus rhinocerus. J Agric Food Chem 61(41):9859–9866
61. Chan SY, Don MM (2013) Biosynthesis and structural characterization of Ag nanoparticles from white rot fungi. Mater Sci Eng C 33(1):282–288
62. Arun G, Eyini M, Gunasekaran P (2014) Green synthesis of silver nanoparticles using the mushroom fungus Schizophyllum commune and its biomedical applications. Biotechnol Bioprocess Eng 19(6):1083–1090
63. Numata M, Hasegawa T, Fujisawa T, Sakurai K, Shinkai S (2004) β-1, 3-Glucan (schizophyllan) can act as a one-dimensional host for creation of novel poly (aniline) nanofiber structures. Org Lett 6(24):4447–4450
64. Shah V, Dobiášová P, Baldrian P, Nerud F, Kumar A, Seal S (2010) Influence of iron and copper nanoparticle powder on the production of lignocellulose degrading enzymes in the fungus Trametes versicolor. J Hazard Mater 178(1–3):1141–1145
65. Jakubiak M, Giska I, Asztemborska M, Bystrzejewska-Piotrowska G (2014) Bioaccumulation and biosorption of inorganic nanoparticles: factors affecting the efficiency of nanoparticle mycoextraction by liquid-grown mycelia of Pleurotus eryngii and Trametes versicolor. Mycol Prog 13(3):525–532
66. Nath BP, Niture SR, Jadhav SD, Boid SO (2015) Biosynthesis and characterization of silver nanoparticles produced by microorganisms isolated from Agaricus bisporus. Int J Curr Microbiol Appl Sci 4(2):330–342
67. Owaid MN, Raman J, Lakshmanan H, Al-Saeedi SSS, Sabaratnam V, Abed IA (2015) Mycosynthesis of silver nanoparticles by Pleurotus cornucopiae var. citrinopileatus and its inhibitory effects against Candida sp. Mater Lett 153:186–190
68. Mouxing FU, Qingbiao LI, Daohua SUN, Yinghua LU, Ning HE, Xu DENG, Huixuan WANG, Huang J (2006) Rapid preparation process of silver nanoparticles by bioreduction and their characterizations. Chin J Chem Eng 14(1):114–117
69. Elumalai S, Devika R, Arumugam P, Kasinathan K (2012) Biosynthesis of silver nanoparticles using the fungus *Pleurotus ostreatus* and their antibacterial activity. J Nanosci Nanoeng Appl 1(2):557
70. Kaur T, Kapoor S, Kalia A (2018) Synthesis of silver nanoparticles from Pleurotus florida, characterization and analysis of their antimicrobial activity. Int J Curr Microbiol Appl Sci 7:4085–4095

71. Latha S (2010) Extracellular biosynthesis, characterization and in vitro antimicrobial potential of silver nanoparticles using myconanofactoris. Bharathidasan University, Tiruchirappalli
72. Sastry M, Mayya KS, Bandyopadhyay K (1997) pH Dependent changes in the optical properties of carboxylic acid derivatized silver colloidal particles. Colloids Surf, A 127(1–3):221–228
73. Sanghi R, Verma P (2009) A facile green extracellular biosynthesis of CdS nanoparticles by immobilized fungus. Chem Eng J 155(3):886–891
74. Meng TX, Furuta S, Fukamizu S, Yamamoto R, Ishikawa H, Arung ET, Shimizu K, Ohga S, Kondo R (2011) Evaluation of biological activities of extracts from the fruiting body of Pleurotus citrinopileatus for skin cosmetics. J Wood Sci 57(5):452–458
75. Egorova EM, Kaba SI, Kubatiev AA (2016) Toxicity of silver nanoparticles obtained by bioreduction as studied on malignant cells: is it possible to create a new generation of anticancer remedies?. In: Nanobiomaterials in cancer therapy, pp 505–542. William Andrew Publishing
76. Dasgupta N, Ranjan S, Mishra D, Ramalingam C (2018) Thermal Co-reduction engineered silver nanoparticles induce oxidative cell damage in human colon cancer cells through inhibition of reduced glutathione and induction of mitochondria-involved apoptosis. Chem Biol Interact 295:109–118
77. Franco-Molina MA, Mendoza-Gamboa E, Sierra-Rivera CA, Gómez-Flores RA, Zapata-Benavides P, Castillo-Tello P, Alcocer-González JM, Miranda-Hernández DF, Tamez-Guerra RS, Rodríguez-Padilla C (2010) Antitumor activity of colloidal silver on MCF-7 human breast cancer cells. J Exp Clin Cancer Res 29(1):1–7
78. Jacob SJP, Finub JS, Narayanan A (2012) Synthesis of silver nanoparticles using Piper longum leaf extracts and its cytotoxic activity against Hep-2 cell line. Colloids Surf B 91:212–214
79. Bhat R, Sharanabasava VG, Deshpande R, Shetti U, Sanjeev G, Venkataraman A (2013) Photo-bio-synthesis of irregular shaped functionalized gold nanoparticles using edible mushroom Pleurotus florida and its anticancer evaluation. J Photochem Photobiol B 125:63–69
80. Philip D (2009) Biosynthesis of Au, Ag and Au–Ag nanoparticles using edible mushroom extract. Spectrochim Acta Part A Mol Biomol Spectrosc 73(2):374–381
81. Sarkar J, Roy SK, Laskar A, Chattopadhyay D, Acharya K (2013) Bioreduction of chloroaurate ions to gold nanoparticles by culture filtrate of Pleurotus sapidus Quel. Mater Lett 92:313–316
82. Senapati US, Sarkar D (2014) Characterization of biosynthesized zinc sulphide nanoparticles using edible mushroom Pleurotuss ostreatu. Indian J Phys 88(6):557–562
83. Manimaran K, Murugesan S, Ragavendran C, Balasubramani G, Natarajan D, Ganesan A, Seedevi P (2020) Biosynthesis of tio 2 nanoparticles using edible mushroom (pleurotus djamor) extract: Mosquito larvicidal, histopathological, antibacterial and anticancer effect. J Cluster Sci:1–12
84. Senapati US, Jha DK, Sarkar D (2015) Structural, optical, thermal and electrical properties of fungus guided biosynthesized zinc sulphide nanoparticles. Res J Chem Sci 2231:33–40
85. Wu HF, Kailasa SK, Shastri L (2010) Electrostatically self-assembled azides on zinc sulfide nanoparticles as multifunctional nanoprobes for peptide and protein analysis in MALDI-TOF MS. Talanta 82(2):540–547
86. Mazumdar H, Haloi N (2011) A study on biosynthesis of iron nanoparticles by Pleurotus sp. J Microbiol Biotechnol Res 1(3):39–49
87. Chen GQ, Zou ZJ, Zeng GM, Yan M, Fan JQ, Chen AW, Yang F, Zhang WJ, Wang L (2011) Coarsening of extracellularly biosynthesized cadmium crystal particles induced by thioacetamide in solution. Chemosphere 83(9):1201–1207
88. Ma L, Peng Y, Wu B, Lei D, Xu H (2013) Pleurotus ostreatus nanoparticles as a new nano-biosorbent for removal of Mn (II) from aqueous solution. Chem Eng J 225:59–67
89. Nasrin T, Roy S, Das TK (2014) Aspergillus foetidus mediated biosynthesis of CdS nano particles and its characterization. Int J Innov Res Sci Eng 2:633–639
90. Borovaya M, Pirko Y, Krupodorova T, Naumenko A, Blume Y, Yemets A (2015) Biosynthesis of cadmium sulphide quantum dots by using Pleurotus ostreatus (Jacq.) P. Kumm. Biotechnol Biotechnol Equip 29(6):1156–1163

91. Bhattacharjee S, Debnath G, Das AR, Saha AK, Das P (2017) Characterization of silver nanoparticles synthesized using an endophytic fungus, Penicillium oxalicum having potential antimicrobial activity. Adv Nat Sci Nanosci Nanotechnol 8(4):045008
92. Prasad R, Kumar V, Kumar M, Wang S (eds) (2018) Fungal nanobionics: principles and applications. Springer, Singapore
93. Sriramulu M, Sumathi S (2017) Photocatalytic, antioxidant, antibacterial and anti-inflammatory activity of silver nanoparticles synthesised using forest and edible mushroom. Adv Nat Sci Nanosci Nanotechnol 8(4):045012
94. Siddiqi KS, Husen A, Rao RA (2018) A review on biosynthesis of silver nanoparticles and their biocidal properties. J Nanobiotechnol 16(1):1–28
95. Yadav KK, Singh JK, Gupta N, Kumar VJJMES (2017) A review of nanobioremediation technologies for environmental cleanup: a novel biological approach. J Mater Environ Sci 8(2):740–757
96. Manzoor-Ul-Haq RV, Patil S, Singh D, Krishnaveni R (2014) Isolation and screening of mushrooms for potent silver nanoparticles production from Bandipora District (Jammu and Kashmir) and their characterization. Int J Curr Microbiol Appl Sci 3:704–714
97. Sonawane H, Bhosle S, Bapat G, Vikram G (2014) Pharmaceutical metabolites with potent bioactivity from mushrooms. J Pharm Res 8(7):969–972
98. Klaus A, Petrovic P, Vunduk J, Pavlovic V, Van Griensven LJLD (2020) The antimicrobial activities of silver nanoparticles synthesized from medicinal mushrooms. Int J Med Mushrooms 22(9)
99. Gurusamy M, Raju R (2021) Biosynthesis of Iron Nanoparticles from Pleurotus florida and its Antimicrobial Activity against Selected Human Pathogens. Indian J Pharm Sci 83(1):45–51
100. Bai RG, Muthoosamy K, Shipton FN, Pandikumar A, Rameshkumar P, Huang NM, Manickam S (2016) The biogenic synthesis of a reduced graphene oxide–silver (RGO–Ag) nanocomposite and its dual applications as an antibacterial agent and cancer biomarker sensor. RSC Adv 6(43):36576–36587
101. Al-Bahrani R, Raman J, Lakshmanan H, Hassan AA, Sabaratnam V (2017) Green synthesis of silver nanoparticles using tree oyster mushroom Pleurotus ostreatus and its inhibitory activity against pathogenic bacteria. Mater Lett 186:21–25
102. Debnath G, Das P, Saha AK (2019) Green synthesis of silver nanoparticles using mushroom extract of Pleurotus giganteus: characterization, antimicrobial, and α-amylase inhibitory activity. Bionanoscience 9(3):611–619
103. Al-Ansari MM, Dhasarathan P, Ranjitsingh AJA, Al-Humaid LA (2020) Ganoderma lucidum inspired silver nanoparticles and its biomedical applications with special reference to drug resistant Escherichia coli isolates from CAUTI. Saudi J Biol Sci 27(11):2993–3002
104. Priyadarshni KC, Mahalingam PU (2019) Biofunctionalization of mycosynthesized silver nanoparticles on selected drug resistant human pathogens. Mater Res Express 6(8):085056
105. Eskandari-Nojedehi M, Jafarizadeh-Malmiri H, Rahbar-Shahrouzi J (2018) Hydrothermal green synthesis of gold nanoparticles using mushroom (Agaricus bisporus) extract: physicochemical characteristics and antifungal activity studies. Green Process Synth 7(1):38–47
106. Jaloot AS, Owaid MN, Naeem GA, Muslim RF (2020) Mycosynthesizing and characterizing silver nanoparticles from the mushroom Inonotus hispidus (Hymenochaetaceae), and their antibacterial and antifungal activities. Environ Nanotechnol Monit Manag 14:100313
107. Zeng D, Zhao J, Luk KH, Cheung ST, Wong KH, Chen T (2019) Potentiation of in vivo anticancer efficacy of selenium nanoparticles by mushroom polysaccharides surface decoration. J Agric Food Chem 67(10):2865–2876
108. Chaturvedi VK, Yadav N, Rai NK, Ellah NHA, Bohara RA, Rehan IF, Marraiki N, Batiha GES, Hetta HF, Singh MP (2020) Pleurotus sajor-caju-mediated synthesis of silver and gold nanoparticles active against colon cancer cell lines: a new era of herbonanoceutics. Molecules 25(13):3091
109. Muthoosamy K, Abubakar IB, Bai RG, Loh HS, Manickam S (2016) Exceedingly higher co-loading of curcumin and paclitaxel onto polymer-functionalized reduced graphene oxide for highly potent synergistic anticancer treatment. Sci Rep 6(1):1–14

110. Gil YG, Kang S, Chae A, Kim YK, Min DH, Jang H (2018) Synthesis of porous Pd nanoparticles by therapeutic chaga extract for highly efficient tri-modal cancer treatment. Nanoscale 10(42):19810–19817
111. Shen HS, Shao S, Chen JC, Zhou T (2017) Antimicrobials from mushrooms for assuring food safety. Compr Rev Food Sci Food Safety 16(2):316–329
112. Sumanth B, Lakshmeesha TR, Ansari MA, Alzohairy MA, Udayashankar AC, Shobha B, Niranjana SR, Srinivas C, Almatroudi A (2020) Mycogenic synthesis of extracellular zinc oxide nanoparticles from xylaria acuta and its nanoantibiotic potential. Int J Nanomed 15:8519
113. Mohiuddin AK (2019) Chemical residues in food grains: the burning health issues in Asian countries. J Nutr Food Sci 2006. Henry Publishing Groups Mohiuddin AK 2(1):100006
114. Sharpe E, Farragher-Gnadt AP, Igbanugo M, Huber T, Michelotti JC, Milenkowic A, Ludlam S, Walker M, Hanes D, Bradley R, Bou-Abdallah F (2021) Comparison of antioxidant activity and extraction techniques for commercially and laboratory prepared extracts from six mushroom species. J Agric Food Res 4:100130
115. Chowdhury MF, Khandaker S, Sarker F, Islam A, Rahman MT, Awual MR (2020) Current treatment technologies and mechanisms for removal of indigo carmine dyes from wastewater: a review. J Mol Liq:114061
116. Begum R, Najeeb J, Sattar A, Naseem K, Irfan A, Al-Sehemi AG, Farooqi ZH (2020) Chemical reduction of methylene blue in the presence of nanocatalysts: a critical review. Rev Chem Eng 36(6):749–770
117. Bhangale HG, Bachhav SG, Sarode KM, Patil DR (2020) Green synthesis of silver nanoparticles using mushroom species, their characterization and catalytic activity. In: Techno-Societal 2018, pp 329–335. Springer, Cham
118. Dheyab MA, Owaid MN, Rabeea MA, Aziz AA, Jameel MS (2020) Mycosynthesis of gold nanoparticles by the Portabello mushroom extract, Agaricaceae, and their efficacy for decolorization of Azo dye. Environ Nanotechnol Monitor Manag 14:100312
119. Rabeea MA, Owaid MN, Aziz AA, Jameel MS, Dheyab MA (2020) Mycosynthesis of gold nanoparticles using the extract of Flammulina velutipes, Physalacriaceae, and their efficacy for decolorization of methylene blue. J Environ Chem Eng 8(3):103841
120. Bhanja SK, Samanta SK, Mondal B, Jana S, Ray J, Pandey A, Tripathy T (2020) Green synthesis of Ag@ Au bimetallic composite nanoparticles using a polysaccharide extracted from Ramaria botrytis mushroom and performance in catalytic reduction of 4-nitrophenol and antioxidant, antibacterial activity. Environ Nanotechnol Monit Manag 14:100341
121. Mondal B, Ray J, Jana S, Bhanja SK, Tripathy T (2018) In situ preparation of Tricholoma mushroom polysaccharide-g-poly (N, N-dimethyl acrylamide-co-acrylic acid)–CuO composite nanoparticles for highly sensitive and selective sensing of Th 4+ in aqueous medium. New J Chem 42(24):19707–19719
122. Sebastian M, Aravind A, Mathew B (2018) Green silver-nanoparticle-based dual sensor for toxic Hg (II) ions. Nanotechnology 29(35):355502
123. Criado P, Fraschini C, Shankar S, Salmieri S, Lacroix M (2021) Influence of cellulose nanocrystals gellan gum-based coating on color and respiration rate of Agaricus bisporus mushrooms. J Food Sci 86(2):420–425
124. Sami R, Elhakem A, Alharbi M, Benajiba N, Almatrafi M, Abdelazez A, Helal M (2021) Evaluation of antioxidant activities, oxidation enzymes, and quality of nano-coated button mushrooms (Agaricus Bisporus) during Storage. Coatings 11(2):149

# Chapter 16
# Therapeutic Importance of Panchagavya


**Sivaji Sathiyaraj, Gunasekaran Suriyakala, Ranganathan Babujanarthanam, and K. Kaviyarasu**

## 1 Introduction

With its systematic approach in Ayurveda, the ancient medicine method considers all the etiological causes, disease condition, patient's psychosomatic condition, diet, and even habits while deciding on the treatment line. Ayurveda mentions various plants, animals, and mineral products for the treatment and positive health maintenance in unique combinations [1]. Ayurveda delineates a combination of five imperative substances obtained from cow namely urine, dung, milk, curd, and ghee. This combination is known as panchagavya (PG), and all these substances are individually known as gavya. A cow is the pillar of Indian culture and rural economy, sustaining our lives, portraying the wealth of cattle and biodiversity. The Ayurveda has extensive references to the importance of PG and its substances in the treatment of various human ailments. All these substances are either used alone or in conjunction with herbs to treat various diseases and disorders such as flu, allergies, sore throat, arthritis, rheumatoid arthritis, asthma, leucoderma, asthma, wound healing, heart disease, renal disorders, gastrointestinal tract disorders, acidity, ulceration, leucorrhoea, alopecia, skin infections/diseases, hyperlipidemia, tuberculosis etc. These substances have been effective against dreaded diseases like diabetes, cancer, and

S. Sathiyaraj · G. Suriyakala · R. Babujanarthanam (✉)
Nano and Energy Bioscience Laboratory, Department of Biotechnology, Thiruvalluvar University, Serkkadu, Vellore, Tamil Nadu 632115, India
e-mail: babukmg@gmail.com

K. Kaviyarasu
UNESCO-UNISA Africa Chair in Nanosciences/Nanotechnology Laboratories, College of Graduate Studies, University of South Africa (UNISA), Muckleneuk Ridge, P.O. Box 392, Pretoria, South Africa

Nanosciences African Network (NANOAFNET), Materials Research Group (MRG), iThemba LABS-National Research Foundation (NRF), 1 Old Faure Road, P.O. Box 722, Somerset West 7129, Western Cape Province, South Africa



K. Kasinathan et al. (eds.), *Nanomaterials for Energy Conversion, Biomedical and Environmental Applications*, Materials Horizons: From Nature to Nanomaterials,
https://doi.org/10.1007/978-981-19-2639-6_16

acquired immunodeficiency deficiency syndrome (AIDS). The activity of PG toward Immunostimulatory, immunomodulatory, and anti-inflammatory is well documented in Ayurveda [2–5]. The five main substances of PG contain more micronutrients, macronutrients, minerals, vitamins, hormones, and beneficial microorganisms. PG and its substance enhance cellular metabolism in prokaryotes under both aerobic and anaerobic conditions, thus producing new secondary metabolites like drugs and enzymes. The present review describes the beneficial health applications and the therapeutic potential for safeguarding human health using PG and its substances.

## *1.1 Cowpathy*

Cowpathy refers to the treatment method using cow products and has emerged as Ayurveda's new domain and provides healing services to a wide variety of human illnesses ranging from common cold to cancer [6]. Cowpathy stimulates immunomodulation by enhancing the response of the adaptive immunity, T&B cell proliferation, cytokine production, and macrophage development; inhibits lymphocyte apoptosis, thus helping in the lymphocyte survival and resistance of infection; impedes the formation of free radicals thereby providing anti-aging, and repair of the damaged DNA effectively [4, 5]. Cowpathy is used in two forms, cow urine therapy and panchagavya therapy, the former uses distilled cow urine, and the latter uses PG for healing purposes.

## *1.2 Panchagavya Therapy*

Panchagavya therapy involves topical application of PG, oral intake of filtered PG and oral intake of Panchagavya ghrita. PG is especially recommended for topical application in the treatment of skin diseases. In all other forms of diseases, a dosage of 50 ml of filtered PG combined with 200 ml of tender coconut water, water, or fruit juice is recommended in oral intake. It is taken in the morning with an empty stomach. Panchagavya ghrita is an Ayurvedic formulation of PG in ghee. Panchagavya ghrita is recommended for oral intake at quarter to a half teaspoon with warm water, before food, once or twice a day [7]. Nevertheless, it is rejected by some groups of people in India and abroad as a mythical or mythological adventure because of its lack of evidence of practice, international recognition. Therefore, it is important to combine science in order to raise awareness among the people around the world. The U.S. patents granted for cow product combinations provide a valid pronouncement for the cow-based products of India. As the major population in India depends on livestock sector, providing a significant attention for this field of research mitigates poverty [8].

## 2 Needs of Cowpathy/Panchagavya Therapy

In recent years major hurdles in allopathic treatments have arisen due to the development of drug resistance in microorganisms, existence of antibiotic residues in the food chain, associated allergies and autoimmune disorder in humans. Immunity is significantly decreased due to contamination from the atmosphere, the excessive inclusion of agrochemicals in agriculture and the existence of pesticides, heavy metals, fungal toxins, etc., in the food chain [9]. Due to the above-mentioned factors, there occurs ineffectiveness of antibiotic drugs, the increased bacterial resistance, frequent infections and decrease in the immunity status of the person. The existence of human cancer also raises the existing situation of shifting habits, and dietary preferences increase the cancer hazards due to chewing of tobacco, smoking, intake of alcohol, atmospheric toxins, occupational health hazards, etc. Methodologies such as radiotherapy, chemotherapy, and surgery are available for cancer treatment, however the success rate is poor mainly with malignant tumors, and moreover, such therapies cause serious side effects that add to the patient's physical and mental distress and the treatments are costly, and even some of the tumors are incurable. Under all the above-mentioned conditions, an alternate therapeutic method is necessary to suppress illnesses, save humans from various ailments, and combat diseases like cancer [10, 11]. PG products are proven to be effective in treating many human diseases and enhancing the immunity and resistance of the body to fight the infections. Also, of dangerous diseases such as cancer, AIDS and diabetes, this sort of alternative therapy has been stated to be effective. People frustrated with heavy allopathy treatment are now using cowpathy drugs and recovering from many diseases because of PG products [12]. Out of 7835 licensed Ayurvedic drug manufacturing firms, several manufacturing firms produces medicinal formulations derived from PG or cow's products. The states of Punjab, Kerala, Karnataka, Madhya Pradesh, Odisha, and Haryana declared 229, 200, 5, 3, 3, and 2 pharmaceutical units manufacturing panchagavya therapy products, respectively. Production and quality control of ayurvedic medicinal products for sale is governed under the provisions of the Drugs and Cosmetics Act, 1940 and the Rules, 1945 [13].

## 3 Cow Urine

Cow urine (CU) is one of the main substances of PG and it has the capability to treat from common cold to cancer [14]. A lot of work has been done to study the therapeutic usage of cow urine and it has been reported that CU can cure AIDS, diabetes, cancer, psoriasis, arthritis, blood pressure, asthma, blockage of the arteries, heart attack, thyroid, eczema, prostrate, migraine, piles, constipation, ulcer, acidity, gynaecological infections, and many other diseases [15]. The CU contains all the beneficial elements such as 24 types of salts, bioactive molecules, hormones, and other chemical components like epithelial growth factors, anti-neoplaston, erythropoietin,

gonadotropins, trypsin inhibitor, Urokinase, allantoin, H-11 beta-iodole-acetic acid, growth hormones, sulphur, phosphates, iron, phosphate, nitrogen, manganese, iron, ammonia, urea, uric acid, sodium, potassium, manganese, copper, carbolic acid, carbonic acid, calcium, vitamins A, B, C, D and E, water 95%, lactose, etc., [16]. Uses of the components present in the CU are given in Table 1. Hence CU is a naturally occurring medicine which increases the deficiency of the elements and minimizes the increased elements in the body. The quality of the CU supports the cure of diseases which are more difficult to cure. CU alone has all those beneficial elements, potentialities and constituents that can eliminate ill effects and imbalances in the body [17, 18]. Due to its enormous therapeutic properties and uses, CU occupies 5 U.S. patents.

**Table 1** Chemical components of cow urine and their uses

| S. No. | Component | Uses |
|---|---|---|
| 1 | Salt | Decreases acidic contents of blood and uses as a germicidal agent |
| 2 | Lactose | Strengthens heart, removes thirst and nervousness |
| 3 | Enzymes | Helpful in digestion and improves immunity |
| 4 | Water | Maintains homeostasis and body temperature |
| 5 | Nitrogen | Involves in blood purification, removes toxins, abnormalities, and activates kidneys |
| 6 | Urea | Germicide |
| 7 | Uric acid | Removes heart swelling or inflammation and toxins |
| 8 | Phosphate | Involves in removing stones from urinary track and improves structure and strength of the bones |
| 9 | Sodium | Blood purifier |
| 10 | Potassium (K) | Cures hereditary rheumatism. Increases appetite. Removes muscular weakness and laziness |
| 11 | Manganese (Mn) | Germicide |
| 12 | Calcium | Improves the strength of the bones, blood purifier and protects the lungs from infections |
| 13 | Carbolic acid | Germicide |
| 14 | Sulphur | Makes vital amino acids |
| 15 | Iron | Haematinic |
| 16 | Vitamins (A, B, C, D, E) | Maintains metabolic and physiological functions of human body |
| 17 | Other minerals | Increase immunity |

## *3.1 U.S. Patents with Respect to CU*

### 3.1.1 Patent No. 6410059

The invention correlates the use of CU as an innovative enhancer and facilitator toward the production of bioactive molecules which includes anti-infective agents. This has massive impact toward decreasing the dosages of antibiotics, medications, and anti-infective agents, thus enhancing the absorption rate of the bio-active molecules which paves a way for cost-effective treatment and lessening side effects.

### 3.1.2 Patent No. 6896907, 7235262

The discovery relates to a novel pharmaceutical composition consisting of a sufficient amount of bioactive fraction from a cow urine distillate. It acts as a facilitator of bioavailability and pharmaceutically suitable additives selected from anticancer substances, antibiotics, drugs, therapeutic and nutraceutical agents, ions, and similar molecules which are focused on the living organisms.

### 3.1.3 Patent No. 7718360

The invention concerns a formulation that is useful for defending and/or restoring DNA from oxidative damage using redistilled cow urine distillate.

### 3.1.4 US Patent No. 7297659

The present investigation emphasizes on the symbiotic mixtures of urine, neem, and garlic either individually or comprising of all possible proportions which are useful in plant's growth and soil enhancer. The treatment shows its usefulness in promoting nutrient accumulation in biomass, promotion of a rapid increase in plant growth, phosphate solubilization, abiotic stress tolerance, inhibiting and controlling pathogenic and phytopathogenic fungi in the plant's rhizosphere and thus enhancing the overall phenolic contents of the plants.

## *3.2 Therapeutic Applications of Cow Urine*

### 3.2.1 Antimicrobial and Anthelmintic Properties

The CU could be used to treat the disease caused by pathogenic bacteria, fungi, and parasitic helminths. From various investigations, CU shows greater inhibition of

gram-positive bacteria compared with gram-negative bacteria [19]. Phenols present in the CU have a significant activity against microbes. The fresh CU consisting of more phenol content results in stronger antimicrobial activity [20]. Various studies demonstrate the cow urine's antifungal activity against *Fusarium oxysporum, Claviceps purpurea, Aspergillus niger, Rhizopus oligosporus, Aspergillus oryzae, Penicillium notatum, Trichoderma Viridae, Aspergillus flavus, Alternaria Solani, Candida albicans, Aspergillus oryzae, Candida tropicalis, Candida parapsilosis, P. aphanidermatum,* and *Candida krusei* [21–23]. CU showed significant anthelmintic activity by triggering paralysis and death of worms in a dose-dependent manner. Krupanidhi et al. [24] performed the anthelmintic experiment using CU and cow urine distillate, thereby indicating that the cow urine distillate possesses more anthelmintic activity compared to CU.

### 3.2.2 Antioxidant Property

Free radicals cause damage to different tissues and attack enzymes, fat and proteins that disrupt normal cell activity or cell membranes, resulting in a chain reaction of destruction that leads to an individual's aging process. These pathogenic effects caused by free radicals can be prevented by the regular usage of CU [25]. The presence of uric acid, volatile fatty acid, A, B, C, D and E vitamins in cow urine are responsible for antioxidant activity of CU [26, 27]. $OH^-$ group of phenolic compounds also has antioxidant activity [28].

### 3.2.3 Anti-Diabetic Properties

Research work on CU revealed that CU has the power of curing diabetes characterized by hyperglycemia, hypertriglyceridemia, and hypercholesterolemia. A Research work has been conducted on alloxan-induced diabetic rats with cow urine distillate and glibenclamide (a standard drug for diabetes). Blood glucose, serum triglycerides and serum cholesterol levels have been significantly reduced by using cow urine distillate compared to glibenclamide [29]. Some of the other research works done by [30, 31] claimed that the antidiabetic activity of CU is due to its antioxidant activity.

### 3.2.4 Wound Healing Property

Research on CU has also highlighted that CU has sufficient antiseptic properties in wound healing and CU requires less time to heal the wound compared to a standard antiseptic cream [32]. Another research on cow urine shows that the cow urine ark has been considerably used in albino rats with diabetic wound as it improves wound healing significantly. The cow urine ark may potentially be effective in curing diabetic wounds by increasing the formulation of granulation tissue and the quality of collagen [33].

### 3.2.5 Bioenhancer

Bioenhancers are substances that do not have their drug activity but develop and increase bioavailability, bioactivity, and drug uptake in combination therapy. Previously, these bio-enhancers were isolated from only plant sources. Currently, it is being isolated in CU, which is usually used in antibiotics, antifungal, and anti-cancer drugs and improves the effectiveness of the antibiotics against pathogens. Bio-enhancing capability has also been observed in CU with other drugs like rifampicin, ampicillin, isoniazid, cyanocobalamin, and clotrimazole. For example, when the rifampicin (anti-tubercular drug) is combined with CU, its bio-enhancement increases by about 3–11 folds against Gram-positive bacteria and 5–7 folds against gram-negative bacteria. Bioenhancer activity of CU has been found to minimize the antibiotic dose per day and treatment period in individuals with tuberculosis [34, 35].

### 3.2.6 Immuno-Modulatory Activity

Research on CU proves that CU enhances the activity of lymphocyte proliferation, and it also enhances adaptive immune response in mice [36, 37].

### 3.2.7 Anti-Urolithiasis Activity

Urolithiasis refers to a condition characterized by the development or occurrence of calculi in the urinary tract [38]. There is a 7–12% lifetime risk for renal calculi among the general population [39]. Cow urine distillate has been shown to have a significant effect on restoring renal function and renal calculi. This type of action might be due to a reduction in excretion of calcium oxalate and the inhibition of calcium oxalate crystal formation by cow's urine [40].

### 3.2.8 Cow Urine Therapy in Cancer Management

Cancer has been a threat to society for a long time. Many scientists worked on the treatment that could cure cancer, but none of the existing therapies came up with an absolute ideal method of curing the disease [41]. From natural products, the key ingredients are available for future discoveries that provide tremendous potential to derive useful knowledge about new chemical structures and their unique modes of action relevant to the production of new drugs that offer a solution to cure cancer and other deadly diseases [42]. 'Cow urine therapy' is one such solution that has been found to be effective in treating cancer. Many patients have experienced significant relief and successfully overcome cancer by Cow urine therapy [15]. Many doctors are now starting to realize that cow urine therapy with conventional medicines positively affects patients. An abundance of research work claims that CU and anti-cancer drugs have been made from cow urine distillate that can cure cancer. Cow urine therapy does

not have any significant side effects for cancer treatment. CU has gained U.S. patents for its therapeutic properties in treating cancer [20]. Along with the antibiotics, the intake of CU decreases the infection caused by bacteria and significantly kills the tumors. Scientists have also found that bio enhancing capability of CU and cow urine distillate enhances and intensifies the activities of anti-cancer drugs. It is also shown that cow urine therapy helps to minimize apoptosis in lymphocyte cells and helps to restore damaged DNA. It can, therefore, be concluded that cow urine therapy, along with drugs will help to cure cancer effectively [43].

## 4 Cow Dung

The undigested food residuals excreted via herbivorous bovine animal species is termed as cow dung. With a mixture of faces and urine in a 3:1 ratio, cow dung majorly comprises cellulose, hemicellulose, and lignin. Cow dung also contains minerals such as potassium, nitrogen, and small quantities of iron, magnesium, manganese, sulphur, cobalt, and copper. Moreover, a native Indian cow also contains higher amounts of phosphorus, copper, zinc, and calcium than the crossbreed cow [44]. Cow dung has a rich microbial diversity, consisting of various bacterial species, protozoa, and yeast [45–48] have isolated many bacterial communities in the cow dung such as *Bacteroides clarus, Alistipes finegoldii, Alistipes sp., Alistipe sputredinis, Alistipes massiliensis, Clostridiales bacterium, Clostridium phytofermentans, Clostridium orbiscindens, Clostridium cylindrosporum, Clostridium sp., Citrobacter koseri, Bacillus thuringiensis, Acinetobacter baumannii, Acinetobacter beijernckii, Escherichia coli, Pseudomonas pseudoalcaligenes, Pseudomonas putida, Pseudomonas sp., Rheinheimera sp., Enterobacter aerogenes, Providencia alcaligenes, Stenotropomonas maltophilia, Rhodobacter sp., Akkermansia muciniphila, Providencia stuartii, Morgarella morganii, Klebsiella oxytoca, Klebsiella pneumoniae, Kluyvera sp., Pasteurella sp.,* and *Mycobacterium vaccae.*

In rural Indian villages, the direct burning of cow dung has been widely used as a fuel source for cooking purposes. The practice of plastering in the wall and floor using cow dung provides insulation during winter and summer seasons. Moreover, the smoke of the burnt cow dung acts as a mosquito repellent and obtained ash is used for cleansing household utensils. Accordingly, the specific use of cow dung among village people represents related native awareness. In India, cow dung is also used as a co-product in agriculture, such as manure, biofertilizer, biopesticides, repellent for pests, and as an energy source. As per Ayurveda, it may also serve as a purifier for all the natural wastes. Cow dung is known as “gold mine” owing to its wide-ranging uses in the fields of natural resources, agriculture, environmental conservation, and therapeutic applications [47].

## *4.1 Therapeutic Applications of Cow Dung*

### 4.1.1 Antimicrobial Activity

Due to its large microbial populations, cow dung has been investigated as a source of potential antimicrobial producers. Muhammad and Amusa [49] successfully used cow dung as an antifungal agent. Their research showed that *T. harzianum, A. niger, B. cereus* and *B. subtilis* isolated from cow dung could retard the growth of *Fusarium oxysporum, Sclerotium rolfsii, Helminthosporium maydis, Pythium aphanidermatum,* and *Rhizoctonia solani* with inhibitory zones of up to 58%. Solvent extract of cow dung has also been tested against *E. coli, Candida* sp., *Pseudomonas* sp., and *S. aureus* by [50] and the findings support the antimicrobial properties of cow dung.

### 4.1.2 Antiseptic and Prophylactic Activity

Fresh cow dung is much preferable over other animal dung due to its valuable antiseptic and prophylactic (prevent from disease) properties. It exterminates the disease-causing micro-organisms and putrefaction [51].

### 4.1.3 Antidepressant Activity

Cow dung has antidepressant properties due to the non-pathogenic bacterium *Mycobacterium vaccae*, the first isolated cow dung bacterium. When *Mycobacterium vaccae* inhales, it increases the neuron growth-stimulating serotonin and norepinephrine production in the brain [52]. The effects of anxiety and learning ability on the mice have also been studied and it showed sufficient evidence that supports the study [53]. Vaccine prepared from killed *Mycobacterium vaccae* has been found to be effective for the treatment of cancer, asthma, psoriasis, and leprosy [54, 55].

## 5 Cow Milk

Cow milk for thousands of years has been associated with good health and wellbeing. Cow milk consists of water, 3.7% fat, 3.2% protein, 4.8% lactose, 0.19% nonprotein nitrogen and 0.7% ash. The major proteins present in cow milk are whey, caseins, and immunoglobulins. Milk-protein is a rich source of biologically active peptide precursors. Bioactive peptides are formed in microbial fermentations by enzymatic protein hydrolysis, or by proteolytic activity of lactic acid bacteria [56]. Milk fat is a lipid complex, and the majority of milk lipids are triglycerides or fatty acid esters associated with glycerol (97–98%), and the rest of the milk lipids are phospholipids

(0.2–1%), free sterols (0.2–0.4%), and a small quantity of free fatty acids. Approximately 62% of milk fat is saturated, 30% is monounsaturated, 4% is polyunsaturated and 4% is of minor fatty acid forms. Lactose is the dominant carbohydrate in dairy products. It is a disaccharide that is formed by galactose and glucose. Lactose forms around 54% of the total solids in non-fat milk. Milk is an important source of minerals, calcium, phosphorus, magnesium, potassium, and trace elements. Milk is the main source of calcium in many countries, particularly in Europe people get about 60–80% of total calcium by consuming milk. Calcium forms soluble complexes and is readily absorbed by milk protein, casein, and phosphorus. Cow milk contains all the vitamins known to be essential to humans. The fat portion of milk is associated with the A, D, E, and K vitamins. Milk also provides variable quantities of water-soluble vitamins such as thiamine, ascorbic acid, niacin, riboflavin, vitamin B6 and B12, pantothenic acid, and folate [57].

## *5.1 Therapeutic Applications of Cow Milk*

### 5.1.1 Osteoporosis

Sufficient intake of milk and other calcium-rich food helps to reduce the risk of osteoporosis, a bone-thinning disorder that has affected about 28 million Americans; three-fourth of them are women [58]. Data from the third National Health and Nutrition Examination Survey reports that higher bone mass and lower fracture rates in older women are associated with more milk consumption in childhood [59]. A study shows that consumption of three servings of fat-free or low-fat milk a day improves skeletal health among older adults [60]. Findings from [61] indicate that regular intake of dairy products in menopausal Korean women can prevent the risk of osteoporosis.

### 5.1.2 Obesity

The unique physical, chemical, and biological properties of milk fat make digestibility easier compared to other fats. Milk rejects the fat cells' tendency to store the calories of the day and increases the amount that is frittered away as heat. Calcium in cow's milk is a vital signaling agent. The calcium interacts with fat cells that provide a signal, which inhibits the storage of fat and induces the burning of fat. Thus, cow's milk helps to make a person fit and healthy [35].

### 5.1.3 Kidney Stones

To assess the impact of calcium intake on kidney stones [62], analyzed the data from 7,982 females aged 65 and older. The study indicates that around 45–54% of females were less likely to develop kidney stones due to the increased calcium dietary intake.

### 5.1.4 Antioxidant Activity

Antioxidant peptides derived from milk are produced in sequence from 5 to 11 hydrophobic amino acids. It includes histidine, proline, tryptophan, and tyrosine which are widely distributed among caseins. It involves in removing or preventing the radical formation by inhibiting the enzymatic and nonenzymatic lipid peroxidation [63]. Cow milk is an important dietary source of calcium, and it can be helpful in many low-calcium-related disorders, including polycystic ovarian syndrome, premenstrual syndrome and periodontal disease [64, 65].

## 6 Curd

Fermentation is the oldest conventional form of processing and storing food to maintain taste, aroma and texture that enrich the human diet. Additionally, fermented foods also enhance digestibility, increase nutritional and therapeutic value. Since Vedic times the role of curd is known in the human diet. Curd is a rich source of protein, calcium, riboflavin, vitamin B6 and B12. This has higher nutritional value than milk. Lactose-intolerant people would digest curd because bacterial fermentation converts the lactose in the milk to lactic acid. Curd is known for its palatability, nutritional and therapeutic properties and curd has a viable bacterial count of 106–107 ml that contains lactobacilli, yeast and mold. A number of variable distinctive bacterial strains are present in the curd, including *L. cremoris, L. acidophilus, S. thermophilus, L. helveticus, L. lactis, L. casei,* and *L. bulgaricus* and these microbes are known for their effective probiotics. These probiotics offer valuable and healthy microflora to the alimentary canal through diet without any risk of adverse effects [66].

## *6.1 Therapeutic Applications of Curd*

### 6.1.1 Enhancing Host Immunity

Probiotics found in the curd support the host's health by improving the immune system. Curd enhances innate immunity by inducing mucosal and systemic host

immunity in the patient by increasing the levels of immunoglobulins, activated macrophages, large quantities of cytokines and natural killer cell activities [67].

### 6.1.2 Anti-Cancer Activity

A good diet is an integral part of the treatment of cancer in the gastrointestinal tract. Eating nutritious food before, during and after cancer treatment makes the patient healthier. But the nutrient requirements vary from individual to individual. Hence, eating a healthy mix of proteins, carbohydrates, vitamins, fats, and minerals (through curd) helps fight cancer. Several animal studies indicate that tumor development and proliferation are prevented by the consumption of fermented milk containing probiotics. Milk fermented by *B. infatis, B. animalis, B. bifidum, L. paracasei* and *L. acidophilus* retards the growth of the breast cancer cell line (MCF7), and its anti-proliferative activity is not linked to bacterial involvement. Thus, along with other curd elements, probiotics in the curd play an important role in halting tumor growth and proliferation [68].

### 6.1.3 Anti-HIV Activity

Scientific research has confirmed that the valuable function of vitamins (B, C, and E), selenium, folic acid, and whey protein, present in curd are very much useful for HIV management. Curd provides a safe, cost-effective, and natural approach, which creates a barrier to microbial infection and effectively reduces HIV infection [69, 70].

### 6.1.4 Anti-Diabetic Activity

In recent decades, Type 2 diabetes mellitus has risen exponentially in the world. This is normally accompanied by increased free radical production and reduced antioxidant defenses. Antioxidant mechanisms of probiotics containing lactic acid bacteria may be attributed to scavenging reactive oxygen species, chelation of metal ions, inhibition of enzymes, and inhibition of ascorbate autoxidation. In vivo studies have further confirmed that *L. acidophilus* and *L. casei* have an antidiabetic effect and reduce oxidative stress [71].

### 6.1.5 Other Benefits to Humans

Curd-based probiotics assist in digestion. Curd helps to overcome extreme summer heat and improves strength and stamina. Curd helps in folic acid deficiency and iron deficiency disorders typically seen in children, pregnant women, and lactating

women who are vulnerable to anemia. Clinical studies in this field are therefore important to evaluate the potential of curd as an effective probiotic [68].

## 7 Ghee

Ghee is one of India's oldest and most popular traditional dairy products. Ghee was produced as far back as 1500 BC, in ancient India. Ghee was a popular cooking element in ancient India. Ghee's chemistry holds the secret to its health benefits. Ghee is made from a mixture of ~65% saturated, ~25% monounsaturated, and ~5% unsaturated fat. The saturated fat majorly consists of 89% short-chain fatty acids which are easily digested. For a balanced diet both saturated and unsaturated fats are required. Cow ghee contains about 5% less saturated fat compared to buffalo ghee. Ghee also contains carotenoids that give the product yellow color. Buffalo ghee, on the contrary, lacks carotenoids but contains biliverdin and bilirubin that is responsible for its greenish tint. Ghee contains vitamins A, D, E, and K with fat solubility, small quantities of essential fatty acids, arachidonic acid, and linoleic acid. Unlike other oils ghee exclusively contains butyric acid; a short-chain fatty acid that contributes to its distinct flavor and fast digestion. However, it is essential for good health up to some extent. Consuming it beyond the individual limit may show detrimental health effects due to the presence of cholesterol content and it is highly saturated in nature [72, 73].

### *7.1 Therapeutic Applications of Ghee*

#### 7.1.1 Wound Healing

Cow ghee in desirable formulation provides better tissue development by contributing its antagonistic action against microbial invasion, which would be a superior treatment for wound healing [74]. According to [75] cow ghee stimulates healing in the wound even without any antibiotic usage, and its role is nearly similar to antibiotics. Cow ghee can cure skin diseases when combined with other selected herbals and can promote wound healing when mixed with honey [35].

#### 7.1.2 Anticarcinogens

The specific components of ghee-fat, such as sphingomyelin, Conjugated Linoleic Acid (CLA), ether lipids, butyric acid, β-carotene, and vitamin A and D, have anticarcinogenic activity [76–79].

### 7.1.3 Healthy Weight Loss

The presence of medium-chain fatty acids in healthy fats such as ghee and coconut oil can improve the burning of fat and help to promote weight loss. Research with 13 trials showed that medium-chain triglycerides helped in reducing body weight, waist and hip circumference, overall fat, and belly fat compared with long-chain triglycerides. Not only this but also CLA, one of the main fatty acids present in ghee, has been associated with reduced mass of body fat [80].

### 7.1.4 Anti-Inflammation

Though inflammation may be a natural immune response to help protect the body against foreign invaders long-term inflammation contributes to chronic disease development [81]. Butyrate, a type of fatty acid present in the ghee has been shown to inhibit inflammation in the in-vitro studies [82].

### 7.1.5 Immunostimulant Activity

The capability of cow ghee toward immunostimulant is demonstrated by an increase in neutrophil adhesion, haemagglutination (HA) titre, and delayed-type hypersensitivity (DTH) responses in rats as reported by [83].

### 7.1.6 Others

Cow ghee is historically recommended for enhancing memory, speech, vision, intelligence, and body resistance to infections. This has anti-aging effects and anti-chollestric activity, which is beneficial for cholesterol and heart disease patients. Cow ghee is a blood purifier; aids wound healing and helps in preventing and treating asthma and paralysis [84].

## 8 Conclusion

Thus, it can be concluded that in future years panchgavya therapy/cowpathy, a modern variant of ancient science, is a promising formulation. It has been found that PG and its ingredients are effective in treating many human diseases and improving the body's immunity and resistance to infection. Even for diseases like cancer and AIDS, this kind of alternative treatment has been stated to be effective. With essential therapeutic possibilities for the good of mankind, panchgavya therapy/cowpathy needs the attention of the scientific community around the world for its validation, recognition, promotion, and popularity. A systematic work needs to be carried out on

the chemical structure, biological activities, microbiology and medicinal aspects, and bioactive compounds in PG and promotional clinical trials in both disease prevention and treatment.

## References


1. Athavale A, Jirankalgikar N, Nariya P, Des S (2012) Evaluation of in-vitro antioxidant activity of panchagavya: a traditional ayurvedic preparation. Int J Pharm Sci Res 3:2543–9. https://doi.org/10.13040/IJPSR.0975-8232.3(8).2543-49
2. Chauhan RS (2003) Panchgavya se rogpratirodhi chamta me vridhi. Prakriti Smarika 9
3. Chauhan RS (2008) Cowpathy: a new version of ancient science. Indian Cow: Sci Econ J 5:39–40
4. Dhama K, Chauhan RS, Singhal L (2005) Anti-cancer activity of cow urine: current status and future directions. Int J Cow Sci 1:1–25
5. Dhama K, Rathore R, Chauhan RS, Tomar S (2005) Panchgavya (cowpathy): an overview. Int J Cow Sci 1:1–5
6. https://saveindiancows.org/cowpathy-and-science/. Accessed 18 Dec 2020
7. Natarajan K (2008) Panchagavya: a manual. Organic Farming Association of India, p 33
8. https://www.pashudhanpraharee.com/importance-of-panchagavya-%E0%A4%AA%E0%A4%82%E0%A4%9A%E0%A4%97%E0%A4%B5%E0%A5%8D%E0%A4%AF-animal-husbandry/. Accessed 18 Dec 2020
9. Dhama K, Chakraborty S, Wani MY, Verma AK, Deb R, Tiwari R, Kapoor S (2013) Novel and emerging therapies safeguarding health of humans and their companion animals: a review. Pak J Biol Sci 16:101. https://doi.org/10.3923/pjbs.2013.101.111
10. Chauhan RS (2004) Panchgavya therapy (cowpathy): current status and future directions. Indian Cow: Sci Econ J 1:3–7
11. Garg N, Chauhan RS (2003) Cow therapy as an alternative to antibiotics. In: Indian science congress, pp 3–7
12. https://govatsfoundation.com/?p=67. Accessed 18 Dec 2020
13. https://pib.gov.in/newsite/PrintRelease.aspx?relid=116073. Accessed 18 Dec 2020
14. Pathak ML, Kumar A (2003) Cow praising and importance of panchyagavya as medicine. Sachitra Ayurveda 5:56–59
15. Jain NK, Gupta VB, Garg R, Silawat N (2010) Efficacy of cow urine therapy on various cancer patients in Mandsaur District, India—a survey. Int J Green Pharm 4. https://doi.org/10.22377/ijgp.v4i1.115
16. Bhadauria H (2002) Gomutra-Ek Chamatkari Aushadhi (Cow urine—a magical therapy). Vishwa Ayurveda Patrika 5:71–74
17. Bartnett B (1988) The miracles of Urine Therapy. Water of Life Institute, Hollywood, Florida
18. Chauhan RS, Singh BP (2000) Panchgavya dwara prakritik chikitsa. Kheti Sansar 3:21–23
19. Nishanth BC, SV PK SV, Kamal D, Sandeep M, Megharaj HK (2010) Cow urine concentrate: a potent agent with antimicrobial and anthelmintic activity. J Pharm Res 3:1025–1027
20. Talokar OW, Belge AR, Belge RS (2013) Clinical evaluation of cow-urine extract special reference to Arsha (Hemmorrhoids). Int J Pharm Sci Invent 2:05–08
21. Deshmukh SS, Rajgure SS, Ingole SP (2012) Antifungal activity of cow urine. IOSR J Pharm 2:27–30
22. Hoh JM, Dhanashree B (2017) Antifungal effect of cow's urine distillate on Candida species. J Ayurveda Integr Med 8:233–237. https://doi.org/10.1016/j.jaim.2017.04.009
23. Rakesh KN, Dileep N, Nawaz NA, Junaid S, Kekuda PT (2013) Antifungal activity of cow urine against fungal pathogens causing rhizome rot of ginger. Environ Ecol 31:1241–1244

24. Krupanidhi K, Kekuda TRP, Bhramarambha BKM, Shrungashree RM, Suchitra SV, Kavya R (2008) Comparative studies on in vitro nematicidal (anthelmintic) activity of cow urine and cow urine. Biotechnol (Rajkot) 2:23
25. Singh AK, Singh PK, Singhal LK, Agrawal DK (2004) Pathogenic effect of free radicals and their prevention through cowpathy. Indian Cow: Sci Econ J 1(2):26–33
26. Joshi DR, Aryal P, Chaudhary MK, BK PK, Yadav SP, Rawal P, Adhikar N, Bhandari R (2019) Study of in-vitro antioxidant and antibacterial activity of cow urine from different altitudinal and climatic region of Nepal. Microbiol Res J Int 29:1–8. https://doi.org/10.9734/mrji/2019/v29i230158
27. Krishnamurthi K, Sivanesan S, Chakrabarti T (2004) Protective effect of distillate and redistillate of cow's urine in human polymorphonuclear leukocytes challenged with established genotoxic chemicals. Biomed Environ Sci 17:247–256
28. Subedi A, Amatya MP, Shrestha TM, Mishra SK, Pokhrel BM (2012) Antioxidant and antibacterial activity of methanolic extract of Machilus odoratissima. Kathmandu Univ J Sci Eng Technol 8:73–80. https://doi.org/10.3126/kuset.v8i1.6045
29. MP G, Joshi AB, Joshi H, Sathyanarayana D, Subrahmanyam EV, Chandrashekhar KS (2010) Antidiabetic potential of cow urine in streptozotocin-induced diabetic rats. 亚洲传统医药 6:8–13
30. Jarald EE, Edwin S, Tiwari V, Garg R, Toppo E (2008) Antidiabetic activity of cow urine and a herbal preparation prepared using cow urine. Pharm Biol 46:789–792. https://doi.org/10.1080/13880200802315816
31. Sachdev DO, Gosavi DD, Salwe KJ (2012) Evaluation of antidiabetic, antioxidant effect and safety profile of gomutra ark in Wistar albino rats. Anc Sci Life 31:84. https://doi.org/10.4103/0257-7941.103180
32. Hirapara HN, Ghori VM, Anovadiya AP, Tripathi CR (2016) Evaluation of wound healing activity of cow urine ark in diabetic Wistar albino rats. J Intercult Ethnopharmacol 5:434. https://doi.org/10.5455/jice.20160923100135
33. Maheshwari AK, Gupta AK, Das AK (2004) Effect of cow urine on wounds. Indian Cow: Sci Econ J 1:19–24
34. Joshi MM (2002) Cow therapy (Panchgavya) and cattle based economy. Inaugural Speech in Vishva Ayurvedas Sammelan on 7:2002
35. Khan MY, Roy M, Saroj BK, Dubey S, Sharma VK (2015) A review-benefits of panchgavya therapy (cowpathy) for health of humans. Asian J Res Pharm Sci 5:115–125. https://doi.org/10.5958/2231-5659.2015.00019.3
36. Chauhan RS, Singh BP, Singhal LK (2001) Immunomodulation with Kamdhenu Ark in mice. J Immunol Immunopathol 3:74–77
37. Kumar P, Singh GK, Chauhan RS, Singh DD (2004) Effect of cow urine on lymphocyte proliferation in developing stages of chicks. Indian Cow: Sci Econ J 1:3–5
38. Wathigo FK, Hayombe A, Maina D (2017) Urolithiasis analysis in a multiethnic population at a tertiary hospital in Nairobi, Kenya. BMC Res Notes 10:158. https://doi.org/10.1186/s13104-017-2474-3
39. Grases F, Costa-Bauza A, Prieto RM (2006) Renal lithiasis and nutrition. Nutr J 5:23. https://doi.org/10.1186/1475-2891-5-23
40. Mondal S, Palbag S (2018) Ethno-pharmacology, chemistry and pharmacology of gomutra. Int Ayurvedic Med J. http://www.iamj.in/posts/images/upload/422_429.pdf
41. Cooper GM, Hausman RE (2007) The cell: a molecular approach, 2000. ASM Press, Washington DC, pp 467–519
42. Yuan H, Ma Q, Ye L, Piao G (2016) The traditional medicine and modern medicine from natural products. Molecules 21:559. https://doi.org/10.3390/molecules21050559
43. http://www.ausib.org/Ausib/Cow-urine-therapy--122-Blog.html. Accessed 18 Dec 2020
44. Gupta KK, Aneja KR, Rana D (2016) Current status of cow dung as a bioresource for sustainable development. Bioresour Bioprocess 3:1–1. https://doi.org/10.1186/s40643-016-0105-9
45. Girija D, Deepa K, Xavier F, Antony I, Shidhi PR (2013) Analysis of cow dung microbiota—a metagenomic approach. Indian J Biotechnol 12:372–378. http://hdl.handle.net/123456789/21863

46. Nene YL (1999) Traditional knowledge system of India and Sri Lanka. In: Utilizing traditional knowledge in agriculture, pp 32–38
47. Randhawa GK, Kullar JS (2011) Bioremediation of pharmaceuticals, pesticides, and petrochemicals with gomeya/cow dung. Int Sch Res Notices 2011:1–7. https://doi.org/10.5402/2011/362459
48. Sawant AA, Hegde NV, Straley BA, Donaldson SC, Love BC, Knabel SJ, Jayarao BM (2007) Antimicrobial-resistant enteric bacteria from dairy cattle. Appl Environ Microbiol 73:156–163. https://doi.org/10.1128/AEM.01551-06
49. Muhammad S, Amusa NA (2003) In-vitro inhibition of growth of some seedling blight inducing pathogens by compost-inhabiting microbes. Afr J Biotechnol 2:161–164. https://doi.org/10.5897/AJB2003.000-1033
50. Sushmita S, Alka M, Arti P (2014) Cow dung—a boon for antimicrobial activity. Life Sci Leafl 55:60–63
51. Dhama K, Rathore R, Chauhan RS, Tomar S (2008) Panchgavya (cowpathy): an overview. Indian Cow: Sci Econ J 5:45–68
52. Lowry CA, Hollis JH, De Vries A, Pan B, Brunet LR, Hunt JR, van Kampen E, Knight DM, Evans AK, Rook GA (2007) Identification of an immune-responsive mesolimbocortical serotonergic system: potential role in regulation of emotional behavior. Neuroscience 146:756–772. https://doi.org/10.1016/j.neuroscience.2007.01.067
53. Matthews DM, Jenks SM (2013) Ingestion of Mycobacterium vaccae decreases anxiety-related behavior and improves learning in mice. Behav Processes 96:27–35. https://doi.org/10.1016/j.beproc.2013.02.007
54. Lehrer A, Bressanelli A, Wachsmann V, Bottasso O, Bay ML, Singh M, Stanford C, Stanford J (1998) Immunotherapy with Mycobacterium vaccae in the treatment of psoriasis. FEMS Immunol Med Microbiol 21:71–77. https://doi.org/10.1111/j.1574-695x.1998.tb01151.x
55. Rook GA, Stanford JL (1988) U.S., Patent No. 4,724,144. Washington, DC: U.S. Patent and Trademark Office
56. Saxelin M, Korpela R, Mayrä-Mäkinen A (2003) Functional dairy products. InDairy processing. Woodhead Publishing, Sawston pp 229–245
57. Miller GD, Jarvis JK, McBean LD (2006) Handbook of dairy foods and nutrition. CRC Press, Boca Raton
58. Armas LAG, Frye CP, Heaney RP (2016) Effect of cow's milk on human health. In: Wilson T, Temple N (eds) Beverage impacts on health and nutrition. Nutrition and health. Humana Press, Cham, pp 131–150. https://doi.org/10.1007/978-3-319-23672-8_9
59. Kalkwarf HJ, Khoury JC, Lanphear BP (2003) Milk intake during childhood and adolescence, adult bone density, and osteoporotic fractures in US women. Am J Clin Nutr 77:257–265. https://doi.org/10.1093/ajcn/77.1.257
60. Heaney RP, McCARRON DA, Dawson-Hughes B, Oparil S, Berga SL, Stern JS, Barr SI, Rosen CJ (1999) Dietary changes favorably affect bone remodeling in older adults. J Am Diet Assoc 99:1228–1233. https://doi.org/10.1016/S0002-8223(99)00302-8
61. Park SJ, Jung JH, Kim MS, Lee HJ (2018) High dairy products intake reduces osteoporosis risk in Korean postmenopausal women: a 4 year follow-up study. Nutr Res Pract 12:436–442. https://doi.org/10.4162/nrp.2018.12.5.436
62. Sorensen MD, Eisner BH, Stone KL, Kahn AJ, Lui LY, Sadetsky N, Stoller ML (2012) Impact of calcium intake and intestinal calcium absorption on kidney stones in older women: the study of osteoporotic fractures. J Urol 187:1287–1292. https://doi.org/10.1016/j.juro.2011.11.109
63. Álvarez-Rosales JD, Ozuna C, Salcedo-Hernández R, Rodríguez-Hernández G (2019) Comparision of antioxidant activity of cow and goat milk during fermentation with lactobacillus acidophilus LA-5. In: Prebiotics and probiotics-potential benefits in nutrition and health. IntechOpen, London. https://doi.org/10.5772/intechopen.88212
64. Heaney RP (2002) Ethnicity, bone status, and the calcium requirement. Nutr Res 22:153–178
65. Miller GD, Jarvis JK, McBean LD (2001) The importance of meeting calcium needs with foods. J Am Coll Nutr 20:168S-185S. https://doi.org/10.1080/07315724.2001.10719029

66. Kore KB, Pattanaik AK, Sharma K, Mirajkar PP (2012) Effect of feeding traditionally prepared fermented milk dahi (curd) as a probiotics on nutritional status, hindgut health and haematology in dogs. 11:35–39. http://hdl.handle.net/123456789/13418
67. Ashraf R, Shah NP (2014) Immune system stimulation by probiotic microorganisms. Crit Rev Food Sci 54:938–956. https://doi.org/10.1080/10408398.2011.619671
68. Milind P, Jyoti M (2014) Curd: a sedative with a bonus bowl of useful side effect. Int Res J Pharm 5:131–135. https://doi.org/10.7897/2230-8407.050328
69. Hummelen R, Hemsworth J, Reid G (2010) Micronutrients, N-acetyl cysteine, probiotics and prebiotics, a review of effectiveness in reducing HIV progression. Nutrients 2:626–651. https://doi.org/10.3390/nu2060626
70. Irvine SL, Hummelen R, Hekmat S, Looman CW, Habbema JDF, Reid G (2010) Probiotic yogurt consumption is associated with an increase of CD4 count among people living with HIV/AIDS. J Clin Gastroenterol 44:e201–e205. https://doi.org/10.1097/MCG.0b013e3181d8fba8
71. Farvin KS, Baron CP, Nielsen NS, Otte J, Jacobsen C (2010) Antioxidant activity of yoghurt peptides: part 2–characterisation of peptide fractions. Food Chem 123:1090–1097. https://doi.org/10.1016/j.foodchem.2010.05.029
72. Sharma H, Zhang X, Dwivedi C (2010) The effect of ghee (clarified butter) on serum lipid levels and microsomal lipid peroxidation. Ayu 31:134. https://doi.org/10.4103/0974-8520.72361
73. Sserunjogi ML, Abrahamsen RK, Narvhus J (1998) A review paper: current knowledge of ghee and related products. Int Dairy J 8:677–688. https://doi.org/10.1016/s0958-6946(98)00106-x
74. Prasad V, Dorle AK (2006) Evaluation of ghee based formulation for wound healing activity. J Ethnopharmacol 107:38–47. https://doi.org/10.1016/j.jep.2006.02.006
75. Prasad V (2002) Evaluation of indigenous formulations for wound healing activity. M. Pharm thesis, Nagpur University, Nagpur, India, pp 35–37
76. Akalln AS, Tokusoglu Ö (2003) A potential anticarcinogenic agent: conjugated linoleic acid (CLA). Pak J Nutr 2:109–110. https://doi.org/10.3923/pjn.2003.109.110
77. Jahreis G, Fritsche J, Möckel P, Schöne F, Möller U, Steinhart H (1999) The potential anticarcinogenic conjugated linoleic acid, cis-9, trans-11 C18: 2, in milk of different species: cow, goat, ewe, sow, mare, woman. Nutr Res 19:1541–1549. https://doi.org/10.1016/S0271-5317(99)00110-4
78. Khanal RC, Olson KC (2004) Factors affecting conjugated linoleic acid (CLA) content in milk, meat, and egg: a review. Pak J Nutr 3:82–98. https://doi.org/10.3923/pjn.2004.82.98
79. Parodi PW (1999) Conjugated linoleic acid and other anticarcinogenic agents of bovine milk fat. J Dairy Sci 82:1339–1349. https://doi.org/10.3168/jds.S0022-0302(99)75358-0
80. Mumme K, Stonehouse W (2015) Effects of medium-chain triglycerides on weight loss and body composition: a meta-analysis of randomized controlled trials. J Acad Nutr Diet 115:249–263. https://doi.org/10.1016/j.jand.2014.10.022
81. Hunter P (2012) The inflammation theory of disease: the growing realization that chronic inflammation is crucial in many diseases opens new avenues for treatment. EMBO Rep 13:968–970. https://doi.org/10.1038/embor.2012.142
82. Segain JP, De La Blétiere DR, Bourreille A, Leray V, Gervois N, Rosales C, Ferrier L, Bonnet C, Blottiere HM, Galmiche JP (2000) Butyrate inhibits inflammatory responses through NFκB inhibition: implications for Crohn's disease. Gut 47:397–403
83. Fulzele SV, Satturwar PM, Dorle AK (2001) 24. Immunostimulant activity of cow's ghee. J Immunol Immunopathol 3:87–88
84. Kuldeep D, Sandip C, Ruchi T (2013) Panchgavya therapy (Cowpathy) in safeguarding health of animals and humans-a review. Res Opin Anim Vet Sci 3:170–178

# Chapter 17
# Role of Antimicrobials Agents and Studies Using Metal Oxide Nanoparticles


**R. Ramesh, G. T. Fathima Mubashira, M. Parasaran, and K. Kaviyarasu**

## 1 Introduction

The appearances of infectious diseases in general pose a severe threat to public health internationally, especially with the emergence of antibiotic-resistant bacterial strains. Generally, both Gram-positive and Gram-negative bacterial strains are causing major health problem over the years [1–5]. For the past few decades, researchers were focusing on the preparation of multifunctional materials in fighting against the antimicrobials and highly infectious disease-causing pathogens, however, the exact interaction of the already available antimicrobial agents becomes inactive with the new types of bacterias and viruses that are arising due to climatic change, lifestyle of humankind, food nature, and other things. Recent advances in the nanomaterial preparation technology focus on the engineered bionanomaterials in curing the infectious diseases caused by the strains and fungi. The antibacterial activity of any drug, as well as the NPs, depends on the shape, size, chemical nature, and biological properties. Size of the particle plays a significant role in the action mechanism of bactericidal activity

R. Ramesh · G. T. Fathima Mubashira · M. Parasaran
Department of Physics, Sacred Heart College (Autonomous), Tirupattur, Tamil Nadu 635601, India

R. Ramesh (✉)
Department of Physics, Islamiah College (Autonomous), Vaniyambadi, Tamil Nadu 635752, India
e-mail: rramesh@shctpt.edu

K. Kaviyarasu
UNESCO-UNISA Africa Chair in Nanosciences/Nanotechnology Laboratories, College of Graduate Studies, University of South Africa (UNISA), Muckleneuk Ridge, PO Box 392, Pretoria, South Africa

Nanosciences African Network (NANOAFNET), Materials Research Group (MRG), iThemba LABS-National Research Foundation (NRF), 1 Old Faure Road Western Cape Province, PO Box 722, Somerset West 7129, South Africa



K. Kasinathan et al. (eds.), *Nanomaterials for Energy Conversion, Biomedical and Environmental Applications*, Materials Horizons: From Nature to Nanomaterials,
https://doi.org/10.1007/978-981-19-2639-6_17

through its propagation into the cell membrane, dysfunction, and disruption of the DNA nucleic acid, etc. [6–10]. Antimicrobial activity of nanoparticles has largely been studied with human pathogenic bacteria such as *Escherichia coli* and *Staphylococcus aureus*. Nowadays, owing to overcoming pollution and harmful radiation makes more prone to infectious diseases and sickness. To overcome this hazardous infection, antimicrobials have been preoccupied as designating agents since late 1928. Thus, it comes under the classification of chemotherapy. Chemotherapy is making avail of synthetic or natural chemical reagents fabricated from microorganisms and plant producing chemical substances for selectively inhibiting the toxic level of cell of infection-causing microorganisms or malignant tumor without disturbing the host cell and tissues [11–16]. It is further systemized into two as antimicrobial agents which impede the progressive development of microorganisms by synthetic or natural means and another as anticancerous drug which impede the uncontrollable growth of cells called cancer and prophylaxis from spreading. Antimicrobial drugs are liberally stratified in a diversity of ways [17, 18].

## *1.1 Efficacy Based on the Way of Action, Source, and Spectrum*

Generally, antimicrobial is categorized partly by their vogue of action. Antimicrobial which demolishes the microbes by preying on the wall and membranes of cell, probably causing the overall death of microorganisms are described as microtidal. Antimicrobial which averts the further accretion of microorganisms is labeled as microstatics. Antimicrobial can be naturally mass produced from fungus resources which stipulate the bacterial cell wall and they often manifest more exhilarated toxicity than synthetic source [19, 20]. Semi-synthetic antimicrobial which are fabricated initially by natural origin and later by modifying into the final product by virtue of chemical reactions. Synthetic antibiotics are depicted to have more efficacious than natural antimicrobial. In this genus, the antimicrobial may be either narrow or broad spectrum. By the denomination of narrow spectrum, it clearly manifests that it can stipulate only a reserved span of microorganisms either only Gram-positive or Gram-negative. On contrasting to narrow spectrum, broad-spectrum antimicrobials are designated to stipulate the vast array of microorganisms inclusive of both Gram-positive and -negative microbes and anaerobes. Usually, the broad-spectrum antimicrobial is barely sanctioned than narrow-spectrum owing to it possess the possession of not killing normal microorganisms on the body of host cell [21] (Table 1).

**Table 1** Broad classification of antimicrobial agents

| S.No | Antimicrobial | Based on their | | | | | |
|---|---|---|---|---|---|---|---|
| | | Type of action | Source | Spectrum | Organism affected | Mechanisms of action | Chemical structure |
| 1 | Penicillin | Bactericidal | Fungi | Narrow spectrum | Antibacterial | Cell wall synthesis inhibitor | Beta -lactam antibiotics |
| 2 | Erythromycin | Bacteriostatic | Actinomycetes | Broad spectrum | Antibacterial | Protein synthesis inhibitor | Macrolide |
| 3 | Chloramphenicol | Bacteriostatic | Actinomycetes | Broad spectrum | Antibacterial | Protein synthesis inhibitor with 50 RNA | Dichloroacetamide |
| 4 | Vancomycin | Bactericidal | Bacteria | Narrow spectrum | Antibacterial | Cell wall synthesis inhibitor | Glycosylated peptide |
| 5 | Sulfonamide | Bactericidal | Synthetic | Broad spectrum | Antifungal & antimalarial | Interfering with inter-mediatory metabolism | Sulfonamide group |
| 6 | Miconazole | Bacteriostatic | Synthetic | Broad spectrum | Antifungal | Cell membrane Synthesis Inhibitor | Imidazole derivatives |
| 7 | Quinolones | Bactericidal | Synthetic | Broad spectrum | Antibacterial & Antifungal | Nucleic acid (DNA) | Quinolones |

## 2 Significance of Chemical Structure, Organisms Affected, and Its Mechanism of Action

To hinge antimicrobial on their chemical structure is crucial considering the discrete skeleton pattern display disparate therapeutic demeanor. It is diverse in β-lactams as group A and aminoglycosides as group B. Antibacterial are agents that impede the accretion of bacteria. Suppressing the accretion of fungi is entitled as antifungal. By abating the growth of virus is locution as antivirus. A single-celled organism used to treat infection caused by protozoa as a single-cell medication is designated as anti-protozoal. Overall, it exemplifies primarily into four categories as cell wall synthesis inhibitor, protein synthesis inhibitor, nuclei acid synthesis inhibitor, cell membrane synthesis inhibitor, and interfere with intermediatory metabolism [22–25].

## 3 Mechanism of Antimicrobial Agents Against Bacteria and Strains

Mechanisms merely intend how an antimicrobial toiled or enact its vogue of maneuver. For the accretion of microbes, there are some crucial proceedings of the incorporation of cell wall, protein, nucleic acid, and cell membrane. If these crucial processes are disturbed or any deformity in their state of vogue is subdivided into four factions, they are hindering cell wall, cell membrane, nucleic acid, and protein synthesis [26–28] (Fig. 1).

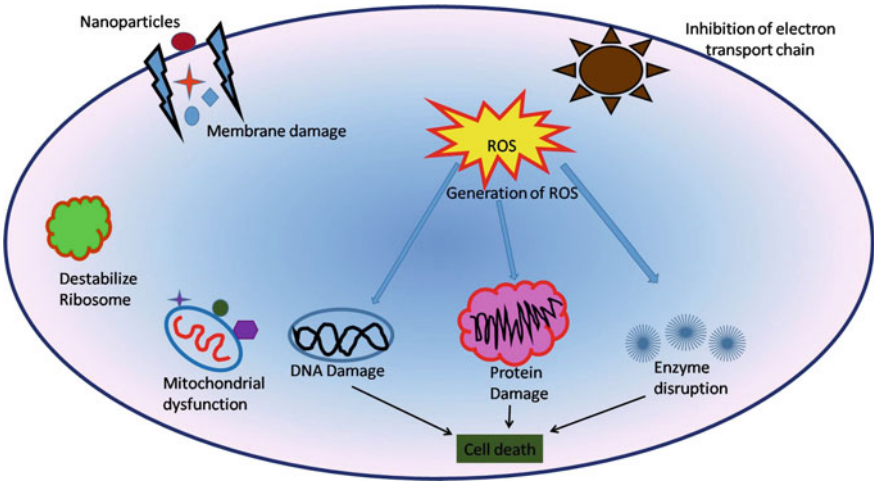


**Fig. 1** Mechanism of action against bacteria and strain

## 4 Effect Due to Cell Wall Incorporation

Mammalian cells and all the other microorganisms contradict one another by their latency of peptidoglycan incarnate of equal amount of N-acetylmuramic acid and N-acetyl glucosamine which is a spunk of cell wall. Impeding the peptidoglycan substratum of cell wall is a major writ for circumventing of bacterial accretion. By avail of β-lactamase drugs including Carbapenems, monobactams, penicillin derivatives. Initially, β-lactamase drugs are restrained with penicillin results in impeding transpeptide reaction thereby activating the enzymes of lytic that break down the bacterial cell wall thereby inhibiting the peptidoglycan which is eased by a protein blended with penicillin. Gram-negative bacteria are scrutinized to possess a thin layer of peptidoglycan which is encompassed by an outer cell [29]. Owing to this perception, the antimicrobial failed to extend that layer thereby β-lactamase drugs portrayed fewer stability than G-positive bacteria which are surrounded by a thick layer of peptidoglycan without the outer wall, that is, a thing that distinct both the microorganisms. Thus, the cell wall of bacteria is envisioned, and the accretion of microbe is ceased.

## 5 Membrane Incorporation

Hinge upon their structure of bacteria and fungi, most of their cells are permeated with a jelly-like fluid imperturbable of water, salts, and protein that is encompassed by a membrane called cytoplasmic membrane and the fluid is cytoplasm that predominant the internal constitution of cell. But viruses do not have cytoplasm to carry out this predomination. However, when this cytoplasmic membrane gets disrupted by an antimicrobial all the ions and its residents will start to flow thereby perturbing the overall accretion of bacteria. Polymyxin portrayed their exceptional riveting towards polysaccharide molecules which are benevolence mostly in Gram-negative bacteria, while polymyxin correlates with the lipopolysaccharide of G-negative bacteria. Thus, while the interaction of polymyxin with polysaccharide, the structure got distorted which upshot the annihilation of osmotic balance and its permeability flourishing, because of molecule exonerate, increased water intake, respiration dilemma of cell result in cell dissolution [30–32]. While polymyxin failed to affect G-positive bacteria owing to their thick cell wall. Daptomycin is utilized to restrain G-positive bacteria acquired from Streptomyces mesoporous, an antibiotic of cyclic lipopeptide accustomed to amusing bacterial infection of skin and intrinsic tissue.

## 5.1 Protein Incorporation

Antimicrobial that quarries the protein coalescence christened as protein synthesis impeder. In the cells of microbes, there are ribosomes concocted into two subunits as 50 s, a larger one, and 30 s, as a smaller one. There are some antibiotics that quarry the 50 s ribosomes are macrolides considering a constituent of clarithromycin, erythromycin, and azithromycin. They chastised the 50 s ribosomes, a larger one endures of the distinct region as A, P, E; these macrolides come in proximity with 50 s RNA, as the ribosomes propel across the m-RNA and coalescence protein. If they inhibit roving along the m-RNA, it won't be able to synthesize protein that is bacteriostatic [33]. Macrolides prevent the elongation of peptide bonds and ribosomes from roving along the m-RNA and translating the actual m-RNA, to forge protein that is employed to tackle pneumonia, H-pylori, gonorrhea, and gastrointestinal tract of infection. Aminoglycosides are bactericidal constituents of gentamycin, tobramycin that target the t-RNA that has anticodon and specific amino acid that is specific to codon. When the t-RNA enters the A side, aminoglycan hunks the t-RNA carrying amino acid from entering aside. Thus, t-RNA is inhibited by aminoglycoside for binding with A side. They are employed to tackle urinary tract infection, pneumonia, meningitis as well as peritonitis impeded by the bacteria of pseudomonas, aerobic Gram-negative, and enterobacteria. Tetracycline is bacteriostatic and perform equivalent reaction as aminoglycosides that instead of targeting 50 s ribosomes, they focused their target towards 30 s ribosomes. It also contradicts the t-RNA from invading this site and to read the codon. If this does not prevail, then protein will not be synthesized effectively [34]. They are employed to tackle Lyme's disease, chlamydia, and anthrax by the avail of doxycycline.

## 5.2 Effect on the DNA\RNA Deformation

Some antibiotics that are targeting the DNA/RNA synthesis specifically are topoisomerase. Whenever a DNA is replicating, it has a downstream called supercoils by dint of which the DNA is coiled up. Topoisomerase has two strands; one strand cuts the one of the phosphodiesters to bond the spunk of DNA and permit the supercoil to be able to levitate and get rid of actual DNA. Another strand takes the DNA fragment that is broken are fused them together. Fluoroquinolones are antimicrobials that are constituents of Ciprofloxacin, Levofloxacin, etc., they hinge DNA/RNA synthesis by stimulating the activity of one strand that cut the DNA, then inhibiting the lysate strand that fused them together [35, 36]. Then the DNA won't be linked up continuously that sequel in fragmented DNA, so it is bactericidal. Nitrofurantoin is one of the dangerous antibiotics that inhibit almost all cell characteristics. This nitrofurantoin enters the cell wall and gets binded to a specific enzyme called nitrofurantoin reductase. These enzymes convert nitrofurantoin into a reactive intermediate that causes damage to DNA, RNA, protein, and cell wall, thus it freckled up almost all syntheses,

both G-positive and G-negative. Metronidazole acts upon by nitroreductase, converts it into active metabolite, disrupts the normal helical structure of DNA, and undergoes fragmentation by nucleases. Daptomycin is used to treat mainly G-positive staphylococcus aureus; its mechanism of action is really fascinated because it forms a pore in the bacterial cell wall membrane, due to its leakage of flux of ions moving in and out causes subsequent depolarization, then the enzyme membrane becomes positively charged. The depolarization of positive charge exists inside the inner side of cell membrane, thereby inhibiting DNA synthesis and protein synthesis. Rifampicin is used to treat leprosy, tuberculosis, as well as hemophilic influenza type B, by using an enzyme DNA-dependent RNA Limerase. Rifampicin inhibits the enzyme that cannot transcribe DNA to m-RNA. If we cannot make the m-RNA, bacteria fails to survive [37]. Thus, the above-mentioned mechanisms clearly tells about how antimicrobe like penicillin kills bacteria, or fungi, or virus. In short, the role of antimicrobe inside microbes is known. Metal oxide nanoparticle is competent to metamorphose of mammalian and bacterial cell, analogous to antimicrobial by dint of metal protein and its transport system of bacteria. They also enumerated an exemplary demeanor of prompting the cell repose activity through multiple implantations or by gene mutation. Wholly, there are three pathways of interrelating bacterial cells with nano-oxide substratum.

## 6 Synergy with Phospholipids Substratum by Metal Oxides

Nano-oxide can rattle the membrane potency and eventuality restrain the charges of oxides and cell wall of microbes together. This is done by merging the positive charge of nano-oxide of metal and negative citation of cell wall catch captivated together by dint of their opposite citation, consequently, allying two charges that bring about oxidative crunch on the cell. Owing to that stress, cell membrane and its intracellular fluids get distorted, which upshot in the liberation of a wide aggregate of ions and molecules thereby crucial recompense to cytoplasmic membrane that effectuate the vital corollary of cell [38]. To conquer this deprivation of microbes, self-engender proton and electron through integral of efflux pump and transport. But it is not legitimate to bear this deprivation. Thus, overall asymmetry of ions is consequently upshot in respiration demise, eventually leading to cell dissolution. This ramification has been displayed through the intercorrelation with CuO, ZnO, $TiO_2$, MgO, and $Fe_2O_3$.

### *6.1 Synergy with Cytosol Protein by Metal Oxides*

The foremost innards among the three is correlating with cytosol protein. It is a semi-fluid that pervades all the embedded phagosome encircled by a cytoplasmic region and cell membrane, omitting nucleus that concocts the cytoplasm. Their aspect is

to ravish molecules and furnish structural reinforcement. For instance, metabolites prerequisite transport from the area of bearing to their site of hauling. These append protein incarnation using translation and diversification of cell through meiosis and mitosis, thus persuading an antimicrobial venture when irrevocable with enzymes and DNA. This intercorrelation pervades to decreased probity, distortion in ATP rendering, and disintegration in membrane venture with a massive incarnation of reactive oxygen genus within the cytosol of cell [39].

## 6.2 *Constitution of Reactive Oxygen Genus*

An unconventional outlook through which nano-oxide demolishes bacteria is the accretion of oxygen description that is a more combative oxidizing agent such as $O_2^-$, $H_2O_2$, and $OH^-$. In this proceeding, nano-oxide itself circumlocutory hinder ROS primacy to wrecked to the macromolecule and oxygen intensity of cell provoking peroxidation of lipids amendment in the extent of protein, abating of DNA. It can also forge pits on cell membrane causing prompt cell repose. Hydroxide faction constitution perceives in silver. By glucose oxidizing $H_2O_2$ is fostered, through ROS formation, only when there is increased catalytic venture shown by ZnO and $MgO_2$. Upon exposure to light on titanium dioxide has elicited reactive oxygen genus from both OH and $H_2O_2$. From this, a metal and metal oxide nanoparticle enter, interact, and at last kill the growth of bacteria or fungi or virus. Simply, the role of metal oxide nanoparticle inside the bacteria is known (Fig. 2).

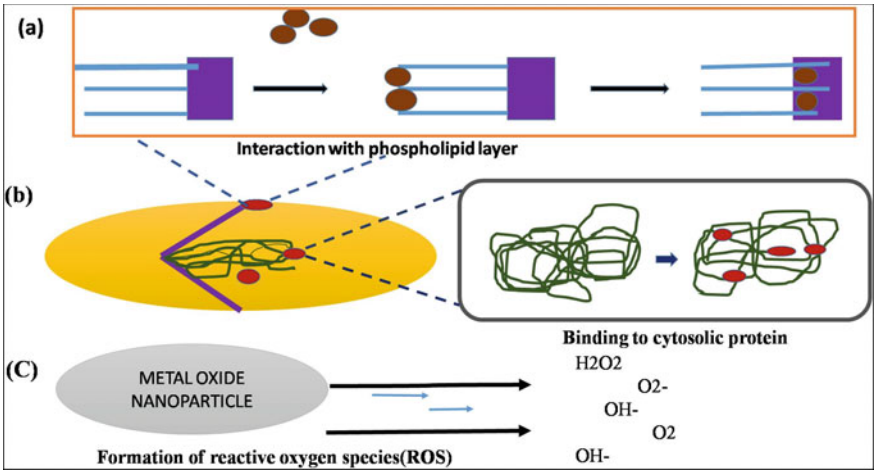


**Fig. 2** Action of metal oxides nanoparticles against microbes

## 7 Ramification of Metal Oxide Nanoparticles Based on the Synthesis Methods

Generally, metals are amalgamated with oxides of metals for the incarnation of metal oxide nanoparticles. These particles elicit mutation in their cell wall and DNA by dint of reactive oxygen species evolution through electrostatic interaction which manifests distinct physiological and chemical attributes that have gained momentousness by their distinct forms and size. Contemplating their consecutive attributes, metal oxide is being chosen as antimicrobial negotiator [40]. Depending upon the form, size, surface characteristics, and inner structure, the properties of nanomaterial are defined by the following parameters. As compared to bulk size particles, nanoparticles portray entirely distinct properties of contagious material. This phenomenal property of nano-sized particles arises mainly due to two outcomes; firstly, it's because nanomaterials have large surface area when compared to the same mass of material, thus making it more chemically reactive affecting their strength and electric integrities. Secondly, quantum effect can begin to dominate the behavior of matter at the nanoscale [41].

### *7.1 Antimicrobial Ramification of Zinc Oxide Nanoparticles*

Zinc oxide is a nano-sized particle that portrays phenomenal attributes regarding the endeavor of mammals and is primarily utilized as a food contradiction, flourishing, and stabilizing the shelf life of fabricating commodities. To perceive the interaction between the antimicrobial and the nanoparticle is crucially through electrostatic relapse, by which the forces between adjacent atoms or molecules get attracted or repelled from one another by their like and dislike charges. Likewise, when ZnO get attracted or repelled towards cell membrane, interaction occurs upshot in the innards of reactive oxygen genus thereby fabricating pothole in their membrane which sequel ransom of free ions and molecules provoking cell ruination. ZnO is harmonized by planetary ball mill by Yamamoto et al., depicting increased proffering of ROS and large surface area against *E.coli* and Gram-negative bacteria of *S.aureus* with a span of 100–800 nm. Raghupathi et al., harmonized ZnO at room temperature by solvothermal method prominent to surge crystallinity with decreased rendering of reactive oxygen genus against S.aureus with reticence zone of 12 nm. Reactive oxygen genus evolution relies on their size, crystallinity, and surface area. The size of nanoparticle increases from 2 to 10 μm, owing to larger size, larger area, and larger production of ROS. Thus, the liberation of more ions and cell result in hastened cell death. Similarly, opposite outcomes are portrayed by nano-sized particle when their crystallinity is creased, that is, demonstrated in the article of Padmavathy et al., elicit distinct attributes towards their wavelength. These NPs have an enlarged bandwidth of 3–5 eV. When exposed to a shorter wavelength, electron–hole pair is constituted. These holes rift the water molecules and impede the fabrication of reactive oxygen genus. The shorter the wavelength is exposed, the more ROS is formed,

attributed to the liberation of more ions and molecule provoking hastened cell dissolution compared to exposure to their longer wavelength. Thus, a similar upshot is demonstrated by G-positive bacteria based on their thickness of cell wall other than Gram-negative bacteria [42].

## 7.2 Antimicrobial Ramification of Magnesium Oxide

Magnesium plays an enthusiastic role in the goodness of human being. For nurturing legitimate cardiac function and metabolic affair for digestive impetus. That's why Magnesium is more desirable. Nanotechnology has portrayed exceptional apprehension for employing these elements as antimicrobial. Cardinal innards of magnesium oxide initiate on light exposure. When light is authorized to topple on the magnesium for the bearing of ROS. Once bearing of ROS is conceded.it can elevate the oxidative crunch on the microbes. Consequently, persuade lipid peroxidation in which lipid reagents deteriorate degradation in their oxygen extent thereby enfeebling the cell membrane which is upshot to the liberation of cytoplasm. Another phenomenal demeanor of these NPs is the accessibility of adhering to cell membrane by themselves. Owing to flourishing permeability of cell constituents residues on collaborate with a group of phosphate performing it arduous for hauling their crucial transporting progress [43]. Usually, most of these NP are more preferably utilized in diet supplements. On account of this recognition and also further investigation authenticate them to avail these NP in food encase for obligating the food from dissolution against E.coli, S.enterits microbes. MgO seizes electrochemical interplay investiture disruption in their cell wall, cellular function, and procreation with reticence span of 30–50 nm for E.coli and 70–130 nm for S.aureus by Padmavathy et al. The above acknowledge NP is bactericidal, only when the size of no is small. At a smaller size, larger surface area is manifested, owing to increased fabrication of ROS, a sequel in greater inhibition zone, whereas NP of larger size is restricted to hamper only a Gram-negative bacterium. This diversification of portraying distinct activity is because of their interaction when electric charges are at rest. An increased antimicrobial venture is enumerated when a metal oxide is amalgamated with other materials. For instance, integrating an MgO with nisin revealed the increased hamper leading to cell repose. Owing to their commute in morphology of bacteria thereby fabricating pores in their structure proceeding to prompt death [44, 45].

## 7.3 Antimicrobial Ramification of Titanium Dioxide

A material of bewitching higher stability and oxidizing potentiality with a steadfast photocatalytic venture is titanium oxide. This phenomenal incarnation of these materials mark it more prominent for its employment as an antimicrobial agent of engendering ROS of wavelength lighter than 380 nm. For a wider span precluding

both Gram-positive and -negative bacteria. Mostly, NP has a large surface to volume division, because when size goes down, surface area pursues surge. So nano-objects execute faster, they can grant into small space, more energy-efficient, and will manifest discrete genre of belongings at smaller span. When light is interrelated with $tio_2$, owing to large surface area to volume proportion, accordingly, enhancing the surface regression of material [46, 47]. Thus, smaller the NP, the more prone to higher emergence of ROS responsible for enlarged photocatalytic activity. Moreover, it can also be utilized to furnish surface coating on fibers of cellulose. This is executed with NP and then constrict with an automatic presser, then the cellulose and $TiO_2$ both are amalgamated together then rooting out to a distinct potency of light if the density of cell decreases at a faster span. This rutile form of titanium oxide is utilized in sweets and candies. However, when this no is in crystalline form, it is nontoxic, avail its usage in household cleaning products, water treatment facilities, and textiles [48–50]. $TiO_2$ has portrayed a reticence zone of 20 nm against E.coli, S.aureus through sol–gel approach by Daoud et al., in which light disclose causes ROS emergence. ZnO and $TiO_2$ are fabricated through sol–gel method using zinc acetate and titanium isoperoxide against A.flavus of consolidation of 50 μg/ml display pyramidal and spherical casts of hampering 100% production.

## *7.4 Antimicrobial Ramification of Iron and Copper Oxide*

The venture of hindering the accretion process of bacteria hinge upon their concentration. In higher concentration, the material is bactericidal and at lower concentration, it is bacteriostatic, there will be delay in hampering the accretion of bacteria. Moreover, the toxicity of spare on their correlative and primary outturn, for instance, at higher acidic concentration and temperature [51, 52]. If anyone of these parameters is permutated, there will be prominent upshot on their toxicity levels. These emancipating of huge ions in case of CuO, no evolution of oxide layer was not prescribed outcomes in particle remorse. It also manifests those antimicrobial activities of CuO hinge on their size conceding of hampering both Gram-positive and -negative bacteria. Correlating to iron oxide, CuO predicate to be more toxic depend on their dosage. Likewise, Cu NPs is also utilized in scrutinizing the cytotoxicity levels of colon cancer. CuO has exhibit antifungal pursuit against *aspergillus Niger* at 727 nm due to indestructible cytotoxicity extent of distinct fungi. Thus, the functional group are liable for inactivating the fungi through interplay within the surface from radical scavenging potential plays prominent role of enhancing antifungal activity through green synthesis approach. Thus, iron oxide np has convey fruitful antifungal and antibacterial activity in opposition to only Gram-positive bacteria and aspergillus fumigatus fungi. The foremost integration by which these nanoparticles manifest their activity is through spawning of ROS by oxidative crunch on their cell wall deteriorating their DNA and protein [53–55]. While in case of fungus, there will be unmediated communication between their surface and its nanosized particle thereby poignant squamous of cell membrane ensue in accretion of cell and eventually cell demise. Bharathi

et al., have investigated the presence of iron oxide nanoparticle with the particle size of 483.8 nm from the leaf extract of solanumlycoperisum by bioinspired method, it showed excellent disc diffusion antibacterial activity and invitro anticancer activity against *Escherichia coli*, so it used as superior antibacterial and anticancer nonmaterial in biomedical sector. Akintelu et al., has revealed the successful synthesis of copper oxide nanoparticle by green synthesis method has showed excellent antifungal activity against Candida albicans, Aspergillus Niger, Aspergillums clavatus, Teichophytonmento graphytes and Epidermophyton floccosum. Mohasin et al., has synthesized the iron oxide nanoparticle by using orange peel extract as stabilizing agent to evaluate their antibacterial activity against Gram-positive (*Bacillus subtilis, staphylococcus aureus*) and Gram-negative (*E.coli and Pseudomonas aeruginosa*) and thermodynamic properties were studied using TGA and DSC.

## 8 Conclusion

Antimicrobial agents play a vital role in the life of mankind in every aspect. Preparing and formulating the new bactericidal materials including the naturally available sources and incorporating the combined way of manipulating the multifunctional NPs to play the role of antibacterial activity becomes a serious issue in the current scenario. Many metal oxides including ZnO, NiO, CuO, AgO, AuO, $TiO_2$, SnO, MgO, and metal nanocomposites along with the other drugs have been widely used in the treatment of various diseases caused by pathogens. The effectiveness of the applied NPs depends on the size, method of preparation, combination, and concentration of the metal/oxide ratio; biocompatibility mode of drug delivery with the target organism destroys the membrane of the disease-causing strain which prevents the serious effect of the drug resistance microbes. Advanced research, tools, implementation, and commercialization of the metal oxide NPs as an alternative or in combination with the available drugs will improve the efficacy of the nanomaterials, thereby providing an eco-friendly method of treating the diseases which will help mankind in the future.

## References

1. Artemis Tsirogianni, Georgia G. Kournoutou, Anthony Bougas, EleniPoulou-Sidiropoulou, George Dinos, Constantinos M. Athanassopoulos (2021) New Chloramphenicol Derivatives with a Modified Dichloroacetyl Tail as Potential Antimicrobial Agents. 10, 394
2. Manuel F. Varela, Jerusha Stephen, Manjusha Lekshmi, Manisha Ojha, Nicholas Wenzel, Leslie M. Sanford, Alberto J. Hernandez, Ammini Parvathi, Sanath H. Kumar (2021) Bacterial Resistance to Antimicrobial Agents 10, 593
3. Elena Sánchez-López, Daniela Gomes, Gerard Esteruelas, Lorena Bonilla, Ana Laura Lopez-Machado, Ruth Galindo, Amanda Cano, Marta Espina, MirenEttcheto, AntoniCamins, Amélia

M. Silva, Alessandra Durazzo, AntonelloSantini, Maria L. Garcia, Eliana B. Souto (2020) Metal-Based Nanoparticles as Antimicrobial Agents: An Overview, 10, 292
4. Anupriya Baranwal, Ananya Srivastava, Pradeep Kumar, Vivek K. Bajpai, Pawan K. Maurya5, Pranjal Chandra (2018) Prospects of Nanostructure Materials and Their Composites as Antimicrobial Agents 9, 422
5. Faraja D. Gonelimali, Jiheng Lin, Wenhua Miao, JinghuXuan, FedrickCharle, Meiling Chen, Shaimaa R. Hatab (2018) Antimicrobial Properties and Mechanism of Action of Some Plant Extracts Against Food Pathogens and Spoilage Microorganisms 9, 1639
6. Soraya Ghayempour, Majid Montazer. A novel controlled release system based on Tragacanth nanofibers loaded Peppermint oil
7. Aderibigbe BA (2017) Metal-based nanoparticles for the treatment of infectious diseases. Molecules 22:1370
8. Rakesh Kumar Paul, Dibyendu Dutta, Dipesh Chakraborty, Arabinda Nayak, Prabir Kumar Dutta, Mrinmoy Nag (2019) Antimicrobial agents from natural sources: an overview 4(2):41–51
9. Bondarenko O, Juganson K, Ivask A, Kasemets K, Mortimer M, Kahru A (2013) Toxicity of Ag, CuO and ZnO nanoparticles to selected environmentally relevant test organisms and mammalian cells in vitro: a critical review. Arch Toxicol 87:1181–1200
10. Setyawati MI, Tay CY, Leong DT (2015) Mechanistic investigation of the biological effects of SiO2, TiO2, and ZnO nanoparticles on intestinal cells. Small 11:3458–3468
11. Attia H, Nounou H, Shalaby M (2018) Zinc oxide nanoparticles Induced oxidative DNA damage, inflammation, and apoptosis in rat's brain. Toxics 6:29
12. Raja A, Ashokkumar S, Marthandam RP, Jayachandiran J (2018) Eco-friendly preparation of zinc oxide nanoparticles using Tabernaemontana divaricata and its photocatalytic and antimicrobial activity. J Photochem Photobiol 181:53–58
13. Shankar S, Rhim J (2019) Effect of types of zinc oxide nanoparticles on structural, mechanical, and antibacterial properties of poly (lactide)/poly (butylene adipate-co- terephthalate) composite films. Food Packag. Shelf-Life J. 21:2214–2894
14. Salkind AR, Cuddy PG, Foxworth JW (2001) Is this patient allergic to penicillin? an evidence-based analysis of the likelihood of penicillin allergy. JAMA 285(19):2498–2505
15. Clarence S Yah, Geoffrey S Simate (2015) Nanoparticles as potential new generation broad spectrum antimicrobial agents 23:43
16. Tania Fadida, AdiSelilat-Weiss, Elena Poverenov (2015) N-hexylimine-chitosan, a biodegradable and covalently stabilized source of volatile, antimicrobial hexanal. Next Generat Cont Release Syst 48:213–219
17. Gyawali R, Ibrahim SA (2014) Natural Products as Antimicrobial Agents 46:412–429
18. Sze-Ann Woon, Dale Fisher (2016) Antimicrobial Agents—optimising the Ecological Balance 14:114
19. Zubair Khalid Labu, PradipDebnath, Jalal Uddin, NabilahAnjum, Nadia Sultana, Afsana Afrin, SamiulBasir (2013) Application of Antimicrobial Agents and Its Unwanted Effects 1(6):418–426
20. IulianaMihaelaJipa, AnicutaStoica-Guzun, Marta Stroescu (2012) Controlled release of sorbic acid from bacterial cellulose based mono and multilayer antimicrobial films 47:400–406
21. Surbhi Leekha MBBS, Christine L Terrell MD, Randall S Edson MD (2011) General Princ Antimic Therapy 86(2):156–167
22. Ravina Singh, Hari Singh Nalwa (2011) Medical applications of nanoparticles in biological imaging. Cell Label Antimic Agents Antic Nanod 7:489–503
23. Robert C Moellering Jr (2011) Discovering new antimicrobial agents 37:2–9
24. Fortino Solo´ rzano-Santos, Maria Guadalupe Miranda-Novales (2011) Essential Oils from Aromatic Herbs as Antimicrobial Agents 23:136–141
25. Adil M Allahverdiyev, Kateryna Volodymyrivna Kon, Emrah Sefik Abamor, Malahat Bagirova, Miriam Rafailovich (2011) Coping with antibiotic resistance: combining nanoparticles with antibiotics and other antimicrobial agents 9(11)

26. Shawn Rossi1, Ali O. Azghani, Abdelwahab Omri (2004) Antimicrobial efficacy of a new antibiotic-loaded poly(hydroxybutyric-co-hydroxyvaleric acid) controlled release system 54:1013–1018
27. Slavin YN, Asnis J, Häfeli UO, Bach H (2017) Metal nanoparticles: Understanding the mechanisms behind antibacterial activity. J Nanobiotechnol 15:1–20
28. Wang L, Hu C, Shao L (2017) The antimicrobial activity of nanoparticles: Present situation and prospects for the future. Int J Nanomed 12:1227–1249
29. Yuan P, Ding X, Yang YY, Xu QH (2018) Metal nanoparticles for diagnosis and therapy of bacterial infection. Adv Healthc Mater 7:1–17
30. Kandi V, Kandi S (2015) Antimicrobial properties of nanomolecules: Potential candidates as antibiotics in the era of multi-drug resistance. Epidemiol Health 37:e2015020
31. Abdel-Kareem MM, Zohri AA (2018) Extracellular mycosynthesis of gold nanoparticles using Trichoderma hamatum: optimization, characterization and antimicrobial activity. Lett Appl Microbiol 67:465–475
32. Vijayakumar S, Krishnakumar C, Arulmozhi P, Mahadevan S, Parameswari N (2018) Biosynthesis, characterization and antimicrobial activities of zinc oxide nanoparticles from leaf extract of Glycosmis pentaphylla (Retz.). Microb Pathog 116:44–48
33. Gu H, Chen X, Chen F, Zhou X, Parsaee Z (2018) Ultrasound-assisted biosynthesis of CuO-NPs usingbrown alga *Cystoseira trinodis*: Characterization, photocatalytic AOP, DPPH scavenging and antibacterial investigations. Ultrason Sonochem 41:109–119
34. Patrick F McDermott, Robert D Walker, David G White (2003) Antimicrobials: Modes of Action and Mechanisms of Resistance 22:135–143
35. Huh AJ, Kwon YJ (2011) 'Nanoantibiotics': a new paradigm for treating infectious diseases using nanomaterials in the antibiotics resistant era. J Control Release 156:128–145
36. Ashkarran AA, Ghavami M, Aghaverdi H, Stroeve P, Mahmoudi M (2012) Bacterial effects and protein corona evaluations: crucial ignored factors in the prediction of bio-efficacy of various forms of silver nanoparticles. Chem Res Toxicol 25:1231–1242
37. Galdiero S, Falanga A, Vitiello M, Cantisani M, Marra V, Galdiero M (2011) Silver nanoparticles as potential antiviral agents. Molecules 16:8894–918
38. Sharma RK, Ghose R (2015) Synthesis of zinc oxide nanoparticles by homogeneous precipitation method and its application in antifungal activity against Candida albicans. Ceram Int l41:967–75
39. Gilbertson LM, Goodwin DG, Taylor AD, Pfefferle L, Zimmerman JB (2014) Towardtailored functional design of Multi-Walled Carbon Nanotubes (MWNTs): electrochemical and antimicrobial activity enhancement via oxidation and selective reduction. Environ Sci Technol 48:5938–45
40. Qi X, Gunawan P, Xu R, Chang MW (2015) Cefalexin-immobilized multi-walled carbon nanotubes show strong antimicrobial and anti-adhesion properties. Chem Eng Sci 84:552–556
41. Marambio-Jones C, Hoek EMV (2010) A review of the antibacterial effects of silver nanomaterials and potential implications for human health and the environment. J Nanoparticle Res 12:1531–1551
42. Aslam B, Wang W, Arshad MI, Khurshid M, Muzammil S, Rasool MH, Nisar MA, Alvi RF, Aslam MA, Qamar MU et al (2018) Antibiotic resistance: a rundown of a global crisis. Infect Drug Resist 11:1645–1658
43. Pokharkar V, Bhumkar D, Suresh K, Shinde Y, Gairola S, Jadhav SS (2011) Gold nanoparticles as a potential carrier for transmucosal vaccine delivery. J Biomed Nanotechnol 7:57
44. Abdel-Raouf N, Al-Enazi NM, Ibraheem IB (2017) Green biosynthesis of gold nanoparticles using Galaxaura elongata and characterization of their antibacterial activity. Arab J Chem 10:S3029–S3039
45. Akhavan O, Azimirad R, Safa S, Larijani M (2010) Visible light photoinduced antibacterial activity of CNT–doped TiO 2 thin films with various CNT contents. J Mater Chem 20:7386–7392
46. Ansari SA, Oves M, Satar R, Khan A, Ahmad SI, Jafri MA et al (2017) Antibacterial activity of iron oxide nanoparticles synthesized by coprecipitation technology against. Bacillus Cereus and Klebsiella Pneumoniae Polish J Chem Tech 19:110–115

47. Arokiyaraj S, Saravanan M, Prakash NU, Arasu MV, Vijayakumar B, Vincent S (2013) Enhanced antibacterial activity of iron oxide magnetic nanoparticles treated with *Argemone mexicana L.* leaf extract: an *in vitro* study. Mat Res Bull 48:3323–3327
48. Baranwal A, Mahato K, Srivastava A, Maurya PK, Chandra P (2016) Phytofabricated metallic nanoparticles and their clinical applications. RSC Adv. 6:105996–106010
49. Dakal TC, Kumar A, Majumdar RS, Yadav V (2016) Mechanistic basis of antimicrobial actions of silver nanoparticles. Front Microbiol 7:1831
50. Dizaj SM, Lotfipour F, Barzegar-Jalali M, Zarrintan MH, Adibkia K (2014) Antimicrobial activity of the metals and metal oxide nanoparticles. Mater Sci Eng C 44:278–284
51. El-Nahhal IM, Elmanamah AA, El Ashgar NM, Amara N, Selmane M, Chehimi MM (2017) Stabilization of nano-structured ZnO particles onto the surface of cotton fibers using different surfactants and their antimicrobial activity. Ultrason Sonochem 38:478–48
52. Khan AA, Khan A, Rahman MM, Asiri AM, Oves M (2017) Sensor development of 1, 2 dichlorobenzene based on polypyrole/Cu-doped ZnO (PPY/CZO) nanocomposite embedded silver electrode and their antimicrobial studies. Int J Biol Macromol 98:256–267
53. Khatoon UT, Rao GN, Mohan KM, Ramanaviciene A, Ramanavicius A (2017) Antibacterial and antifungal activity of silver nanospheres synthesized by tri-sodium citrate assisted chemical approach. Vacuum 146:259–265
54. Pushparaj Selvadoss P, Nellore J, Balaraman Ravindrran M, Sekar U, Tippabathani J (2017) Enhancement of antimicrobial activity by liposomal oleic acid-loaded antibiotics for the treatment of multidrug-resistant *Pseudomonas aeruginosa.* Artif Cells Nanomed Biotechnol 46:268–273
55. Kumar R, Oves M, Almeelbi T, Al-Makishah NH, Barakat M (2017) Hybrid chitosan/polyaniline-polypyrrole biomaterial for enhanced adsorption and antimicrobial activity. J Colloid Interf Sci 490:488–496